LUNG IMAGING IN RESPIRATORY FAILURE

EDITED BY: Paolo Pelosi, Lorenzo Ball and Patricia R. M. Rocco
PUBLISHED IN: Frontiers in Physiology and Frontiers in Medicine

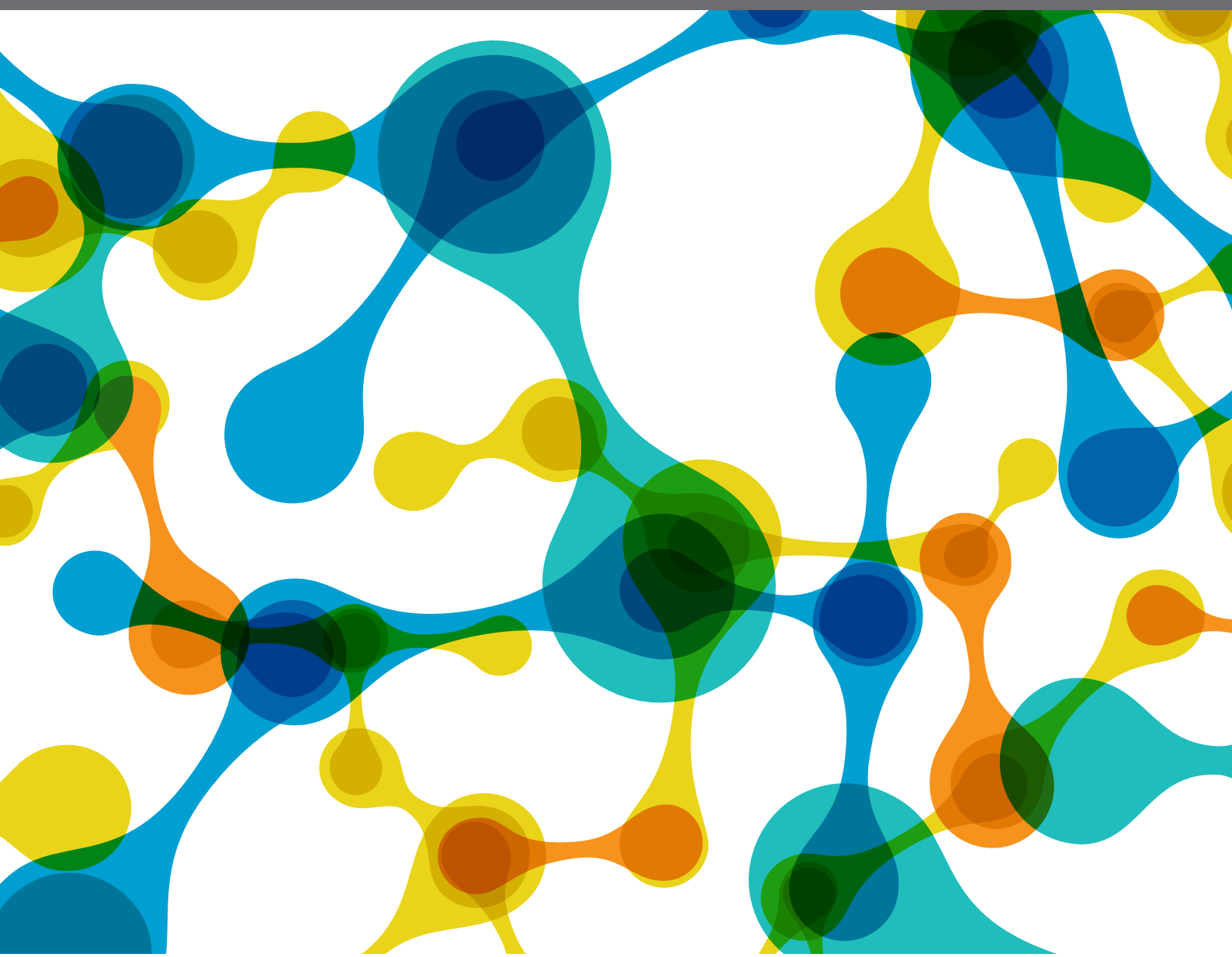

frontiers Research Topics

frontiers

ISSN 1664-8714
ISBN 978-2-88974-758-0
DOI 10.3389/978-2-88974-758-0

About Frontiers

Frontiers is more than just an open-access publisher of scholarly articles: it is a pioneering approach to the world of academia, radically improving the way scholarly research is managed. The grand vision of Frontiers is a world where all people have an equal opportunity to seek, share and generate knowledge. Frontiers provides immediate and permanent online open access to all its publications, but this alone is not enough to realize our grand goals.

Frontiers Journal Series

The Frontiers Journal Series is a multi-tier and interdisciplinary set of open-access, online journals, promising a paradigm shift from the current review, selection and dissemination processes in academic publishing. All Frontiers journals are driven by researchers for researchers; therefore, they constitute a service to the scholarly community. At the same time, the Frontiers Journal Series operates on a revolutionary invention, the tiered publishing system, initially addressing specific communities of scholars, and gradually climbing up to broader public understanding, thus serving the interests of the lay society, too.

Dedication to Quality

Each Frontiers article is a landmark of the highest quality, thanks to genuinely collaborative interactions between authors and review editors, who include some of the world's best academicians. Research must be certified by peers before entering a stream of knowledge that may eventually reach the public - and shape society; therefore, Frontiers only applies the most rigorous and unbiased reviews.
Frontiers revolutionizes research publishing by freely delivering the most outstanding research, evaluated with no bias from both the academic and social point of view. By applying the most advanced information technologies, Frontiers is catapulting scholarly publishing into a new generation.

What are Frontiers Research Topics?

Frontiers Research Topics are very popular trademarks of the Frontiers Journals Series: they are collections of at least ten articles, all centered on a particular subject. With their unique mix of varied contributions from Original Research to Review Articles, Frontiers Research Topics unify the most influential researchers, the latest key findings and historical advances in a hot research area! Find out more on how to host your own Frontiers Research Topic or contribute to one as an author by contacting the Frontiers Editorial Office: frontiersin.org/about/contact

LUNG IMAGING IN RESPIRATORY FAILURE

Topic Editors:
Paolo Pelosi, University of Genoa, Italy
Lorenzo Ball, University of Genoa, Italy
Patricia R. M. Rocco, Federal University of Rio de Janeiro, Brazil

Citation: Pelosi, P., Ball, L., Rocco, P. R. M., eds. (2022). Lung Imaging in Respiratory Failure. Lausanne: Frontiers Media SA. doi: 10.3389/978-2-88974-758-0

Table of Contents

frontiers in Physiology

EDITORIAL
published: 03 March 2022
doi: 10.3389/fphys.2022.862647

Editorial: Lung Imaging in Respiratory Failure

Lorenzo Ball[1,2]*, *Patricia R. M. Rocco*[3] *and Paolo Pelosi*[1,2]

[1] *Department of Surgical Sciences and Integrated Diagnostics (DISC), University of Genoa, Genoa, Italy,* [2] *Anesthesia and Intensive Care, Ospedale Policlinico San Martino, IRCCS per l'Oncologia e le Neuroscienze, Genoa, Italy,* [3] *Laboratory of Pulmonary Investigation, Carlos Chagas Filho Institute of Biophysics, Federal University of Rio de Janeiro, Rio de Janeiro, Brazil*

Keywords: computed tomography, ARDS, lung imaging, electrical impedance tomography (EIT), lung ultrasonography (LUS), respiratory failure, intensive care

Editorial on the Research Topic

Lung Imaging in Respiratory Failure

The last two decades have seen increasing interest toward delivering personalized treatments to patients admitted to the intensive care unit (ICU) with acute respiratory failure (ARF), in particular acute respiratory distress syndrome (ARDS) (Pelosi et al., 2021). However, identifying simple clinical characteristics allowing targeted respiratory support and other treatments is challenging. Lung imaging techniques are capable of describing different phenotypes of lung injury as well as the effects of ventilatory support on the respiratory system (Ball et al., 2017b), and have shown promising results as tools to guide mechanical ventilation strategies in ARDS (Constantin et al., 2019). Moreover, research in the field of imaging applied to respiratory failure has been boosted by the ongoing COVID-19 pandemics, providing valuable clinical information that helped clinicians in the timely development of appropriate strategies in such a rapidly evolving scenario (Grasselli et al., 2020; Ball et al., 2021a). This editorial summarizes the articles enclosed in this Frontiers Research Topic "Lung Imaging in Respiratory Failure."

An introductory review highlights how different imaging techniques depict specific pathophysiological aspects of the lungs and how their quantitative analysis can provide functional information on the respiratory system (Musch). Despite being widely used, each imaging technique has specific methodological pitfalls that require elucidation in the future. A systematic review focusing on lung ultrasound (LUS) explored its diagnostic accuracy in discriminating different patterns of lung injury (Yuan et al.). Several lung imaging techniques were often used to measure or estimate lung recruitment, namely the amount of non-aerated lung that can be aerated following changes in ventilator settings or recruitment maneuvers. A systematic review covering studies using LUS, computed tomography (CT), and electrical impedance tomography (EIT) concluded that the estimation of lung recruitment based on lung imaging techniques is poorly standardized and that the ability of imaging techniques to predict lung recruitment in ARDS remains uncertain (Pierrakos et al.). On the other hand, a simple scoring system of chest X-ray, the Radiographic Assessment of Lung Edema, showed good diagnostic accuracy for identifying patients with ARDS according to the Berlin definition (Zimatore et al.).

Several papers in this Research Topic focused on bedside imaging techniques such as EIT and LUS. In an interesting experimental study, authors propose a sophisticated analysis of EIT-derived parameters, combined with airway pressure data, to derive information concerning transpulmonary pressure, exploiting the relationships between respiratory mechanics partitioning and regional heterogeneity of ventilation in ARDS (Scaramuzzo et al.). Such estimate might provide important information to improve the understanding of respiratory support in ARDS,

OPEN ACCESS

Edited and reviewed by:
Andrew John Halayko, University of Manitoba, Canada

***Correspondence:**
Lorenzo Ball
lorenzo.ball@unige.it

Specialty section:
This article was submitted to Respiratory Physiology, a section of the journal Frontiers in Physiology

Received: *26 January 2022*
Accepted: *03 February 2022*
Published: *03 March 2022*

Citation:
Ball L, Rocco PRM and Pelosi P (2022) Editorial: Lung Imaging in Respiratory Failure. Front. Physiol. 13:862647. doi: 10.3389/fphys.2022.862647

in a context where the esophageal pressure monitoring is still underused in the clinical practice (Akoumianaki et al., 2014). In addition to its role in adult chest imaging, LUS has an established role in the pediatric setting, also for the particularly favorable acoustic window that characterizes these patients. In a review covering 10 years of research in this field, benefits, limitations, and possible future challenges of pediatric LUS are discussed (Musolino et al.). In another research article, the efficiency of deep learning and artificial intelligence to classify lung ultrasound images in the pediatric setting is explored with good results (Magrelli et al.).

Another application of artificial intelligence proposed in this article collection is semi-automated segmentation of lung images obtained with CT. This high-resolution technique is a recognized standard for the assessment of lung aeration (Pesenti et al., 2016) as well as lung recruitment in ARDS (Gattinoni et al., 2006) and COVID-19 (Ball et al., 2021b), but manual delimitation of lung is time consuming (Reske et al., 2010; Ball et al., 2017a). Computer-based approaches using neural networks performed acceptably in two original research papers when applied to both human and experimental animal CT scans with different lung findings, including in repeated scans aimed at measuring lung recruitability (Herrmann P., et al.; Maiello et al.).

In other research papers included in this Research Topic, lung imaging techniques and their derived parameters were used as endpoints to assess the effects of specific changes in respiratory support strategies. In an experimental study in pigs receiving one-lung ventilation and thoracic surgery, lateral compared to supine positioning was associated with higher relative perfusion, regardless of the presence of intravascular hypovolemia (Wittenstein et al.). Another research paper investigated the dependency on positive end-expiratory pressure (PEEP) of patients receiving non-invasive respiratory support for COVID-19-related ARF; the authors observed, using EIT, that lung de-recruitment during a PEEP-decrease trial was associated with failure of non-invasive respiratory support (Rauseo et al.). These findings might improve the understanding of the role of non-invasive respiratory support in COVID-19, while avoidance of intubation is often feasible but in certain patients associated with a high risk of developing self-inflicted lung injury (Battaglini et al., 2021). In another study, the effects of PEEP were studied in invasively ventilated brain injured critically ill patients using quantitative CT and assessing the effect on intracranial pressure (Robba et al.). In an experimental study using dynamic four-dimensional computed tomography, the authors explored the role of inhomogeneity in determining the expiratory kinetics of gases in different lung regions, highlighting how poorly aerated regions might be particularly susceptible to ventilator-induced lung injury (Herrmann J., et al.).

Finally, two papers used imaging techniques addressed specific controversies regarding the concept of mechanical power. This parameter was proposed as a parameter to guide mechanical ventilation parameters in patients with ARDS (Gattinoni et al., 2016; Silva et al., 2019). However, several aspects concerning its calculation remain controversial. In a model of ARDS, a correlation between mechanical power and neutrophilic inflammation was confirmed using positron emission tomography (Scharffenberg et al.). However, in another experimental study using CT and EIT, mechanical power was reduced with the decrease in the respiratory rate alone, while maintaining constant CO_2 levels through the use of extracorporeal membrane oxygenation at increasing gas flows. The reduction in respiratory rate worsened lung atelectasis despite reducing mechanical power (Spinelli et al.).

We are grateful to the authors and reviewers that contributed to this Research Topic, covering a wide range of interesting and challenging aspects of innovative applications of lung imaging techniques of respiratory failure from research to clinical practice.

AUTHOR CONTRIBUTIONS

LB, PR, and PP drafted and revised this editorial. All authors contributed to the article and approved the submitted version.

REFERENCES

Akoumianaki, E., Maggiore, S. M., Valenza, F., Bellani, G., Jubran, A., Loring, S. H., et al. (2014). The application of esophageal pressure measurement in patients with respiratory failure. *Am. J. Respir. Crit. Care Med.* 189, 520–531. doi: 10.1164/rccm.201312-2193CI

Ball, L., Braune, A., Corradi, F., Brusasco, C., Garlaschi, A., Kiss, T., et al. (2017a). Ultra-low-dose sequential computed tomography for quantitative lung aeration assessment-a translational study. *Intensive Care Med. Exp.* 5, 19. doi: 10.1186/s40635-017-0133-6

Ball, L., Robba, C., Herrmann, J., Gerard, S. E., Xin, Y., Mandelli, M., et al. (2021a). Lung distribution of gas and blood volume in critically ill COVID-19 patients: a quantitative dual-energy computed tomography study. *Crit. Care Lond. Engl.* 25, 214. doi: 10.1186/s13054-021-03610-9

Ball, L., Robba, C., Maiello, L., Herrmann, J., Gerard, S. E., Xin, Y., et al. (2021b). Computed tomography assessment of PEEP-induced alveolar recruitment in patients with severe COVID-19 pneumonia. *Crit. Care Lond. Engl.* 25, 81. doi: 10.1186/s13054-021-03477-w

Ball, L., Vercesi, V., Costantino, F., Chandrapatham, K., and Pelosi, P. (2017b). Lung imaging: how to get better look inside the lung. *Ann. Transl. Med.* 5, 294. doi: 10.21037/atm.2017.07.20

Battaglini, D., Robba, C., Ball, L., Silva, P. L., Cruz, F. F., Pelosi, P., et al. (2021). Noninvasive respiratory support and patient self-inflicted lung injury in COVID-19: a narrative review. *Br. J. Anaesth.* 127, 353–364. doi: 10.1016/j.bja.2021.05.024

Constantin, J.-M., Jabaudon, M., Lefrant, J.-Y., Jaber, S., Quenot, J.-P., Langeron, O., et al. (2019). Personalised mechanical ventilation tailored to lung morphology versus low positive end-expiratory pressure for patients with acute respiratory distress syndrome in France (the LIVE study): a multicentre, single-blind, randomised controlled trial. *Lancet Respir. Med.* 7, 870–880. doi: 10.1016/S2213-2600(19)30138-9

Gattinoni, L., Caironi, P., Cressoni, M., Chiumello, D., Ranieri, V. M., Quintel, M., et al. (2006). Lung recruitment in patients with the acute respiratory distress syndrome. *N. Engl. J. Med.* 354, 1775–1786. doi: 10.1056/NEJMoa052052

Gattinoni, L., Tonetti, T., Cressoni, M., Cadringher, P., Herrmann, P., Moerer, O., et al. (2016). Ventilator-related causes of lung injury: the mechanical power. *Intensive Care Med.* 42, 1567–1575. doi: 10.1007/s00134-016-4505-2

Grasselli, G., Tonetti, T., Protti, A., Langer, T., Girardis, M., Bellani, G., et al. (2020). Pathophysiology of COVID-19-associated acute respiratory distress syndrome: a multicentre prospective observational study. *Lancet Respir. Med.* 8, 1201–1208. doi: 10.1016/S2213-2600(20)30370-2

Pelosi, P., Ball, L., Barbas, C. S. V., Bellomo, R., Burns, K. E. A., Einav, S., et al. (2021). Personalized mechanical ventilation in acute respiratory distress syndrome. *Crit. Care Lond. Engl.* 25, 250. doi: 10.1186/s13054-021-03686-3

Pesenti, A., Musch, G., Lichtenstein, D., Mojoli, F., Amato, M. B. P., Cinnella, G., et al. (2016). Imaging in acute respiratory distress syndrome. *Intensive Care Med.* 42, 686–698. doi: 10.1007/s00134-016-4328-1

Reske, A. W., Reske, A. P., Gast, H. A., Seiwerts, M., Beda, A., Gottschaldt, U., et al. (2010). Extrapolation from ten sections can make CT-based quantification of lung aeration more practicable. *Intensive Care Med.* 36, 1836–1844. doi: 10.1007/s00134-010-2014-2

Silva, P. L., Ball, L., Rocco, P. R. M., and Pelosi, P. (2019). Power to mechanical power to minimize ventilator-induced lung injury? *Intensive Care Med. Exp.* 7, 38. doi: 10.1186/s40635-019-0243-4

Conflict of Interest: The authors declare that the research was conducted in the absence of any commercial or financial relationships that could be construed as a potential conflict of interest.

frontiers in Physiology

ORIGINAL RESEARCH
published: 09 April 2021
doi: 10.3389/fphys.2021.663313

Atelectasis, Shunt, and Worsening Oxygenation Following Reduction of Respiratory Rate in Healthy Pigs Undergoing ECMO: An Experimental Lung Imaging Study

*Elena Spinelli[1], Giulia Colussi[1], Gaia Dal Santo[2], Eleonora Scotti[1], Ines Marongiu[2], Erica Garbelli[2], Alessandra Mazzucco[3], Daniele Dondossola[2,4], Raquel Maia[1,5], Michele Battistin[1], Osvaldo Biancolilli[1], Lorenzo Rosso[2,3], Stefano Gatti[6] and Tommaso Mauri[1,2]**

[1] Department of Anesthesia, Critical Care and Emergency, Fondazione Istituto di Ricovero e Cura a Carattere Scientifico (IRCCS) Ca' Granda Ospedale Maggiore Policlinico, Milan, Italy, [2] Department of Pathophysiology and Transplantation, University of Milan, Milan, Italy, [3] Thoracic Surgery and Lung Transplantation Unit, Fondazione Istituto di Ricovero e Cura a Carattere Scientifico (IRCCS) Ca' Granda Ospedale Maggiore Policlinico, Milan, Italy, [4] General and Liver Transplant Surgery Unit, Fondazione Istituto di Ricovero e Cura a Carattere Scientifico (IRCCS) Ca' Granda Ospedale Maggiore Policlinico, Milan, Italy, [5] Department of Intensive Care Medicine, Hospital Professor Doutor Fernando Fonseca, Amadora, Portugal, [6] Center for Preclinical Research, Fondazione Istituto di Ricovero e Cura a Carattere Scientifico (IRCCS) Ca' Granda Ospedale Maggiore Policlinico, Milan, Italy

OPEN ACCESS

Edited by:
Lorenzo Ball, University of Genoa, Italy

Reviewed by:
Alysson Roncally Silva Carvalho, University of Porto, Portugal
Carmen Silvia Valente Barbas, University of São Paulo, Brazil

***Correspondence:**
Tommaso Mauri
tommaso.mauri@unimi.it

Specialty section:
This article was submitted to Respiratory Physiology, a section of the journal Frontiers in Physiology

Received: *02 February 2021*
Accepted: *04 March 2021*
Published: *09 April 2021*

Citation:
Spinelli E, Colussi G, Dal Santo G, Scotti E, Marongiu I, Garbelli E, Mazzucco A, Dondossola D, Maia R, Battistin M, Biancolilli O, Rosso L, Gatti S and Mauri T (2021) Atelectasis, Shunt, and Worsening Oxygenation Following Reduction of Respiratory Rate in Healthy Pigs Undergoing ECMO: An Experimental Lung Imaging Study. Front. Physiol. 12:663313. doi: 10.3389/fphys.2021.663313

Rationale: Reducing the respiratory rate during extracorporeal membrane oxygenation (ECMO) decreases the mechanical power, but it might induce alveolar de-recruitment. Dissecting de-recruitment due to lung edema vs. the fraction due to hypoventilation may be challenging in injured lungs.

Objectives: We characterized changes in lung physiology (primary endpoint: development of atelectasis) associated with progressive reduction of the respiratory rate in healthy animals on ECMO.

Methods: Six female pigs underwent general anesthesia and volume control ventilation (Baseline: PEEP 5 cmH_2O, Vt 10 ml/kg, I:E = 1:2, FiO_2 0.5, rate 24 bpm). Veno-venous ECMO was started and respiratory rate was progressively reduced to 18, 12, and 6 breaths per minute (6-h steps), while all other settings remained unchanged. ECMO blood flow was kept constant while gas flow was increased to maintain stable $PaCO_2$.

Measurements and Main Results: At Baseline (without ECMO) and toward the end of each step, data from quantitative CT scan, electrical impedance tomography, and gas exchange were collected. Increasing ECMO gas flow while lowering the respiratory rate was associated with an increase in the fraction of non-aerated tissue (i.e., atelectasis) and with a decrease of tidal ventilation reaching the gravitationally dependent lung regions ($p = 0.009$ and $p = 0.018$). Intrapulmonary shunt increased ($p < 0.001$) and arterial PaO_2 decreased ($p < 0.001$) at lower rates. The fraction of non-aerated lung was correlated with longer expiratory time spent at zero flow ($r = 0.555$, $p = 0.011$).

Conclusions: Progressive decrease of respiratory rate coupled with increasing CO_2 removal in mechanically ventilated healthy pigs is associated with development of lung atelectasis, higher shunt, and poorer oxygenation.

Keywords: extracorporeal membrane oxygenation, respiratory rate, atelectasis, shunt, expiratory time

INTRODUCTION

Veno-venous extracorporeal membrane oxygenation (ECMO) is a rescue strategy for patients with severe acute respiratory distress syndrome (ARDS) not responsive to conventional positive pressure ventilation (Combes et al., 2020). In the last few years, the use of ECMO increased worldwide since the H1N1 epidemic in 2009 and following publication of large clinical trials and observational analyses showing positive impact on mortality (Peek et al., 2009; Combes et al., 2018). ECMO support allows a reduction in mechanical ventilation load. Indeed, during ECMO, gas exchange becomes almost independent from the applied ventilation, and the latter can be reduced drastically, enhancing lung rest (Pesenti et al., 1982). Even though decreased ventilation is key to ECMO success and lung protection, physiological data supporting specific strategies are scant and published clinical trials implemented "ultra-protective ventilation" with very different settings (Gattinoni et al., 1986; Terragni et al., 2009; Bein et al., 2013; Combes et al., 2019).

In the present study, we focused on the physiological effects of decreasing respiratory rate. In usual clinical management of severe ARDS patients, respiratory rate is gradually reduced after start of ECMO but with highly variable targets (Spinelli et al., 2020); large clinical trials used rates ranging between 24 and 5 breaths per minute (Pesenti et al., 1982; Gattinoni et al., 1986; Peek et al., 2009; Terragni et al., 2009; Bein et al., 2013; Combes et al., 2018, 2019), and only two animal studies reported some physiological benefits of reduced respiratory rate during extracorporeal support, but rates differed widely, averaging 14 vs. 5 breaths per minute (Grasso et al., 2014; Araos et al., 2019). Thus, the physiological targets to guide the reduction of respiratory rate during ECMO are still unclear.

Lowering the respiratory rate leads to a reduction in the mechanical power applied to the lungs, and any decrease should be associated with improved lung protection (Marini et al., 2020). This is true only if all other determinants of ventilator-induced lung injury (VILI) remain stable (Marini et al., 2020). By contrast, previous experimental study described development of atelectasis when expiration becomes longer than 4 s (Neumann et al., 1998), and this might increase ventilation heterogeneity (Mauri et al., 2013), lung strain (Bellani et al., 2011), and atelectrauma (Caironi et al., 2010). Moreover, to maintain stable gas exchange, lower respiratory support requires higher extracorporeal oxygenation and CO_2 removal, which might be associated with altered physiology (e.g., increased intrapulmonary shunt; Fanelli et al., 2016; Spinelli et al., 2020).

The aim of this study was to describe the physiological effects of the progressive reduction of the respiratory rate and concomitant increase of extracorporeal CO_2 removal during ECMO in terms of non-aerated lung fraction measured by CT scan (primary endpoint), ventilation maldistribution, increased shunt, and hypoxemia due to low values of the respiratory exchange ratio (RER) of the natural lung. Since dissecting atelectasis caused by the compressive forces of lung edema vs. those due to hypoventilation may be challenging in injured lungs, we took a step backward and studied progressive reduction of respiratory rate and increased CO_2 removal in a large animal ECMO model with healthy lungs.

Abbreviations: VILI, ventilator-induced lung injury; IV, intravenous; RR, respiratory rate; Crs, respiratory system compliance; Clung, lung compliance; Ccw, chest wall compliance; RER, respiratory exchange ratio; MAP, mean arterial pressures; PAPm, mean pulmonary artery pressures; WP, wedge pressure; BE, base excess; NL, natural lung; EIT, electrical impedance tomography; BF, blood flow; GF, gas flow; ML, membrane lung.

MATERIALS AND METHODS

The study was approved by the Italian Ministry of Health (protocol n. 749/2019) and conducted according to the European Directive 2010/63/EU on the protection of animals used for scientific purposes and Italian legislative decree 26/2014. The research protocol was approved by the Institutional Animal Care Committee.

Anesthesia, Animal Preparation, and Instrumentation

In compliance with local recommendations, pigs arrived at the experimental facility the day before the start of the study and fasted for 24 h with free access to water. Six healthy female pigs (40 ± 4 kg) were sedated by intramuscular injection of medetomidine 0.025 mg/kg and tiletamine/zolazepam 5 mg/kg. Then, an auricular vein was cannulated and, after administration of ceftriaxone 1 g and tramadol 50 mg, continuous intravenous (IV) infusion of Propofol was titrated to maintain the animal on spontaneous breathing and SpO_2 100% while oxygen was provided via face mask. Surgical tracheostomy was performed in the supine position under additional local anesthesia (Lidocaine 2%). After endotracheal tube was inserted through the tracheostomy and fixed, mechanical ventilation was started (see Baseline ventilation settings below) and general anesthesia was maintained by IV Propofol 5–10 mg/kg/h, Medetomidine 2.5–10.0 μg/kg/h, and Pancuronium bromide 0.3–0.5 mg/kg/h. Depth of anesthesia was adjusted to ensure no sign of distress, such as unexplained tachycardia, arterial hypertension, and horripilation. Ringer lactate was administered at 100 ml/h during surgery and along the whole study, unless otherwise indicated by hemodynamic requirements (see the hemodynamic protocol below). Ceftriaxone 1 g IV and tramadol 50 mg IV were repeated after 12 h.

Vascular accesses were obtained by surgical exposure. An arterial catheter (Seldicath, 5 Fr and 8 cm, Prodimed, France) was inserted in the left common carotid artery. A three-lumen central venous catheter (Arrow, 7 Fr, Teleflex, Ireland) and a pulmonary artery catheter (Swan Ganz, 5 Fr, Edwards, USA) were inserted and advanced in the left external jugular vein. Positioning of pulmonary artery catheter was achieved by direct visualization of pulmonary artery and wedge pressures.

An esophageal balloon catheter (5 Fr, Cooper Surgical, CT, USA) was inserted and inflated with the recommended volume of air. Correct positioning and calibration were confirmed by the standard occlusion test with external compressions.

Baseline Ventilation Settings and Data Collection

During the whole experiment, apart from surgical procedures, animals were kept prone.

From tracheostomy to the end of Baseline data collection, volume-controlled mechanical ventilation (Evita XL, Drager, Germany) was set as follows:

- Fraction of inspired oxygen (FiO_2) = 0.5
- Tidal volume (Vt) = 10 ml/kg body weight
- Respiratory rate (RR) = 24 breaths per minute
- Positive end-expiratory pressure (PEEP) = 5 cmH_2O
- Inspiratory to expiratory time ratio (I:E) = 1:2

A heat and moisture exchange filter was part of the ventilator circuit.

Data from respiratory mechanics, hemodynamics, arterial, and mixed venous blood gas analysis, volumetric capnography (Respironics NM3 monitor, Philips, The Netherlands), and quantitative CT scan (Lightspeed, General Electric, USA) were collected at the end of the instrumentation phase (Baseline).

The variables collected were as follows:

- Respiratory mechanics: mean airway pressure (mPaw), tidal volume (Vt), plateau airway pressure (Pplat), total PEEP (PEEPtot), and change between inspiratory and expiratory esophageal pressure (ΔPes) by 3-s inspiratory and expiratory holds. From these, static respiratory system compliance (Crs) was calculated as Vt/(Pplat – PEEPtot), lung compliance (Clung) as Vt/((Pplat – PEEPtot) – ΔPes), and chest wall compliance (Ccw) as Vt/ΔPes (Mauri et al., 2016b). We also calculated mechanical power per minute by standard formula (Marini et al., 2020). Finally, we recorded tracings of airway pressure and flow and we measured the time spent by the respiratory system at zero flow during expiration (T_{EXP} at zero flow: the time between the zero expiratory flow and the start of inspiratory flow for the next breath), as the average of 5 breaths.
- Hemodynamics: mean arterial pressures (MAP), mean pulmonary artery pressures (PAPm), pulmonary capillary wedge pressure (WP) at end expiration, cardiac output (CO) via thermodilution technique (Vigilance, Baxter Edwards Critical Care, Edwards E6 Lifesciences, USA), heart rate (HR), central venous pressure (CVP) at end expiration, and mixed venous oxygen saturation (SvO_2).
- Blood gas values: arterial pH, $PaCO_2$, PaO_2, Base Excess (BE), and lactates. Oxygen consumption through the natural lung (VO_{2NL}) and intrapulmonary shunt calculated with Riley's method were also calculated from mixed venous and arterial blood gases by standard formulas (Zanella et al., 2016; Radermacher et al., 2017).
- Volumetric capnography: CO_2 elimination by the natural lung (VCO_{2NL}); alveolar partial pressure of oxygen (PAO_2) calculated as:

$$PAO_2 = FiO_2 * (P_{atm} - PH2O) - PaCO_2/RER_{NL} + FiO_2 * PaCO_2 * (1 - ER_{NL})/RER_{NL}$$

Where RER_{NL} is the respiratory exchange ratio of the natural lung and was calculated as (Dickstein, 2020):

$$RER_{NL} = VCO_{2NL}/VO_{2NL}$$

- CT scan: chest CT scans (Lightspeed®, General Electric, USA) were acquired during a respiratory hold performed at end expiration. Acquired images were processed offline for quantitative analysis, as previously described (Gattinoni et al., 2006). Briefly, lung boundaries were manually drawn on each slice and analyzed using a dedicated software program (Maluna 3.17, Göttingen, Germany). After processing each slice of a series, total lung weight expressed in grams of tissue was calculated by standard formulas and frequency distribution of lung CT numbers expressed in Hounsfield units (HUs) was computed. From this, lung units were classified as non-aerated (density > −100 HU), poorly aerated (−100 to −500 HU), and normally aerated (−500 to −900 HU). The percentages of non-aerated, poorly aerated, and normally aerated tissue were measured both for the whole lungs and for non-dependent (from halfway of the lungs up) and dependent (from halfway down) regions.
- Electrical impedance tomography (EIT): EIT data (Pulmovista, Drager, Lubeck, Germany) were continuously recorded for 2–3 min, during which end-expiratory and end-inspiratory holds were performed. From offline analysis, we measured the tidal ventilation distribution and the regional respiratory system compliances in two equal-size regions (non-dependent from halfway up and dependent from halfway down), as previously described (Mauri et al., 2016a; Scaramuzzo et al., 2020a).

Extracorporeal Membrane Oxygenation

After Baseline data collection, animals were turned supine and veno-venous ECMO was started. ECMO circuit consisted of draining line, pump, return line (heparin-coated 3/8 polyvinylchloride circuit and Bio-pump BPX-80, Medtronic Italia SpA, Milan, Italy), membrane lung (EOS ECMO PMP oxygenator, Livanova, London, UK), return line heater, oxygen supply, and pressure transducer (positioned on the draining line) and was primed with balanced solution at a controlled temperature of 38°C. The left iliac and right external jugular veins were surgically cannulated (wire-reinforced venous cardiopulmonary bypass cannula, 18 Fr 36 cm, Sorin Group Italia srl, Mirandola, Italy) after an IV heparin bolus of 80 UI/kg, and ECMO was started by a gradual increase of blood flow (BF) up to 1.5 L/min. Then, heparin infusion was started at 40 UI/kg/h and titrated to obtain an Activated Coagulation Time of 180–210 s, measured every 1–2 h.

Once stable, animals were turned prone again.

Study Protocol

After start of ECMO and return to the prone position, ventilation continued with the abovementioned settings (FiO_2 = 0.5, Vt = 10 ml/kg, PEEP = 5 cmH_2O, I:E = 1:2) and RR was promptly decreased to 18 bpm for 6 h. BF was maintained at 1.5 L/min

for the whole study and ECMO sweep 100% oxygen gas flow (GF) was increased to maintain stable $PaCO_2$ at values equal to Baseline ± 5 mmHg (arterial blood gases were performed every 30 min and GF adjusted by 0.5 L/min steps until stability for two subsequent measures). Toward the end of the RR 18 time period, data collection was performed again (see ECMO data collection below). Then, respiratory rate was decreased to 12 bpm for 6 h, leaving all other ventilation settings unchanged and adjusting ECMO GF as described above. Toward the end of the 6-h RR 12 period, ECMO data collection was performed again (see below). Finally, respiratory rate was reduced to 6 for the last 6 h, ECMO GF was adjusted to obtain stable $PaCO_2$, and ECMO data collection was repeated toward the end. All animals completed the protocol.

Toward the end of each 6-h study phase, all the abovementioned Baseline data collection was repeated. The following relevant data on ECMO support were collected, too:

- Extracorporeal CO_2 elimination ($VCO_{2\ ML}$) was measured by measuring the fraction of CO_2 within the gas exiting the ECMO membrane lung and multiplying this by the actual ECMO GF.
- Oxygen consumption through the ECMO membrane lung (VO_{2ML}) was calculated from pre- and post-lung blood gas analyses by standard formulas (Zanella et al., 2016).
- The RER of the membrane lung was calculated as:

$$RER_{ML} = VCO_{2\ ML}/VO_{2\ ML} \quad (1)$$

Hemodynamic Protocol

Balanced electrolytes solution and norepinephrine were infused according to a standardized protocol, with a target of MAP above 60 mmHg. Every step of the protocol was applied only if the preceding one failed. If MAP was <60 mmHg:

- Balanced solution (Ringer) 250 ml bolus was administered, and infusion restarted at 150 ml/h;
- If MAP remained <60 mmHg, solution bolus was repeated and infusion was continued at 150 ml/h;
- If not responding to fluids, norepinephrine was started and titrated to obtain MAP >60 mmHg, with infusion at 150 ml/h.

When MAP rose above 70 mmHg, hemodynamic support was de-escalated according to the same protocol.

Statistical Analysis

Study sample size was similar to previous similar studies (Pesenti et al., 1982; Neumann et al., 1998; Grasso et al., 2014). We calculated that six animals would have allowed us to detect an increase in the fraction of non-aerated tissue measured by CT scan with power of 0.8, alpha 0.05, and very large effect size (1.5). Data are shown as mean ± standard deviation. Comparisons between variables at each study time point were performed by one-way repeated measures ANOVA. Comparisons of non-aerated lung fractions at each time point in the non-dependent and dependent lung regions were performed by two-way repeated measures ANOVA. Holm–Sidak test was applied for *post-hoc* analyses. Correlations between variables were tested by Pearson's coefficient. Statistical significance was defined by $p < 0.05$ (two-tailed). Statistical analysis was performed using Sigma Plot 11.0 (Systat Software Inc., CA, USA).

RESULTS

Progressive Reduction of Respiratory Rate and ECMO Support

Respiratory rate decreased from 24 to 6 bpm while CO_2 removal ($p < 0.001$) gradually increased. Extracorporeal oxygenation ($p < 0.001$) increased after ECMO start and then remained stable (**Table 1**). ECMO provided around 40% of total VO_2, with minimal differences between study steps, while the ECMO VCO_2 increased progressively with the reduction of the respiratory rate, up to around 60% of total VCO_2 at 6 breaths per minute (**Table 1**). Arterial partial pressure of CO_2 remained stable throughout all study phases ($p = 0.146$; **Table 1**).

Effects of Lower Respiratory Rate and Higher Extracorporeal CO_2 Removal by ECMO

The percentage of collapsed non-aerated lung tissue in the whole lungs measured by CT scan (i.e., lung atelectasis) significantly increased at lower respiratory rate and higher ECMO CO_2 extraction (**Figure 1A** and **Table 1**). Development of atelectasis was mirrored by a reduction of the normally aerated lung tissue ($p = 0.011$), without change in total lung weight (i.e., no lung edema) measured by CT scan ($p = 0.260$; **Table 1**).

The increase in non-aerated compartment measured by CT scan was more pronounced in the gravitationally dependent lung regions (Dep vs. NDep $p = 0.022$, study steps $p = 0.007$, interaction $p < 0.001$; **Figure 1B**). EIT data showed that collapse of the dependent lung caused a reduction of regional tidal volume at lower respiratory rate ($p = 0.018$), likely caused by decreased local respiratory system compliance ($p = 0.012$; **Table 1**). **Figure 2** shows CT and EIT images for RR 24 and RR 6 study phase from a representative animal.

Progressive decrease of respiratory rate and increase of CO_2 removal by ECMO were associated with increased intrapulmonary shunt ($p < 0.001$; **Figure 3A**) and with decreased PaO_2 ($p < 0.001$; **Figure 3B**). FiO_2 remained unchanged as per study protocol. Moreover, there was a reduction in arterial blood pH ($p = 0.004$) with decrease in base excess ($p < 0.001$) and bicarbonates ($p < 0.001$), possibly due to metabolic compensation for some respiratory alkalosis at Baseline (**Table 2**).

As respiratory rate decreased and ECMO CO_2 extraction increased, mechanical power decreased ($p < 0.001$) in comparison to the RR 24 Baseline value (**Table 2**). At lower respiratory rates, plateau pressure ($p < 0.001$) and mean airway pressure ($p = 0.021$) slightly increased, while respiratory system compliance decreased (**Table 2**). Partitioned mechanics showed that lung compliance remained stable at increasing level of CO_2 removal by ECMO, while chest wall compliance decreased (**Table 2**).

TABLE 1 | Physiological effects of progressive reduction of respiratory rate and increase of extracorporeal CO_2 removal during ECMO support—Part 1.

Variables°	RR 24 Baseline	RR 18 + ECMO	RR 12 + ECMO	RR 6 + ECMO	*P*-value#
ECMO					
$VCO_{2\ NL}$, % total	100 ± 0	82 ± 7*	68 ± 13*	39 ± 7*	**<0.001**
$VCO_{2\ ML}$, % total	0 ± 0	18 ± 7*	32 ± 13*	61 ± 7*	**<0.001**
$VO_{2\ NL}$, % total	100 ± 0	60 ± 11*	59 ± 9*	62 ± 7*	**<0.001**
$VO_{2\ ML}$, % total	0 ± 0	40 ± 11*	41 ± 9*	38 ± 7*	**<0.001**
Gas exchange					
$PaCO_2$, mmHg	34.6 ± 3.8	30.7 ± 2.7	33.1 ± 4.0	32.4 ± 2.3	0.146
PaO_2/FiO_2	526 ± 46	501 ± 49	509 ± 35	436 ± 46*	**<0.001**
Computed tomography scan					
Non-aerated lung (atelectasis), %	3 ± 2	3 ± 2	6 ± 4	12 ± 9*	**0.009**
Poorly-aerated lung, %	39 ± 7	39 ± 11	44 ± 11	46 ± 12	0.270
Normally-aerated lung, %	58 ± 8	58 ± 12	50 ± 14	42 ± 11*	**0.011**
Total lung weight, g	661 ± 119	647 ± 125	632 ± 95	695 ± 106	0.260
Electrical impedance tomography					
Vt_{NDep}, %	29 ± 5	29 ± 6	34 ± 10	38 ± 11*	**0.018**
Vt_{Dep}, %	71 ± 5	71 ± 6	66 ± 10	62 ± 11*	**0.018**
Crs_{NDep}, ml/cmH_2O	12 ± 2	9 ± 2	11 ± 3	12 ± 3	0.127
Crs_{Dep}, ml/cmH_2O	30 ± 8	24 ± 3*	23 ± 5*	20 ± 6*	**0.012**

#*One-way RM ANOVA.*

**p < 0.05 Post-Hoc Holm–Sidak method vs. RR 24 Baseline value.*

°*ECMO, extracorporeal membrane oxygenation; $VCO_{2\ NL}$, VCO_2 natural lung; $VCO_{2\ ML}$, VCO_2 membrane lung; $VO_{2\ NL}$, VO_2 natural lung; $VO_{2\ ML}$, VO_2 membrane lung; $PaCO_2$, arterial partial pressure of carbon dioxide; PaO_2, arterial partial pressure of oxygen; FiO_2, inspiratory fraction of oxygen; Vt_{NDep}, tidal volume, non-dependent lung region; Vt_{Dep}, tidal volume, dependent lung region; Crs_{NDep}, respiratory system compliance, non-dependent region; Crs_{Dep}, respiratory system compliance, dependent region. Significant p-values are presented in bold characters.*

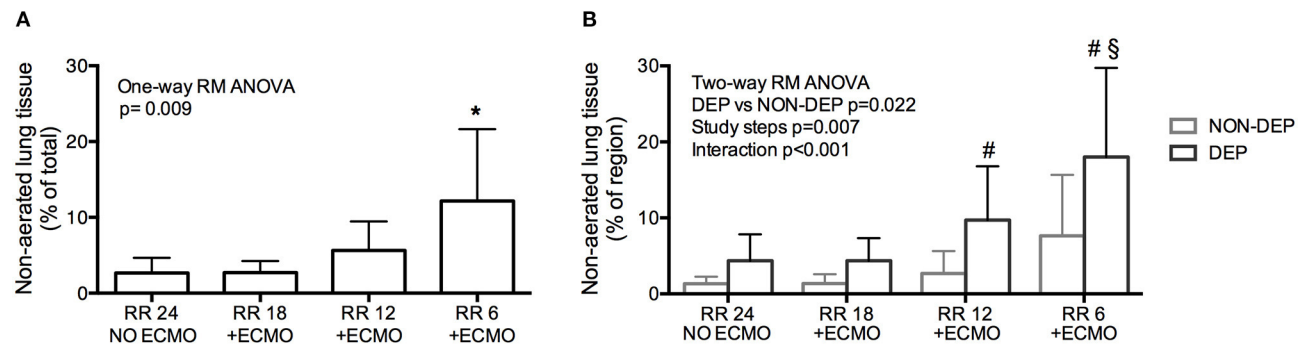

FIGURE 1 | Development of atelectasis (non-aerated lung tissue) in healthy pigs undergoing Extracorporeal Membrane Oxygenation (ECMO) with progressive decrease of respiratory rate. **(A)** Development of atelectasis as increase of the % of Non-aerated lung tissue. **(B)** Regional atelectasis as increase of the % of non-aerated lung tissue in gravitationally dependent and non-dependent regions. *$p < 0.05$ *Post-Hoc* Holm–Sidak method vs. Baseline. #$p < 0.05$ *Post-Hoc* Holm–Sidak method DEP vs. NON-DEP within study steps. §$p < 0.05$ *Post-Hoc* Holm–Sidak method vs. Baseline within region (DEP).

Finally, despite stable systemic arterial pressure and cardiac output, mean pulmonary artery pressure increased at lower RR ($p < 0.05$; **Figure 3C** and **Table 2**).

Determinants of Physiological Impairments

In an effort to more precisely identify the mechanisms underlying poorer respiratory physiology, we explored correlations between physiologic changes induced by lower respiratory rate and higher ECMO CO_2 extraction and the abovementioned observed effects.

The percentage of non-aerated lung tissue was correlated with the expiratory time spent at zero flow ($r = 0.555$; **Figure 4A**) and not with the mean or the plateau airway pressure ($r = -0.333$ and $r = 0.102$, respectively). The percentage of non-aerated lung was correlated also with the RER_{ML} ($r = 0.702$; **Figure 4B**), indicating that development of atelectasis may be more likely when ECMO is predominantly used to remove CO_2.

Intrapulmonary shunt was correlated with the SvO_2 and with the % of VO_2 granted by ECMO ($r = 0.419$ and $r = 0.664$, respectively; **Figure 5A**). Increasing ECMO CO_2 extraction

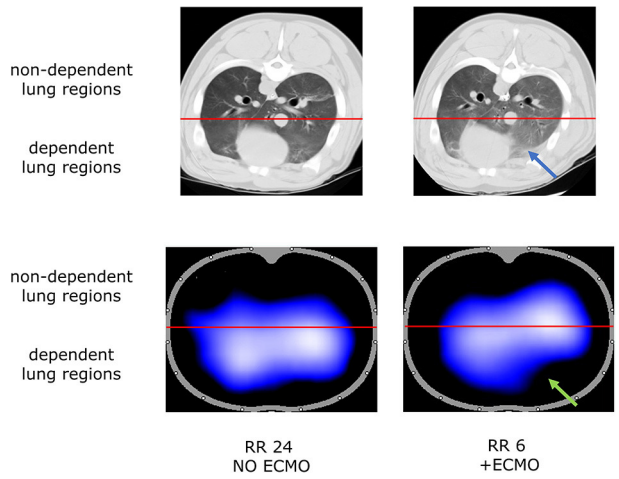

FIGURE 2 | Representative CT scan (aeration at end expiration, **Top**) and Electrical Impedance Tomography (ventilation at end-inspiration, **Bottom**) images during RR 24 and RR 6 step from one representative animal. Blue arrow indicates lung collapse at CT scan; green arrow indicates the correspondent loss of aeration detected by EIT analysis.

decreased the RER_{NL} (Baseline 0.74 ± 0.09 vs. RR18 0.87 ± 0.11 vs. RR12 0.78 ± 0.12 vs. RR6 0.46 ± 0.13, $p < 0.001$), resulting in lower alveolar PAO_2 (RR24 312 ± 6 mmHg vs. RR18 321 ± 4 mmHg vs. RR12 315 ± 7 mmHg vs. RR6 300 ± 12 mmHg; $p < 0.001$). Systemic PaO_2 was significantly correlated with PAO_2 ($r = 0.568$; **Figure 5B**).

DISCUSSION

Study main findings are that progressive decrease of respiratory rate coupled with increased extracorporeal CO_2 removal by ECMO leads to reduced mechanical power, but it is also associated with development of atelectasis, higher intrapulmonary shunt, and lower oxygenation in a large animal model of ECMO with healthy lungs. Development of atelectasis may be caused by longer motionless expiratory time (zero flow during expiration) and predominance of CO_2 removal over oxygen delivery by the ECMO membrane lung. Increased shunt, evident already during the RR 18 phase, instead, may be correlated to oxygen transfer by ECMO, leading to higher mixed venous saturation. Finally, poorer systemic oxygenation may be caused by lower RER of the natural lung, yielding reduced alveolar O_2 tension.

Seminal ECMO studies proposed reduction to very low frequency ventilation (3–5 breaths per minute) as optimal strategy for lung rest (Gattinoni et al., 1986). The two most recent randomized clinical trials on ECMO in severe ARDS applied much higher rates: fixed 10 breaths per minute in the CESAR trial (Peek et al., 2009) and an average of 23–24 breaths per minute in the more recent EOLIA study (Combes et al., 2018), leaving equipoise and clinical uncertainty. A study in pigs with acute lung injury described that rate of ∼14 breaths per minute during extracorporeal CO_2 removal was associated with lower levels of systemic and pulmonary inflammatory mediators in comparison to standard mechanical ventilation with ∼30 breaths per minute (Grasso et al., 2014). However, the two ventilation strategies were applied only for 3 h. A more recent experimental study on animal model of ARDS compared different ventilation strategies for 24 h during ECMO. The one termed "near-apneic" with a rate of 5 breaths per minute showed decreased histologic lung injury score in comparison to other strategies with higher RR. However, the "near-apneic" strategy was also associated with impaired respiratory mechanics (Araos et al., 2019). Thus, physiological targets guiding the decrease of respiratory rate after ECMO start remain an open issue.

The aim of mechanical ventilation during ECMO is to decrease the risk of VILI (Marini et al., 2020), and reduction of respiratory rate is usually a key component of this strategy (Pesenti et al., 1982; Gattinoni et al., 1986; Peek et al., 2009; Terragni et al., 2009; Bein et al., 2013; Combes et al., 2018, 2019). As expected, in the present study, respiratory rate was associated with significantly decreased *mechanical power*, with larger reduction at lower rates, potentially suggesting linear correlation between reduced respiratory rate and lung protection (at constant inspiratory flow). However, progressive decrease of respiratory rate (especially at values lower than 12 breaths per minute) was also associated with development of atelectasis. Atelectasis may trigger two key mechanisms of VILI, potentially outweighing the beneficial effects of decreased mechanical power, namely, reduced baby lung size (i.e., the normally aerated lung fraction) causing increased *lung strain* (Bellani et al., 2011) and larger fraction of lung units opening and closing during the respiratory cycle (*atelectrauma*) causing additional local stress by the sudden diffusion of gas flow between the epithelial cells (Caironi et al., 2010). A larger fraction of atelectasis occurred in the dependent lung, suggesting that this region may be particularly prone to these detrimental mechanisms, as shown by a previous publication (Scaramuzzo et al., 2020b).

Reduced respiratory rate after ECMO start was also associated with increased intrapulmonary shunt and lower arterial oxygenation, confirming previous observations in ARDS patients (Fanelli et al., 2016; Spinelli et al., 2020). Higher shunt and poorer oxygenation may not be detrimental *per se* for the lungs. However, in clinical practice, they could lead to use of higher PEEP levels and more aggressive recruitment during ECMO and, in turn, with increased risk of *overdistension* and *barotrauma* (Mauri et al., 2016a), further increasing the risk of undermining the benefits of reduced mechanical power.

We described increased pulmonary artery pressure at lower respiratory rate that may stress the right heart function, which is a major determinant of ARDS outcome (Mekontso Dessap et al., 2016).

In summary, our data indicate that progressive decrease of respiratory rate after ECMO start is associated with lung-protective effects but may place the basis for mechanisms potentially promoting VILI.

Deeper understanding of the mechanisms that caused the abovementioned physiological effects may be key to tailor personalized ventilation and ECMO settings. A previous study showed that expiratory time longer than 4 s promotes lung collapse in a large animal model of ARDS (Neumann et al., 1998). Our results are in line with those findings: expiratory time was 6.7 s during the RR 6 phase (the one associated

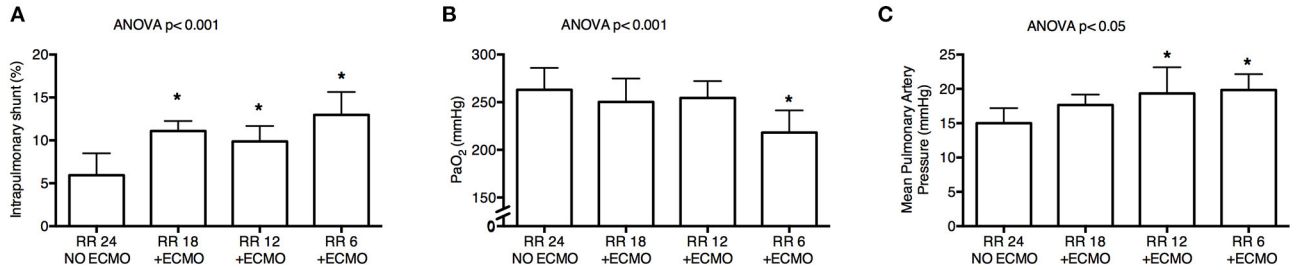

FIGURE 3 | Physiological effects of lower respiratory rate and higher extracorporeal CO_2 removal by ECMO. Progressive decrease of respiratory rate induced significant increase of intrapulmonary shunt calculated with Riley's method **(A)**, poorer systemic oxygenation **(B)**, and higher mean pulmonary artery pressure **(C)**. RR, respiratory rate; ECMO, extracorporeal membrane oxygenation; PaO_2, arterial partial pressure of oxygen. *$p < 0.05$ *Post-Hoc* Holm–Sidak method vs. Baseline.

TABLE 2 | Physiological effects of progressive reduction of respiratory rate and increase of extracorporeal CO_2 removal during ECMO support—Part 2.

Variables°	RR24 Baseline	RR18 + ECMO	RR12 + ECMO	RR6 + ECMO	*P*-value#
Respiratory mechanics					
Pplat, cmH_2O	14 ± 1	17 ± 2*	17 ± 1*	17 ± 1*	**<0.001**
mPaw, cmH_2O	9 ± 1	10 ± 1	9 ± 2	8 ± 1	0.183
Mechanical power, J/min	9.7 ± 1.0	8.8 ± 1.7	5.4 ± 0.8*	3.4 ± 0.7*	**<0.001**
T_{EXP} at zero flow, s	0.1 ± 0.2	0.4 ± 0.3	1.2 ± 0.5*	4.3 ± 0.8*	**<0.001**
Crs, ml/cmH_2O	44 ± 6	34 ± 3*	34 ± 4*	34 ± 3*	**<0.001**
Ccw, ml/cmH_2O	90 ± 14	74 ± 14	67 ± 18*	62 ± 9*	**0.014**
Clung, ml/cmH_2O	88 ± 26	68 ± 24	77 ± 27	81 ± 26	0.475
Vt/EELV ratio	0.54 ± 0.06	0.52 ± 0.08	0.63 ± 0.16	0.62 ± 0.15	0.063
Hemodynamics					
MAP, mmHg	106 ± 8	116 ± 15	109 ± 9	101 ± 24	0.450
HR, bpm	93 ± 7	104 ± 14	98 ± 21	96 ± 21	0.681
PAPm, mmHg	15 ± 2	18 ± 2	19 ± 3*	20 ± 2*	**0.036**
PCWP, mmHg	6 ± 2	6 ± 1	6 ± 2	8 ± 2	0.265
CO, L/min	5.2 ± 0.5	4.7 ± 0.4	4.4 ± 0.8	4.6 ± 0.6	0.228
CVP, mmHg	2 ± 2	3 ± 1	3 ± 3	5 ± 2	0.119
SvO_2, %	69 ± 4	80 ± 6	77 ± 5	76 ± 7	**0.008**
Arterial acid–base balance					
pH	7.54 ± 0.03	7.55 ± 0.04	7.50 ± 0.04*	7.49 ± 0.02*	**0.004**
$HCO3^-$, mmol/L	29.6 ± 1.7	26.8 ± 2.1*	26.5 ± 1.4*	24.7 ± 1.8*	**<0.001**
BE, mmol/L	10.5 ± 10.3	8.2 ± 10.9*	7.4 ± 11.1*	5.7 ± 10.2*	**<0.001**
Lac, mmol/L	1.0 ± 0.3	0.7 ± 0.2	0.7 ± 0.4	0.6 ± 0.3	0.066

#*One-way RM ANOVA.*

**p < 0.05 Post-Hoc Holm–Sidak method vs. RR 24 Baseline value.*

°*Pplat, plateau pressure; mPaw, mean airway pressure; T_{EXP} at zero flow, expiratory time at zero flow; Crs, static respiratory system compliance; Ccw, chest wall compliance; Clung, lung compliance; EELV, end-expiratory lung volume measured by CT scan; MAP, mean arterial pressure; HR, heart rate; PAPm, mean pulmonary arterial pressure; PCWP, pulmonary capillary wedge pressure; CO, cardiac output; CVP, central venous pressure; SvO_2, mixed venous saturation; BE, base excess; Lac, plasma lactates. Significant p-values are presented in bold characters.*

with larger fraction of atelectasis) vs. 3.3 s during RR 12 and 2.2 s for RR 18. We also described a more direct association between the development of atelectasis and the "no motion" time at end expiration. This phenomenon is probably due to lack of fresh gas replacement favoring reabsorption and it seems reasonable from a physiological point of view as collapse more likely occurs when the alveolar pressure reaches its lowest level (Duggan et al., 2005). Larger fraction of atelectasis was also correlated with predominance of CO_2 extraction over O_2 delivery by the ECMO membrane lung: this might be due to collapse of instable lung units with a low ventilation–perfusion ratio, which may have increased at lower respiratory rates by reduced alveolar ventilation. Indeed, these units are more prone to collapse due to the shift of alveolar nitrogen to relatively denitrogenated venous blood (Dantzker et al., 1975). Interestingly, shorter expiratory time spent at zero flow would not influence the latter mechanism and atelectasis would develop anyway, while a lower concentration of oxygen in the ECMO sweep gas flow might be protective.

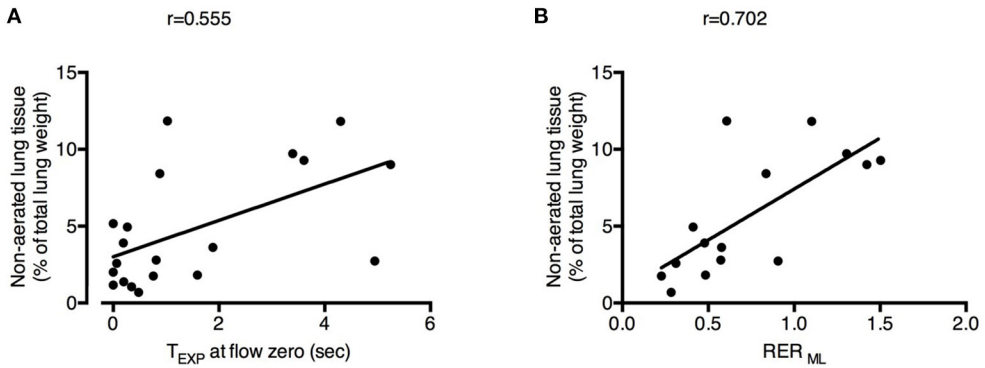

FIGURE 4 | Physiological changes induced by decreased respiratory rate and increased extracorporeal CO_2 removal associated with the development of atelectasis. Increased expiratory time spent at zero flow (T_{EXP} at flow zero) **(A)** and higher Respiratory Exchange Ratio of the membrane lung (RER ML) **(B)** were correlated with higher fraction of non-aerated lung tissue (i.e., atelectasis). See text for methodological details. Number of observations were $n = 20$ in **(A)** due to unavailability of calculation of expiratory time at flow zero in one of the animals and $n = 15$ in **(B)** due to impossibility of blood withdrawal to calculate RER ML in one of the animals.

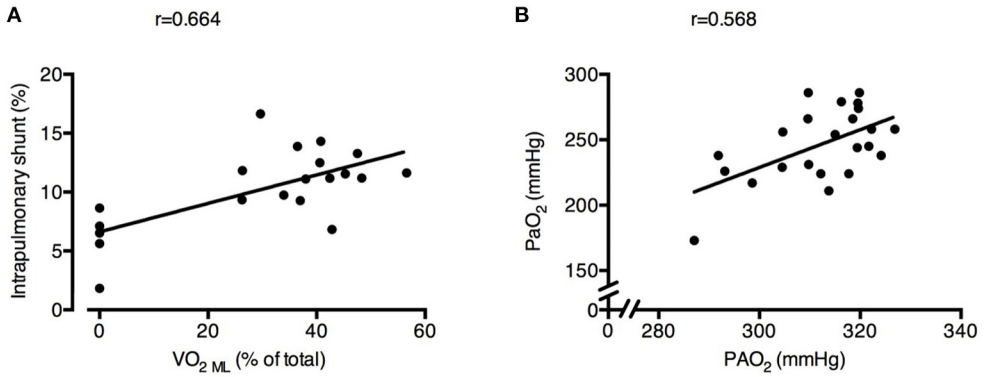

FIGURE 5 | Physiological changes induced by decreased respiratory rate and increased extracorporeal CO_2 removal associated with increased intrapulmonary shunt and poorer arterial oxygenation. Higher oxygen transfer by the ECMO membrane lung (VO_2 ML) was correlated with larger intrapulmonary shunt fraction **(A)**. Alveolar O_2 pressure (PAO_2) was correlated with systemic arterial partial pressure of O_2 (PaO_2) **(B)**. See text for methodological details. Number of observations were $n = 20$ in **(A)** due to impossibility of blood withdrawal to calculate VO_2ML in one of the animals and $n = 23$ in **(B)** due to blood gas analyzer failure for one arterial sample.

We showed that increased intrapulmonary shunt was proportional to oxygen delivery by ECMO and to mixed venous saturation: blunting of hypoxic vasoconstriction by higher oxygenation of venous blood is known to increase shunt and could be the underlying mechanism (Spinelli et al., 2020). In the future, personalized ECMO settings might be aimed at minimizing these effects.

Finally, arterial and alveolar O_2 tensions were correlated in our study, as expected in healthy lungs (Riley and Cournand, 1949). Decreased arterial and alveolar PO_2 at lower respiratory rates were caused by lower RER of the natural lung due to higher CO_2 extraction by ECMO. Of note and as previously described, the RER of the natural lung decreased only at very high CO_2 extraction rate by ECMO and relatively low FiO_2 at the ventilator and may not be particularly relevant during standard clinical use (Abrams et al., 2020).

Personalized respiratory rate in ARDS patients on ECMO may be chosen as the one associated with reduced mechanical power without increase in atelectasis. For example, continuous dynamic EIT monitoring could identify the lowest respiratory rate avoiding decrease of the dependent lung ventilation. On average, among the respiratory rates explored in this study, 12 breaths per minute was associated with decreased mechanical power and minimal detrimental effects.

This study has relevant limitations in the design of the experiment. First, the respiratory rates were not randomized since, to increase the clinical impact, we decided to assess the detrimental effects of progressive decrease of respiratory rate and not to compare selected target respiratory rates, which would have been anyway debatable. The development of atelectasis likely occurred by interaction of decreased rate and time under controlled mechanical ventilation and paralysis. The progressive decrease in chest wall compliance might be a confounding factor, possibly due to surgical procedures, and time under paralysis and anesthesia, while the lack of change in lung compliance with decreasing RR might be explained by the relatively small amount

of atelectasis. Second, tidal volume was left unchanged during the study, while it is usually decreased after ECMO start in the clinical practice reduction. However, further hypoventilation due to reduced tidal volume might have amplified the unphysiological effects that we measured (e.g., atelectasis). Third, some ECMO centers increase PEEP in severe ARDS patients after ECMO start (Schmidt et al., 2019) to limit de-recruitment while we left unchanged low PEEP level of 5 cmH_2O. Higher PEEP might counteract the decrease in EELV due to atelectasis. Fourth, the study was performed exclusively on healthy animals, which limits clinical significance, but our choice is intended to remove the problem of discriminating between hypoventilation-induced atelectasis and loss of aeration due to lung injury and edema, which are predominant mechanisms leading to loss of aeration in ARDS.

CONCLUSIONS

In the end, our study is an exploratory investigation to test the physiological effects of reduced respiratory rate *per se* during ECMO. Progressive decrease of respiratory rate and increased CO_2 extraction in a large animal model of ECMO with healthy lungs are associated with not only decreased mechanical power but also development of atelectasis, higher intrapulmonary shunt, and lower arterial oxygenation. We observed mild but potentially detrimental physiological effects that deserve attention in order to personalize optimal ventilation and ECMO interaction guaranteeing protective respiratory mechanics and minimal adverse events.

DATA AVAILABILITY STATEMENT

The raw data supporting the conclusions of this article will be made available by the authors, without undue reservation.

ETHICS STATEMENT

The study was approved by the Italian Ministry of Health (protocol n. 749/2019) and conducted according to the European Directive 2010/63/EU on the protection of animals used for scientific purposes and Italian legislative decree 26/2014. The research protocol was approved by the Institutional Animal Care Committee.

AUTHOR CONTRIBUTIONS

ESp, ESc, LR, SG, and TM: substantial contributions to the conception or design of the work. ESp, GC, GD, ESc, IM, EG, AM, DD, RM, MB, OB, and TM: acquisition, analysis, interpretation of data for the work, and agreement to be accountable for all aspects of the work in ensuring that questions related to the accuracy or integrity of any part of the work are appropriately investigated and resolved. All authors: drafting the work or revising it critically for important intellectual content and final approval of the version submitted for publication.

FUNDING

This present study was supported by institutional funding of the Department of Anesthesia, Critical Care and Emergency, Fondazione IRCCS Ca' Granda Ospedale Maggiore Policlinico, Milan, Italy (Ricerca corrente 2019) and by a grant from the Italian Ministry of Health, Rome, Italy (Ricerca Finalizzata 2016, project GR-2016-02362428).

ACKNOWLEDGMENTS

We wish to thank Samanta Oldoni for the logistical support in the animal laboratory.

REFERENCES

Abrams, D., Pesenti, A., Brochard, L., and Brodie, D. (2020). Reply to Dickstein: extracorporeal CO_2 removal and the alveolar gas equation. *Am. J. Respir. Crit. Care Med.* 202, 1058–1059. doi: 10.1164/rccm.202005-1923LE

Araos, J., Alegria, L., Garcia, P., Cruces, P., Soto, D., Erranz, B., et al. (2019). Near-apneic ventilation decreases lung injury and fibroproliferation in an acute respiratory distress syndrome model with extracorporeal membrane oxygenation. *Am. J. Respir. Crit. Care Med.* 199, 603–612. doi: 10.1164/rccm.201805-0869OC

Bein, T., Weber-Carstens, S., Goldmann, A., Müller, T., Staudinger, T., Brederlau, J., et al. (2013). Lower tidal volume strategy (≈3 ml/kg) combined with extracorporeal CO_2 removal versus 'conventional' protective ventilation (6 ml/kg) in severe ARDS: the prospective randomized Xtravent-study. *Intensive Care Med.* 39, 847–856. doi: 10.1007/s00134-012-2787-6

Bellani, G., Guerra, L., Musch, G., Zanella, A., Patroniti, N., Mauri, T., et al. (2011). Lung regional metabolic activity and gas volume changes induced by tidal ventilation in patients with acute lung injury. *Am. J. Respir. Crit. Care Med.* 183, 1193–1199. doi: 10.1164/rccm.201008-1318OC

Caironi, P., Cressoni, M., Chiumello, D., Ranieri, M., Quintel, M., Russo, S. G., et al. (2010). Lung opening and closing during ventilation of acute respiratory distress syndrome. *Am. J. Respir. Crit. Care Med.* 181, 578–586. doi: 10.1164/rccm.200905-0787OC

Combes, A., Fanelli, V., Pham, T., and Ranieri, V. M. (2019). European society of intensive care medicine trials group and the "strategy of ultra-protective lung ventilation with extracorporeal CO_2 removal for new-onset moderate to severe ARDS" (SUPERNOVA) investigators. Feasibility and safety of extracorporeal CO_2 removal to enhance protective ventilation in acute respiratory distress syndrome: the SUPERNOVA study. *Intensive Care Med.* 45, 592–600. doi: 10.1007/s00134-019-05567-4

Combes, A., Hajage, D., Capellier, G., Demoule, A., Lavoué, S., Guervilly, C., et al. (2018). Extracorporeal membrane oxygenation for severe acute respiratory distress syndrome. *N. Engl. J. Med.* 378, 1965–1975. doi: 10.1056/NEJMoa1800385

Combes, A., Schmidt, M., Hodgson, C. L., Fan, E., Ferguson, N. D., Fraser, J. F., et al. (2020). Extracorporeal life support for adults with acute respiratory distress syndrome. *Intensive Care Med*. 46, 2464–2476. doi: 10.1007/s00134-020-06290-1

Dantzker, D., Wagner, P., and West, J. B. (1975). Instability of lung units with low Va/Q ratios during O_2 breathing. *J. Appl. Physiol.* 38, 886–895. doi: 10.1152/jappl.1975.38.5.886

Dickstein, M. L. (2020). Extracorporeal CO_2 removal and the alveolar gas equation. *Am. J. Respir. Crit. Care Med.* 202, 1057–1058. doi: 10.1164/rccm.202005-1609LE

Duggan, M., Kavanagh, B. P., and Warltier, D. C. (2005). Pulmonary atelectasis: a pathogenic perioperative entity. *Anesthesiology* 102, 838–854. doi: 10.1097/00000542-200504000-00021

Fanelli, V., Ranieri, M. V., Mancebo, J., Moerer, O., Quintel, M., Morley, S., et al. (2016). Feasibility and safety of low-flow extracorporeal carbon dioxide removal to facilitate ultra-protective ventilation in patients with moderate acute respiratory distress sindrome. *Crit. Care* 20:36doi: 10.1186/s13054-016-1211-y

Gattinoni, L., Caironi, P., Cressoni, M., Chiumello, D., Ranieri, V. M., Quintel, M., et al. (2006). Lung recruitment in patients with the acute respiratory distress syndrome. *N. Engl. J. Med.* 354, 1775–1786. doi: 10.1056/NEJMoa052052

Gattinoni, L., Pesenti, A., Mascheroni, D., Marcolin, R., Fumagalli, R., Rossi, F., et al. (1986). Low-frequency positive-pressure ventilation with extracorporeal CO_2 removal in severe acute respiratory failure. *JAMA* 256, 881–886. doi: 10.1001/jama.1986.03380070087025

Grasso, S., Stripoli, T., Mazzone, P., Pezzuto, M., Lacitignola, L., Centonze, P., et al. (2014). Low respiratory rate plus minimally invasive extracorporeal Co_2 removal decreases systemic and pulmonary inflammatory mediators in experimental acute respiratory distress syndrome. *Crit. Care Med.* 42, e451–e460. doi: 10.1097/CCM.0000000000000312

Marini, J. J., Rocco, P. R. M., and Gattinoni, L. (2020). Static and dynamic contributors to ventilator-induced lung injury in clinical practice. Pressure, energy, and power. *Am. J. Respir. Crit. Care Med.* 201, 767–774. doi: 10.1164/rccm.201908-1545CI

Mauri, T., Bellani, G., Confalonieri, A., Tagliabue, P., Turella, M., Coppadoro, A., et al. (2013). Topographic distribution of tidal ventilation in acute respiratory distress syndrome: effects of positive end-expiratory pressure and pressure support. *Crit. Care Med.* 41, 1664–1673. doi: 10.1097/CCM.0b013e318287f6e7

Mauri, T., Eronia, N., Turrini, C., Battistini, M., Grasselli, G., Rona, R., et al. (2016a). Bedside assessment of the effects of positive end-expiratory pressure on lung inflation and recruitment by the helium dilution technique and electrical impedance tomography. *Intensive Care Med.* 42, 1576–1587. doi: 10.1007/s00134-016-4467-4

Mauri, T., Yoshida, T., Bellani, G., Goligher, E. C., Carteaux, G., Rittayamai, N., et al. (2016b). Esophageal and transpulmonary pressure in the clinical setting: meaning, usefulness and perspectives. *Intensive Care Med.* 42, 1360–1373. doi: 10.1007/s00134-016-4400-x

Mekontso Dessap, A., Boissier, F., Charron, C., Bégot, E., Repessé, X., Legras, A., et al. (2016). Acute cor pulmonale during protective ventilation for acute respiratory distress syndrome: prevalence, predictors, and clinical impact. *Intensive Care Med.* 42, 862–870. doi: 10.1007/s00134-015-4141-2

Neumann, P., Berglund, J. E., Fernández Mondéjar, E., Magnusson, A., and Hedenstierna, G. (1998). Dynamics of lung collapse and recruitment during prolonged breathing in porcine lung injury. *J. Appl. Physiol.* 85, 1533–1543. doi: 10.1152/jappl.1998.85.4.1533

Peek, G. J., Mugford, M., Tiruvoipati, R., Wilson, A., Allen, E., Thalanany, M. M., et al. (2009). Efficacy and economic assessment of conventional ventilatory support versus extracorporeal membrane oxygenation for severe adult respiratory failure (CESAR): a multicentre randomised controlled trial. *Lancet* 374, 1351–1363. doi: 10.1016/S0140-6736(09)61069-2

Pesenti, A., Kolobow, T., Buckhold, D. K., Pierce, J. E., Huang, H., and Chen, V. (1982). Prevention of hyaline membrane disease in premature lambs by apneic oxygenation and extracorporeal carbon dioxide removal. *Intensive Care Med.* 8, 11–17. doi: 10.1007/BF01686848

Radermacher, P., Maggiore, S. M., and Mercat, A. (2017). Fifty years of research in ARDS. Gas exchange in acute respiratory distress syndrome. *Am. J. Respir. Crit. Care Med.* 196, 964–984. doi: 10.1164/rccm.201610-2156SO

Riley, R. L., and Cournand, A. (1949). Ideal alveolar air and the analysis of ventilation-perfusion relationships in the lungs. *J. Appl. Physiol.* 1, 825–847. doi: 10.1152/jappl.1949.1.12.825

Scaramuzzo, G., Spadaro, S., Dalla Corte, F., Waldmann, A. D., Böhm, S. H., Ragazzi, R., et al. (2020a). Personalized positive end-expiratory pressure in acute respiratory distress syndrome: comparison between optimal distribution of regional ventilation and positive transpulmonary pressure. *Crit. Care Med.* 48, 1148–1156. doi: 10.1097/CCM.0000000000004439

Scaramuzzo, G., Spinelli, E., Spadaro, S., Santini, A., Tortolani, D., Dalla Corte, F., et al. (2020b). Gravitational distribution of regional opening and closing pressures, hysteresis and atelectrauma in ARDS evaluated by electrical impedance tomography. *Crit. Care* 24:622. doi: 10.1186/s13054-020-03335-1

Schmidt, M., Pham, T., Arcadipane, A., Agerstrand, C., Ohshimo, S., Pellegrino, V., et al. (2019). Mechanical ventilation management during extracorporeal membrane oxygenation for acute respiratory distress syndrome. An international multicenter prospective cohort. *Am. J. Respir. Crit. Care Med.* 200, 1002–1012. doi: 10.1164/rccm.201806-1094OC

Spinelli, E., Mauri, T., Carlesso, E., Crotti, S., Tubiolo, D., Lissoni, A., et al. (2020). Time-course of physiologic variables during extracorporeal membrane oxygenation and outcome of severe acute respiratory distress syndrome. *ASAIO J.* 66, 663–670. doi: 10.1097/MAT.0000000000001048

Terragni, P. P., Del Sorbo, L., Mascia, L., Urbino, R., Martin, E. L., Birocco, A., et al. (2009). Tidal volume lower than 6 ml/kg enhances lung protection: role of extracorporeal carbon dioxide removal. *Anesthesiology* 111, 826–835. doi: 10.1097/ALN.0b013e3181b764d2

Zanella, A., Salerno, D., Scaravilli, V., Giani, M., Castagna, L., Magni, F., et al. (2016). A mathematical model of oxygenation during venovenous extracorporeal membrane oxygenation support. *J. Crit. Care* 36, 178–186. doi: 10.1016/j.jcrc.2016.07.008

Conflict of Interest: TM received personal fees from Fisher & Paykel, Drager, Mindray, and BBraun outside of the present work.

The remaining authors declare that the research was conducted in the absence of any commercial or financial relationships that could be construed as a potential conflict of interest.

frontiers in Physiology

ORIGINAL RESEARCH
published: 26 May 2021
doi: 10.3389/fphys.2021.672823

Accuracy of the Radiographic Assessment of Lung Edema Score for the Diagnosis of ARDS

Claudio Zimatore[1,2], Luigi Pisani[1,3,4], Valeria Lippolis[5], Melissa A. Warren[6], Carolyn S. Calfee[7], Lorraine B. Ware[6,8], Anna Geke Algera[1], Marry R. Smit[1], Salvatore Grasso[2] and Marcus J. Schultz[1,3]*

[1] Department of Intensive Care, Academic Medical Center, Amsterdam, Netherlands, [2] Department of Emergency and Organ Transplantation, School of Medicine, University of Bari Aldo Moro, Bari, Italy, [3] Mahidol-Oxford Tropical Medicine Research Unit (MORU), Mahidol University, Bangkok, Thailand, [4] Department of Anesthesia and Perioperative Medicine, Regional General Hospital F. Miulli, Acquaviva delle Fonti, Italy, [5] Department of Intensive Care, Mater Dei Hospital, Bari, Italy, [6] Division of Allergy, Pulmonary and Critical Care Medicine, Department of Medicine, Vanderbilt University School of Medicine, Nashville, TN, United States, [7] Department of Medicine and Department of Anesthesia, Cardiovascular Research Institute, University of California, San Francisco, San Francisco, CA, United States, [8] Department of Pathology, Microbiology and Immunology, Vanderbilt University School of Medicine, Nashville, TN, United States

OPEN ACCESS

Edited by:
Peter Markus Spieth, University Hospital Carl Gustav Carus, Germany

Reviewed by:
Alysson Roncally Silva Carvalho, University of Porto, Portugal
Sam Bayat, Université Grenoble Alpes, France

***Correspondence:**
Claudio Zimatore
claudiozimatore@gmail.com

Specialty section:
This article was submitted to Respiratory Physiology, a section of the journal Frontiers in Physiology

Received: *26 February 2021*
Accepted: *28 April 2021*
Published: *26 May 2021*

Citation:
Zimatore C, Pisani L, Lippolis V, Warren MA, Calfee CS, Ware LB, Algera AG, Smit MR, Grasso S and Schultz MJ (2021) Accuracy of the Radiographic Assessment of Lung Edema Score for the Diagnosis of ARDS. Front. Physiol. 12:672823. doi: 10.3389/fphys.2021.672823

Background: Bilateral opacities on chest radiographs are part of the Berlin Definition for Acute Respiratory Distress Syndrome (ARDS) but have poor interobserver reliability. The "Radiographic Assessment of Lung Edema" (RALE) score was recently proposed for evaluation of the extent and density of alveolar opacities on chest radiographs of ARDS patients. The current study determined the accuracy of the RALE score for the diagnosis and the prognosis of ARDS.

Methods: *Post-hoc* analysis of a cohort of invasively ventilated intensive care unit (ICU) patients expected to need invasive ventilation for >24 h. The Berlin Definition was used as the gold standard. The RALE score was calculated for the first available chest radiograph after start of ventilation in the ICU. The primary endpoint was the diagnostic accuracy for ARDS of the RALE score. Secondary endpoints included the prognostic value of the RALE score for ICU and hospital mortality, and the association with ARDS severity, and the PaO_2/FiO_2. Receiver operating characteristic (ROC) curves were constructed, and the optimal cutoff was used to determine sensitivity, specificity and the negative and positive predictive value of the RALE score for ARDS.

Results: The study included 131 patients, of whom 30 had ARDS (11 mild, 15 moderate, and 4 severe ARDS). The first available chest radiograph was obtained median 0 [0 to 1] days after start of invasive ventilation in ICU. Compared to patients without ARDS, a higher RALE score was found in patients with ARDS (24 [interquartile range (IQR) 16–30] *vs.* 6 [IQR 3–11]; $P < 0.001$), with RALE scores of 20 [IQR 14–24], 26 [IQR 16–32], and 32 [IQR 19–36] for mild, moderate and severe ARDS, respectively, ($P = 0.166$). The area under the ROC for ARDS was excellent (0.91 [0.86–0.96]). The best cutoff for ARDS diagnosis was 10 with 100% sensitivity, 71% specificity, 51%

positive predictive value and 100% negative predictive value. The RALE score was not associated with ICU or hospital mortality, and weakly correlated with the PaO_2/FiO_2.

Conclusion: In this cohort of invasively ventilated ICU patients, the RALE score had excellent diagnostic accuracy for ARDS.

Keywords: invasive ventilation, acute respiratory distress syndrome (ARDS), lung imaging, chest X ray, chest radiogprahs, diagnostic capacity, prognostic capacity, rale score

INTRODUCTION

The chest radiograph is a frequently used imaging tool in intensive care unit (ICU) patients (Trotman-Dickenson, 2003; Graat et al., 2006), although its clinical value has been disputed (Graat et al., 2005). Findings on chest radiographs are an important part of the Berlin Definition for acute respiratory distress syndrome (ARDS Definition Task Force et al., 2012), despite the low interobserver reliability that does not improve with training (Rubenfeld et al., 1999; Goddard et al., 2018). Also, the description of chest radiographs findings remains mostly subjective. Recently, therefore, the "Radiographic Assessment of Lung Edema" (RALE) score was proposed (Warren et al., 2018), a numeric scoring system in which the chest is divided into four quadrants that are each scored on a numerical scale for extent of consolidation *and* density of opacification. The RALE score is calculated by summing the product of the scores for consolidation and density of opacification of the four quadrants, and can range from 0 to 48.

While the first description of the RALE score focused on validating the score against gravimetric quantification and testing the association between the score and outcome in patients with ARDS (Warren et al., 2018), it could be that this score also has discriminating properties to diagnose ARDS in invasively ventilated ICU patients who may or may not have ARDS. In addition, with every new scale or score, it is necessary to externally validate its capacity, feasibility and reliability (Patrick and Chiang, 2000; Keszei et al., 2010; Kottner et al., 2011).

The objective of the current study was two–fold. The first objective was to determine whether the RALE score has diagnostic properties for ARDS, and prognostic properties in ICU patients. The second objective was to assess the feasibility and interobserver reliability of the RALE score. These objectives were studied using the chest radiographs of patients in a well–defined cohort of invasively ventilated ICU patients (Vercesi et al., 2018). The hypotheses tested were that the RALE score has a good diagnostic accuracy for ARDS, and that the RALE score has prognostic value in invasively ventilated ICU patients, independent of the diagnosis of ARDS.

MATERIALS AND METHODS

Study Design and Settings

This study was a *post-hoc* analysis of a single–center observational study performed in the ICU of the Amsterdam University Medical Centers, location Academic Medical Center (AMC) between November 2016 and June 2017 (Vercesi et al., 2018; Pisani et al., 2019). The Institutional Review Board of the AMC approved the original study and waived the need for informed consent from individual patients because data used in this study had been collected as part of standard care for patients with acute respiratory failure (approval W17_353 # 17.411).

Inclusion and Exclusion Criteria

Patients were eligible for participation in the original study if they: (a) were expected to receive invasive ventilation for at least 24 h at the moment of screening, (b) received ventilation with a minimum of 5 cm H_2O positive end–expiratory pressure (PEEP); and (c) had a chest radiograph or lung CT scan within the first 24 and 48 h of start of invasive ventilation, respectively. As the original study focused on the diagnostic value of lung ultrasound plus pulse oximetry for moderate or severe ARDS, the original study had two exclusion criteria, namely: (a) no lung ultrasound study made within 48 h of start of invasive ventilation; and (b) conditions potentially compromising reliability of pulse oximetry, including carbon monoxide poisoning. The number of excluded patients because of these reasons, though, was very low. An additional exclusion criterion for the current analysis was the absence of a chest radiograph during the first 2 days of invasive ventilation in the ICU.

Data Collection

Collection of data involved demographic characteristics including age, gender, height, weight, and body mass index; disease severity scores including the acute physiology and chronic health evaluation IV score and the simplified acute physiology score II; and ventilation characteristics including FiO_2, minute volume, PEEP, maximum airway pressure (P_{max}), respiratory rate, tidal volume, and blood gas analysis results.

ARDS Diagnosis

Acute respiratory distress syndrome was diagnosed according to the Berlin Definition for ARDS (ARDS Definition Task Force et al., 2012). For this, a panel of independent experienced clinicians assessed presence or absence of ARDS, strictly using the 4 components of the Berlin Definition for ARDS, i.e., new or worsening respiratory symptoms within 1 week of a known medical clinical insult; a $PaO_2/FiO_2 < 300$ mm Hg at a minimum of 5 cm H_2O PEEP; bilateral opacities on the chest radiograph or computed tomography (CT) exam, not explained by effusions, collapse or nodules; and respiratory

Consolidation[a]

Consolidation Score	Extent of alveolar opacities
0	None
1	< 25 %
2	25 – 50 %
3	50 – 75 %
4	> 75 %

Density[b]

Density Score	Density of alveolar opacities
1	Hazy
2	Moderate
3	Dense

Final RALE Score[c]

Right Lung	Left Quadrant
Upper Quadrant	Upper Quadrant
Cons x Den = Q1 Score	Cons x Den = Q3 Score
Lower Quadrant	Lower Quadrant
Cons x Den = Q2 Score	Cons x Den = Q4 Score

Total RALE = Q1 + Q2 + Q3 + Q4

[a] Consolidation is scored for each quadrant
[b] Density is scored for each quadrant having a consolidation > 0
[c] If Quadrant consolidation Score is 0 than Quadrant score il 0

Calculation of the RALE score for radiograph

Score	Q1	Q2	Q3	Q4	Total
Consolidation	2	1	3	4	
Density	3	3	3	3	
Quadrant Score	2 x 3 = 6	1 x 3 = 3	3 x 3 = 9	4 x 3 = 12	**30**

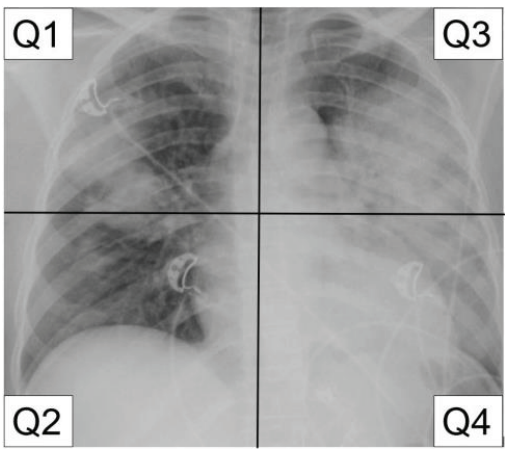

FIGURE 1 | Consolidation and density scoring in the RALE score.

failure not fully explained by cardiac failure or fluid overload. Of note, the clinicians applying the criteria in the Berlin Definition for ARDS could not calculate the RALE score, as this score was developed and reported in the literature after their assessments.

RALE Score

Two independent researchers (CZ and VL) scored the first available chest radiograph after start of mechanical ventilation in ICU patients. These researchers were unaware of clinical information or presence or absence of ARDS, as well as the results of assessments of the above–mentioned physicians who applied the criteria in the Berlin Definition. In short, as shown in **Figure 1**, the lung fields on the chest radiograph were divided into four quadrants by a vertical line over the spine and a horizontal line at the level of the first branch of the left main bronchus, exactly as described in the seminal publication on the RALE score (Warren et al., 2018). Each quadrant was assigned a number, and the extent of alveolar opacities (the consolidation score, from 0 to 4) and density of alveolar opacities (the density score, from 1 to 3) was determined. If the consolidation score was 0, the density score was 0. The final RALE score was the sum of the product of the consolidation and density score for each quadrant. Thus, the final RALE score ranged from minimum 0 to maximum 48.

Endpoints

The primary endpoint was the diagnostic accuracy for ARDS of the RALE score. Secondary endpoints included the prognostic value of the RALE score for ICU and hospital mortality, correlation between the RALE score and ARDS severity, and the inter-observer reliability for the RALE scoring, the correlation with the PaO_2/FiO_2 at the moment the chest radiograph was obtained.

Statistical Analysis

Demographic data, and clinical and outcome variables were presented as frequencies with percentages for categorical variables and as medians with interquartile ranges for continuous variables.

To determine the reliability of the RALE score, the interobserver variability (Keszei et al., 2010) between the primary scorer and a second independent investigator was tested on the entire cohort of the patients. For this, a two–way mixed consistency average measures intraclass correlation coefficient (ICC) was calculated. A Bland–Altman plot and a scatter plot were used to visualize the agreement between independent viewers. For the primary analysis only the scores attributed by the primary scorer were used.

To determine the diagnostic accuracy of the RALE score for ARDS, the Area Under the Receiver Operating Characteristic

curve (AUROC) with 95% confidence intervals (CI) was calculated. Diagnostic accuracy was considered "excellent" if AUROC was between 0.9 and 1, "very good" between 0.8 and 0.9, "good" between 0.7 and 0.8, "sufficient" between 0.6 and 0.7, and "bad" between 0.5 and 0.6 (Šimundić, 2009). The best cutoffs, the maximum difference between true positive and false positive, were obtained with the Youden index (Youden, 1950) (sensitivity + specificity − 1). Sensitivity, specificity, positive and negative predictive values were calculated using this cutoff.

Next, RALE scores were compared between patients without ARDS, and patients with mild, moderate or severe ARDS, and local polynomial regression (LOWESS curve fitting) was used to assess the correlation between RALE score with PaO_2/FiO_2, PEEP, FiO_2, and P_{Max}.

Finally, to determine the prognostic accuracy for ICU or hospital mortality, ROCs were constructed and analyzed in the same way as for determining the diagnostic accuracy for ARDS.

Statistical significance was considered when $P < 0.05$. All analyses were performed using IBM SPSS Statistics 24.0 and graphs built using Prism 8 (GraphPad software, version 8.4.2).

RESULTS

Patients

Patient flow is shown in **Figure 2**. Of the 152 patients in the original cohort, 131 patients fulfilled the additional criteria for participation in the current analysis. Of them, 101 were diagnosed as not having ARDS, and 30 fulfilled the Berlin Definition for ARDS (11, 15, and 4 patients with mild, moderate and severe ARDS, respectively). Demographic and ventilatory characteristics are presented in **Table 1**.

The ICC for applying the RALE score was excellent (0.95 [95%– CI 0.92–0.96]). The Bland–Altman plot showed a strong agreement and the scatter plot suggests high degree of agreement between the two independent researchers (**Supplementary Figure 1**).

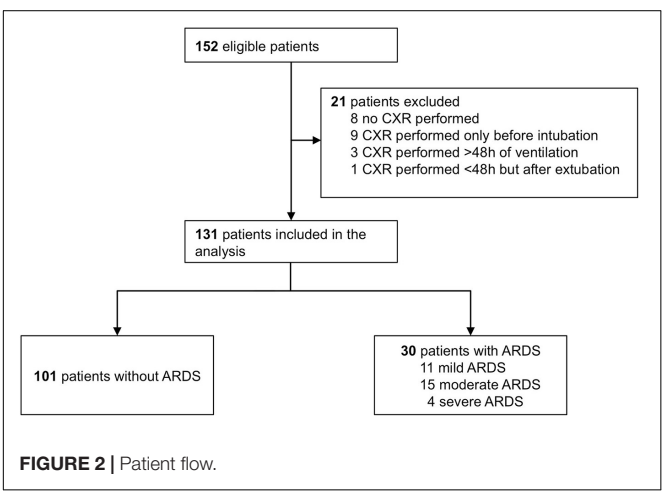

FIGURE 2 | Patient flow.

TABLE 1 | Baseline characteristics, outcomes and ventilatory characteristics of patients at the moment of the chest radiograph.

	No ARDS	Mild ARDS	Moderate ARDS	Severe ARDS
Baseline characteristics and outcomes				
Age, years	62 [51,72]	65 [52,71]	55 [24,69]	54 [37,59]
Gender, male	59 (58)	5 (45)	11 (73)	3 (75)
BMI, kg/m^2	25 [23,28]	26 [24,28]	26 [23,33]	24 [23,29]
SAPS	37 [15,52]	24 [15,53]	20 [3,49]	52 [12,61]
SOFA	10 [7,12]	9 [6,11]	11 [8,13]	13 [11,15]
APACHE II score	22 [17,27]	20 [15,31]	19 [13,24]	24 [15,27]
ICU mortality	32 (32)	3 (27)	3 (20)	4 (100)
Hospital mortality	41 (41)	3 (27)	3 (20)	4 (100)
Duration of ventilation	3 [1,8]	5 [2,17]	12 [7,18]	11 [1,21]
VFD 28, days	19 [0,25]	18 [0,24]	15 [0,20]	0 [0,0]
Ventilation characteristics*x*				
FiO_2, %	40 [30,50]	50 [40,65]	50 [40,60]	100 [93,100]
Minute volume, L/min	8.7 [6.9,10.8]	10.3[9.3,12.9]	10.8[9.4,12.7]	11.4[4.9,13.5]
PEEP, cm H_2O	5 [5,8]	8 [7,10]	12 [8,15]	15 [11,15]
P_{max}, cm H_2O	22 [16,27]	28 [26,35]	31 [27,36]	35 [31,39]
RR measured, breath/min	18 [16,24]	26 [22,32]	27 [21,30]	23 [13,30]
V_T, ml/kg PWB	8.2 [6.7,9.3]	8.5 [6.1,10.1]	6.9 [4.8,8.8]	5.4 [2.6,9.4]
SpO_2, %	98 [96,100]	96 [93,99]	95 [94,98]	89 [78,95]
PaO_2, mm Hg	89 [80,102]	80 [69,93]	77 [67,80]	75 [61,92]
PaO2 to FiO2 ratio	253 [173,321]	159 [131,212]	143 [123,177]	78 [62,92]

Values are medians [interquartile range] or numbers (percentage).
Abbreviations: ARDS, acute respiratory distress syndrome; SAPS, simplified acute physiology score; SOFA, sequential organ failure assessment; APACHE, acute physiology and chronic health; VFD 28, ventilator-free days at day 28; FiO2, fraction of inspired oxygen; PEEP, positive end–expiratory pressure; Pmax, maximum airway pressure; RR, respiratory rate; VT, tidal volume; PBW, predicted body weight; SpO2, pulse oximetry saturation; PaO2, arterial oxygen pressure; and PaCO2, arterial carbon dioxide pressure.

The Diagnostic Performance of the RALE Score

The RALE score was higher in ARDS patients compared to patients without ARDS (24 [16–30] *vs.* 6 [3–11]; $P < 0.001$) and had an excellent area under the ROC for ARDS (**Figure 3**). The best cutoff for ARDS diagnosis was 10 (Youden's index = 0.710) with 100% sensitivity, 71% specificity, 51% positive predicted value and 100% negative predicted value. Although the RALE scores increased with ARDS severity, differences between the severity groups were non–significant (20 [14–24], 26 [16–32] and 32 [19–36] in mild, moderate and severe ARDS, respectively; $P = 0.166$).

The Prognostic Value of the RALE Score

The prognostic capacity of the RALE score for ICU – and hospital mortality was poor (**Figure 4**).

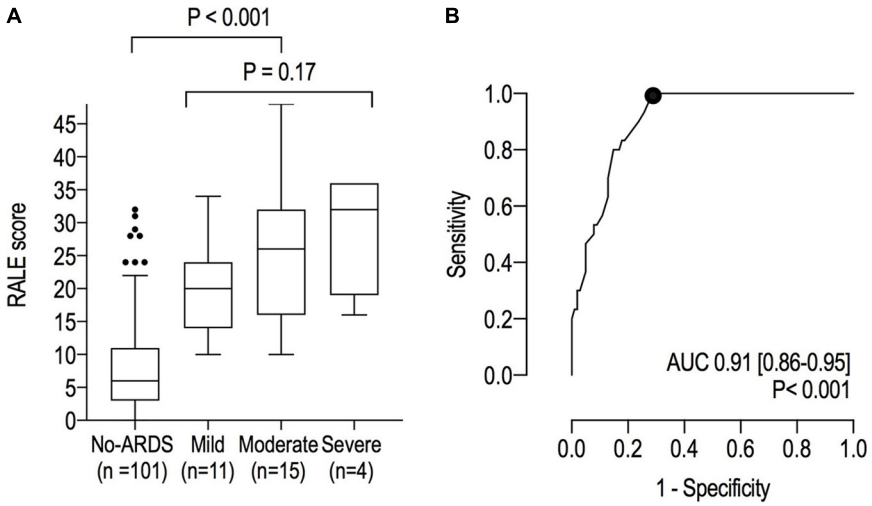

FIGURE 3 | (A) RALE scores in patients with ARDS and those without ARDS; **(B)** Receiver Operating Characteristic curves for ARDS. The dot represents the optimal cutoff.

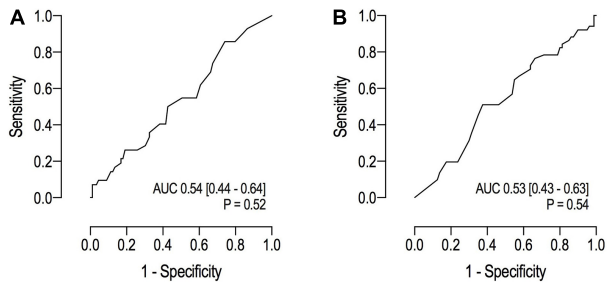

FIGURE 4 | (A) Receiver operating characteristic curves for ICU mortality; **(B)** Receiver operating characteristic curves for hospital mortality.

Correlation With PaO_2/FiO_2

The correlation between RALE score and PaO_2/FiO_2 was weak (R^2 linear = 0.21; **Supplementary Figure 2**). No meaningful association was detectable between the RALE score and PEEP levels recorded at the moment of the CXR.

DISCUSSION

The findings of this *post-hoc* analysis of cohort of well–defined invasively ventilated critically ill patients expected not to be extubated within 24 h can best be summarized as follows: (a) the RALE score is higher in patients with ARDS compared to patients not fulfilling the Berlin Definition for ARDS, (b) the diagnostic performance for ARDS of the RALE score is excellent, with a cutoff of 10 showing excellent sensitivity and moderate specificity; (c) though has poor prognostic value in a mixed cohort of patients with may or may not have ARDS; (d) the RALE score increases from mild to severe ARDS, though this finding was not statistically significant; and (e) the RALE score correlates weakly with the PaO_2/FiO_2.

This study has several strengths. It used the data of a prospective study in which consecutive patients expected to be intubated for at least 24 h were included. The original study as well as the current re–analysis had only few exclusion criteria, increasing its generalizability. Only eight patients were excluded because of a missing chest radiograph. The chest radiographs used for calculating the RALE score were as close as possible to start of invasive ventilation in the ICU, and always with a PEEP $\geq$ 5 cm H_2O. ARDS was diagnosed using the present "gold standard," i.e., the Berlin Definition for ARDS, applied by independent physicians with extensive experience in using it. Finally, as a measure against bias, clinicians involved in applying the criteria in the Berlin Definition for ARDS were unaware of the RALE score, and *vice versa*, the investigators calculating the RALE score remained blinded for the presence of absence of ARDS.

One salient finding was the high agreement between the two researchers with regard to the RALE score in individual cases. This new numeric score seemed easy to learn and calculate, and gave a uniform interpretation of chest radiographs, in line with the seminal report on use of the RALE score (Warren et al., 2018). It is noticeable that the Berlin Definition investigators demonstrated low interobserver reliability which did not improve with training (Goddard et al., 2018). Thus, one could argue to use this new score as a finding to make diagnosing ARDS easier.

The findings of the current study are at least in part in line with the finding in the seminal study on this new score, i.e., that higher RALE scores are found in patients with more injured lungs, according to the PaO_2/FiO_2. One difference between the two studies was that in the current study the RALE score was calculated in much "broader" population of invasively ventilated ICU patients, i.e., not only patients with ARDS, but also patients at risk of this complication. The RALE score demonstrated an excellent diagnostic accuracy for ARDS, and may be taken into consideration in future refinements of the radiological criteria

of the Berlin Definition of ARDS. The increase in RALE score from mild, to moderate and severe ARDS was not statistically significant, in agreement with a recent study focusing on the evolution of the RALE score in 108 patients with ARDS (Kotok et al., 2020). However, it must be mentioned that the number of patients with ARDS, in particular severe ARDS, was low.

Although we could not find an association between baseline RALE and mortality, a recent study proposes that the change in RALE score in the first days is associated with survival in ARDS (Jabaudon et al., 2020). Also in patients with pneumonia from coronavirus disease, both the visually scored and RALE score and the ones computed from artificial intelligence algorithms were associated with poor outcomes (Ebrahimian et al., 2021).

While the RALE score had a weak association with ARDS categories based on degree of hypoxemia, scores could independently increase the diagnostic performance and the outcome prediction. This should be tested in future cohorts of invasively ventilated ICU patients. This study has other limitations. The study included a relatively small number of patients, resulting in a low number of patients with ARDS, and especially few patients with severe ARDS. In addition, this was a single center study with all available patients being used without a formal power calculation performed beforehand. It will be important to confirm the results of the current study performing the RALE score in a multicenter setting.

In conclusion, the RALE score provides a reliable interpretation of signs of lung edema on chest radiographs in invasively ventilated ICU patients. The RALE score has an excellent diagnostic accuracy for ARDS in such patients but has only a weak correlation with PaO_2/FiO_2 and no associations with patient outcomes. Additional validation of the cutoff and performance of the RALE score is needed in larger cohorts.

DATA AVAILABILITY STATEMENT

The raw data supporting the conclusions of this article will be made available by the authors, without undue reservation.

ETHICS STATEMENT

Ethical review and approval was not required for the study on human participants in accordance with the local legislation and institutional requirements. Written informed consent for participation was not required for this study in accordance with the national legislation and the institutional requirements.

AUTHOR CONTRIBUTIONS

MJS, LW, CC, MW, SG, CZ, and LP contributed to conception and design of the study. CZ, LP, and VL organized the database. CZ and LP performed the statistical analysis. CZ wrote the first draft of the manuscript. LP, VL, AA, and MRS wrote sections of the manuscript. MJS and LP supervised the project and revised the present manuscript. All authors contributed to the manuscript revision, read, and approved the submitted version.

SUPPLEMENTARY MATERIAL

The Supplementary Material for this article can be found online at: https://www.frontiersin.org/articles/10.3389/fphys.2021.672823/full#supplementary-material

REFERENCES

ARDS Definition Task Force, Ranieri, V. M., Rubenfeld, G. D., Thompson, B. T., Ferguson, N. D., Caldwell, E., et al. (2012). Acute respiratory distress syndrome. *JAMA.* 307, 2526–2533. doi: 10.1001/jama.2012.5669

Ebrahimian, S., Homayounieh, F., Rockenbach, M. A. B. C., Putha, P., Raj, T., Dayan, I., et al. (2021). Artificial intelligence matches subjective severity assessment of pneumonia for prediction of patient outcome and need for mechanical ventilation: a cohort study. *Sci. Rep.* 11:858. doi: 10.1038/s41598-020-79470-0

Goddard, S. L., Rubenfeld, G. D., Manoharan, V., Dev, S. P., Laffey, J., Bellani, G., et al. (2018). The randomized educational acute respiratory distress syndrome diagnosis study: a trial to improve the radiographic diagnosis of acute respiratory distress syndrome. *Crit. Care Med.* 46, 743–748. doi: 10.1097/ccm.0000000000003000

Graat, M. E., Hendrikse, K. A., Spronk, P. E., Korevaar, J. C., Stoker, J., and Schultz, M. J. (2006). Chest radiography practice in critically ill patients: a postal survey in the Netherlands. *BMC Med. Imaging* 6:8. doi: 10.1186/1471-2342-6-8

Graat, M. E., Stoker, J., Vroom, M. B., and Schultz, M. J. (2005). Can we abandon daily routine chest radiography in intensive care patients? *J. Intensive Care Med.* 20, 238–246. doi: 10.1177/0885066605277212

Jabaudon, M., Audard, J., Pereira, B., Jaber, S., Lefrant, J. Y., Blondonnet, R., et al. (2020). Early changes over time in the radiographic assessment of lung edema score are associated with survival in ARDS. *Chest* 158:2394.

Keszei, A. P., Novak, M., and Streiner, D. L. (2010). Introduction to health measurement scales. *J. Psychosom. Res.* 68, 319–323. doi: 10.1016/j.jpsychores.2010.01.006

Kotok, D., Yang, L., Evankovich, J. W., Bain, W., Dunlap, D. G., Shah, F., et al. (2020). The evolution of radiographic edema in ARDS and its association with clinical outcomes: a prospective cohort study in adult patients. *J. Crit. Care* 56, 222–228. doi: 10.1016/j.jcrc.2020.01.012

Kottner, J., Audige, L., Brorson, S., Donner, A., Gajewski, B. J., Hróbjartsson, A., et al. (2011). Guidelines for reporting reliability and agreement studies (GRRAS) were proposed. *Int. J. Nurs. Stud.* 48, 661–671. doi: 10.1016/j.ijnurstu.2011.01.016

Patrick, D. L., and Chiang, Y. P. (2000). Measurement of health outcomes in treatment effectiveness evaluations: conceptual and methodological challenges. *Med. Care.* 38(suppl. 9)II, 14–25. doi: 10.1097/00005650-200009002-00005

Pisani, L., Vercesi, V., van Tongeren, P. S. I., Lagrand, W. K., Leopold, S. J., Huson, M. A. M., et al. (2019). The diagnostic accuracy for ARDS of global versus regional lung ultrasound scores - a post hoc analysis of an observational study in invasively ventilated ICU patients. *Intensive Care Med. Exp.* 7(Suppl. 1):44. doi: 10.1186/s40635-019-0241-6

Rubenfeld, G. D., Caldwell, E., Granton, J., Hudson, L. D., and Matthay, M. A. (1999). Interobserver variability in applying a radiographic definition for ARDS. *Chest* 116, 1347–1353. doi: 10.1378/chest.116.5.1347

Šimundić, A.-M. (2009). Measures of diagnostic accuracy: basic definitions. *EJIFCC* 19, 203–211.

Trotman-Dickenson, B. (2003). Radiology in the intensive care unit (Part I). *J. Int. Care Med.* 18, 198–210. doi: 10.1177/0885066603251897

Vercesi, V., Pisani, L., van Tongeren, P. S. I., Lagrand, W. K., Leopold, S. J., Huson, M. M. A., et al. (2018). External confirmation and exploration of the kigali modification for diagnosing moderate or severe ARDS. *Intensive Care Med.* 44, 523–524. 10.1007/s00134-018-5048-5

Warren, M. A., Zhao, Z., Koyama, T., Bastarache, J. A., Shaver, C. M., Semler, M. W., et al. (2018). Severity scoring of lung oedema on the chest radiograph is associated with clinical outcomes in ARDS. *Thorax* 73, 840–846. doi: 10.1136/thoraxjnl-2017-211280

Youden, W. J. (1950). Index for rating diagnostic tests. *Cancer* 3, 32–35. doi: 10.1002/1097-0142(1950)3:1<32::aid-cncr2820030106>3.0.co;2-3

Conflict of Interest: The authors declare that the research was conducted in the absence of any commercial or financial relationships that could be construed as a potential conflict of interest.

frontiers in Physiology

SYSTEMATIC REVIEW
published: 04 June 2021
doi: 10.3389/fphys.2021.666941

Assessment of the Effect of Recruitment Maneuver on Lung Aeration Through Imaging Analysis in Invasively Ventilated Patients: A Systematic Review

Charalampos Pierrakos[1,2]*, *Marry R. Smit*[1], *Laura A. Hagens*[1], *Nanon F. L. Heijnen*[3], *Markus W. Hollmann*[4,5], *Marcus J. Schultz*[1,4,6,7], *Frederique Paulus*[1] and *Lieuwe D. J. Bos*[1,4,8]

[1] Department of Intensive Care, Amsterdam UMC, University of Amsterdam, Amsterdam, Netherlands, [2] Department of Intensive Care, Brugmann University Hospital, Université Libre de Bruxelles, Brussels, Belgium, [3] Department of Intensive Care, Maastricht UMC+, Maastricht, Netherlands, [4] Laboratory of Experimental Intensive Care and Anesthesiology, Amsterdam UMC, University of Amsterdam, Amsterdam, Netherlands, [5] Department of Anesthesiology, Amsterdam UMC, University of Amsterdam, Amsterdam, Netherlands, [6] Mahidol–Oxford Tropical Medicine Research Unit (MORU), Mahidol University, Bangkok, Thailand, [7] Nuffield Department of Medicine, University of Oxford, Oxford, United Kingdom, [8] Department of Respiratory Medicine, Amsterdam UMC, University of Amsterdam, Amsterdam, Netherlands

OPEN ACCESS

Edited by:
Lorenzo Ball, University of Genoa, Italy

Reviewed by:
Carmen Silvia Valente Barbas, University of São Paulo, Brazil
Alysson Roncally Silva Carvalho, University of Porto, Portugal

***Correspondence:**
Charalampos Pierrakos
charalampos.pierrakos@chu-brugmann.be

Specialty section:
This article was submitted to Respiratory Physiology, a section of the journal Frontiers in Physiology

Received: *11 February 2021*
Accepted: *20 April 2021*
Published: *04 June 2021*

Citation:
Pierrakos C, Smit MR, Hagens LA, Heijnen NFL, Hollmann MW, Schultz MJ, Paulus F and Bos LDJ (2021) Assessment of the Effect of Recruitment Maneuver on Lung Aeration Through Imaging Analysis in Invasively Ventilated Patients: A Systematic Review. Front. Physiol. 12:666941. doi: 10.3389/fphys.2021.666941

Background: Recruitment maneuvers (RMs) have heterogeneous effects on lung aeration and have adverse side effects. We aimed to identify morphological, anatomical, and functional imaging characteristics that might be used to predict the RMs on lung aeration in invasively ventilated patients.

Methods: We performed a systemic review. Studies included invasively ventilated patients who received an RM and in whom re-aeration was examined with chest computed tomography (CT), electrical impedance tomography (EIT), and lung ultrasound (LUS) were included.

Results: Twenty studies were identified. Different types of RMs were applied. The amount of re-aerated lung tissue after an RM was highly variable between patients in all studies, irrespective of the used imaging technique and the type of patients (ARDS or non-ARDS). Imaging findings suggesting a non-focal morphology (i.e., radiologic findings consistent with attenuations with diffuse or patchy loss of aeration) were associated with higher likelihood of recruitment and lower chance of overdistention than a focal morphology (i.e., radiological findings suggestive of lobar or segmental loss of aeration). This was independent of the used imaging technique but only observed in patients with ARDS. In patients without ARDS, the results were inconclusive.

Conclusions: ARDS patients with imaging findings suggestive of non-focal morphology show most re-aeration of previously consolidated lung tissue after RMs. The role of imaging techniques in predicting the effect of RMs on re-aeration in patients without ARDS remains uncertain.

Keywords: electrical impedance tomography, computed tomography, lung ultrasound, overdistention, recruitment maneuvers, ARDS

INTRODUCTION

A lung recruitment maneuver (RM) is a dynamic and transient increase in transpulmonary pressure aiming at (re-)opening collapsed lung parts and increasing end-expiratory lung volume (Lapinsky and Mehta, 2005). In theory, opening of collapsed or "non-aerated" lung areas decreases shunt, improving both oxygenation and removal of CO_2 (Hedley-Whyte et al., 1964; Neumann et al., 1999). Furthermore, atelectatic areas might cause stress on, or deformation of, aerated regions, resulting in additional injury of lung parenchyma (Gattinoni et al., 2012). Accordingly, decreasing atelectatic areas with RM could protect the lungs, a strategy often referred to as the "open lung concept" (Hes, 2015).

The value of RMs without the use of any imaging monitoring is disputed, as, so far, clinical studies have failed to show benefit with regard to patient-centered outcomes—and even suggest harm (Cavalcanti et al., 2017). The absence of net benefit might be explained by the heterogeneity and unpredictable effects of RMs on lung aeration (Sahetya and Brower, 2017; Mancebo et al., 2019). The pressure threshold that should be overpassed during RMs to open atelectatic lung units is multifactorial and cannot be calculated precisely (Sahetya and Brower, 2017; Gattinoni et al., 2017). Furthermore, any increase in airways pressure will result in higher pressures in all lung parts, also those that are "open," and these areas might be harmed by overdistention (Gattinoni et al., 2019). Thus, the benefit of RMs needs to be balanced between re-aeration and overdistention.

Changes in lung morphology indicative of re-aeration or overdistention can be estimated using lung imaging (Gattinoni et al., 2020). Various imaging techniques like chest computed tomography (CT), electrical impedance tomography (EIT), and lung ultrasound (LUS) have been suggested to be useful to evaluate lung morphology and function in an individual patient (Godet et al., 2015). We performed a systematic review to describe imaging-based methods to assess re-aeration after RMs in patients receiving invasive ventilation at the intensive care unit or the operating room. In this review, we focus on the variability of imaging-based method definitions and the clinical utility of baseline imaging characteristics.

METHODS

This protocol was designed in accordance with Preferred Reporting Items for Systematic Reviews and Meta-Analyses (PRISMA) guidelines (Liberati et al., 2009). The study protocol has been registered on PROSPERO (CRD42020188056).

Eligibility Criteria

The PICO used to define eligibility criteria are the following: (1) *P* (population): invasive mechanical ventilation either in the intensive care unit (ICU) or the operating room (OR) with or without ARDS, (2) *I* (intervention): recruitment maneuver of any sort, (3) *C* (comparison): LUS and/or EIT and/or CT was used to evaluate re-aeration of previously consolidated lung tissue, (4) *O*: baseline image characteristics were reported and evaluated for their predictive value of recruitment.

Only original studies written in English were included, whereas animal studies, case reports, comments, letters, and studies that enrolled pediatric patients were not included.

Information Sources and Search

We searched EMBASE using PubMed on December 15, 2020 using the following key words: *((“diagnostic imaging” [Subheading] OR (“diagnostic” [All Fields] AND “imaging” [All Fields]) OR “diagnostic imaging” [All Fields] OR “ultrasound” [All Fields] OR “ultrasonography” [MeSH Terms] OR “ultrasonography” [All Fields] OR “ultrasound” [All Fields] OR “ultrasonics” [MeSH Terms] OR “ultrasonics” [All Fields]) OR (“ct” [All Fields]) OR “computed tomography” [All Fields]) OR ((“IEEE Int Conf Electro Inf Technol” [Journal] OR “eit” [All Fields]) OR “(electrical impedance tomography” [All Fields])) AND ((“positive-pressure respiration” [MeSH Terms] OR (“positive-pressure” [All Fields] AND “respiration” [All Fields]) OR “positive-pressure respiration” [All Fields] OR “peep” [All Fields]) AND Recruitment [All Fields]).*

Study Selection

The identified studies were assessed for inclusion criteria based on title and then on abstract. For all selected papers, the full text was read and discussed between two authors (CP and LB). Studies that fulfilled the inclusion criteria were included in this review.

Data Collection

For each included study, we collected data related to patient characteristics and whether they referred to ARDS patients or not. The type of recruitment maneuver that was used was categorized as (a) sustained inflation, (b) sigh, (c) pressure-control ventilation, and (d) variable ventilation (Rocco et al., 2010). We recorded the criteria that were used to define a "responder" to recruitment and the baseline characteristics to identify factors that differentiate between "responders" and "non-responders." For those studies including patients with ARDS, we documented whether authors classified patients as having "focal" (i.e., radiological attenuations with lobar or segmental distributions) or "non-focal" (i.e., radiological attenuation with diffuse or patchy distribution) abnormal lung morphology.

Bias Assessment

The Quality Assessment of Diagnostic Accuracy Studies-2 (QUADAS-2) was used for the assessment of the methodologic quality of selected studies (Whiting, 2011). The four recommended domains (i.e., patient selection, index test, reference standard, and flow/timing) were assessed for low, high, or unclear risk of bias. As for the reference standard domain, CT was considered the "gold standard" for assessing lung re-aeration. Given the insufficient evidence to classify LUS or EIT as adequate reference tests to assess lung aeration, we considered the risk of bias to be high. Concerns regarding applicability for the first three domains were also assessed and scored as low, high, or unclear.

Synthesis of Results

The following data were combined into a table: patient group that was studied, number of patients, type of recruitment and

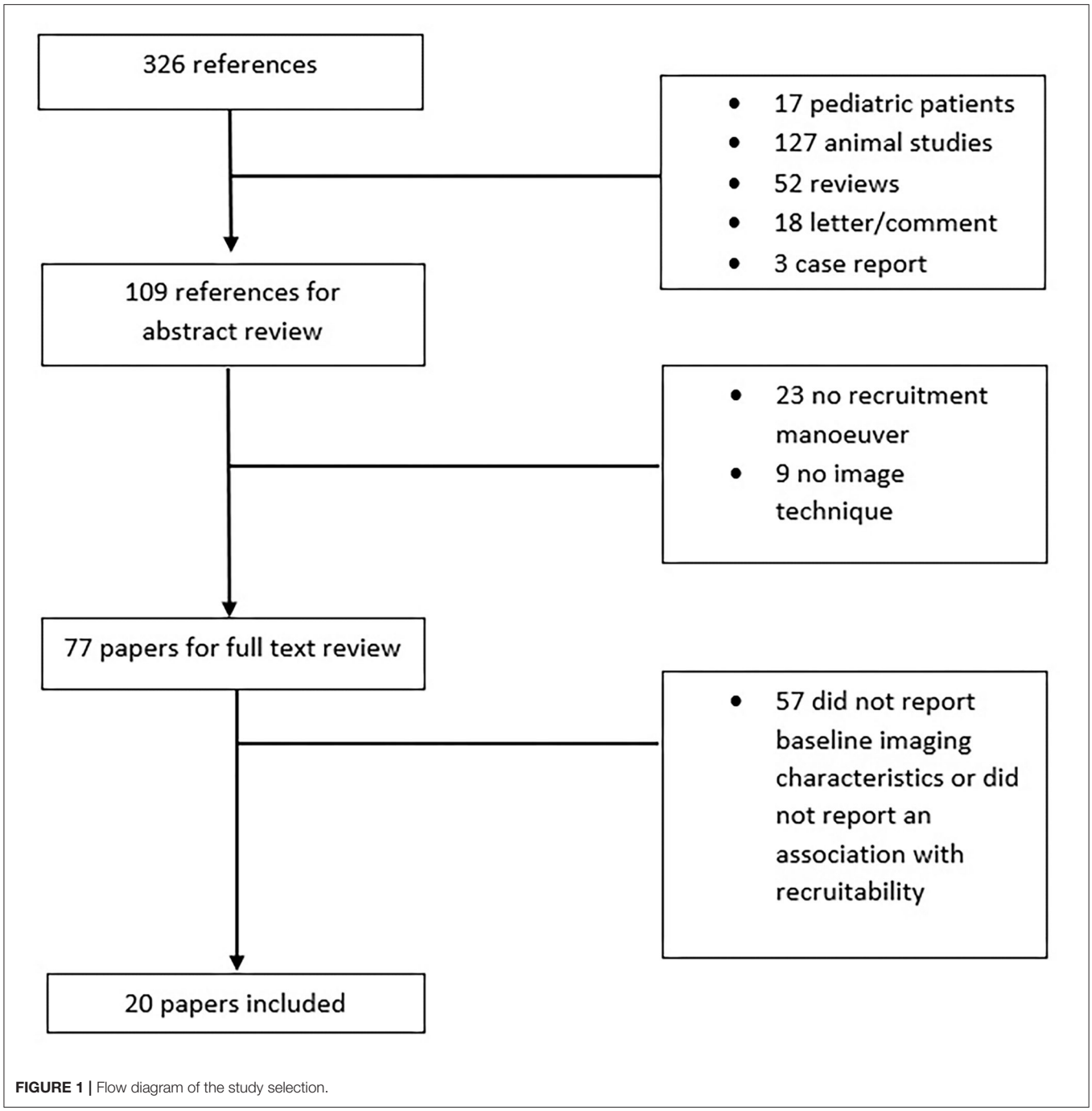

FIGURE 1 | Flow diagram of the study selection.

maximal airway pressure reached, assessment of re-aeration of lung tissue, and criteria to define "responder." The main findings of the study regarding heterogeneity in re-aerated lung tissue and differences between "responders" and "non-responders" were also shown. We further synthesized the current evidence for heterogeneity and prediction of recruitment response in an overview table, stratified per imaging method that was used. Finally, we linked the morphological characteristics derived from different imaging techniques of responders and non-responders in an overview figure.

RESULTS

Included Studies

The described search resulted in 326 articles of which 249 were excluded based on the title and abstract review. Twenty out of the remaining 77 studies were included in this review based on full text review (**Figure 1**) and are summarized in **Table 1**. Seventeen studies included deeply sedated patients, while sedation level was not mentioned in the other three studies. All patients in the included studies were in supine position during RM.

TABLE 1 | Studies included in this review.

References	Patients	N	RM	Pmax	Imaging modality	Recruitment definition method	Outcome
He et al., 2020	ICU (deeply sedated)	30	PC	NG	EIT	Ratio overdistended to recruited pixels	RM resulted in a high variability of the changes in the ration of overdistended to recruited pixels measured with EIT. No differences in the EELI and GI between responders and not responders to RM
Généreux et al., 2020	OR (deeply sedated)	45	SI	30 cm H_2O	LUS	12 areas derived LUS score	RM did not result in a significant improvement in LUS score
Karsten et al., 2019	ICU (NM)	15	Sigh	40 cm H_2O	EIT	Local compliance (ODCL index)	RM resulted in the complete disappearance of collapsed units (ODCLindex) in all studied patients, but there was a high variation of the overdistention extension (19 ± 17%). After RM, the proportion of collapsed units was highly variable (0–50%), independent of the selected PEEP (5–13 cm H_2O)
Zhao et al., 2019	ARDS (deeply sedated)	3	Sigh	35 cm H_2O	EIT	Increase in ventilation in dependent areas	Those with ventilation distribution predominantly in the most dependent regions are likely non-responders to RM
Camporota et al., 2019	ARDS (sedation level not mentioned)	47	SI	45 cm H_2O	CT	Proportion of re-aerated lung tissue compared with the total lung weight	RM resulted in a variable change in aerated lung tissue with a mean of 24.3% (−2–76). All patients were on ECMO and had a very high percentage of non-aerated lung tissue. Non-recruitable tissue varied between 50 and 80% of total lung weight
Eichler et al., 2018	OR (deeply sedated)	37	Sigh	40 cm H_2O	EIT	EELI slope	A downward course of EELI may indicate the need for RM ($EELI_{30sec}/EELI_{0sec}$ <1). This pattern of EELI inversed after RM and PEEP increase
Tang et al., 2017	ARDS (deeply sedated)	40	PC	35 cm H_2O	LUS	Regasification score	RM resulted in significant changes in aeration in the anterior and lateral areas, but not in the posterior areas
Longo et al., 2017	OR (deeply sedated)	40	Sigh	35 cm H_2O	LUS	Resolution of atelectasis	RM resolved atelectasis in all but 2/20 (10%) of the patients. The RM effect was assessed with TOE
Eronia et al., 2017	ICU (deeply sedated)	16	SI	40 cm H_2O	EIT	EELI slope	A downward course of end-expiratory lung impedance may indicate the need for RM (10 min delta EELI >10%). This pattern of EELI inversed after RM and PEEP increase
Chiumello et al., 2016	ARDS (sedation level not mentioned)	22	Sigh	NG	CT	Proportion of re-aerated lung tissue compared with the total lung weight	Responders to RM (increase in tissue >-100 HU) had higher amount of non-inflated tissue at PEEP 5 cmH_2O ($r^2 = 0.44$). This relation disappears when responders are defined by increase in tissue >-500 HU ($r^2 = 0.002$)
*Caironi et al., 2015	ARDS (deeply sedated)	14	PC	45 cm H_2O	CT	Proportion of re-aerated lung tissue compared with the total lung weight	Responders to RM had higher total lung weights. RM results in a highly variable recruitment of non-aerated lung tissue. This is independent of the severity of disease and baseline PEEP
de Matos et al., 2012	ARDS (deeply sedated)	51	PC	60 cm H_2O	CT	Sectional lung weight re-aerated	RM resulted in variable aeration of previously non-aerated lung tissue: 45% (25–53). Responders to RM did not have a higher initial amount of non-aerated tissue (PEEP 10 cmH_2O; $r^2 = 0.03$)
Rode et al., 2012	ARDS (deeply sedated)	17	Sigh	30 cm H_2O	LUS	Crater-like consolidations' borders leveling and abutting pleural line	RM resolved most (92%) of crater–like subpleural consolidations visible during ZEEP
Bouhemad et al., 2011	ARDS (deeply sedated)	40	SI	40 cm H_2O	LUS	Increase lung re-aeration score	RM was unlikely to affect consolidations in posterior and caudal regions. RM responders were more likely to have non-focal rather than focal lung morphology

(Continued)

TABLE 1 | Continued

References	Patients	N	RM	Pmax	Imaging modality	Recruitment definition method	Outcome
Constantin et al., 2010	ARDS (deeply sedated)	19	SI	40 cm H_2O	CT	Proportion of re-aerated lung volume compared with the total lung volume	RM responders were more likely to have non-focal than focal lung morphology at ZEEP. Hyperinflation during RM is predicted by the lung volume between −800 and −900 HU in ZEEP ($r^2 = 0.77$)
*Caironi et al., 2010	ARDS (deeply sedated)	68	PC	45 cm H_2O	CT	Proportion of re-aerated lung tissue compared with the total lung weight	RM responders had more opening and closing lung tissue at PEEP 5 cm H_2O. RM responders had a homogeneous cephalo-caudal distribution of non-aerated areas, while non-responders had a linear cephalo-caudal increase in non-aerated areas
Gattinoni et al., 2006	ARDS (sedation level not mentioned)	68	PC	45 cm H_2O	CT	Proportion of re-aerated lung tissue compared with the total lung weight	RM had a variable effect on opening of lung tissue (median 9% range −10–60%). RM response was predicted by recruitment of lung tissue after increase in PEEP from 5 to 15 cm H_2O ($r^2 = 0.72$). RM response was predicted by the amount of non-aerated tissue at PEEP 5 cm H_2O
Borges et al., 2006	ARDS (deeply sedated)	26	PC	60 cm H_2O	CT	Proportion of re-aerated lung tissue compared with the total lung weight and proportion of re-aerated lung volume compared with the total lung volume	RM shows different responses with variation in lung opening pressures. RM at 40 cmH2O resulted in response in <50%, while this increased to 93% at 60 cm H_2O
*Nieszkowska et al., 2004	ARDS (sedation level not mentioned)	32	Sigh	NG	CT	Volume increase in non-aerated or poorly aerated areas	RM responders more frequently had non-focal morphology rather than focal (lobar) morphology (recruited volume: 572 ± 25 vs. 249 ± 159 ml). RM did not result in overinflation in patients with a diffuse morphology
Vieira et al., 1999	ARDS (sedation level not mentioned)	14	Sigh	45 cm H_2O	CT	Total lung volume increases	RM responders more frequently had a non-focal morphology. RM responders more frequently had a biphasic lung density histogram with a peak at −700 to −900 HU >50 ml at ZEEP is related to a higher amount of overinflation with RM

OR, operating room; N, number of enrolled patients; Pmax, maximum pressure used for recruitment maneuver; RM, lung recruitment maneuver; SI, sustained inflation; PC, pressure control; LUS, lung ultrasound; EIT, electrical impedance tomography; CT, computed tomography; ODCL, overdistention collapse index; PEEP, positive end-expiratory pressure; ZEEP, zero end-expiratory pressure; EELI, end expiratory lung impedance; LIL, left inferior lobe; TOE, transesophageal echocardiography; HU, Hounsfield units; COPD, chronic obstructive pulmonary disease.
**Retrospective study.*

The majority of the included studies enrolled ARDS patients exclusively (14 studies, 70%). Three studies (15%) included a mixed population of intensive care unit patients, and in three studies (15%), patients undergoing elective operation were included. Three studies had the primary goal of quantification of potential for lung recruitment (Gattinoni et al., 2006; Camporota et al., 2019) or recruitment prediction (Constantin et al., 2010). Regarding lung imaging techniques, most of the studies (10 studies, 50%) assessed chest CT scan, followed by LUS (five studies, 25%) and EIT (five studies, 25%). Notably, chest CT was only used in studies that included patients with ARDS.

Quality characteristics of the included studies, in relation to the aim of this systematic review, are presented in **Supplementary Table 1**. In two studies, there was a high concern regarding applicability of population selection. These two studies included a highly selective population, i.e., patients after cardiac surgery (Longo et al., 2017) or patients who underwent tracheostomy (Eichler et al., 2018).

Recruitment Methodology and Identification of "Responders"

In eight studies (42%), a sigh, in six studies (31%), a pressure-control method, and in five studies (26%), a sustained inflation were used for the RM (**Table 1**). Applied maximum airway pressure varied widely, between 30 and 60 cm H_2O. Classification of responders depended on the imaging technique used (**Table 2**). None of the studies defined the criteria to identify "responders" beforehand. Patients were classified *post-hoc* as "responders" and "non-responders" based on the median value of the study population in studies that quantified re-aeration by CT imaging. Recruitment "responders" generally had an increase in aeration of non-aerated lung tissue of more than 20% (**Figure 2**).

TABLE 2 | Findings related to the assessment of recruitment after recruitment maneuver application.

Imaging modality	Definition of "recruitment"	Base-line PEEP	Maximum applied pressure (mean and range)
LUS	Decrease four points in LUS score (Généreux et al., 2020) Maximum increase in regasification score (Tang et al., 2017) Disappearance of atelectasis or B-lines (Bouhemad et al., 2011; Rode et al., 2012; Longo et al., 2017)	ZEEP (Bouhemad et al., 2011; Rode et al., 2012; Tang et al., 2017; Généreux et al., 2020), 6 cm H_2O (Longo et al., 2017)	34 cm H_2O [30–40]
EIT	Any decrease in ODCLindex (Karsten et al., 2019) Reverse in EELI ratio from <1 to >1 (Eronia et al., 2017; Longo et al., 2017; Zhao et al., 2019) Changes in the pixel ratio of overdistention to recruitment >15% (He et al., 2020)	ZEEP (Karsten et al., 2019; He et al., 2020), 5–8 cm H_2O (Zhao et al., 2019), PEEP/FiO_2 table PEEP(Eronia et al., 2017), 8 cm H_2O (Eichler et al., 2018)	39 cm H_2O [35–40]
CT	Decrease in non-aerated weight of lung (>-100 HU) (Borges et al., 2006; Gattinoni et al., 2006; Caironi et al., 2010, 2015; de Matos et al., 2012; Chiumello et al., 2016; Camporota et al., 2019) Decrease in non-aerated and poorly aerated weight of lung (>-500 HU; Chiumello et al., 2016) Increase in the volume of gas penetrating in non-aerated areas (>-500 HU; Borges et al., 2006) Increase in the volume of gas penetrating in non-aerated and poorly aerated areas (>-500 HU; Vieira et al., 1999; Nieszkowska et al., 2004; Constantin et al., 2010)	ZEEP (Vieira et al., 1999; Nieszkowska et al., 2004; Constantin et al., 2010), 5 cm H_2O (Gattinoni et al., 2006; Constantin et al., 2010; Caironi et al., 2015; Chiumello et al., 2016; Camporota et al., 2019), 10 cm H_2O (de Matos et al., 2012), 5–10 cm H_2O (Borges et al., 2006)	48 cm H_2O [40–60]

PEEP, positive end-expiratory pressure; ZEEP, zero end-expiratory pressure; LUS, lung ultrasound; EIT, electrical impedance tomography; CT, computed tomography; EELI, end expiratory lung impedance; HU, Hounsfield units; ODCL, overdistention collapse index.

Heterogeneity in Re-aeration and Prediction of Positive Response to RM

Re-aeration after RM varied widely between studies, independent of the used image technique (**Table 3**). Unsurprisingly, most CT imaging studies showed that around 50% of patients are "non-responders" to recruitment because the median value was used as the cutoff value (Borges et al., 2006; Gattinoni et al., 2006; Caironi et al., 2015; Vieira et al., 1999; Camporota et al., 2019). Studies that used other imaging techniques did not mention the proportion of "non-responders," though recruitment was described as "highly variable" (Karsten et al., 2019; Généreux et al., 2020).

Imaging findings related to the amount of re-aerated lung tissue in patients with ARDS were the extent of lost aeration before RM, the distribution of non-aerated areas (craniocaudal and anteroposterior distribution), the morphology of non-aerated areas (e.g., crater-like consolidation), and functional lung characteristics related to tidal recruitment (tidal opening/closing tissue; **Table 3**). Findings that are more likely to resemble a diffuse or patchy loss of aeration (i.e., non-focal morphology) were suggestive of an increased likelihood of positive response to RMs (**Figure 3**). This was independent on the image technique employed.

Only one study addressed the prediction of response to RM in patients in the operating room. A decreasing pattern of end-expiratory lung impedance (EELI) evaluated with EIT was found to be related to the amount of re-aerated lung tissue (Eichler et al., 2018; **Table 3**).

Overdistention

Overdistention was assessed in studies that used CT or EIT only, as LUS cannot be used for this purpose. Studies employing CT imaging showed the average percentage of overdistended lung volume to vary between 0 and 20% (**Figure 2**). EIT studies revealed the average overdistention secondary to RMs across patients to range between 5 and 30% (Karsten et al., 2019). Nevertheless, local overdistention in non-dependent areas may exceed 60% of that area (Eronia et al., 2017). "Non-responders" identified by CT had a higher increase in hyperinflated lung tissue compared with "responders" (**Figure 2**).

DISCUSSION

The results of this systematic review can be summarized as follows: (a) data that quantify the potential for lung recruitment based on imaging are limited, (b) the definition of positive response to RMs was highly variable, and (c) patients with imaging characteristics suggestive for a non-focal morphology of ARDS seemed to show more re-aeration at RMs with moderate inspiratory pressures.

The included studies used a wide range of maximum airway pressures to recruit lung tissue. Most collapsed areas can be

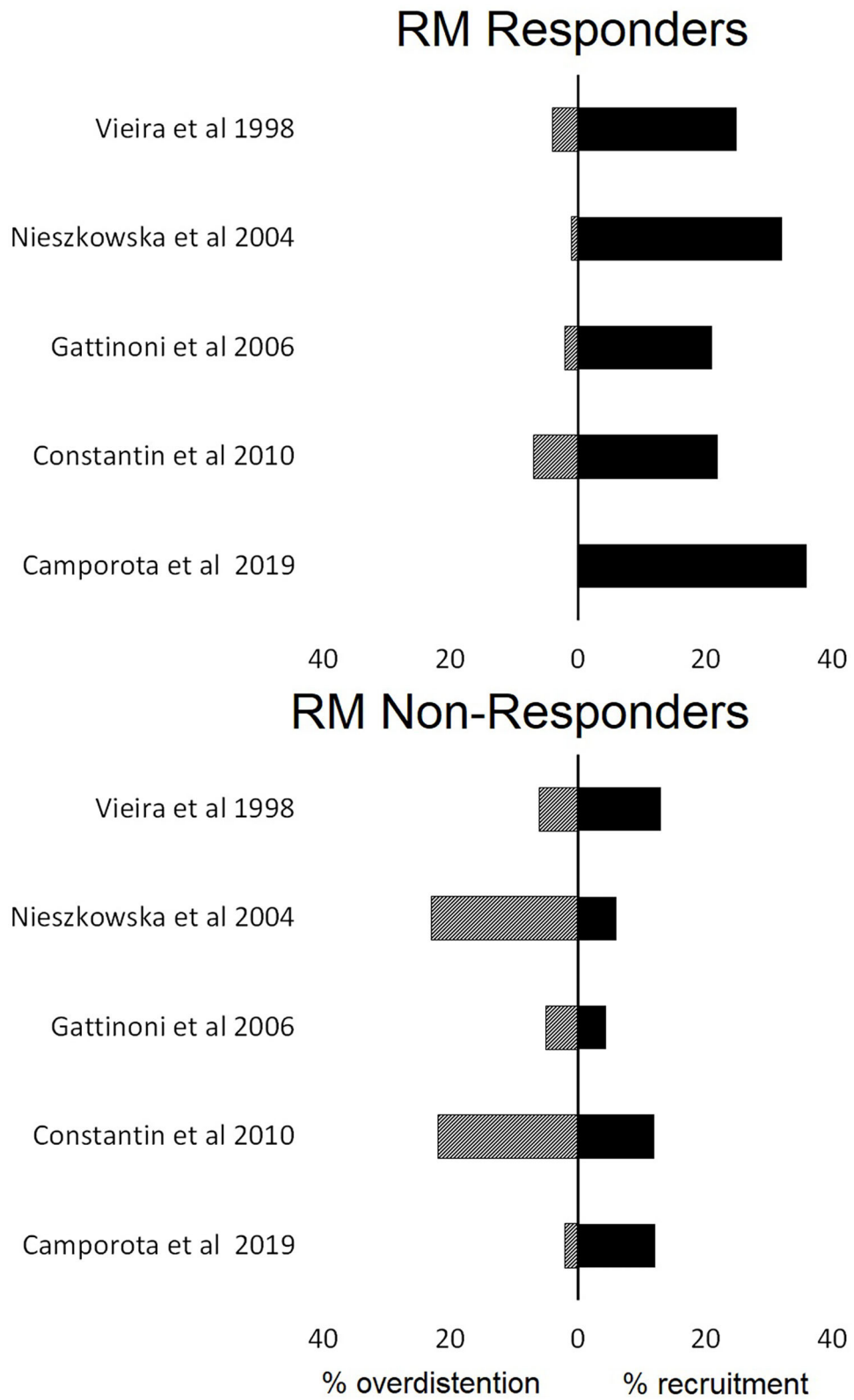

FIGURE 2 | The proportions of lung recruitment and lung overdistention in patients who were characterized responders or not responders to lung recruitment maneuvers (RM) based on computed tomography findings.

TABLE 3 | Observed recruitment maneuver re-aeration effect and findings related to potential for lung re-aeration after recruitment maneuver according to the imaging module and the presence or not ARDS.

	ARDS	Non-ARDS
Observed lung re-aeration with imaging analysis		
LUS	8% of evaluated consolidations did not respond to RM (Rode et al., 2012)	No change of LUS score after RM (Généreux et al., 2020)
	27% of patients had a re-aeration score ≥8 and an increase in lung volume more than 600 ml after RM (Bouhemad et al., 2011)	10% of patients do not respond to RM (Longo et al., 2017)
EIT	Extremely high variability in changes of the ratio between overdistention and collapsed ration (He et al., 2020)	Variable* compromise between the extension of lung collapse and overdistention after RM (Karsten et al., 2019)
CT	High variability* of potential recruitment tissue (Caironi et al., 2015)	
	Potential recruitable tissue: 45% (range 5–75%; de Matos et al., 2012)	
	Potential recruitable tissue: 9% (range −10–60%; Gattinoni et al., 2006)	
	Potential recruitable tissue: 24.3% (range −2–76; Camporota et al., 2019)	
	High variability of opening lung pressures (Caironi et al., 2015)	
Findings that predicted more lung re-aeration		
LUS	Anterior located consolidations (Bouhemad et al., 2011; Tang et al., 2017)	
	Crater-like sub-pleural consolidations (Rode et al., 2012)	
EIT	Predominant ventilation in non-dependent areas (Zhao et al., 2019)	Decreasing pattern of EELI (delta EELI >10% or EELI index <1; Eronia et al., 2017; Eichler et al., 2018)
CT	Not aerated tissue (>-100 HU) >25–30% of total lung tissue (Gattinoni et al., 2006; Chiumello et al., 2016)	
	Non-focal lung morphology (Nieszkowska et al., 2004; Constantin et al., 2010)	
	Homogeneous cephalo-caudal distribution of 40–50% non-aeration area (Caironi et al., 2010)	
	Opening and closing lung tissue (141 ± 81 g; Caironi et al., 2010)	

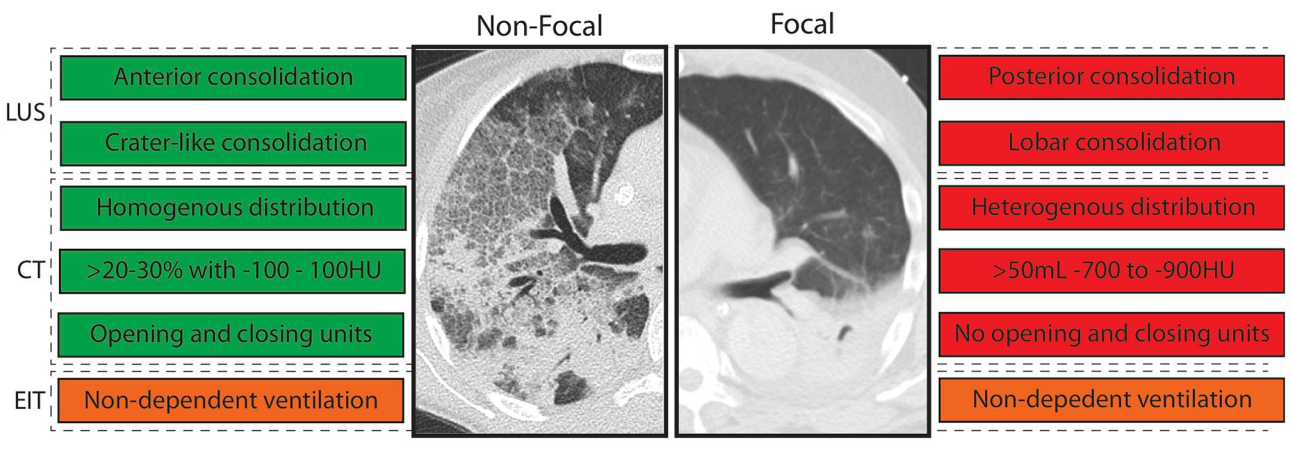

FIGURE 3 | Imaging abnormalities that predicted response to recruitment maneuvers (RM) stratified per morphology. LUS, lung ultrasound; EIT, electrical impedance tomography; CT, computed tomography; HU, Houndsfield units; green, imaging abnormality in line with responder to RM; red, imaging abnormality in line with non-responder to RM; orange, imaging abnormality in line with responder with high uncertainty. Text boxes on the left: consistent with non-focal morphology. Text boxes on the right: consistent with focal morphology.

opened, but frequently only at very high airway pressures (Cressoni et al., 2017). Borges et al. found opening pressures of 60 cmH_2O in patients with ARDS to be common, with coexistence of areas opening at lower and higher pressures in the majority of patients (Borges et al., 2006). In clinical practice, maximum airway pressure is often selected based on the hemodynamic fragility of the patient rather than the expected pressure needed for lung recruitment (Santos et al., 2015). This might explain why CT compared with LUS and EIT studies revealed higher recruitment pressures as transfer for CT imaging requires more hemodynamically stable patients (Constantin et al., 2019). Recent RCTs suggest airway pressures above 50 cm H_2O to be associated with serious adverse events, even when the patient is exposed to it for a short period of time (Cavalcanti et al., 2017; Hodgson et al., 2019). As the different components that attribute to the compliance of the respiratory system (compliance of the lung and chest wall as well as intra-abdominal pressure) cannot be easily separated in clinical practice (Umbrello and Chiumello, 2018),

assessing the RMs' effect with imaging techniques is important in clinical practice. Rather than defining the pressure at which the lung can be opened, it is more important to determine whether recruitment can be achieved with moderate airway pressures. In other words, when comparing patients with a similar expected risk of side effects due to a transient increase in inspiratory pressures, a patient who responds to the RM with reaeration of previously collapsed lung tissue may still benefit, but a patient without this response may not.

This review also revealed several challenges associated with the quantification of lung *re-aeration* with image technics: there is poor agreement between imaging techniques, and there is no universal definition of recruitment response. Chiumello et al. found poor agreement between CT and LUS with respect to assessment of re-aeration, which is not unexpected since LUS is a semiquantitative method assessing only the subpleural areas (Chiumello et al., 2018). Furthermore, the role of LUS in assessing overdistention is currently unknown (Bouhemad et al., 2015). Pleural line displacement identified with LUS, as well the number of A-lines are relevant indexes that are currently being studied (Martins and Nogué, 2020; Tonelotto et al., 2020). EIT quantifies collapsed lung units based on local changes in compliance (Costa et al., 2009). However, compliance might be more related to the improvement or deterioration of already ventilated lung units than the real recruitment of atelectatic lung units (Chiumello et al., 2016). Even though CT is considered the gold standard in detecting lung recruitment, defining the degree of re-aeration remains challenging. Potentially recruitable lung tissue, determined by CT, is mainly expressed as percentage of total lung volume since absolute values depend on lung dimensions. However, expressing recruitment as percentage implies mathematical coupling with the total atelectatic volume, which is at least debatable (de Matos et al., 2012). Gattinoni et al. introduced the terms "high" and "low" recruitment responders based on the median percentage of potentially recruitable lung tissue determined by CT (Gattinoni et al., 2006). Worth mentioning, different median percentages of potentially recruitable tissue were reported in later studies (Camporota et al., 2019; de Matos et al., 2012), probably due to heterogeneity in inclusion characteristics and application of various maximum airway pressures. Given that recruitment is a continuous spectrum that depends on applied airway pressure and several imaging characteristics, speaking about "responders" from "non-responders" is a false dichotomization.

We set out to determine the role of imaging techniques in predicting the lung response to RM. The main strength of this review is the systematic and integrative approach. We excluded studies that based assessment of recruitment on mechanical or oxygenation variables as those can be influenced by factors other than recruitment of lung tissue, which is also known as the recruitment paradox (Amato and De Santis Santiago, 2016). We also acknowledge several limitations. First, we had to perform secondary analyses of many included studies as they were not intended to quantify potential for lung re-aeration, limiting statistical comparisons between groups. Second, we did not directly compare imaging techniques. Each method has intrinsic limitations, such as visualization of the subpleural region only for LUS and the need for patient transport for CT, which justify preferential use of one technique over another in specific situations. Of note, the definition and method of recruitment varied between studies even when the same image technique was used, which made direct comparisons impossible. Third, given the undefined role of LUS and EIT in the assessment of recruitment, a significant number of trials had an unclear risk of bias.

All features predictive of increased lung re-aeration after RM are consistent with a non-focal morphology of ARDS. Patients with focal ARDS lack, by definition, ventral consolidations not limited to the subpleural space and show a heterogeneous distribution of consolidation with less opening and closing, which renders them very unlikely to be recruitable. In line with this notion, patients with non-focal morphology were typically recruitable, while patients with focal morphology were not (Puybasset et al., 2000; Constantin et al., 2010). Notably, atelectasis is usually located in the dorsal lung areas in patients without lung injury requiring invasive mechanical ventilation (Longo et al., 2017; Pereira et al., 2018) implying a "focal" morphology. This may explain the lack of RM efficiency to increase lung aeration in invasively ventilated patients in the operating room (Généreux et al., 2020). Although the results of this review are not conclusive for patients without ARDS, it stresses the need for further research into lung morphology and its relation to lung re-aeration with robust imaging technics in these patients.

By integrating data from multiple studies to morphological classifications, we present a framework used to better design and interpret future studies. We have to acknowledge that this classification is imperfect, as one EIT study that only included three patients suggested that predominant ventilation in the non-dependent areas predicted recruitment, while this is not a feature that is consistent with non-focal morphology of ARDS. The relation between re-aeration and improvement in ventilation perfusion mismatch and heart function was not evaluated in this review (Karbing et al., 2020). Furthermore, in this review, we investigated the imaging techniques' role in predicting RM effects in deeply sedated patients without considering the optimal level of PEEP that would be required after recruitment to keep the lung open. Rather than a final classification, we suggest that the morphological classification is a good starting point to further improve from, with the addition of other predictors. Furthermore, more attention should be drawn to the quantification of overdistention rather than measurement of re-aeration alone. Balancing the assessment of negative and positive effects may improve our understanding as to what patients may or may not benefit from RMs.

CONCLUSIONS

We conclude that defining positive response to RMs using imaging techniques is challenging and not yet well-elucidated. Variations in RM method, population selection, as well as

different imaging techniques should be taken into consideration in future studies. Given the adverse events associated with high maximum airway pressures, only the lungs of specific patients can be re-aerated with moderate maximum airway pressures. Lung ultrasound and CT characteristics consistent with non-focal morphology of ARDS are predictive of more re-aeration in response to recruitment maneuver. The morphological characteristics related to successful response to RMs in patients without ARDS have not been studied to date.

DATA AVAILABILITY STATEMENT

The original contributions presented in the study are included in the article/**Supplementary Material**, further inquiries can be directed to the corresponding author/s.

AUTHOR CONTRIBUTIONS

CP performed the literature search, drafted the manuscript, and approved the submitted version of the manuscript. MRS, LH, NH, MH, and FP revised the manuscript for critical content and approved the submitted version of the manuscript. MJS and LB conceived the study, revised the manuscript for critical content, and approved the submitted version of the manuscript. All authors contributed to the article and approved the submitted version.

SUPPLEMENTARY MATERIAL

The Supplementary Material for this article can be found online at: https://www.frontiersin.org/articles/10.3389/fphys.2021.666941/full#supplementary-material

REFERENCES

Amato, M. B. P., and De Santis Santiago, R. R. (2016). The recruitability paradox. *Am. J. Respir. Crit. Care Med.* 193, 1192–1194. doi: 10.1164/rccm.201601-0178ED

Borges, J. B., Okamoto, V. N., Matos, G. F., Caramez, M. P., Arantes, P. R., Barros, F., et al. (2006). Reversibility of lung collapse and hypoxemia in early acute respiratory distress syndrome. *Am. J. Respir. Crit. Care Med.* 174, 268–278. doi: 10.1164/rccm.200506-976OC

Bouhemad, B., Brisson, H., Le-Guen, M., Arbelot, C., Lu, Q., and Rouby, J. J. (2011). Bedside ultrasound assessment of positive end-expiratory pressure-induced lung recruitment. *Am. J. Respir. Crit. Care Med.* 183, 341–347. doi: 10.1164/rccm.201003-0369OC

Bouhemad, B., Mongodi, S., Via, G., and Rouquette, I. (2015). Ultrasound for "lung monitoring" of ventilated patients. *Anesthesiology* 122, 437–447. doi: 10.1097/ALN.0000000000000558

Caironi, P., Carlesso, E., Cressoni, M., Chiumello, D., Moerer, O., Chiurazzi, C., et al. (2015). Lung recruitability is better estimated according to the Berlin definition of acute respiratory distress syndrome at standard 5 cm H2O rather than higher positive end-expiratory pressure: a retrospective cohort study. *Crit. Care Med.* 43, 781–790. doi: 10.1097/CCM.0000000000000770

Caironi, P., Cressoni, M., Chiumello, D., Ranieri, M., Quintel, M., Russo, S. G., et al. (2010). Lung opening and closing during ventilation of acute respiratory distress syndrome. *Am. J. Respir. Crit. Care Med.* 181, 578–586. doi: 10.1164/rccm.200905-0787OC

Camporota, L., Caricola, E. V., Bartolomeo, N., Di Mussi, R., Wyncoll, D. L. A., Meadows, C. I. S., et al. (2019). Lung recruitability in severe acute respiratory distress syndrome requiring extracorporeal membrane oxygenation. *Crit. Care Med.* 47,1177–1183. doi: 10.1097/CCM.0000000000003837

Cavalcanti, A. B., Suzumura, É. A., Laranjeira, L. N., Paisani, D. M., Damiani, L. P., Guimarães, H. P., et al. (2017). Effect of lung recruitment and titrated Positive End-Expiratory Pressure (PEEP) vs low PEEP on mortality in patients with acute respiratory distress syndrome - a randomized clinical trial. *JAMA* 318, 1335–1345. doi: 10.1001/jama.2017.14171

Chen, L., Del Sorbo, L., Grieco, D. L., Junhasavasdikul, D., Rittayamai, N., Soliman, I., et al. (2019). Potential for lung recruitment estimated by the recruitment-to-inflation ratio in acute respiratory distress syndrome. *Am. J. Respir. Crit. Care Med.* 201, 178–187. doi: 10.1164/rccm.201902-0334OC

Chiumello, D., Marino, A., Brioni, M., Cigada, I., Menga, F., Colombo, A., et al. (2016). Lung recruitment assessed by respiratory mechanics and computed tomography in patients with acute respiratory distress syndrome what is the relationship? *Am. J. Respir. Crit. Care Med.* 193, 1254–1263. doi: 10.1164/rccm.201507-1413OC

Chiumello, D., Mongodi, S., Algieri, I., Vergani, G. L., Orlando, A., and Via, G. (2018). Assessment of lung aeration and recruitment by ct scan and ultrasound in acute respiratory distress syndrome patients*. *Crit. Care Med.* 46, 1761–1768. doi: 10.1097/CCM.0000000000003340

Constantin, J. M., Grasso, S., Chanques, G., Aufort, S., Futier, E., and Sebbane, M. (2010). Lung morphology predicts response to recruitment maneuver in patients with acute respiratory distress syndrome. *Crit. Care Med.* 38, 1108–1117. doi: 10.1097/CCM.0b013e3181d451ec

Constantin, J. M., Jabaudon, M., Lefrant, J. Y., Jaber, S., Quenot, J. P., Langeron, O., et al. (2019). Personalised mechanical ventilation tailored to lung morphology versus low positive end-expiratory pressure for patients with acute respiratory distress syndrome in France (the LIVE study): a multicentre, single-blind, randomised controlled trial. *Lancet Respir. Med.* 7, 870–880. doi: 10.1016/S2213-2600(19)30138-9

Costa, E. L., Borges, J. B., Melo, A., Suarez-Sipmann, F., Toufen, C. Jr, Bohm, S. H., et al. (2009). Bedside estimation of recruitable alveolar collapse and hyperdistension by electrical impedance tomography. *Intens. Care Med.* 35, 1132–1137. doi: 10.1007/s00134-009-1447-y

Cressoni, M., Chiumello, D., Algieri, I., Brioni, M., Chiurazzi, C., Colombo, A., et al. (2017). Opening pressures and atelectrauma in acute respiratory distress syndrome. *Intens. Care Med.* 43, 603–611. doi: 10.1007/s00134-017-4754-8

de Matos, G. F., Stanzani, F., Passos, R. H., Fontana, M. F., Albaladejo, R., and Caserta, R. E. (2012). How large is the lung recruitability in early acute respiratory distress syndrome: a prospective case series of patients monitored by computed tomography. *Crit. Care* 16:R4. doi: 10.1186/cc10602

Eichler, L., Mueller, J., Grensemann, J., Frerichs, I., Zöllner, C., and Kluge, S. (2018). Lung aeration and ventilation after percutaneous tracheotomy measured by electrical impedance tomography in non-hypoxemic critically ill patients: a prospective observational study. *Ann. Intens. Care* 8:110. doi: 10.1186/s13613-018-0454-y

Eronia, N., Mauri, T., Maffezzini, E., Gatti, S., Bronco, A., Alban, L., et al. (2017). Bedside selection of positive end-expiratory pressure by electrical impedance tomography in hypoxemic patients: a feasibility study. *Ann. Intens. Care* 7:76. doi: 10.1186/s13613-017-0299-9

Gattinoni, L., Caironi, P., Cressoni, M., Chiumello, D., Ranieri, V. M., Quintel, M., et al. (2006). Lung recruitment in patients with the acute respiratory distress syndrome. *N. Engl. J. Med.* 354, 1775–1786. doi: 10.1056/NEJMoa052052

Gattinoni, L., Carlesso, E., and Caironi, P. (2012). Stress and strain within the lung. *Curr. Opin. Crit. Care* 18, 42–47. doi: 10.1097/MCC.0b013e32834f17d9

Gattinoni, L., Collino, F., Maiolo, G., Rapetti, F., Romitti, F., Tonetti, T., et al. (2017). Positive end-expiratory pressure: How to set it at the individual level. *Ann. Transl. Med.* 5:288.

Gattinoni, L., Collino, F., Maiolo, G., Rapetti, F., Romitti, F., Tonetti, T., et al. (2017). Positive end-expiratory pressure: how to set it at the individual level. *Ann. Transl. Med.* 5:288. doi: 10.21037/atm.2017.06.64

Gattinoni, L., Marini, J. J., and Quintel, M. (2020). Recruiting the acutely injured lung: how and why? *Am. J. Respir. Crit. Care Med.* 201, 130–132. doi: 10.1164/rccm.201910-2005ED

Généreux, V., Chassé, M., Girard, F., Massicotte, N., Chartrand-Lefebvre, C., and Girard, M. (2020). Effects of positive end-expiratory pressure/recruitment manoeuvres compared with zero end-expiratory pressure on atelectasis during open gynaecological surgery as assessed by ultrasonography: a randomised controlled trial. *Br. J. Anaesth.* 124, 101–109. doi: 10.1016/j.bja.2019.09.040

Godet, T., Constantin, J. M., Jaber, S., and Futier, E. (2015). How to monitor a recruitment maneuver at the bedside. *Curr. Opin. Crit. Care* 21, 253–258. doi: 10.1097/MCC.0000000000000195

He, H., Chi, Y., Long, Y., Yuan, S., Frerichs, I., Möller, K., et al. (2020). Influence of overdistension/recruitment induced by high positive end-expiratory pressure on ventilation-perfusion matching assessed by electrical impedance tomography with saline bolus. *Crit. Care*. 29:586. doi: 10.1186/s13054-020-03301-x

Hedley-Whyte, J., Laver, M. B., and Bendixen, H. H. (1964). Effect of changes in tidal ventilation on physiologic shunting. *Am. J. Physiol.* 206, 891–897. doi: 10.1152/ajplegacy.1964.206.4.891

Hes, D. R. (2015). Recruitment maneuvers and PEEP titration. *Respir. Care* 60, 1688–1704. doi: 10.4187/respcare.04409

Hodgson, C. L., Cooper, D. J., Arabi, Y., King, V., Bersten, A., Bihari, S., et al. (2019). Maximal recruitment open lung ventilation in acute respiratory distress syndrome (PHARLAP): a phase II. Multicenter randomized controlled clinical trial. *Am. J. Respir. Crit. Care Med*. 200, 1363–1372. doi: 10.1164/rccm.201901-0109OC

Karbing, D. S., Panigada, M., Bottino, N., Spinelli, E., Protti, A., Rees, S. E., et al. (2020). Changes in shunt, ventilation/perfusion mismatch, and lung aeration with PEEP in patients with ARDS: a prospective single-arm interventional study. *Crit. Care* 24, 1–13. doi: 10.1186/s13054-020-2834-6

Karsten, J., Voigt, N., Gillmann, H.-J., and Stueber, T. (2019). Determination of optimal positive end-expiratory pressure based on respiratory compliance and electrical impedance tomography: a pilot clinical comparative trial. *Biomed. Eng. Biomed. Tech.* 64, 135–145. doi: 10.1515/bmt-2017-0103

Lapinsky, S. E., and Mehta, S. (2005). Bench-to-bedside review: recruitment and recruiting maneuvers. *Crit Care* 9, 60–65. doi: 10.1186/cc2934

Liberati, A., Altman, D. G., Tetzlaff, J., Mulrow, C., Gøtzsche, P. C., Ioannidis, J. P., et al. (2009). The PRISMA statement for reporting systematic reviews and meta-analyses of studies that evaluate health care interventions: explanation and elaboration. *PLoS Med.* 21:e1000100. doi: 10.1371/journal.pmed.1000100

Longo, S., Siri, J., Acosta, C., Palencia, A., Echegaray, A., Chiotti, I., et al. (2017). Lung recruitment improves right ventricular performance after cardiopulmonary bypass: a randomised controlled trial. *Eur. J. Anaesthesiol.* 34, 66–74. doi: 10.1097/EJA.0000000000000559

Mancebo, J., Mercat, A., and Brochard, L. (2019). Maximal lung recruitment in ARDS: a nail in the coffin. *Am. J. Respir. Crit. Care Med.* 200, 1331–1333. doi: 10.1164/rccm.201908-1615ED

Martins, S. R., and Nogué, R. (2020). Vertical displacement of pleura: a new method for bronchospasm evaluation? *Ultrasound J.* 12, 10–13. doi: 10.1186/s13089-020-00184-5

Neumann, P., Rothen, H. U., Berglund, J. E., Valtysson, J., Magnusson, A., and Hedenstierna, G. (1999). Positive end-expiratory pressure prevents atelectasis during general anaesthesia even in the presence of a high inspired oxygen concentration. *Acta Anaesthesiol. Scand.* 43, 295–301. doi: 10.1034/j.1399-6576.1999.430309.x

Nieszkowska, A., Lu, Q., Vieira, S., Elman, M., Fetita, C., and Rouby, J. J. (2004). Incidence and regional distribution of lung overinflation during mechanical ventilation with positive end-expiratory pressure. *Crit. Care Med.* 32, 1496–1503. doi: 10.1097/01.CCM.0000130170.88512.07

Pereira, S. M., Tucci, M. R., Morais, C. C. A., Simões, C. M., Tonelotto, B. F. F., Pompeo, M. S., et al. (2018). Individual positive end-expiratory pressure settings optimize intraoperative mechanical ventilation and reduce postoperative atelectasis. *Anesthesiology* 129, 1070–1081. doi: 10.1097/ALN.0000000000002435

Puybasset, L., Gusman, P., Muller, J.-C., Cluzel, P., Coriat, P., Rouby, J.-J., et al. (2000). Regional distribution of gas and tissue in acute respiratory distress syndrome. III. Consequences for the effects of positive end-expiratory pressure. *Intens. Care Med.* 26, 1215–1227. doi: 10.1007/s0013400 51340

Rocco, P. R., Pelosi, P., and De Abreu, M. G. (2010). Pros and cons of recruitment maneuvers in acute lung injury and acute respiratory distress syndrome. *Expert Rev. Respir. Med.* 4, 479–489. doi: 10.1586/ers.10.43

Rode, B., Vučić, M., Siranović, M., Horvat, A., Krolo, H., Kelečić, M., et al. (2012). Positive end-expiratory pressure lung recruitment: comparison between lower inflection point and ultrasound assessment. *Wien Klin Wochenschr.* 124, 842–847. doi: 10.1007/s00508-012-0303-1

Sahetya, S. K., and Brower, R. G. (2017). Lung recruitment and titrated PEEP in moderate to severe ARDS. *JAMA* 318:1327. doi: 10.1001/jama.2017.13695

Santos, R. S., Silva, P. L., Pelosi, P., and Rocco, P. R. (2015). Recruitment maneuvers in acute respiratory distress syndrome: the safe way is the best way. *World J. Crit. Care Med.* 4, 278–286 doi: 10.5492/wjccm.v4.i4.278

Tang, K. Q., Yang, S. L., Zhang, B., Liu, H. X., Ye, D. Y., Zhang, H. Z., et al. (2017). Ultrasonic monitoring in the assessment of pulmonary recruitment and the best positive end-expiratory pressure. *Medicine* 96:e8168. doi: 10.1097/MD.0000000000008168

Tonelotto, B., Pereira, S. M., Tucci, M. R., Vaz, D. F., Vieira, J. E., Malbouisson, L. M., et al. (2020). Intraoperative pulmonary hyperdistention estimated by transthoracic lung ultrasound: a pilot study. *Anaesth. Crit. Care Pain Med.* 39, 825–831. doi: 10.1016/j.accpm.2020.09.009

Umbrello, M., and Chiumello, D. (2018). Interpretation of the transpulmonary pressure in the critically ill patient. *Ann. Transl. Med.* 6, 383–383. doi: 10.21037/atm.2018.05.31

Vieira, S. R., Puybasset, L., Lu, Q., Richecoeur, J., Cluzel, P., Coriat, P., et al. (1999). A scanographic assessment of pulmonary morphology in acute lung injury: significance of the lower inflection point detected on the lung pressure- volume curve. *Am. J. Respir. Crit. Care Med*. 159, 1612–1623. doi: 10.1164/ajrccm.159.5.9805112

Whiting, P. F. (2011). QUADAS-2: a revised tool for the quality assessment of diagnostic accuracy studies. *Ann. Intern. Med.* 155:529. doi: 10.7326/0003-4819-155-8-201110180-00009

Zhao, Z., Lee, L. C., Chang, M. Y., Frerichs, I., Chang, H. T., Gow, C. H., et al. (2019). The incidence and interpretation of large differences in EIT-based measures for PEEP titration in ARDS patients. *J. Clin. Monit. Comput.* 10. doi: 10.07/s10877-019-00396-8

Conflict of Interest: The authors declare that the research was conducted in the absence of any commercial or financial relationships that could be construed as a potential conflict of interest.

frontiers in Physiology

ORIGINAL RESEARCH
published: 19 July 2021
doi: 10.3389/fphys.2021.693736

Calculation of Transpulmonary Pressure From Regional Ventilation Displayed by Electrical Impedance Tomography in Acute Respiratory Distress Syndrome

Gaetano Scaramuzzo[1], Savino Spadaro[1], Elena Spinelli[2], Andreas D. Waldmann[3], Stephan H. Bohm[3], Irene Ottaviani[1], Federica Montanaro[1], Lorenzo Gamberini[4], Elisabetta Marangoni[1], Tommaso Mauri[2,5] and Carlo Alberto Volta[1]*

[1] Department of Translational Medicine and for Romagna, University of Ferrara, Ferrara, Italy, [2] Department of Anesthesia, Critical Care and Emergency, Fondazione IRCCS Ca' Granda Ospedale Maggiore Policlinico, Milan, Italy, [3] Department of Anesthesiology and Intensive Care Medicine, Rostock University Medical Center, Rostock, Germany, [4] Department of Anaesthesia, Intensive Care and Prehospital Emergency, Ospedale Maggiore Carlo Alberto Pizzardi, Bologna, Italy, [5] Department of Pathophysiology and Transplant, University of Milan, Milan, Italy

OPEN ACCESS

Edited by:
Paolo Pelosi,
University of Genoa, Italy

Reviewed by:
Carmen Silvia Valente Barbas,
University of São Paulo, Brazil
Hsin-Kuo Bruce Ko,
Taipei Veterans General Hospital, Taiwan

***Correspondence:**
Gaetano Scaramuzzo
scrgtn@unife.it

Specialty section:
This article was submitted to Respiratory Physiology, a section of the journal Frontiers in Physiology

Received: 11 April 2021
Accepted: 14 June 2021
Published: 19 July 2021

Citation:
Scaramuzzo G, Spadaro S, Spinelli E, Waldmann AD, Bohm SH, Ottaviani I, Montanaro F, Gamberini L, Marangoni E, Mauri T and Volta CA (2021) Calculation of Transpulmonary Pressure From Regional Ventilation Displayed by Electrical Impedance Tomography in Acute Respiratory Distress Syndrome. Front. Physiol. 12:693736. doi: 10.3389/fphys.2021.693736

Transpulmonary driving pressure (DP_L) corresponds to the cyclical stress imposed on the lung parenchyma during tidal breathing and, therefore, can be used to assess the risk of ventilator-induced lung injury (VILI). Its measurement at the bedside requires the use of esophageal pressure (Peso), which is sometimes technically challenging. Recently, it has been demonstrated how in an animal model of ARDS, the transpulmonary pressure (P_L) measured with Peso calculated with the absolute values method ($P_L = Paw - Peso$) is equivalent to the transpulmonary pressure directly measured using pleural sensors in the central-dependent part of the lung. We hypothesized that, since the P_L derived from Peso reflects the regional behavior of the lung, it could exist a relationship between regional parameters measured by electrical impedance tomography (EIT) and driving P_L (DP_L). Moreover, we explored if, by integrating airways pressure data and EIT data, it could be possible to estimate non-invasively DP_L and consequently lung elastance (EL) and elastance-derived inspiratory P_L (PI). We analyzed 59 measurements from 20 patients with ARDS. There was a significant intra-patient correlation between EIT derived regional compliance in regions of interest (ROI1) ($r = 0.5$, $p = 0.001$), ROI2 ($r = -0.68$, $p < 0.001$), and ROI3 ($r = -0.4$, $p = 0.002$), and DP_L. A multiple linear regression successfully predicted DP_L based on respiratory system elastance (Ers), ideal body weight (IBW), roi1%, roi2%, and roi3% ($R^2 = 0.84$, $p < 0.001$). The corresponding Bland-Altmann analysis showed a bias of −1.4e-007 cmH_2O and limits of agreement (LoA) of −2.4–2.4 cmH_2O. EL and PI calculated using EIT showed good agreement ($R^2 = 0.89$, $p < 0.001$ and $R^2 = 0.75$, $p < 0.001$) with the esophageal derived correspondent variables. In conclusion, DP_L has a good correlation with EIT-derived parameters in the central lung. DP_L, PI, and EL can be estimated with good accuracy non-invasively combining information coming from EIT and airway pressure.

Keywords: driving pressure, transpulmonary pressure, acute respiratory distress syndrome, precision medicine, electric impedance tomography

INTRODUCTION

Monitoring transpulmonary pressure can be important in patients affected by acute respiratory distress syndrome (ARDS) (ARDS Definition Task Force et al., 2012; Chiumello et al., 2014). Pressure measured at airway opening, indeed, does not yield information about the different components of the respiratory system, i.e., the chest wall and the lung. Chest wall and lung elastance (EL) can differ unpredictably such that, patients having the same airway pressures can have significantly different transpulmonary pressures (Gattinoni et al., 2004; Chiumello et al., 2008). The current approach to evaluate transpulmonary pressure (P_L) is based on the use of esophageal pressure (Peso) and assumes that it could be a good surrogate for pleural pressure (Grieco et al., 2017). The transpulmonary driving pressure (DP_L), i.e., the variation of transpulmonary pressure between end-expiration and end-inspiration, corresponds to the cyclical stress imposed on the lung parenchyma. Unlike driving pressure calculated from airway opening pressure (DP), DP_L is the pressure imposed on the lung during the tidal breathing, since it does not consider the amount of pressure needed to overcome the chest-wall compartment (Loring and Malhotra, 2015). Evaluating DP_L can be important to limit the stress on the lung parenchyma and, therefore, may be useful to monitor the risk for ventilator-induced lung injury (VILI). Recently, it has been demonstrated in an animal model of ARDS how transpulmonary pressure calculated with the classical absolute subtractive method (i.e., P_L = Paw—Peso) corresponds to the transpulmonary pressure in the central to dependent lung (Yoshida et al., 2018). When we consider transpulmonary pressure, we should consider that its value is not unique along with the whole lung but changes regionally according to regional differences in pleural pressures which reflects the forces acting in favor of lung collapse or opening (regional heterogeneity of core disease, gravitational distribution of edema, and mediastinum weight) (Silva and Gama de Abreu, 2018). Electrical impedance tomography (EIT) is a non-invasive monitoring technique that can help to monitor regional lung ventilation distribution at the bedside (Frerichs et al., 2017; Yoshida et al., 2019; Scaramuzzo et al., 2020c). Since the P_L derived from Peso reflects the behavior of the central to dependent part of the lung, we aimed to evaluate the relationship between regional mechanics variables, derived by EIT, and transpulmonary pressure in patients affected by ARDS. Moreover, we tested if, by integrating the information from EIT and airway opening pressure, we could predict non-invasively DP_L. Finally, we wanted to verify if EL and the elastance-based inspiratory P_L derived by EIT, agree with the one classically calculated using esophageal manometry.

METHODS

This is a secondary analysis of data collected from a database of patients affected by ARDS enrolled in a previous study (Scaramuzzo et al., 2020b) in two university hospital intensive care units (Arcispedale Sant'Anna Hospital, Ferrara, Italy and at Cà Granda IRCCS, Milano). The study was approved by the ethics committee of the Sant' Anna Hospital, Ferrara, Italy (Protocol n. 171098) and Milan (protocol no. 625_2018). The selection criteria for the current data analysis were: ARDS according to the Berlin criteria (ARDS Definition Task Force et al., 2012), EIT images for at least 2 min containing an end-inspiratory and end-expiratory pauses, simultaneous recording of airway opening pressure, and airway flow and Peso. Enrolled patients were all mechanically ventilated in volume-controlled ventilation (VCV) with a tidal volume (TV) = 6 ml/kg/IBW. An occlusion test was performed for each patient (Baydur et al., 1982) to assess the correct positioning of the esophageal balloon. All patients were sedated and paralyzed, as per clinical decision and no recruitment maneuver was performed before the measurements. We collected three measures from each patient at three different levels of PEEP, based on clinical practice, transpulmonary pressure, and EIT. The method for PEEP setting guided by EIT and P_L was described previously by Scaramuzzo et al. (2020b).

Respiratory Mechanics

The following mechanical measurements were collected from the airway opening pressure end-inspiratory and end-expiratory pauses: TV, total positive end-expiratory pressure (PEEP), peak pressure (peak), and plateau pressure (Pplat). The DP of the respiratory system was calculated as Pplat-PEEP. The elastance of the respiratory system (Ers) was calculated as $Ers = DP/TV$ and was expressed in cmH_2O/L. Transpulmonary pressure (P_L) was calculated as the difference between airway pressure and Peso (P_L = Pao–Peso) and DP_L as the difference between end-inspiratory and end-expiratory P_L. EL was calculated as $EL = DP_L/TV$ while chest-wall elastance (Ecw) as Ecw = Ers–EL. The elastance-derived inspiratory P_L (PI) was calculated as PI = Pplat–[Pplat*(Ecw/Ers)].

EIT Analysis

An average of 10 respiratory acts was used to analyze EIT and the regional analysis was conducted by dividing the EIT image into four craniocaudal regions of interest (ROI_N; ROI1: most ventral; ROI4: most dorsal). The percentage of tidal ventilation ($ROI\%_N$) in four ROIs was calculated as the fraction of tidal delivered to the ROI in the analyzed acts and was expressed in percentage (Frerichs et al., 2017). The weighted regional compliance in the four ROIs was calculated as follows:

$$RC_{ROI} = \frac{\frac{TV \times ROI\%}{DP}}{IBW}$$

and expressed as $ml/cmH_2O/kg$ of ideal body weight (IBW).

Statistical Analysis

Data are expressed as median [IQR]. Repeated measures correlation (rmcorr) [Bakdash and Marusich (2020)]. R package version 0.4.1. https://CRAN.R-project.org/package=rmcorr) was used to test correlation among variables with repeated measures. To predict measured DP_L, a linear regression analysis [panel linear model, plm (Croissant and Millo, 2008)] accounting for the longitudinal characteristic of the data (cross-sectional time-series data) was used. Time of sampling and patient ID were considered as fixed factors. The pooled OLS estimation method was used, and the following variables were entered as predictors, based on their clinical meaningfulness and the results of rmcorr: IBW, Ers

TABLE 1 | Main characteristics of the patients and the pooled measurements.

Gender	*M* = 13; *F* = 7
Age (years)	63 [53–72]
BMI (Kg/m^2)*	28 [24–33]
SAPS II	53 [45–66]
Days from ICU admission	4 [2–5]
PaO2/FiO2*	149 [96–211]
PaCO2 (mmHg)*	57 [47–68]
FiO2 (%)*	50 [43–60]
Respiratory rate (bpm)	19 [15–24]
Tidal volume (ml/kg IBW)	6.3 [6.1–7.0]
Mild/Moderate/Severe ARDS	6/9/5
Tidal volume (ml)	375 [346–440]
Respiratory rate (acts/min)	19[16–24]
Peak pressure (cmH2O)	31[28–39]
Plateau pressure (cmH2O)	23[19–28]
PEEP (cmH2O)	13 [9.2–15]
Driving pressure (cmH2O)	10 [8.7–13]
End inspiratory P_L (cmH2O)	8.7 [5.6–13]
End-expiratory P_L (cmH2O)	1.3 [-0.27–3.3]
Transpulmonary driving pressure (cmH2O)	7 [5.8–9.1]
RS Elastance (cmH2O/L)	27 [21–33]
Lung elastance (cmH2O/L)	18 [14–23]
ROI1 tidal distribution (%)	19 [15–22]
ROI2 tidal distribution (%)	37 [33–42]
ROI3 tidal distribution (%)	31 [27–35]
ROI4 tidal distribution (%)	13 [8.3–17]
Regional compliance ROI1 (ml/cmH2O/kg)	0.12 [0.096–0.15]
Regional compliance ROI2 (ml/cmH2O/kg)	0.25 [0.18–0.3]
Regional compliance ROI2 (ml/cmH2O/kg)	0.19 [0.15–0.25]
Regional compliance ROI2 (ml/cmH2O/kg)	0.072 [0.043–0.12]

*BMI, body mass index; SAPSII, simplified acute physiology score II; ICU, intensive care unit; $_{PaO2}/_{FiO2}$, partial pressure of arterial oxygen on the inspired fraction of oxygen ratio; PEEP, positive end-expiratory pressure; MAP, mean arterial blood pressure; IBW, ideal body weight; P_L, transpulmonary pressure; RS, respiratory system. *, at ICU admission.*

(derived by TV and DP), roi1%, roi2, and roi3%. The resulting EIT-derived driving transpulmonary pressure (named $DP_{L,EIT}$) was used to calculate EL as $EL_{EIT} = TV/DP_{L,EIT}$. The EIT PI was calculated as PI_{EIT} = Pplat—[Pplat((Ers–EL_{EIT}) /Ers)]. Bias and limits of agreement (LOA) with mean bias ± 2 sds were calculated as per the Bland-Altman approach (Bland and Altman, 1986) between EIT- and Peso-derived DP_L, EL, and PI. To evaluate if the PEEP titration technique or the number of quadrants infiltrated at the chest x-ray could affect the agreement between the two techniques, we performed an additional linear regression between EIT and Peso-derived DP_L (as shown in **Supplementary Material**). The statistical analysis was conducted using GraphPad Prism 8.4.3 for Windows (GraphPad Software, San Diego, California USA, www.graphpad.com) and R 4.0.4 (R Foundation for Statistical Computing, Vienna, Austria) [R Core Team (2021). R: A language and environment for statistical computing. R Foundation for Statistical Computing, Vienna, Austria. URL https://www.R-project.org/.]. *P*-values < 0.05 were considered statistically significant.

TABLE 2 | Repeated measures correlation (rmcorr) analysis between electrical impedance tomography (EIT)- derived and esophageal-derived parameters.

	Intra-patient correlation coefficient	*p*-value
Relative ventilation, ROI1 (%)	−0.35	0.03
Relative ventilation, ROI2 (%)	−0.45	0.003
Relative ventilation, ROI3 (%)	0.40	0.01
Relative ventilation, ROI4 (%)	0.40	0.01
Regional compliance/IBW (ml/cmH_2O/kg)—ROI1	−0.50	0.001
Regional compliance/IBW (ml/cmH_2O/kg)—ROI2	−0.68	<0.001
Regional compliance/IBW (ml/cmH_2O/kg)—ROI3	−0.47	0.002
Regional compliance/IBW (ml/cmH_2O/kg)—ROI4	−0.12	0.47

Correlation coefficients for rmcorr analysis between EIT and esophageal-derived measures.

RESULTS

Population Characteristics

Of the 60 measurements considered for the analysis, 59 were analyzed (one excluded after quality check). The measures were derived from 20 patients, 13 males and 7 females, aged 63 [53–72] years with a median body mass index (BMI) of 28 [24–33] kg/m^2, and a PaO_2/FiO_2 of 149 [96–211], and average PEEP 13[9.2–15] cmH_2O. Each patient had three measures in which PEEP was set according to three different methods (clinical practice, transpulmonary pressure, and EIT). The characteristics of the population are resumed in **Table 1**. Additional information on lung mechanics and the effect of PEEP titration on lung recruitment/derecruitment has been already published previously by Scaramuzzo et al. (2020b).

Correlation

The repeated measures correlation analysis showed a significant intra-patient correlation between DP_L and regional tidal distribution, which was negative in ROI1 ($r = -0.35$, $p = 0.03$) and ROI2($r = -0.45$, $p = 0.003$) and positive in ROI3 ($r = 0.4$, $p = 0.01$) and ROI4 ($r = 0.4$, $p = 0.01$, **Table 2**). A stronger correlation was found with regional compliance in ROI1 ($r = -0.5$, $p = 0.001$), ROI2 ($r = -0.68$, $p < 0.001$), and ROI3 ($r = -0.47$, $p = 0.002$), while there was no significant correlation between DP_L and regional compliance in ROI4 ($r = -0.12$, $p = 0.47$, **Table 2**; **Figure 1**).

EIT Derived Parameters Calculation

Five regressors were used to perform the linear regression with DP_L as the dependent variable: Ers, IBW, roi%1, roi%2, and roi%3. A significant regression was found, with an R^2 of 0.84 ($p < 0.001$) and predicted DP_L ($DP_{L,EIT}$) was equal to

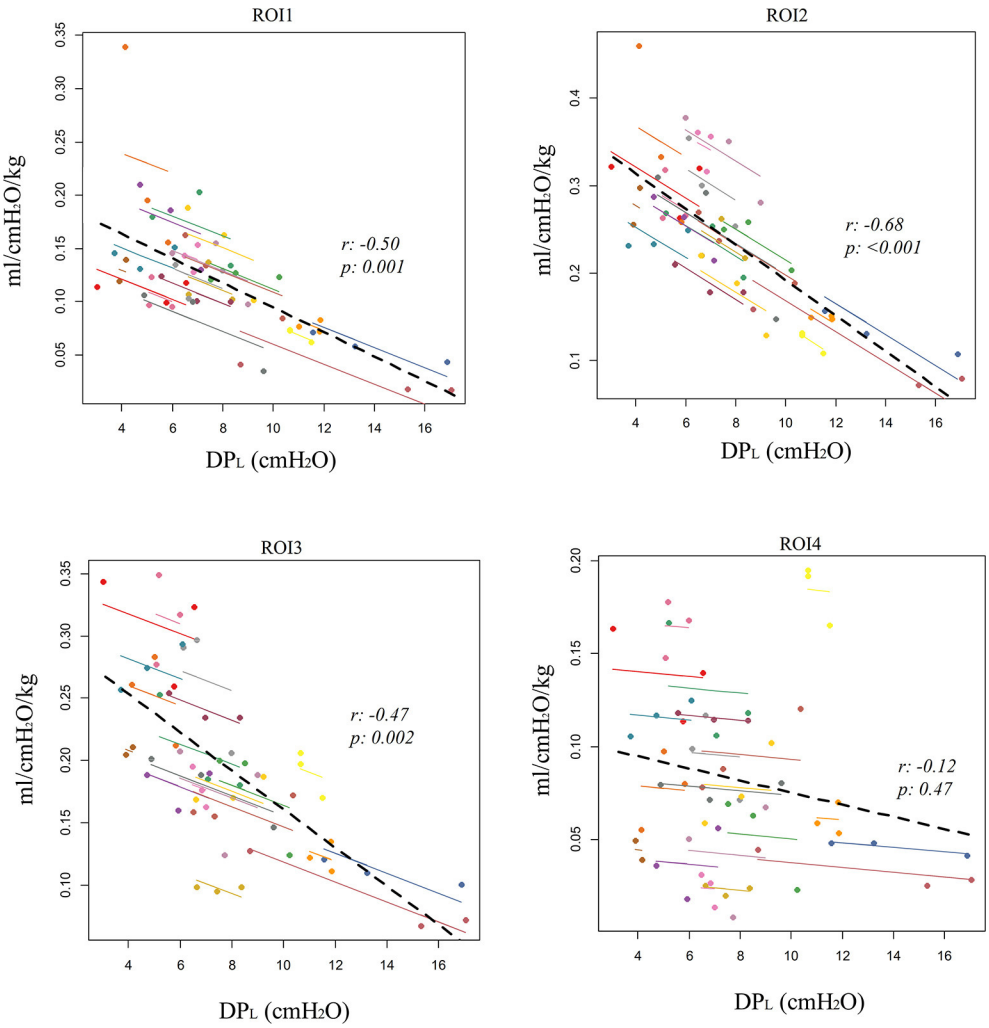

FIGURE 1 | Correlation between electrical impedance tomography (EIT)-derived regional compliance in the four craniocaudal regions of interest (ROI1, ventral lung; ROI4, dorsal lung) and esophageal-derived transpulmonary driving pressure (DP_L). Repeated measures correlation (rmcorr).

$DP_{L,EIT}$ = k + α · IBW + β · Ers + γ · roi1% + δ · roi2% + e· roi3% being $k = 16.64$; $\alpha = 0.074683$; $\beta = 0.230941$; $\gamma = -0.21449$; $\delta = -0.15974$; $e = -0.32996$ (**Figure 2A**; **Supplementary Table S1**). The corresponding Bland-Altmann between the EIT and Peso-derived measures showed a bias of −1.4e-007 and an LoA of −2.4–2.4 cmH_2O (**Figure 2B**). The linear regression between $EL_{EIT,}$ and EL resulted in an $R^2 = 0.89$ ($p < 0.0001$), while the corresponding Bland-Altmann analysis showed a bias of −0.11 ± and an LoA of −6.8–6.5 cmH2O/L (**Figures 2C,D**). The EIT-derived inspiratory PL predicted well the corresponding Peso derived value ($R^2 = 0.75$, $p < 0.0001$) and with a good agreement [bias of −0.007 ± and an LoA of −5.6–5.6 cmH_2O/L (**Figures 2E,F**)]. The PEEP titration technique did not provide different results in terms of the agreement between the two techniques (**Supplementary Figure S2**), but in patients with a higher number of quadrants infiltrated at the chest x-ray, the agreement was higher (**Supplementary Figure S3**).

DISCUSSION

In this study, we investigated the relationship between the EIT-derived parameters and DP_L in patients affected by ARDS. We found that regional ventilation distribution correlates well with DP_L, especially in the central part of the lung. The highest correlation was found with regional compliance in the ventral-central part of the lung. Moreover, by using EIT and airway opening pressure derived data, we were able to predict DP_L, EL and lung inspiratory transpulmonary pressure with good accuracy.

Lung monitoring has been increasingly used in the last few years to personalize mechanical ventilation (Pereira et al., 2018; Beitler et al., 2019; Scaramuzzo et al., 2020b) in different settings, especially in ARDS. ARDS requires, indeed, more precise fine-tuned ventilation, since the wide and unpredictable characteristics of the disease, especially the amount of alveolar and interstitial edema, make it difficult to develop a standard

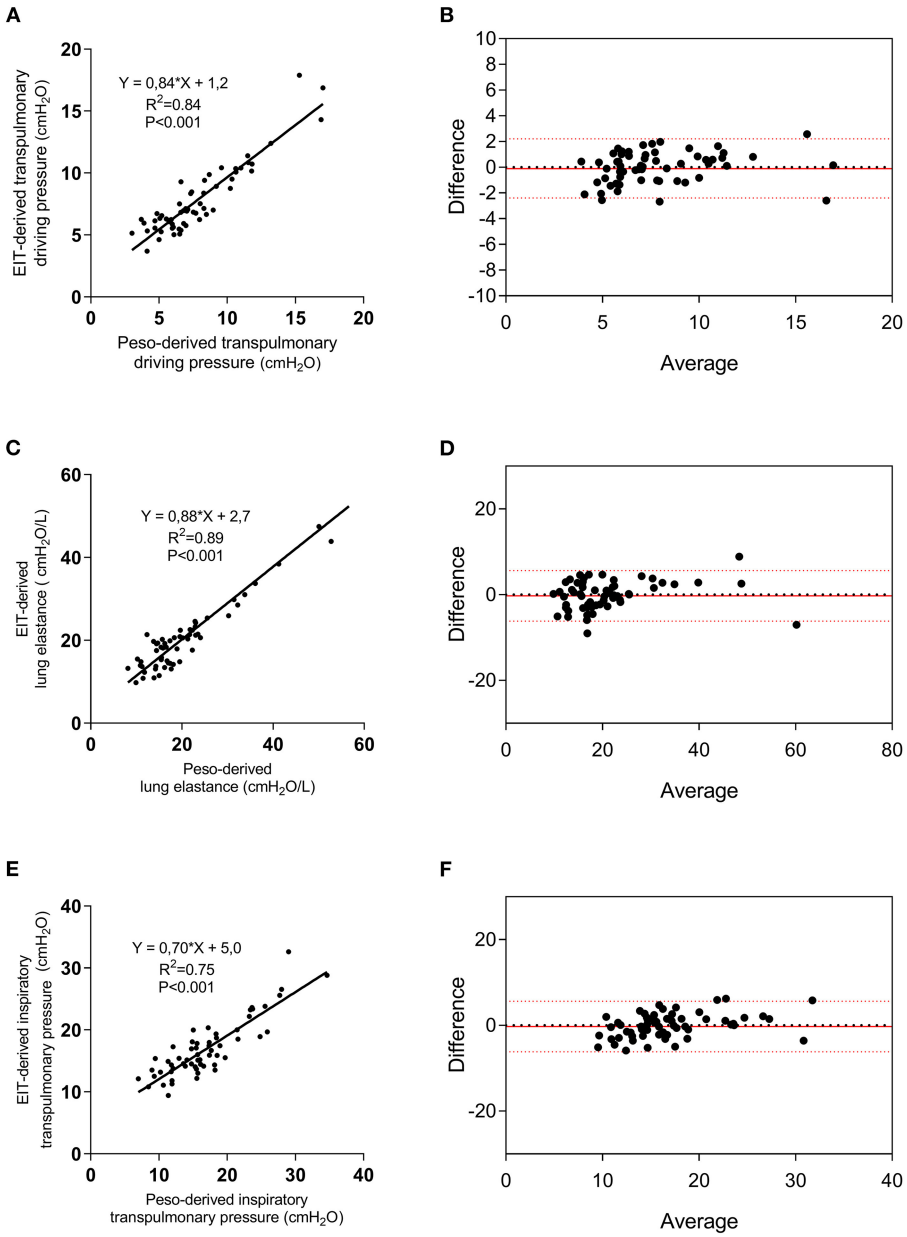

FIGURE 2 | Electrical impedance tomography derived and measured DP_L, lung elastance (EL), and elastance-derived inspiratory lung pressure. Linear regression between EIT-derived and measured DP_L **(A)**, EL **(C)**, and lung inspiratory pressure **(E)**, and relative Bland-Altmann plots **(B,D,F)**. EIT, electrical impedance tomography; Peso, esophageal pressure.

that fits all the patients and conditions. Personalizing mechanical ventilation in patients affected by ARDS aims to keep under control different variables, each one affecting the different components of VILI pathophysiology (Nieman et al., 2017; Tonetti et al., 2017; Pinto et al., 2020). DP_L is the pressure to which the lung parenchyma is cyclically exposed during tidal breathing and represents the stress applied to the lung, not considering the pressure needed to overcome the chest-wall resistance. Since pleural pressure is not easily accessible to the bedside, Peso has been classically used to indirectly calculate transpulmonary pressure (Talmor et al., 2008; Beitler et al., 2019; Scaramuzzo et al., 2020a). However, Peso monitoring is invasive, can be technically challenging or not feasible in some patients, and requires precise calibration and interpretation. By exploring the intra-patient correlation of EIT-derived parameters and DP_L, we found that a change in DP_L correlates negatively with a change of ventilation distribution in ROI1 and ROI2 while positively with a change in ROI3 and ROI4. This means that, when changing PEEP in patients with ARDS, an increase in relative ventilation in the dependent lung is related to a rise in

DP_L. This can be explained by the increased lung deformation which is related to a dorsal shift of ventilation but raises some questions on PEEP titration aiming to maximize dorsal ventilation (Pelosi et al., 2018). The association was even stronger when analyzing regional compliance, especially in the ROI2, which corresponds to the central-ventral ROI. Surprisingly, no significant correlation was found between change DP_L and regional compliance in ROI4, meaning that the esophageal-derived DP_L is less informative than thought on the regional characteristics of the dorsal part of the lung, despite the dorsal lung has been classically associated with the concept of PEEP titration guided by transpulmonary pressure. The central lung region corresponds to the position where the esophagus and, therefore, the esophageal catheter are supposed to be and explains why the stronger correlations have been found in the central lung ROIs.

We found that by integrating EIT and airway opening pressure information, DP_L can be predictable with good reliability and low bias. Specifically, esophageal derived DP_L was derived from IBW, Ers, and the relative ventilation in ROI1, ROI2, and ROI3. This is not the first attempt to evaluate non-invasively DP_L and EL. Lundin et al. (2015) recently introduced a method to estimate transpulmonary pressure from changes in end-expiratory lung volume (ΔEELV) following a PEEP step. Despite this approach is intriguing, it does need to perform a PEEP titration including the need to reach low or even zero PEEP. This is not problematic in patients undergoing general anesthesia which is the context of method validation but is less feasible in patients with ARDS, where the removal of PEEP can cause clinically important effects. Recently, Yoshida et al. (2018) demonstrated how transpulmonary pressure calculated using the subtractive method from Peso reflects the local behavior of the central to dependent lung. We hereby confirm this finding. Is has to be tested if this approach could be used to evaluate directly measured non-dependent lung DP, being at the moment still not possible to estimate local end-expiratory transpulmonary pressure and, therefore, the corresponding DP_L of this area.

We evaluated if also the inspiratory transpulmonary pressure, calculated using the elastance-derived method (Grasso et al., 2012) could be predicted by EIT. This parameter, indeed, has been demonstrated to be highly indicative of the transpulmonary pressure directly measured in the non-dependent lung (Yoshida et al., 2018). We found that EIT could predict its value with high accuracy, just by deriving lung and chest wall elastances by $P_{L,EIT}$. This simple calculation, if implemented on available bedside EIT machines, would allow having continuously and non-invasively a good predictor of non-dependent transpulmonary pressure and, therefore, of the risk of barotrauma in this part of the lung.

We demonstrated that by using EIT data, it is possible to quantify DP_L and EL, as commonly calculated by the esophageal balloon. The immediate advantage of this is the possibility of measuring DP_L continuously and in patients in which the esophageal catheter positioning is technically challenging or the signal is not reliable. Moreover, we confirmed that P_L reflects the behavior of the central regions of the lung. Future studies need to evaluate if EIT can be used to calculate transpulmonary pressure in the other lung regions, allowing therefore to have at the bedside, regional transpulmonary pressure data. This information is currently not derivable by any non-invasive monitoring tool and could be precious in assessing regional early indicators of VILI.

This study has some limitations. First, it is derived from a limited number of observations and a small number of patients enrolled in two centers. Second, we used only one EIT machine to retrieve the percentage of relative ventilation in the ROI which is implemented with lung contouring based on the anthropometric characteristics of the patient. If this approach and the parameters derived in the regression equation can be applied also to the other EIT devices has to be confirmed (Lionheart, 2004). Third, in the protocol, we explored the correlation between DP_L measured using the esophageal balloon and EIT, by using a database of repeated measures at different levels of PEEP. Since regional DP can be modified by TV, future studies need to evaluate the impact of this parameter on regional transpulmonary pressure and the agreement between the two techniques. Finally, the population was characterized by patients affected mainly by ARDS associated with pneumonia or sepsis. None of the patients had a highly asymmetrical ARDS. The replicability of the findings must be, therefore, explored in this specific form of ARDS, due to the highly variable local forces, especially for their influence on the esophageal balloon signal (as shown in **Supplementary Figure S3**). No patient with COVID-19 was enrolled in this study and, therefore, also the applicability of this technique to patients with COVID-19 has to be tested. In conclusion, DP_L correlated with EIT-derived regional parameters, especially in the central lung. DP_L, EL, and inspiratory transpulmonary lung pressures can be non-invasively estimated by integrating EIT-derived and airway opening pressure-derived data.

DATA AVAILABILITY STATEMENT

The data that support the findings of this study are available from the corresponding author upon reasonable request.

ETHICS STATEMENT

The studies involving human participants were reviewed and approved by Sant' Anna Hospital, Ferrara, Italy (Protocol no. 171098) and Milan (protocol no. 625_2018). The patients/participants provided their written informed consent to participate in this study.

AUTHOR CONTRIBUTIONS

GS, SS, CV, and TM conceived of and coordinated the study. AW participated in its design and helped to draft and review the manuscript. IO, EM, and LG contributed to the interpretation of data and were involved in revising the manuscript. AW, SB, FM, and ES contributed to analysis and interpretation of data and were involved in revising the manuscript. AW contributed technical help during data analysis and revision of the final manuscript. GS and SS performed the statistical analysis and

helped to carry out the data analysis. All authors meet all authorship requirements of the International Committee of Medical Journal Editors. All authors read and approved the final manuscript.

FUNDING

The present study was supported by a research grant from SIAARTI (Italian society of anesthesia and intensive care medicine) and from institutional funding of the Department of Morphology, Surgery and Experimental Medicine, Section of Anesthesia and Intensive Care, University of Ferrara, Italy.

SUPPLEMENTARY MATERIAL

The Supplementary Material for this article can be found online at: https://www.frontiersin.org/articles/10.3389/fphys.2021.693736/full#supplementary-material

REFERENCES

ARDS Definition Task Force, Ranieri, V. M., Rubenfeld, G. D., Thompson, B. T., Ferguson, N. D., Caldwell, E., et al. (2012). Acute respiratory distress syndrome: the Berlin Definition. *JAMA* 307, 2526–2533. doi: 10.1001/jama.2012.5669

Bakdash, J. Z., and Marusich, L. R. (2020). *rmcorr: Repeated Measures Correlation. R package version 0.4.1*. Available online at: https://CRAN.R-project.org/package=rmcorr (accessed April 1, 2021).

Baydur, A., Behrakis, P. K., Zin, W. A., Jaeger, M., and Milic-Emili, J. (1982). A simple method for assessing the validity of the esophageal balloon technique. *Am. Rev. Respir. Dis.* 126, 788–791. doi: 10.1164/arrd.1982.126.5.788

Beitler, J. R., Sarge, T., Banner-Goodspeed, V. M., Gong, M. N., Cook, D., Novack, V., et al. (2019). Effect of Titrating Positive End-Expiratory Pressure (PEEP) with an esophageal pressure–guided strategy vs an empirical high PEEP-Fio2 strategy on death and days free from mechanical ventilation among patients with acute respiratory distress syndrome: a randomized clinical trial. *JAMA* 321, 846–857. doi: 10.1001/jama.2019.0555

Bland, J. M., and Altman, D. G. (1986). Statistical methods for assessing agreement between two methods of clinical measurement. *Lancet Lond. Engl.* 1, 307–310. doi: 10.1016/S0140-6736(86)90837-8

Chiumello, D., Carlesso, E., Cadringher, P., Caironi, P., Valenza, F., Polli, F., et al. (2008). Lung stress and strain during mechanical ventilation for acute respiratory distress syndrome. *Am. J. Respir. Crit. Care Med.* 178, 346–355. doi: 10.1164/rccm.200710-1589OC

Chiumello, D., Cressoni, M., Colombo, A., Babini, G., Brioni, M., Crimella, F., et al. (2014). The assessment of transpulmonary pressure in mechanically ventilated ARDS patients. *Intensive Care Med.* 40, 1670–1678. doi: 10.1007/s00134-014-3415-4

Croissant, Y., and Millo, G. (2008). Panel data econometrics in R: the plm package. *J. Stat. Softw.* 27, 1–43. doi: 10.18637/jss.v027.i02

Frerichs, I., Amato, M. B. P., van Kaam, A. H., Tingay, D. G., Zhao, Z., Grychtol, B., et al. (2017). Chest electrical impedance tomography examination, data analysis, terminology, clinical use and recommendations: consensus statement of the TRanslational EIT developmeNt stuDy group. *Thorax* 72, 83–93. doi: 10.1136/thoraxjnl-2016-208357

Gattinoni, L., Chiumello, D., Carlesso, E., and Valenza, F. (2004). Bench-to-bedside review: chest wall elastance in acute lung injury/acute respiratory distress syndrome patients. *Crit. Care Lond. Engl.* 8, 350–355. doi: 10.1186/cc2854

Grasso, S., Terragni, P., Birocco, A., Urbino, R., Del Sorbo, L., Filippini, C., et al. (2012). ECMO criteria for influenza A (H1N1)-associated ARDS: role of transpulmonary pressure. *Intensive Care Med.* 38, 395–403. doi: 10.1007/s00134-012-2490-7

Grieco, D. L., Chen, L., and Brochard, L. (2017). Transpulmonary pressure: importance and limits. *Ann. Transl. Med.* 5:285. doi: 10.21037/atm.2017.07.22

Lionheart, W. R. B. (2004). EIT reconstruction algorithms: pitfalls, challenges and recent developments. *Physiol. Meas.* 25, 125–142. doi: 10.1088/0967-3334/25/1/021

Loring, S. H., and Malhotra, A. (2015). Driving pressure and respiratory mechanics in ARDS. *N. Engl. J. Med.* 372, 776–777. doi: 10.1056/NEJMe1414218

Lundin, S., Grivans, C., and Stenqvist, O. (2015). Transpulmonary pressure and lung elastance can be estimated by a PEEP-step manoeuvre. *Acta Anaesthesiol. Scand.* 59, 185–196. doi: 10.1111/aas.12442

Nieman, G. F., Satalin, J., Andrews, P., Aiash, H., Habashi, N. M., and Gatto, L. A. (2017). Personalizing mechanical ventilation according to physiologic parameters to stabilize alveoli and minimize ventilator induced lung injury (VILI). *Intensive Care Med. Exp.* 5:8. doi: 10.1186/s40635-017-0121-x

Pelosi, P., Rocco, P. R. M., and Gama de Abreu, M. (2018). Close down the lungs and keep them resting to minimize ventilator-induced lung injury. *Crit. Care* 22:72. doi: 10.1186/s13054-018-1991-3

Pereira, S. M., Tucci, M. R., Morais, C. C. A., Simões, C. M., Tonelotto, B. F. F., Pompeo, M. S., et al. (2018). Individual positive end-expiratory pressure settings optimize intraoperative mechanical ventilation and reduce postoperative atelectasis. *Anesthesiology* 129, 1070–1081. doi: 10.1097/ALN.0000000000002435

Pinto, E. F., Santos, R. S., Antunes, M. A., Maia, L. A., and Padilha, G. A. de A., Machado, J., et al. (2020). Static and dynamic transpulmonary driving pressures affect lung and diaphragm injury during pressure-controlled versus pressure-support ventilation in experimental mild lung injury in rats. *Anesthesiology* 132, 307–320. doi: 10.1097/ALN.0000000000003060

R Core Team (2021). *R: A Language and Environment for Statistical Computing. R Foundation for Statistical Computing, Vienna, Austria*. Available online at: https://www.R-project.org/.

Scaramuzzo, G., Ball, L., Pino, F., Ricci, L., Larsson, A., Guérin, C., et al. (2020a). Influence of positive end-expiratory pressure titration on the effects of pronation in acute respiratory distress syndrome: a comprehensive experimental study. *Front. Physiol.* 11:179. doi: 10.3389/fphys.2020.00179

Scaramuzzo, G., Spadaro, S., Dalla Corte, F., Waldmann, A. D., Böhm, S. H., Ragazzi, R., et al. (2020b). Personalized positive end-expiratory pressure in acute respiratory distress syndrome: comparison between optimal distribution of regional ventilation and positive transpulmonary pressure. *Crit. Care Med.* 48, 1148–1156. doi: 10.1097/CCM.0000000000004439

Scaramuzzo, G., Spinelli, E., Spadaro, S., Santini, A., Tortolani, D., Dalla Corte, F., et al. (2020c). Gravitational distribution of regional opening and closing pressures, hysteresis and atelectrauma in ARDS evaluated by electrical impedance tomography. *Crit. Care Lond. Engl.* 24:622. doi: 10.1186/s13054-020-03335-1

Silva, P. L., and Gama de Abreu, M. (2018). Regional distribution of transpulmonary pressure. *Ann. Transl. Med.* 6:385. doi: 10.21037/atm.2018.10.03

Talmor, D., Sarge, T., Malhotra, A., O'Donnell, C. R., Ritz, R., Lisbon, A., et al. (2008). Mechanical ventilation guided by esophageal pressure in acute lung injury. *N. Engl. J. Med.* 359, 2095–2104. doi: 10.1056/NEJMoa0708638

Tonetti, T., Vasques, F., Rapetti, F., Maiolo, G., Collino, F., Romitti, F., et al. (2017). Driving pressure and mechanical power: new targets for VILI prevention. *Ann. Transl. Med.* 5:286. doi: 10.21037/atm.2017.07.08

Yoshida, T., Amato, M. B. P., Grieco, D. L., Chen, L., Lima, C. A. S., Roldan, R., et al. (2018). Esophageal manometry and regional transpulmonary pressure in lung injury. *Am. J. Respir. Crit. Care Med.* 197, 1018–1026. doi: 10.1164/rccm.201709-1806OC

Yoshida, T., Piraino, T., Lima, C. A. S., Kavanagh, B. P., Amato, M. B. P., and Brochard, L. (2019). Regional ventilation displayed by electrical impedance tomography as an incentive to decrease PEEP. *Am. J. Respir. Crit. Care Med.* doi: 10.1164/rccm.201904-0797LE

Conflict of Interest: The authors declare that the research was conducted in the absence of any commercial or financial relationships that could be construed as a potential conflict of interest.

frontiers in Physiology

ORIGINAL RESEARCH
published: 28 July 2021
doi: 10.3389/fphys.2021.707119

Effects of Lung Injury on Regional Aeration and Expiratory Time Constants: Insights From Four-Dimensional Computed Tomography Image Registration

Jacob Herrmann[1], Sarah E. Gerard[2], Wei Shao[3], Yi Xin[4], Maurizio Cereda[5], Joseph M. Reinhardt[2,6], Gary E. Christensen[7,8], Eric A. Hoffman[2,6,9] and David W. Kaczka[2,6,10]*

[1]Department of Biomedical Engineering, Boston University, Boston, MA, United States, [2]Department of Radiology, University of Iowa, Iowa City, IA, United States, [3]Department of Radiology, Stanford University, Stanford, CA, United States, [4]Department of Radiology, University of Pennsylvania, Philadelphia, PA, United States, [5]Department of Anesthesiology and Critical Care, University of Pennsylvania, Philadelphia, PA, United States, [6]Roy J. Carver Department of Biomedical Engineering, University of Iowa, Iowa City, IA, United States, [7]Department of Electrical and Computer Engineering, University of Iowa, Iowa City, IA, United States, [8]Department of Radiation Oncology, University of Iowa, Iowa City, IA, United States, [9]Department of Internal Medicine, University of Iowa, Iowa City, IA, United States, [10]Department of Anesthesia, University of Iowa, Iowa City, IA, United States

OPEN ACCESS

Edited by:
Chun Y. Seow, University of British Columbia, Canada

Reviewed by:
Gaetano Perchiazzi, Uppsala University, Sweden
Alysson Roncally Silva Carvalho, University of Porto, Portugal

***Correspondence:**
Jacob Herrmann
jakeherr@bu.edu

Specialty section:
This article was submitted to Respiratory Physiology, a section of the journal Frontiers in Physiology

Received: *09 May 2021*
Accepted: *30 June 2021*
Published: *28 July 2021*

Citation:
Herrmann J, Gerard SE, Shao W, Xin Y, Cereda M, Reinhardt JM, Christensen GE, Hoffman EA and Kaczka DW (2021) Effects of Lung Injury on Regional Aeration and Expiratory Time Constants: Insights From Four-Dimensional Computed Tomography Image Registration. Front. Physiol. 12:707119. doi: 10.3389/fphys.2021.707119

Rationale: Intratidal changes in regional lung aeration, as assessed with dynamic four-dimensional computed tomography (CT; 4DCT), may indicate the processes of recruitment and derecruitment, thus portending atelectrauma during mechanical ventilation. In this study, we characterized the time constants associated with deaeration during the expiratory phase of pressure-controlled ventilation in pigs before and after acute lung injury using respiratory-gated 4DCT and image registration.

Methods: Eleven pigs were mechanically ventilated in pressure-controlled mode under baseline conditions and following an oleic acid model of acute lung injury. Dynamic 4DCT scans were acquired without interrupting ventilation. Automated segmentation of lung parenchyma was obtained by a convolutional neural network. Respiratory structures were aligned using 4D image registration. Exponential regression was performed on the time-varying CT density in each aligned voxel during exhalation, resulting in regional estimates of intratidal aeration change and deaeration time constants. Regressions were also performed for regional and total exhaled gas volume changes.

Results: Normally and poorly aerated lung regions demonstrated the largest median intratidal aeration changes during exhalation, compared to minimal changes within hyper- and non-aerated regions. Following lung injury, median time constants throughout normally aerated regions within each subject were greater than respective values for poorly aerated regions. However, parametric response mapping revealed an association between larger intratidal aeration changes and slower time constants. Lower aeration and faster time constants were observed for the dependent lung regions in the supine position. Regional

gas volume changes exhibited faster time constants compared to regional density time constants, as well as better correspondence to total exhaled volume time constants.

Conclusion: Mechanical time constants based on exhaled gas volume underestimate regional aeration time constants. After lung injury, poorly aerated regions experience larger intratidal changes in aeration over shorter time scales compared to normally aerated regions. However, the largest intratidal aeration changes occur over the longest time scales within poorly aerated regions. These dynamic 4DCT imaging data provide supporting evidence for the susceptibility of poorly aerated regions to ventilator-induced lung injury, and for the functional benefits of short exhalation times during mechanical ventilation of injured lungs.

Keywords: mechanical ventilation, ventilator-induced lung injury, respiratory mechanics, computed tomography, image registration

INTRODUCTION

Repetitive recruitment and derecruitment of lung tissue during mechanical ventilation is associated with atelectrauma, a harmful process contributing to ventilator-induced lung injury and associated with progressively deteriorating overall condition (Slutsky and Ranieri, 2013; Gaver et al., 2020). Intratidal derecruitment occurs predominantly during exhalation, when the reduction of gas volume and distending pressure allows the collapse of atelectatic regions. Alveolar permeability, pulmonary edema, and surfactant dysfunction contribute to increased susceptibility to derecruitment in injured lungs (Gatto et al., 2004), such that atelectrauma is likely to occur in regions that are poorly aerated (Broche et al., 2017, 2019; Fardin et al., 2021). Regional distributions of intratidal recruitment and derecruitment have been inferred by comparing static or quasi-static computed tomography (CT) images acquired at end-expiration vs. end-inspiration (Crotti et al., 2001; Carvalho et al., 2008; Cereda et al., 2017). Clinical CT imaging cannot resolve structural details of individual alveoli and alveolar ducts, making it impossible to conclude whether an increase in CT density corresponds to partial derecruitment, uniform deflation without any derecruitment, or any combination thereof (Cereda et al., 2019). Nonetheless, progression of lung injury is associated with poor or unstable aeration in CT (Cereda et al., 2017; Xin et al., 2018). However, recruitment and derecruitment are not instantaneous responses to changes in transpulmonary pressure, but rather occur gradually over time, with heterogeneous rates of re-inflation and collapse (Bates and Irvin, 2002). Thus, to determine which regions of the lung may be at risk for atelectrauma, one must not only quantify how much aeration changes within a given region during exhalation, but also how quickly such deaeration occurs.

Several lung-protective modalities are predicated on the maintenance of lung recruitment by shortening the time allowed for exhalation (Jain et al., 2016), with support from experimental evidence provided by *in vivo* microscopy at the alveolar level near the pleural surface (Gatto et al., 2004; Carney et al., 2005), dynamic CT (Neumann et al., 1998a,b; Markstaller et al., 2001), and synchrotron radiation phase-contrast imaging with sub-acinar spatial resolution (Fardin et al., 2021). Previous studies involving dynamic CT imaging have assumed exponential decay of regional aeration (i.e., changes in fraction of gas per unit volume of lung tissue, assessed by changes in regional CT density) in response to instantaneous changes in applied airway pressure (**Figure 1**). These studies demonstrated regional discrepancies in exhalation deaeration rates, but were limited in the ability to spatially localize these measurements.

The goal of this study was to quantify regional rates of lung deaeration during passive exhalation, using four-dimensional computed tomography (4DCT) dynamic imaging (Herrmann et al., 2017) and 4D image registration (Zhao et al., 2016; Herrmann et al., 2020a) to track localized aeration changes with high spatial resolution. In addition to assessment of aeration based on CT density, it is also possible to account for specific gas volume changes using an intensity-corrected Jacobian determinant, which is more strongly correlated to specific ventilation (Ding et al., 2012). In this study, we quantified regional CT density and gas volume time constants before and after acute lung injury in anesthetized porcine subjects. We also investigated potential factors that influence the distribution of these regional time constants, including location on the gravitational axis as well as regional aeration at end-inspiration, end-expiration, and predicted equilibrium. Our study therefore provides new insights into how the rate of tidal aeration changes occur within normally and poorly aerated regions during passive exhalation. Portions of these data were presented in abstract form at meetings of the American Society of Anesthesiologists (Kaczka et al., 2020) and the American Thoracic Society (Herrmann et al., 2020b).

MATERIALS AND METHODS

All experimental procedures were approved by the University of Iowa Institute for Animal Care and Use Committee (Protocol Number 5061428). Two other studies of respiratory mechanics, involving regional dynamic deformation (Herrmann et al., 2020a) and gas transport (Herrmann et al., 2021), were previously published using data collected from the subjects used in

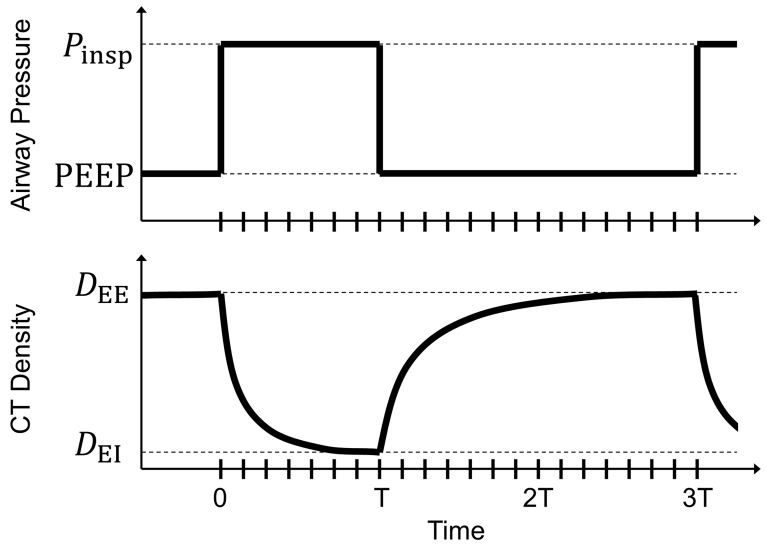

FIGURE 1 | Schematic of a step change in airway pressure producing a decaying exponential response in voxel computed tomography (CT) density. At end-inspiration, airway pressure changes from inspiratory pressure (P_{insp}) to positive end-expiratory pressure (PEEP) with an inspiratory:expiratory ratio of 1:2. Voxel CT density changes from an end-inspiratory level (D_{EI}) to an end-expiratory level (D_{EE}). Tick marks along the horizontal axis indicate the corresponding breath phases of retrospectively gated four-dimensional computed tomographic images. The duration of inspiration (T) is half that of exhalation (2 T).

this study. Eleven pigs were used in this study, weighing between 9 and 13 kg.

Ventilation and CT imaging were performed before and after an acute lung injury induced by infusion of 0.08 $cm^3\ kg^{-1}$ oleic acid into the internal jugular vein over 15 min. Maturation of lung injury was confirmed by a ratio of arterial oxygen tension to inspired oxygen fraction less than 300 mm Hg with at least 5 cm H_2O of positive end-expiratory pressure (PEEP). Each subject was then mechanically ventilated in a pressure-controlled modality for 30 min, using a FabianHFO hybrid oscillator/ventilator (ACUTRONIC Medical Systems AG, Switzerland). During baseline conditions, F_iO_2 was set to 40%, but was increased to maintain $S_pO_2 \geq 90\%$ following lung injury. Respiratory rate varied between 20 and 32 min^{-1}, with inspiratory-to-expiratory (I:E) ratio of 1:2. Sampling frequency for the ventilator waveforms was 200 Hz. Ventilator driving pressure was adjusted to obtain arterial CO_2 tension (P_aCO_2) in the target range of 30–60 mm Hg, while maintaining mean airway pressure ($\overline{P}_{aw}$) at 12 cm H_2O. Each 30-min ventilation interval was followed by an arterial blood gas analysis and 4DCT scan sequence, without interrupting mechanical ventilation (Herrmann et al., 2017). Before each ventilation interval, a 30-second recruitment maneuver to 35 cm H_2O of airway pressure was used to restore a control mechanical and physiological state. After completion of the experimental protocol, subjects were euthanized with an intravenous solution of pentobarbital sodium and phenytoin sodium (1 ml + 0.2 ml kg^{-1}).

Computed tomography scans were acquired using a Siemens SOMATOM Force (Siemens Healthineers, Germany) in an axial scanning mode, with 5.76 cm of axial coverage and 0.6 mm slice thickness. Subjects were continuously scanned for 30 s at 80 kVp tube voltage and 150 mA tube current, with 250 ms scanner rotation period, yielding an extensive series of x-ray projection data. Projection data were then retrospectively binned according to both the scanner rotation angle and acquisition timing relative to the periodic ventilation cycle (Herrmann et al., 2017), resulting in a sequence of distinct sinograms each corresponding to a specific ventilation phase. Each sinogram sequence was then reconstructed with isotropic 0.6 mm spatial resolution to obtain a 4DCT image sequence, yielding between 13 and 21 volumetric images in each sequence (depending on sampling constraints imposed by the choice of respiratory rate). The temporal sampling frequency for 21-phase image sequences was 7 Hz during ventilation at 20 min^{-1}, which is faster than the 4 Hz rotation frequency of the scanner. Each sequence was periodic in the temporal (i.e., phase) dimension, such that the choice of the "initial" image in the sequence was arbitrary. Voxels corresponding to spatial positions within the lungs were identified by a fully automated segmentation algorithm using a deep convolutional neural network (Gerard et al., 2018, 2020), generating a distinct lung mask for each image phase.

The periodic motion of respiratory structures was estimated using a deformable image registration technique, using four-dimensional cubic B-splines ensuring smoothness across both spatial and temporal dimensions (Metz et al., 2011). Fluctuations in CT voxel density due to variations in fractional gas content were compensated using a sum of squared tissue volume differences (SSTVD) similarity cost function (Gorbunova et al., 2008; Yin et al., 2009; Zhao et al., 2016), implemented in the Elastix library (Klein et al., 2010). After registration, the estimated transformations were used to deform images to align structures with a single, arbitrarily

selected reference phase. The phase most closely aligned with the end of inspiration was manually identified by the lowest level of aeration according to time-varying histograms of CT intensity. End-expiratory phase was then determined according to the 1:2 I:E ratio for all subjects. The elapsed time since end-inspiration was determined for each expiratory phase according to the fixed time interval associated with each phase interval.

Before exponential regression, images were downsampled to 1.2 mm isotropic resolution, to reduce the influence of noise on parameter estimation. The time-varying intensity within each voxel during exhalation only was fit to an exponential model:

$$\hat{I}_n = D_0 + (D_\infty - D_0) \bullet \left(1 - e^{-t_n/\tau_D}\right) \quad (1)$$

where $\hat{I}_n$ is the spatially varying estimate of actual CT intensity, I_n, at each ventilation phase n corresponding to elapsed expiratory time t_n, and D_0, D_∞, and τ_D are the spatially varying estimates of initial density, equilibrium density, and density time constant, respectively. Equilibrium density D_∞ is defined as the predicted value of CT intensity after a prolonged exhalation of infinite duration, i.e., as $t_n \to \infty$. Note that initial density and end-inspiratory density are the same, whereas the equilibrium density and end-expiratory density are not necessarily the same, especially if the duration of exhalation is longer than five times the time constant. **Figure 1** illustrates the concept of exponential decay in voxel aeration following a step change in airway pressure. Parameters were estimated by minimizing the sum of squared residuals between model-predicted intensity $\hat{I}_n$ and actual image itensity I_n for each ventilation phase n.

Regional time constants were estimated for changes in gas volume, by computing regressions for the specific air volume change by corrected Jacobian (SACJ; Ding et al., 2012) instead of density. The Jacobian determinant $|\mathcal{J}_{n\to 0}|$ describes the ratiometric total volume change of a voxel between ventilation phase n and the end-inspiratory reference phase 0:

$$|\mathcal{J}_{n\to 0}| = \frac{V_n}{V_0} \quad (2)$$

Specific air volume change by corrected Jacobian adjusts the Jacobian determinant to account for changes in voxel intensity as well, assuming that gas and tissue exhibit CT intensities of −1,000 and 0 HU, respectively (Ding et al., 2012):

$$\mathrm{SACJ}_n = |\mathcal{J}_{n\to 0}| \frac{I_n}{I_0} - 1 \quad (3)$$

Note that SACJ as defined is zero at end-inspiration, and negative at end-expiration if there is a loss of gas volume in the corresponding region.

The coefficient of determination and F statistic for each regression were computed to determine whether the exponential regression significantly contributed to prediction of variability. Voxels for which the F test yielded $p > 0.05$ were excluded from further analysis. Regional time constants were grouped and analyzed in several different ways. Time constants were grouped by aeration level using standard thresholds for CT intensity: hyper-aerated below −900 HU, normally aerated between −900 and −500 HU, poorly aerated between −500 and −100 HU, and non-aerated above −100 HU. Time constants were grouped by relative height in the gravitational field given by the position along the dorsal-ventral axis for subjects in the supine position. Time constants were grouped according to location on a parametric response map (PRM) corresponding to the initial and equilibrium densities of each voxel. Finally, time constants were grouped according to the nonequilibrated difference between end-expiratory density and predicted equilibrium density. For reference, an overall time constant for lung exhalation was obtained by applying Equation (1) to the exhaled gas volume measured at the proximal end of the endotracheal tube by the mechanical ventilator. Dynamic elastance was estimated by the quotient of driving pressure and tidal volume, assuming that inspiratory flow was nearly zero at end-inspiration.

RESULTS

Table 1 shows summarized ventilation parameters across all 11 subjects. The oleic acid injury model produced significantly lower ratios of alveolar oxygen tension to inspired oxygen fraction, meeting the criteria for severe (three subjects), moderate (seven subjects), and mild (one subject) acute respiratory distress syndome (ARDS). Injury was also associated with significantly higher dynamic elastance, respiratory rate, and inspiratory pressures. There was no significant difference in PEEP or tidal volume.

Figure 2 shows regional aeration at end-inspiration, intratidal aeration change, and the time constant of expiratory deaeration in a representative subject before and after lung injury. Voxels were excluded if exponential regression did not significantly contribute to prediction of variability compared to the mean at the 0.05 significance level. The majority of excluded voxels were either hyper-aerated or non-aerated with little or no intratidal change in aeration, and thus relatively constant aeration throughout exhalation. Upon close visual inspection, such voxels often constituted airways, pulmonary vasculature, and areas of nonrecruiting atelectasis.

Figure 3A shows the average volume fractions of hyper-, normally, poorly, and non-aerated lung. **Figures 3B,C** show the intratidal change in density (i.e., the difference between end-expiratory and end-inspiratory densities), as well as the

TABLE 1 | Summarized parameters for ventilation and respiratory system mechanics, before and after lung injury (mean ± SD).

	Baseline	Injured
Positive end-expiratory pressure (cmH_2O)	8.1 ± 1.5	7.7 ± 0.9
Inspiratory pressure (cmH_2O)	20.8 ± 1.6	25.4 ± 3.3*
Tidal volume (ml kg^{-1})	9.1 ± 1.7	7.5 ± 2.4
P_aO_2:F_IO_2 ratio (mmHg)	481 ± 85	136 ± 56*
Dynamic elastance (cmH_2O L^{-1})	143 ± 32	248 ± 59*

*Asterisks indicate a statistically significant difference between baseline and injured conditions according to a paired samples t-test (*p < 0.001). P_aO_2:F_IO_2 ratio, quotient of arterial oxygen partial pressure and inspired oxygen fraction.*

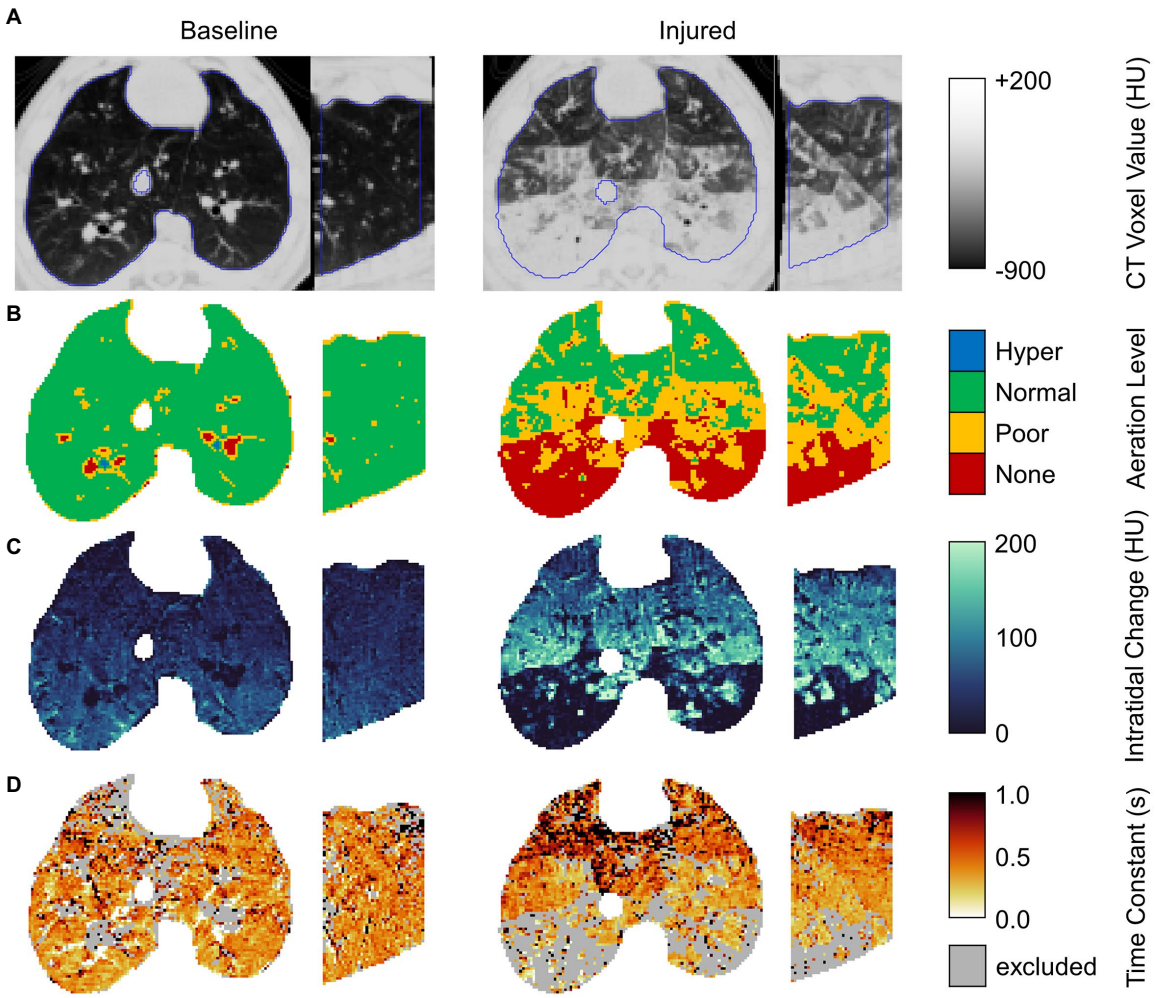

FIGURE 2 | Example axial and sagittal views from images of a single representative subject before and after lung injury. From top to bottom, rows show **(A)** the end-expiratory CT image with lung segmentation (blue line); **(B)** end-expiratory aeration level; **(C)** the intratidal density change given by the difference between end-inspiratory and end-expiratory densities; and **(D)** the regional density time constant (excluding voxels for which exponential regression did not significantly contribute to prediction of variability at the 0.05 significance level).

remaining nonequilibrated density change (i.e., the difference between predicted equilibrium density and end-expiratory density). The vast majority of intratidal variation in density occurred in regions that were normally or poorly aerated. Intratidal density change per voxel was largest in poorly aerated regions after lung injury. Overall, voxel densities equilibrated to within 20% of the expected change.

Figure 4 shows the regional density and SACJ time constants grouped according to aeration level, as well as the mechanical time constants for the entire respiratory system based on exhaled volume. Regional density time constants were typically larger (i.e., slower) than the overall time constants, but of the same order of magnitude. By contrast, the regional SACJ time constants were closer in magnitude to the overall time constant of the respiratory system. Regions with normal and poor aeration tended to exhibit slower regional time constants compared to hyper- and non-aerated regions. Although the overall time constants were reduced after lung injury, the regional density time constants were longer compared to baseline conditions.

Figure 5 shows a strong correlation between regional density and SACJ time constants, with SACJ time constants consistently faster than density time constants in the same region. This trend was observed before and after lung injury.

Figure 6 highlights the contributions of gravitational stress and lung weight on regional aeration dynamics. Dorsal proximity in the supine position was associated with reduced aeration at end-expiration and end-inspiration, with a larger intratidal change in aeration, and with a faster density time constant. Lung injury resulted in a reduction of aeration at all height levels, especially in the dorsal lung. Lung injury was also associated with larger intratidal changes in aeration, particularly in the middle regions between ventral and dorsal portions. These middle regions generally exhibited poor aeration at end-expiration. Compared to baseline conditions, the density

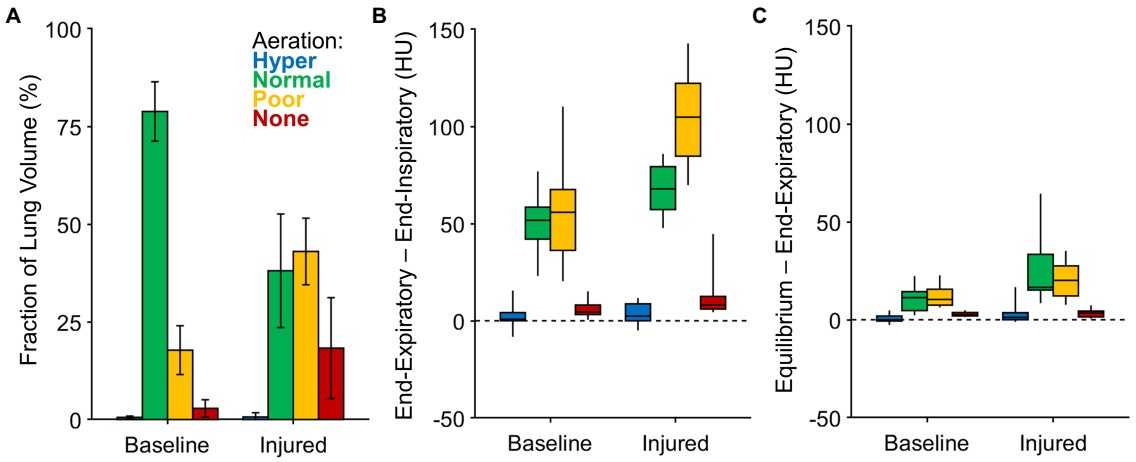

FIGURE 3 | Aeration levels at end-expiration, end-inspiration, and predicted equilibrium. **(A)** The fraction of imaged lung volume at each end-expiratory aeration level. **(B)** The intratidal density change or the difference between end-expiratory density and end-inspiratory density, among voxels at each aeration level. **(C)** The nonequilibrated remaining density change or the difference between predicted equilibrium density and end-expiratory density, among voxels at each aeration level.

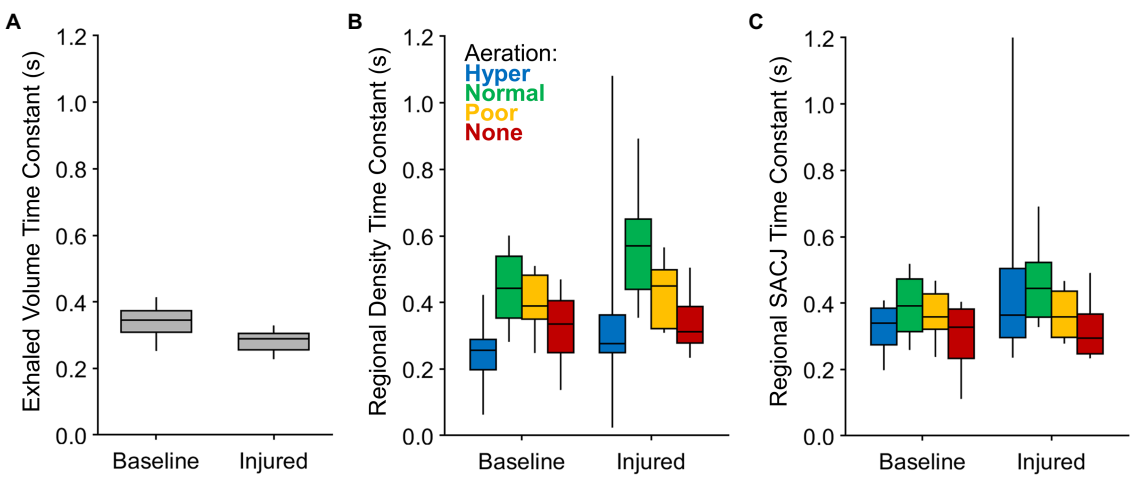

FIGURE 4 | Expiratory time constants estimated for **(A)** the entire lung based on exponential regression of exhaled volume measured at the proximal end of the endotracheal tube; **(B)** lung regions based on exponential regression of density changes among voxels at each aeration level; and **(C)** lung regions based on exponential regression of specific air volume change by corrected Jacobian (SACJ) among voxels at each aeration level.

time constants were not different after lung injury for any height level.

Figure 7A shows the average PRMs between end-expiratory and end-inspiratory density. The PRM in lung imaging typically depicts a two-dimensional histogram of lung voxels exhibiting each combination of end-expiratory and end-inspiratory density. In this figure, the predicted equilibrium density is used *in lieu* of the dynamic end-expiratory density, since PRMs are usually obtained quasi-statically *via* imaging during end-expiratory breathholds. Horizontal distance to the line of identity indicates the predicted density change between end-inspiration and equilibrium (i.e., after infinite exhalation duration). It is worth noting that a nonzero fraction of voxels was mapped above the line of identity, wherein density paradoxically decreases during exhalation. **Figure 7B** also shows how the distribution of density time constants depends on location within the PRM. In **Figure 7B**, the visualization represents not probability density but rather the median density time constant across subjects of voxels with end-expiratory and end-inspiratory aeration corresponding to that same location on the PRM. Data in this figure are aggregated from all subjects, such that any locations on the PRM without representation from at least half of all subjects were left blank. Regardless of lung condition, time constants were slower in regions that were normally aerated at both end-inspiration and end-expiration, compared to regions that were poorly aerated or non-aerated. However, there

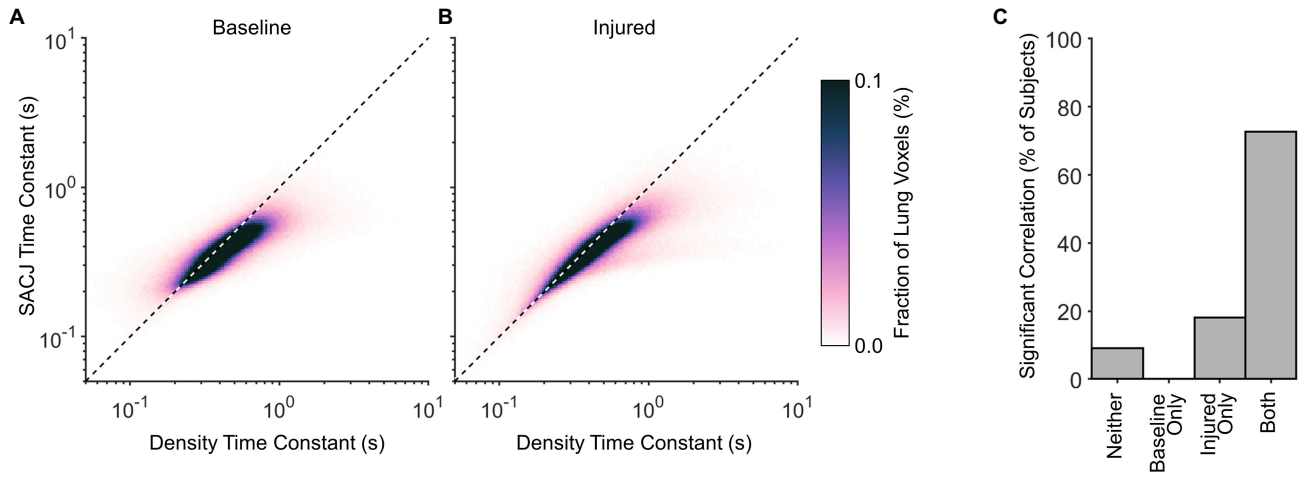

FIGURE 5 | Correlation between regional time constants estimated for density changes and specific air volume change by corrected Jacobian (SACJ). Average probability density distributions are shown for **(A)** baseline and **(B)** injured conditions, including voxels for which both exponential regressions significantly predicted variability in the respective signals at the 0.05 significance level. Dashed line indicates identity. **(C)** The fraction of subjects exhibiting significant correlations between density and SACJ time constants before and/or after lung injury.

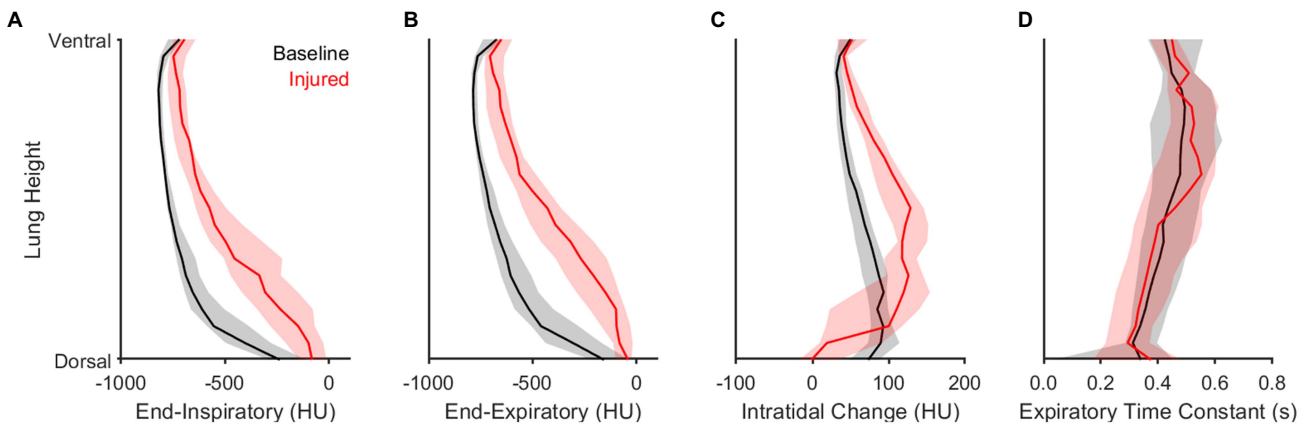

FIGURE 6 | Influence of height and lung condition on regional intratidal density variation. Panels show median and interquartile range at each relative height level along the dorsal-ventral axis for **(A)** end-inspiratory density, **(B)** end-expiratory density, **(C)** the difference between end-expiratory and end-inspiratory densities, and **(D)** the density time constant.

was also an effect of intratidal aeration change. Regions that were poorly aerated tended to have faster time constants when the predicted equilibrium change was small, and slower time constants when the predicted change was large. **Figure 7C** shows the nonequilibrated density change remaining at end-expiration (i.e., the difference between predicted equilibrium density and end-expiratory density). Similar to the observed distribution in **Figure 7B**, regions with larger predicted density changes also exhibited larger degrees of nonequilibration, as well as slower time constants.

Figure 8A expresses the average probability density distribution in terms of the nonequilibrated density change, rather than the end-inspiratory density usually shown in PRMs as in **Figure 7**. This depiction emphasizes that injured regions with the largest degree of nonequilibrated density change also exhibited poor aeration at predicted equilibrium (i.e., between −500 and −100 HU). **Figure 8B** shows the corresponding median density time constants, again linking large nonequilibrated density change to slower time constants, especially in regions with normal aeration at predicted equilibrium (i.e., between −900 and −500 HU).

Figure 9 shows the nonequilibrated density change as a normalized quantity, to represent the fractional convergence at end-expiration. The density time constant in this figure is also normalized by the duration of exhalation, which allows the resulting probability density distribution to be contextualized to the theoretical prediction for convergence of a single time constant exponential decay. The theoretical prediction provides a reliable lower bound for the nonequilibrated aeration changes. Regions with density time

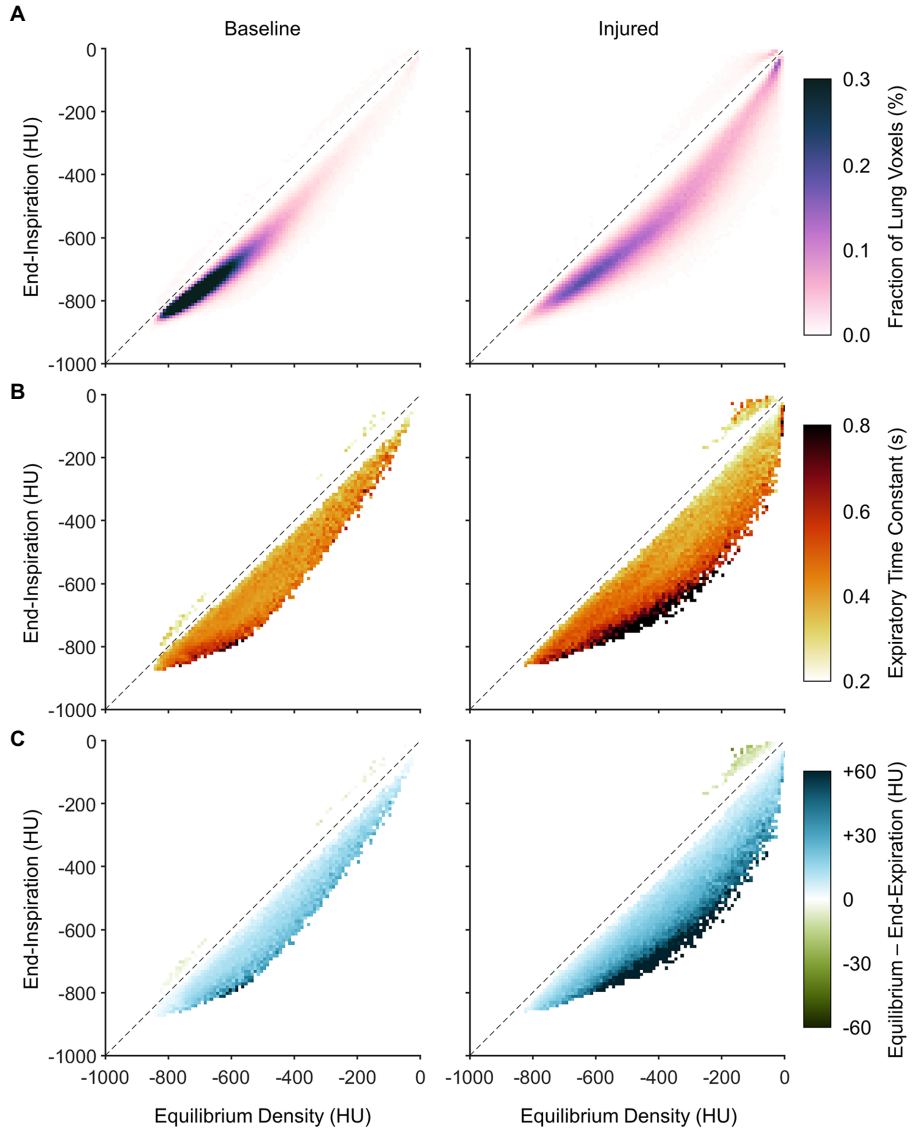

FIGURE 7 | Distributions of dynamic aeration characteristics before and after lung injury with respect to location on the parametric response map (PRM), aggregated across all subjects. **(A)** Aggregate PRM showing the average probability density distribution of lung voxels with a given initial (or end-inspiratory) density and equilibrium density. Note that equilibrium density is not necessarily equal to end-expiratory density. The dashed line is the line of identity, indicating no change between end-inspiration and equilibrium. **(B)** Median density time constants, shown wherever at least half of the subjects exhibited at least five voxels each at the corresponding location of the PRM. **(C)** The median difference between equilibrium density and end-expiratory density, using the same inclusion criteria as **(B)**.

constant less than one fifth of the total exhalation duration tended to exhibit nearly complete equilibration.

Figures 10, 11 show the distributions of regional density change and gas volume change from end-inspiration as expiratory time increases. Regions with poor aeration exhibit the largest changes in density, and also the largest changes in gas volume. Changes in gas volume were magnified by low initial gas volume in regions that were poorly or non-aerated at end-inspiration. Regional gas volume reduced up to 33% under baseline conditions over longer exhalations, and up to 80% after lung injury. Restricting gas volume changes to less than 40% after injury would have required exhalation times less than 0.2 s according to the exponential regression.

DISCUSSION

This study presents a retrospective analysis of regional expiratory deaeration dynamics in mechanically ventilated pigs before and after lung injury. Previous studies of regional exhalation time constants using CT imaging have been limited to two-dimensional

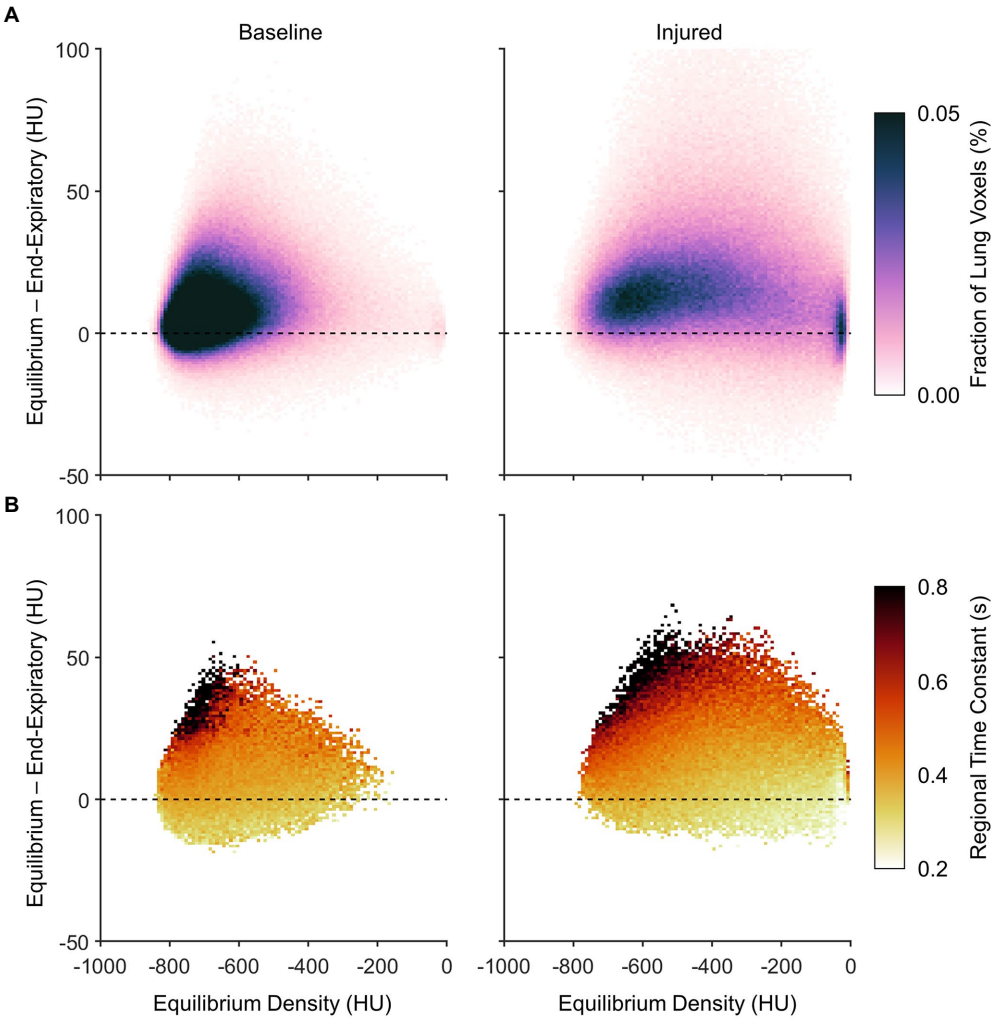

FIGURE 8 | Characteristics of nonequilibrating density at end-expiration according to the difference between predicted equilibrium density and end-expiratory density, aggregated across all subjects. **(A)** Average probability density distribution, with increasing vertical distance from the dashed line indicating an increasing lack of convergence to the equilibrium density by end-expiration. **(B)** Median expiratory time constants, shown wherever at least half of the subjects exhibited at least five voxels each at the corresponding locations of **(A)**.

analyses and slower imaging speeds, permitting only coarse resolution of large spatial regions over relatively long expiratory durations (Neumann et al., 1998a,b; Markstaller et al., 2001). These studies were limited by a lack of anatomic specificity (i.e., lung tissue was moving through the image plane during acquisition), such that a given region of analysis in the image may have yielded different structures at each point in time. Additionally, slower sampling rates limited the faster time constants that could have been reliably estimated. In this study, we reconstructed volumetric sections of lung tissue with 5.6 cm axial coverage and temporal sampling rates of up to 21 images per breath. Together with 4DCT image registration, this study enabled a higher resolution analysis of local aeration changes over shorter time scales. Our use of image registration also enabled calculation of specific air volume changes by the so-called "corrected" Jacobian determinant (SACJ). The primary findings of this study include (1) a tendency for poorly aerated regions to exhibit large intratidal density changes and slow time constants; (2) a potential for preventing derecruitment of poorly aerated regions with shorter exhalation times; (3) a large discrepancy between the overall mechanical time constant of the respiratory system and regional deaeration time constants; (4) a potential for regions with slow time constants to remain nonequilibrated at end-expiration, especially in the injured lung; and (5) the gravitational dependence of regional time constants that is independent of lung injury.

It may be inferred from **Figure 10** that shortening the allowable expiratory time during mechanical ventilation offers protection against derecruitment to regions of "unstable inflation," or poor aeration. If instead an extended exhalation time is allowed, these poorly aerated regions at end-inspiration experience the greatest change in density, suggesting increased

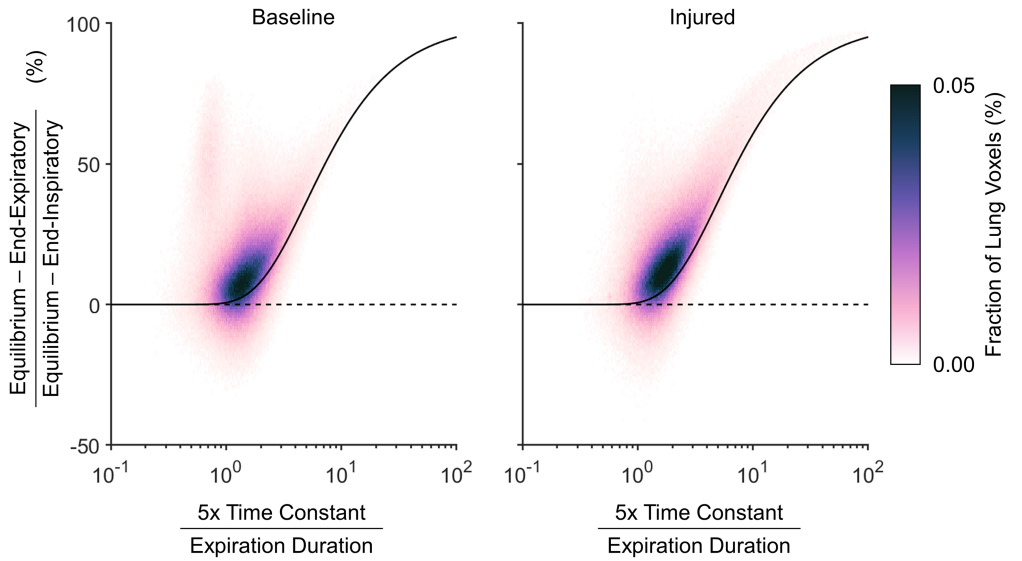

FIGURE 9 | Relative nonequilibrated density change remaining at end-expiration, according to the difference between predicted equilibrium density and end-expiratory density normalized by the total expected density change from end-inspiration to equilibrium, shown with respect to the estimated density time constant normalized by the total duration allowed for exhalation. A voxel with an estimated density time constant less than one fifth of the exhalation duration is expected to converge to within 0.7%. The black line shows theoretical expected convergence for exponential decay.

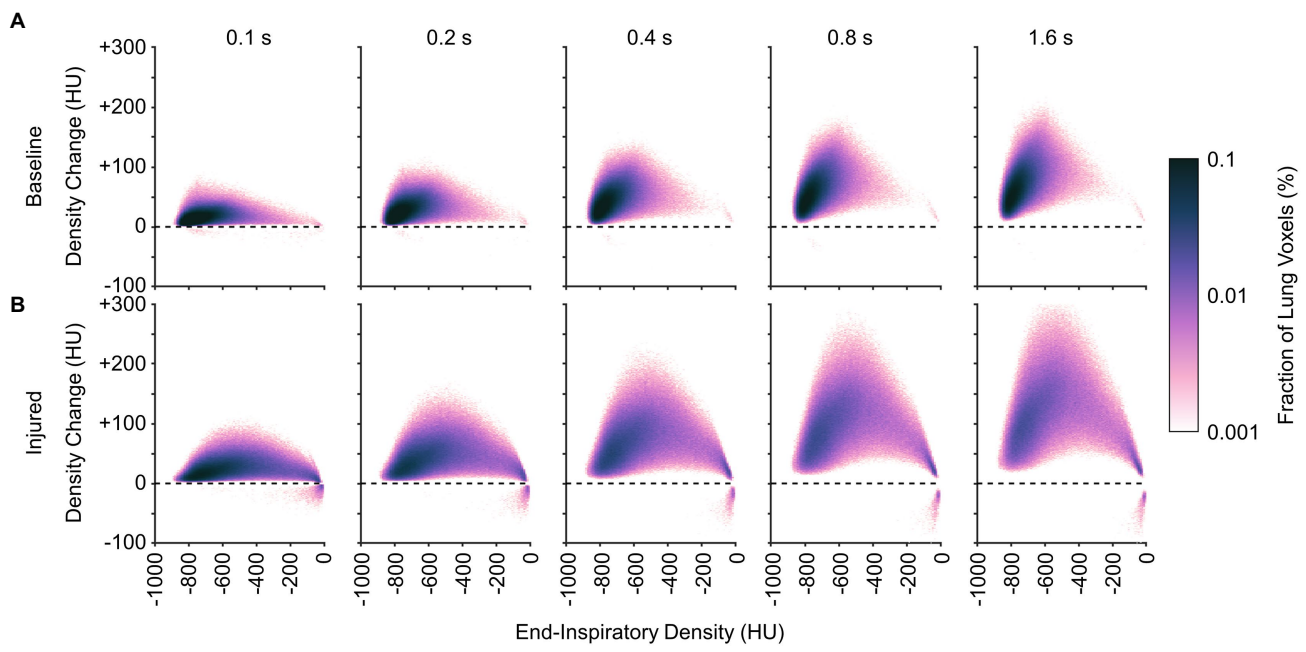

FIGURE 10 | Average distributions of density change at different time points during exhalation **(A)** before and **(B)** after lung injury. Density change was estimated from exponential regression.

proclivity for collapse during exhalation. It should be noted that the same change in density has a larger effect on poorly aerated compared to normally aerated regions. The relative change in gas volume is amplified by the lower initial gas volume in poorly aerated regions. For example, normally aerated regions at end-expiration are less susceptible to derecruitment, whereas poorly aerated regions may not tolerate similar degrees of deaeration. **Figure 11** highlights this discrepancy, with up to 80% loss of gas volume in poorly aerated regions of the injured lung during prolonged exhalation, compared to just 33% at baseline. For our lung injury model, ensuring a comparable upper limit of relative gas volume change requires a reduction

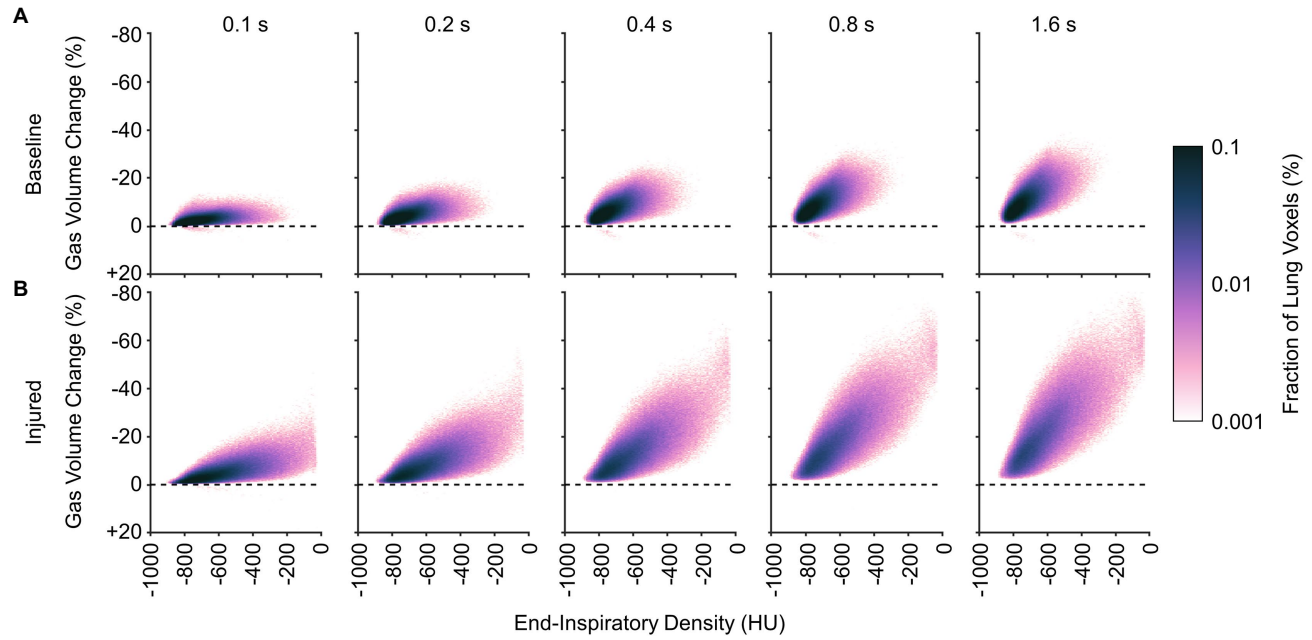

FIGURE 11 | Average distributions of relative gas volume change at different time points during exhalation **(A)** before and **(B)** after lung injury.

of the exhalation duration to 0.2 s or shorter. There are also wide ranges of time constants in poorly aerated regions (**Figure 8**), with an association between slower time constants and larger changes in CT density (**Figure 7**). Thus, limiting exhalation time prevents the largest changes in density from occurring, perhaps providing more stability to poorly aerated regions.

The mechanical time constant for the entire respiratory system, as estimated by exponential regression of exhaled gas volume, was 10–50% faster compared to the regional density time constants, as estimated by exponential regression of CT density (**Figure 4**). Neumann et al. (1998a) also reported lower mechanical time constants (estimated by the product of respiratory system resistance and compliance) compared to CT density changes. The product of average resistance and compliance in their study was approximately 0.4 s both before and after oleic acid injury, compared to time constants ranging 0.7–1.4 s based on CT density changes (Neumann et al., 1998a). Furthermore, these authors found no correlation between CT density time constants and mechanical time constants, reasoning that extraneous mechanisms of density change (e.g., blood volume fluctuations; Porra et al., 2017) confound a meaningful relationship between overall mechanical time constants and regional CT density time constants (Neumann et al., 1998a).

The specific air volume change by corrected Jacobian (SACJ) utilizes an intensity-corrected Jacobian determinant to account for changes in gas volume only, yielding strong correlations to specific ventilation, at least as estimated by xenon-CT imaging (Ding et al., 2012). We computed exponential regression of regional SACJ variation over time, in an attempt to determine whether the regional SACJ time constants provided a better correspondence to the overall mechanical time constant of the entire respiratory system. Indeed, the discrepancy between overall and regional time constants was reduced using SACJ instead of CT density (**Figure 3**). This finding demonstrates that the rate of gas volume change is consistently faster than the rate of aeration change (**Figure 5**), both globally and regionally. This suggests that increases in regional tissue volume, due to blood influx and/or fluid accumulation, occur on a slower time scale compared to corresponding reductions in gas volume. It is worth noting that gas exchange relies on gas volume change specifically (i.e., the turnover of alveolar gas), as opposed to the CT density change (which reflects the relative amounts of tissue vs. gas in a voxel). Therefore, the observation that gas volume changes occur faster than density changes provides some justification for the efficacy of lung-protective strategies with short exhalation: enough time for alveolar gas turnover but not enough time for alveolar collapse (Bates et al., 2020). Although relative gas volume changes estimated by SACJ may be more appropriate for representation of the regional mechanical response, the primary objective of our study was to evaluate the dynamics of regional CT density instead of gas volume, since regional density is associated with atelectasis (Gatto et al., 2004; Broche et al., 2017; Fardin et al., 2021) and atelectrauma (Cereda et al., 2017). It is therefore important to consider that the mechanical time constant of the respiratory system, which can be easily estimated at the bedside during mechanical ventilation, may substantially underestimate regional exhalation time constants. Electrical impedance tomography may offer a low-resolution

bedside alternative for measurement of aeration dynamics (Karagiannidis et al., 2018; Victor et al., 2019).

Cereda et al. (2017) identified locations on the PRM associated with the highest risk of injury progression and complete loss of aeration over the course of multiple hours. These high risk locations were characterized by voxels with "unstable inflation," including those normally or poorly aerated at end-inspiration, but poorly or non-aerated at end-expiration. Several ventilatory strategies may reduce the fraction of lung operating in the high risk category, such as prone positioning (Xin et al., 2018) and use of PEEP. However, within the high risk PRM locations, there is still great variability of the dynamic characteristics of aeration change from end-inspiration to end-expiration. The 4DCT dynamic approach used in our study may supplement risk categorization based solely on end-inspiratory and end-expiratory densities, by contributing new information about precisely how density changes in each voxel between two endpoints. Importantly, our approach highlights the benefit of using short expiratory times as an alternative lung-protective strategy, to prevent derecruitment of high-risk lung regions. Such strategies include inverse ratio ventilation, airway pressure release ventilation, or time-controlled adaptive ventilation (Nieman et al., 2020).

Quasi-static imaging during end-expiratory breathholds likely overestimates the extent of aeration loss. The lung exhibits a wide distribution of region time constants, with some regions equilibrating over 10-fold longer time scales than others (**Figure 4**). Mechanical nonequilibration may contribute substantially to the measurement of regional aeration. Thus dynamic CT imaging, without interruption of mechanical ventilation, may yield more clinically relevant information. Even if gas flow is completely occluded, intrapulmonary gas redistribution and pendelluft may still affect the measurement of regional aeration, as well as time-dependent changes in regional recruitment (Bates and Irvin, 2002). Decreasing CT density during exhalation, evidenced in **Figure 7**, is a counterintuitive phenomenon that may indicate out-of-phase gas redistribution (Kaczka et al., 2011; Perchiazzi et al., 2014).

Limitations

Our particular CT reconstruction technique relies on an assumption of temporal periodicity in the motion of thoracic structures (Herrmann et al., 2017). Asynchronous motion (e.g., due to cardiac contractions) may produce motion artifact and blurring. Furthermore, lung recruitment and derecruitment at the microscale exhibit irregularity over time (Broche et al., 2017), such that breath-to-breath variability of regional density may not be periodic. In our study, such irregular density variations are averaged over 30 s of CT scanning. The limited axial field-of-view provided by this imaging technique encompasses only a portion of the total lung volume. Apical and basal lung regions may exhibit different aeration responses. In addition, mean airway pressure was explicitly controlled in this study rather than PEEP, although all PEEP settings were between 5 and 10 cm H_2O (**Table 1**). Neumann et al. (1998a) report faster time constants in an oleic acid model of lung injury when subjects were allowed to exhale to atmospheric pressure compared to 5 cm H_2O PEEP yet no consistent difference in response to different PEEP levels greater than 10 cm H_2O (Neumann et al., 1998b), highlighting the nonlinearity of respiratory system mechanics during passive exhalation.

We also did not determine the inspiratory time constants in our study. Given the 1:2 I:E ratio used in our study, only seven sequential images during inspiration could be reconstructed – potentially too few time points to ensure reliable regression especially in regions with longer time constants. Neumann et al. (1998a) also report faster time constants in pigs with an oleic acid model of lung injury during exhalation compared to inspiration, reasoning that the injured lung may tend to derecruit faster than it recruits.

Finally, our model for ARDS relied on oleic acid infusion into the central venous circulation, which mimics certain features of the fat emboli syndrome (Ballard-Croft et al., 2012). While the exact mechanism of injury from oleic acid remains elusive, it is associated with increased vascular permeability, as well as patchy, heterogenous edema in the airspaces and interstitium (Wang et al., 2008). Neumann et al. (1998a) noted differences in regional time constants among the oleic acid, saline lavage, and endotoxin models of lung injury. Unfortunately, CT imaging alone cannot distinguish between intraalveolar vs. interstitial edema in the poorly aerated regions we identified, at least for the spatial resolution of our scanner. Accordingly, one should exercise caution in generalizing our results in a small animal model of porcine oleic acid injury to mechanically ventilated humans with the acute respiratory distress syndrome. The underlying etiology of respiratory failure may yield differences in regional lung recruitability and dynamic behavior, as well as differences in noninjurious ventilatory approaches.

Conclusion

Mechanical time constants for the entire respiratory system based on exhaled gas volume may underestimate the regional time constants of deaeration based on 4DCT imaging. After lung injury, poorly aerated regions tend to experience larger intratidal changes in aeration over shorter time scales compared to normally aerated regions. However, within these poorly aerated regions, the largest intratidal aeration changes occur over the longest time scales. These dynamic imaging results provide supporting evidence for the susceptibility of poorly aerated regions to ventilator-induced lung injury, and for the protective benefits of short exhalation times during mechanical ventilation of acutely injured lungs.

DATA AVAILABILITY STATEMENT

The raw data supporting the conclusions of this article will be made available by the authors, without undue reservation.

ETHICS STATEMENT

The animal study was reviewed and approved by University of Iowa Institute for Animal Care and Use Committee.

AUTHOR CONTRIBUTIONS

JH and DK conceived the study, collected the data, and wrote the manuscript. JH, SG, WS, YX, MC, JR, GC, EH, and DK analyzed the data and revised the manuscript. All authors contributed to the article and approved the submitted version.

FUNDING

This work was supported by the Office of the Assistant Secretary of Defense for Health Affairs, through the Peer Reviewed Medical Research Program under Award Numbers W81XWH-16-1-0434 and W81XWH-20-1-0696. Opinions, interpretations, conclusions, and recommendations are those of the authors and are not necessarily endorsed by the Department of Defense. This study was also supported by the Department of Anesthesia at the University of Iowa Hospital and Clinics, and by National Institutes of Health awards R41 HL140640, R01 CA166703, and R01 HL142625. This work utilized a CT scanner that was purchased with funding from National Institutes of Health Shared Instrumentation Grant 1S10OD018526. This research was supported in part through high-performance computing resources provided by The University of Iowa, Iowa City, Iowa.

ACKNOWLEDGMENTS

Andrea Fonseca da Cruz, Bakir Hajdarevic, Eli Schmidt, Chelsea Sloan, and Kelly M. Stark assisted with performing the experimental protocol. Melissa Saylor, Jarron Atha, and Shayna Hogue assisted with computed tomographic imaging. Ahmed Halaweish, Mathew K. Fuld, and Siemens Healthineers (Forchheim, Germany) provided technical assistance for image reconstruction. Andrea Fonseca da Cruz, Eli Schmidt, Charles A. Mascardo, and Ethan L. Chen assisted with manual image segmentation. ZOLL Medical Corporation generously loaned a portable ventilator for use in animal experiments. The authors are deeply grateful for all of their contributions to this investigation.

REFERENCES

Ballard-Croft, C., Wang, D., Sumpter, L. R., Zhou, X., and Zwischenberger, J. B. (2012). Large-animal models of acute respiratory distress syndrome. *Ann. Thorac. Surg.* 93, 1331–1339. doi: 10.1016/j.athoracsur.2011.06.107

Bates, J. H. T., Gaver, D. P., Habashi, N. M., and Nieman, G. F. (2020). Atelectrauma versus volutrauma: A tale of two time-constants. *Crit. Care Explor.* 2:e0299. doi: 10.1097/CCE.0000000000000299

Bates, J. H. T., and Irvin, C. G. (2002). Time dependence of recruitment and derecruitment in the lung: a theoretical model. *J. Appl. Physiol.* 93, 705–713. doi: 10.1152/japplphysiol.01274.2001

Broche, L., Perchiazzi, G., Porra, L., Tannoia, A., Pellegrini, M., Derosa, S., et al. (2017). Dynamic mechanical interactions between neighboring airspaces determine cyclic opening and closure in injured lung. *Crit. Care Med.* 45, 687–694. doi: 10.1097/CCM.0000000000002234

Broche, L., Pisa, P., Porra, L., Degrugilliers, L., Bravin, A., Pellegrini, M., et al. (2019). Individual airway closure characterized in vivo by phase-contrast CT imaging in injured rabbit lung. *Crit. Care Med.* 47, e774–e781. doi: 10.1097/CCM.0000000000003838

Carney, D., DiRocco, J., and Nieman, G. F. (2005). Dynamic alveolar mechanics and ventilator-induced lung injury. *Crit. Care Med.* 33, S122–S128. doi: 10.1097/01.CCM.0000155928.95341.BC

Carvalho, A. R., Spieth, P. M., Pelosi, P., Vidal Melo, M. F., Koch, T., Jandre, F. C., et al. (2008). Ability of dynamic airway pressure curve profile and elastance for positive end-expiratory pressure titration. *Intensive Care Med.* 34, 2291–2299. doi: 10.1007/s00134-008-1301-7

Cereda, M., Xin, Y., Goffi, A., Herrmann, J., Kaczka, D. W., Kavanagh, B. P., et al. (2019). Imaging the injured lung: mechanisms of action and clinical use. *Anesthesiology* 131, 716–749. doi: 10.1097/ALN.0000000000002583

Cereda, M., Xin, Y., Hamedani, H., Bellani, G., Kadlecek, S., Clapp, J., et al. (2017). Tidal changes on CT and progression of ARDS. *Thorax* 72, 981–989. doi: 10.1136/thoraxjnl-2016-209833

Crotti, S., Mascheroni, D., Caironi, P., Pelosi, P., Ronzoni, G., Mondino, M., et al. (2001). Recruitment and derecruitment during acute respiratory failure: a clinical study. *Am. J. Respir. Crit. Care Med.* 164, 131–140. doi: 10.1164/ajrccm.164.1.2007011

Ding, K., Cao, K., Fuld, M. K., Du, K., Christensen, G. E., Hoffman, E. A., et al. (2012). Comparison of image registration based measures of regional lung ventilation from dynamic spiral CT with Xe-CT. *Med. Phys.* 39, 5084–5098. doi: 10.1118/1.4736808

Fardin, L., Broche, L., Lovric, G., Mittone, A., Stephanov, O., Larsson, A., et al. (2021). Imaging atelectrauma in ventilator-induced lung injury using 4D X-ray microscopy. *Sci. Rep.* 11:4236. doi: 10.1038/s41598-020-77300-x

Gatto, L. A., Fluck, R. R., and Nieman, G. F. (2004). Alveolar mechanics in the acutely injured lung: role of alveolar instability in the pathogenesis of ventilator-induced lung injury. *Respir. Care* 49, 1045–1055.

Gaver, D. P., Nieman, G. F., Gatto, L. A., Cereda, M., Habashi, N. M., and Bates, J. H. T. (2020). The POOR get POORer: a hypothesis for the pathogenesis of ventilator-induced lung injury. *Am. J. Respir. Crit. Care Med.* 202, 1081–1087. doi: 10.1164/rccm.202002-0453CP

Gerard, S. E., Herrmann, J., Kaczka, D. W., Musch, G., Fernandez-Bustamante, A., and Reinhardt, J. M. (2020). Multi-resolution convolutional neural networks for fully automated segmentation of acutely injured lungs in multiple species. *Med. Image Anal.* 60:101592. doi: 10.1016/j.media.2019.101592

Gerard, S. E., Herrmann, J., Kaczka, D. W., and Reinhardt, J. M. (2018). "Transfer learning for segmentation of injured lungs using coarse-to-fine convolutional neural networks," in *Image Analysis for Moving Organ, Breast, and Thoracic Images. RAMBO 2018, BIA 2018, TIA 2018. Lecture Notes in Computer Science, vol 11040*. eds. D. Stoyanov, Z. Taylor, B. Kainz, G. Maicas, R. Beichel, A. Martel, et al. (Basel, Switzerland: Springer International Publishing), 191–201.

Gorbunova, V., Lol, P., Ashraf, H., Dirksen, A., Nielsen, M., and de Bruijne, M. (2008). Weight preserving image registration for monitoring disease progression in lung CT. *Med. Image Comput. Comput. Assist. Interv.* 11, 863–870. doi: 10.1007/978-3-540-85990-1-104

Herrmann, J., Gerard, S. E., Reinhardt, J. M., Hoffman, E. A., and Kaczka, D. W. (2021). Regional gas transport during conventional and oscillatory ventilation assessed by xenon-enhanced computed tomography. *Ann. Biomed. Eng.*. doi:10.1007/s10439-021-02767-2 [Epub ahead of print].

Herrmann, J., Gerard, S. E., Shao, W., Hawley, M. L., Reinhardt, J. M., Christensen, G. E., et al. (2020a). Quantifying regional lung deformation using four-dimensional computed tomography: a comparison of conventional and oscillatory ventilation. *Front. Physiol.* 11:14. doi: 10.3389/fphys.2020.00014

Herrmann, J., Gerard, S. E., Shao, W., Xin, Y., Cereda, M., Reinhardt, J. M., et al. (2020b). "Expiratory de-aeration occurs faster in poorly- vs. normally-aerated regions of the injured lung." in *Annual Meeting of the American Thoracic Society* (Virtual); August 5–10, 2020, A4107.

Herrmann, J., Hoffman, E. A., and Kaczka, D. W. (2017). Frequency-selective computed tomography: applications during periodic thoracic motion. *IEEE Trans. Med. Imaging* 36, 1722–1732. doi: 10.1109/TMI.2017.2694887

Jain, S. V., Kollisch-Singule, M., Sadowitz, B., Dombert, L., Satalin, J., Andrews, P., et al. (2016). The 30-year evolution of airway pressure release ventilation (APRV). *Intensive Care Med. Exp.* 4:11. doi: 10.1186/s40635-016-0085-2

Kaczka, D. W., Cao, K., Christensen, G. E., Bates, J. H. T., and Simon, B. A. (2011). Analysis of regional mechanics in canine lung injury using forced oscillations and 3D image registration. *Ann. Biomed. Eng.* 39, 1112–1124. doi: 10.1007/s10439-010-0214-0

Kaczka, D. W., Herrmann, J., Gerard, S. E., Shao, W., Xin, Y., Cereda, M., et al. (2020). "Regional aeration and expiratory time constants during pressure-controlled ventilation in porcine lung injury." in *Annual Meeting of the American Society of Anesthesiologists* (Virtual); October 3–7, 2020, A3037.

Karagiannidis, C., Waldmann, A. D., Róka, P. L., Schreiber, T., Strassmann, S., Windisch, W., et al. (2018). Regional expiratory time constants in severe respiratory failure estimated by electrical impedance tomography: a feasibility study. *Crit. Care* 22:221. doi: 10.1186/s13054-018-2137-3

Klein, S., Staring, M., Murphy, K., Viergever, M. A., and Pluim, J. P. W. (2010). Elastix: A toolbox for intensity-based medical image registration. *IEEE Trans. Med. Imaging* 29, 196–205. doi: 10.1109/TMI.2009.2035616

Markstaller, K., Eberle, B., Kauczor, H. U., Scholz, A., Bink, A., Thelen, M., et al. (2001). Temporal dynamics of lung aeration determined by dynamic CT in a porcine model of ARDS. *Br. J. Anaesth.* 87, 459–468. doi: 10.1093/bja/87.3.459

Metz, C. T., Klein, S., Schaap, M., van Walsum, T., and Niessen, W. J. (2011). Nonrigid registration of dynamic medical imaging data using nD+t B-splines and a groupwise optimization approach. *Med. Image Anal.* 15, 238–249. doi: 10.1016/j.media.2010.10.003

Neumann, P., Berglund, J. E., Mondéjar, E. F., Magnusson, A., and Hedenstierna, G. (1998a). Dynamics of lung collapse and recruitment during prolonged breathing in porcine lung injury. *J. Appl. Physiol.* 85, 1533–1543. doi: 10.1152/jappl.1998.85.4.1533

Neumann, P., Berglund, J. E., Mondéjar, E. F., Magnusson, A., and Hedenstierna, G. (1998b). Effect of different pressure levels on the dynamics of lung collapse and recruitment in oleic-acid-induced lung injury. *Am. J. Respir. Crit. Care Med.* 158, 1636–1643. doi: 10.1164/ajrccm.158.5.9711095

Nieman, G. F., Gatto, L. A., Andrews, P., Satalin, J., Camporota, L., Daxon, B., et al. (2020). Prevention and treatment of acute lung injury with time-controlled adaptive ventilation: physiologically informed modification of airway pressure release ventilation. *Ann. Intensive Care* 10:3. doi: 10.1186/s13613-019-0619-3

Perchiazzi, G., Rylander, C., Derosa, S., Pellegrini, M., Pitagora, L., Polieri, D., et al. (2014). Regional distribution of lung compliance by image analysis of computed tomograms. *Respir. Physiol. Neurobiol.* 201, 60–70. doi: 10.1016/j.resp.2014.07.001

Porra, L., Broche, L., D'Egrugilliers, L., Albu, G., Malaspinas, I., Doras, C., et al. (2017). Synchrotron imaging shows effect of ventilator settings on intra breath cyclic changes in pulmonary blood volume. *Am. J. Respir. Cell Mol. Biol.* 57, 459–467. doi: 10.1165/rcmb.2017-0007OC

Slutsky, A. S., and Ranieri, V. M. (2013). Ventilator-induced lung injury. *N. Engl. J. Med.* 369, 2126–2136. doi: 10.1056/NEJMra1208707

Victor, M., Melo, J., Roldán, R., Nakamura, M., Tucci, M., Costa, E., et al. (2019). Modelling approach to obtain regional respiratory mechanics using electrical impedance tomography and volume-dependent elastance model. *Physiol. Meas.* 40:45001. doi: 10.1088/1361-6579/ab144a

Wang, H. M., Bodenstein, M., and Markstaller, K. (2008). Overview of the pathology of three widely used animal models of acute lung injury. *Eur. Surg. Res.* 40, 305–316. doi: 10.1159/000121471

Xin, Y., Cereda, M., Hamedani, H., Pourfathi, M., Siddiqui, S., Meeder, N., et al. (2018). Unstable inflation causing injury insight from prone position and paired computed tomography scans. *Am. J. Respir. Crit. Care Med.* 198, 197–207. doi: 10.1164/rccm.201708-1728OC

Yin, Y., Hoffman, E. A., and Lin, C.-L. (2009). Mass preserving nonrigid registration of CT lung images using cubic B-spline. *Med. Phys.* 36, 4213–4222. doi: 10.1118/1.3193526

Zhao, B., Christensen, G. E., Hyun Song, J., Pan, Y., Gerard, S. E., Reinhardt, J. M., et al. (2016). "Tissue-volume preserving deformable image registration for 4DCT pulmonary images." in *Proceedings of the IEEE Conference on Computer Vision and Pattern Recognition Workshops*; June 26–July 01, 41–49.

Conflict of Interest: JH and DK are co-founders and shareholders of OscillaVent, Inc. and consultants for ZOLL Medical Corporation. JR and EH are co-founders and shareholders of VIDA Diagnostics, Inc., and GC is paid licensing fees from VIDA Diagnostics, Inc.

Publisher's Note: All claims expressed in this article are solely those of the authors and do not necessarily represent those of their affiliated organizations, or those of the publisher, the editors and the reviewers. Any product that may be evaluated in this article, or claim that may be made by its manufacturer, is not guaranteed or endorsed by the publisher.

frontiers in Medicine

SYSTEMATIC REVIEW
published: 10 August 2021
doi: 10.3389/fmed.2021.705960

Diagnosis Accuracy of Lung Ultrasound for ARF in Critically Ill Patients: A Systematic Review and Meta-Analysis

*Xueyan Yuan, Ling Liu, Wei Chang, Zongsheng Wu, Lili Huang, Yali Chao, Xinxing Lu, Jianfeng Xie, Yi Yang and Haibo Qiu**

Jiangsu Provincial Key Laboratory of Critical Care Medicine, Department of Critical Care Medicine, Zhongda Hospital, School of Medicine, Southeast University, Nanjing, China

Background: Acute respiratory failure (ARF) is a commonly distressing condition in critically ill patients. Its early recognition and treatment may improve clinical outcomes. Mounting evidence suggests that lung ultrasound (LUS) could be an alternative to chest X-ray (CXR) or computed tomography (CT) for the diagnosis of ARF in critically ill patients. This meta-analysis aimed to determine whether LUS can be an alternative tool used to investigate the cause of ARF or thoracic pathologies associated with the diagnosis of ARF in critically ill patients.

Method: A systematic literature search of the PubMed, Web of Science, Embase, and Cochrane Library databases was conducted from inception to March 2020. Two researchers independently screened studies investigating the accuracy of LUS with CXR or CT for adult critically ill patients with ARF. Data with baseline, true positives, false positives, false negatives, and true negatives were extracted. The study quality was assessed using the Quality Assessment of Diagnostic Accuracy Studies-2 tool. The pooled sensitivity and specificity were obtained using a bivariate model.

Results: Eleven studies, including 1,232 patients, were included in the meta-analysis. Most studies were of low quality. LUS had a pooled sensitivity of 92% (95% confidence interval [CI]: 85–96) and a pooled specificity of 98% (95% CI: 94–99). The area under the summary receiver operating characteristic curve was 98% (95% CI: 97–99). The sensitivity and specificity of LUS to identify different pathological types of ARF were investigated. For consolidation (1,040 patients), LUS had a sensitivity of 89% and a specificity of 97%. For pleural effusion (279 patients), LUS had a pooled sensitivity of 95% and a specificity of 99%. For acute interstitial syndrome (174 patients), LUS had a pooled sensitivity of 95% and a specificity of 91%.

Conclusions: LUS is an adjuvant tool that has a moderate sensitivity and high specificity for the diagnosis of ARF in critically ill patients.

Systematic Review Registration: The study protocol was registered with PROSPERO (CRD42020211493).

Keywords: lung ultrasound, diagnostic accuracy, consolidation, acute interstitial syndrome, acute respiratory failure

OPEN ACCESS

Edited by:
Piero Valentini, Università Cattolica del Sacro Cuore, Italy

Reviewed by:
Luigi Vetrugno, University of Udine, Italy
Marek Nalos, Nepean Hospital, Australia
Maged Hassan, Alexandria University, Egypt

****Correspondence:***
Haibo Qiu
haiboq2000@163.com

Specialty section:
This article was submitted to Pulmonary Medicine, a section of the journal Frontiers in Medicine

Received: *14 May 2021*
Accepted: *12 July 2021*
Published: *10 August 2021*

Citation:
Yuan X, Liu L, Chang W, Wu Z, Huang L, Chao Y, Lu X, Xie J, Yang Y and Qiu H (2021) Diagnosis Accuracy of Lung Ultrasound for ARF in Critically Ill Patients: A Systematic Review and Meta-Analysis. Front. Med. 8:705960. doi: 10.3389/fmed.2021.705960

INTRODUCTION

Acute respiratory failure (ARF) is a commonly distressing condition in critically ill patients with increased incidence (1). The common causes of ARF include pneumonia, sepsis, heart failure, and chronic obstructive pulmonary disease (COPD) (1, 2). In most cases, patients with ARF present in conditions not suitable for the establishment of accurate diagnosis at the early stage of illness, which may compromise the outcomes (3, 4). Early recognition and treatment of ARF may play an important role in improving clinical outcomes.

The diagnosis of the underlying causes of ARF is dependent on chest imaging, with unreliable results. Chest X-ray (CXR) is recommended as the first-line imaging modality for the diagnosis of ARF in intensive care units (ICUs), but the limited supine films result in diminished diagnostic accuracy for consolidation (5). The "gold standard" modality, chest computed tomography (CT), has considerable limitation, although it currently offers a higher accurate diagnosis for lung lesions (6). This is related to the difficulties and risks of transportation, radiation exposure, and costs (7).

Lung ultrasound (LUS) is possibly a reliable diagnostic approach that can be used in critically ill patients (8). Studies have shown that the diagnostic accuracy of LUS for pneumonia was well-established (9–11). Available data have also suggested that LUS had a high diagnostic performance for commonly encountered conditions, such as pulmonary embolism and pneumothorax (12, 13). Furthermore, LUS is portable, inexpensive, radiation-free, non-invasive, and real-time at the bedside. Thus, LUS may be a potential alternative to chest radiography or CT for the diagnosis of ARF.

This systematic literature review and meta-analysis aimed to assess the diagnostic performance (including sensitivity and specificity) of LUS for the different pathological types of critically ill patients with ARF.

METHODS

We conducted this systematic review and meta-analysis to assess the diagnostic efficacy of LUS in ARF in accordance with the Preferred Reporting Items for Systematic Reviews and Meta-analyses (PRISMA) guidelines for Diagnostic Test Accuracy (14). The meta-analysis was prospectively registered at https://www.crd.york.ac.uk/prospero/ with the registration number CRD42020211493.

Search Strategy and Study Selection

Two researchers (XY and LH) independently conducted an electronic database search, including PubMed, Embase, the Cochrane Library, and Web of Science databases, to identify potentially eligible studies published from inception to March 2020. The search strategy included controlled vocabulary (i.e., Medical Subject Headings) and free-text words for two basic concepts: (1) ultrasonography and (2) ARF, respiratory insufficiency, and ventilatory depression. The search strategy details are presented in **Supplementary Table 1**. Two researchers (XY and ZW) selected and evaluated the titles and abstracts of the retrieved literature. All disagreements between the two researchers were resolved by the intervention of a third expert (WC).

This systematic review and meta-analysis included all English-language articles describing retrospective and prospective observational studies. Studies were included if they (i) enrolled adult patients with clinically suspected or confirmed ARF caused by any etiology, (ii) compared the diagnostic accuracy of LUS for ARF with radiography or CT, and (iii) included more than 20 consecutive patients. The following studies were excluded: case reports, studies with abstracts without full text available, animal studies, and pediatric studies. The outcomes were all data concerning diagnostic accuracy including sensitivity, specificity, pooled positive likelihood ratio (PLR), pooled negative likelihood ratio (NLR), and diagnostic odds ratio (DOR) with 95% confidence intervals (CIs). PLR and NLR indicate the reliability of the results. The higher the PLR value, the greater the probability of the diagnosis of ARF with LUS. Meanwhile, NLR has a contrasting concept. A higher DOR indicates a higher diagnostic accuracy.

Data Extraction

Two researchers (XL and YC) independently extracted the data including the number of true positives, false positives, false negatives, and true negatives with prepared data extraction forms. When the information we needed was not explicitly obtained in the selected studies, a 2×2 table was built to calculate the required data. Additionally, other data, including the year of the studies, settings, origins of patients, sample sizes, causes of ARF, ultrasound equipment, lung areas examined, and expertise of operators, were obtained.

Quality Assessment

The Quality Assessment of Diagnostic Accuracy Studies-2 tool (QUADAS-2) was performed to assess the methodological quality of the selected studies (15). Studies with potential risk of bias for any domains were identified to have high risk of bias overall. Overall quality was independently determined by two researchers (XY and YC) with discrepancies solved by consensus.

Data Analysis and Synthesis

The statistical analysis was performed in the raw data according to the European Association for Technology Assessment recommendations (16). The quality of the included studies was assessed using QUADAS-2 with Review Manager 5.3. The pooled sensitivity and specificity were obtained using a bivariate model with Stata 15.0. The Midas module included in the Stata statistical package was used to construct forest plots. Heterogeneity was estimated using the Q-test and the I^2 statistic, and significant heterogeneity was considered when the P-value was <0.05 or I^2 was $>50\%$. The summary receiver operating characteristic (SROC) curves were plotted to estimate the true positivity and specificity. Meanwhile, Fagan's nomogram and likelihood ratio plot were performed to assess the clinical applicability of LUS in diagnosing ARF. The causes of heterogeneity in the studies were identified using subgroup analysis and meta-regression analysis. A sensitivity analysis was performed to assess the stability of the

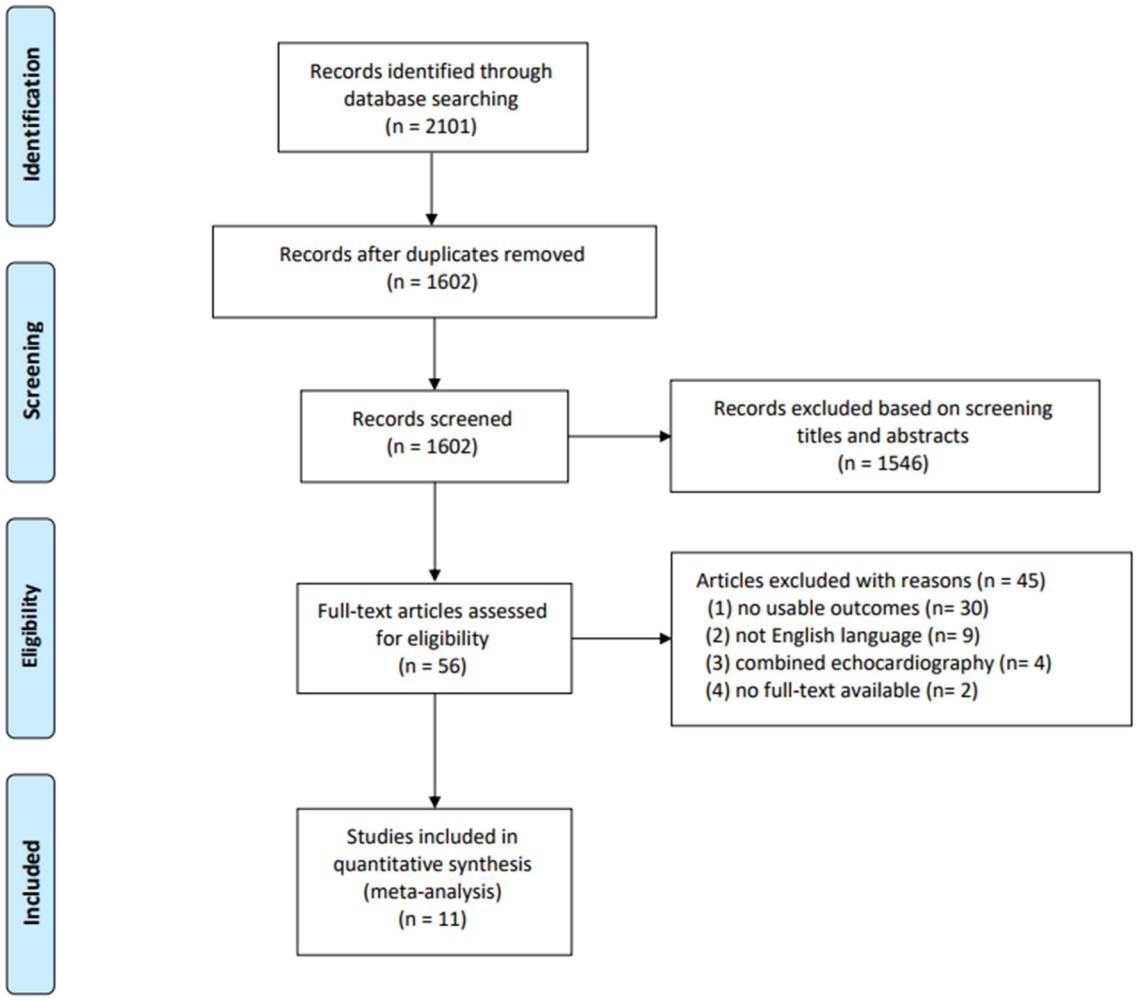

FIGURE 1 | Flowchart of the selection process for the included studies.

results. Publication bias was estimated with Deeks' funnel plot asymmetry test, and significant publication bias was considered when the *P*-value was <0.10.

RESULTS

Literature Search

Of the 2,102 studies obtained through the databases and references, 2,046 were excluded by screening the titles and abstracts. A total of 56 potentially eligible studies remained, of which 11 studies (1,232 patients) were finally included in the quantitative analyses (17–27). The details of the study selection and reasons for excluding studies are presented in **Figure 1**.

Study Characteristics and Quality Assessment

All characteristics of the included studies are summarized in **Table 1**. All the included studies were conducted between 2004 and 2019. Ten studies, comprising 776 patients, had a prospective design (17–25, 27). Of the 11 included studies, five evaluated the diagnostic accuracy of LUS compared with CT (18, 21, 23, 24, 27). It is unclear whether the ultrasound operators were blinded to the results of chest radiography or CT in two studies (19, 21). Details of the performance of LUS are summarized in **Supplementary Table 2**.

The quality assessment is presented in **Figure 2**. Most studies were of low quality according to the QUADAS-2 criteria. Concerning patient selection, some studies were at high risk of bias and compromised the applicability (18, 20, 24). One study was at high risk of bias but did not compromise the applicability in an index test (19). Considering the flow and timing, one study was at high risk of bias but did not compromise the applicability (19).

Diagnostic Accuracy of LUS in Critically Ill Patients With ARF

The overall pooled sensitivity and specificity of LUS were 92% (95% CI: 85–96) and 98% (95% CI: 94–99), respectively

TABLE 1 | Characteristics of the included studies and patients.

Study	Year	Setting	Country	Design	Number of patients and lung regions in the LUS protocol	Cause of ARF	Reference standard	Blind in reference standard
Lichtenstein et al. (17)	2004	Surgical ICU	France	Prospective	ARDS ($n = 32$) and healthy controls ($n = 10$), total lung regions ($n = 384$)	ARDS (27 insulted to the lung, 5 insulted to secondary reason)	CXR	Yes
Lichtenstein et al. (18)	2004	Medical ICU	France	Prospective	ARF ($n = 60$), total lung regions ($n = 118$)	–	CT	Yes
Copetti et al. (19)	2008	ICU	Italy	Prospective	ARDS ($n = 18$) and APE ($n = 40$), total hemi-thoraces ($n = 10$)	ARDS (4 insulted to the lung, 11 insulted to secondary reason)	CXR	Unclear
Lichtenstein et al. (20)	2008	ICU	France	Prospective	ARF ($n = 260$), lung regions were unknown	COPD, cardiogenic pulmonary edema, pneumonia, acute asthma, pulmonary embolism, pneumothorax	CT/CXR	Yes
Rocco et al. (21)	2008	Mixed ICU	Italy	Prospective	Trauma, requiring mechanical ventilation ($n = 22$): total lung regions ($n = 180$)	Thoracic trauma	CT	Unclear
Xirouchaki et al. (22)	2011	Mixed ICU	Greece	Prospective	Mechanical ventilation ($n = 42$): total of hemi-thoraces ($n = 84$)	–	CXR	Yes
Refaat and Abdurrahman (23)	2013	Chest ICU	Egypt	Prospective	ARF ($n = 90$), lung regions were unknown	–	CT	Yes
Daabis et al. (24)	2014	ICU	Egypt	Prospective	ARF ($n = 93$), lung regions were unknown	–	CT	Yes
Bass et al. (25)	2015	Mixed ICU	USA	Prospective	Mechanical ventilation ($n = 77$), lung regions were unknown	–	CXR	Yes
See et al. (26)	2018	ICU	Singapore	Retrospective	ARDS ($n = 216$) and non-ARDS ($n = 240$), total hemi-thoraces ($n = 12$)	ARDS (100 insulted to lung, 356 insulted to the secondary reason)	CXR	Yes
Chiumello et al. (27)	2019	ICU	Italy	Prospective	ARDS ($n = 32$); total hemi-thoraces ($n = 12$)	ARDS (25 insulted to the lung, 7 insulted to secondary reason)	CT	Yes

LUS, lung ultrasound; ARF, acute respiratory failure; ARDS, acute respiratory distress; CXR, chest X-ray; CT, computed tomography.

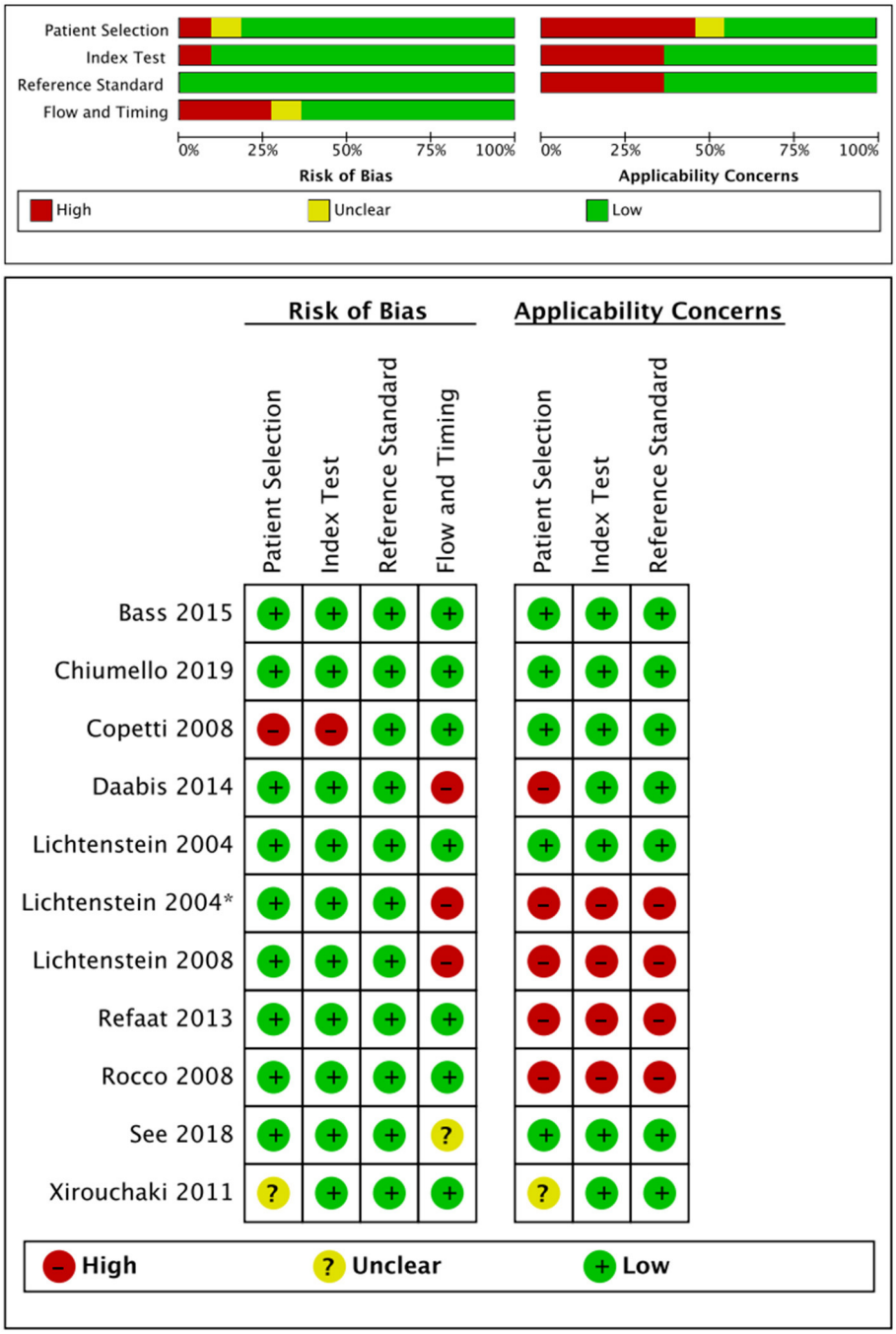

FIGURE 2 | Risk of bias and applicability concerns assessment according to the QUADAS-2. QUADAS-2, Quality Assessment of Diagnostic Accuracy Studies Score-2.

(**Figure 3**). In addition, the overall area under the SROC curve (AUC) of LUS was 98% (95% CI: 97–99), indicating that LUS had a high diagnostic value for ARF (**Figure 4**). The sensitivity, specificity, PLR, NLR, and DOR of different types of pathology were investigated, and the main results are presented in **Table 2**. For consolidation, eight studies, comprising 1,040 patients, were included (17–20, 22, 23, 26, 27). The pooled sensitivity and specificity of LUS were 89 and 97%, respectively. The PLR, NLR, and DOR were 31.9, 0.11, and 284, respectively. Six studies, comprising 279 patients, reported the raw data for pleural effusion (17, 19, 21–23, 27). LUS had a pooled sensitivity of 95% and a specificity of 99%. The PLR, NLR, and DOR were 88.1, 0.05, and 1,750, respectively. Four studies, comprising 174 patients, reported the accuracy of LUS to identify acute interstitial

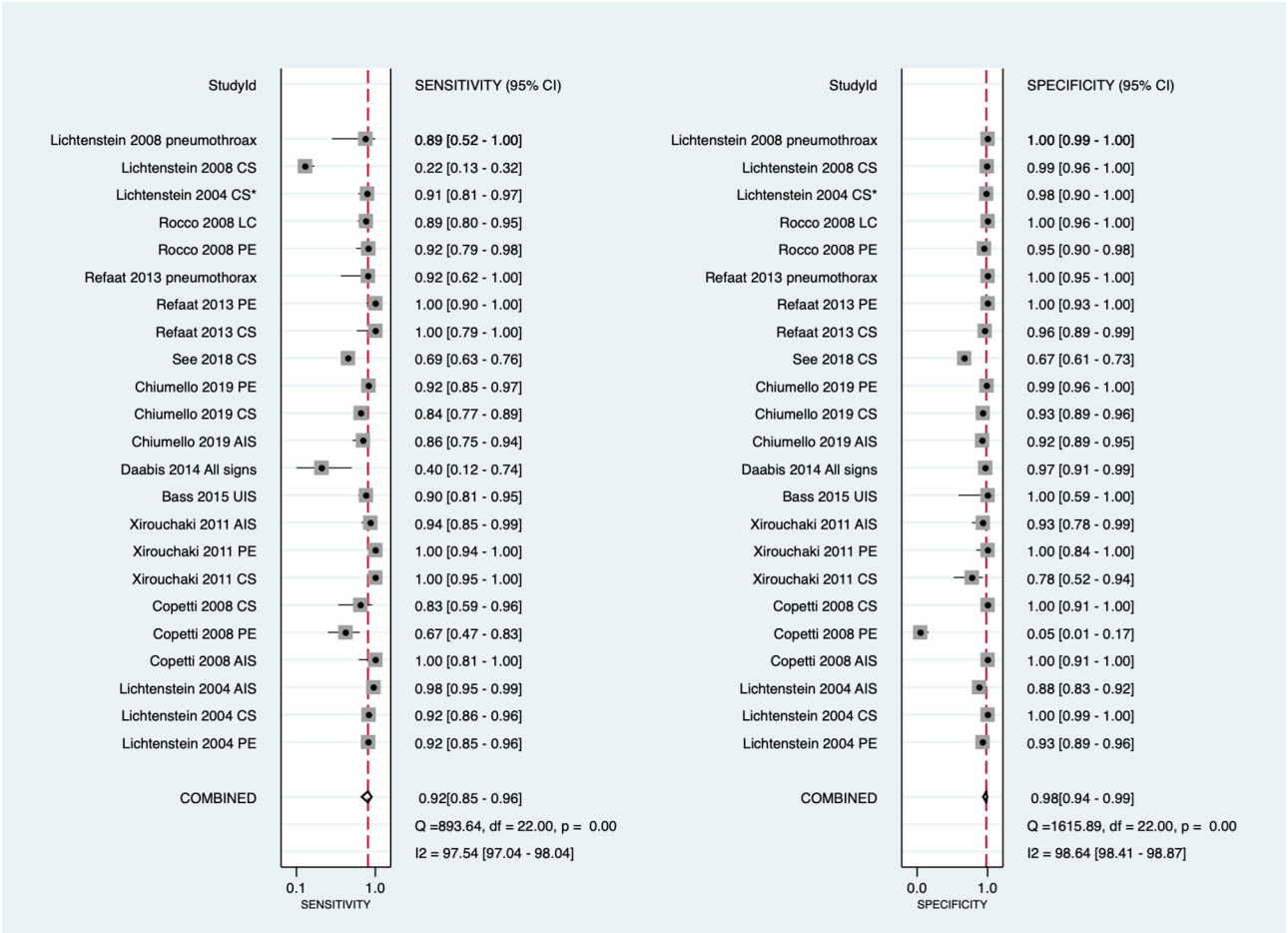

FIGURE 3 | Forest plot of the sensitivity and specificity in the overall studies. Several studies used repeated measurements per patient (e.g., measurements on different types of pathology episodes and different lung fields). *Daabis et al. (24) included all profiles including A, AB, B, B+PLAPS, and lung point. CI, confidence interval; LUS, lung ultrasound; CS, consolidation; PE, pleural effusion; LC, lung contusion; AIS, acute interstitial syndrome; B, B lines; PLAPS, post-erolateral alveolar and/or pleural syndrome; UIS, ultrasound interstitial syndrome.

syndrome (AIS) (17, 19, 22, 27). The sensitivity and the specificity were 95 and 91%, respectively. Furthermore, the PLR, NLR, and DOR were 10.8, 0.06, and 196, respectively. Pneumothorax was investigated in two studies (20, 23). The pooled sensitivity and specificity for pneumothorax of LUS were 90 and 100%, respectively. Lung contusion was examined in one study (21), which reported an LUS sensitivity and specificity of both 89%. The SROC curves for different types of pathology are presented in **Supplementary Figure 1**.

Causes of Heterogeneity

The significant heterogeneity in the meta-analysis was performed according to the dispersion of studies in the ROC plane. An influence analysis was performed to examine the potential sources of heterogeneity in **Supplementary Figure 2**. The results suggested that there was no outlier for consolidation, PE, and AIS. To further explore the heterogeneity of the included studies, the secondary analysis according to different reference standards (CT or CXR) was performed (**Table 3**). With CT as the reference standard, the sensitivity and specificity of LUS for the diagnosis of consolidation were 86 and 95%. With CXR as the reference standard, LUS had sensitivities of 73 and 97% and specificities of 99 and 90% to identify consolidation and AIS, respectively.

Assessment of Clinical Applicability

Fagan's nomogram on the pre-test and post-test probability of LUS for diagnosing ARF in critically ill patients is shown in **Supplementary Figure 3**. Fagan's nomogram showed that the pooled PLR and NLR were 51 and 0.08, respectively.

Publication Bias

Deeks' funnel plot asymmetry test was performed to examine publication bias (**Figure 5**), which showed that there was no significant publication bias in this study ($P = 0.39$).

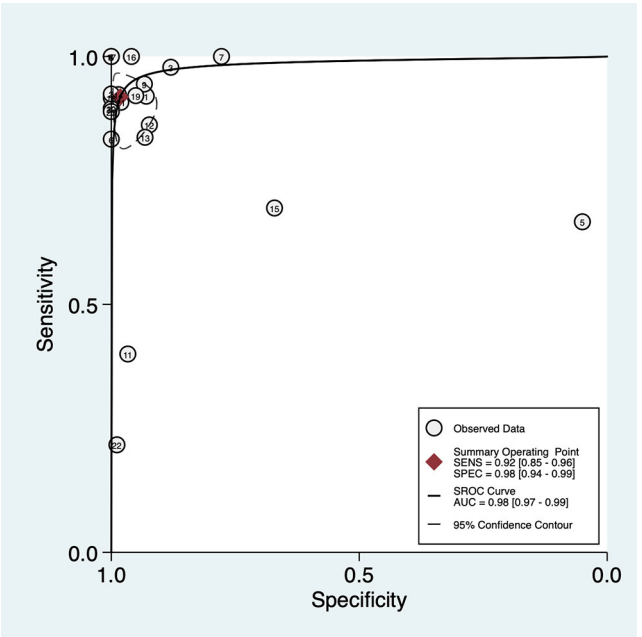

FIGURE 4 | Summary of the receiver operating characteristic curve (SROC) of lung ultrasound in critically ill patients with acute respiratory failure. AUC, area under curve.

TABLE 2 | Diagnostic performance of lung ultrasound in critically ill patients with acute respiratory failure.

	Consolidation	AIS	PE	Pneumothorax
No. of studies (patients)	8 (1,040)	4 (174)	6 (279)	3 (332)
SEN (95% CI) (%)	89 (66–97)	95 (88–98)	95 (82–99)	90 (70–99)
SPE (95% CI) (%)	97 (88–99)	91 (88–94)	99 (47–100)	100 (0.99–100)
PLR (95% CI)	31.9 (7.4–137.2)	10.8 (8.1–14.6)	88.1 (0.8–9193.2)	244.2 (34.3–1737.9)
NLR (95% CI)	0.11 (0.03–0.41)	0.06 (0.02–0.13)	0.05 (0.01–0.21)	0.13 (0.05–0.38)
DOR (95% CI)	284 (41–1,970)	196 (85–453)	1750 (4–6,93,798)	1849 (184–18,622)

PE, pleural effusion; AIS, acute interstitial syndrome; DOR, diagnostic odds ratio; PLR, positive likelihood ratio; NLR, negative likelihood ratio; CI, confidence interval.

DISCUSSION

In this systematic review and meta-analysis, 11 studies were included, and the diagnostic value of LUS was investigated. The results indicated that LUS had an overall moderate sensitivity of 92% (95% CI: 85–96) and high specificity of 98% (95% CI: 94–99) for diagnosing of ARF in critically ill patients. The secondary analysis was performed to determine the significant heterogeneity, and the result showed that LUS had a low sensitivity but high specificity in diagnosing consolidation regardless of whether CXR or CT was used as the reference standard. LUS had a high sensitivity but low specificity to identify AIS in ARF with CXR as the reference standard.

LUS, as a convenient approach, has routinely been used in critically ill patients and has been identified to be effective in evaluating ICU conditions such as pneumonia (9) and pneumothorax (13). Despite the pervasive use of LUS in critically ill patients, few studies have focused on the diagnostic value of LUS in ARF. This meta-analysis demonstrates that LUS had a moderate sensitivity and high specificity to identify ARF when compared with CXR or CT. The results are relatively different from those of a recent meta-analysis in which the pooled sensitivity and specificity for the diagnostic accuracy of LUS in critically ill patients with respiratory symptoms were 95 and 94%, respectively (28). In this study, the authors only focused on the diagnostic accuracy of LUS with CT as the reference standard. Staub et al. have also explored the diagnostic value of LUS in adults with respiratory symptoms (29). However, they mainly focused on patients with pneumonia, acute heart failure, and exacerbations of COPD in the emergency department. They reported that LUS had sensitivity of ∼85–95% and specificity of 75–90%. This result is possibly attributed to the heterogeneity of the population included in these studies.

Common pathological types, including consolidation, AIS, and PE in ARF, were the main concern in the present study. LUS in ARF with PE had higher sensitivity and specificity than consolidation and AIS. LUS was low sensitive but highly specific for the diagnosis of consolidation in critically ill patients with ARF. However, although AIS is central to the BLUE protocol (30), LUS had a high sensitivity but low specificity to identify AIS in this study. This may be explained by the fact that LUS can detect the interstitial edema surrounding an isolated consolidation, even if deep consolidations are not detected (31). These results are consistent with the results of a recent study. Chinardet et al. (32) have demonstrated that LUS was useful in evaluating consolidation after PE drainage in acute respiratory distress syndrome (ARDS). However, there were only 10 patients in this study.

Due to the rapid development of ARF, early changes in lung morphology can occur, which can be assessed by LUS. This review identified that LUS might be a valuable resource as an adjunct or replacement for CXR and CT in critically ill patients with ARF in clinical practice. Compared with CXR and CT, LUS has some advantages in addition to its diagnostic accuracy. LUS is convenient and can be performed right at the bedside (33, 34). Furthermore, LUS is inexpensive and can be used worldwide, especially in areas where medical sources are limited. Considering these advantages, LUS is considered a routine imaging modality for critically ill patients, especially for patients with unstable conditions. LUS is simply performed, but it must be methodologically learned. The main disadvantage of LUS that restricts its use is it is highly operator dependent (9). The heterogeneity of the observation-dependent nature of LUS may affect the reliability of the study results. Furthermore, similar with CXR and CT, the images obtained in LUS are only considered useful when these are combined with clinical information. Hence, combined with clinical information, well-trained operators select LUS as their preferred choice of modality.

TABLE 3 | Summary of the performance of different reference standards for the diagnosis of ARF in critically ill patients.

	No. of studies (patients)	SEN (%) (95% CI)	SPE (%) (95% CI)	PLR (95% CI)	NLR (95% CI)	DOR (95% CI)
REFERENCE STANDARD: CT						
Consolidation	3 (182)	86 (82–90)	95 (92–97)	15.5 (8.9–26.9)	0.13 (0.07–0.24)	192 (37–980)
REFERENCE STANDARD: CXR						
Consolidation	4 (598)	73 (68–78)	99 (97–100)	32.4 (3.0–353.1)	0.12 (0.01–2.29)	330 (23–4725)
AIS	3 (142)	97 (94–99)	90 (86–94)	11.6 (4.8–27.7)	0.04 (0.02–0.07)	342 (138–848)

PE, pleural effusion; AIS, acute interstitial syndrome; DOR, diagnostic odds ratio; PLR, positive likelihood ratio; NLR, negative likelihood ratio; CI, confidence interval; CT, computed tomography; CXR, chest X-ray.

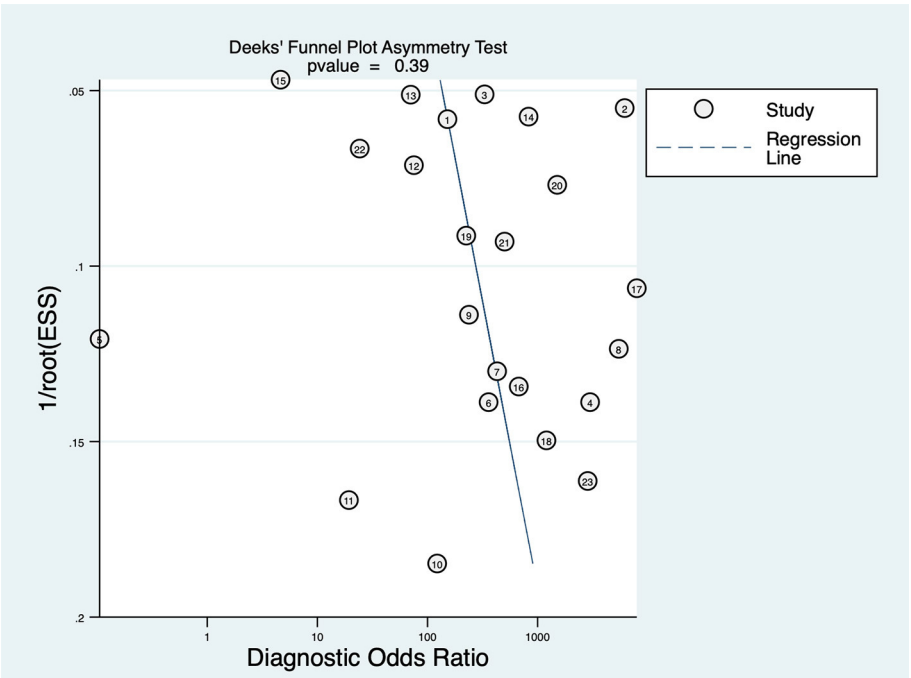

FIGURE 5 | Graph of Deeks' funnel plot asymmetry.

Our results revealed substantial heterogeneity in the included studies, and the reasons for heterogeneity were investigated by subgroup analysis. First, the study comprised several different pathologies, including consolidation, AIS, PE, LC, and pneumothorax. This may affect the diagnostic accuracy because different pathologies have different values in diagnosing ARF. To reduce heterogeneity, we further investigated the sensitivity and specificity of the main pathologies, including consolidation, AIS, PE, and pneumothorax. The heterogeneity was subject to these aspects in pioneering meta-analysis on the diagnosis of LUS (10, 11). Second, several included studies were of low quality. The different study qualities can lead to heterogeneity. A previous study by Llamas-Álvarez et al. (9) has attributed the heterogeneity to the study quality, and the diagnostic accuracy of LUS improved by stratifying the study quality.

This meta-analysis has several limitations. First, this meta-analysis included a limited number of studies, with only two studies involving 100 participants or more (20, 26). This may lead to the non-repeatability of the results, and the results need to be interpreted carefully. Second, only four different pathologies were investigated for heterogeneity in our study. Although we performed subgroup analysis, the heterogeneity could not be fully explained because there were more manifestations of these four pathologies in LUS. Third, the study quality was limited by the included literature due to the secondary analysis.

CONCLUSIONS

This systematic review and meta-analysis demonstrated that LUS had moderate sensitivity and high specificity for diagnosing ARF in critically ill patients when compared with CXR or CT. LUS seems to be a well-validated modality to investigate the cause of ARF or thoracic pathology associated with the diagnosis. However, large-scale studies are needed to confirm the role of LUS in critically ill patients with ARF.

DATA AVAILABILITY STATEMENT

The original contributions presented in the study are included in the article/**Supplementary Material**, further inquiries can be directed to the corresponding author/s.

AUTHOR CONTRIBUTIONS

HQ and XY conceptualized and designed the study, collected and organized the data, and drafted the initial manuscript. LH, ZW, YC, and XL collected and organized the data, reviewed the included articles, and conducted the analyses. WC collected and organized the data and reviewed the included articles. LL and JX conceptualized and designed the study, and critically reviewed and revised the manuscript. YY conceptualized and designed the study, coordinated and supervised data collection, and critically reviewed and revised the manuscript. All authors read and approved the final manuscript.

FUNDING

This work was supported by the National Natural Science Foundation of China (81930058), Jiangsu Provincial Special Program of Medical Science (BE2019749), and National Science and Technology Major Project for Control and Prevention of Major Infectious Diseases of China (2017ZX10103004).

SUPPLEMENTARY MATERIAL

The Supplementary Material for this article can be found online at: https://www.frontiersin.org/articles/10.3389/fmed.2021.705960/full#supplementary-material

REFERENCES

1. Stefan MS, Meng-Shiou S, Pekow PS, Rothberg MB, Steingrub JS, Lagu T, et al. Epidemiology and outcomes of acute respiratory failure in the United States, 2001 to 2009: a national survey. *J Hosp Med.* (2013) 8:76–82. doi: 10.1002/jhm.2004
2. Singh Lamba T, Sharara RS, Leap J, Singh AC. Management of respiratory failure. *Crit Care Nurs Q.* (2016) 39:94–109. doi: 10.1097/CNQ.0000000000000103
3. Wallbridge P, Steinfort D, Tay TR, Irving L, Hew M. Diagnostic chest ultrasound for acute respiratory failure. *Respir Med.* (2018) 141:26–36. doi: 10.1016/j.rmed.2018.06.018
4. Ray P, Birolleau S, Lefort Y, Becquemin MH, Beigelman C, Isnard R, et al. Acute respiratory failure in the elderly: etiology, emergency diagnosis and prognosis. *Crit Care.* (2006) 10:R82. doi: 10.1186/cc4926
5. Xirouchaki N, Kondili E, Prinianakis G, Malliotakis P, Georgopoulos D. Impact of lung ultrasound on clinical decision making in critically ill patients. *Intensive Care Med.* (2014) 40:57–65. doi: 10.1007/s00134-013-3133-3
6. Aliaga M, Forel JM, De Bourmont S, Jung B, Thomas G, Mahul M, et al. Diagnostic yield and safety of CT scans in ICU. *Intensive Care Med.* (2015) 41:436–43. doi: 10.1007/s00134-014-3592-1
7. Brenner DJ, Hall EJ. Computed tomography–an increasing source of radiation exposure. *N Engl J Med.* (2007) 357:2277–84. doi: 10.1056/NEJMra072149
8. Volpicelli G, Elbarbary M, Blaivas M, Lichtenstein DA, Mathis G, Kirkpatrick AW, et al. International evidence-based recommendations for point-of-care lung ultrasound. *Intensive Care Med.* (2012) 38:577–91. doi: 10.1007/s00134-012-2513-4
9. Llamas-Álvarez AM, Tenza-Lozano EM, Latour-Pérez J. Accuracy of lung ultrasonography in the diagnosis of pneumonia in adults: systematic review and meta-analysis. *Chest.* (2017) 151:374–82. doi: 10.1016/j.chest.2016.10.039
10. Chavez MA, Shams N, Ellington LE, Naithani N, Gilman RH, Steinhoff MC, et al. Lung ultrasound for the diagnosis of pneumonia in adults: a systematic review and meta-analysis. *Respir Res.* (2014) 15:50. doi: 10.1186/1465-9921-15-50
11. Alzahrani SA, Al-Salamah MA, Al-Madani WH, Elbarbary MA. Systematic review and meta-analysis for the use of ultrasound versus radiology in diagnosing of pneumonia. *Crit Ultrasound J.* (2017) 9:6–16. doi: 10.1186/s13089-017-0059-y
12. Squizzato A, Rancan E, Dentali F, Bonzini M, Guasti L, Steidl L, et al. Diagnostic accuracy of lung ultrasound for pulmonary embolism: a systematic review and meta-analysis. *J Thromb Haemost.* (2013) 11:1269–78. doi: 10.1111/jth.12232
13. Ding W, Shen Y, Yang J, He X, Zhang M. Diagnosis of pneumothorax by radiography and ultrasonography: a meta-analysis. *Chest.* (2011) 140:859–66. doi: 10.1378/chest.10-2946
14. Liberati A, Altman DG, Tetzlaff J, Mulrow C, Gøtzsche PC, Ioannidis JP, et al. The PRISMA statement for reporting systematic reviews and meta-analyses of studies that evaluate healthcare interventions: explanation and elaboration. *BMJ.* (2009) 339:b2700. doi: 10.1136/bmj.b2700
15. Whiting PF, Rutjes AW, Westwood ME, Mallett S, Deeks JJ, Reitsma JB, et al. QUADAS-2: a revised tool for the quality assessment of diagnostic accuracy studies. *Ann Intern Med.* (2011) 155:529–36. doi: 10.7326/0003-4819-155-8-201110180-00009
16. Campbell JM, Klugar M, Ding S, Carmody DP, Hakonsen SJ, Jadotte YT, et al. Diagnostic test accuracy: methods for systematic review and meta-analysis. *Int J Evid Based Healthc.* (2015) 13:154–62. doi: 10.1097/XEB.0000000000000061
17. Lichtenstein D, Goldstein I, Mourgeon E, Cluzel P, Grenier P, Rouby JJ. Comparative diagnostic performances of auscultation, chest radiography, and lung ultrasonography in acute respiratory distress syndrome. *Anesthesiology.* (2004) 100:9–15. doi: 10.1097/00000542-200401000-00006
18. Lichtenstein DA, Lascols N, Mezière G, Gepner A. Ultrasound diagnosis of alveolar consolidation in the critically ill. *Intensive Care Med.* (2004) 30:276–81. doi: 10.1007/s00134-003-2075-6
19. Copetti R, Soldati G, Copetti P. Chest sonography: a useful tool to differentiate acute cardiogenic pulmonary edema from acute respiratory distress syndrome. *Cardiovascular Ultrasound.* (2008) 6:16–25. doi: 10.1186/1476-7120-6-16
20. Lichtenstein DA, Mezière GA. Relevance of lung ultrasound in the diagnosis of acute respiratory failure: the BLUE protocol. *Chest.* (2008) 134:117–25. doi: 10.1378/chest.07-2800
21. Rocco M, Carbone I, Morelli A, Bertoletti L, Rossi S, Vitale M, et al. Diagnostic accuracy of bedside ultrasonography in the ICU: feasibility of detecting pulmonary effusion and lung contusion in patients on respiratory support after severe blunt thoracic trauma. *Acta Anaesthesiol Scand.* (2008) 52:776–84. doi: 10.1111/j.1399-6576.2008.01647.x
22. Xirouchaki N, Magkanas E, Vaporidi K, Kondili E, Plataki M, Patrianakos A, et al. Lung ultrasound in critically ill patients: comparison with bedside chest radiography. *Intensive Care Med.* (2011) 37:1488–93. doi: 10.1007/s00134-011-2317-y
23. Refaat R, Abdurrahman L. The diagnostic performance of chest ultrasonography in the up-to-date work-up of the critical care setting. *Egypt J Radiol Nucl Med.* (2013) 44:779–89. doi: 10.1016/j.ejrnm.2013.09.001
24. Daabis R, Banawan L, Rabea A, Elnakedy A, Sadek A. Relevance of chest sonography in the diagnosis of acute respiratory failure: comparison with current diagnostic tools in intensive care units. *Egypt J Chest Dis Tuberc.* (2014) 63:979–85. doi: 10.1016/j.ejcdt.2014.05.005
25. Bass CM, Sajed DR, Adedipe AA, West TE. Pulmonary ultrasound and pulse oximetry versus chest radiography and arterial blood gas analysis for the diagnosis of acute respiratory distress syndrome: a pilot study. *Crit Care.* (2015) 19:282–92. doi: 10.1186/s13054-015-0995-5

26. See KC, Ong V, Tan YL, Sahagun J, Taculod J. Chest radiography versus lung ultrasound for identification of acute respiratory distress syndrome: a retrospective observational study. *Crit Care.* (2018) 22:203. doi: 10.1186/s13054-018-2105-y
27. Chiumello D, Umbrello M, Sferrazza Papa GF, Angileri A, Gurgitano M, Formenti P, et al. Global and regional diagnostic accuracy of lung ultrasound compared to CT in patients with acute respiratory distress syndrome. *Crit Care Med.* (2019) 47:1599–606. doi: 10.1097/CCM.0000000000003971
28. Winkler MH, Touw HR, van de Ven PM, Twisk J, Tuinman PR. Diagnostic accuracy of chest radiograph, and when concomitantly studied lung ultrasound, in critically ill patients with respiratory symptoms: a systematic review and meta-analysis. *Crit Care Med.* (2018) 46:e707–14. doi: 10.1097/CCM.0000000000003129
29. Staub LJ, Mazzali Biscaro RR, Kaszubowski E, Maurici R. Lung ultrasound for the emergency diagnosis of pneumonia, acute heart failure, and exacerbations of chronic obstructive pulmonary disease/asthma in adults: a systematic review and meta-analysis. *J Emerg Med.* (2019) 56:53–69. doi: 10.1016/j.jemermed.2018.09.009
30. Lichtenstein DA. BLUE-protocol and FALLS-protocol: two applications of lung ultrasound in the critically ill. *Chest.* (2015) 147:1659–70. doi: 10.1378/chest.14-1313
31. Volpicelli G, Caramello V, Cardinale L, Mussa A, Bar F, Frascisco MF. Detection of sonographic B-lines in patients with normal lung or radiographic alveolar consolidation. *Med Sci Monit.* (2008) 14:CR122–8.
32. Chinardet B, Brisson H, Arbelot C, Langeron O, Rouby JJ, Lu Q. Ultrasound assessment of lung consolidation and reaeration after pleural effusion drainage in patients with Acute Respiratory Distress Syndrome: a pilot study. *Acta Anaesthesiol Belg.* (2016) 67:29–35.
33. Mojoli F, Bouhemad B, Mongodi S, Lichtenstein D. Lung ultrasound for critically ill patients. *Am J Respir Crit Care Med.* (2019) 199:701–14. doi: 10.1164/rccm.201802-0236CI
34. Brogi E, Bignami E, Sidoti A, Shawar M, Gargani L, Vetrugno L, et al. Could the use of bedside lung ultrasound reduce the number of chest x-rays in the intensive care unit? *Cardiovasc. Ultrasound.* (2017) 15:23. doi: 10.1186/s12947-017-0113-8

Conflict of Interest: The authors declare that the research was conducted in the absence of any commercial or financial relationships that could be construed as a potential conflict of interest.

frontiers in Physiology

ORIGINAL RESEARCH
published: 27 August 2021
doi: 10.3389/fphys.2021.693448

Classification of Lung Disease in Children by Using Lung Ultrasound Images and Deep Convolutional Neural Network

Silvia Magrelli[1]*, *Piero Valentini*[2,3]*, *Cristina De Rose*[2], *Rosa Morello*[2] and *Danilo Buonsenso*[2,3,4]

[1] Independent Researcher, Zurich, Switzerland, [2] Department of Woman and Child Health and Public Health, Fondazione Policlinico Universitario A. Gemelli IRCCS, Rome, Italy, [3] Global Health Research Institute, Istituto di Igiene, Università Cattolica del Sacro Cuore, Rome, Italy, [4] Dipartimento di Scienze Biotecnologiche di Base, Cliniche Intensivologiche e Perioperatorie, Università Cattolica del Sacro Cuore, Rome, Italy

OPEN ACCESS

Edited by:
Lorenzo Ball,
University of Genoa, Italy

Reviewed by:
Cindy Thamrin,
Woolcock Institute of Medical Research, Australia
Jonathan E. Elliott,
Oregon Health and Science University, United States

***Correspondence:**
Silvia Magrelli
silvia.magrelli@gmail.com
Piero Valentini
piero.valentini@policlinicogemelli.it

Specialty section:
This article was submitted to Respiratory Physiology, a section of the journal Frontiers in Physiology

Received: 11 April 2021
Accepted: 05 August 2021
Published: 27 August 2021

Citation:
Magrelli S, Valentini P, De Rose C, Morello R and Buonsenso D (2021) Classification of Lung Disease in Children by Using Lung Ultrasound Images and Deep Convolutional Neural Network. Front. Physiol. 12:693448. doi: 10.3389/fphys.2021.693448

Bronchiolitis is the most common cause of hospitalization of children in the first year of life and pneumonia is the leading cause of infant mortality worldwide. Lung ultrasound technology (LUS) is a novel imaging diagnostic tool for the early detection of respiratory distress and offers several advantages due to its low-cost, relative safety, portability, and easy repeatability. More precise and efficient diagnostic and therapeutic strategies are needed. Deep-learning-based computer-aided diagnosis (CADx) systems, using chest X-ray images, have recently demonstrated their potential as a screening tool for pulmonary disease (such as COVID-19 pneumonia). We present the first computer-aided diagnostic scheme for LUS images of pulmonary diseases in children. In this study, we trained from scratch four state-of-the-art deep-learning models (VGG19, Xception, Inception-v3 and Inception-ResNet-v2) for detecting children with bronchiolitis and pneumonia. In our experiments we used a data set consisting of 5,907 images from 33 healthy infants, 3,286 images from 22 infants with bronchiolitis, and 4,769 images from 7 children suffering from bacterial pneumonia. Using four-fold cross-validation, we implemented one binary classification (healthy vs. bronchiolitis) and one three-class classification (healthy vs. bronchiolitis vs. bacterial pneumonia) out of three classes. Affine transformations were applied for data augmentation. Hyperparameters were optimized for the learning rate, dropout regularization, batch size, and epoch iteration. The Inception-ResNet-v2 model provides the highest classification performance, when compared with the other models used on test sets: for healthy vs. bronchiolitis, it provides 97.75% accuracy, 97.75% sensitivity, and 97% specificity whereas for healthy vs. bronchiolitis vs. bacterial pneumonia, the Inception-v3 model provides the best results with 91.5% accuracy, 91.5% sensitivity, and 95.86% specificity. We performed a gradient-weighted class activation mapping (Grad-CAM) visualization and the results were qualitatively evaluated by a pediatrician expert in LUS imaging: heatmaps highlight areas containing diagnostic-relevant LUS imaging-artifacts, e.g., A-, B-, pleural-lines, and consolidations. These complex patterns are automatically learnt from the data, thus

avoiding hand-crafted features usage. By using LUS imaging, the proposed framework might aid in the development of an accessible and rapid decision support-method for diagnosing pulmonary diseases in children using LUS imaging.

Keywords: deep-learning CNN, bronchiolitis, pneumonia, children, lung ultrasonography

1. INTRODUCTION

Bronchiolitis is a viral acute lower respiratory-tract infection and the most common reason for hospitalization and intensive-care-unit admission of children worldwide (Choi and Lee, 2012; Øymar et al., 2014).

The diagnosis of infants with bronchiolitis is difficult: there exists no unambiguous definition of the disease; the diagnosis is based on clinical evaluation and anamnesis (Ralston et al., 2014) hence determined by different conditions such as age and variability in the disease state. Furthermore, many of these parameters are based on subjective clinical findings and can be diversely interpreted by different physicians, according to their clinical experience. Finally, bronchiolitis can require serial observations over time, which in turn presents several challenges when performed in emergency departments.

Community acquired pneumonia (CAP) is also pervasive and a frequent cause of pediatric morbidity and mortality (Liu et al., 2015). A diagnosis of CAP, similarly to that of bronchiolitis, relies mainly on medical history and clinical examination. However, these methods suffer from poor sensitivity and specificity hence, to confirm CAP, physicians need to prescribe medical imaging techniques such as chest X-ray (Bradley et al., 2011; World Health Organization, 2014; Shah et al., 2017).

There is growing research interest (Ralston et al., 2014; Collins and Varmus, 2015) in discovering objective parameters that are easy to measure and that could help the physician to perform a more accurate evaluation of children possibly infected with a respiratory disease, thus to make prompt clinical decisions.

Ultrasound technology (US) is one of the most often used imaging diagnostic tools for physicians and radiologists, due to its relative safety, portability, repeatability, cost effectiveness, and operator comfort. Examinations can be carried out, after appropriate training, even by non-specialist radiologists [point-of-care ultrasound, POCUS (Kessler et al., 2017)]. Therefore, US imaging presents several major advantages over other medical imaging modalities such as magnetic resonance imaging (MRI), computed tomography (CT), and X-ray.

In the last few decades, lung ultrasound (LUS) imaging supported clinical examinations for neonatal and pediatric respiratory diseases, as a valid tool for evaluating the lung parenchyma (Dunn and Fry, 1961; Bauld and Schwan, 1974; Volpicelli et al., 2012; Rosenfield et al., 2015). This avoids unnecessary exposure of children to ionizing radiation (Buonsenso et al., 2019a). Several studies have demonstrated the usefulness of LUS imaging in the diagnosis and follow-up of community-acquired pneumonia (Berce et al., 2019; Musolino et al., 2019; Najgrodzka et al., 2019; Buonsenso et al., 2021) and, in particular, of bronchiolitis (Basile et al., 2015; Di Mauro et al., 2019; Supino et al., 2019; Buonsenso et al., 2021).

In an attempt to objectively quantify respiratory distress, many scoring systems were developed on the bases of the visual features generated by the interaction between the ultrasound beam and the lung (Supino et al., 2019; Buonsenso et al., 2020e). The appearance of these features varies according to the specific composition of the lung periphery. In general, the main lung ultrasound features of lung inflammatory diseases include irregular pleural line; short and long vertical artifacts; white-lung; consolidations and effusions. However, despite documented medical evidence (Lichtenstein et al., 1997, 2009; Reißig and Kroegel, 2003; Jambrik et al., 2004; Soldati et al., 2006; Volpicelli et al., 2006; Copetti et al., 2008; Gargani et al., 2008) and extensive acoustic studies (Dunn and Fry, 1961; Bauld and Schwan, 1974; Dunn, 1974, 1986; Pedersen and Ozcan, 1986; Mikhak and Pedersen, 2002; Volpicelli et al., 2012), the interpretation of the lung ultrasound features is subjectively made by the clinician/sonographer. US imaging also presents unique challenges, such as low imaging-quality caused by noise and artifacts, and high inter- and intra-observer variability across different institutes and manufacturers of US systems. To address these challenges, it is essential to develop advanced automatic US image-analysis methods in order to make US diagnosis, assessment, and image-guided interventions/therapy more objective, accurate, and intelligent.

In the past 7 years, deep learning (LeCun et al., 2015), a subfield of machine learning (ML), also due to improvements in device capabilities (computing power, memory capacity, power consumption, image sensor resolution, and optics) has seen a dramatic resurgence, with striking improvements in the performance and cost-effectiveness of vision-based applications (Voulodimos et al., 2018). It solves problems that are beyond human capability or that were previously considered intractable, and it demonstrates huge potential for various automatic tasks in medical-image analysis (Greenspan et al., 2016; Litjens et al., 2017; Shen et al., 2017; Ker et al., 2018). Therefore, it receives increasing attention by the medical-imaging scientific community (Esteva et al., 2019).

Recent works uncovered the deep-learning potential to perform automatic US image-analysis tasks, including detection, classification, segmentation, biometric measurements, registration, and quality assessment, as well as emerging tasks such as image-guided interventions and therapy (Anas et al., 2015). It was also successfully applied, in medical US imaging analysis to different anatomical structures: breast (Bian et al., 2017; Hiramatsu et al., 2017), thyroid (Ma et al., 2017), heart/cardiac (Ghesu et al., 2016; Pereira et al., 2017), brain (Milletari et al., 2015; Sombune et al., 2017), fetus (Yaqub et al., 2017), and many other organs and body parts (see Liu et al., 2019 for a review). However, only a limited amount of studies investigated the performances of deep neural networks on lung

ultrasound images, and these studies mainly focus on detecting and extracting domain specific, hand-crafted features such as A-lines, B-lines (also known as vertical artifacts), pleural lines (Carrer et al., 2020), pleural effusions, and consolidations, with B-line detection being the most common task (Kulhare et al., 2018; Wang et al., 2019; van Sloun and Demi, 2020).

The recent outbreak of the novel 2019 coronavirus (COVID-19) has required the development of fast diagnostic techniques, among which the chest X-ray is key. Given the paucity of radiologists and expertise in the field, in order to provide physicians with valid assistance for accurate diagnosis, there is an increased interest in quickly developing AI systems. Recently, there have been many publications that focused on using deep neural networks over raw chest X-ray images rather than learning hand-engineered features by using deep neural networks.

For instance, Wang et al. (2020) designed COVID-Net, an open-source deep convolutional neural network that was specifically tailored for the task of detecting COVID-19 cases from chest X-ray images. The authors also introduced COVIDx, an open-access benchmark data set that comprises 13,975 chest X-ray images across 13,870 patient cases. The COVID-Net achieves 93.3% test accuracy in classifying images from individuals who belong to three different classes: healthy, non-COVID pneumonia, and COVID-19.

Another example is the study from Apostolopoulos and Mpesiana (Apostolopoulos and Mpesiana, 2020) who applied transfer learning on state-of-the-art CNN architectures for classification tasks that involve COVID-19 as one of the target classes. Specifically, they used a database of chest X-ray scans that contain 224 images of patients with COVID-19, 700 images of people infected with non-COVID pneumonia, and 504 images of healthy individuals. The best performance model (VGG19) achieved an accuracy of 98.75% in classifying the following multi-class problem: normal vs. COVID-19 pneumonia vs. bacterial pneumonia. Whereas, an accuracy of 93.48% was reached for the multi-class problem: normal vs. COVID-19 pneumonia vs. viral and bacterial pneumonia.

All the above mentioned studies used deep learning and raw chest X-ray images for either binary (normal vs. COVID-19) or 3-class (normal vs. pneumonia vs. COVID-19) classification problems. These studies provided evidence that deep neural networks can achieve impressively high performance when applied to lung medical imaging without the need for explicitly designed and extracted problem-oriented features to be fed into the neural network. Therefore, these works confirm the idea that deep-learning techniques have the potential to change the design paradigm of the computer-aided diagnostics (CADx) systems (Bian et al., 2017) and provide physicians with refined interpretations of medical imaging (McBee et al., 2018).

Less attention has been given to the use of deep learning for the automation of lung disease classification from raw ultrasound images. Nonetheless, LUS has been shown to play an invaluable role in the diagnosis, management, and prognosis of COVID-19 in all age groups (Bonadia et al., 2020; Buonsenso et al., 2020a; Smith et al., 2020; Volpicelli et al., 2020, 2021) including children (Musolino et al., 2021) and pregnant women (Buonsenso et al., 2020b; Inchingolo et al., 2020). Remarkably, LUS has a diagnostic accuracy similar to that of chest X-ray in COVID-19 patients (Lieveld et al., 2020; Pare et al., 2020; Tung-Chen et al., 2020).

Only recently, Born et al. (2021) presented a VGG16-based CNN, POCOVID-Net, pre-trained on ImageNet (Deng et al., 2009), and then fine-tuned it by using their data set, the largest publicly available LUS data set for COVID-19: 1,204 COVID-19, 704 bacterial pneumonia, and 1,326 healthy images. Their convolutional neural network was able to differentiate among patients who were diagnosed with COVID-19, those who were affected by bacterial pneumonia, and healthy individuals, thus achieving an overall accuracy of 89%.

Inspired by the above research results on COVID-19, obtained by applying deep-learning techniques to raw medical imaging, we analyse the performance of different state-of-the-art convolutional neural networks for the diagnosis of childhood pulmonary disease. In this first study we included a large set of LUS images from children with lower-respiratory-tract infections; this represents a real practice scenario in the pediatrics department, for children affected by the most important pediatric respiratory conditions (pneumonia and bronchiolitis), as well as healthy subjects.

In order to achieve automatic feature extraction, we applied deep-learning techniques directly to raw LUS images. For this purpose, we trained from scratch the following state-of-the-art deep-learning models: VGG19, Xception, Inception-v3, and Inception-ResNet-v2. In this work, we assess the performance of one binary classification problem and one three-class classification problem, including LUS images of healthy infants, those with bronchiolitis, and those with bacterial pneumonia.

2. METHODS

2.1. Participants

For the purpose of this study, we considered three group of patients enrolled in clinical studies at the Agostino Gemelli University Hospital between the end of 2018 and the beginning of 2019:

- Healthy: 33 healthy infants (18 males, 15 females; mean age: 2.83 ± 2.89 months)
- Bronchiolitis: 22 infants with bronchiolitis (13 males, 9 females; mean age: 2.78 ± 2.96 months)
- Bacterial pneumonia: 7 children with bacterial pneumonia (4 males, 3 females; mean age: 7 years $\pm$ 6.85 years).

Healthy infants were defined as children completely healthy without comorbidities.

Infants with bronchiolitis were diagnosed through an integrated approach based on clinical (Seattle Children's Hospital, 2011) and ultrasound assessment (Buonsenso et al., 2019b; Supino et al., 2019). Radiological evaluation and laboratory tests (e.g., oxygen saturation) were also performed, when necessary, as recommended by clinical practice guidelines (Subcommittee on Diagnosis and Management of Bronchiolitis, 2006; Ralston et al., 2014). All patients suspected to have bronchiolitis underwent a routine clinical assessment based on Seattle Children's Hospital clinical scores (Seattle Children's Hospital, 2011). This is a clinical score created by

Seattle Children's Hospital in 2011, to evaluate children with bronchiolitis and to distinguish those in need of hospitalization from those who could be discharged. The score is based on the consideration of

- respiratory rate
- retractions: subcostal, intercostal, or supraclavicular retractions; nasal flaring; or bobbing of the head
- signs of dyspnea: reduction/suspension of feeding, reduction/suspension of vocalization, agitation, drowsiness, or confusion
- auscultation: inspiratory wheeze, expiratory wheeze, or reduction of air penetration.

The clinical diagnosis of CAP was made in accordance with the British Thoracic Society guidelines (Harris et al., 2011). At the first evaluation, all children with suspected CAP underwent: medical history, clinical evaluation, and blood tests, including complete blood count (CBC) with white blood cell (WBC), and C-reactive protein (CRP). Definitive diagnoses of bacterial pneumonia were confirmed by both chest X-ray and lung ultrasound.

Only the children that underwent complete LUS scanning as described below, have been included in the analyses. Images from each patient were collected during multiple sessions, therefore they display a disease with different severity in the same patient. Images and videos have been collected during the study protocol "Utility of lung ultrasound in children with lower respiratory tract infections", approved by the Ethic Committee of the Fondazione Policlinico Universitario A. Gemelli IRCCS, Rome, Italy (prot 36173/19, ID 2729). Written informed consent was obtained before data collection by the caregiver of the study participants. All the private information of patients was anonymized.

2.2. Lung Scanning Procedure

LUS imaging was performed with the ultrasound machine ESAOTE MyLab^{TM} 40 using a linear probe (12–6 MHz). Images and clips were stored and archived. In order to guarantee agreement in the methodology and acquisition, all LUS scanning were performed by two physicians, Danilo Buonsenso and Cristina De Rose, with more than 5 years of experience in LUS clinical practice and teaching and already several papers published together (Buonsenso et al., 2020c,d; Pata et al., 2020; Rose et al., 2020). The scans were made by investigating the anterior, lateral, and posterior regions of the thorax, according to a protocol used by the Italian Academy of Thoracic Ultrasound (ADET) and recently published in a COVID-19 protocol (Taccari and Buonsenso, 2020).

The following lung ultrasound features were evaluated to better define the prognosis of the infants with bronchiolitis and, in particular, to identify those children who are in need of supplementary oxygen (Basile et al., 2015; Taveira et al., 2018; Buonsenso et al., 2019b; Supino et al., 2019):

- presence of an irregular pleural line;
- absence of pleural effusion;
- presence of short vertical artifacts;
- presence of long vertical artifacts: multiple, non-confluent, and/or confluent, unevenly distributed, possibly involving several lung areas, possibly bilaterally distributed, and with "spared areas" in the single area involved;
- presence of area(s) of white-lung;
- presence of single or multiple subpleural consolidations (even $>$ 1 cm in size), associated with multiple long non-confluent or confluent vertical perilesional artifacts.

Lung ultrasound features considered for the aetiological diagnosis of bacterial pneumonia were as follows (Berce et al., 2019; Buonsenso et al., 2021):

- irregular pleural line;
- subpleural pulmonary parenchymal lesion (consolidation and atelectasis; $>$ 2 cm, and in particular $>$ 4 cm);
- presence of bronchograms, its characteristics (air or fluid), morphology (arboriform or dot-like/linear), position (deep if $>$ 2 cm far from the pleura or superficial if close to the pleura), dynamicity during breath (fix, poorly dynamic, or clearly dynamic);
- presence and type of pleural effusion: simple (anechogenic and dependent on gravity) or complex (presence of septa, hyperechogenic spot, following the lung through the apex and not dependent on gravity, requiring drainage).

We also report the lung ultrasound features that were evaluated for healthy infants, especially in the first 3 months of life (Buonsenso et al., 2020d):

- absence of irregularities of the pleural line;
- absence of pleural effusion;
- absence of subpleural consolidations;
- presence of short vertical artifacts;
- presence of long vertical artifacts single and/or multiple, non-confluent and/or confluent, with possible uneven distribution and/or involving multiple lung areas with a prevalence of the right and/or left hemithorax, depending on the gestational age and the current age of the patient.

2.3. Data Acquisition

The set of available lung ultrasound images were ordered by the patients and manually categorized by medical operators into three different diagnoses: healthy infants, infants with bronchiolitis, and children with bacterial pneumonia. The resulting data set of all available images is organized as follows:

1. Healthy: 5,907 images: 5,193 bmp images validated by human raters and 714 bmp images automatically extracted from videos and validated by human raters.
2. Bronchiolitis: 3,286 images: 2,516 bmp images validated by human raters and 770 automatically extracted from videos and validated by human raters.
3. Bacterial pneumonia: 4,769 images: 206 bmp images validated by human raters and 4,563 automatically extracted from videos and validated by human raters.

Every patient contributes to multiple ultrasound images (mean = 226.1 $\pm$ 287.4), with a minimum of 43 images, collectively taken from different sessions. To estimate the accuracy of the

classifiers, we used four-fold cross-validation stratified by the number of samples per class. In order to avoid the unbalanced data problem, we sampled images from the original data set of available images as follows. Data were split on a patient level, hence we organized the folds in such a way that all the images belonging to a particular subject were assigned to only one-fold and, consequently to only one of the following subsets: training set, validation set, test set (i.e., there was no overlap patient-wise among the training, validation, and test data sets). Where possible, the subset of patients was matched by age and gender, and it was distributed randomly between the folds as per the above mentioned constraints. Each of the four final data sets used for four-fold cross-validation is organized as follows:

1. Healthy: 2,000 images: 1,000 bmp images for the training set, 500 images for the validation set and 500 images for the test set.
2. Bronchiolitis: 2,000 images: 1,000 bmp images for the training set, 500 images for the validation set and 500 images for the test set.
3. Bacterial pneumonia: 2,000 images: 1,000 bmp images for the training set, 500 images for the validation set and 500 images for the test set.

2.4. Convolutional Neural Networks

Deep learning constitutes the state-of-the-art set of applied machine-learning techniques and frameworks currently used both in the research and industry fields to perform automated tasks such as signal classification, regression, image segmentation. Such frameworks are also currently used in the medical domain to draw meaningful results from medical data: for instance, the automated classification or segmentation of magnetic resonance imaging (MRI), computed tomography (CT), and X-ray images.

One fundamental class of deep neural networks, applied mostly in analyzing visual imagery, is represented by convolutional neural networks (CNNs). In fact, CNNs are able to process data expressed as tensors, called feature maps, i.e., three-dimensional arrays. For instance, an RGB image is a 3D tensor with two spatial axes (height and width), as well as three depth axes (also called the channels axis). Each depth channel accounts for a single color component: red, green, or blue.

The typical CNN architecture is structured as a series of stages. The fundamental data structure being the layer: a data processing module that takes one or more tensors as input and returns one or more tensors as outputs. Most of deep learning consists of chaining together simple layers that will implement a form of progressive information distillation over the input data: a succession of increasingly refined data filters are applied by going deeper in the CNNs. These layers can either be stateless or have a state; the weights are the state of the layers. Weights are tensors learned with stochastic gradient descent and, collectively, they constitute the knowledge of a neural network. CNNs are usually constructed making use of different types of layers: convolutional layers, pooling layers, fully connected layers, and others.

The feature extraction process takes place in both convolutional and pooling layers, whereas the classification process occurs in the fully connected layer. It is important to note that the topology of a neural network defines a hypothesis space for the target distribution, i.e., the distribution over which the final system performance must be trained. In fact, machine learning (hence deep learning) accomplishes the task of looking for useful representations of some desired distribution of data, within a predefined space of possibilities, by using a feedback signal as search guidance, i.e., backpropagating gradients through the CNNs. Every time a network topology is chosen, the space of possible hypotheses is constrained in some way: specifically a series of tensor operations are chosen to be used for mapping input data to output data. Training a neural network means finding a good set of values for the weight tensors involved in the tensor operations that map inputs into outputs thus enabling a single model (or hypothesis) for the target data distribution to be selected.

2.4.1. Convolutional Layer

The convolutional layer is the base layer of a CNN. In a convolutional layer, during the inference process, patches from the layer input feature map are extracted and transformed into output feature map (response map) by applying the same convolution operation to each patch.

The output feature map is a 3D tensor with the width, height, and an arbitrary number of depth channels. Every channel in the depth axis stands for a filter and the response map is a 2D tensor that indicates the response of the filter over the input. Filters encode specific aspects of the input data, i.e., features. As the activation map is obtained by performing convolution between the filter and the input, the filter parameters are spatially invariant. Therefore, CNNs are particularly efficient when processing images: as the visual world translation is invariant, only a limited amount of training data is needed to learn representations with great generalization ability. CNNs can also learn spatial hierarchies of patterns: the first convolutional layer will learn small local patterns such as edges; a second convolutional layer will learn larger patterns with features of the first layers as building blocks, and so on.

2.4.2. Pooling Layer

Usually, a pooling layer follows a convolutional layer. The pooling layer is applied to reduce the spatial dependency of the computed features maps, hence to increase robustness to changes in the position of the feature in the image and to better exploit the resulting feature hierarchy. This is achieved by downsampling the feature maps in order to keep them reasonable in number.

The downsampling can be performed through the use of different techniques such as max-pooling and average pooling. The max-pooling operation, similarly to the convolution operation, extracts local patches from the input feature maps and outputs the maximum value of each channel in the original visual patch. The average pooling, instead, outputs the average value of each channel over the patch. Max-pooling tends to perform better than average pooling, as the maximal presence of specific features are more informative than their average presence.

2.4.3. Fully Connected Layer

Fully connected layers are final layers in a CNN where each neuron is completely connected to other neurons. These layers are responsible for the final classification results. In a fully connected layer, the rectified linear unit (ReLU) activation function is commonly used:

$$ReLU(x) = \begin{cases} 0, & x < 0 \\ x, & x \geq 0 \end{cases} \quad (1)$$

Softmax activation function is usually utilized to predict output images in the very last fully connected layer:

$$Softmax(x_i) = \frac{e^{x_i}}{\sum_{y=1}^{m} e^{x_y}} \quad (2)$$

where x_i and m represent input data and the number of classes, respectively.

2.4.4. Hyper-Parameter Optimization

Deep-neural-network performance depends on a wide range of hyper-parameter choices, subject to fine tuning during the training process and include, among others, the CNN architecture, an optimization process, and regularization (Hutter et al., 2019).

A CNN optimization configuration involves selecting the optimizer to be used to update the network weights through stochastic gradient descent. The learning rate of the optimizer defines the magnitude of the modifications to the model weights in response to the estimated error. By applying a learning rate that changes during training (i.e., adaptive learning rate), increased performance and a faster convergence can often be achieved. For instance, a learning-rate decay formula might be used to reduce the learning rate at each iteration i (e.g., end of each mini-batch) as follows:

$$learning\_rate_i = learning\_rate_{i-1} * \left(\frac{1}{1 + decay * (i-1)}\right) \quad (3)$$

Regularization is a design principle for augmenting a primary optimization objective (e.g., how well a learned model fits its training data) by taking into account a secondary objective: a penalization term with respect to those representations that are less desirable due to less compact. In weight regularization, for example, a cost is associated with the loss function of the network in order to constrain the CNN weight values to be small and the distribution of weight values to be regular. The cost might be proportional to either the absolute value of the weight coefficients (L1-regularization) or to the squared value of the weight coefficients (L2-regularization). The dropout regularization technique consists of introducing noise in the output values of a layer by randomly setting a fraction of them to zero, i.e., dropping them out, during the training phase. The idea behind this is to prevent the CNN from retaining the patterns that are less significant.

2.5. Experimented CNN Architectures

CNN architectures are crafted by stacking different types of layers and can result in networks that have very deep structures. We here present an overview of some of the most relevant, in literature, existing CNN architectures that have been trained and tested in this experimental investigation.

2.5.1. VGG19

The VGG19 CNN architecture (Simonyan and Zisserman, 2015) was introduced in 2014, as an improvement of the well-known VGG16. The main contribution resulted in an increased depth of the network and by the replacement of the 11 × 11 and 5 × 5 with small 3 × 3 convolutional filters. The network consists of 19 layers (16 convolutional layers, 3 fully connected layers, 5 max-pooling layers and 1 Softmax layer). The default input image size of VGG19 is 224 × 224 pixels. VGG19 showed a significant improvement on classification tasks with respect to the ImageNet Challenge 2014 and compared to other popular networks such as AlexNet and GoogleNet.

2.5.2. Inception-v3

Inception CNN was introduced by Szegedy et al. (2016) at Google in 2013–2014. This is a popular CNN architecture, aimed at reaching performance efficiency by utilizing suitably factorized convolutions and aggressive regularization (see section 2.4.4). Factorized convolutions are effectively applied in CNN convolutional layers to simultaneously perform spatial convolution in each channel and linear projection across channels. These and other techniques can effectively preserve the spatial information and maintain the accuracy with significantly less computation (Wang et al., 2017). The default input image size of Inception-v3 is 299 × 299 pixels. The network input is processed by several parallel convolutional branches that work independently and whose outputs are then merged back into a single tensor. The most basic form of an Inception module has three to four branches that start with a 1 × 1 convolution, are followed by a 3 × 3 convolution, and end with the concatenation of the resulting features. This structure enables the network to learn, separately rather than jointly, spatial features and channel-wise features. The rationale behind this approach is the fact that each channel might be highly autocorrelated across space, but might not be highly correlated with other channels.

2.5.3. Xception

Xception (Chollet, 2017) is a CNN architecture roughly inspired by Inception. Xception stands for extreme Inception. In fact, it adopts an extreme form of an Inception module: the process of learning channel-wise features is fully separated from that of learning spatial features. Moreover, the Xception network substitutes Inception modules with depth wise separable convolutions. They are depth wise convolutions (a spatial convolution where every input channel is handled separately) followed by a point-wise convolution (a 1 × 1 convolution). Xception and Inception-v3 have approximately the same number of parameters and the same default image size. However, Xception makes a more efficient use of model parameters with respect to Inception; therefore, it shows better runtime

performance and higher accuracy large-scale data sets such as on ImageNet.

2.5.4. Inception-ResNet-v2

Inception-ResNet-v2 (Szegedy et al., 2017) is a CNN architecture that belongs to the Inception CNN family and incorporates residual connection as a replacement of the filter concatenation stage of the Inception architecture. A residual connection resides in reintroducing previous representations by skipping one or more layers (through the so-called "shortcut connections") and by summing by a past output tensor to a later output tensor. This helps to prevent information loss along the data-processing flow. The authors reported, on the one hand, a significant improvement of the recognition performance but, on the other, a substantial increase of the training speed compared to standard for the Inception architectures. The default input size for this model is 299 × 299 pixels.

2.6. Data Pre-processing

All ultrasound images were read into an RGB format to ensure that the model input shape is compatible with the used CNN models. Images containing artifacts, such as calipers, text, lines, and tick marks, were not considered in the current analysis. In fact, such patterns are detrimental for accurate image classification. Therefore, we used a simple template-matching module to detect and discard, prior to feeding the data set into the learning architecture, the ultrasound images that have these structures. The remaining images were cropped to remove uninformative data, such as dark borders and text, thus resulting in images with a resolution that span between 546 × 410 and 175 × 409 pixels. All images were then resized to the default input size of the used neural network (224 × 224 pixels for VGG19; 299 × 299 pixels for Inception-v3, Xception, and Inception-ResNet-v2) and were normalized to ensure every pixel value is between −1 and 1.

2.7. Data Augmentation

In order to avoid overfitting, we applied the technique of data augmentation (Perez and Wang, 2017) on the three-class classification problem. Data augmentation consists of artificially increasing the number of existing samples, by applying a number of random transformations: this yields close-to-real biomedical images that are likely to well represent the target data distribution.

The performance of different affine transformations were evaluated: flips (horizontal, vertical), angle rotations, translational pixel shifts, regional zoom, random Gaussian noise, and blurring by various amounts.

We found that the best performances are achieved by using a horizontal flip and width shift range of 10%. In fact, these transformations provide realistic lung ultrasound images. Horizontal flip produces horizontally-mirrored images of the lung, which might represent the occurrence of the clinical condition displayed in the original image but in the opposite lung. Similarly, a width shift range of 10% can represent a lung from a slightly older patient. The images were expanded from 3,000 lung ultrasound images to 100,000 artificial images. It should be noted that augmentation was only done for the training data set; the validation and the testing data sets were not touched.

2.8. Experimental Setup

Keras (Chollet, 2015), a compact, high-level and easy-to-learn Python library for deep learning, coupled with TensorFlow backend (Abadi et al., 2016) in Python 3.7 was used to train the deep-learning models from scratch.

Several python libraries [Qt (Nokia Corp., 2012), OpenCV (Bradski, 2000), Sklearn (Buitinck et al., 2013)] were used for the statistical analysis and the software implementation, including the development of a software system that uses the learned model for classifying images of healthy children and those with either bronchiolitis or pneumonia.

All experiments were performed on a workstation Intel® Xenon® CPU E5-2680 @ 2.70 GHz (2 processors) with Windows 10 operating system using GeForce RTX™ 2080 Ti GPU graphics card.

2.9. Model Selection

In this section, we provide a brief description of the CNNs employed for LUS images classification. All CNN models (VGG19, Xception, Inception-v3 and Inception-ResNet-v2) were trained from scratch with random initialization weights. The default densely connected classifier (from ImageNet) on top of the network, for all Keras models, were replaced with new fully-connected layers having the correct number of output classes.

The trained neural networks share some common hyper-parameters. More specifically, all CNNs were compiled using the optimization method called RMSProp, a momentum (Sutskever et al., 2013) with a decay of 0.9; and all the convolutional layers were activated by the rectified linear unit (ReLU). In all our experiments, we trained all the CNNs with batch sizes of 20 for 50 epochs, except for Inception-ResNet-v2 that was trained with a batch size of 10.

As for the three-class classification problems, we performed a hyper-parameter optimization (see section 2.4.4) with respect the following parameters:

- the learning rate was experimentally iterated between the value 1e-3 and value 1e-7: 1e-6 was selected;
- the dropout regularization was set to 0.5 in all experiments;
- l2-regularization: the following values have been iteratively evaluated 5e-4, 4e-5, 1e-5, 0: 0 was selected;
- exponential learning rate decay was set to either 0.94 or 0: 0 was selected.

2.10. Performance Metrics

Five criteria were used for evaluating the performances of deep-learning models.

$$Accuracy = (TN + TP)/(TN + TP + FN + FP) \quad (4)$$

Accuracy is the ratio of the number of true samples to the total number of samples.

$$Sensitivity = TP/(TP + FN) \quad (5)$$

Sensitivity, also known as true positive rate (TPR) or recall, is the probability that a patient with a certain condition is correctly diagnosed.

$$Specificity = TN/(TN + FP) \quad (6)$$

Specificity is the probability that people without a certain diagnosis are not erroneously diagnosed as suffering from that disease. It can however analogously be called true-negative rate. Precision, also known as true positive accuracy (TPA), is defined in (7):

$$Precision = TP/(TP + FP) \quad (7)$$

Precision denotes the proportion of positive predicted values (PPV) that are correctly real positives.

$$F1 - Score = 2 * ((Precision * Recall)/(Precision + Recall)) \quad (8)$$

The F1-Score is a measure of the accuracy of a model on a data set. This is defined as the harmonic mean of precision and recall. TP, FP, TN, and FN given in Equations (4–8) represent the number of true-positives, false-positives, true-negatives, and false-negatives, respectively.

The terms positive and negative are used to refer to the presence or absence of a condition of interest: bacterial pneumonia, bronchiolitis, or being healthy. True-positives (TP) are the number of examples correctly labeled as positives. False-positives (FP) refer to the number of samples incorrectly labeled as positive. False-positives (FP) refer to negative examples incorrectly labeled as positive. True-negatives (TN) correspond to negatives correctly labeled as negative. Finally, false-negatives (FN) refer to positive examples incorrectly labeled as negative.

3. RESULTS

3.1. Experimental Results

In this paper, we performed one binary classification (healthy vs. bronchiolitis) and one three-class classification (healthy vs. bronchiolitis vs. bacterial pneumonia) out of three classes. The four-fold cross-validation method was used with four state-of-the-art deep learning models (Inception-v3, Inception-ResNet-v2, Xception, VGG19) trained from scratch. Fifty percent of the data is reserved for the training set, 25% of the data is allocated to the validation set, and the remaining 25% is reserved for the testing test. The experiments were repeated four times, until each 25%-part of the original data set was tested.

The results of all the experiments are listed in **Table 1**: it shows a detailed comparison of all trained models in terms of precision, sensitivity, F1-scores, specificity, and accuracy for each fold; the average classification performances of the model were also calculated.

For experiments classifying healthy vs bronchiolitis we found that the Inception-ResNet-v2 model provided the best results with a sensitivity of 97.75%, an accuracy of 97.75%, and a precision of 98.25%. Inception-v3 and Xception had similar performances. VGG19 was the worst and achieved accuracy of only 92.25%, a sensitivity of 91%, and a precision of 91.75%.

TABLE 1 | Classification metrics.

Healthy vs. Bronchiolitis					
	Precision	**Sensitivity**	**F1-score**	**Specificity**	**Accuracy**
Inception-v3					
Fold 1	92	91	91	100	91
Fold 2	95	95	95	95.4	95
Fold 3	99	99	99	97.2	99
Fold 4	91	89	89	79.2	89
Average	94.25	93.5	92.95	92.95	93.5
Inception-ResNet-v2					
Fold 1	99	99	99	99.2	99
Fold 2	98	97	97	97.2	97
Fold 3	99	99	99	99	99
Fold 4	97	96	96	92.6	96
Average	98.25	97.75	97.75	97	97.75
Xception					
Fold 1	92	91	91	100	91
Fold 2	97	97	97	100	97
Fold 3	99	99	99	100	99
Fold 4	95	94	94	94	94
Average	95.75	95.25	95.25	98.5	95.25
VGG19					
Fold 1	90	89	88	89	94
Fold 2	92	92	92	95.2	92
Fold 3	96	96	96	95	96
Fold 4	89	87	87	74.8	87
Average	91.75	91	90.75	88.5	92.25
Healthy vs. Bronchiolitis vs. Bacterial Pneumonia					
	Precision	**Sensitivity**	**F1-score**	**Specificity**	**Accuracy**
Inception-v3					
Fold 1	92	92	92	88.68	92
Fold 2	92	91	91	99.75	91
Fold 3	94	92	92	99.79	92
Fold 4	92	91	91	95.26	91
Average	92.5	91.5	91.5	95.86	91.5
Inception-ResNet-v2					
Fold 1	96	96	96	98.01	96
Fold 2	90	87	87	99.69	87
Fold 3	88	82	81	100	82
Fold 4	88	82	81	100	82
Average	90.5	86.75	86.25	99.42	86.75
Xception					
Fold 1	96	96	96	93.97	96
Fold 2	89	83	82	100	83
Fold 3	82	68	61	100	68
Fold 4	95	95	95	95.45	95
Average	90.5	85.5	83.5	97.35	85.5
VGG19					
Fold 1	91	90	90	81.11	90
Fold 2	90	89	89	94.01	89
Fold 3	96	96	96	93.49	96
Fold 4	89	87	87	87.79	87
Average	91.5	90.5	90.5	89.1	90.5

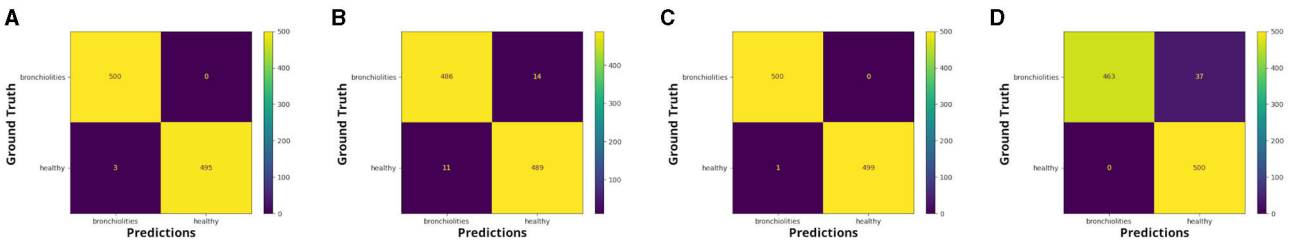

FIGURE 1 | Confusion matrices: healthy vs. bronchiolitis, respectively for **(A)** fold 1, **(B)** fold 2, **(C)** fold 3, and **(D)** fold 4.

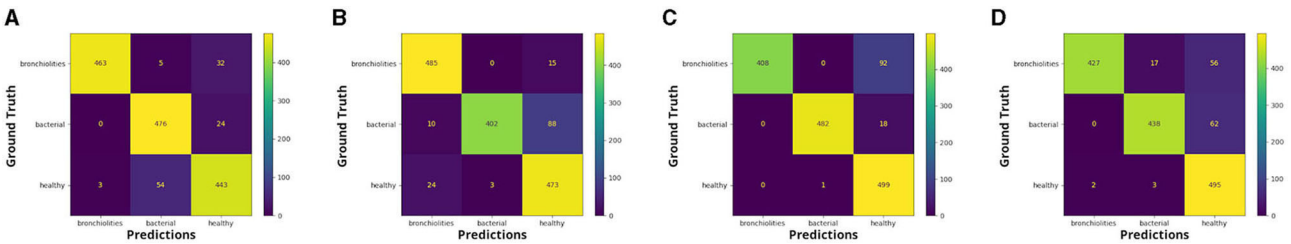

FIGURE 2 | Confusion matrices: healthy vs. bacterial pneumonia vs. bronchiolitis, respectively for **(A)** fold 1, **(B)** fold 2, **(C)** fold 3, and **(D)** fold 4.

For experiments classifying healthy vs bronchiolitis vs bacterial pneumonia, we found that the Inception-v3 model provided the best results with a sensitivity of 91.5%, a precision of 92.5%, and an accuracy of 91.5%.

The confusion matrices in **Figures 1**, **2** report the number of TP, TN, FP, and FN results of our experiments for each fold. We can observe that, for the comparison between healthy and bronchiolitis, the number of false-negative predictions (FN) and the number of false-positive predictions (FP) are very low.

In the medical context, and in particular for the diagnosis of bronchiolitis, the minimization of false-negative predictions is crucial because not identifying the disease could lead to treatment delay, hence to the aggravation of symptoms, and poor medical outcomes.

We see that for the comparison healthy vs bronchiolitis vs. bacterial pneumonia, false-positive predictions (FP) are higher for the groups of healthy infants and those with bronchiolitis. This is probably due to the fact that infants show artifactual patterns that are similar to those patterns usually observed in pulmonary diseases.

We can notice from the matrices that there are cases in which LUS images correctly classified in the binary classification problem were then attributed to the incorrect class in the three-class classification problem by the best performance model, Inception-v3.

3.2. Statistical Results

In order to analyse statistically significant differences among ages of the different diagnostic groups, we performed Kruskal-Wallis H-tests. According to the result of the Kruskal-Wallis H-test, age does not statistically differ between the group of infants with bronchiolitis and the healthy infants (chi-squared = 0.28869, df = 1, p-value = 0.5911 $>$ 0.05). Instead, the age of the children with bacterial pneumonia differs significantly from the age of children in the other two groups: healthy and bronchiolitis (chi-squared = 20.559, df = 2, p-value = 3.433e-05 $<$ 0.05).

3.3. EXplainable Artificial Intelligence Results

EXplainable Artificial Intelligence (XAI) is a newly emerging discipline of AI (Doran et al., 2017) that seeks to develop a series of ML techniques that enable non-expert audiences to better understand and manage results obtained by artificial intelligence (Holzinger et al., 2017). In fact, deep-learning models are usually perceived as "black boxes," they receive an input and learn representations that are in general difficult to extract and to present in a human-intelligible form. Although this concept is partially valid for certain types of deep-learning models, this is definitely not true for CNNs. Indeed, CNNs learn representations of visual concepts hence are highly responsive to visualization. We present a visualization study performed by using the best performance model (Inception-v3) that classifies images as belonging to three different diagnostic groups (i.e., bronchiolitis, pneumonia, and healthy). We applied three state-of-the-art eXplainable Artificial Intelligence approaches that are specifically tailored for convolutional neural networks: visualization of CNN filters, visualization of activation maps, and visualization of gradient-weighted class activation mapping (Grad-CAM).

3.3.1. Visualizing CNN Filters

We can describe a deep network as a multistage information-distillation operation (see section 2.4): the information goes through successive layers, it becomes increasingly purified over successive filtering operations and is finally more informative

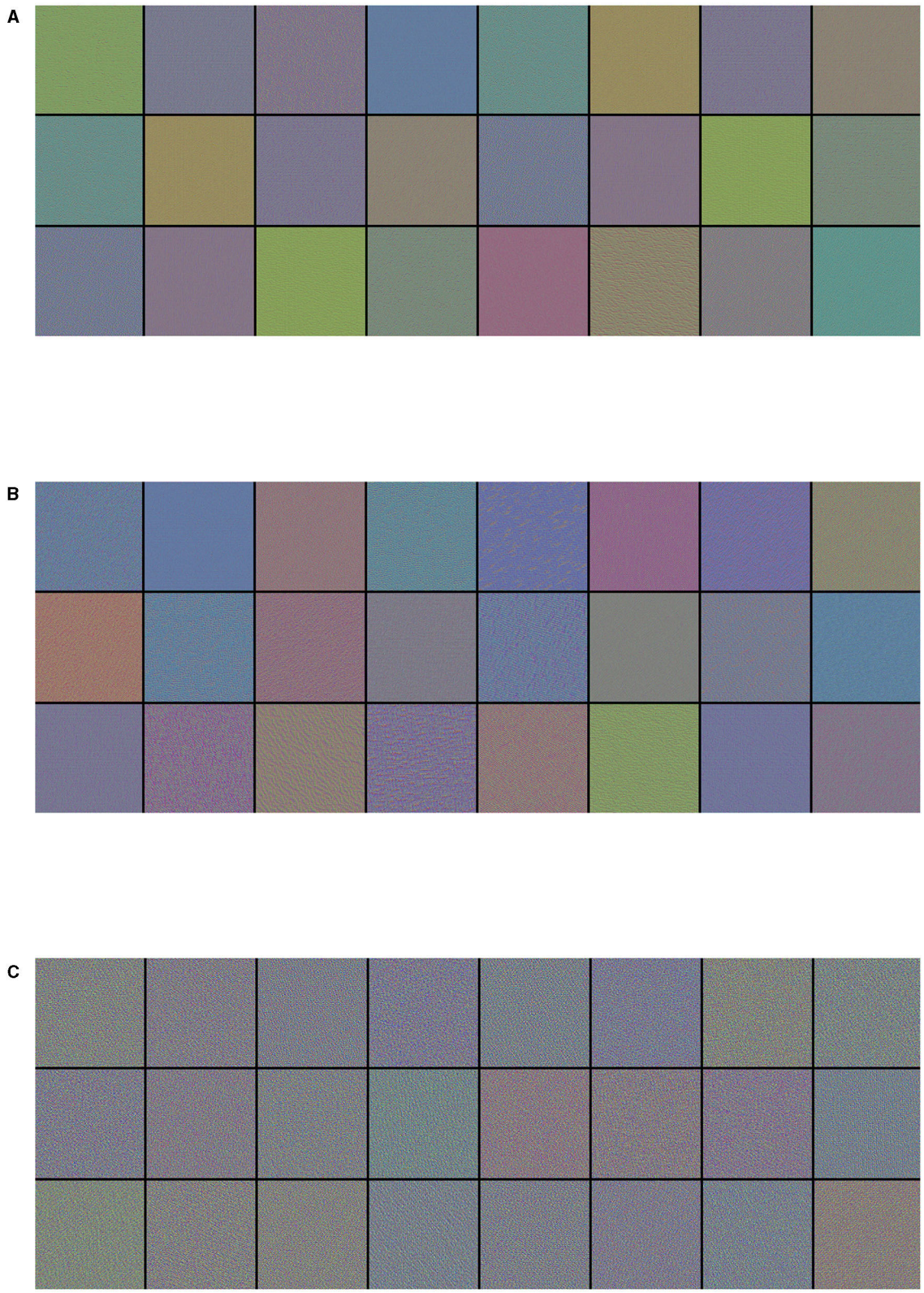

FIGURE 3 | Visualization of **(A)** the first 24 filters from the first convolutional layer, **(B)** the first 24 filters from the third convolutional layer, and **(C)** the first 24 filters from the fifth convolutional layer of the best performance model (Inception-v3) on the three-class classification problem. Filters act as collections of edge detectors, detect background, contours, and texture-like patterns.

for the task at hand. In fact, deep convolutional models learn a collection of filters that are increasingly refined and complex, the deeper the layers become. Specifically, each layer in a CNN learns a collection of filters such that their inputs can be expressed as a combination of the filters.

Visualizing CNN filters enables us to understand precisely which visual patterns or concepts each filter in a CNN is receptive to, therefore it permits us to observe how CNN layers see the world.

The filters from the first convolutional layers learned by the best performance model (Inception-v3) for the three-class classification problem are displayed in **Figure 3**. These filters encode colors, simple directional edges and, in some cases, colored edges that can be found in ultrasound images of lungs; the texture-like patterns of the filters become more complex, the deeper the layer becomes.

As a CNN is a hierarchical-modular network of convolutional filters that are probabilistically combined together, the way it works differs from the nature of human vision, which is not purely convolutional and it is organized in more sophisticated functionalities that involve motor control (Bressler, 1995). Nonetheless, colors, simple directional edges, and texture-like patterns extracted by a deep-learning model can provide useful insights that could help physicians diagnose lung diseases.

3.3.2. Visualizing Intermediate Activations

Visualizing intermediate activations (i.e., intermediate output of the activation function) consists of displaying, given a certain input, the feature maps that are output by various convolutions and by pooling layers in a network. Intermediate CNN outputs enable us to visualize the result of applying individual CNN filters to an input image, thus enabling us to visualize how an input is decomposed into the different filters learned by the network. In fact, feature maps are presence maps of learned visual concepts over a picture. Given as input an ultrasound

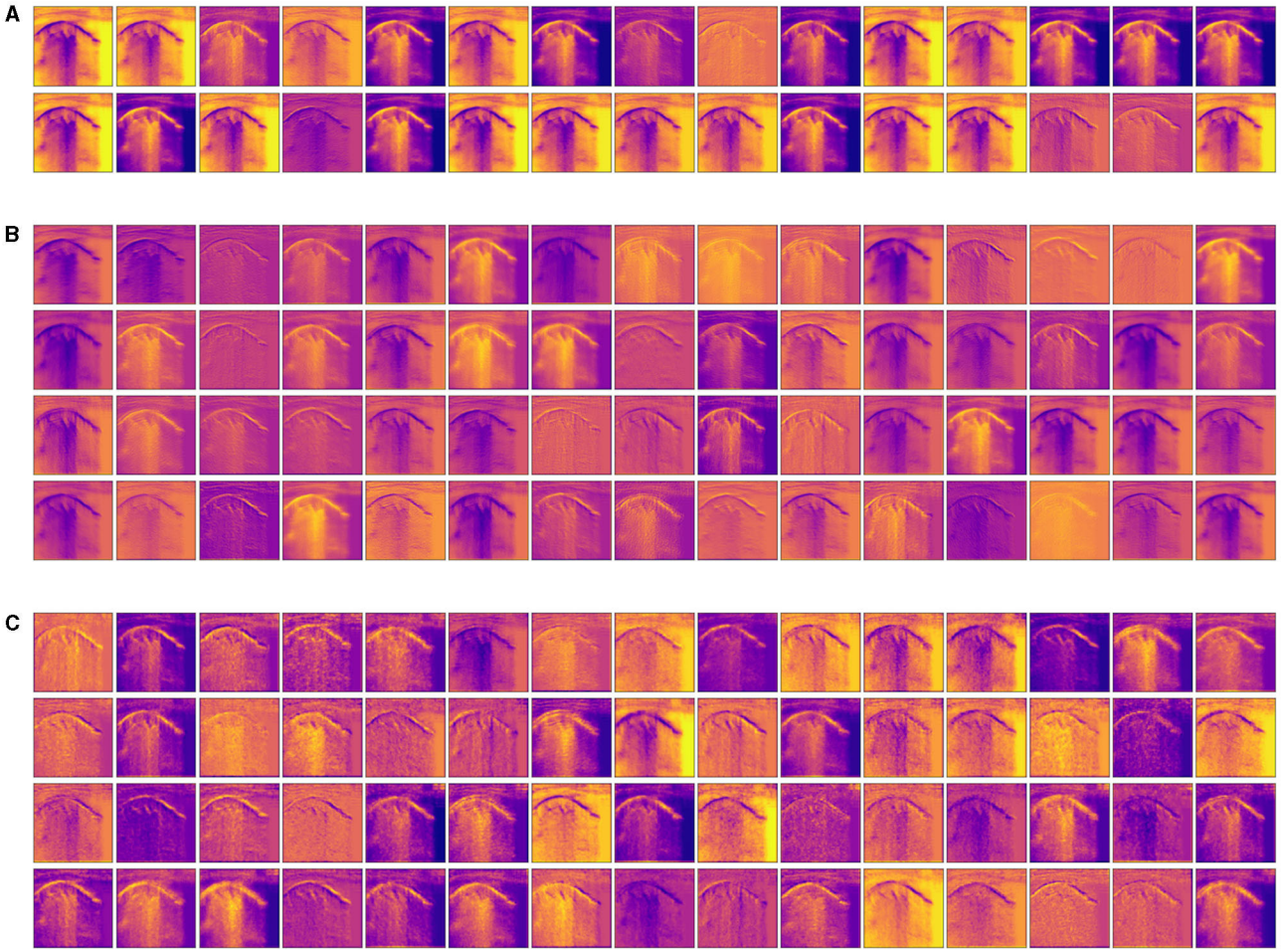

FIGURE 4 | Visualization of the activation maps from **(A)** the first, **(B)** the third, and **(C)** the fourth convolutional layer of the best performance model (Inception-v3) on the three-class classification problem, when fed with an image of a lung with bronchiolitis. Filters act as collections of edge detectors, detect background, contours, and texture-like patterns. When going deeper in the layers, the filters enhance differently vertical artifacts and small consolidation-like patterns that are typical of bronchiolitis.

image of a lung with bronchiolitis, in order to gain further insight into its performance and learned behavior, we show some visualizations of the activations from intermediate layers of the best performance model (Inception-v3) for the three-class classification problem. We observe in **Figure 4**, that different filters in the first convolutional layers activate distinct parts of

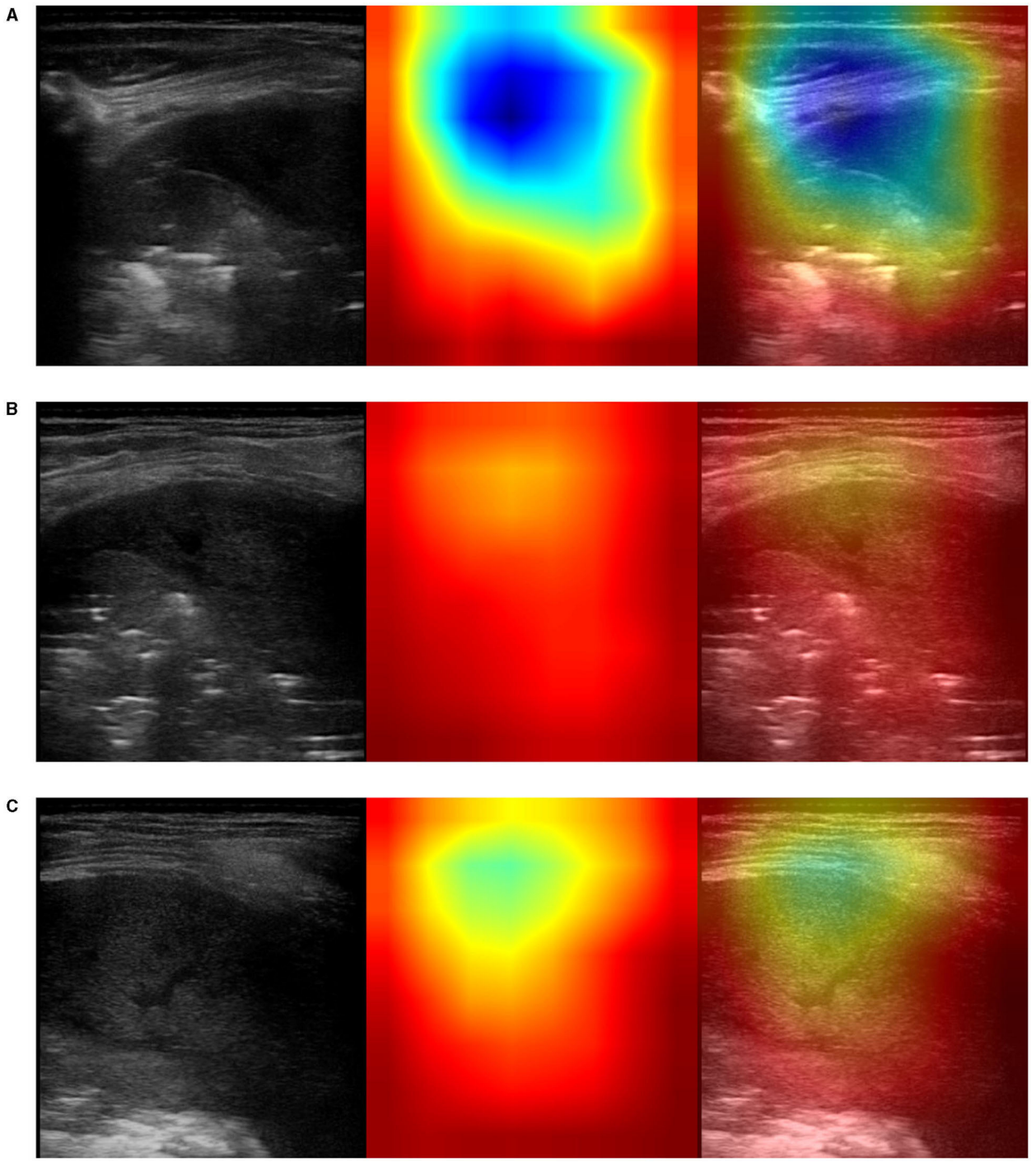

FIGURE 5 | Example of lung ultrasound images correctly predicted by the best performance model (Inception-v3) as bacterial pneumonia. **Left**: original LUS image; **middle**: Grad-CAM visualization; **right**: the class activation mapping transparently overlaid on the original LUS image. Note that red and orange regions correspond to high scores for the predicted class and correctly highlight diagnostic-relevant features: **(A)** severe consolidations with fluid bronchogram and dynamic air bronchogram, **(B)** severe consolidations with fluid bronchogram and dynamic air bronchogram, complicated pleural effusions, **(C)** fibrinous pleural effusions with pulmonary atelectasis.

the ultrasound image. Some filters act as collections of edge detectors; some other filters detect the background, and others detect the contours and texture-like patterns. It is evident how the activations have almost entirely preserved and split the information present in the original image. When going deeper in the layers, filters enhance in different ways the B-lines and small consolidation-like patterns that are typical of bronchiolitis. At the same time, the images become a little blurry, due to the max-pooling operations. As more and more pooling layers are introduced, the extracted features become increasingly abstract the deeper the layers become: this is an important and universal characteristic of the representations learned by deep neural networks. As explained in section 2.4, the deep neural network acts as an information distillation pipeline, where activations of the higher layers carry less information about the specific input being seen, and more information about the target (i.e., the class being learned: bronchiolitis, pneumonia, or healthy lung), thus helping the complete network to finally classify the image properly but without providing us with much visual information. The sparsity of the activations increases together with the depth of the network: in the last layers, many feature maps are blank, meaning that the pattern encoded by the filters is not present in the input image. The representation learned by the filter at this stage is much more abstract and not directly present in the original image. This resembles human perception: after observing a scene for a few seconds, humans remember which particular categories of objects were present in their field of view but cannot recall the exact appearance of those objects. Although these visual concepts might be different from how a human interprets images, they might be useful in helping physicians make diagnoses.

3.3.3. Visualizing Class-Activation Mapping

This visualization technique can be used to shed light on the reason a CNN model decides that an ultrasound image belongs to a certain class of diagnosis. Class-activation mapping highlights the parts of an image that are identified by means of the learned model, thus, they show where in the picture the features that characterize a diagnosis are located. In our examples, the red/orange areas are considered by the model to output the class prediction: the brighter the red color is, the higher the probability of the predicted class of diagnosis is.

In particular, we used the specific implementation that is described in "Grad-CAM: Visual Explanations from Deep Networks via Gradient-based Localization" (Selvaraju et al., 2017). We produced Grad-CAM visualizations for all LUS images belonging to the testing set and a set of corresponding images, each showing (1) the ultrasound images used as input to the optimal model, for the three-class classification problem, (2) the GRAD-Cam visualization, and (3) the overlapping of the lung ultrasound image and the class activation mapping. Examples of resulting images are shown in **Figures 5**–**7**.

The resulting images, together with the origin class and the predicted class by the optimal model, were qualitatively evaluated by a pediatrician expert in lung ultrasound. His comments are reported in section 4.

4. DISCUSSION

4.1. Summary of Findings

To the best of our knowledge, this is the first study using deep-learning techniques and raw lung ultrasound images (LUS) for the purpose of diagnosing bronchiolitis and bacterial pneumonia in children. We trained from scratch state-of-the-art deep neural networks on a large data set - a training-set size of 2,000 LUS images for the binary classification problem. An initial training-set size of 3,000 LUS images was expanded with data augmentation to contain 100,000 artificially-created images for the three-class classification problem. We carried out comparisons with results from four different CNN networks trained using four-fold cross-validation: VGG19, Xception, Inception-v3, and Inception-ResNet-v2. The optimization of the supervised classifier was performed jointly with the optimization of the neural network.

We provide strong evidence that the automatic detection from lung ultrasound imaging, of pulmonary diseases in children, is a promising future research direction to be investigated. In particular, as shown in **Table 1**, we obtained high performance for the three-class classification problem involving healthy infants and those with cases of bronchiolitis and bacterial pneumonia: an average accuracy, sensitivity, and F1-score of 91.5%, and with precision and specificity, respectively, of 92.5 and 95.86%.

4.2. Clinical Significance

It is important to note that no hand-crafted features were considered in our algorithm pipeline. Nonetheless, biologically relevant features were automatically selected and extracted from the LUS images by the optimal deep-learning model. The Grad-CAM (see section 3.3.3), enables us to understand which areas in an image are mostly considered by the model to make its decision about the diagnosis. Dr. Buonsenso, a pediatrician expert in lung ultrasound, with more than 5 years of experience in LUS diagnosis and teaching, analyzed both the results of the classification by the optimal deep-learning model and the Grad-CAM visualizations. The purpose was to evaluate whether diagnostically relevant visual features in pulmonary diseases were highlighted by the Grad-CAM hence taken into consideration by the optimal deep-learning model for predicting the diagnosis. The model correctly identified almost all the images belonging to the group of children with bacterial pneumonia. The majority of the Grad-CAM also localized the domain-specific features that are taken into account by physicians when formulating a diagnosis of bacterial pneumonia: for example, larger consolidations with air and/or liquid bronchograms and pleural effusions, either simple (anaecogenic fluid) or complex (with fibrinae and septae, see **Figure 5**). Similarly, the model achieved high accuracy in classifying images belonging to infants with bronchiolitis. Consistently, the Grad-CAM detected diagnostically-relevant features (see **Figure 6**). In particular, in the case of bronchiolitis, the Grad-CAM often and

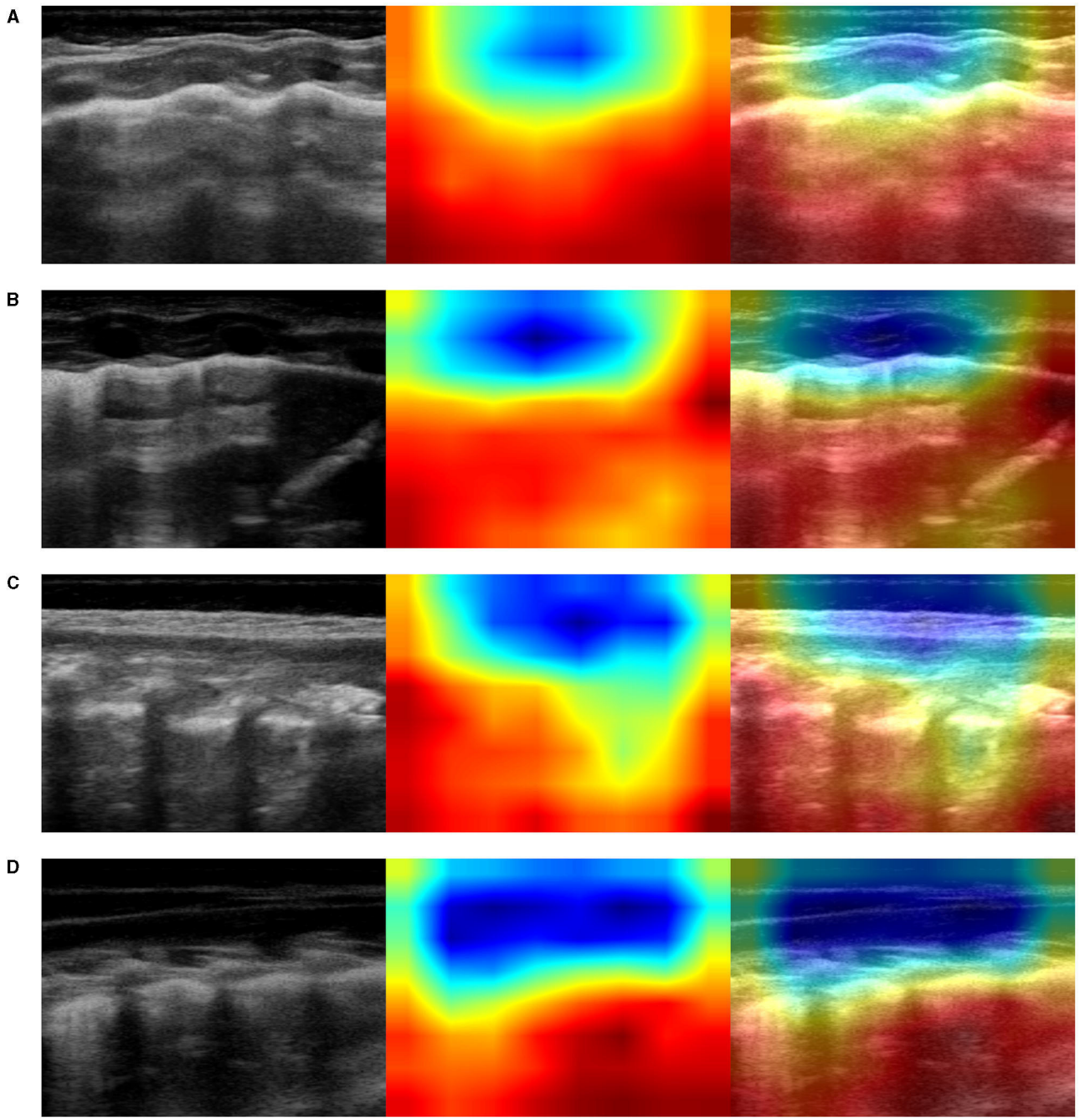

FIGURE 6 | Example of lung ultrasound images correctly predicted by the best performance model (Inception-v3) as bronchiolitis. **Left**: original LUS image; **middle**: class activation mapping produced by the Grad-CAM visualization; **right**: the class activation mapping overlaid transparently on the original LUS image. Note that red and orange regions correspond to high scores for the predicted class and correctly highlight diagnostic-relevant features: **(A)** irregular short vertical artifacts; **(B)** irregular pleural line, subpleural consolidation > 2 cm, confluent short and long vertical artifacts; **(C)** irregular subpleural line, microconsolidations, short vertical artifacts; and **(D)** white-lung.

suitably pointed out areas of short and long artifacts (either isolated or confluent), pleural line irregularities (with or without pleural effusions), large consolidations with air bronchograms, and small subpleural consolidations. The model showed the best performance when distinguishing larger consolidations and vertical artifacts, especially when they were long and confluent. Finally, the model showed great performance also in recognizing LUS images of healthy infants, even in presence of long vertical artifacts that might be characteristic of different conditions, see **Figure 7**.

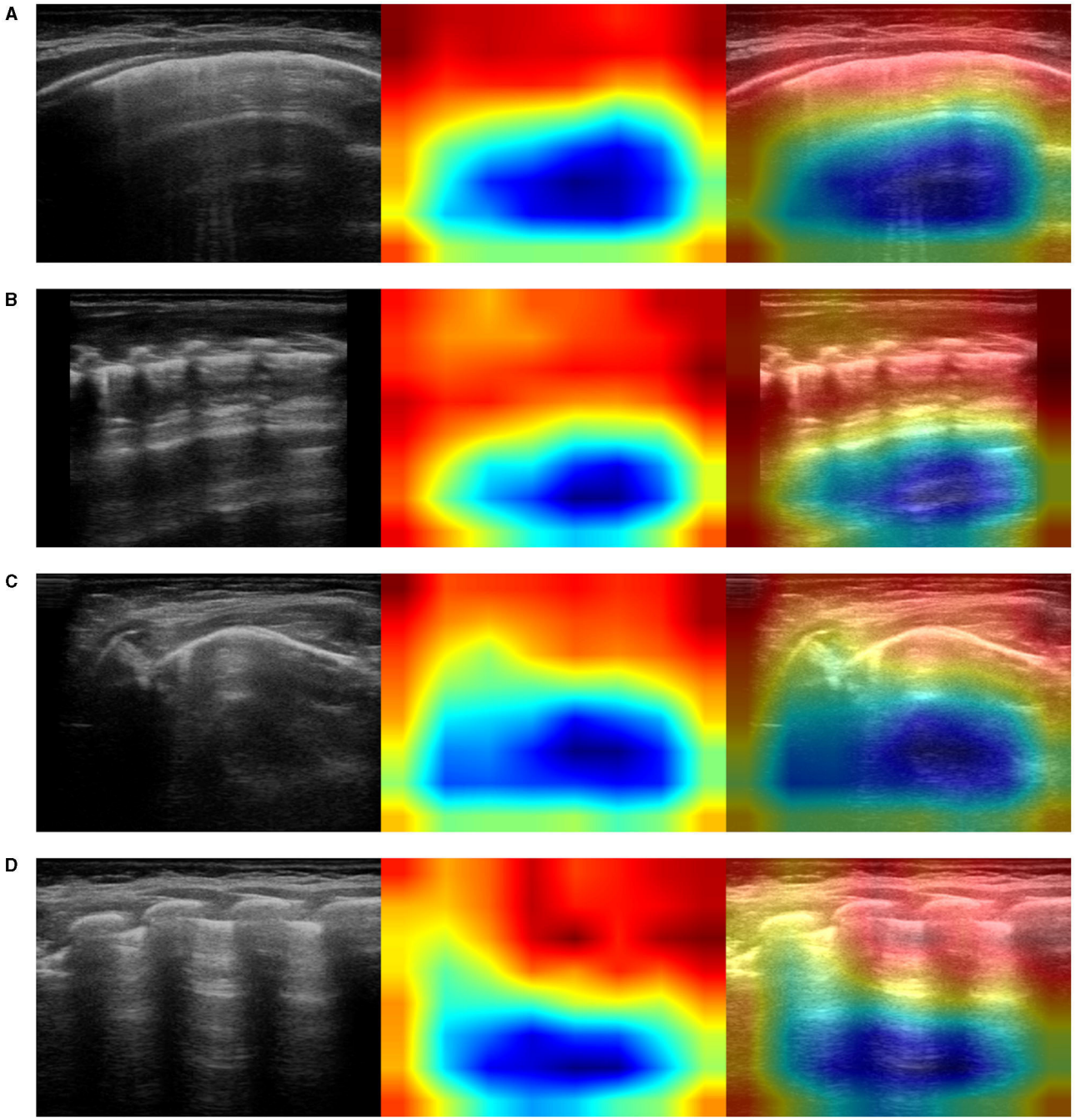

FIGURE 7 | Examples of lung ultrasound images **(A–D)** from healthy infants correctly predicted by the best performance model (Inception-v3). **Left**: original LUS image; **middle**: class activation mapping produced by the Grad-CAM visualization; **right**: the class activation mapping overlaid transparently on the original LUS image. Note that red and orange regions correspond to high scores for the predicted class and correctly highlight diagnostic-relevant features: regular pleural lines; presence of short vertical artifacts; presence of long vertical artifacts single and/or multiple, non-confluent and/or confluent, with possible uneven distribution and/or involving multiple lung areas with a prevalence of the right and/or left hemithorax, depending on the gestational age and the current age of the patient.

4.3. Comparison With Other Studies

Few studies, for the purpose of assisting medical doctors make their diagnoses, have been dedicated to the investigation of lung diseases by applying deep-learning techniques to raw LUS images. For instance, Born et al. (2021) crafted a VGG16-based convolutional neural network pre-trained on ImageNet and successfully performed three-class classification problems involving cases of COVID-19 patients with bacterial

pneumonia and healthy individuals. Following a different approach, we did not modify the structure of the original CNNs, except for the classifier. We also used random weights instead of those trained on ImageNet: lung ultrasound images are fundamentally different from those contained in the ImageNet data set, likely characterized by features that diverge from those identified with the use of the ImageNet data set.

Similar deep-learning approaches were extensively validated on CT scans and chest X-ray for COVID-19 diagnoses and were previously applied to pediatric pulmonary diseases by using chest X-ray images.

Ozturk et al. (2020) presented a deep neural network based on a DarkNet model for the automatic COVID-19 detection using chest X-ray images. They implemented 17 convolutional layers with LeakyReLU as activation function and introduced different filtering on each layer. The model achieved an accuracy of 98.08% for binary classes (normal vs. COVID-19) and 87.02% for multi-class cases (COVID-19 vs. no-findings vs. pneumonia). In work more comparable to our study, Narin et al. (2021) conducted experiments with three binary classification problems by using transfer learning on five pre-trained convolutional neural-network-based models (ResNet-50, ResNet-101, ResNet-152, Inception-v3, and Inception-ResNet-v2), and they tested their performance with five-fold cross-validation. They found that the pre-trained ResNet-50 model provides the highest classification performance (96.1% accuracy for normal vs. COVID-19, 99.5% accuracy for COVID-19 vs. viral pneumonia, and 99.7% accuracy for COVID-19 vs. bacterial pneumonia).

In the field of pediatric pulmonary imaging, an interesting study by Liang and Zheng (2020) proposed a deep-learning network that combines residual structures and dilated convolution with the purpose of diagnosing pneumonia by using raw chest X-ray images from children from 1 to 5 years of age. Their data set involved a total of 6,090 chest X-ray images, 4,117 images from children with pneumonia, and 1,973 images from healthy infants. Their method obtained an accuracy of 90%, a recall rate of 96.7%, and the F1-score of 92.7% on pneumonia classification tasks. A similar approach, developed by Saraiva. et al. (2019), obtained an average accuracy of over 95% on a binary classification problem for detecting pneumonia cases from chest X-ray images. Our results are competitive when compared to those obtained by using both X-ray and LUS imaging modalities, both in pediatric studies regarding cases of pneumonia (Liang and Zheng, 2020) and in recent investigations involving patients with different kinds of pneumonia (i.e., COVID-19 and bacterial pneumonia). In fact, our Inception-ResNet-v2 model achieves 97.75% accuracy, 97.75% sensitivity, and 97% specificity for healthy vs. bronchiolitis, whereas the Inception-v3 model provides the best results with 91.5% accuracy, 91.5% sensitivity, and 95.86% specificity for healthy vs. bronchiolitis vs. bacterial pneumonia.

Interestingly, a study from Correa et al. (2018) examined brightness profiles of pleural lines in children younger than 5 years of age; they were associated with three possible diagnoses: pneumonia, healthy, and bone. The authors used a feed-forward neural network composed of three layers and sigmoid as an activation function. Their approach achieves a sensitivity of 90.9% and a specificity of 100% in detecting vectors associated with pneumonia consolidation. The results of their study support our findings that filters of the first convolutional layers learned by the optimal model respond mainly to color features (see section 3.3.1), with brightness being expressible as a linear combination of RGB color components. Furthermore, when inspecting the convolutional filters (**Figure 3**), and activation maps (**Figure 4**) of the first convolutional layers, we can see that they also responded to edges and texture-like patterns (see sections 3.3.1 and 3.3.2). This observation, when considered together with the fact that the Grad-CAM highlights areas of medical interest, suggests that, when taking its decision over the classification outcome, the network looks predominantly at those specific patterns.

A fair amount of research is devoted to the use of deep-learning approaches for analysing LUS images by focusing on training deep neural networks on isolated, hand-crafted features that are considered diagnostically valid, i.e., A-lines, vertical artifacts, pleural lines (Carrer et al., 2020), pleural effusions, and also consolidations, with vertical artifact (i.e., B-lines) detection the most common task (Kulhare et al., 2018; Wang et al., 2019; van Sloun and Demi, 2020). See McDermott et al. (2021), for a review. Conversely, we opted for applying deep neural networks to raw images, because this usually permits avoiding the introduction of typical errors caused by inaccurate results of image pre-processing steps (e.g., image segmentation and decomposition) and cognitive biases or confidence in spatial relationships between pixels and could lead to the discovery of unexpected associations that would remain otherwise undetected (Poplin et al., 2018). Furthermore, feeding the deep neural network with raw images enables us to take better advantage of deep-learning potential: (1) the automatic detection of the appropriate predictive visual features from the training data enables the feature extraction without requiring features to be hand-engineered; (2) feature interaction and hierarchy can be exploited jointly within the intrinsic deep architecture of a neural network; (3) the three steps of feature selection, feature extraction and supervised classification, can be realized within the optimization of the same deep architecture, and the performance can be tuned more easily in a systematic fashion. As a result, the models achieved very high performances in both classification tasks. We can also observe that the optimal model appears to be able to distinguish the specific appearance of visual features (such as B-lines, consolidations etc.) in different diagnoses, rather than merely being able to look for the presence or absence of them. In fact, growing evidence indicates that artifacts can have a different semeiotic, according to each disease (Soldati et al., 2016, 2019).

4.4. Limitations

Although our data set contains a large number of images, it suffers from a limitation due to the relatively small number of individuals, particularly children with pneumonia. It is important to observe that only two out of three groups of children were matched by age: healthy infants (age: 2.83 $\pm$ 2.89 months) and

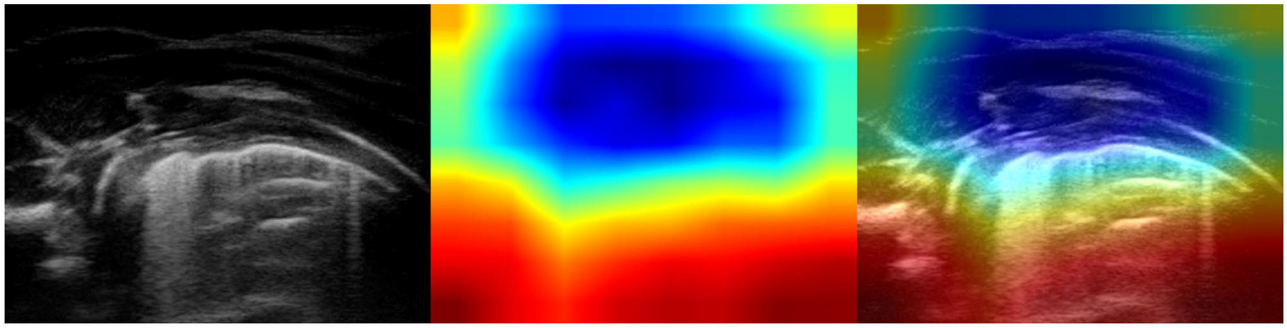

FIGURE 8 | Example of lung ultrasound image of a healthy lung incorrectly classified as bronchiolitis by the best performance model (Inception-v3). **(Left)** Original LUS image; **(Middle)** Class activation mapping produced by the Grad-CAM visualization; **(Right)** The class activation mapping overlaid transparently on the original LUS image. Note that red and orange regions correspond to high scores for the predicted class and highlight multiple, confluent long vertical artifacts. These visual features are typical of bronchiolitis but can also be observed in very young healthy infants (∼ 6 months of life). Therefore, the optimal model "mistake" results in the recognition of multiple long vertical artifacts.

infants with bronchiolitis (age: 2.50 ± 2.67 months). The age of children suffering from bacterial pneumonia (age: 6.17 ± 6.77 years) is statistically different from that of the subjects in the other two groups. The patient populations of our study reflect real-life clinical situations, i.e., bronchiolitis tends to affect younger infants with respect to bacterial pneumonia. Although the obtained results are promising, they might not be generalizable to patients of all ages. The main features of lung pathology (e.g., consolidations, pleural effusions, and bronchograms) were demonstrated to be the same across all age groups, from newborns to adults, the only exception being vertical artifacts. Although vertical artifacts are traditionally considered as a sign of interstitial disease, rather than one of a healthy lung, they can be morphologically different in a healthy lung, in a pathological lung and in the case of diverse diseases (Soldati et al., 2016, 2019). For instance, we recently showed that the healthy younger infants (∼6 months of life) can have a lung ultrasound pattern characterized by multiple vertical lung artifacts (Buonsenso et al., 2020d). This is probably due to the immature development of the lung in the first months of life. In line with these results, our models, misinterpreted some cases of healthy infants, whose images were characterized by the presence of multiple, often confluent, vertical artifacts (see **Figure 8**, for an example), such as with bronchiolitis. In a real-life scenario the "age-effect" should have no impact on the interpretation of LUS features. However, from a methodological point of view, further studies should address this issue and, in order to achieve better classification performance, should therefore focus on training deep neural networks, by using more diverse examples of LUS images that contain vertical artifacts from both healthy infants and patients with interstitial disease. In fact, the correct diagnosis of bronchiolitis and, in particular, the possibility of making a distinction between acute bronchiolitis and pneumonia are crucial in young infants because this age group bears the highest global mortality rate for both bronchiolitis and pneumonia. As these two conditions require different management (antibiotics are needed only in case of pneumonia), the differentiation of these two conditions by point-of-care lung ultrasound, particularly in poor settings, could be particularly relevant from a global health perspective.

Another limitation of our study is certainly related to data acquisition. We did not set up a standard procedure for obtaining images from the ultrasound probe, i.e., zoom, gain, mechanical index, and focus positioning were perhaps not always the same in every patient. When those images were either oversaturated or extremely dark, the model made a few objective mistakes by misinterpreting some images of healthy lungs as images that displayed lungs with bacterial pneumonia (**Figure 9**): input perturbations might have been confused with consolidations by the model. The ability to set the proper settings depends on the experience of the sonographer, and different settings can lead to different lung ultrasound patterns, even when scanning the very same areas. Establishing standard settings is probably one of the main challenges of using lung ultrasound imaging. Only recently, and much later with respect to the time of our data acquisition, researchers of the Italian Academy of Thoracic Ultrasound proposed a standardization with respect to the use of LUS in the management of COVID-19 patients by specifying imaging and device settings, among the other procedures, with the aim of reaching a more globally unified approach for comparisons between different human- and computer-aided studies; hence a better understanding of the role of LUS in the diagnosis of COVID-19 (Soldati et al., 2020).

4.5. Applications and Future Directions

At present, we have implemented a simple decision support tool (computer aided diagnosis system or CADx) that can assist medical doctors in formulating their diagnoses: given as input a sequence of LUS images, our system is able to suggest a diagnosis on the basis of the majority of the CNN classification votes obtained over all images belonging to a patient. The diagnosis spans over the three above-mentioned diagnostic groups: healthy subjects and patients with bacterial pneumonia or bronchiolitis. The final decision of the diagnosis is eventually taken by the medical personnel, with the help of the Grad-CAM that is displayed for each LUS image belonging to a specific patient.

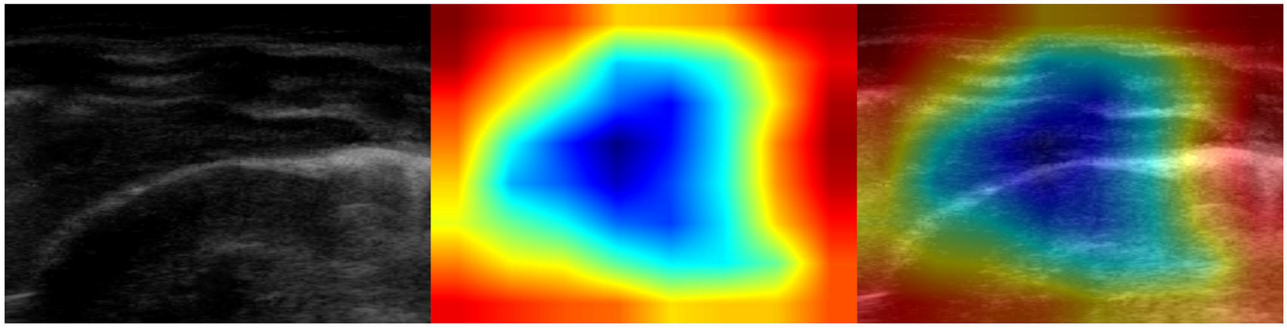

FIGURE 9 | Example of lung ultrasound image of a healthy lung incorrectly classified as bacterial pneumonia by the best performance model (Inception-v3). **(Left)** Original LUS image; **(Middle)** Class activation mapping produced by the Grad-CAM visualization; **(Right)** The class activation mapping overlaid transparently on the original LUS image. Note that red and orange regions corresponds to high scores for the predicted class and highlight what might be confused with consolidations, being the image really dark. This mistake helps us to better understand how the training set should be balanced with a more comprehensive inclusion of the different visual features.

The explainable method gives quantitative feedback (in terms of probability) on the rationale behind the decision taken by the model hence might also be useful for instructional purposes (Muse and Topol, 2020).

When validated adequately, the method we propose could help to simplify and accelerate the diagnosis of pulmonary diseases, and if extended, in the future, might enable the differentiation among different types of bacterial and viral pneumonia (including COVID-19). Considering the fact that deep learning usually performs better when the available data points represent well the distribution at end, our future works will be to collect ultrasound image sets that are greater and better balanced, with respect to age groups, ethnicity and device settings, despite the fact that methodical data collection is time-consuming and challenging due to the paucity of data. Particular attention could be given to the anomaly detection problem (Chandola et al., 2009). In most classification tasks the presence of one or more negative (alien or abnormal) classes constitutes a challenge, especially considering the lack of data of these classes and the openness of the problem. A typical solution to overcome this problem is to use supervised anomaly detection thus build a predictive model for normal vs. anomaly classes that might then contain data belonging to other illnesses not contemplated by the actual classification. Different techniques have been used to address the anomaly detection problem and could be adopted in future works: generative adversarial networks for anomaly detection (Schlegl et al., 2019) and the methods based on one class classification (Ruff et al., 2018). Many other approaches could be investigated to refine our results: careful choices for the topology of a neural network, extensive use of transfer learning in compatible domains, exploring other deep-learning methods, for example, with the objective of emphasizing robustness and explainability (Roberts and Tsiligkaridis, 2020). Additionally, our approach might be combined with the classification of disease severity (Supino et al., 2019) or with LUS image quality assessment module (Baum et al., 2021).

5. CONCLUSIONS

In conclusion, our study represents a first step for the development of a CADx system that is able to assess and classify pediatric LUS images as belonging to different pulmonary diseases. When extensively validated, such a system could reduce the daily burden of clinicians, could assist them in making more accurate diagnoses, and could enable better comparisons of images obtained during follow-up. Moreover, CADx systems could provide a second opinion to expert radiologists and remote training assistance, which could be particularly useful in remote geographic areas with a limited availability of diagnostic tools.

DATA AVAILABILITY STATEMENT

The raw data supporting the conclusions of this article will be made available by the authors, without undue reservation.

ETHICS STATEMENT

The studies involving human participants were reviewed and approved by ethics committee of the Fondazione Policlinico Universitario A. Gemelli IRCCS Rome, Italy. (prot 36173/19, ID 2729). Written informed consent to participate in this study was provided by the participants' legal guardian/next of kin.

AUTHOR CONTRIBUTIONS

SM, PV, and DB conceptualized the study. DB, CD, and RM performed the lung ultrasound scans. SM was responsible for the deep-learning studies. SM and DB wrote the first draft of the manuscript. All authors read and approved the last version of the manuscript.

REFERENCES

Abadi, M., Barham, P., Chen, J., Chen, Z., Davis, A., Dean, J., et al. (2016). "Tensorflow: a system for large-scale machine learning," in *12th USENIX Symposium on Operating Systems Design and Implementation (OSDI 16)* (Savannah, GA: USENIX Association), 265–283.

Anas, E. M. A., Seitel, A., Rasoulian, A., John, P. S., Pichora, D., Darras, K., et al. (2015). Bone enhancement in ultrasound using local spectrum variations for guiding percutaneous scaphoid fracture fixation procedures. *Int. J. Comput. Assist. Radiol. Surg.* 10, 959–969. doi: 10.1007/s11548-015-1181-6

Apostolopoulos, I. D., and Mpesiana, T. A. (2020). COVID-19: automatic detection from x-ray images utilizing transfer learning with convolutional neural networks. *Phys. Eng. Sci. Med.* 43, 635–640. doi: 10.1007/s13246-020-00865-4

Basile, V., Mauro, A. D., Scalini, E., Comes, P., Lofú, I., Mostert, M., et al. (2015). Lung ultrasound: a useful tool in diagnosis and management of bronchiolitis. *BMC Pediatr.* 15:63. doi: 10.1186/s12887-015-0380-1

Bauld, T. J., and Schwan, H. P. (1974). Attenuation and reflection of ultrasound in canine lung tissue. *J. Acoust. Soc. Am.* 56, 1630–1637. doi: 10.1121/1.1903488

Baum, Z. M. C., Bonmati, E., Cristoni, L., Walden, A., Prados, F., Kanber, B., et al. (2021). *Image Quality Assessment for Closed-Loop Computer-Assisted Lung Ultrasound*. Available online at: https://arxiv.org/abs/2008.08840. doi: 10.1117/12.2581865

Berce, V., Tomazin, M., Gorenjak, M., Berce, T., and Lovrenčič, B. (2019). The usefulness of lung ultrasound for the aetiological diagnosis of community-acquired pneumonia in children. *Sci. Rep.* 9:17957. doi: 10.1038/s41598-019-54499-y

Bian, C., Lee, R., Chou, Y., and Cheng, J. (2017). "Boundary regularized convolutional neural network for layer parsing of breast anatomy in automated whole breast ultrasound," in *Medical Image Computing and Computer Assisted Intervention - MICCAI 2017 - 20th International Conference*, eds M. Descoteaux, L. Maier-Hein, A. M. Franz, P. Jannin, D. L. Collins, and S. Duchesne (Quebec City, QC: Springer), 259-266. doi: 10.1007/978-3-319-66179-7_30

Bonadia, N., Carnicelli, A., Piano, A., Buonsenso, D., Gilardi, E., Kadhim, C., et al. (2020). Lung ultrasound findings are associated with mortality and need for intensive care admission in COVID-19 patients evaluated in the emergency department. *Ultrasound Med. Biol.* 46, 2927–2937. doi: 10.1016/j.ultrasmedbio.2020.07.005

Born, J., Wiedemann, N., Cossio, M., Buhre, C., Brändle, G., Leidermann, K., et al. (2021). Accelerating detection of lung pathologies with explainable ultrasound image analysis. *Appl. Sci.* 11:672. doi: 10.3390/app11020672

Bradley, J. S., Byington, C. L., Shah, S. S., Alverson, B., Carter, E. R., Harrison, C., et al. (2011). The management of community-acquired pneumonia in infants and children older than 3 months of age: clinical practice guidelines by the pediatric infectious diseases society and the infectious diseases society of America. *Clin. Infect. Dis.* 53, e25–e76. doi: 10.1093/cid/cir625

Bradski, G. (2000). *The OpenCV Library. Dr. Dobb's Journal of Software Tools*. Available online at: https://opencv.org/

Bressler, S. L. (1995). Large-scale cortical networks and cognition. *Brain Res. Rev.* 20, 288–304. doi: 10.1016/0165-0173(94)00016-I

Buitinck, L., Louppe, G., Blondel, M., Pedregosa, F., Mueller, A., Grisel, O., et al. (2013). "API design for machine learning software: experiences from the scikit-learn project," in *ECML PKDD Workshop: Languages for Data Mining and Machine Learning* (Prague), 108–122.

Buonsenso, D., Brancato, F., Valentini, P., Curatola, A., Supino, M., and Musolino, A. M. (2019a). The use of lung ultrasound to monitor the antibiotic response of community-acquired pneumonia in children: a preliminary hypothesis. *J. Ultrasound Med.* 39, 817–826. doi: 10.1002/jum.15147

Buonsenso, D., Musolino, A., Ferro, V., Rose, C. D., Morello, R., Ventola, C., et al. (2021). Role of lung ultrasound for the etiological diagnosis of acute lower respiratory tract infection (ALRTI) in children: a prospective study. *J. Ultrasound* 1–13. doi: 10.1007/s40477-021-00600-z

Buonsenso, D., Musolino, A. M., Gatto, A., Lazzareschi, I., Curatola, A., and Valentini, P. (2019b). Lung ultrasound in infants with bronchiolitis. *BMC Pulm. Med.* 19:159. doi: 10.1186/s12890-019-0925-4

Buonsenso, D., Pata, D., and Chiaretti, A. (2020a). COVID-19 outbreak: less stethoscope, more ultrasound. *Lancet Respir. Med.* 8:e27. doi: 10.1016/S2213-2600(20)30120-X

Buonsenso, D., Raffaelli, F., Tamburrini, E., Biasucci, D. G., Salvi, S., Smargiassi, A., et al. (2020b). Clinical role of lung ultrasound for diagnosis and monitoring of COVID-19 pneumonia in pregnant women. *Ultrasound Obstetr. Gynecol.* 56, 106–109. doi: 10.1002/uog.22055

Buonsenso, D., Rose, C. D., Morello, R., Lazzareschi, I., and Valentini, P. (2020c). Aspiration pneumonia in children with neurological disorders: a new indication for lung ultrasound? A case series. *J. Ultrasound*. doi: 10.1007/s40477-020-00520-4

Buonsenso, D., Soldati, G., Curatola, A., Morello, R., Rose, C. D., Vacca, M. E., et al. (2020d). Lung ultrasound pattern in healthy infants during the first 6 months of life. *J. Ultrasound Med.* 39, 2379–2388. doi: 10.1002/jum.15347

Buonsenso, D., Tomá, P., Scateni, S., Curatola, A., Morello, R., Valentini, P., et al. (2020e). Lung ultrasound findings in pediatric community-acquired pneumonia requiring surgical procedures: a two-center prospective study. *Pediatr. Radiol.* 50, 1560–1569. doi: 10.1007/s00247-020-04750-w

Carrer, L., Donini, E., Marinelli, D., Zanetti, M., Mento, F., Torri, E., et al. (2020). Automatic pleural line extraction and COVID-19 scoring from lung ultrasound data. *IEEE Trans. Ultrason. Ferroelectr. Frequency Control* 67, 2207–2217. doi: 10.1109/TUFFC.2020.3005512

Chandola, V., Banerjee, A., and Kumar, V. (2009). Anomaly detection. *ACM Comput. Surveys* 41, 1–58. doi: 10.1145/1541880.1541882

Choi, J., and Lee, G. L. (2012). Common pediatric respiratory emergencies. *Emerg. Med. Clin. N. Am.* 30, 529–563. doi: 10.1016/j.emc.2011.10.009

Chollet, F. (2015). *Keras*. Available online at: https://keras.io

Chollet, F. (2017). "Xception: deep learning with depthwise separable convolutions," in *Proceedings of the IEEE Conference on Computer Vision and Pattern Recognition* (Honolulu, HI), 1251–1258. doi: 10.1109/CVPR.2017.195

Collins, F. S., and Varmus, H. (2015). A new initiative on precision medicine. *N. Engl. J. Med.* 372, 793–795. doi: 10.1056/NEJMp1500523

Copetti, R., Soldati, G., and Copetti, P. (2008). Chest sonography: a useful tool to differentiate acute cardiogenic pulmonary edema from acute respiratory distress syndrome. *Cardiovasc. Ultrasound* 6:16. doi: 10.1186/1476-7120-6-16

Correa, M., Zimic, M., Barrientos, F., Barrientos, R., Román-Gonzalez, A., Pajuelo, M. J., et al. (2018). Automatic classification of pediatric pneumonia based on lung ultrasound pattern recognition. *PLoS ONE* 13:e206410. doi: 10.1371/journal.pone.0206410

Deng, J., Dong, W., Socher, R., Li, L.-J., Li, K., and Fei-Fei, L. (2009). "Imagenet: a large-scale hierarchical image database," in *2009 IEEE Conference on Computer Vision and Pattern Recognition* (Miami, FL), 248–255. doi: 10.1109/CVPR.2009.5206848

Di Mauro, D., Ammirabile, A., Quercia, M., Panza, R., Capozza, M., Manzionna, M. M., et al. (2019). Acute bronchiolitis: Is there a role for lung ultrasound? *Diagnostics* 9:172. doi: 10.3390/diagnostics9040172

Doran, D., Schulz, S., and Besold, T. R. (2017). *What Does Explainable AI Really Mean? A New Conceptualization of Perspectives*. Available online at: arxiv.org/abs/1710.00794

Dunn, F. (1974). Attenuation and speed of ultrasound in lung. *J. Acoust. Soc. Am.* 56, 1638–1639. doi: 10.1121/1.1903489

Dunn, F. (1986). Attenuation and speed of ultrasound in lung: dependence upon frequency and inflation. *J. Acoust. Soc. Am.* 80, 1248–1250. doi: 10.1121/1.393818

Dunn, F., and Fry, W. J. (1961). Ultrasonic absorption and reflection by lung tissue. *Phys. Med. Biol.* 5, 401–410. doi: 10.1088/0031-9155/5/4/302

Esteva, A., Robicquet, A., Ramsundar, B., Kuleshov, V., DePristo, M., Chou, K., et al. (2019). A guide to deep learning in healthcare. *Nat. Med.* 25, 24–29. doi: 10.1038/s41591-018-0316-z

Gargani, L., Frassi, F., Soldati, G., Tesorio, P., Gheorghiade, M., and Picano, E. (2008). Ultrasound lung comets for the differential diagnosis of acute cardiogenic dyspnoea: a comparison with natriuretic peptides. *Eur. J. Heart Fail.* 10, 70–77. doi: 10.1016/j.ejheart.2007.10.009

Ghesu, F. C., Krubasik, E., Georgescu, B., Singh, V., Zheng, Y., Hornegger, J., et al. (2016). Marginal space deep learning: efficient architecture for volumetric image parsing. *IEEE Trans. Med. Imag.* 35, 1217–1228. doi: 10.1109/TMI.2016.2538802

Greenspan, H., van Ginneken, B., and Summers, R. M. (2016). Guest editorial deep learning in medical imaging: overview and future promise of an exciting new technique. *IEEE Trans. Med. Imag.* 35, 1153–1159. doi: 10.1109/TMI.2016.2553401

Harris, M., Clark, J., Coote, N., Fletcher, P., Harnden, A., McKean, M., et al. (2011). British thoracic society guidelines for the management of community acquired pneumonia in children: update 2011. *Thorax* 66(Suppl. 2), ii1–ii23. doi: 10.1136/thoraxjnl-2011-200598

Hiramatsu, Y., Muramatsu, C., Kobayashi, H., Hara, T., and Fujita, H. (2017). "Automated detection of masses on whole breast volume ultrasound scanner: false positive reduction using deep convolutional neural network," in *Medical Imaging 2017: Computer-Aided Diagnosis, Vol. 10134*, eds S. G. Armato III and N. A. Petrick (Orlando, FL: International Society for Optics and Photonics), 717–722. doi: 10.1117/12.2254581

Holzinger, A., Biemann, C., Pattichis, C. S., and Kell, D. B. (2017). *What Do We Need to Build Explainable AI Systems for the Medical Domain?* Available online at: https://arxiv.org/abs/1712.09923

Hutter, F., Kotthoff, L., and Vanschoren, J., (eds.). (2019). *Automated Machine Learning*. Cham: Springer International Publishing. doi: 10.1007/978-3-030-05318-5

Inchingolo, R., Smargiassi, A., Moro, F., Buonsenso, D., Salvi, S., Giacomo, P. D., et al. (2020). The diagnosis of pneumonia in a pregnant woman with coronavirus disease 2019 using maternal lung ultrasound. *Am. J. Obstetr. Gynecol.* 223, 9–11. doi: 10.1016/j.ajog.2020.04.020

Jambrik, Z., Monti, S., Coppola, V., Agricola, E., Mottola, G., Miniati, M., et al. (2004). Usefulness of ultrasound lung comets as a nonradiologic sign of extravascular lung water. *Am. J. Cardiol.* 93, 1265–1270. doi: 10.1016/j.amjcard.2004.02.012

Ker, J., Wang, L., Rao, J., and Lim, T. (2018). Deep learning applications in medical image analysis. *IEEE Access* 6, 9375–9389. doi: 10.1109/ACCESS.2017.2788044

Kessler, D., Ng, L., Tessaro, M., and Fischer, J. (2017). Precision medicine with point-of-care ultrasound. *Pediatr. Emerg. Care* 33, 206–209. doi: 10.1097/PEC.0000000000001050

Kulhare, S., Zheng, X., Mehanian, C., Gregory, C., Zhu, M., Gregory, K., et al. (2018). "Ultrasound-based detection of lung abnormalities using single shot detection convolutional neural networks," in *Simulation, Image Processing, and Ultrasound Systems for Assisted Diagnosis and Navigation* (Cham: Springer Verlag), 65–73. doi: 10.1007/978-3-030-01045-4_8

LeCun, Y., Bengio, Y., and Hinton, G. (2015). Deep learning. *Nature* 521, 436–444. doi: 10.1038/nature14539

Liang, G., and Zheng, L. (2020). A transfer learning method with deep residual network for pediatric pneumonia diagnosis. *Comput. Methods Prog. Biomed.* 187:104964. doi: 10.1016/j.cmpb.2019.06.023

Lichtenstein, D., Méziére, G., Biderman, P., Gepner, A., and Barré, O. (1997). The comet-tail artifact. *Am. J. Respir. Crit. Care Med.* 156, 1640–1646. doi: 10.1164/ajrccm.156.5.96-07096

Lichtenstein, D., Méziére, G., and Seitz, J. (2009). The dynamic air bronchogram. *Chest* 135, 1421–1425. doi: 10.1378/chest.08-2281

Lieveld, A. W., Kok, B., Schuit, F. H., Azijli, K., Heijmans, J., van Laarhoven, A., et al. (2020). Diagnosing COVID-19 pneumonia in a pandemic setting: lung ultrasound versus CT (LUVCT) –a multicentre, prospective, observational study. *ERJ Open Res.* 6, 539–2020. doi: 10.1183/23120541.00539-2020

Litjens, G., Kooi, T., Bejnordi, B. E., Setio, A. A. A., Ciompi, F., Ghafoorian, M., et al. (2017). A survey on deep learning in medical image analysis. *Med. Image Anal.* 42, 60–88. doi: 10.1016/j.media.2017.07.005

Liu, L., Oza, S., Hogan, D., Perin, J., Rudan, I., Lawn, J. E., et al. (2015). Global, regional, and national causes of child mortality in 2000–13, with projections to inform post-2015 priorities: an updated systematic analysis. *Lancet* 385, 430–440. doi: 10.1016/S0140-6736(14)61698-6

Liu, S., Wang, Y., Yang, X., Lei, B., Liu, L., Li, S. X., et al. (2019). Deep learning in medical ultrasound analysis: a review. *Engineering* 5, 261–275. doi: 10.1016/j.eng.2018.11.020

Ma, J., Wu, F., Jiang, T., Zhu, J., and Kong, D. (2017). Cascade convolutional neural networks for automatic detection of thyroid nodules in ultrasound images. *Med. Phys.* 44, 1678–1691. doi: 10.1002/mp.12134

McBee, M. P., Awan, O. A., Colucci, A. T., Ghobadi, C. W., Kadom, N., Kansagra, A. P., et al. (2018). Deep learning in radiology. *Acad. Radiol.* 25, 1472–1480. doi: 10.1016/j.acra.2018.02.018

McDermott, C., Łącki, M., Sainsbury, B., Henry, J., Filippov, M., and Rossa, C. (2021). Sonographic diagnosis of COVID-19: A review of image processing for lung ultrasound. *Front. Big Data* 4:612561. doi: 10.3389/fdata.2021.612561

Mikhak, Z., and Pedersen, P. C. (2002). Acoustic attenuation properties of the lung: an open question. *Ultrasound Med. Biol.* 28, 1209–1216. doi: 10.1016/S0301-5629(02)00561-6

Milletari, F., Ahmadi, S.-A., Kroll, C., Hennersperger, C., Tombari, F., Shah, A., et al. (2015). "Robust segmentation of various anatomies in 3d ultrasound using hough forests and learned data representations," in *Medical Image Computing and Computer-Assisted Intervention-MICCAI 2015*, eds N. Navab, J. Hornegger, W. M. Wells, and A. Frangi (Cham: Springer International Publishing), 111–118. doi: 10.1007/978-3-319-24571-3_14

Muse, E. D., and Topol, E. J. (2020). Guiding ultrasound image capture with artificial intelligence. *Lancet* 396:749, doi: 10.1016/S0140-6736(20)31875-4

Musolino, A. M., Supino, M. C., Buonsenso, D., Papa, R. E., Chiurchiú, S., Magistrelli, A., et al. (2021). Lung ultrasound in the diagnosis and monitoring of 30 children with coronavirus disease 2019. *Pediatr. Pulmonol.* 56, 1045–1052. doi: 10.1002/ppul.25255

Musolino, A. M., Tomá, P., Supino, M. C., Scialanga, B., Mesturino, A., Scateni, S., et al. (2019). Lung ultrasound features of children with complicated and noncomplicated community acquired pneumonia: a prospective study. *Pediatr. Pulmonol.* 54, 1479–1486. doi: 10.1002/ppul.24426

Najgrodzka, P., Buda, N., Zamojska, A., Marciniewicz, E., and Lewandowicz-Uszyńska, A. (2019). Lung ultrasonography in the diagnosis of pneumonia in children—a metaanalysis and a review of pediatric lung imaging. *Ultrasound Q.* 35, 157–163. doi: 10.1097/RUQ.0000000000000411

Narin, A., Kaya, C., and Pamuk, Z. (2021). Automatic detection of coronavirus disease (COVID-19) using x-ray images and deep convolutional neural networks. *Pattern Anal. Appl.* 24, 1207–1220. doi: 10.1007/s10044-021-00984-y

Nokia Corp. (2012). *QT: Cross-Platform Application and UI Framework*. Nokia Corp. Available online at: http://qt.nokia.com/

Øymar, K., Skjerven, H. O., and Mikalsen, I. B. (2014). Acute bronchiolitis in infants, a review. *Scand. J. Trauma Resuscit. Emerg. Med.* 22:23. doi: 10.1186/1757-7241-22-23

Ozturk, T., Talo, M., Yildirim, E. A., Baloglu, U. B., Yildirim, O., and Rajendra Acharya, U. (2020). Automated detection of covid-19 cases using deep neural networks with x-ray images. *Comput. Biol. Med.* 121:103792. doi: 10.1016/j.compbiomed.2020.103792

Pare, J., Camelo, I., Mayo, K., Leo, M., Dugas, J., Nelson, K., et al. (2020). Point-of-care lung ultrasound is more sensitive than chest radiograph for evaluation of COVID-19. *West. J. Emerg. Med.* 21, 771–778. doi: 10.5811/westjem.2020.5.47743

Pata, D., Valentini, P., Rose, C. D., Santis, R. D., Morello, R., and Buonsenso, D. (2020). Chest computed tomography and lung ultrasound findings in COVID-19 pneumonia: a pocket review for non-radiologists. *Front. Med.* 7:375. doi: 10.3389/fmed.2020.00375

Pedersen, P. C., and Ozcan, H. S. (1986). Ultrasound properties of lung tissue and their measurements. *Ultrasound Med. Biol.* 12, 483–499. doi: 10.1016/0301-5629(86)90220-6

Pereira, F., Bueno, A., Rodriguez, A., Perrin, D., Marx, G., Cardinale, M., et al. (2017). Automated detection of coarctation of aorta in neonates from two-dimensional echocardiograms. *J. Med. Imag.* 4:014502. doi: 10.1117/1.JMI.4.1.014502

Perez, L., and Wang, J. (2017). *The Effectiveness of Data Augmentation 1in Image Classification Using Deep Learning*. Available online at: https://arxiv.org/abs/1712.04621

Poplin, R., Varadarajan, A. V., Blumer, K., Liu, Y., McConnell, M. V., Corrado, G. S., et al. (2018). Prediction of cardiovascular risk factors from retinal fundus photographs via deep learning. *Nat. Biomed. Eng.* 2, 158–164. doi: 10.1038/s41551-018-0195-0

Ralston, S. L., Lieberthal, A. S., Meissner, H. C., Alverson, B. K., Baley, J. E., Gadomski, A. M., et al. (2014). Clinical practice guideline: the diagnosis,

management, and prevention of bronchiolitis. *Pediatrics* 134, e1474–e1502. doi: 10.1542/peds.2014-2742

Reißig, A., and Kroegel, C. (2003). Transthoracic sonography of diffuse parenchymal lung disease. *J. Ultrasound Med.* 22, 173–180. doi: 10.7863/jum.2003.22.2.173

Roberts, J., and Tsiligkaridis, T. (2020). *Ultrasound Diagnosis of COVID-19: Robustness and Explainability*. Available online at: https://arxiv.org/abs/2012.01145

Rose, C. D., Inchingolo, R., Smargiassi, A., Zampino, G., Valentini, P., and Buonsenso, D. (2020). How to perform pediatric lung ultrasound examinations in the time of COVID -19. *J. Ultrasound Med.* 39, 2081–2082. doi: 10.1002/jum.15306

Rosenfield, D., Kwan, C., and Fischer, J. (2015). Point-of-care ultrasound: an emerging technology in canadian paediatrics. *Paediatr. Child Health* 20, 67–68. doi: 10.1093/pch/20.2.67

Ruff, L., Vandermeulen, R., Goernitz, N., Deecke, L., Siddiqui, S. A., Binder, A., et al. (2018). "Deep one-class classification," in *Proceedings of the 35th International Conference on Machine Learning, Vol. 80* (Stockholm), eds J. Dy and A. Krause, 4393–4402.

Saraiva., A., Ferreira., N., Lopes de Sousa., L., Costa., N., Sousa., J., Santos., D., et al. (2019). "Classification of images of childhood pneumonia using convolutional neural networks," in *Proceedings of the 12th International Joint Conference on Biomedical Engineering Systems and Technologies, Vol. 2* (Prague: SciTePress), 112–119. doi: 10.5220/0007404301120119

Schlegl, T., Seeböck, P., Waldstein, S. M., Langs, G., and Schmidt-Erfurth, U. (2019). f-AnoGAN: fast unsupervised anomaly detection with generative adversarial networks. *Med. Image Anal.* 54, 30–44. doi: 10.1016/j.media.2019.01.010

Seattle Children's Hospital (2011). *Criteria and Respiratory Score*. Available online at: http://www.tecpedu.net/uploads/1/4/9/1/14912848/bronchiolitis_algorithm_1_1.pdf (accessed September 30, 2018).

Selvaraju, R. R., Cogswell, M., Das, A., Vedantam, R., Parikh, D., and Batra, D. (2017). "Grad-cam: visual explanations from deep networks via gradient-based localization," in *Proceedings of the IEEE International Conference on Computer Vision (ICCV)* (Venice), 618–626. doi: 10.1109/ICCV.2017.74

Shah, S. N., Bachur, R. G., Simel, D. L., and Neuman, M. I. (2017). Does this child have pneumonia?: the rational clinical examination systematic review. *JAMA* 318, 462–471. doi: 10.1001/jama.2017.9039

Shen, D., Wu, G., and Suk, H.-I. (2017). Deep learning in medical image analysis. *Annu. Rev. Biomed. Eng.* 19, 221–248. doi: 10.1146/annurev-bioeng-071516-044442

Simonyan, K., and Zisserman, A. (2015). "Very deep convolutional networks for large-scale image recognition," in *3rd International Conference on Learning Representations, ICLR 2015*, eds Y. Bengio and Y. LeCun (San Diego, CA).

Smith, M. J., Hayward, S. A., Innes, S. M., and Miller, A. S. C. (2020). Point-of-care lung ultrasound in patients with COVID-19—a narrative review. *Anaesthesia* 75, 1096–1104. doi: 10.1111/anae.15082

Soldati, G., Demi, M., Inchingolo, R., Smargiassi, A., and Demi, L. (2016). On the physical basis of pulmonary sonographic interstitial syndrome. *J. Ultrasound Med.* 35, 2075–2086. doi: 10.7863/ultra.15.08023

Soldati, G., Demi, M., Smargiassi, A., Inchingolo, R., and Demi, L. (2019). The role of ultrasound lung artifacts in the diagnosis of respiratory diseases. *Expert Rev. Respir. Med.* 13, 163–172. doi: 10.1080/17476348.2019.1565997

Soldati, G., Smargiassi, A., Inchingolo, R., Buonsenso, D., Perrone, T., Briganti, D. F., et al. (2020). Proposal for international standardization of the use of lung ultrasound for patients with COVID-19. *J. Ultrasound Med.* 39, 1413–1419. doi: 10.1002/jum.15285

Soldati, G., Testa, A., Silva, F. R., Carbone, L., Portale, G., and Silveri, N. G. (2006). Chest ultrasonography in lung contusion. *Chest* 130, 533–538. doi: 10.1378/chest.130.2.533

Sombune, P., Phienphanich, P., Phuechpanpaisal, S., Muengtaweepongsa, S., Ruamthanthong, A., and Tantibundhit, C. (2017). "Automated embolic signal detection using deep convolutional neural network," in *2017 39th Annual International Conference of the IEEE Engineering in Medicine and Biology Society (EMBC)* (Jeju Island), 3365–3368. doi: 10.1109/EMBC.2017.8037577

Subcommittee on Diagnosis and Management of Bronchiolitis (2006). Diagnosis and management of bronchiolitis. *Pediatrics* 118, 1774–1793. doi: 10.1542/peds.2006-2223

Supino, M. C., Buonsenso, D., Scateni, S., Scialanga, B., Mesturino, M. A., Bock, C., et al. (2019). Point-of-care lung ultrasound in infants with bronchiolitis in the pediatric emergency department: a prospective study. *Eur. J. Pediatr.* 178, 623–632. doi: 10.1007/s00431-019-03335-6

Sutskever, I., Martens, J., Dahl, G., and Hinton, G. (2013). "On the importance of initialization and momentum in deep learning," in *Proceedings of the 30th International Conference on Machine Learning, Vol. 28*, eds S. Dasgupta and D. McAllester (Atlanta, GA), 1139–1147.

Szegedy, C., Ioffe, S., Vanhoucke, V., and Alemi, A. A. (2017). "Inception-v4, inception-resnet and the impact of residual connections on learning," in *Proceedings of the Thirty-First AAAI Conference on Artificial Intelligence, AAAI'17* (San Francisco, CA: AAAI Press), 4278–4284.

Szegedy, C., Vanhoucke, V., Ioffe, S., Shlens, J., and Wojna, Z. (2016). "Rethinking the inception architecture for computer vision," in *Proceedings of the IEEE Conference on Computer Vision and Pattern Recognition (CVPR)* (Las Vegas, NV). doi: 10.1109/CVPR.2016.308

Taccari, F. and Buonsenso, D. (2020). COVID-19 and lung ultrasound: reflections on the "light beam." *J. Ultrasound Med.* 40, 1037–1038. doi: 10.1002/jum.15468

Taveira, M., Yousef, N., Miatello, J., Roy, C., Claude, C., Boutillier, B., et al. (2018). Un score échographique pulmonaire simple peut-il prédire la durée de ventilation des nourrissons atteints de bronchiolite aigusévére? *Arch. Pédiatr.* 25, 112–117. doi: 10.1016/j.arcped.2017.11.005

Tung-Chen, Y., de Gracia, M. M., Dìez-Tascón, A., Alonso-González, R., Agudo-Fernández, S., Parra-Gordo, M. L., et al. (2020). Correlation between chest computed tomography and lung ultrasonography in patients with coronavirus disease 2019 (COVID-19). *Ultrasound Med. Biol.* 46, 2918–2926. doi: 10.1016/j.ultrasmedbio.2020.07.003

van Sloun, R. J. G., and Demi, L. (2020). Localizing b-lines in lung ultrasonography by weakly supervised deep learning, *in-vivo* results. *IEEE J. Biomed. Health Inform.* 24, 957–964. doi: 10.1109/JBHI.2019.2936151

Volpicelli, G., Elbarbary, M., Blaivas, M., Lichtenstein, D. A., Mathis, G., Kirkpatrick, A. W., et al. (2012). International evidence-based recommendations for point-of-care lung ultrasound. *Intens. Care Med.* 38, 577–591. doi: 10.1007/s00134-012-2513-4

Volpicelli, G., Gargani, L., Perlini, S., Spinelli, S., Barbieri, G., Lanotte, A., et al. (2021). Lung ultrasound for the early diagnosis of COVID-19 pneumonia: an international multicenter study. *Intens. Care Med.* 47, 444–454. doi: 10.1007/s00134-021-06373-7

Volpicelli, G., Lamorte, A., and Villén, T. (2020). What's new in lung ultrasound during the COVID-19 pandemic. *Intens. Care Med.* 46, 1445–1448. doi: 10.1007/s00134-020-06048-9

Volpicelli, G., Mussa, A., Garofalo, G., Cardinale, L., Casoli, G., Perotto, F., et al. (2006). Bedside lung ultrasound in the assessment of alveolar-interstitial syndrome. *Am. J. Emerg. Med.* 24, 689–696. doi: 10.1016/j.ajem.2006.02.013

Voulodimos, A., Doulamis, N., Doulamis, A., and Protopapadakis, E. (2018). Deep learning for computer vision: a brief review. *Comput. Intell. Neurosci.* 2018:7068349. doi: 10.1155/2018/7068349

Wang, L., Lin, Z. Q., and Wong, A. (2020). COVID-net: a tailored deep convolutional neural network design for detection of COVID-19 cases from chest x-ray images. *Sci. Rep.* 10:19549. doi: 10.1038/s41598-020-76550-z

Wang, M., Liu, B., and Foroosh, H. (2017). "Factorized convolutional neural networks," in *2017 IEEE International Conference on Computer Vision Workshops (ICCVW)* (Venice). doi: 10.1109/ICCVW.2017.71

Wang, X., Burzynski, J. S., Hamilton, J., Rao, P. S., Weitzel, W. F., and Bull, J. L. (2019). Quantifying lung ultrasound comets with a convolutional neural network: Initial clinical results.

Comput. Biol. Med. 107, 39–46. doi: 10.1016/j.compbiomed.2019.02.002

World Health Organization (2014). *Revised WHO Classification and Treatment of Pneumonia in Children at Health Facilities: Evidence Summaries*. Geneva: World Health Organization.

Yaqub, M., Kelly, B., Papageorghiou, A. T., and Noble, J. A. (2017). A deep learning solution for automatic fetal neurosonographic diagnostic plane verification using clinical standard constraints. *Ultrasound Med. Biol.* 43, 2925–2933. doi: 10.1016/j.ultrasmedbio.2017.07.013

Conflict of Interest: The authors declare that the research was conducted in the absence of any commercial or financial relationships that could be construed as a potential conflict of interest.

Publisher's Note: All claims expressed in this article are solely those of the authors and do not necessarily represent those of their affiliated organizations, or those of the publisher, the editors and the reviewers. Any product that may be evaluated in this article, or claim that may be made by its manufacturer, is not guaranteed or endorsed by the publisher.

frontiers in Physiology

ORIGINAL RESEARCH
published: 09 September 2021
doi: 10.3389/fphys.2021.728243

A Pilot Study on Electrical Impedance Tomography During CPAP Trial in Patients With Severe Acute Respiratory Syndrome Coronavirus 2 Pneumonia: The Bright Side of Non-invasive Ventilation

Michela Rauseo, Lucia Mirabella, Donato Laforgia, Angela Lamanna, Paolo Vetuschi, Elisa Soriano, Daniele Ugliola, Elena Casiello, Livio Tullo and Gilda Cinnella*

Department of Anesthesia and Intensive Care, University of Foggia, Foggia, Italy

OPEN ACCESS

Edited by:
Paolo Pelosi, University of Genoa, Italy

Reviewed by:
Carmen Silvia Valente Barbas, University of São Paulo, Brazil
Marie-Cécile Niérat, INSERM U1158 Neurophysiologie Respiratoire Expérimentale et Clinique, France
Thomas Poulard, Neuromuscular Physiology and Evaluation Laboratory, Neuromuscular Investigation Center, Institute of Myology, France contributed to the reviewer M-CN
Cesare Gregoretti, Azienda Ospedaliera Universitaria Policlinico Paolo Giaccone, Italy

***Correspondence:**
Michela Rauseo
michela.rauseo@unifg.it

Specialty section:
This article was submitted to Respiratory Physiology, a section of the journal Frontiers in Physiology

Received: *21 June 2021*
Accepted: *17 August 2021*
Published: *09 September 2021*

Citation:
Rauseo M, Mirabella L, Laforgia D, Lamanna A, Vetuschi P, Soriano E, Ugliola D, Casiello E, Tullo L and Cinnella G (2021) A Pilot Study on Electrical Impedance Tomography During CPAP Trial in Patients With Severe Acute Respiratory Syndrome Coronavirus 2 Pneumonia: The Bright Side of Non-invasive Ventilation. Front. Physiol. 12:728243. doi: 10.3389/fphys.2021.728243

Background: Different severe acute respiratory syndrome coronavirus 2 (SARS-CoV-2) pneumonia phenotypes were described that match with different lung compliance and level of oxygenation, thus requiring a personalized ventilator setting. The burden of so many patients and the lack of intensive care unit (ICU) beds often force physicians to choose non-invasive ventilation (NIV) as the first approach, even if no consent has still been reached to discriminate whether it is safer to choose straightforward intubation, paralysis, and protective ventilation. Under such conditions, electrical impedance tomography (EIT), a non-invasive bedside tool to monitor lung ventilation and perfusion defects, could be useful to assess the response of patients to NIV and choose rapidly the right ventilatory strategy.

Objective: The rationale behind this study is that derecruitment is a more efficient measure of positive end expiratory pressure (PEEP)-dependency of patients than recruitment. We hypothesized that patients who derecruit significantly when PEEP is reduced are the ones that do not need early intubation while small end-expiratory lung volume (ΔEELV) variations after a single step of PEEP de-escalation could be predictive of NIV failure.

Materials and Methods: Consecutive patients admitted to ICU with confirmed SARS-CoV-2 pneumonia ventilated in NIV were enrolled. Exclusion criteria were former intubation or NIV lasting $>$ 72 h. A trial of continuos positive airway pressure (CPAP) 12 was applied in every patient for at least 15 min, followed by the second period of CPAP 6, either in the supine or prone position. Besides standard monitoring, ventilation of patients was assessed by EIT, and end-expiratory lung impedance (ΔEELI) (%) was calculated as the difference in EELI between $CPAP_{12}$ and $CPAP_6$. Tidal volume (Vt), Ve, respiratory rate (RR), and FiO_2 were recorded, and ABGs were measured. Data were analyzed offline using the dedicated software. The decision to intubate or continue NIV was in charge of treating physicians, independently from study results. Outcomes of patients in terms of intubation rate and ICU mortality were recorded.

Results: We enrolled 10 male patients, with a mean age of 67 years. Six patients (60%) were successfully treated by NIV until ICU discharge (Group S), and four patients failed NIV and were intubated and switched to MV (Group F). All these patients died in ICU. During the supine CPAP decremental trial, all patients experienced an increase in RR and Ve. ΔEELI was < 40% in Group F and > 50% in Group S. In the prone trial, ΔEELI was > 50% in all patients, while RR decreased in Group S and remained unchanged in Group F.

Conclusion: ΔEELI < 40% after a single PEEP de-escalation step in supine position seems to be a good predictor of poor recruitment and CPAP failure.

Keywords: SARS-CoV-2, electrical impedance tomography, awake prone positioning, CPAP, non-invasive ventilation

INTRODUCTION

At present time, more than 1 year since the severe acute respiratory syndrome coronavirus 2 (SARS-CoV-2) pandemic broke out, its physiopathology and clinical course are much better understood. However, to speak with Sir W. Churchill, "the best is not good enough," since many key points of this threatening disease are still far from being fully elucidated, notably as regards therapeutic options, while the number of cases that require respiratory support is far from being subsided. Hence, clinicians all over the world still have to face the impossibility to guarantee tracheal intubation for everyone (Grasselli et al., 2020), and non-invasive respiratory support becomes sometimes an obliged choice. Presently, an increasing amount of studies are reporting successful treatment of SARS-CoV-2 pneumonia in non-intubated patients, ventilated with moderate to high level of positive airways pressure (PEEP/CPAP) (8–12 cmH_2O) and cycles of awake proning (Bamford et al., 2020; Whang et al., 2021). Accurate selection of patients, appropriate PEEP/CPAP setting, and correct timing for switching to invasive mechanical ventilation in non-responders to the non-invasive approach are thus of paramount importance and still remain among the most debated topics in the intensive care unit (ICU) environment and more (Lee et al., 2021; Tseng et al., 2021).

Hypoxemia severity and oxygenation response to PEEP/CPAP application are weak indexes of lung recruitability (Dantzker, 1982; Chen et al., 2020), and this is even more evident in SARS-CoV-2 pneumonia, since patients with a same degree of severity of arterial desaturation may present with different clinical phenotypes, ranging from normal respiratory rate (RR) to marked dyspnea and near normal to decreased respiratory system compliance (Crs), where compliance is a measure of the lung expandability. It refers to the ability of the lung to stretch and expand (Gattinoni et al., 2020a,b,c). In fact, the most challenging patients are the ones that under non-invasive ventilation keep normal $PaCO_2$, RR, and adequate minute ventilation (12–14 l/min) (He et al., 2019), with preserved lung mechanics, in whom PaO_2/FiO_2 do not respond to the application of increasing PEEP levels. These patients are at high risk for developing self-inflicted lung injury (PSILI) (Brochard et al., 2017; Grieco et al., 2019; Yoshida et al., 2020) and require intubation as early as possible. Assessing if a patient is recruiter or not can thus guide the decision to keep non-invasive ventilation or intubate. A recruiter can be defined as a patient who responds to PEEP in terms of better oxygenation, hemodynamic stability, improvement of respiratory compliance, and lung mechanics. However, lung recruitability is uneasy to measure at the bedside and even more difficult in non-intubated patients. Recently, Chen et al. (2020) proposed a single-breath bedside method to measure lung recruitment by using the so-called compliance of the recruited lung: the ratio between the loss in end-expiratory lung volume (ΔEELV) after a reduction of PEEP, and driving pressure (DP) itself. However, this R/I index can be used only in sedated and mechanically ventilated patients. We hypothesized that the same physiological principle could be applied to patients under non-invasive ventilation with PEEP/CPAP, to screen the ones that are PEEP-dependent: after a drop in PEEP/CPAP, a reduction in EELV, and thus an increase in ΔEELV, should indicate that lung maintains a good elasticity and is able to deform. These lungs are affected by the pressure change and respond to the PEEP, so the clinician should insist with CPAP maximized at 12 cmH_2O (He et al., 2019). In contrast, a stable EELV, and thus a small ΔEELV, with no changes in other parameters such as RR or Ve, would indicate that patients have an airway opening pressure (AOP) > 12 cmH_2O (Chen et al., 2018) and thus PEEP must be increased over 12 cmH_2O to reach alveoli, or that lungs are already stiff and fibrotic. These patients should be better rapidly switched to invasive mechanical ventilation. Thus, a delay in understanding this process, in a patient with spontaneous breathing, may worsen PSILI or may delay intubation and reduce the chances for survival. Under this hypothesis, ΔEELV could be a predictor of CPAP failure and the need for switching to invasive mechanical ventilation.

Electrical impedance tomography (EIT) is a non-invasive and easy to use bedside tool that dynamically shows regional tidal volume (Vt) distribution. EIT has been demonstrated a

Abbreviations: ΔEELI, Variation of End Expiratory Lung Impedence; ΔEELV, variation of End expiratory Lung Volume; GI, Global Impedence; ROI, Region of Interest; NIV, Non Invasive ventilation; MV, Mechanical Ventilation; RR, Respiratory Rate; Ve, Minute ventilation; Vt, Tidal Volume; PSILI, Patient Self Inflicted Lung Injury; R/I, Recruitment to Inflaction Ratio; AOP, Airway Opening Pressure; DP, Driving Pressure; BP, Blood Pressure; HR, Heart rate; ABG, Aterial Blood Gas Analysis ; Crs, Respiratory system compliance; Cs, Static Compliance ; V/Q, Ventilation/Perfusion ratio.

valid instrument to assess regional ventilation and PEEP-induced recruitment in many experimental and clinical studies (Cinnella et al., 2015; Sosio et al., 2019). However, to our knowledge, no data are available on the use of EIT to monitor lung recruitability under non-invasive ventilation in patients with COVID-19.

Thus, we launched the present observational pilot study in patients admitted in ICU with SARS-CoV-2 pneumonia treated by non-invasive ventilation with PEEP/CPAP and cycles of the prone position. This study was aimed at (a) estimating PEEP-dependency at the bedside by using EIT to measure ΔEELV by end-expiratory lung impedance variations (ΔEELI) after a drop in PEEP; (b) evaluating the relationship between PEEP-dependency and outcome of patients, in terms of intubation and survival rate; (c) assessing if EIT may be useful to identify responders to the prone position, by continuously monitoring the ventilation redistribution following changes of the position.

MATERIALS AND METHODS

Patients

After Ethics Committee approval and written informed consent, all consecutive patients with COVID-19 admitted to our academic hospital ICU from March 2021 to April 2021 were enrolled. Inclusion criteria were as follows: admission from the emergency room within 24 h from symptoms onset, non-invasive mechanical ventilation for clinical decision, age $\geq$ 18 years, and confirmed SARS-CoV-2 infection from a respiratory tract sample by PCR-based tests. Exclusion criteria were as follows: prior admission to the ward, prior intubation, hemodynamic instability, defined as systolic blood pressure (BP) $<$ 90 mmHg or mean BP $<$ 60 mmHg, contraindication to EIT use (presence of pacemaker), impossibility to correctly place EIT belt, and refusal to participate in this study.

Patients underwent standard monitoring: ECG, heart rate (HR), RR, FiO_2, SaO_2, and urinary output. The radial artery was cannulated, and the catheter connected to the pressure transducer of the MostCare monitor (MostCareup, Vigon, Italy) and/or the IntelliVue Philips X3 monitor (Philips Medizin Systeme Böblingen GmbH, Böblingen Germany).

Intravascular pressure measurements were adjusted to zero at atmospheric pressure and leveled to the mid-axillary line. Analysis of arterial blood gases was performed (GEM Premier 4000, Werfen, United Kingdom).

All patients were ventilated using a Respironics V60 Ventilator (Philips N.V., Netherlands) in CPAP mode and connected to a full-face mask (Respironics FitLife, Philips) as the interface. Vt, RR, and minute ventilation (Ve) were measured from the ventilator.

Electrical impedance tomography is a non-invasive imaging technique that gives you a special view of inside the lungs. In a cross-sectional projection, the distribution of the tidal volume in the thorax is shown. The derived image shows ventilated and non-ventilated areas of the lungs and their changes as a function of time.

The EIT (PulmoVista 500, Draeger Medical GmbH, Germany) was applied as follows: a rubber belt containing 16 electrodes was placed around the chest between the fourth and fifth intercostal space and connected to the EIT monitor (Draeger/GoeMFII EIT Evaluation Kit 2, Draeger Medical GmbH). The correct position and signal quality were assessed on the monitor screen as described (Cinnella et al., 2015). At every study step, the EIT images were divided into four quadrants, to obtain two ventral and two dorsal regions of interest (ROIs), as already described (Cinnella et al., 2015; Sosio et al., 2019). Real-time impedance curves represent ventilation over time. Changes in the overall cross-section are reflected by the global impedance curve. This curve strongly correlates with the volume curve of the ventilator and with the applied/inhaled total volume. The regional impedance changes (i.e., tidal variations) serve to compare different lung regions. The numerical values indicate the volume distribution, which together adds up to 100% of the global value unless the overall window size (ROI setting) is changed.

Data Analysis

The operator was always the same. We recorded EELI according to a validated method (Sosio et al., 2019). Later, the patient was connected to a V60 Philips Respirator, and the recordings were taken in the four study steps (**Figure 1**).

The Dräger (SW EITdiag V1.6 (Draeger Lübeck, Germany), is a dedicated software tool for advanced PC-based analysis of EIT data files that have been previously recorded with PulmoVista 500 or other devices applying the technique of electrical impedance tomography. EITdiag reconstructs EIT images and uses various previously published approaches for data interpretation with respect to regional and temporal inhomogeneity of the lung function (Lowhagen et al., 2010).

An offline analysis was performed with the EITdiag software on impedance data to calculate global lung impedance and ΔEELI. The end-inspiratory trend view is used to compare two different tidal images and their regional tidal volume distribution. It helps to identify inhomogeneities, recruitment, derecruitment, overdistension, and the redistribution of Vt when changing the PEEP setting on the ventilator.

Recorded data included demographics [age, gender, and body mass index (BMI)], comorbidities, previous pharmacological treatments, disease chronology [time from onset of symptoms and from hospital admission to initiation of respiratory support, and ICU length of stay (LOS)], symptoms at ICU admission, vital signs [temperature, mean arterial pressure (MAP), and heart rate], laboratory parameters (blood test, coagulation, and biochemical), non-respiratory sequential organ failure assessment (non-respiratory SOFA) and APACHE II scores, and outcome in ICU and hospital.

Interventions

A physician not involved in this study was responsible for the care of patients. All patients were awake and mildly sedated with dexmedetomidine 0.3–1.2 mcg/kg/h. A standardized protocol for hemodynamic management was applied to ensure fluid volume optimization, as already described (Cinnella et al., 2015).

This study was performed in four steps as follows (**Figures 1**, **2**): (a) in the supine position, CPAP was set at 12 cmH_2O, and the first series of the measurement was performed (T1s); (b) CPAP was then decreased to 6 cmH_20, and the series of the second measurement was recorded (T2s);

FIGURE 1 | Study steps protocol.

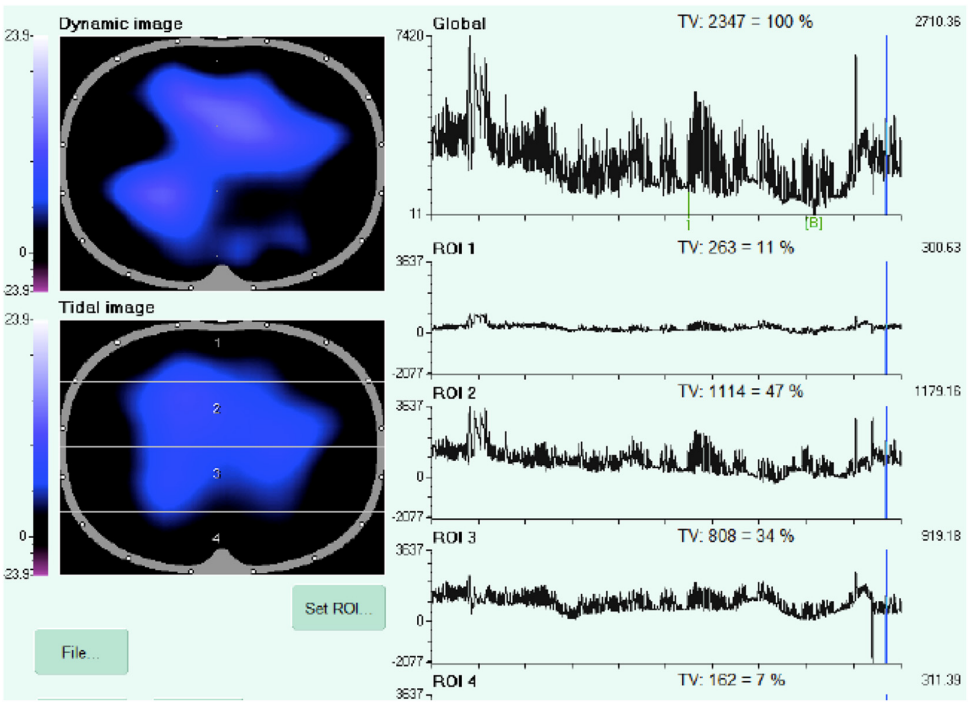

FIGURE 2 | EIT ventilation dynamic distribution image from one CPAP decremental trial. The screenshot shows the distribution of the tidal volume in a cross sectional full screen view of the patient thorax in the caudal-cranial direction.

(c) patients were then turned to the prone position, CPAP was again set to 12 cmH_2O, and the third series of measurements was performed (T1p); (d) CPAP was decreased to 6 cmH_2O (T2s), and the last measurement was performed. Every step lasted 15 min. The whole procedure lasted 1 h plus the time necessary for turning patients to the prone position. After the final steps, the physician in charge decided whether the patients can be kept in the prone position or not and set CPAP according to her/his clinical judgment. The decision to switch to intubation and invasive mechanical ventilation was taken by treating physicians independently from study results.

During every step, Vt, RR, and minute ventilation (Ve) were recorded together with data from the EIT as already described (Cinnella et al., 2015). BP, HR, SaO_2, and a baseline ABG were collected, together with blood screen of the day, as per ward policy.

Statistical Analysis

Data are expressed as percentage, mean ± SD, since they are normally distributed (Shapiro–Wilk test, $p > 0.05$). We used the one-way ANOVA to assess differences between $CPAP_{12}$ and $CPAP_6$ and differences between supine and prone positions. A p value < 0.05 was considered significant. Statistical analysis was performed using Statistica 10.0 (TIBCO software Inc., Palo Alto, CA, United States; Statsoft Italia srl 2011; available at: www.statsoft.com).

RESULTS

In this study, 10 men patients were included, with a mean age of 67 (range 51–81) years, a weight of 85 ± 20 kg, and a BMI of 20 ± 15.

The mean time lapse from the appearance of symptoms to ICU admission was within a range of 7–10 days.

Six patients were successfully discharged from the ICU to ward after 12 ± 2 days, without being intubated (**Table 1**). The remaining four patients failed the non-invasive ventilation (NIV) trial, were intubated, and mechanically ventilated within 48 h post trial. All these patients died in ICU (mean ICU stay 14 ± 3.5 days, range 14–20 days.

TABLE 1 | Demographics data and outcome.

Patient	Sex	Age (y-o)	BMI (Kg/m^2)	Comorbidities	Outcome
1	M	80	33	HTN	ICU discharge Day 12th
2	M	57	28	None	ICU discharge Day 7th
3	M	79	32	HTN	Dead Day 10th post ETT
4	M	77	30	HTN	ICU discharge Day 12th
5	M	80	26	HTN, CKI	Dead Day 4th post ETT
6	M	68	33	HTN	Dead Day 21st (24 h post ETT)
7	M	60	29	HTN, DM II	Dead Day 32nd
8	M	51	28	None	ICU discharge Day 6th
9	M	55	29	None	ICU discharge Day 9th
10	M	60	26	HTN	ICU discharge Day 5th

BMI, body mass index; ETT, endotracheal tube; HTN, hypertension; CKI, chronic kidney injury; DM II, Diabetes Mellitus Type II.

In the whole group, baseline PaO_2/FiO_2 was 180 ± 20 and remained unchanged during the study (NS). RR and Ve increased when going from CPAP 12 to CPAP 6, both in supine (RR 18 ± 2 in T1s to 28 ± 2 bpm in T2s; Ve 8.3 ± 1.2 to 12.5 ± 3.2 L × min^{-1}) and prone positions (RR 17 ± 2 in T1p to 26 ± 3 bpm in T2p; Ve 8.5 ± 0.6 to 11.6 ± 2.7 L × min^{-1}; $p < 0.05$), while Vt remained stable in every patient (**Table 2**).

A posteriori analysis of survivors vs. non-survivors showed that ΔEELI (**Table 2**) was > 50% in all survivors and remained stable in both supine and prone positions (58 ± 6% and 62 ± 8%, respectively, $p = 0.05$). In non-survivors, ΔEELI was 28 ± 4%, with small or no changes in the supine trial, and increased up to 63 ± 9% (<0.01) during the prone trial. Ve increased on the last phase of the trial (**Figure 3**). In **Figures 4**, **5**, EITdiag MatLab analysis from two representative patients (one survivor and one non-survivor) is shown.

The four patients intubated were ventilated with 6 ml/kg/PBW and PEEP of 12 ± 2 cmH_2O. Measurement of respiratory mechanics showed a plateau pressure (Pplat) < 30 cmH_2O in all patients, with mean static compliance (Cs) of 40 ± 4 ml/cmH_2O; patients #3 and 7 had an AOP of 13 ± 2 cmH_2O, and patients # 5 and 6 were not recruiters (R/I < 0.5).

DISCUSSION

The main findings of the present pilot study are that patients with SARS-CoV-2 pneumonia under non-invasive ventilation may have two distinct behaviors to a CPAP decremental trial: (a) ΔEELI > 50% either in the supine or prone position, indicating lung recruitability, associated with NIV success; (b) ΔEELI < 40% in the supine position, indicating non-recruiter lungs (phenotype L) or AOP > 12 cmH_2O, associated with NIV failure; (c) in patients who failed NIV, an increased ΔEELI% exclusively during proning may be due to a better V/Q matching.

The novelty of our study is that we performed a decremental CPAP trial in awake SARS-CoV-2 patients and used EIT, a non-invasive, bedside tool that does not require specific competencies in respiratory mechanic assessment, to assess the changes in lung volume. Thus, we applied in our patients the same physiological principle used in intubated and mechanically ventilated patients to discriminate between recruiters and non-recruiters (Perier et al., 2020; van der Zee et al., 2020; Kotani and Shono, 2021; Shono et al., 2021).

Before discussing our results, a short excursus on NIV state-of-the-art in SARS-CoV-2 pneumonia is required. In fact, the time course of findings from trials focused on non-invasive respiratory support reflects the difficulties that everybody, everywhere, had to face in front of a new syndrome of such a sprawling aspect as SARS-CoV-2. Retrospectively, one can bitterly meditate on the ATS/ERS guidelines (Rochwerg et al., 2017), on the use of NIV in *de novo* acute respiratory failure and critical viral illness pandemic statement: "*we are unable to offer a recommendation*," just before the SARS-CoV-2 pandemic explosion. Later, the panel added: "*. . .we consider prior recommendations against the use of NIV for pandemic as unsupportable.*" Nonetheless, the worldwide fight against SARS-CoV-2 started from ATS/ERS first statement, so that the earliest international guidelines on COVID

TABLE 2 | Respiratory parameters during CPAP trials, in both positions.

	Supine		Prone		*P* value
	CPAP 12 cmH_2O	CPAP 6 cmH_2O	CPAP 12 cmH_2O	CPAP 6 cmH_2O	
Vt (ml)	450 ± 100	430 ± 150	500 ± 80	460 ± 90	$P = 0.2$
RR (breaths per minute)	18 ± 2	28 ± 2*	17 ± 2	26 ± 3*	$P < 0.05$
Ve (l/min)	8.3 ± 1.2	12.5 ± 3.2*	8.5 ± 0.6	11.6 ± 2.7*	$P < 0.05$
PaO_2/FiO_2	180 ± 20	170 ± 20	220 ± 10	190 ± 10	NS
ΔEELI Global (%) NIV failure	28 ± 4		63 ± 9 #		$P < 0.01$
ΔEELI Global (%) NIV success	58 ± 6		62 ± 8 #		$P = 0.05$

**$CPAP_{12}$ vs. $CPAP_6$; # Supine vs. Prone position. NS, not significant.*

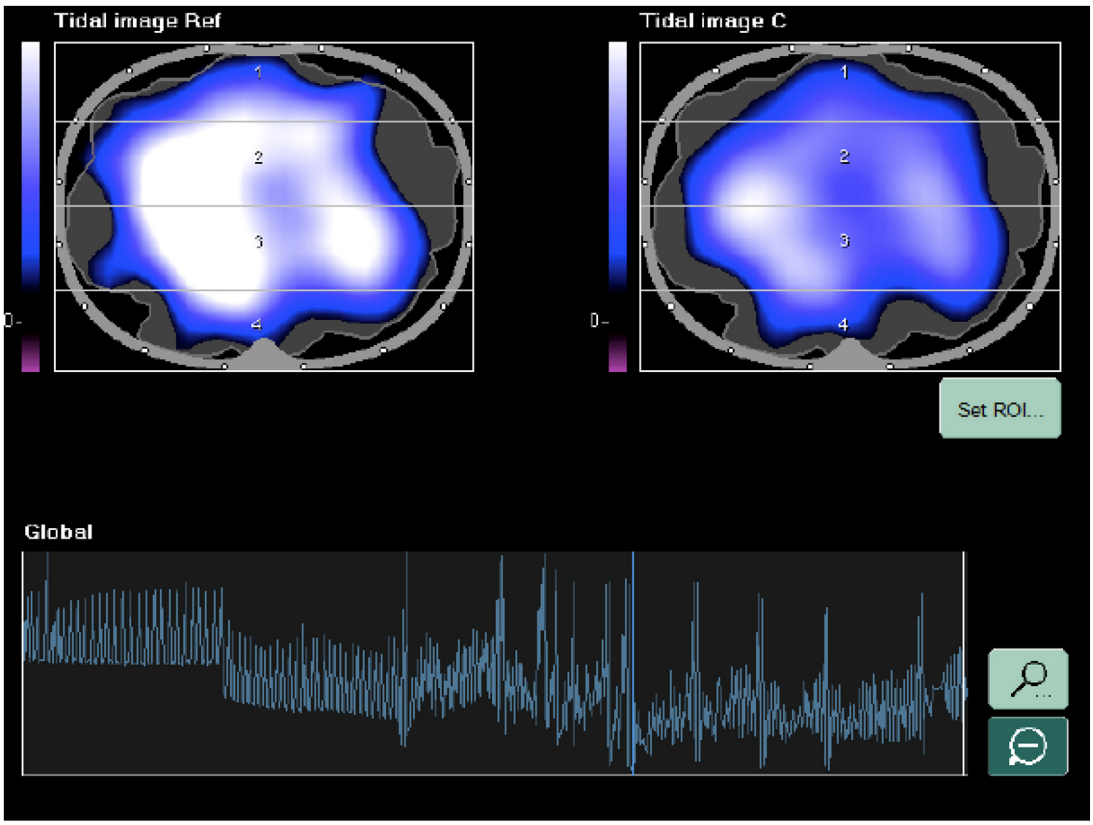

FIGURE 3 | Analysis from one CPAP decremental trial and change in ventilation distribution in a patient who failed NIV and died (the huge variability of the signal in the final step of the trial highlights the fatigue).

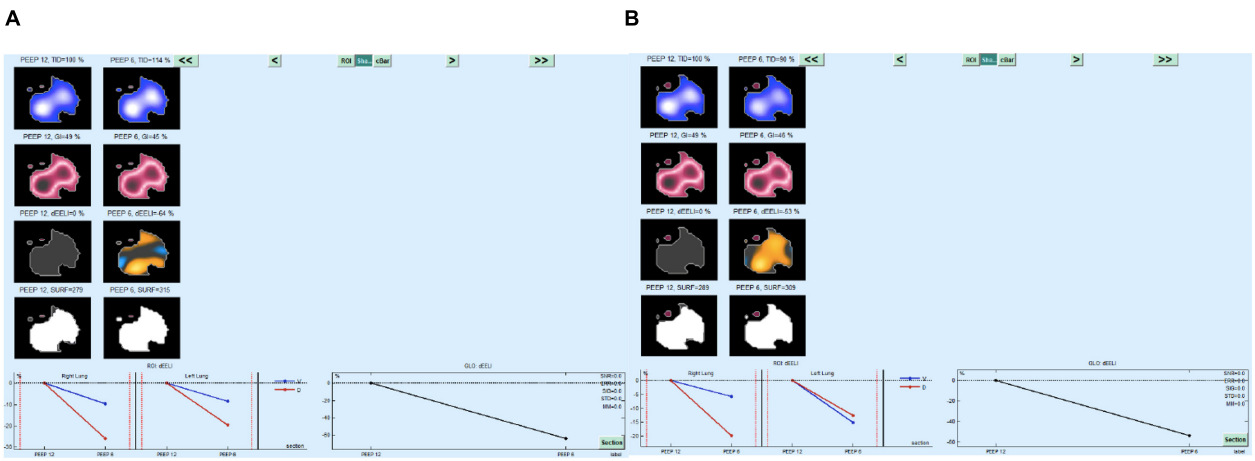

FIGURE 4 | EITdiag MatLAb Analysis of the decremental CPAP trial in a patient who survived, **(A)** supine, **(B)** prone. Note the ΔEELI% > 50 in both body positions.

19 (Whang et al., 2021) did not recommend NIV in such patients. However, it became soon evident that the situation had gone out of control and 1,000 patients had to be treated non-invasively because the alternate choice was not respiratory support at all. Paradigmatic of this struggle is the amendments made by National COVID-19 Clinical Evidence Taskforce (NCCET) (Whang et al., 2021) that deleted the following statement from its revised guidelines "*in patients with hypoxemia associated with COVID-19, do not routinely use NIV*" (Whang et al., 2021). Since then, a number of studies dealt with the COVID-19 outcome prediction (Tseng et al., 2021), early vs. late intubation (Lee et al., 2021), and criteria for NIV and prediction of NIV failure

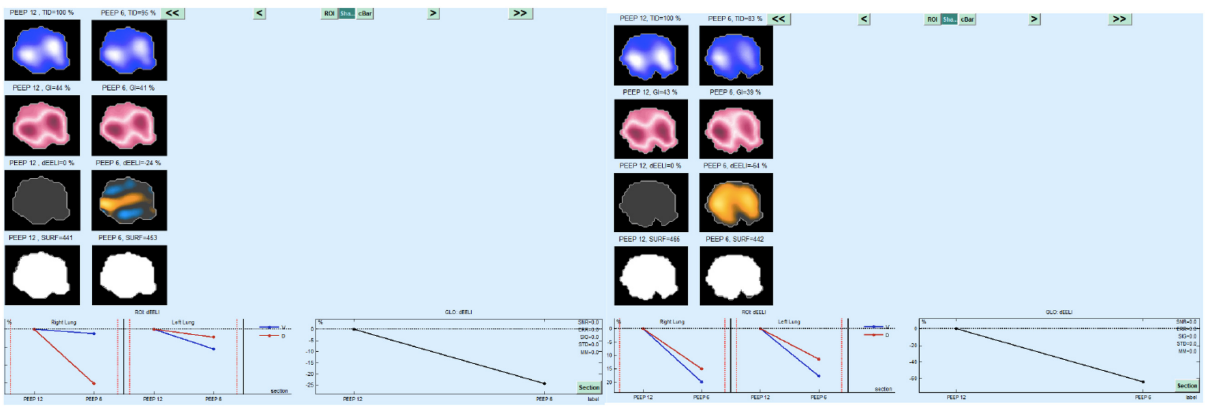

FIGURE 5 | EITdiag MatLAb Analysis of the decremental CPAP trial in a patient who died, **(A)** supine, **(B)** prone. Note the ΔEELI% < 40 in supine postion and > 50 in prone postion.

(Bellani et al., 2017; He et al., 2019), so that at present, the debate is still going and no definite recommendations are available, while patients are still largely ventilated with NIV, mainly in non-ICU departments and often by non-ICU trained physicians. An effort to provide clear and simple means to early discriminate patients that require intubation is thus needed, perhaps more due to ethical reasons than purely speculative ones.

Severe acute respiratory syndrome coronavirus 2 pneumonia may present with two phenotypes which identification is pivotal to apply the right mechanical ventilation strategy (Gattinoni et al., 2020a): type L, characterized by low elastance, low V/Q ratio, lung weight, and recruitability, and type H, defined by high elastance, right to left shunt, lung weight, and recruitability. Recruitability is defined as the possibility to open up collapsed areas of the lung by positive pressure. The "classical" lung-protective strategy (Gattinoni et al., 2006, 2020a,b,c), based on limiting Vt and plateau pressure is not required for type L but should be actively implemented in type H. However, it is not easy to distinguish between the two types because the lung weight cannot be measured clinically, and the method to evaluate recruitability is unclear, while a method to measure V/Q matching at the bedside has not been established. Under such conditions, EIT was proposed not only to evaluate recruitability but also to assess regional ventilation homogeneity, thus allowing to determine the optimum PEEP at the time of measurement. As a result, this approach could be of help to set ventilation to attenuate regional dynamic strain and inhomogeneity of transpulmonary pressure. Morais et al. (2021) presented three cases of mechanically ventilated patients with COVID-19 with acute hypoxemic respiratory failure (AHRF) and ARDS that had similar levels of oxygenation but variable respiratory system compliance. In this case series, different characteristics of the regional ventilation profile were evidenced by EIT that was thus helpful in understanding the etiology of hypoxemia at the bedside. Tomasino et al. (2020) used EIT to identify the characteristics of COVID-19 pneumonia and to decide whether to use high PEEP or prone positioning.

In this study, PEEP de-escalation affected most of the respiratory parameters in all patients, disclosing two behaviors that matched with a clinically significant difference in the outcome of patients. Interestingly, the two behaviors were evident in the supine position and not in the prone position: the four patients that failed NIV had only slight variations in terms of ΔEELI when kept in the supine position, probably because in this position, lung stiffness, alveolar collapse, and V/Q mismatch play a major role than in prone position (Cornejo et al., 2013; Yoshida et al., 2013; Scaravilli et al., 2015; Aguirre-Bermeo et al., 2018; Telias et al., 2020). In fact, this hypothesis was confirmed by respiratory mechanic data obtained after intubation in these patients showing that two of them were not recruiters (R/I < 0.5), and the remaining two had an AOP > 12 cmH_2O, signs of their need for mechanical ventilation and higher PEEP levels. These four patients had already signs of fatigue on their admission to the ICU, and it could be argued that NIV would probably have not been indicated for them from the beginning. However, since their PaO_2/FiO_2 was acceptable when compared with other patients, they underwent an NIV trial. In contrast, the six patients in whom NIV was successful (all discharged from ICU) had a significant increase in ΔEELI when PEEP was reduced, both in supine and prone positions, and in our opinion, this can be explained still by soft lungs and high recruitability, since the end-expiratory trend view or ΔEELI-trend view is used to monitor regional changes of ΔEELI. ΔEELI is strongly correlated with the changes in ΔEELV. The ΔEELI trend is useful to assess the changes in lung volume, for example, after changing the PEEP and after recruitment maneuvers for the reopening of dorsal atelectases and for the detection of derecruitment of individual lung areas.

Paradoxically, it could be argued that the prone position could mask NIV failure precisely because of its favorable effects. In fact, the physiological rationale behind prone positioning in typical ARDS is to reduce ventilation/perfusion mismatching, hypoxemia, and shunting (Cornejo et al., 2013; Scaravilli et al., 2015; Aguirre-Bermeo et al., 2018). When a patient is in the prone

position, the pleural pressure gradient between dependent and non-dependent lung regions decreases as a result of gravitational effects and matching of conformational shape of the lung to the chest cavity. This generates more homogenous lung aeration and strain distribution, thus enhancing recruitment of dorsal lung units (Telias et al., 2020), while the regional distribution of pulmonary blood flow is not altered, with perfusion predominating toward the dorsal lung due to non-gravitational factors. In patients with spontaneous breathing, respiratory physiology under prone position is the same plus the effect of diaphragm contraction, since its muscular mass is mainly *posterior*, when in the prone position, it exerts on lungs a more uniform distribution of stress (Yoshida et al., 2013). Lung regional hyperinflation may thus be reduced (Telias et al., 2020). Therefore, the prone position allows an improvement in ventilatory homogeneity with a relatively constant perfusion pattern, and a subsequent reduction in shunting is observed together with an increase in EELV. In fact, none of our patients had a severe respiratory failure (they would not have been in NIV), so that all responded to proning with the expected EELV increase, but the physiological and clinical meaning of these data is different in the two groups. The benefit of prone position in terms of V/Q matching did probably overcome the role played by OAP or lung stiffness in those patients who were not recruitable, and this could explain why all did have a ΔEELI $>$ 50% when switched from 12 to 6 cmH_2O in pronation.

In contrast, in the supine position, the damages of lung inflammation and edema are more evident. Due to the increased weight of the lung, alveolar collapse may predominantly occur in the dependent lung regions, and the resulting arterial hypoxemia is worsened by diaphragmatic contractions that cause gas displacement from non-dependent to dependent lung areas, the so-called pendelluft phenomenon (Yoshida et al., 2013). Moreover, strong inspiratory effort causes large negative pressure in the thorax and increased transpulmonary pressure that can cause or aggravate lung injury, generating the so-called PSILI, whose pathological changes are irreversible and worsen the prognosis (Brochard et al., 2017; Grieco et al., 2019; Yoshida et al., 2020). Under such conditions, a lung that is PEEP-dependent, i.e., recruitable, will lose volume when PEEP is decreased while a lung stiff or with AOP will remain quite unaffected.

CONCLUSION

Although our results need to be confirmed by larger data set and further RCTs should be conducted to evaluate whether the use of the EIT could, in fact, help to detect different phenotypes and clustering patients able to tolerate NIV, our data seem to suggest that a PEEP de-escalation trial in the supine position can be useful to discriminate lung recruitability in patients with SARS-CoV-2 under NIV.

DATA AVAILABILITY STATEMENT

The original contributions presented in the study are included in the article/supplementary material, further inquiries can be directed to the corresponding author/s.

ETHICS STATEMENT

The studies involving human participants were reviewed and approved by Comitato Etico Azienda Ospedaliero Universitaria Policlinico Riuniti di Foggia. The patients/participants provided their written informed consent to participate in this study.

AUTHOR CONTRIBUTIONS

MR and GC conceived the presented idea. MR wrote the first draft. DL performed the measurements. AL and LM verified the analytical methods. PV, ES, DU, EC, and LT encouraged MR to investigate the use of the EIT in patients with COVID-19 and supervised the findings of this study. GC contributed to the final manuscript. All authors discussed the results.

ACKNOWLEDGMENTS

The authors would like to thank all the personnel of our ICU involved in this dramatic period.

REFERENCES

Aguirre-Bermeo, H., Turella, M., Bitondo, M., Grandjean, J., Italiano, S., Festa, O., et al. (2018). Lung volumes and lung volume recruitment in ARDS: a comparison between supine and prone position. *Ann. Intensive Care* 8:25.

Bamford, P., Bentley, A., Dean, J., Whitmore, D., and Wilson-Baig, N. (2020). *Intensive Care Society ICS Guidance for Prone Positioning of the Conscious COVID Patient*. Available online at: https://emcrit.org/wp-content/uploads/2020/04/2020-04-12-Guidance-for-conscious-proning.pdf

Bellani, G., Laffey, J. G., Pham, T., Madotto, F., Fan, E., Brochard, L., et al. (2017). Noninvasive Ventilation of Patients with Acute Respiratory Distress Syndrome. Insights from the LUNG SAFE Study. *Am. J. Respir. Crit. Care Med.* 195, 67–77. doi: 10.1164/rccm.201606-1306OC

Brochard, L., Slutsky, A., and Pesenti, A. (2017). Mechanical ventilation to minimize progression of lung injury in acute respiratory failure. *Am. J. Respir. Crit. Care Med.* 195, 438–442. doi: 10.1164/rccm.201605-1081CP

Chen, L., Del Sorbo, L., Grieco, D. L., Junhasavasdikul, D., Rittayamai, N., Soliman, I., et al. (2020). Potential for lung recruitment estimated by the recruitment-to-inflation ratio in acute respiratory distress syndrome: a clinical trial. *Am. J. Respir. Crit. Care Med.* 201, 178–187. doi: 10.1164/rccm.201902-0334oc

Chen, L., Del Sorbo, L., Grieco, D. L., Shklar, O., Junhasavasdikul, D., Telias, I., et al. (2018). Airway closure in acute respiratory distress syndrome: an underestimated and misinterpreted phenomenon. *Am. J. Respir. Crit. Care Med.* 197, 132–136.

Cinnella, G., Grasso, S., Raimondo, P., D'Antini, D., Mirabella, L., Rauseo, M., et al. (2015). Physiological Effects of the Open Lung Approach in Patients with Early, Mild, Diffuse Acute Respiratory Distress Syndrome: an Electrical Impedance Tomography Study. *Anesthesiology* 123, 1113–1121. doi: 10.1097/ALN.0000000000000862

Cornejo, R. A., Díaz, J. C., Tobar, E. A., Bruhn, A. R., Ramos, C. A., González, R. A., et al. (2013). Effects of prone positioning on lung protection in patients

with acute respiratory distress syndrome. *Am. J. Respir. Crit. Care Med.* 188, 440–448.

Dantzker, D. R. (1982). Gas exchange in the adult respiratory distress syndrome. *Clin. Chest Med.* 3, 57–67. doi: 10.1016/s0272-5231(21)00144-1

Gattinoni, L., Caironi, P., Cressoni, M., Chiumello, D., Ranieri, V. M., Quintel, M., et al. (2006). Lung recruitment in patients with the acute respiratory distress syndrome. *N. Engl. J. Med.* 354, 1775–1786.

Gattinoni, L., Chiumello, D., Caironi, P., Busana, M., Romitti, F., Brazzi, L., et al. (2020a). COVID-19 pneumonia: different respiratory treatments for different phenotypes?. *Intensive Care Med.* 46, 1099–1102. doi: 10.1007/s00134-020-06033-2

Gattinoni, L., Chiumello, D., and Rossi, S. (2020b). COVID-19 pneumonia: ARDS or not?. *Crit. Care* 24, 154.

Gattinoni, L., Coppola, S., Cressoni, M., Busana, M., Rossi, S., and Chiumello, D. (2020c). Covid-19 does not lead to a «typical» acute respiratory distress syndrome. *Am. J. Respir. Crit. Care Med.* 201, 1299–1300. doi: 10.1164/rccm.202003-0817le

Grasselli, G., Tonetti, T., Protti, A., Langer, T., Girardis, M., Bellani, G., et al. (2020). Pathophysiology of COVID-19-associated acute respiratory distress syndrome: a multicentre prospective observational study. *Lancet Respir. Med.* 8, 1201–1208. doi: 10.1016/S2213-2600(20)30370-2

Grieco, D. L., Menga, L. S., Eleuteri, D., and Antonelli, M. (2019). Patient self-inflicted lung injury: implications for acute hypoxemic respiratory failure and ARDS patients on non-invasive support. *Minerva Anestesiol.* 85, 1014–1023.

He, H., Sun, B., Liang, L., Li, Y., Wang, H., Wei, L., et al. (2019). A multicenter RCT of noninvasive ventilation in pneumonia-induced early mild acute respiratory distress syndrome. *Crit. Care* 23:300. doi: 10.1186/s13054-019-2575-6

Kotani, T., and Shono, A. (2021). Roles of Electrical Impedance Tomography in Determining a Lung Protective Strategy for Acute Respiratory Distress Syndrome in the Era of Coronavirus Disease 2019. *JMA J.* 4, 81–85.

Lee, C. P., Yip, Y. Y., Chan, A. K., Ko, C. P., and Joynt, G. M. (2021). Early intubation versus late intubation for COVID-19 patients: an in situ simulation identifying factors affecting performance and infection control in airway management. *Anaesth. Intensive Care*. doi: 10.1177/0310057X211007862 [Online ahead of print]

Lowhagen, K., Lundin, S., and Stenqvist, O. (2010). Regional intratidal gas distribution in acute lung injury and acute respiratory distress syndrome: assessed by electric impedance tomography. *Minerva Anestesiol.* 76:1024.

Morais, C. C. A., Safaee Fakhr, B., De Santis Santiago, R. R., Di Fenza, R., Marutani, E., Gianni, S., et al. (2021). Bedside electrical impedance tomography unveils respiratory "chimera" in COVID-19. *Am. J. Respir. Crit. Care Med.* 203, 120–121. doi: 10.1164/rccm.202005-1801im

Perier, F., Tuffet, S., Maraffi, T., Alcala, G., Victor, M., Haudebourg, A. F., et al. (2020). Electrical impedance tomography to titrate positive end-expiratory pressure in COVID-19 acute respiratory distress syndrome. *Crit. Care* 24:678. doi: 10.1186/s13054-020-03414-3

Rochwerg, B., Brochard, L., Elliott, M. W., Hess, D., Hill, N. S., Nava, S., et al. (2017). Official ERS/ATS clinical practice guidelines: noninvasive ventilation for acute respiratory failure. *Eur. Respir. J.* 50:1602426. doi: 10.1183/13993003.02426-2016

Scaravilli, V., Grasselli, G., Castagna, L., Zanella, A., Isgrò, S., Lucchini, A., et al. (2015). Prone Positioning improves oxygenation in spontaneously breathing nonintubated patients with hypoxemic acute respiratory failure: a retrospective study. *J. Crit. Care* 30, 1390–1394. doi: 10.1016/j.jcrc.2015.07.008

Shono, A., Kotani, T., and Frerichs, I. (2021). Personalisation of therapies in COVID-19 associated acute respiratory distress syndrome, using electrical impedance tomography. *J. Crit. Care Med.* 7, 62–66. doi: 10.2478/jccm-2020-0045

Sosio, S., Bellani, G., Villa, S., Lupieri, E., Mauri, T., and Foti, G. (2019). A Calibration Technique for the Estimation of Lung Volumes in Nonintubated Subjects by Electrical Impedance Tomography. *Respiration* 98, 189–197. doi: 10.1159/000499159

Telias, I., Katira, B. H., and Brochard, L. (2020). Is the prone position helpful during spontaneous breathing in patients with COVID-19?. *JAMA* 323, 2265–2267. doi: 10.1001/jama.2020.8539

Tomasino, S., Sassanelli, R., Marescalco, C., Meroi, F., Vetrugno, L., and Bove, T. (2020). Electrical impedance tomography and prone position during ventilation in COVID-19 pneumonia: case reports and a brief literature review. *Semin. Cardiothorac. Vasc. Anesth.* 24, 287–292. doi: 10.1177/1089253220958912

Tseng, L., Hittesdorf, E., Berman, M. F., Jordan, D. A., Yoh, N., Elisman, K., et al. (2021). Predicting Poor Outcome of COVID-19 Patients on the Day of Admission with the COVID-19 Score. *Crit Care Res. Pract.* 2021:5585291. doi: 10.1155/2021/5585291

van der Zee, P., Somhorst, P., Endeman, H., and Gommers, D. (2020). Electrical impedance tomography for positive end-expiratory pressure titration in COVID-19 related ARDS. *Am. J. Respir. Crit. Care Med.* 202, 280–284. doi: 10.1164/rccm.202003-0816le

Whang, Z., Whang, Y., Yang, Z., Wu, H., Liang, J., Liang, H., et al. (2021). The use of non-invasive ventilation in COVID-19: a systematic review. *Int. J. Infect. Dis.* 106, 254–261.

Yoshida, T., Grieco, D. L., Brochard, L., and Fujino, Y. (2020). Patient self-inflicted lung injury and positive end-expiratory pressure for safe spontaneous breathing. *Curr. Opin. Crit. Care.* 26, 59–65. doi: 10.1097/MCC.0000000000000691

Yoshida, T., Torsani, V., Gomes, S., De Santis, R. R., Beraldo, M. A., Costa, E. L., et al. (2013). Spontaneous effort causes occult pendelluft during mechanical ventilation. *Am. J. Respir. Crit. Care Med.* 188, 1420–1427. doi: 10.1164/rccm.201303-0539oc

Conflict of Interest: The authors declare that the research was conducted in the absence of any commercial or financial relationships that could be construed as a potential conflict of interest.

Publisher's Note: All claims expressed in this article are solely those of the authors and do not necessarily represent those of their affiliated organizations, or those of the publisher, the editors and the reviewers. Any product that may be evaluated in this article, or claim that may be made by its manufacturer, is not guaranteed or endorsed by the publisher.

frontiers in Physiology

ORIGINAL RESEARCH
published: 10 September 2021
doi: 10.3389/fphys.2021.717269

Effects of Body Position and Hypovolemia on the Regional Distribution of Pulmonary Perfusion During One-Lung Ventilation in Endotoxemic Pigs

Jakob Wittenstein[1], Martin Scharffenberg[1], Xi Ran[1,2], Yingying Zhang[1,3], Diana Keller[1], Sebastian Tauer[1], Raphael Theilen[1], Yusen Chai[1], Jorge Ferreira[1], Sabine Müller[1], Thomas Bluth[1], Thomas Kiss[1,4], Marcus J. Schultz[5], Patricia R. M. Rocco[6], Paolo Pelosi[7,8], Marcelo Gama de Abreu[1,9,10] and Robert Huhle[1]*

[1] Department of Anaesthesiology and Intensive Care Medicine, Pulmonary Engineering Group, University Hospital Carl Gustav Carus Dresden at Technische Universität Dresden, Dresden, Germany, [2] Department of Intensive Care, Chongqing General Hospital, University of Chinese Academy of Science, Chongqing, China, [3] Department of Anesthesiology, Affiliated Hospital of Southwest Medical University, Luzhou, China, [4] Department of Anaesthesiology, Intensive-, Pain- and Palliative Care Medicine, Radebeul Hospital, Academic Hospital of the Technische Universität Dresden, Radebeul, Germany, [5] Department of Intensive Care and Laboratory of Experimental Intensive Care and Anaesthesiology, Academic Medical Center, University of Amsterdam, Amsterdam, Netherlands, [6] Laboratory of Pulmonary Investigation, Carlos Chagas Filho Institute of Biophysics, Federal University of Rio de Janeiro, Rio de Janeiro, Brazil, [7] Department of Surgical Sciences and Integrated Diagnostics, University of Genoa, Genoa, Italy, [8] Anesthesia and Critical Care, San Martino Policlinico Hospital, Istituto di Ricovero e Cura a Carattere Scientifico (IRCCS) for Oncology and Neurosciences, Genoa, Italy, [9] Department of Intensive Care and Resuscitation, Anesthesiology Institute, Cleveland Clinic, Cleveland, OH, United States, [10] Department of Outcomes Research, Anesthesiology Institute, Cleveland Clinic, Cleveland, OH, United States

OPEN ACCESS

Edited by:
Andrew T. Lovering,
University of Oregon, United States

Reviewed by:
Susan Hopkins,
University of California, San Diego, United States
Erik Richard Swenson,
University of Washington, United States

***Correspondence:**
Marcelo Gama de Abreu
gamadem@ccf.org

Specialty section:
This article was submitted to Respiratory Physiology, a section of the journal Frontiers in Physiology

Received: 30 May 2021
Accepted: 10 August 2021
Published: 10 September 2021

Citation:
Wittenstein J, Scharffenberg M, Ran X, Zhang Y, Keller D, Tauer S, Theilen R, Chai Y, Ferreira J, Müller S, Bluth T, Kiss T, Schultz MJ, Rocco PRM, Pelosi P, Gama de Abreu M and Huhle R (2021) Effects of Body Position and Hypovolemia on the Regional Distribution of Pulmonary Perfusion During One-Lung Ventilation in Endotoxemic Pigs. Front. Physiol. 12:717269. doi: 10.3389/fphys.2021.717269

Background: The incidence of hypoxemia during one-lung ventilation (OLV) is as high as 10%. It is also partially determined by the distribution of perfusion. During thoracic surgery, different body positions are used, such as the supine, semilateral, lateral, and prone positions, with such positions potentially influencing the distribution of perfusion. Furthermore, hypovolemia can impair hypoxic vasoconstriction. However, the effects of body position and hypovolemia on the distribution of perfusion remain poorly defined. We hypothesized that, during OLV, the relative perfusion of the ventilated lung is higher in the lateral decubitus position and that hypovolemia impairs the redistribution of pulmonary blood flow.

Methods: Sixteen juvenile pigs were anesthetized, mechanically ventilated, submitted to a right-sided thoracotomy, and randomly assigned to one of two groups: (1) intravascular normovolemia or (2) intravascular hypovolemia, as achieved by drawing ∼25% of the estimated blood volume (n = 8/group). Furthermore, to mimic thoracic surgery inflammatory conditions, *Escherichia coli* lipopolysaccharide was continuously infused at 0.5 μg kg^{-1} h^{-1}. Under left-sided OLV conditions, the animals were further randomized to one of the four sequences of supine, left semilateral, left lateral, and prone positioning. Measurements of pulmonary perfusion distribution with fluorescence-marked microspheres, ventilation distribution by electrical impedance tomography, and gas exchange were then performed during two-lung ventilation in a supine position and after 30 min in each position and intravascular volume status during OLV.

Results: During one-lung ventilation, the relative perfusion of the ventilated lung was higher in the lateral than the supine position. The relative perfusion of the non-ventilated lung was lower in the lateral than the supine and prone positions and in semilateral compared with the prone position. During OLV, the highest arterial partial pressure of oxygen/inspiratory fraction of oxygen (PaO_2/F_IO_2) was achieved in the lateral position as compared with all the other positions. The distribution of perfusion, ventilation, and oxygenation did not differ significantly between normovolemia and hypovolemia.

Conclusions: During one-lung ventilation in endotoxemic pigs, the relative perfusion of the ventilated lung and oxygenation were higher in the lateral than in the supine position and not impaired by hypovolemia.

Keywords: one-lung ventilation, OLV, pulmonary perfusion, thoracic anesthesia, hypovolemia, body position, HPV, gravity

INTRODUCTION

During one-lung ventilation (OLV), the incidence of relevant hypoxemia can be as high as 10% and can be associated with postoperative complications (Kazan et al., 2009). The incidence of hypoxemia is mainly determined by the pulmonary blood flow to the ventilated and non-ventilated lung, with the latter representing the intrapulmonary right-to-left shunt. During OLV, hypoxic pulmonary vasoconstriction (HPV) redirects pulmonary blood flow toward the ventilated lung. In turn, regional pulmonary blood flow is influenced by gravity (Szegedi et al., 2010), local mechanical forces (Alfery et al., 1981), and intravascular volume status (Deem et al., 1995), as summarized in the west-zone model (West et al., 1964). Furthermore, the atelectasis and hypo-ventilated zones and the hyper-inflated areas of the ventilated lung contribute to perfusion-ventilation mismatch and have an additive effect on shunting in the non-ventilated lung (Hedenstierna et al., 1986). Body position may further influence the distribution of pulmonary perfusion because of different gravitational and ventilation distributions in corresponding positions. Finally, the geometry of the vascular tree that branches asymmetrically plays an important role in the spatial distribution of pulmonary blood flow (Glenny and Robertson, 2011).

One-lung ventilation is required for different thoracic procedures to allow access to the surgical field. Depending on the surgical access, a patient can be placed in a supine, semilateral, lateral, or prone position. While the lateral decubitus position is most frequently used, the prone position is needed for certain esophageal and spinal surgery approaches. In addition, the supine position is required during mediastinal and cardiac surgery, and the semilateral position is used during open thoracic aortic repair (Crawford position). Currently, it is not known how these positions compare with respect to the distribution of regional pulmonary perfusion and gas exchange. Furthermore, during thoracic surgery, the incidence of major bleeding leading to acute intravascular hypovolemia can reach up to 5% (Schirren et al., 2015). It has been proposed that acute intravascular hypovolemia may alter hypoxic pulmonary vasoconstriction (Deem et al., 1995) and thereby gas exchange. However, the effect of hypovolemia on the distribution of pulmonary blood flow during OLV is not well-determined.

In this study, we aimed to determine the distribution of pulmonary blood flow during commonly used body positions for thoracic surgery during normo- and hypovolemia in pigs undergoing one-lung ventilation. We hypothesized that the pulmonary blood flow of the ventilated lung would be highest in the lateral decubitus position. We also hypothesized that intravascular hypovolemia impairs the redistribution of pulmonary blood flow because of an altered hypoxic pulmonary vasoconstriction.

METHODS

The Institutional Animal Care and Welfare Committee and the Government of the State of Saxony, Germany, approved the study (DD24.1-5131/449/71, TVV 69/2018). All the animals in this study received humane care in compliance with the Principles of Laboratory Animal Care formulated by the National Society for Medical Research and the US National Academy of Sciences Guide for the Care and Use of Laboratory Animals. This study also complied with the relevant aspects of the Animal Research: Reporting of *In Vivo* Experiments (ARRIVE) guidelines (Percie du Sert et al., 2020). The animals were kept at a controlled temperature and a light-dark cycle with free access to water and food.

Abbreviations: CV, Coefficient of variation; EIT, Electrical impedance tomography; E_{RS}, Elastance of the respiratory system; EVLWI, Extravascular lung water index; F_IO_2, Inspired fraction of oxygen; GEDVI, Global end-diastolic volume index; HPV, Hypoxic pulmonary vasoconstriction; I:E, Inspiratory to expiratory time ratio; ITBVI, Intrathoracic blood volume index; LPS, Lipopolysaccharide; OLV, One-lung ventilation; PEEP, Positive end-expiratory pressure; PICCO, Pulse Contour Cardiac Output; Pmean, Mean airway pressure; Ppeak, Peak airway pressure; PVRI, Pulmonary vascular resistance index; $Q_{rel,I}$, Relative pulmonary blood flow; RR, Respiratory rate; R_{RS}, Resistance of the respiratory system; SVRI, Systemic vascular resistance index; TLV, Two-lung ventilation; V_T, Tidal volume.

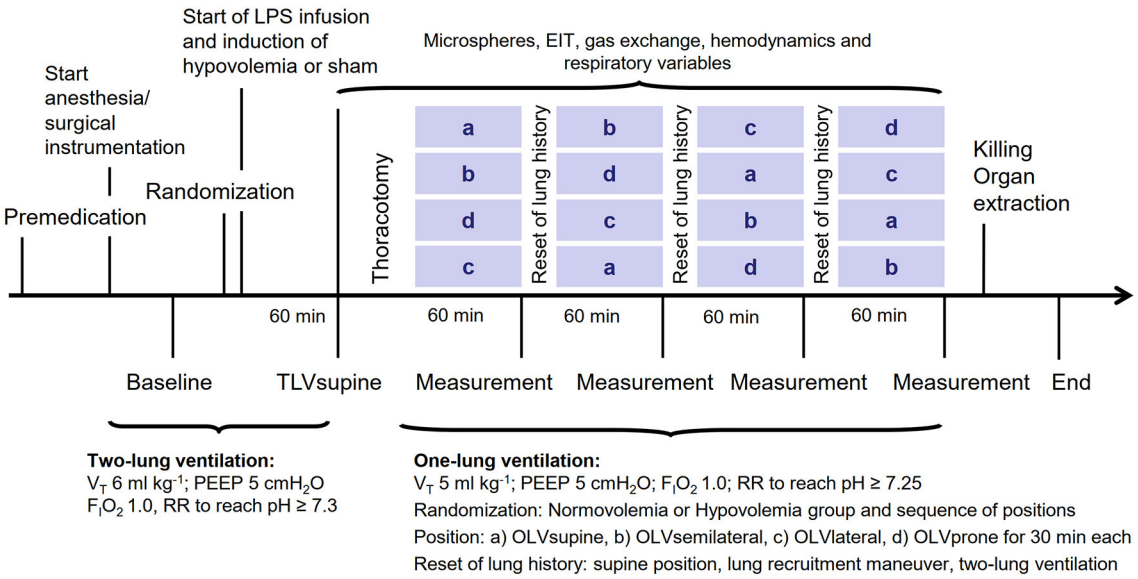

FIGURE 1 | The time course of the interventions and measurements. LPS, lipopolysaccharide; V_T, tidal volume; PEEP, positive end-expiratory pressure; F_IO_2, fraction of inspired oxygen; RR, respiratory rate; microspheres, measurement of regional pulmonary perfusion; EIT, electrical impedance tomography.

Experimental Protocol

The time course of the experiments is presented in **Figure 1**. Sixteen female pigs (German landrace, weighing 35–49 kg, Danish Specific Pathogen Free Certification, www.spf.dk) were intramuscularly sedated with midazolam (1 mg kg^{-1}) and ketamine (10 mg kg^{-1}). Intravenous anesthesia was induced and maintained with midazolam (bolus of 0.5–1 mg kg^{-1}, followed by 1 mg kg^{-1} h^{-1}) and ketamine (bolus of 3–4 mg kg^{-1}, followed by 15 mg kg^{-1} h^{-1}). Muscle paralysis was achieved with atracurium (bolus 3–4 mg kg^{-1}, followed by 3 mg kg^{-1} h^{-1}). The intravascular volume was maintained with a crystalloid solution (E153; Serumwerk Bernburg AG, Bernburg, Germany) at a rate of 5 ml kg h^{-1}. The mean arterial pressure was kept >60 mmHg by norepinephrine and colloid infusion, as appropriate. Colloids were used in the case of increasing hemoglobin. Furthermore, the animals were ventilated in a volume-controlled mode: a fraction of inspired oxygen (F_IO_2) of 1, a tidal volume (V_T) of 6 ml kg^{-1}, a positive end-expiratory pressure (PEEP) of 5 cm H_2O, an inspiratory: expiratory (I:E) ratio of 1:1, a constant gas flow of 25 L/min, and a respiratory rate (RR) adjusted to arterial pH >7.3.

All skin incisions were preceded by the infiltration of 2–5 ml lidocaine 2%. After the surgical preparation of the right internal carotid artery, a pulse contour cardiac output (PiCCO) catheter (20 cm; Pulsion Medical Systems SE, Feldkirchen, Germany) was inserted to continuously monitor the arterial pressure. A 7.5 Fr. pulmonary artery catheter (Opticath; Abbott, Abbott Park, IL, United States) was used to measure cardiac output (CO), and pulmonary artery pressure was advanced through an 8.5 Fr. sheath placed in the right external jugular vein until typical pulmonary arterial pressure waveforms were observed. Urine was collected with a bladder catheter inserted through a median mini-laparotomy. For lung separation, a left-sided double-lumen tube (39 Fr., Silbroncho Fuji, Tokyo, Japan) was placed through a tracheotomy, where the bronchial tip was inserted into the left main bronchus, under fiberoptic control conditions (AmbuaScope 3 and AmbuaView, Ambu GmbH, Bad Nauheim, Germany). In another investigation, the results of which are being published elsewhere, a left-sided video-assisted thoracoscopy was performed, where three pressure sensors were attached to the parietal pleura in the left hemithorax, as described previously (Kiss et al., 2019). Thereafter, the baseline measurements of gas exchange, respiratory signals, hemodynamics, and the distribution of ventilation by electrical impedance tomography (EIT) were performed (baseline).

The animals were randomly assigned to normovolemia or hypovolemia. For the induction of moderate hypovolemia, 25% of the calculated blood volume, estimated as 70 ml kg^{-1} (Hannon et al., 1990), was drawn from the central venous catheter. To mimic the inflammatory response to surgical trauma due to major thoracic surgery (Takenaka et al., 2006; Sánchez-Pedrosa et al., 2018), 0.5 μg/kg/h of lipopolysaccharides (LPS) from *E. coli* O111:B4 (Sigma-Aldrich, St. Louis, MO, United States) was continuously infused through the central venous line. In previous studies, a low-dose LPS infusion was shown to reduce hypoxic pulmonary vasoconstriction (Reeves and Grover, 1974; Theissen et al., 1991). An hour after the start of LPS infusion, the two-lung ventilation supine (TLVsupine) measurements of regional pulmonary perfusion (microspheres), gas exchange, respiratory signals, hemodynamics, and the distribution of ventilation were performed. Thereafter, the animals were randomly submitted to one of four sequences during OLV according to a Latin square design, namely, (1) a-b-c-d, (2) b-d-a-c, (3) d-c-b-a, and (4) c-a-d-b (30 min per body position, crossover), with a = supine, b = left semilateral, c = left lateral, and d =

prone position. To mimic a thoracic surgery, a right-sided thoracotomy was performed between the medial-clavicular and anterior axillary lines in the 4th−5th intercostal space by placing a rib spreader. For OLV, a volume-controlled mode was used: V_T of 5 ml kg^{-1}, F_IO_2 of 1, PEEP of 5 cmH_2O, I:E of 1:1, and RR of 30–35 min^{-1} titrated to achieve an arterial pH of >7.25 and a flow of 25 L min^{-1}. Thirty minutes after placing the animals in the respective body positions (OLVsupine, OLVsemilateral, OLVlateral, OLVprone), the measurements of regional pulmonary perfusion, gas exchange, respiratory signals, hemodynamics, and the distribution of ventilation were performed. To reset lung history between interventions, the animals were placed in the supine position and disconnected from the ventilator. An alveolar recruitment maneuver was then performed, with two-lung ventilation resuming thereafter until the normalization of gas exchange, before the start of each position.

Measurements

Measurement of Regional Pulmonary Blood Flow

The distribution of regional pulmonary blood flow was marked with IV-administered fluorescence and color-labeled 15-μm diameter microspheres (Thermo Fisher Scientific, Waltham, MA, United States). The colors used were blue, blue-green, yellow-green, orange, and red. To avoid bias, the colors were randomly assigned at any given time point. Immediately before injection, the microspheres were vortexed, sonicated for 90 s, and drawn into 2-ml syringes. All the injections were performed for over 60 s to average the blood flow over several cardiac and respiratory cycles. During the injection, $\sim 1.5 \times 10^6$ microspheres were administered.

Postmortem lungs were extracted *en bloc* and flushed with 50 ml kg^{-1} of a hydroxyethyl starch 130/0.4 solution (Voluven, Fresenius Kabi, Bad Homburg, Germany) and air-dried by continuous tracheal airflow for 7 days with a continuous pressure of 25 cm H_2O. The lungs were then coated with a one-component polyurethane foam (BTI Befestigungstechnik, Ingelfingen, Germany), suspended vertically in a square box, and embedded in a rapidly setting urethane foam (polyol and isocyanate; Elastogran, Lemförde, Germany).

The foam block was then cut into cubes of $\sim$1.2 cm^3. Each cube was weighed and assigned a three-dimensional coordinate. The samples were then soaked for 7 days in 3 ml of 2-ethoxyethyl acetate (Aldrich Chemical Co. LLC, Milwaukee, WI, United States) to retrieve the fluorescent dye. The fluorescence was read in a luminescence spectrophotometer (LS-50B; Perkin-Elmer, Beaconsfield, United Kingdom), with the measured intensity of fluorescence in each probe then being normalized according to its weight (x_i). The relative pulmonary blood flow $Q_{rel,i}$ of a probe i was also determined according to:

$$Q_{rel,i} = \frac{x_i}{\frac{1}{n}\sum x_i}$$

with the denominator holding the mean relative blood flow of one lung per time point. The mean normalized relative blood flow was, therefore, 1.

The distributions of pulmonary blood flow along the craniocaudal, ventrodorsal, and left-right axes under each of the experimental conditions were assessed by linear regression. Additionally, a three-dimensional reconstruction of the lung was performed, considering the spatial coordinates of each lung piece and the pulmonary blood flow at each of the x (left-right), y (dorsal-ventral), and z (caudal-cranial) coordinates. Color mapping was performed to identify the regional distribution of pulmonary blood flow based on $Q_{rel,i}$. The color map was then normalized by the maximum Q_{rel} under each of the experimental conditions, resulting in a color scale ranging from white (0, lowest perfusion) to red (1, highest perfusion). The relative centers of perfusion along the left-right axes, the dorsal-ventral, and the caudal-cranial axis were calculated by.

$$CoP_x = \frac{1}{\sum Q_{rel,i}(x,y,z)} \sum_{x=0}^{1} x \cdot \sum_{y,z} Q_{rel,i}(x,y,z)$$

with the three body directions represented by x, y, and z. The coefficient of variation (ratio of the SD to the mean in percent) of mean pulmonary perfusion was calculated to determine the spatial heterogeneity of pulmonary perfusion distribution.

Electrical Impedance Tomography

Electrical impedance tomography measurements were conducted with an operating frequency of 130 kHz and 50 frames s^{-1}. Raw measured EIT data were then filtered at 50 Hz and reconstructed using PulmoVista® 500 (Drägerwerk AG & Co. KGaA, Lubeck, Germany), a commercially available software. Each EIT image of the resulting reconstructed temporal image series consisted of 32 × 32 pi. The reconstruction of these images was carried out as described in detail by the group of authors of this study (Bluth et al., 2019). The global region of interest was a half-sphere covering the left hemisphere of the EIT, thus, only containing the ventilated lung, as described previously (Wittenstein et al., 2020). The center of ventilation was defined as the median of tidal impedance changes (surrogate for ventilation) along the dorsoventral axis and left-right axis of the left lung and expressed as a percentage, with 0% representing most dorsal and most left and 100% most ventral and most central lung zones.

Gas Exchange and Hemodynamics

Arterial and mixed venous blood samples were analyzed using a blood gas analyzer (ABL 80 Flex Basic, Radiometer Medical, Copenhagen, Denmark). The mean arterial and pulmonary artery pressures were measured continuously, and cardiac output was determined with a pulmonary artery catheter using a conventional thermodilution method. Extravascular lung water (EVLW, a surrogate for lung injury), intrathoracic blood volume (ITBV), and global end-diastolic blood volume (GEDV, a surrogate for cardiac preload), systemic vascular resistance (SVR, a surrogate for cardiac afterload), and stroke volume (SV) were determined using the PiCCO catheter. The values were then normalized to body surface area [pulmonary vascular resistance index (PVRI), systemic vascular resistance index (SVRI), global end-diastolic volume index (GEDVI), and

intrathoracic blood volume index (ITBVI), respectively] and body weight [extravascular lung water index (EVLWI)), as reported previously (Kelley et al., 1973). Furthermore, PiCCO was not used to guide fluid treatment, since the normal values of pigs lie outside the reference ranges for humans (Längin et al., 2020).

Respiratory Signals

Airway flow was measured with the internal sensors of the ventilator. On the other hand, airway pressure was measured at the y-piece with a custom-made measurement system composed of a pressure transducer (163PC01D48-PCB; FirstSensors AG, Berlin, Germany) and corresponding hardware and software for amplification and recording (custom-built software written in LabVIEW, National Instruments, Austin, TX, United States). Furthermore, respiratory system elastance (E_{RS}) and resistance (R_{RS}) were determined by the multiple linear regression of the linear equation of motion composed of the R_{RS} and E_{RS} two-compartmental model of the respiratory system.

Statistical Analyses

Sample size calculation was based on the perfusion measurements of relative perfusion distribution by positron-emission tomography using ^{68}Ga-labeled microspheres from a previous study of the group of authors on pigs under two-lung ventilation conditions and different levels of PEEP (Bluth et al., 2019). In this study, we expected that the relative perfusion of the ventilated lung during OLV would be higher than during TLV. Assuming an effect size of 2, we estimated that eight animals per group would yield a power of 80% to detect the difference in the distributions of pulmonary perfusion between TLV and OLV in the supine, semilateral, lateral, and prone positions, with $\alpha = 0.01$ corrected for multiple comparisons. The data were presented as mean and SD if not stated otherwise. The statistical analysis was conducted with SPSS (Version 27, IBM Corp., Armonk, NY, United States). Significance was accepted at $P < 0.05$. The differences between the two groups, respective body positions, and the sequences of interventions were compared using a linear mixed-effects model with repeated measures, using composite ventilation-position (levels: TLVsupine, OLVsupine, OLVsemilateral, OLVlateral, and OLVprone) as the within-subject factor and with group and sequence as between subject-factors. The significance of the within-subject factors was corrected for sphericity according to Greenhouse–Geisser. Pairwise *post-hoc* multiple comparisons were also performed according to least significant difference (LSD) when appropriate.

RESULTS

Characteristics of Animal and Experimental Protocol

Body weight, total time of anesthesia, total time on mechanical ventilation, the cumulative doses of crystalloids and colloids, and total urine output did not differ significantly between normovolemia and hypovolemia, while the cumulative norepinephrine dose was higher in hypovolemia than in normovolemia (**Table 1**). Hemoglobin was not different between the groups ($P = 0.593$). In the hypovolemia group, 755 ± 80 ml of blood was drawn (**Table 1**), resulting in a significant decrease in ITBVI (baseline: 765 ± 79 ml m^{-2} vs. TLVsupine: 619 ± 122 ml m^{-2}; $P = 0.006$) and GEDVI (baseline: 612 ± 63 ml m^{-2} vs. TLVsupine: 496 ± 98 ml m^{-2}; $P = 0.006$) at TLVsupine *vs.* baseline. In all the animals, the LPS infusion resulted in a significant increase in PVRI at TLVsupine vs. baseline (baseline: 150 ± 53 dyn s cm^{-5} m^{-2}; TLVsupine: 365 ± 243 dyn s cm^{-5} m^{-2}; $P = 0.006$) and SVRI (baseline: 1,153 ± 237 dyn s cm^{-5} m^{-2}; TLVsupine: 1,602 ± 579 dyn s cm^{-5} m^{-2}; $P = 0.014$).

TABLE 1 | Characteristics of the animal and experimental protocol.

Variable	Normovolemia	Hypovolemia	*P* =
Body weight [kg]	43.5 ± 1.4	43.1 ± 4.6	0.803
Total anesthesia time [min]	713 ± 52	738 ± 81	0.493
LPS total dose [μg]	178.6 ± 13.6	187.2 ± 25.8	0.422
Aspirated blood volume [ml]	0 ± 0	755 ± 80	≤0.001
Crystalloid infusion [ml kg^{-1}]	47 ± 6	46 ± 10	0.847
Colloids [mlkg^{-1}]	7 ± 6	8 ± 8	0.843
Norepinephrine [μg kg^{-1}]	3 ± 5	52 ± 53	0.036
Cumulative urine output [mL]	945 ± 489	809 ± 303	0.514

Mean ± SD; significance was accepted at P < 0.05. Differences between the two groups were compared by Student's t-test.

Regional Pulmonary Blood Flow (Primary Endpoint)

Compared with TLVsupine, the OLV resulted in the shift of perfusion toward the ventilated left lung, irrespective of position (**Figures 2**, **3**, **Table 2**). During OLV, the relative perfusion of the ventilated lung was higher in the lateral as compared with the supine position, while the relative perfusion of the non-ventilated lung was lower in the lateral position as compared with the supine and prone positions, and in the semilateral compared with the prone position. The relative perfusions of the ventilated and non-ventilated lungs were not different between normovolemia and hypovolemia.

In the ventilated left lung, the center of relative perfusion along the left-right axis shifted toward the hilum during OLVsemilateral, OLVlateral, and OLVprone as compared with OLVsupine. Along the dorsal-ventral axis, the perfusion shifted toward the dorsal during OLVsemilateral, OLVlateral, and OLVprone as compared with OLVsupine. Along the caudal-cranial axis, the perfusion shifted toward the cranial in the semilateral position as compared with TLVsupine. The center of perfusion did not differ between normovolemia and hypovolemia (**Table 2**).

The spatial heterogeneity of relative perfusion in the ventilated left lung was highest during TLVsupine and lowest during OLV in the prone position, while there was no difference between normovolemia and hypovolemia (**Table 2**).

Regional Ventilation (EIT)

In the ventilated left lung, the center of ventilation along the left-right axis shifted toward the lung hilum during OLV in

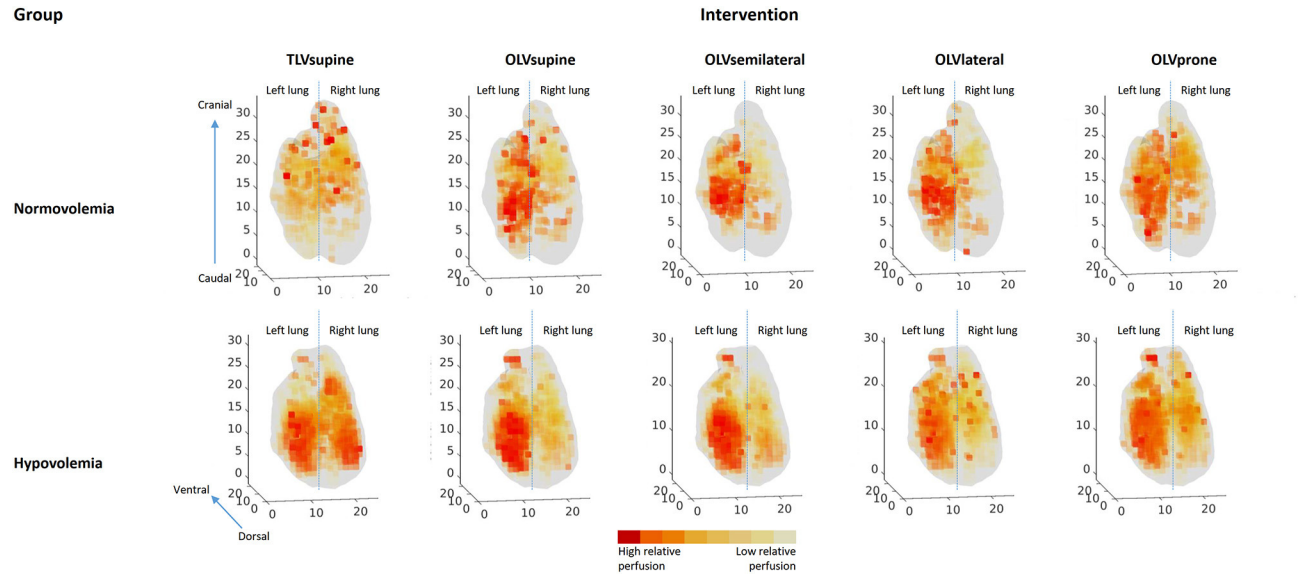

FIGURE 2 | Representative three-dimensional perfusion maps for one animal from each group. Lungs are shown from the dorsal with the left lung on the left side and right lung on the right side. Axes are divided in cm. Lighter colors represent lower relative pulmonary perfusions, while darker colors represent higher relative pulmonary perfusions.

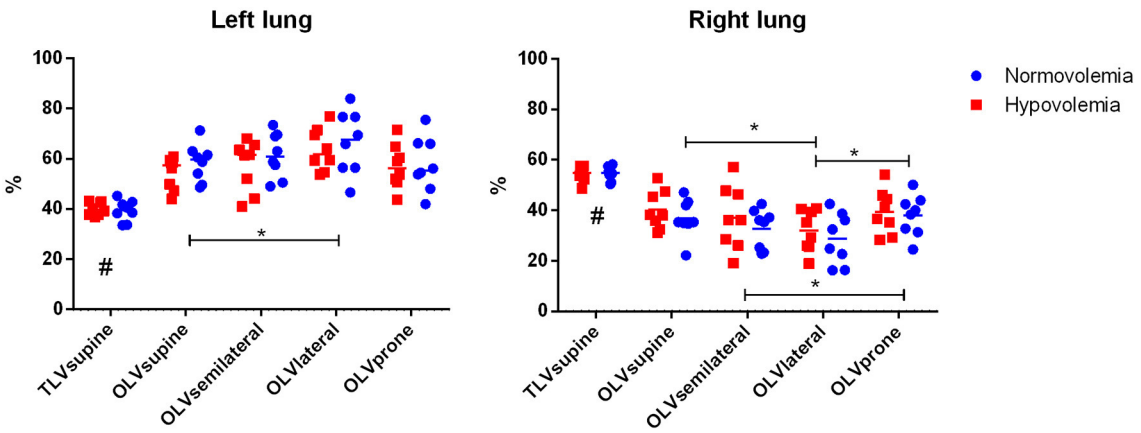

FIGURE 3 | Relative perfusion of the left and right lungs. Mean and single values. Significance was accepted at $P < 0.05$. Differences between the two groups, respective body positions, and the sequences of interventions were compared using a linear mixed-effects model with repeated measures, with TLVsupine, OLVsupine, OLVsemilateral, OLVlateral, and OLVprone as within-subject factors and with group and sequence as fixed between subject-factors. The significance of the within-subject factors was corrected for sphericity according to Greenhouse–Geisser. Pairwise *post-hoc* multiple comparisons were performed according to LSD when appropriate. #$P < 0.05$ TLVsupine vs. all the others, *$P < 0.05$. The relative perfusions of the ventilated and the non-ventilated lungs were not different between normo- and hypovolemia ($P = 0.457$ and $P = 0.418$, respectively). Mixed effects position × group ventilated lung: $P = 0.852$ and mixed effects position × group non-ventilated lung: $P = 0.891$.

all positions as compared with TLVsupine. Furthermore, it also shifted toward the lung hilum during OLV in the prone as compared with the lateral position (**Table 3**). In addition, the center of ventilation along the dorsal-ventral axis of the left lung shifted toward the dorsal during OLV in the prone as compared with the supine position. The center of ventilation along the left-right and dorsoventral axes did not differ among the groups (**Table 3**).

Gas Exchange

The variables of gas exchange are summarized in **Table 4**, where PaO_2/F_IO_2 differed significantly between TLVsupine and OLV in all the positions. It was higher in the lateral as compared with the other positions during OLV, while there was no difference between normovolemia and hypovolemia. Additionally, $PaCO_2$ in the arterial blood gas analysis differed significantly between TLVsupine and OLV in all the positions, while it was not

TABLE 2 | Perfusion of the left lung.

Variable	Group	TLVsupine		OLVsupine		OLVsemilateral		OLVlateral		OLVprone		Sequence *P* =	Group *P* =	Position *P* =	ME *P* =
Center of perfusion left-right axis [% from left]	Normo	30.7 ± 5.0	p	28.8 ± 3.6	se, l, p	31.6 ± 2.6	p	31.1 ± 4.2	p	32.8 ± 2.6		0.614	0.695	≤0.001	0.368
	Hypo	28.5 ± 4.9		29.0 ± 3.3		29.9 ± 3.5		30.8 ± 3.1		33.4 ± 2.7					
Center of perfusion dorsal-ventral axis [% from dorsal]	Normo	27.5 ± 3.6		28.9 ± 3.0	sl, l, p	27.1 ± 3.1		27.3 ± 2.9		27.5 ± 3.0		0.673	0.948	0.025	0.627
	Hypo	27.5 ± 4.4		28.3 ± 3.9		27.7 ± 4.1		27.5 ± 3.3		27.7 ± 3.8					
Center of perfusion caudal-cranial axis [% from caudal]	Normo	45.4 ± 6.0	sl	46.0 ± 5.2		46.8 ± 4.6		46.1 ± 4.7		45.2 ± 3.1		0127	0.462	0.048	0.444
	Hypo	42.9 ± 3.7		44.2 ± 4.1		46.1 ± 4.5		45.0 ± 4.0		45.3 ± 3.5					
CV of relative perfusion %	Normo	157.9 ± 19.1	sl, l, p	154.4 ± 11.2		151.4 ± 15.9		147.2 ± 10.3		139.4 ± 10.4	s, se	0.026	0.075	≤0.001	0.104
	Hypo	180.0 ± 24.3		153.4 ± 14.7		152.9 ± 14.9		145.4 ± 8.4		143.8 ± 8.0					

Mean ± SD; Normo, normovolemia group; Hypo, hypovolemia group; TLV, two-lung ventilation; OLV, one-lung ventilation; CV, coefficient of variation; ME, mixed effects position × group. Significance was accepted at P < 0.05. The differences between the two groups, respective body positions, and the sequences of interventions were compared using a linear mixed-effects model with repeated measures, with TLVsupine, OLVsupine, OLVsemilateral, OLVlateral, and OLVprone as within-subject factors and with group and sequence as fixed between subject-factors. The significance of the within-subject factors was corrected for sphericity according to Greenhouse–Geisser. Pairwise post-hoc multiple comparisons were performed according to least significant difference (LSD) when appropriate. s P < 0.05 vs. OLVsupine, se P < 0.05 vs. OLVsemilateral, l P < 0.05 vs. OLVlateral, and p P < 0.05 vs. OLVprone.

TABLE 3 | Electrical impedance tomography of the left lung.

Variable	Group	TLVsupine		OLVsupine		OLVsemilateral	OLVlateral		OLVprone		Sequence *P* =	Group *P* =	Position *P* =	ME *P* =
CoVleftright [% from left)	Normo	51.1 ± 3.9	s, se, l, p	50 ± 3.6		56.5 ± 4.3	55 ± 3.7	p	54.8 ± 3.4		0.527	0.456	≤0.001	0.743
	Hypo	51.6 ± 3.2		51.8 ± 3.4		56.5 ± 1.8	56.3 ± 2.3		54.3 ± 3.6					
CoVdorso-ventral [% from dorsal]	Normo	49.6 ± 1.9		49.2 ± 1.6	p	49.8 ± 1.5	49.6 ± 1.4		48.9 ± 1.4		0.822	0.636	0.040	0.958
	Hypo	49.1 ± 2.2		49.3 ± 1.6		50 ± 1.2	50 ± 1		49.4 ± 1.8					

Mean ± SD; Normo, normovolemia group; Hypo, hypovolemia group; TLV, two-lung ventilation; OLV, one-lung ventilation; CoV, center of ventilation along the left-right and dorso-ventral axes; ME, mixed effects position × group. Significance was accepted at P < 0.05. Differences between the two groups, respective body positions, and the sequences of interventions were compared using a linear mixed-effects model with repeated measures, with TLVsupine, OLVsupine, OLVsemilateral, OLVlateral, and OLVprone as within-subject factors and with group and sequence as fixed between subject factors. The significance of the within-subject factors was corrected for sphericity according to Greenhouse–Geisser. Pairwise post-hoc multiple comparisons were performed according to LSD when appropriate. s P < 0.05 vs. OLVsupine, se P < 0.05 vs. OLVsemilateral, l P < 0.05 vs. OLVlateral, and p P < 0.05 vs. OLVprone.

different for the different positions during OLV, and there was no group difference. Arterial pH also differed significantly between TLVsupine and OLV in all the positions, while it was similar in the different positions during OLV. Arterial pH was lower in hypovolemic as compared with normovolemic animals. Mixed venous oxygen saturation was significantly different between TLVsupine and OLVsupine and between OLVsemilateral and OLVprone. Furthermore, the mixed venous oxygen saturation was higher during OLVlateral compared with OLVsupine and OLVprone. There was no difference between the two groups.

Hemodynamic and Respiratory Variables

Hemodynamic and respiratory variables are summarized in the (**Supplementary Material Tables 1**, **2**).

DISCUSSION

In a model of thoracic surgery and OLV with normovolemia and moderate hypovolemia in pigs, we found that (1) the relative pulmonary blood flow of the ventilated lung was highest in the lateral position and lowest in the supine position; (2) the relative pulmonary blood flow of the non-ventilated lung was lowest in the lateral position and highest in the supine and prone positions; (3) the spatial heterogeneity of pulmonary blood flow of the ventilated lung was lowest in the prone position; (4) PaO_2/F_IO_2 during OLV was highest in the lateral position; and (5) hypovolemia did not influence the distribution of perfusion, irrespective of body position.

To the knowledge of the authors, this is the first *in vivo* study that systematically investigated the effects of body position and intravascular volume status on the distribution of relative pulmonary perfusion during OLV in a clinically relevant model of thoracic surgery. Previous physiological studies have investigated the effects of OLV through either a closed chest or minor surgeries (Bardoczky et al., 2000; Szegedi et al., 2010). In contrast, major surgeries trigger the inflammatory cascade (Hannon et al., 1990; Kiss et al., 2019), which can blunt HPV (Himmat et al., 2018) and interfere with the distribution of pulmonary perfusion. We also used LPSs to mimic the inflammatory response to major thoracic surgery, which was previously shown to reliably reduce hypoxic pulmonary vasoconstriction (Reeves and Grover, 1974; Theissen et al., 1991) while not altering hemodynamics significantly (Traber et al., 1989). Another strength of this study is that normovolemia and moderate hypovolemia (Silva et al., 2013), both of which may occur during thoracic surgery (Nakamura et al., 2015) and can influence HPV (Deem et al., 1995), were addressed. We chose the left semilateral and lateral decubitus positions because of the fact that the effects of mediastinal compression are more pronounced in the left than in the right semilateral and lateral positions (Chang et al., 2002).

Effects of Body Position on Regional Pulmonary Perfusion and Ventilation

The finding that the relative perfusion of the ventilated lung was highest in the lateral decubitus position during OLV is in line with clinical data (Bardoczky et al., 2000; Szegedi et al., 2010). In the lateral decubitus position, gravitational

TABLE 4 | Gas exchange.

Variable	Group	BL	TLVsupine		OLVsupine		OLVsemilateral	OLVlateral		OLVprone	Sequence *P* =	Group *P* =	Position *P* =	ME *P* =
pHa	Normo	7.38 ± 0.04	7.39 ± 0.03	s, se, l, p	7.29 ± 0.08	l	7.28 ± 0.1	7.31 ± 0.08		7.29 ± 0.08	0.481	0.304	≤0.001	0.629
	Hypo	7.42 ± 0.07	7.39 ± 0.06		7.23 ± 0.13		7.25 ± 0.11	7.26 ± 0.12		7.25 ± 0.11				
$PaCO_2$ [mmHg]	Normo	54 ± 6	53 ± 5	s, se, l, p	65 ± 13		66 ± 12	63 ± 11		64 ± 13	0.464	0.425	≤0.001	0.273
	Hypo	50 ± 12	51 ± 7		72 ± 17		69 ± 13	69 ± 15		69 ± 15				
F_IO_2/PaO_2 [mmHg]	Normo	509 ± 50	562 ± 45	s, se, l, p	78 ± 18		89 ± 20	123 ± 45	s, se, p	78 ± 9	0.936	0.878	≤0.001	0.940
	Hypo	504 ± 105	565 ± 64		85 ± 26		80 ± 24	101 ± 14		94 ± 24				
SaO_2 [%]	Normo	100 ± 1	99 ± 4	s, se, l, p	90 ± 7		91 ± 6	95 ± 5	s	91 ± 8	0.862	0.578	≤0.001	0.603
	Hypo	100 ± 1	100 ± 0		85 ± 10		90 ± 9	94 ± 5		89 ± 8				
SvO_2 [%]	Normo	77 ± 7	78 ± 12	s, se, p	64 ± 9		64 ± 10	76 ± 9	s, p	65 ± 13	0.862	0.578	≤0.001	0.459
	Hypo	78 ± 6	79 ± 6		62 ± 14		65 ± 12	67 ± 12		61 ± 16				

Mean ± SD; Normo, normovolemia group; Hypo, hypovolemia group; BL, baseline; TLV, two-lung ventilation; OLV, one-lung ventilation; pHa, arterial pH, F_IO_2, fraction of inspired oxygen; PaO_2, arterial partial pressure of oxygen; $PaCO_2$, arterial partial pressure of carbon dioxide, SaO_2, arterial oxygen saturation; SvO_2, mixed venous oxygen saturation; ME, mixed effects position × group. Significance was accepted at $P < 0.05$. Differences between the two groups, respective body positions, and the sequences of interventions were compared using a linear mixed-effects model with repeated measures, with TLVsupine, OLVsupine, OLVsemilateral, OLVlateral, and OLVprone as within-subject factors and with group and sequence as fixed between subject-factors. The significance of the within-subject factors was corrected for sphericity according to Greenhouse–Geisser. Pairwise post-hoc multiple comparisons were performed according to LSD when appropriate. s $P < 0.05$ vs. OLVsupine, se $P < 0.05$ vs. OLVsemilateral, l $P < 0.05$ vs. OLVlateral, and p $P < 0.05$ vs. OLVprone.

forces, in addition to HPV, reduce the blood flow of the non-ventilated lung. Furthermore, HPV also allows ventilation-perfusion matching by reducing perfusion to poorly oxygenated lung tissue through smooth muscle contractions in primarily low-resistance pulmonary arteries (Weir et al., 2005). In addition to HPV, hypercapnic pulmonary vasoconstriction (HCPV) reduces perfusion to hypo-ventilated and, therefore, hypercapnic lung regions (Dorrington et al., 2010). In the supine and prone positions, HPV, HCPV, and regional mechanical forces determine regional pulmonary perfusion, while gravity does not influence the shift of perfusion toward the ventilated lung (Szegedi et al., 2010). In addition to the geometry of the vascular tree, which branches asymmetrically (Glenny and Robertson, 2011) regional mechanical forces in the ventilated lung determine the distribution of pulmonary blood flow. Regional mechanical forces are defined by tissue deformation, thorax shape (Tawhai et al., 2009), and mechanical ventilation (Alfery et al., 1981). High airway pressures can divert the blood flow from the ventilated to the non-ventilated lung by compressing the capillaries. In fact, peak, mean, and plateau airway pressures were higher during OLVsupine as compared with OLVlateral, possibly contributing to lower relative perfusion of the ventilated lung in this position.

HPV, HCPV, gravity, and regional mechanical forces as well as lung volume do not only influence the distribution of blood flow toward the ventilated and non-ventilated lung but also determine its regional distribution within the ventilated lung. In fact, during OLV, the lateral position center of perfusion along the left-right axis shifted toward the lung hilum as compared with the supine position, while the center of ventilation along the left-right axis shifted toward peripheral lung areas as compared with the supine position, possibly resulting in improved ventilation-perfusion matching. This might represent another mechanism of better gas exchange for this body position during OLV.

During OLV in the semilateral position, HPV is augmented by gravity. In line with our results, in a small clinical trial arterial saturation as a surrogate for regional pulmonary perfusion was not different between semilateral and lateral position (Watanabe et al., 2000). Thirty-three adult patients undergoing right thoracotomy with left OLV were divided into three groups: supine position ($n = 11$), left semilateral decubitus position ($n = 9$), and left lateral decubitus position ($n = 13$). The final PaO_2 and SaO_2 at the end of the OLV were lowest in the supine position, while there was no difference between the semilateral and lateral decubitus positions (Watanabe et al., 2000).

Gas Exchange

The fact that PaO_2/F_IO_2 was higher during OLV in lateral as compared with the supine, semilateral, and prone positions can be explained by the differences in regional pulmonary perfusion, namely, the lower perfusion of the non-ventilated lung and the better ventilation-perfusion matching of the ventilated lung. The gas exchange itself, especially hypercapnia, may influence intrapulmonary shunt and HPV (Benumof et al., 1976). However, $PaCO_2$ did not differ significantly during OLV in the four positions and the groups. Nevertheless, arterial pH was lower in the hypovolemia group. Furthermore, lower arterial pH has the potential to increase HPV (Brimioulle et al., 1990). In this study, the lower arterial pH in the hypovolemia group might have counteracted the deleterious effects of hypovolemia on HPV, resulting in similar regional perfusions for both groups. However, the differences in the arterial pH between the groups were small and most likely clinically irrelevant.

Intravascular Volume Status

The finding rejects the hypothesis that intravascular hypovolemia influences regional pulmonary perfusion, which is in contrast with previous studies. In isolated rat lungs perfused with plasma, HPV was weakened, when compared with lungs perfused with blood (McMurtry et al., 1977; Deem et al., 1998). Similar results were found in isolated rat, cat, and rabbit lungs (Hakim and Malik, 1988). In this experiment, we performed low-dose LPS infusions in both groups, which altered pulmonary vascular resistance (Theissen et al., 1991), possibly masking the further effects of acute intravascular hypovolemia on the distribution of pulmonary perfusion. As stated, during OLV in the supine and prone positions, the distribution of regional perfusion to the ventilated and non-ventilated lungs is mainly determined with HPV, HCPV, and lung volume, with gravity playing a minor role. Therefore, the most pronounced effects of acute intravascular hypovolemia would be expected in these positions. However, even in OLVsupine and OLVprone, we found no differences between the groups, supporting the claim that an acute moderate hemorrhage during thoracic surgery only has a minor effect on the distribution of pulmonary perfusion.

Possible Clinical Implications

The results suggest that the lateral decubitus position may serve as a means to improve the distribution of perfusion and oxygenation during OLV. In fact, during OLV in the supine, semilateral, and prone positions, but not the lateral decubitus position, the central venous oxygen saturation was lower than 70%, indicating tissue hypoxia (Sevuk et al., 2016) in the normovolemia group. Interestingly, moderate hypovolemia did not influence the distribution of perfusion and shunting, challenging the concept that the intravascular volume expansion in patients with volume depletion might be useful for the reversal of hypoxemia during OLV.

Limitations

This study has several limitations. First, the thoracic surgery model did not fully represent the clinical scenario, especially because of the lack of the surgical manipulation of the lungs and its potential effects on atelectasis in the dependent lung and pulmonary vascular resistance. Furthermore, the absolute values of ITBVI, GEDVI, and EVLWI in this study need to be interpreted with caution, since there were no reference tables and they vary between species (Längin et al., 2020). Additionally, HPV is more pronounced in pigs than in humans and other species (Tucker and Rhodes, 2001). Thus, we could not extrapolate the findings directly to human patients. Second, we addressed only the short-term effects of the different body positions during OLV, although OLV is usually limited to short periods. Third, we did not measure lactate as a surrogate of organ hypoxia. However, we determined

mixed venous oxygen saturation, which is an important marker for the oxygen supply of organs (Janotka and Ostadal, 2021).

CONCLUSIONS

During OLV in endotoxemic pigs, the relative perfusion of the ventilated lung and oxygenation were higher in the lateral than the supine position and not impaired by hypovolemia.

DATA AVAILABILITY STATEMENT

The raw data supporting the conclusions of this article will be made available by the authors, without undue reservation.

ETHICS STATEMENT

The animal study was reviewed and approved by Landesdirektion Sachsen, 09105 Chemnitz.

AUTHOR CONTRIBUTIONS

JW, MS, TK, RH, and MG planned and designed the study. JW, MS, XR, DK, ST, RT, and RH conducted the experiments. JW, MS, YC, TB, TK, MS, PR, PP, MG, and RH were involved in the analyses of the data. JW, XR, YZ, DK, ST, RT, YC, JF, SM, and RH cut and soaked the lungs and measured and analyzed fluorescence. JW, MS, MJS, TB, TK, PR, PP, MG, and RH wrote the draft of the manuscript. All authors have read and approved the submitted manuscript, agreed to be accountable for the content of the article, and agreed with its publication.

FUNDING

This study was supported by departmental funds.

ACKNOWLEDGMENTS

We thank the research fellows of the Pulmonary Engineering Group, University Hospital Carl Gustav Carus, and Technische Universität Dresden, Germany, for their assistance in conducting the experiments.

SUPPLEMENTARY MATERIAL

The Supplementary Material for this article can be found online at: https://www.frontiersin.org/articles/10.3389/fphys.2021.717269/full#supplementary-material

REFERENCES

Alfery, D. D., Benumof, J. L., and Trousdale, F. R. (1981). Improving oxygenation during one-lung ventilation in dogs: the effects of positive end-expiratory pressure and blood flow restriction to the nonventilated lung. *Anesthesiology* 55, 381–385. doi: 10.1097/00000542-198110000-00008

Bardoczky, G. I., Szegedi, L. L., d'Hollander, A. A., Moures, J. M., de Francquen, P., and Yernault, J. C. (2000). Two-lung and one-lung ventilation in patients with chronic obstructive pulmonary disease: the effects of position and F(IO)2. *Anesth. Analg.* 90, 35–41. doi: 10.1097/00000539-200001000-00008

Benumof, J. L., Mathers, J. M., and Wahrenbrock, E. A. (1976). Cyclic hypoxic pulmonary vasoconstriction induced by concomitant carbon dioxide changes. *J. Appl. Physiol.* 41, 466–469. doi: 10.1152/jappl.1976.41.4.466

Bluth, T., Kiss, T., Kircher, M., Braune, A., Bozsak, C., Huhle, R., et al. (2019). Measurement of relative lung perfusion with electrical impedance and positron emission tomography: an experimental comparative study in pigs. *Br. J. Anaesth.* 123, 246–254. doi: 10.1016/j.bja.2019.04.056

Brimioulle, S., Lejeune, P., Vachiery, J. L., Leeman, M., Melot, C., and Naeije, R. (1990). Effects of acidosis and alkalosis on hypoxic pulmonary vasoconstriction in dogs. *Am. J. Physiol.* 258, H347–353. doi: 10.1152/ajpheart.1990.258.2.H347

Chang, H., Lai-Fook, S. J., Domino, K. B., Schimmel, C., Hildebrandt, J., Robertson, H. T., et al. (2002). Spatial distribution of ventilation and perfusion in anesthetized dogs in lateral postures. *J. Appl. Physiol.* 92, 745–62. doi: 10.1152/japplphysiol.00377.2001

Deem, S., Bishop, M. J., and Alberts, M. K. (1995). Effect of anemia on intrapulmonary shunt during atelectasis in rabbits. *J. Appl. Physiol.* 79, 1951–1957. doi: 10.1152/jappl.1995.79.6.1951

Deem, S., Swenson, E. R., Alberts, M. K., Hedges, R. G., and Bishop, M. J. (1998). Red-blood-cell augmentation of hypoxic pulmonary vasoconstriction: hematocrit dependence and the importance of nitric oxide. *Am. J. Respir. Crit. Care Med.* 157, 1181–1186. doi: 10.1164/ajrccm.157.4.9707165

Dorrington, K. L., Balanos, G. M., Talbot, N. P., and Robbins, P. A. (2010). Extent to which pulmonary vascular responses to PCO2 and PO2 play a functional role within the healthy human lung. *J. Appl. Physiol.* 108, 1084–1096. doi: 10.1152/japplphysiol.90963.2008

Glenny, R. W., and Robertson, H. T. (2011). Determinants of pulmonary blood flow distribution. *Compr. Physiol.* 1, 39–59. doi: 10.1002/cphy.c090002

Hakim, T. S., and Malik, A. B. (1988). Hypoxic vasoconstriction in blood and plasma perfused lungs. *Respir. Physiol.* 72, 109–121. doi: 10.1016/0034-5687(88)90083-7

Hannon, J. P., Bossone, C. A., and Wade, C. E. (1990). Normal physiological values for conscious pigs used in biomedical-research. *Lab. Anim. Sci.* 40, 293–298.

Hedenstierna, G., Tokics, L., Strandberg, A., Lundquist, H., and Brismar, B. (1986). Correlation of gas exchange impairment to development of atelectasis during anaesthesia and muscle paralysis. *Act aAnaesthesiol. Scand.* 30, 183–191. doi: 10.1111/j.1399-6576.1986.tb02393.x

Himmat, S., Alzamil, A., Aboelnazar, N., Hatami, S., White, C., Dromparis, P., et al. (2018). A decrease in hypoxic pulmonary vasoconstriction correlates with increased inflammation during extended normothermic *ex vivo* lung perfusion. *Artif. Organs.* 42, 271–279. doi: 10.1111/aor.13017

Janotka, M., and Ostadal, P. (2021). Biochemical markers for clinical monitoring of tissue perfusion. *Mol. Cell. Biochem.* 476, 1313–1326. doi: 10.1007/s11010-020-04019-8

Kazan, R., Bracco, D., and Hemmerling, T. M. (2009). Reduced cerebral oxygen saturation measured by absolute cerebral oximetry during thoracic surgery correlates with postoperative complications. *Br. J. Anaesth.* 103, 811–816. doi: 10.1093/bja/aep309

Kelley, K. W., Curtis, S. E., Marzan, G. T., Karara, H. M., and Anderson, C. R. (1973). Body surface area of female swine. *J. Anim. Sci.* 36, 927–930. doi: 10.2527/jas1973.365927x

Kiss, T., Bluth, T., Braune, A., Huhle, R., Denz, A., Herzog, M., et al. (2019). Effects of positive end-expiratory pressure and spontaneous breathing activity on regional lung inflammation in experimental acute respiratory distress syndrome. *Crit. Care Med.* 47, e358–e365. doi: 10.1097/CCM.0000000000003649

Längin, M., Konrad, M., Reichart, B., Mayr, T., Vandewiele, S., Postrach, J., et al. (2020). Hemodynamic evaluation of anesthetized baboons and piglets by transpulmonary thermodilution: normal values and interspecies differences with respect to xenotransplantation. *Xenotransplantation* 27:e12576. doi: 10.1111/xen.12576

McMurtry, I. F., Hookway, B. W., and Roos, S. (1977). Red blood cells play a crucial role in maintaining vascular reactivity to hypoxia in isolated rat lungs. *Chest*. 71(2 suppl):253–256. doi: 10.1378/chest.71.2_Supplement.253

Nakamura, H., Saji, H., Kurimoto, N., Shinmyo, T., and Tagaya, R. (2015). Impact of intraoperative blood loss on long-term survival after lung cancer resection. *Ann. Thorac. Cardiovasc. Surg.* 21, 18–23. doi: 10.5761/atcs.oa.13-00312

Percie du Sert, N., Hurst, V., Ahluwalia, A., Alam, S., Avey, M. T., Baker, M., et al. (2020). The ARRIVE guidelines 2.0: updated guidelines for reporting animal research. *PLoS Biol*. 18:e3000410. doi: 10.1371/journal.pbio.3000410

Reeves, J. T., and Grover, R. F. (1974). Blockade of acute hypoxic pulmonary hypertension by endotoxin. *J. Appl. Physiol*. 36, 328–332. doi: 10.1152/jappl.1974.36.3.328

Sánchez-Pedrosa, G., VaraAmeigeiras, E., Casanova Barea, J., Rancan, L., SimónAdiego, C. M., and GaruttiMartínez, I. (2018). Role of surgical manipulation in lung inflammatory response in a model of lung resection surgery. *Interact. Cardiovasc. Thorac. Surg.* 27, 870–877. doi: 10.1093/icvts/ivy198

Schirren, M., Sponholz, S., Oguhzan, S., Kudelin, N., Ruf, C., Trainer, S., et al. (2015). Intraoperative Blutungen in der Thoraxchirurgie. *Chirurg* 86, 453–458. doi: 10.1007/s00104-015-2999-8

Sevuk, U., Altindag, R., Baysal, E., Yaylak, B., Adiyaman, M. S., Akkaya, S., et al. (2016). The effects of hyperoxaemia on tissue oxygenation in patients with a nadir haematocrit lower than 20% during cardiopulmonary bypass. *Perfusion* 31, 232–239. doi: 10.1177/0267659115595281

Silva, P. L., Guldner, A., Uhlig, C., Carvalho, N., Beda, A., Rentzsch, I., et al. (2013). Effects of intravascular volume replacement on lung and kidney function and damage in nonseptic experimental lung injury. *Anesthesiology* 118, 395–408. doi: 10.1097/ALN.0b013e31827e554c

Szegedi, L. L., D'Hollander, A. A., Vermassen, F. E., Deryck, F., and Wouters, P. F. (2010). Gravity is an important determinant of oxygenation during one-lung ventilation. *Acta Anaesthesiol. Scand*. 54, 744–750. doi: 10.1111/j.1399-6576.2010.02238.x

Takenaka, K., Ogawa, E., Wada, H., and Hirata, T. (2006). Systemic inflammatory response syndrome and surgical stress in thoracic surgery. *J. Crit. Care*. 21, 48–53; discussion 53-55. doi: 10.1016/j.jcrc.2005.07.001

Tawhai, M. H., Nash, M. P., Lin, C.-L., and Hoffman, E. A. (2009). Supine and prone differences in regional lung density and pleural pressure gradients in the human lung with constant shape. *J. Appl. Physiol*. 107, 912–20. doi: 10.1152/japplphysiol.00324.2009

Theissen, J. L., Loick, H. M., Curry, B. B., Traber, L. D., Herndon, D. N., and Traber, D. L. (1991). Time course of hypoxic pulmonary vasoconstriction after endotoxin infusion in unanesthetized sheep. *J. Appl. Physiol*. 70, 2120–2125. doi: 10.1152/jappl.1991.70.5.2120

Traber, D. L., Flynn, J. T., Herndon, D. N., Redl, H., Schlag, G., and Traber, L. D. (1989). Comparison of the cardiopulmonary responses to single bolus and continuous infusion of endotoxin in an ovine model. *Circ. Shock*. 27, 123–138.

Tucker, A., and Rhodes, J. (2001). Role of vascular smooth muscle in the development of high altitude pulmonary hypertension: an interspecies evaluation. *High Alt. Med. Biol.* 2, 173–189. doi: 10.1089/152702901750265288

Watanabe, S., Noguchi, E., Yamada, S., Hamada, N., and Kano, T. (2000). Sequential changes of arterial oxygen tension in the supine position during one-lung ventilation. *Anesth. Analg.* 90, 28–34. doi: 10.1097/00000539-200001000-00007

Weir, E. K., López-Barneo, J., Buckler, K. J., and Archer, S. L. (2005). Mechanisms of disease acute oxygen-sensing mechanisms. *N. Engl. J. Med*. 353, 2042–2055. doi: 10.1056/NEJMra050002

West, J. B., Dollery, C. T., and Naimark, A. (1964). Distribution of blood flow in isolated lung; relation to vascular and alveolar pressures. *J. Appl. Physiol.* 19, 713–724. doi: 10.1152/jappl.1964.19.4.713

Wittenstein, J., Scharffenberg, M., Ran, X., Keller, D., Michler, P., Tauer, S., et al. (2020). Comparative effects of flow vs. volume-controlled one-lung ventilation on gas exchange and respiratory system mechanics in pigs. *Intensive Care Med. Exp*. 8(Suppl. 1):24. doi: 10.1186/s40635-020-00308-0

Conflict of Interest: MG received consultation fees from Dräger, Ambu, GE Healthcare, and ZOLL.

The remaining authors declare that the research was conducted in the absence of any commercial or financial relationships that could be construed as a potential conflict of interest.

Publisher's Note: All claims expressed in this article are solely those of the authors and do not necessarily represent those of their affiliated organizations, or those of the publisher, the editors and the reviewers. Any product that may be evaluated in this article, or claim that may be made by its manufacturer, is not guaranteed or endorsed by the publisher.

frontiers in Physiology

METHODS
published: 14 September 2021
doi: 10.3389/fphys.2021.676118

Using Artificial Intelligence for Automatic Segmentation of CT Lung Images in Acute Respiratory Distress Syndrome

Peter Herrmann[1], Mattia Busana[1], Massimo Cressoni[2], Joachim Lotz[3], Onnen Moerer[1], Leif Saager[1], Konrad Meissner[1], Michael Quintel[1,4] and Luciano Gattinoni[1]*

[1] Department of Anesthesiology, University Medical Center Göttingen, Göttingen, Germany, [2] Unit of Radiology, IRCCS Policlinico San Donato, Milan, Italy, [3] Institute for Diagnostic and Interventional Radiology, University Medical Center Göttingen, Göttingen, Germany, [4] Department of Anesthesiology, DONAUISAR Klinikum Deggendorf, Deggendorf, Germany

Knowledge of gas volume, tissue mass and recruitability measured by the quantitative CT scan analysis (CT-qa) is important when setting the mechanical ventilation in acute respiratory distress syndrome (ARDS). Yet, the manual segmentation of the lung requires a considerable workload. Our goal was to provide an automatic, clinically applicable and reliable lung segmentation procedure. Therefore, a convolutional neural network (CNN) was used to train an artificial intelligence (AI) algorithm on 15 healthy subjects (1,302 slices), 100 ARDS patients (12,279 slices), and 20 COVID-19 (1,817 slices). Eighty percent of this populations was used for training, 20% for testing. The AI and manual segmentation at slice level were compared by intersection over union (IoU). The CT-qa variables were compared by regression and Bland Altman analysis. The AI-segmentation of a single patient required 5–10 s vs. 1–2 h of the manual. At slice level, the algorithm showed on the test set an IOU across all CT slices of 91.3 ± 10.0, 85.2 ± 13.9, and 84.7 ± 14.0%, and across all lung volumes of 96.3 ± 0.6, 88.9 ± 3.1, and 86.3 ± 6.5% for normal lungs, ARDS and COVID-19, respectively, with a U-shape in the performance: better in the lung middle region, worse at the apex and base. At patient level, on the test set, the total lung volume measured by AI and manual segmentation had a R^2 of 0.99 and a bias −9.8 ml [CI: +56.0/−75.7 ml]. The recruitability measured with manual and AI-segmentation, as change in non-aerated tissue fraction had a bias of +0.3% [CI: +6.2/−5.5%] and −0.5% [CI: +2.3/−3.3%] expressed as change in well-aerated tissue fraction. The AI-powered lung segmentation provided fast and clinically reliable results. It is able to segment the lungs of seriously ill ARDS patients fully automatically.

Keywords: ARDS, fully automatic lung segmentation, deep learning, U-Net, LabVIEW, DeepLTK, Maluna, mechanical ventilation

OPEN ACCESS

Edited by:
Lorenzo Ball,
University of Genoa, Italy

Reviewed by:
Alysson Roncally Silva Carvalho,
University of Porto, Portugal
Sarah Gerard,
The University of Iowa, United States
Robert Huhle,
Dresden University of Technology, Germany

****Correspondence:***
Peter Herrmann
pherrmann@med.uni-goettingen.de

Specialty section:
This article was submitted to Respiratory Physiology, a section of the journal Frontiers in Physiology

Received: *04 March 2021*
Accepted: *17 August 2021*
Published: *14 September 2021*

Citation:
Herrmann P, Busana M, Cressoni M, Lotz J, Moerer O, Saager L, Meissner K, Quintel M and Gattinoni L (2021) Using Artificial Intelligence for Automatic Segmentation of CT Lung Images in Acute Respiratory Distress Syndrome. Front. Physiol. 12:676118. doi: 10.3389/fphys.2021.676118

INTRODUCTION

The quantitative analysis of lung tomography [quantitative CT scan analysis (CT-qa)] images has been used extensively for more than 20 years and has significantly improved our knowledge of the pathophysiology of the acute respiratory distress syndrome (ARDS; ARDS Definition Task Force et al., 2012). Indeed, with CT-qa we have clarified how densities are

distributed in ARDS, advancing the concept of the "baby lung" (Gattinoni et al., 1987; Bone, 1993; Gattinoni and Pesenti, 2005), showing how densities redistribute in prone position (Gattinoni et al., 1991; Pelosi et al., 1998; Cornejo et al., 2013), and explaining the mechanisms by which positive end-expiratory pressure (PEEP) acts (Pelosi et al., 1994). Determining the change in the non-aerated tissue fraction at two end-expiratory pressure levels, i.e., 5 and 45 cmH_2O, is considered the gold standard for assessing recruitment in ARDS (Gattinoni et al., 2006). We were recently able to show that CT-qa can also provide valuable information for the respiratory management of COVID-19 (Chiumello et al., 2020). A precise segmentation [the inclusion of a structure into a region of interest (ROI) for the subsequent analysis] of the lung is mandatory for a reliable CT-qa. The actual segmentation procedure in several hospitals required constisten manual intervention. The time requirement and need of expert personal has serious hindered a broder adoption of CT-qa in clinical practice.

The application of machine learning techniques to image processing is currently of rapidly growing interest in the medical community (Seo et al., 2020a). Artificial neural networks (ANN) are a subfield of machine learning in which the underlying mathematical algorithm simulates the organization of the brain. By doing so, increasingly complicated tasks, such as voice and face recognition, recommender systems etc., which, until recently were considered impossible for a machine, have become part of our everyday life. The term deep learning (DL) goes back to around 2006 (Hinton et al., 2006). LeCun et al. (2015) explained DL in detail in 2015. Goodfellow et al. (2018) published an excellent textbook on DL in 2018. DL uses ANNs with many hidden layers. The larger the amount of data, the better DL works. Certain neural Network architectures such as the so-called convolutional neural networks (CNNs) are used specifically for image recognition. DL with CNNs are very common in medicine today (Chartrand et al., 2017; Litjens et al., 2017; Suzuki, 2017; Yasaka et al., 2018; Currie et al., 2019; Chassagnon et al., 2020; Al-Fatlawi et al., 2021; Guimarães et al., 2021; Jünger et al., 2021; Schwartz et al., 2021; Sułot et al., 2021; Wang C. et al., 2021; Yi et al., 2021).

There are two interesting CNN architectures for image segmentation. The "SegNet" developed by Badrinarayanan et al. (2017) and the U-Net developed by Ronneberger et al. (2015). SegNet was developed as an efficient architecture for semantic pixel-wise segmentation. It is primarily developed to recognize and classify in street scenes, streets, sidewalks, buildings, cars and pedestrians. SegNet was already used for Medical Image Segmentation (Sravani, 2019; Almotairi et al., 2020; Hu et al., 2020; Lei et al., 2021). The U-Net, was mainly developed for segmenting neuronal structures in electron microscopic stacks and light microscopic cell and tissue sections and works very effectively with comparatively little training data. In recent years, U-Net has been used successfully in medicine to segment certain structures and organs in chest x-rays and CT images (Zhou et al., 2018; Alom et al., 2019; Dong et al., 2019; Jeong et al., 2019; Hojin et al., 2020; Seo et al., 2020b; Umapathy et al., 2020; Causey et al., 2021; Ghosh et al., 2021; Wang Z. et al., 2021; Yan and Zhang, 2021). Some working groups have also segmented lungs in the CT images (Skourt et al., 2018; Park et al., 2020; Zhou et al., 2020; Chen et al., 2021; Jalali et al., 2021; Kumar Singh et al., 2021; Qiblawey et al., 2021). In a current publication, in the course of the COVID-19 pandemic, lung CT image segmentation with SegNet and U-Net was compared with each other, whereby the lungs segmented better with U-Net (Saood and Hatem, 2021). Gerard et al. (2020, 2021) developed a multi-resolution 3D-SegNet-CNN for the segmentation of inflamed, fibrotic and also ARDS lungs from the CT. This very interesting model consists of a high-res and a low-res Network and showed very good results. Seg3DNet is a fully convolutional CNN, but it uses less memory than SegNet and U-Net and can therefore process 3D images. There are now several modifications of the U-Net, such as U-Net ++ (Zhou et al., 2018), Res-U-Net (Umapathy et al., 2020), Recurrent Res-U-Net (Alom et al., 2019), 3D U-Net (Park et al., 2020), and more. Hofmanninger et al. (2020) trained a U-Net with 231 clinical cases (231 volumes with 108,248 slices). This data set contained different pathologies, reconstruction kernels, slice thicknesses, etc. This 2D U-Net231 showed surprisingly good results in the lung series tested. Hofmanninger et al. were able to show that automatic lung segmentation in routine clinical imaging is primarily a problem of data diversity. This was a very interesting aspect for us because we are working with clinical data. Due to the complexity of Networks such as 3DSegNet or the U-Net modifications, we decided to implement the 2D-U-Net.

The successful application of DL to the segmentation process of CT lung images in ARDS would greatly increase the use of CT-qa. It would become available to clinical practice for monitoring relevant variables, such as the size of the lung, the severity of lung injury, hyperinflation, recruitability, differentiate atelectatic and consolidated tissue, and assess parenchymal homogeneity. We developed a DL algorithm, based on the graphical programming language LabVIEW to automatically and efficiently analyze and segment acutely injured lungs over the full spectrum of ARDS severity.

MATERIALS AND EQUIPMENT

Dataset Descriptions

The CT scan dataset used in this study (n patients = 100, n slices = 12,279) was extracted from an ARDS dataset in which we included the patients enrolled into different trials or physiological studies from 2003 to 2018 the Policlinico Hospital in Milan. The CTs of these ARDS patients were taken during an end inspiratory pause at 45 cm of water (recruitment) and at 5 and 15 cm of water during end expiratory pressure. The CT scan of these patients were performed within 4.1 $\pm$ 2.6 days after admission into the hospital. To this ARDS group, we added acquired CT scans from 20 COVID-19 patients (n slices = 1,817) from the San Paolo hospital, Milan and CT scans from 15 patients with normal lungs (n slices = 1,302) from the Medical University of Göttingen. From the included patients, we obtained 15,398 CT slices which were all manually segmented. We did not exclude any lung slice. Computed Tomography scans from eighty percent of the patients, randomly selected (n patients = 108, n slices = 11,932)

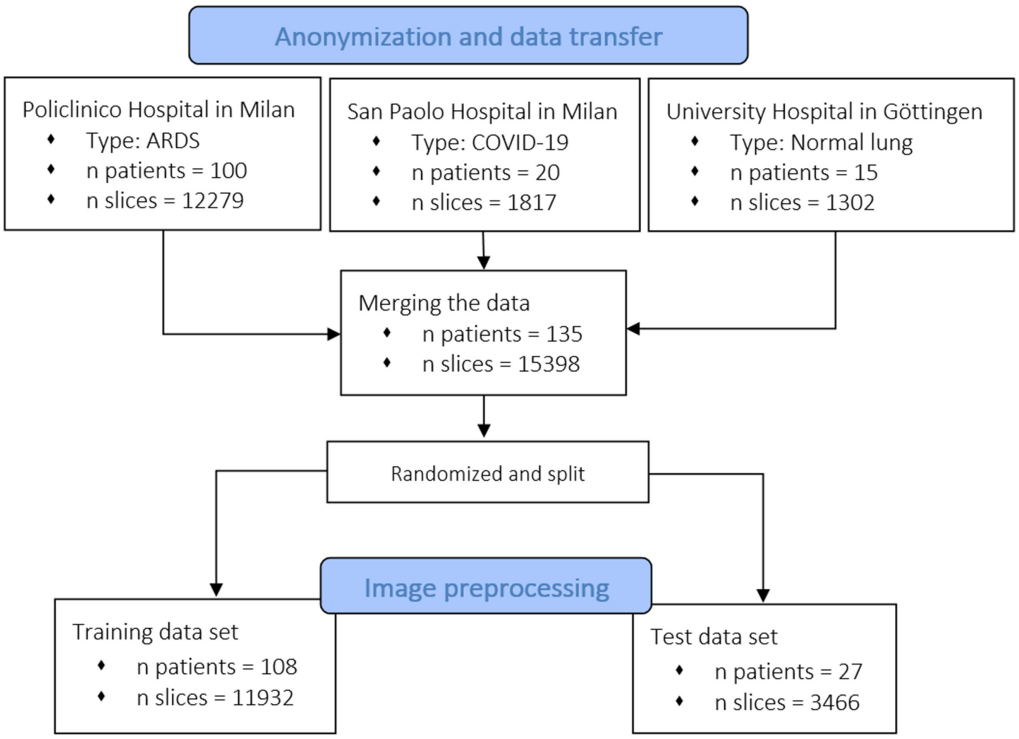

FIGURE 1 | Flowchart of the inclusion of patients and related CT scans. We collected data from different centers, from healthy and acute respiratory distress syndrome (ARDS) lungs. As shown, the model was also trained and tested with recently acquired COVID-19 lungs.

were used for training of the algorithm and the remaining 20% (*n* patients = 27, *n* slices = 3,466) for the testing dataset. The characteristics of the dataset used in this study are summarized in **Figure 1** and the characteristics of the patient population are presented in **Table 1**. The technical characteristics of the CT used to acquire the images are reported in **Table 2**. The ethics committee was notified and permission to use the data was granted (Göttingen Application Number 14/12/12).

Hardware and Software Used

We used a DELL Precision 5820 Tower with 32 GB RAM, a 3.70 GHz Intel (R) Xeon (R) W-2135 CPU and Windows 10 64-bit operating system. An Nvidia Quadro P 5000 with 16 GB GDDR5 RAM and 2560 CUDA cores was used as the graphics card. We used the same hardware for segmentation, quantitative analysis, and training. The U-Net was programmed with LabVIEW, NI-Vision (NI, Austin, TX, United States) and the Add-On Toolkit DeepLTK (Ngene, Yerevan, Armenia). There are many frameworks for DL (Caffe, Keras, TensorFlow, Theano, and Torch) on the market, but they mainly support the Python and C/C++ programming language. The DL toolkit, developed by Ngene, is a high abstraction level API providing the possibility to build, configure, train, evaluate and deploy deep neural Networks in the LabVIEW programming environment

TABLE 1 | Summary of the datasets used to train and test the convolutional neural network.

	Train dataset		Test dataset		Sum	
	Patients (n°)	Slices (n°)	Patients (n°)	Slices (n°)	Patients (n°)	Slices (n°)
Normal lung	8	716	7	586	15	1,302
ARDS	89	10,222	11	2,057	100	12,279
COVID-19	11	994	9	823	20	1,817
Sum	108	11,932	27	3,466	135	15,398

TABLE 2 | Technical characteristics of the CT scanner used.

Hospital	San Paolo Hospital Milan	Policlinico Hospital Milan	University Hospital Göttingen	
CT Scanner	GE Light Speed Qx/i	Siemens Somaton Definiton Flash	GE Lightspeed VCT	Siemens Sensation 16
KVP	120 kV, 140 kV	120 kV, 140 kV	140 kV	120 kV, 140 kV
Slice Thickness	2.0, 2.5, and 5.0 mm	5.0 mm	5.0 mm	5.0 mm
Pixel Spacing	0.6–0.8 mm	0.6–0.7 mm	0.6–0.7 mm	0.6–0.7 mm
Convolution Kernel	STANDARD	B30f, B31f, B40f	LUNG	B41f, B75f
Filter Type	BODY FILTER	0, FLAT, WEDGE_3	BODY FILTER	0
Patient Position	FFS, HFS	FFS	FFS	FFS, HFS

(Ngene, 2021). The GPU acceleration functionality of the toolkit is based on Nvidia's CUDA and CUDNN toolkit, by calling corresponding shared libraries. CUDA is a parallel computing platform and programming model using a GPU for general purpose computing, and CUDNN is a GPU-accelerated library of primitives for deep neural Networks.

METHODS

Image Preprocessing

Anonymized CT scans of the lungs obtained in the Policlinico Hospital Milan, San Paolo Hospital Milan and the University Hospital Göttingen were stored in DICOM (Digital Imaging and COmmunication in Medicine) format (*.dcm) on DVD data carriers. In addition, a corresponding file with the coordinates of the manually drawn ROI was saved for each DICOM file (*.xroi). These *.xroi files were created as follows. All reference segmentations (ground truth) were carried out manually and/or semi-automatically by experienced intensive care physicians using our own software (Maluna 3.14, Maluna 2020). The coordinates of these lung masks were then saved for each CT in a so-called *.xroi file (same file name as the Dicom image file name). They are loaded automatically when the DICOM image is loaded and placed as an ROI over the original image. Lung-specific calculations can be carried out within this ROI.

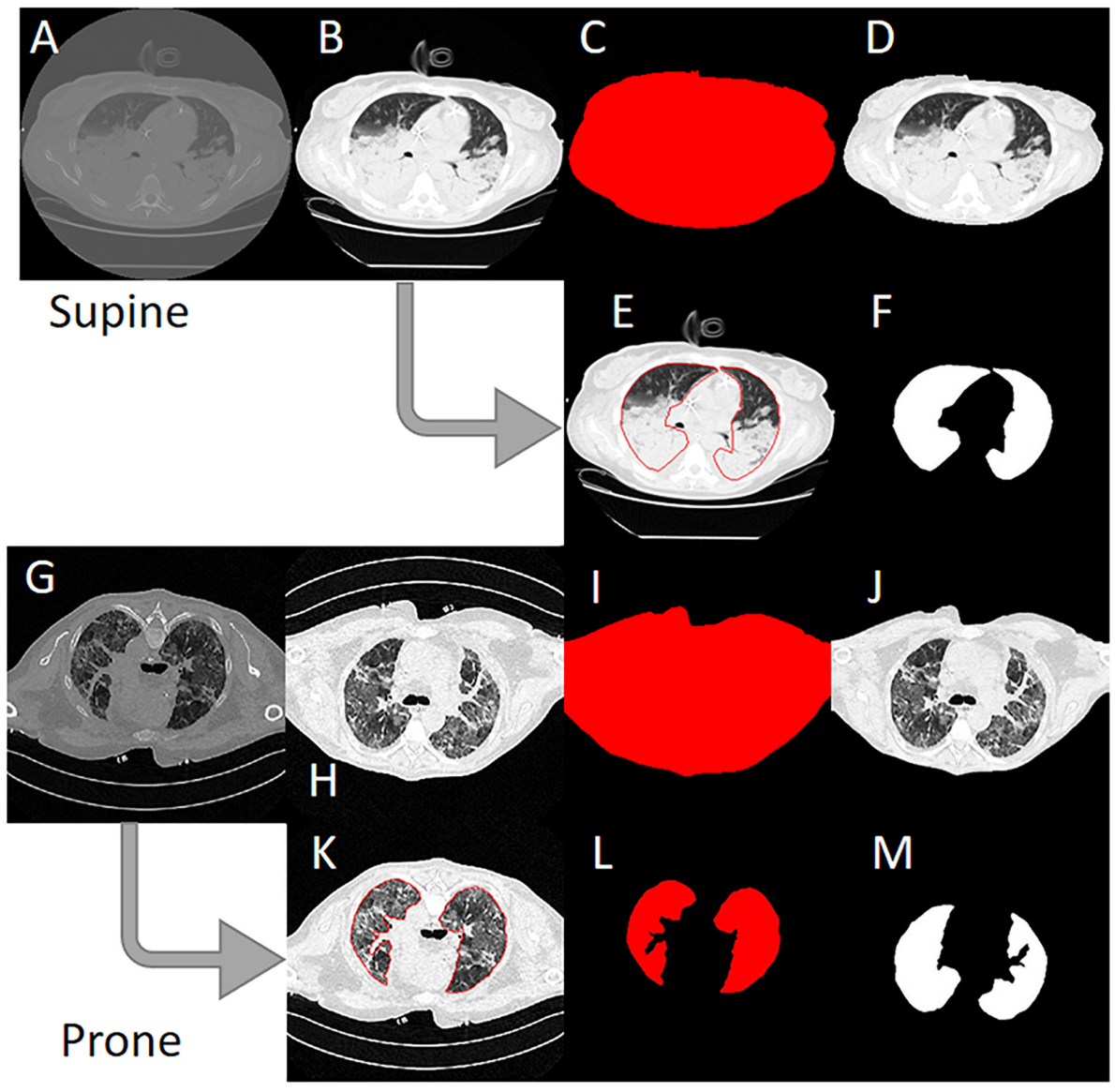

FIGURE 2 | Image preprocessing steps to create the input data for the artificial neural network. **(A)** Original 16-bit gray value Digital Imaging and COmmunication in Medicine (DICOM) image. **(B)** 16-bit HU image. **(C)** 8-bit image. **(D)** Binary thorax mask. **(E)** Masked image. **(F)** Normalized image. **(G)** Manually drawn ROI. **(H)** Binary mask created from the region of interest (ROI). **(I)** Normalized lung mask (ground truth). **(K)** Rotated prone image. **(L)** Rotated prone mask.

Before the ANN could be trained with the lung CTs, the original DICOM images were preprocessed (**Figure 2**). In a first step, the gray values were converted into Hounsfield units (HUs) from the original 16-bit DICOM image (A,G) using the DICOM attributes "Rescale Intercept" (×0028, ×1,052) and "Rescale Slope" (×0028, ×1,053). The resulting image was then scaled to the range −1,024 HU to +100 HU and then converted into an 8-bit image (B,H). An 8-bit image is one with 256 levels of gray. A binary thorax mask was created (C, I) using a threshold and particle filter (Klapsing et al., 2017). Image B (H) was then masked in order to remove superfluous information from the image (D, J). In the final step, the pixels were normalized to the range between −1 and +1. This was done by subtracting 128 from each pixel and then dividing the result by 128.

To create the lung mask (known as "ground truth"), the ROI coordinates loaded from the *.xroi file drawn as an ROI in image E (K) are converted into a binary mask (F, L). Then, as with the lung image, the mask is normalized to the range −1 to +1 (I). For the CT images that were not obtained with the patient in the supine position, the images and masks were rotated accordingly (H, I M). To check the position of the patient, we used the DICOM attribute "patient position" (×0018, ×5,100). A total of 11,932 images and their manually generated ROI coordinates were preprocessed in this way and then loaded into the ANN. The image preprocessing was carried out with our own software Maluna 2020.

The ANN

Structure of the ANN

The network we use is based on the U-Net architecture. The U-Net was programmed with the graphical programming language LabVIEW, with which we had many years of experience in the development of software for image analysis. The unique concept of U-Net is that it is able to generate a new, altered image as the output from an input image, after appropriate processing. This is very useful for generating segmentation images. The U-Net is a so-called fully convolutional network. Our U-Net programmed with LabVIEW is shown in **Figure 3**.

The architecture has a symmetric "U" shape and consists of two major parts: a contraction path (left side) and an expansion path (right side). The path follows the typical architecture of a convolution neural network. It consists of the repeated application of two convolution layers, each layer with batch normalization, followed by an activation function. In all convolution layers we use a filter kernel size of 3 × 3 pixels. For each convolution we used the so called "SAME" padding type, which means there is automatically enough padding that the output image of the convolution layer has the same dimensions as the input image.

In the original U-Net by Ronneberger, the image is filtered twice with 64 convolution filters in the first level of the contraction path. Due to insufficient graphics memory, we had to modify the original U-Net a bit. In the first level of the contraction path, the preprocessed lung CT image is therefore filtered twice with only 32 different convolution kernels. We used a filter kernel size of 3 × 3 pixels. A copy of this batch of 32 filtered images is transferred to the right part of the network. In the original U-Net, the next step is a max pooling layer for down sampling. We used a 3 × 3 convolution layer with stride 2, which halves the size of the input image (from 512 × 512 to 256 × 256 pixels) and doubled in the number of filtered images (from 32 to 64 images or channels). This principle, i.e., twice convolution filtering, halving the image size, and doubling the number of channels, is followed until we finally get a stack of 1,024 channels with a size of 16 × 16 pixels (this size is approximately in the range of an acinus). Since these small images no longer have any resemblance to the original image, but show certain extracted properties of the image, i.e., corners, edges, structures, they are also referred to as feature maps. These feature

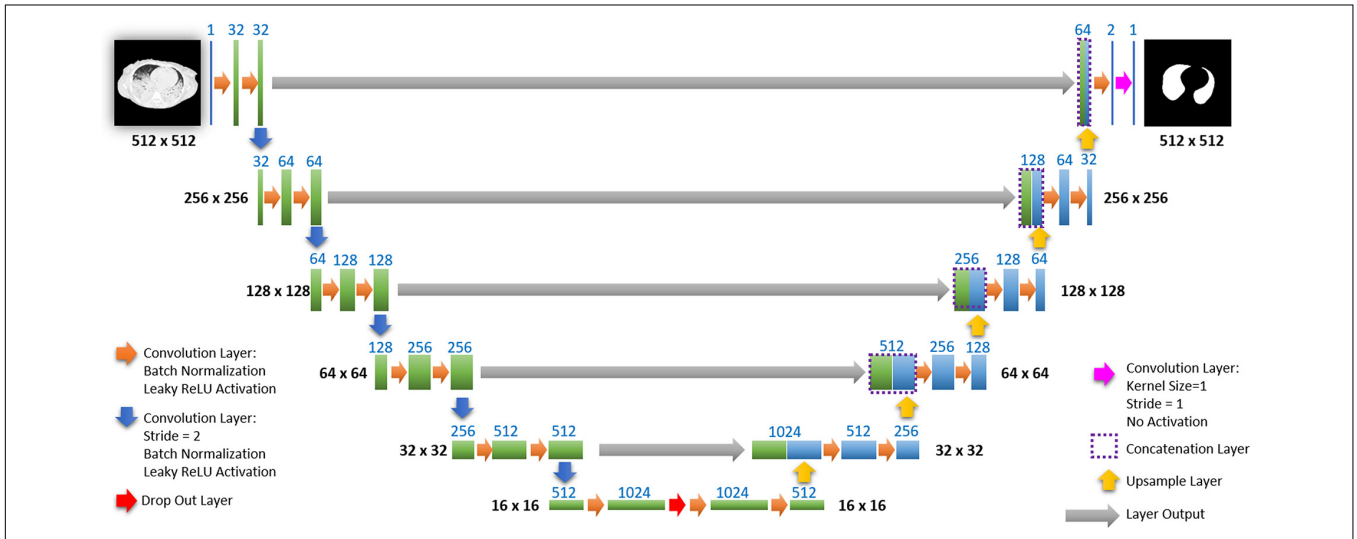

FIGURE 3 | Our used U-Net architecture. Each green or blue box corresponds to a multi-channel feature map. The number of channels is shown above the box. The specifications 512 × 512 to 16 × 16 (in the lowest resolution) show the *x*, *y* dimensions in pixels of the input and output images (or feature maps).

maps are processed further in the expansion path (right part) of the U-Net.

Each step on the expansion path consists of upsampling the feature map, followed by a convolution layer ("up-convolution") which halves the number of feature channels and doubles the size of the input image. Then, a concatenation is carried out with the corresponding feature map from the contraction path (left part of the U-Net) followed by two convolution layers with batch normalization and an activation function. In the lowest path with the lowest resolution (16 × 16 pixels, 1,024 feature channels) a drop-out layer (with probability set to 0.4) was programmed between two convolutional layers.

Preprocessed lung CT-images are input to the contracting path, and lung mask predictions are output from a final layer following the expansive path. This final output layer is a 1 × 1 convolutional layer with no activation and a single filter. Batch normalization and dropout are proven methods of avoiding overfitting with CNNs (Srivastava et al., 2014; Ioffe and Szegedy, 2015).

Convolution Layers

The input image is first processed by a set number of convolution filters that have a fixed pixel size. In our case the size was 3 × 3 pixels. This filter then moves in a constant step size (stride) like a window from left to right over the pixels of the input image. After each pass, the filter skips to the next-lower row. The so-called padding is used to determine how the filter should behave when it hits the edge of the matrix. We use "SAME" padding. With "SAME" padding and Stride 1, the convolution layer output will have the same spatial dimensions as its input. With a 3 × 3 pixel filter, nine pixels of the input image are simultaneously connected to the filter (local connectivity) and are convolved to a new value.

The following equation shows the computation of the discrete convolution

$$O[i,j] = \sum_{p=\frac{-S}{2}}^{\frac{S}{2}} \sum_{q=\frac{-S}{2}}^{\frac{S}{2}} [i-p, j-q] \cdot K[p,q] \tag{1}$$

$$O = I \cdot K(convolution) \tag{2}$$

where I is the Input Image, O is the Output Image, K is the Filter Kernel, and S is the Filter Size.

Depending on the property and number of filters, the convolution layer is able to recognize and extract individual features in the input data. These can be lines, edges or certain shapes (**Figure 4**). The step size of the filter determines whether the output image should have the same size as the input image, or whether it should be reduced in size. For example, for downsampling we chose a stride of 2 to halve the size of the input image. For upsampling we use an upsampling layer. This layer increases the dimensionality (rows and columns) of output feature maps by doubling the values (stride = 2).

Activation Function

In the activation function of the neural network, you decide whether the neuron fires or not. There are different types of activation functions such as sigmoid function, tangent function, rectified linear unit (ReLU) and leaky rectified linear unit (LReLU). In our case we used LReLU. LReLU s are one attempt to fix the "dying ReLU" problem. Instead of the function being zero when $x < 0$, a leaky ReLU will instead have a small negative slope like 0.1 or 0.3 (Maas et al., 2013; Goodfellow et al., 2018). That is, the function computes:

$$f(x) = 1(x < 0) \cdot (\alpha \cdot x) + 1(x \geq 0) \cdot (x) \tag{3}$$

where α is a small constant. So, if the input x is greater than 0, then the output is x. If the input is less than 0, the output will be alpha α times the input.

In the DeepLTK toolkit LReLU activation function uses 0.1 as a hardcoded alpha parameter.

Batch Normalization

Batch normalization is a layer that allows every layer of the network to perform learning more independently. Batch normalization can be used as a regularization strategy to avoid overfitting the model. The layer is added to the sequential model to standardize the input or the outputs. It can be used at several points between the layers of the model. It is often inserted just after defining the sequential model and after the convolution and pooling layers. Batch normalization is a technique that has been widely used over the years and has proven to be very effective in several DL tasks. It uses the mean and variance computed within a small data stack to normalize its features during activation (Ioffe and Szegedy, 2015).

Dropout Layer

Dropouts are the regularization technique that is used to prevent overfitting in the model. Dropouts are added to randomly switching some percentage of neurons of the network. When the neurons are switched off, the incoming and outgoing connections to those neurons are also switched off. This prevents units from co-adapting too much (Srivastava et al., 2014).

Initialization of the Weights in the ANN

With each pass through a layer, the variance should remain as constant as possible. This prevents the signal from increasing toward infinity or vanishing to zero. This means that the weights in the network must be initialized so that the variance for x and y remains the same. This initialization process is known as Xavier initialization (Glorot and Bengio, 2010). We use Xavier initialization for all the weights in our U-Net.

Training of the U-Net

The ANN programmed in this manner was trained with 11,932 CT slice images of lungs and the associated manually drawn lung masks (ground truth). The training was performed on 113,784 iterations. One iteration includes miniBatch sampling (we use a miniBatch size of 12) → Forward Propagation → Loss Evaluation (the predicted masks were compared to the manually generated lung masks) → Back Propagation and update of the weights in the network. In simple terms the network then tried to minimize the error between the manual mask and the mask generated in each iteration by selecting the appropriate combinations of convolution filters with more than

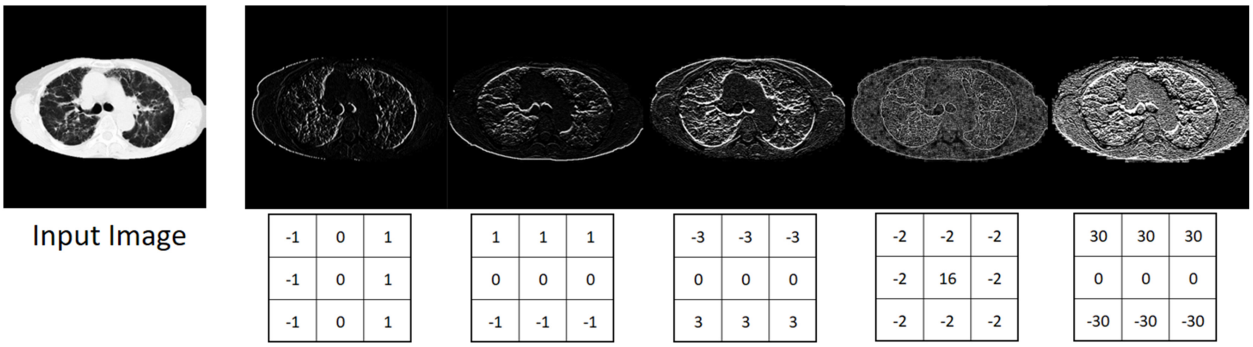

FIGURE 4 | Input image and five different output images generated with different convolution kernels.

6,000 different convolution kernels used. This took about 1.4 s. The complete training duration was 44.2 h. Return values are the evaluated loss value and a value for the current iteration. We used the Mean Square Error Regression Loss function. The course of the learning curve is shown in **Figure 5**. The complete training process is shown in **Figure 6**.

Testing of the Trained Model

The trained U-Net was tested on 3,466 CT lung slice images from 27 patients. The predicted ROIs were used to segment each slice and the whole lung CT-qa was then performed. Briefly, the lung is composed by two compartments with very different densities: tissue, with a density close to the one of water (0 HUs), and gas, with a density of −1,000 HU. For each voxel:

$$V_{gas} = \frac{-CT(HU)}{1,000} \cdot V_{voxel} \tag{4}$$

$$\rho_L = \frac{CT + 1,000}{1,000} \tag{5}$$

$$Tissue\ mass = \rho_L \cdot V_{voxel} \tag{6}$$

The voxel gas volume and voxel tissue mass were multiplied by the total number of voxels to obtain the total tissue mass and the total gas volume. Lung tissue was classified according to its gas/tissue content as not inflated (CT number between +100 and −100), poorly aerated (CT number between −101 and −500), normally inflated (CT number between −501 and −900), and hyper-inflated (CT number between −901 and −1,000) (Cressoni et al., 2013).

We estimated recruitability as:

$$Recruitability = \frac{non\ aerated\ tissue_{5cmH_2O} - non\ aerated\ tissue_{45cmH_2O}}{non\ aerated\ tissue_{5cmH_2O}} \tag{7}$$

The first formula indicates the fraction of gasless tissue which regains inflation increasing the pressure. The complete testing workflow is shown in **Figure 7**.

Statistical Analysis

The masks obtained by manual and artificial segmentation were compared by the intersection over nion (IoU) metric method. The variables computed by CT quantitative analysis after manual and artificial Intelligence (AI)-segmentation were compared by linear regression, and Bland-Altman analysis, and calculating 95% confidence intervals to evaluate the agreement between the masks. Student's t test was used to test the difference between the means of normally distributed values. Otherwise, we used the Wilcoxon test. Two-tailed p values < 0.05 were considered statistically significant. All statistical analyses were performed using R 4.1 (The R Project for Statistical Computing).

Intersection Over Union Metric

The IoU, also known as the Jaccard index, is an established method for determining the segmentation quality of segmented images. It is used to quantify the correspondence between the manually created lung mask (ground truth) and the lung mask predicted by the trained model. The IoU metric measures the number of pixels common to the manually created masks and the prediction masks divided by the total number of pixels present in both masks. A value of 1 indicates a 100% agreement of the masks and 0 means no agreement (Nowozin, 2014).

The following equation shows the computation of the IoU:

$$IoU = \frac{|A \cap B|}{|A \cup B|} \tag{8}$$

where A is the manual generated mask (ground truth) and B is the predicted mask.

RESULTS

Slices-Level Performance

For all lung scans, the agreement between manual and AI-segmentation (IoU metric) was 87% ± 10% in the test set, as shown in **Table 3**. In **Figure 8** we show the agreement between manually and AI-segmentation in the training and test sets along the cranio-caudal axis in normal lungs (Panel A), ARDS (Panel B), and COVID-19 (Panel C). Regardless of the lung type, the mean agreement between manual and AI segmentation across

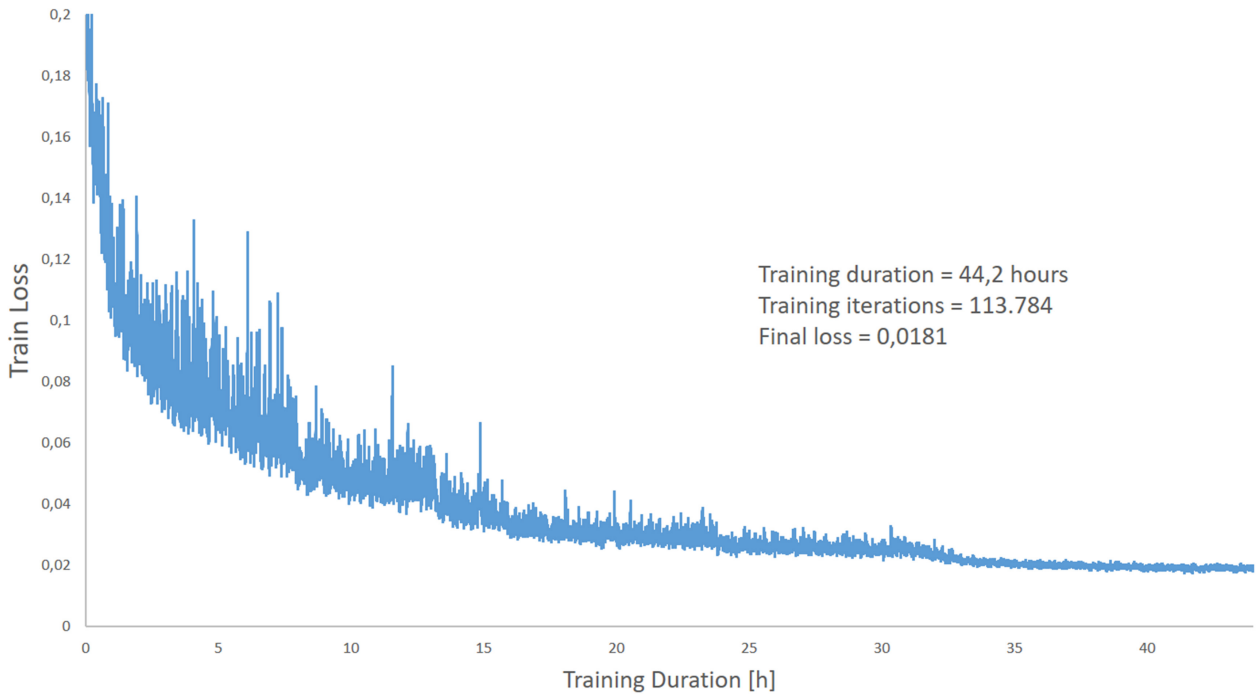

FIGURE 5 | Graphical representation of the loss during the training period over 44.2 h.

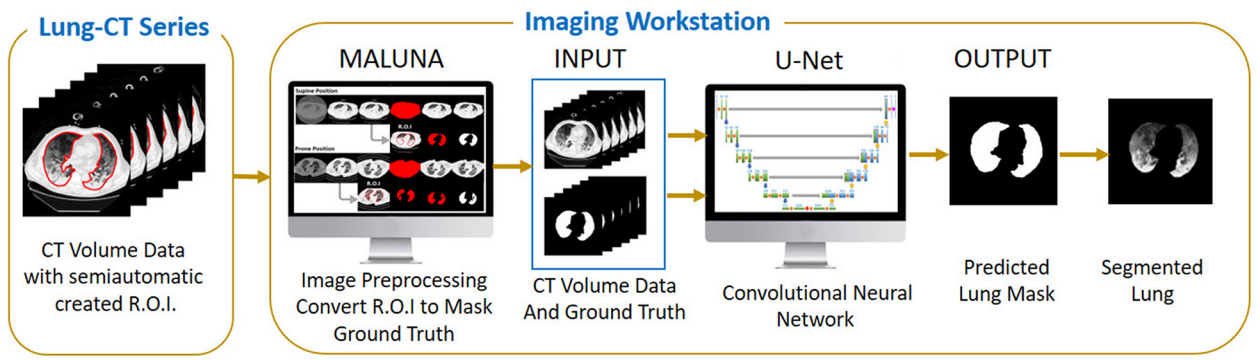

FIGURE 6 | The complete training workflow.

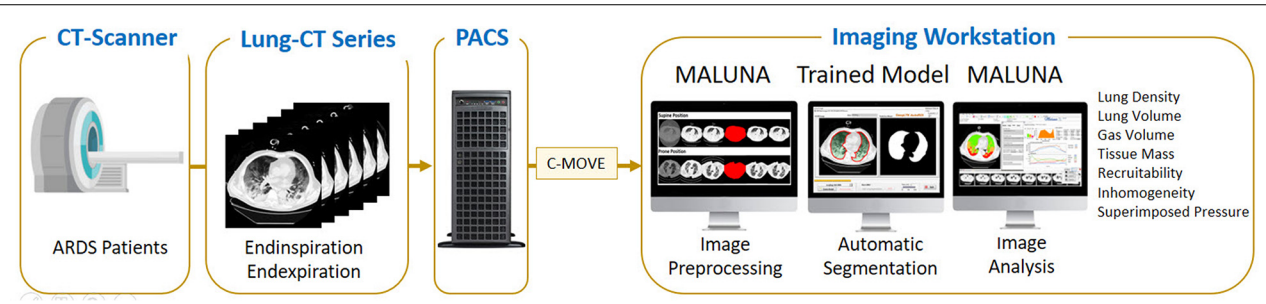

FIGURE 7 | The complete test and analyzing workflow.

TABLE 3 | Mean Intersection over Union calculated per slices and per volumes.

	$IoU_{mean} \pm SD$ per slices	*N* Slices	$IoU_{mean} \pm SD$ per volumes	*N* volumes
Normal lung	91.3 ± 10.1%	586	96.3 ± 0.6%	9
ARDS	85,2 ± 13.9%	2,057	88.9 ± 3.1%	30
COVID-19	84,7 ± 14.0%	823	86.3 ± 6.5%	12
All lungs	87.3 ± 10.0%	3,466	89.6 ± 5.1%	51

all CT slices was 91.3 ± 10.0, 85.2 ± 13.9, and 84.7 ± 14.0%, and across all lung volumes 96.3 ± 0.6, 88.9 ± 3.1, and 86.3 ± 6.5% for normal lungs, ARDS and COVID-19, respectively. In this test set, we found that the agreement between manual and AI-segmented lungs followed an inverse U-shape: higher in the central regions of the thorax and lower at the apex or near in the pleural recesses. Note that in these regions, the absolute amount of lung tissue is just a small fraction (4.1 ± 2.0%) of the entire parenchyma. The worst results were obtained in severe ARDS compared with moderate and mild ARDS (**Figures 8D–F**). **Figure 9** shows the worst segmentation results, mainly in the peripheral zones of the lung slices. In addition to the IOU metric, the difference in lung volume between ground truth and predicted mask can also be seen. **Figure 10** shows the best segmentation results with up to 99% agreement (IOU = 99%) in normal lungs.

Patient-Level Performance

Lung Volume

The regressions and the Bland Altman analysis of the total lung volumes (gas + tissue volume) computed with manual and AI-segmentation both in the training set and in the test set are summarized in **Supplementary Figure 6**. As shown, the regression lines in these sets were close to identity. The Bland Altman plots on the sets showed biases of −3.1 ml [CI +13.0/−19.1] and −9.8 ml [CI: +56.0/−75.7 ml], respectively.

Lung Tissues

In the CT-qa, the overinflated, well-aerated, poorly aerated and non-aerated tissue fractions were almost identical in the manually or AI-segmentated images. Indeed, the R^2 of the linear regressions between manual and AI-segmentation on overinflated, well-aerated and poorly aerated and non-aerated tissue was 0.99, 0.99, 0.98, and 0.91, respectively. The Bland Altman analyses comparing overinflated (p = 0.99), well-aerated (p = 0.91), poorly aerated (p = 0.91), and non-aerated tissues (p = 0.53) obtained after manual and AI-segmentation on the test set is summarized in **Figure 11**. The whole lung tissue fraction in all cases is 41.8 ± 17.2% in manual segmentation and 41.1 ± 16.2% (p = 0.85).

Recruitability

Assessment of recruitability is likely the most relevant variable that can be measured with CT-qa. In **Supplementary Figure 7**,

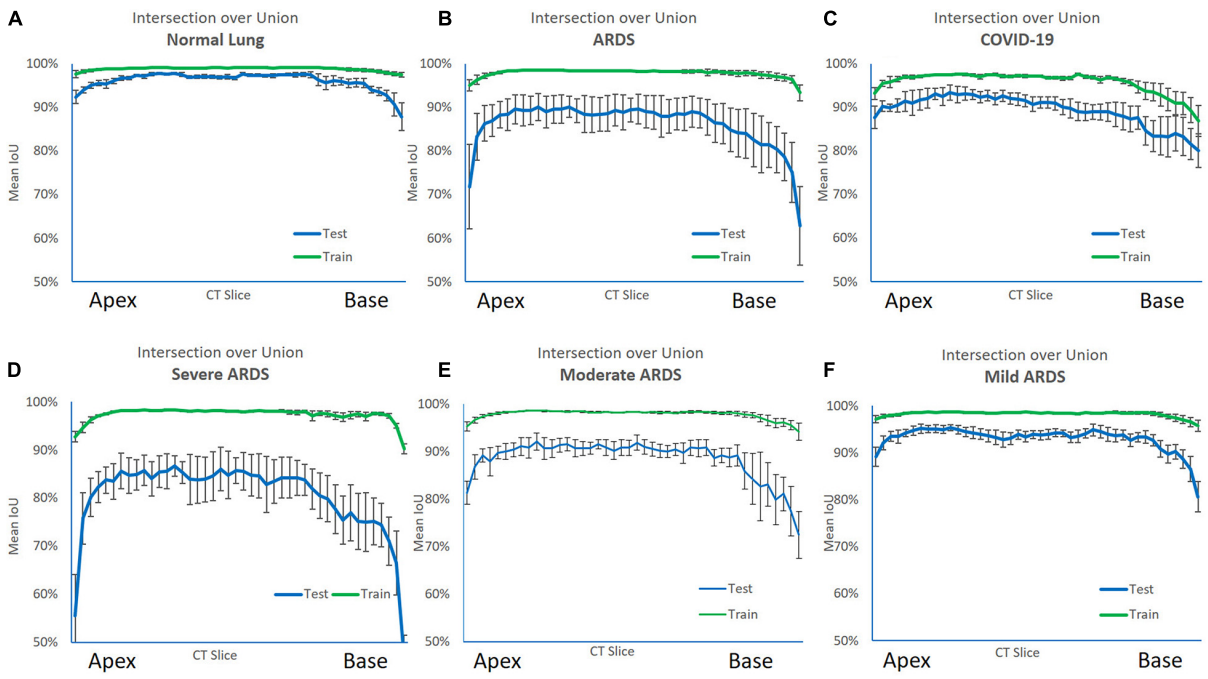

FIGURE 8 | Intersection over Union (IoU) metric performance on the training (green line) and test set (blue line) along the cranio-caudal axis in normal lungs **(A)**, ARDS **(B)**, COVID-19 **(C)**, severe ARDS **(D)**, moderate ARDS **(E)**, and mild ARDS **(F)**. As shown, in the training set, the AI algorithm almost perfectly matched the manual segmentation. In the test set the performance was slightly poorer. The Figure also shows the anatomical distribution of the error. Indeed, the algorithm was able to achieve a higher performance in the middle of the lung, while at the apex and the base, locations where also for a trained eye is sometimes difficult to distinguish the lung parenchyma from the surrounding structures and the pleural effusion, as is the case with severe ARDS **(D)**, it struggled more.

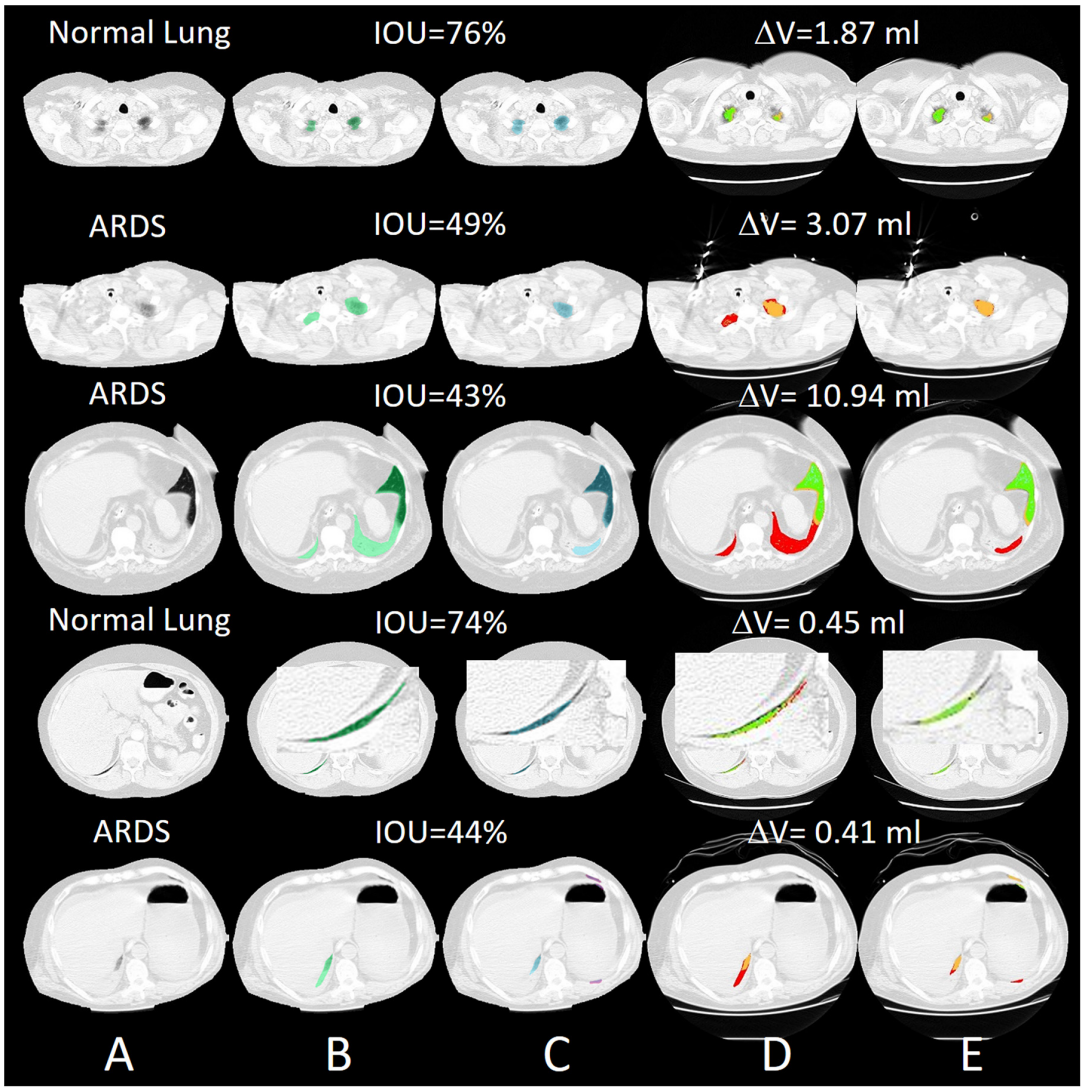

FIGURE 9 | Selected slices with very poor segmentation results with an IOU of up to 43% in ARDS Lung. Most of the lungs were poorly recognized in the peripheral areas. **(A)** preprocessed CT, **(B)** ground truth (transparent green), **(C)** predicted mask (transparent blue), **(D)** quantitative calculations within the manual ROI and **(E)** quantitative calculations within the automatic ROI (green = normally aerated, blue = overextended, orange = badly aerated and red = not aerated).

we report the recruitment fraction computed for the manual and AI-segmented lungs in the test set. The recruitment is expressed both as variations of non-aerated tissue (panel A) and as a variation of well-aerated tissue (panel B). The agreement between the two techniques is within +6.2 and −5.5% (bias +0.3%) when the recruitment is expressed as variation of the percentage of non-aerated tissue and between +2.3 and −3.3% (bias −0.5) when expressed as variation of the percentage of well-aerated tissue.

Inaccuracies

To determine the inaccuracies of manual and AI-segmentation we assumed that the lung weight should not change in the same individual when increasing the airway pressure from 5 to 15 and to 45 cmH_2O. A difference in lung weight between the two airway pressure levels can be considered as a sign of segmentation inaccuracy. As shown in **Table 4**, the average lung weight differences between 5 and 15 cmH_2O or between 5 and 45 cmH_2O obtained by manual and AI-segmentation were negligible. However, in the individual patients the differences could be as high as 336 g.

Workload

The complete training of the neural Network up to the level used in this analysis lasted 44.2 h. The learning curve of the algorithm is reported in **Figure 5**. With our current configuration the analysis of an unknown single CT slice requires 0.041 ± 0.007 s. Therefore, automatic segmentation of a complete lung CT-scan with approximately 100 slices of 5.0 mm thickness, required approximately 5 s.

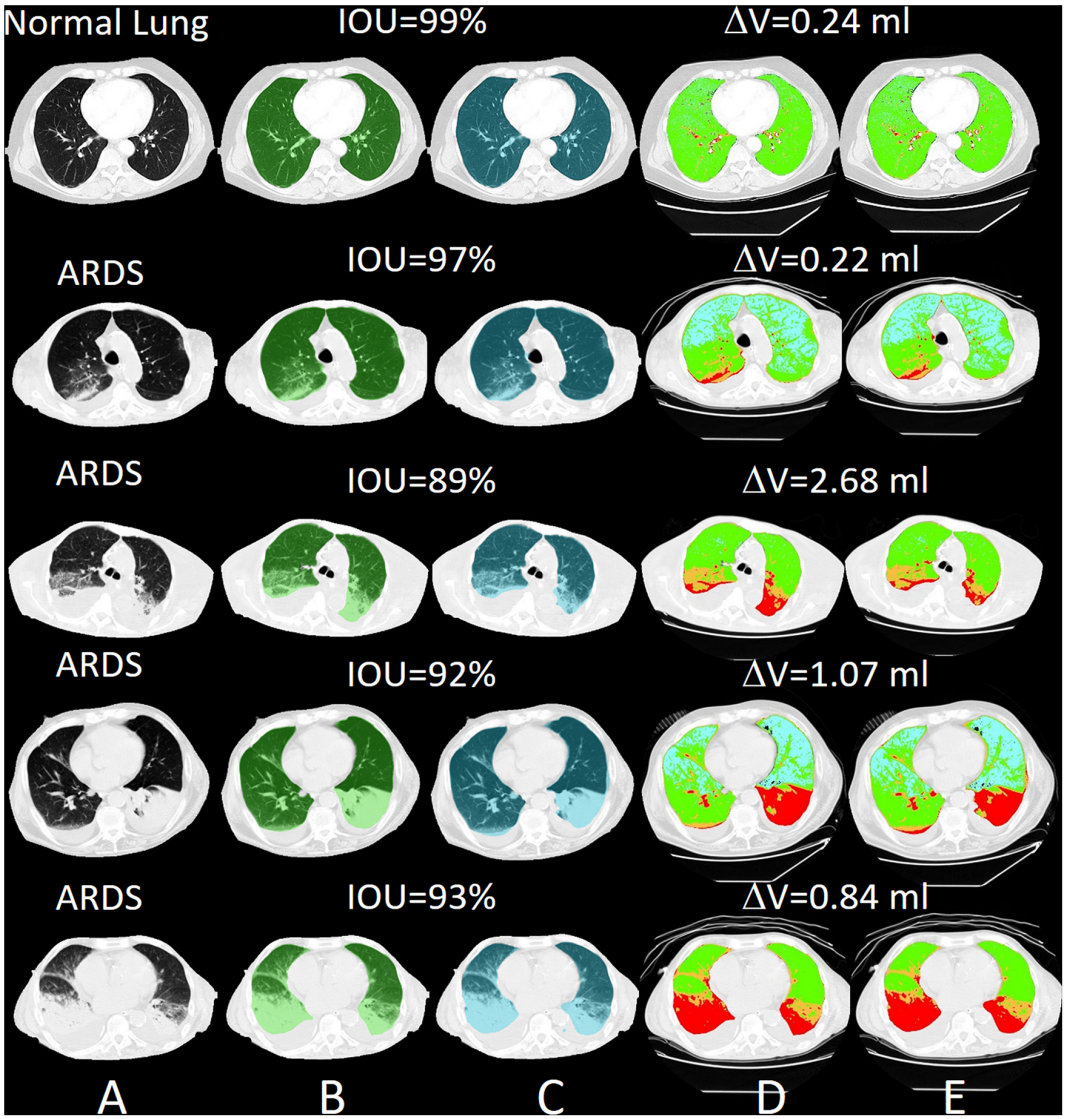

FIGURE 10 | Selected slices with very good segmentation results with an IOU of up to 99% with normal lungs. The differences in lung volume between manually and automatically segmented lungs are 0.24 ml. **(A)** preprocessed CT, **(B)** ground truth (transparent green), **(C)** predicted mask (transparent blue), **(D)** quantitative calculations within the manual ROI and **(E)** quantitative calculations within the automatic ROI (green = normally aerated, blue = over-inflated, orange = poorly aerated and red = not aerated).

DISCUSSION

In this study, we found that automatic lung segmentation performed by a properly trained neural network provided lung contours in close agreement with the ones obtained by manual segmentation. When comparing lung CT slices with the original Ronneberger network (Hofmanninger et al., 2020, **Table 3**: test data set for lung slice only), the IOU of damaged lungs is in a similar range (85% vs. 80–87% for trauma and 85% vs. 83–91% for atelectasis). In the case of normal lungs, however, the results are worse in comparison (91% vs. 94%). The automatic approach completed segmentation of the entire lung in 5–10 s making immediately available the CT-qa. Therefore, the whole process from DICOM image extraction to the lung CT-qa with data on the fractions of inflated, well aerated, poorly aerated and non-aerated tissue, as well as lung recruitability can be completed in just a few minutes. Beyond their use for research, these data may prove important for the clinical diagnosis and respiratory therapy. Indeed, the greatest limitation in implementing CT-qa in the everyday clinical practice is the amount of man-hours required for lung segmentation. This study presents a possible solution to this problem. The trained model is not perfect, as it showed weaknesses in the edge regions of the apex and base, especially in severely damaged lung areas that are difficult to identify even for a trained radiologist. These represent, however, only a minor fraction

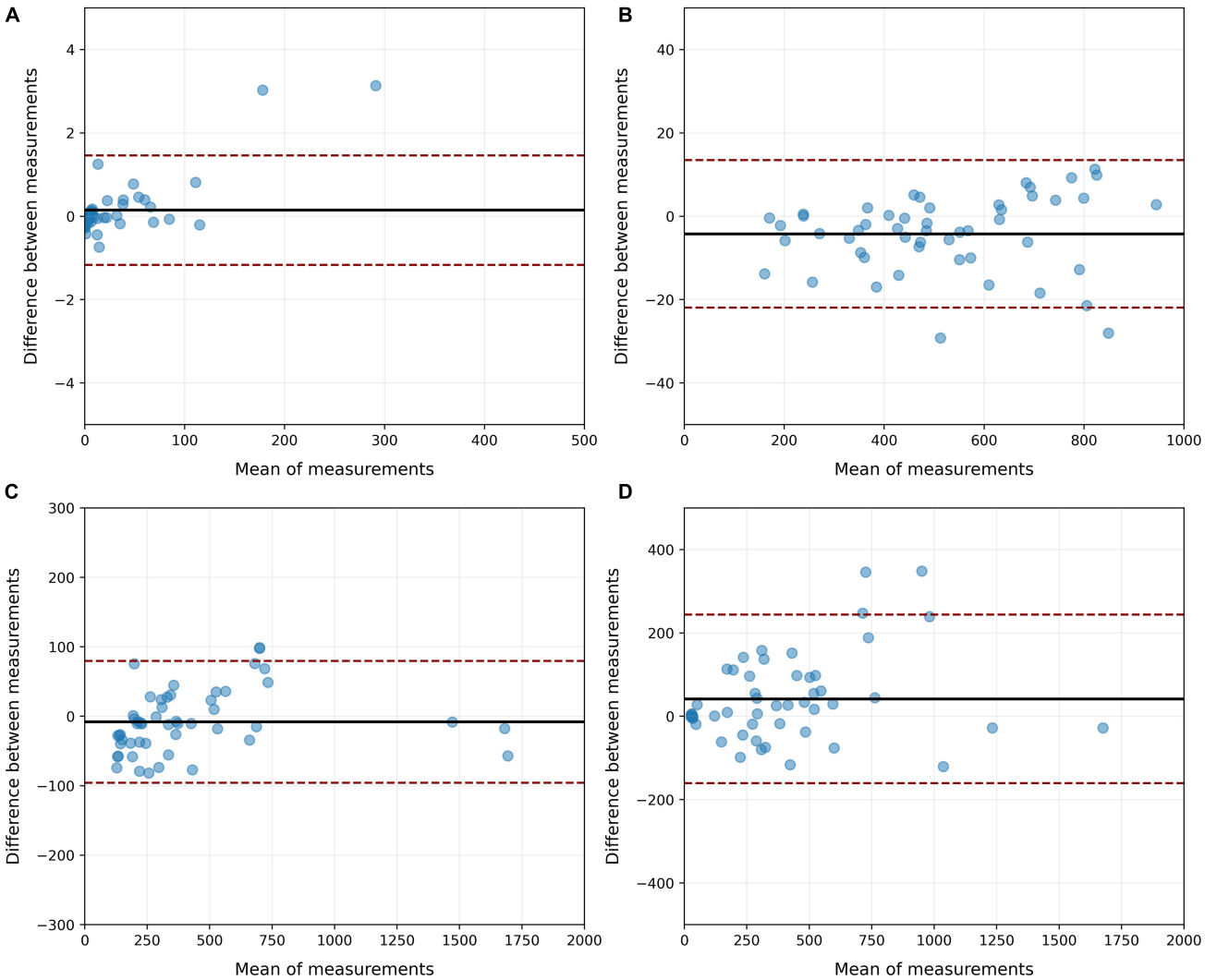

FIGURE 11 | Bland Altman analysis of the agreement between manual and AI-segmentation on the test set when CT-qa was used to measure the over-inflated **(A)**, well-aerated **(B)**, poorly inflated **(C)** and non-aerated **(D)** tissues on the test set. As shown, biases never exceeded 50 g. The largest CI were, as expected, in the non-aerated tissue, where also for a trained eye is, at times, difficult to distinguish parenchyma from pleural effusion.

of the total lung parenchyma that this should not exceed 10% of the entire lung mass. Overall, the results obtained are fully adequate for pathophysiological decision processes and consequent clinical application.

We may wonder to which extent one may be confident in the AI-segmentation compared to the manual one. In ARDS, image segmentation is especially difficult as, in some cases, it is almost impossible to discriminate the edge of the lung parenchyma from a pleural effusion, so common in ARDS (Chiumello et al., 2013), particularly in the most dependent lung regions and most severe ARDS forms. However, this problem is also present in manual segmentation. Indeed, when the CT scan of the same lung is taken under different operating conditions, for example, at different airway pressures, we observed, as in previous studies, differences in lung weights which, on average were rather trivial (∼10–20 g), but they could be as high as 336 g in the individual patient. These variations may result either from the segmentation procedure and/or from actual changes in lung weight, primarily due to a possible airway pressure-dependent blood shift. It is unfortunately impossible to determine how much of the weight variation is due to an intrathoracic blood shift or to inaccuracies of the segmentation process. The decrease in intrathoracic blood volume we estimated in a previous work (Chiumello et al., 2007) with increasing airway pressures was about 100 ml, leading to a small decrease in lung weight. In the present study, we found more pronounced variations of lung weight between 5 and 45 cmH_2O than between 5 and 15 cmH_2O. Indeed, especially in the train set, we found maximum differences in lung weight between the two pressure levels as large as 336 g, making unlikely that blood shift alone accounted for the entire variation. Indeed, at 5 cmH_2O it is more difficult, even for trained personnel, to discriminate between parenchyma and

TABLE 4 | Differences in lung weight detected at different airway pressures.

Train dataset				Test dataset			
		Manual	Automatic			Manual	Automatic
5–15 cmH_2O	Mean (g)	−6.5	1.2	5–15 cmH_2O	Mean (g)	17.2	−14.8
	SD (g)	64.7	60.5		SD (g)	83.9	54.3
	Min (g)	−227.5	−168.5		Min (g)	−103.0	−150.4
	Max (g)	173.2	196.2		Max (g)	194.8	42.6
5–45 cmH_2O	Mean	7.5	14.5	5–45 cmH_2O	Mean	39.8	−2.6
	SD (g)	93.8	92.6		SD (g)	92.1	72.4
	Min (g)	−226.0	−231.9		Min (g)	−94.8	−145.7
	Max (g)	336.0	339.8		Max (g)	150.7	101.8

pleural effusion, a process that is easier at 45 cmH_2O. Therefore, manual segmentation is intrinsically associated with some degree of inaccuracy. Interestingly, as shown in **Table 3**, AI had the same degree of inaccuracy and closely mimicked the manual segmentation. Moreover, the more severe the ARDS, i.e., the extent of the densities and pleural effusions that are is present in approximately 80% of ARDS patients (Gattinoni et al., 1986), the greater the probability of inaccuracy. As opposed to the CT images of the training set, the lungs of the patients in the test CT were more poorly segmented, which may indicate a slight overfitting of the CNNs.

The most relevant quantitative CT variables that may have an impact on clinical management are the recruitability and the volume of the lung open to the gas. The latter is frequently referred to as "baby lung," since in ARDS its size may resemble that of a 3-year-old child. The baby lung is represented by the amount of normally aerated tissue, which conventionally includes the voxels between −500 and −900 HUs (Gattinoni et al., 1986). AI-segmentation performed remarkably well under this definition, with an overall agreement within few grams. Knowledge of the baby lung and its associated gas volume will allow a straightforward measurement of the strain occurring during mechanical ventilation. Determining the strain, i.e., the ratio of tidal volume plus PEEP volume to the FRC, is a fundamental information when setting the ventilator, since excessive strain is a primary cause of ventilation-induced lung injury (Chiumello et al., 2008).

The recruitability can be estimated either by assessing the amount of lung tissue which regains aeration, or by measuring the increase in the size of the baby lung when the airway pressure is increased. This allows the normal aeration of pulmonary units, which were previously collapsed or simply poorly inflated. Measuring recruitment as a non-aerated tissue fraction difference had a bias of +0.3% (CI: +6.2/−5.5%) on the test set. We believe, from a clinical standpoint, that these numbers are more than adequate to define the recruitability, which is usually roughly defined as a binary variable, i.e., the patient is either a "recruiter" or a "non-recruiter." A more precise definition of recruitability, which may range from 0% to more than 50% of the total lung mass, that would be easily clinically available with AI-segmentation, may represent an important step ahead when tailoring mechanical ventilation or setting PEEP. When we defined recruitment as changes in the baby lung dimensions, AI performed extremely well compared with manual segmentation.

Most of the advances on our pathophysiological understanding of ARDS derive from the quantitative CT scan analysis. An easy availability of the CT-qa may play an important role in setting a proper ventilation and, maybe more importantly, to avoid harmful approaches.

LIMITATIONS

In the original U-Net, the original input image is first convoluted with 64 filters. Due to hardware limitations, this was not possible with our U-Net, so we started with 32 convolution filters. We have found that in the edge areas of the lungs, especially with very badly damaged lung tissue, segmentation is much worse. In addition, the lung CTs unknown to the model are segmented more poorly than the trained lung CTs, which indicates on the one hand that the Network is slightly overfitted, or on the other hand, that training was carried out with too few lung CT variations. Our ANN was developed with NI-LabVIEW, NI-Vision and the Deep Learning Toolkit from Ngene (DeepLTK). These are all commercial, license-protected software products. This means that an application cannot be used freely. The DeepLTK still has a number of limitations: IOU and Dice coefficient are the only metrics so far. More will be added in the next releases. Shape quality performance metrics like ASSD or BF-Score are not yet supported. The only optimization algorithm is Stochastic gradient descent. Further algorithms such as Adam, Adagrad, AdaDelta, RMSProp, and Nesterov are being developed for the next releases. So far, Mean Squared Error is the only loss type for 3D data. Cross Entropy loss is currently only available for 1D data. But it will be available for 3D data in the next update. It is a specific of DeepLTK toolkit (at the moment) that the complete dataset is preloaded on the CPU RAM (as a 4D single precision floating point array) to speed up miniBatch fetching and feeding to the Network for the training process. As during the training process, the whole dataset will be utilized for several (hundreds of) epochs, it is reasonable to preload decoded dataset and store it on the RAM to speed up the training process. Loading a miniBatch of data from disk is also reasonable, in case of large datasets, and at the cost of speed, but currently it is not implemented in the toolkit. A 3D semantic segmentation architecture is still not possible with the DeepLTK.

CONCLUSION

The trained model based on the U-Net can automatically segment the lungs in the CT with the limitations mentioned. The automatic segmentation of a full lung CT scan with approximately 100 sections with a slice thickness of 5.0 mm took approximately 5 s, compared to manual segmentation which can take up to an hour. Due to the still poor performance compared to Python-based CNNs, we plan to further improve the U-Net developed with LabVIEW and optimize it for the detection of differently damaged lung areas. We are convinced that the

widest possible variety of different lung pathologies and CT reconstruction parameters can significantly improve a suitable segmentation CNN. Therefore, we will increase the amount of input data through augmentation by varying the brightness, contrast, gamma and grain of the CT images and applying them to an increasing number and variety of lung pathologies. We plan to further modify the Network architecture through tests, while changing the miniBatch size, varying the probability of dropout layers, and varying the training parameters (i.e., optimizer, loss type, momentum, weight decay, and training type) are interventions for future research and further improvement. This should widen the field of potential applications and increase the already convincing validity of image data processing. In order to play with all these possibilities, one will require greatly advanced hardware with much better performance compared with the hardware used for this study.

The development of a reliable clinical diagnostic system, able to perform the automatic detection and consecutively the quantitative analysis of lung tissues immediately after performance of a lung CT scan seems conceivable and also practicable. Such a tool would have significant impact on diagnosing and selecting the appropriate therapeutic interventions for each individual patient suffering from severe lung injury.

DATA AVAILABILITY STATEMENT

The raw data supporting the conclusions of this article will be made available by the authors, without undue reservation.

AUTHOR CONTRIBUTIONS

PH: study design, programming of the ANN, data collection, data analysis, figure design, and writing. MB: data analysis, statistical interpretation, figure design, and writing. MC: data collection, data interpretation, and image processing. LS, OM, KM, MQ, and LG: study design, data analysis, data interpretation, and writing. JL: data analysis, data interpretation, and revision of the manuscript. All authors critically revised and accepted the manuscript in its current form.

FUNDING

The present work has been funded by the Department of Anesthesiology, University Medical Center Göttingen, Göttingen, Germany and an unrestricted grant for lung injury-related research from Sartorius AG, Göttingen, Germany.

ACKNOWLEDGMENTS

We would like to thank Robert Ventzki and Silvio Rizzoli for the short-term loan of the DELL workstation, without which the training of the artificial neural network would not have been possible. We also thank Alik Sargsyan (Developer of the DeepLTK Toolkit and Founder & CEO of Ngene, Armenia) for the valuable tips on programming the first artificial neural Network with the DeepLTK Toolkit for LabVIEW.

SUPPLEMENTARY MATERIAL

The Supplementary Material for this article can be found online at: https://www.frontiersin.org/articles/10.3389/fphys.2021.676118/full#supplementary-material

REFERENCES

Al-Fatlawi, A., Malekian, N., García, S., Henschel, A., Kim, I., Dahl, A., et al. (2021). Deep Learning Improves Pancreatic Cancer Diagnosis Using RNA-Based Variants. *Cancers* 13:2654. doi: 10.3390/cancers13112654

Almotairi, S., Kareem, G., Aouf, M., Almutairi, B., and Salem, M. A. (2020). Liver Tumor Segmentation in CT Scans Using Modified SegNet. *Sensors* 20:1516. doi: 10.3390/s20051516

Alom, M. Z., Yakopcic, C., Hasan, M., Taha, T. M., and Asari, V. K. (2019). Recurrent residual U-Net for medical image segmentation. *J. Med. Imaging* 6:014006. doi: 10.1117/1.JMI.6.1.014006

ARDS Definition Task Force, V. M., Rubenfeld, G. D., Thompson, B. T., Ferguson, N. D., Caldwell, E., et al. (2012). Acute respiratory distress syndrome: the Berlin Definition. *JAMA* 307, 2526–2533.

Badrinarayanan, V., Kendall, A., and Cipolla, R. (2017). SegNet: a deep convolutional encoder-decoder architecture for image segmentation. *IEEE Trans. Pattern Anal. Mach. Intell.* 39, 2481–2495. doi: 10.1109/tpami.2016.2644615

Bone, R. C. (1993). The ARDS lung. New insights from computed tomography. *JAMA* 269, 2134–2135. doi: 10.1001/jama.1993.03500160104042

Causey, J., Stubblefield, J., Qualls, J., Fowler, J., Cai, L., Walker, K., et al. (2021). An Ensemble of U-Net Models for Kidney Tumor Segmentation with CT images. *IEEE/ACM Trans. Comput. Biol. Bioinform.* doi: 10.1109/TCBB.2021.3085608 [Epub ahead of print].

Chartrand, G., Cheng, P. M., Vorontsov, E., Drozdzal, M., Turcotte, S., Pal, C. J., et al. (2017). Deep Learning: a Primer for Radiologists. *Radiographics* 37, 2113–2131. doi: 10.1148/rg.2017170077

Chassagnon, G., Vakalopolou, M., Paragios, N., and Revel, M. P. (2020). Deep learning: definition and perspectives for thoracic imaging. *Eur. Radiol.* 30, 2021–2030. doi: 10.1007/s00330-019-06564-3

Chen, K. B., Xuan, Y., Lin, A. J., and Guo, S. H. (2021). Lung computed tomography image segmentation based on U-Net Network fused with dilated convolution. *Comput. Methods Programs Biomed.* 18:106170. doi: 10.1016/j.cmpb.2021.106170

Chiumello, D., Busana, M., Coppola, S., Romitti, F., Formenti, P., Bonifazi, M., et al. (2020). Physiological and quantitative CT-scan characterization of COVID-19 and typical ARDS: a matched cohort study. *Intensive Care Med.* 46, 2187–2196. doi: 10.1007/s00134-020-06281-2

Chiumello, D., Carlesso, E., Aliverti, A., Dellacà, R. L., Pedotti, A., Pelosi, P. P., et al. (2007). Effects of volume shift on the pressure-volume curve of the respiratory system in ALI/ARDS patients. *Minerva Anestesiol.* 73, 109–118.

Chiumello, D., Carlesso, E., Cadringher, P., Caironi, P., Valenza, F., Polli, F., et al. (2008). Lung stress and strain during mechanical ventilation for acute respiratory distress syndrome. *Am. J. Respir. Crit. Care Med.* 178, 346–355.

Chiumello, D., Marino, A., Cressoni, M., Mietto, C., Berto, V., Gallazzi, E., et al. (2013). Pleural effusion in patients with acute lung injury: a CT scan study. *Crit. Care Med.* 41, 935–944. doi: 10.1097/ccm.0b013e318275892c

Cornejo, R. A., Diaz, J. C., Tobar, E. A., Bruhn, A. R., Ramos, C. A., Gonzalez, R. A., et al. (2013). Effects of prone positioning on lung protection in patients with acute respiratory distress syndrome. *Am. J. Respir. Crit. Care Med.* 188, 440–448.

Cressoni, M., Gallazzi, E., Chiurazzi, C., Marino, A., Brioni, M., Menga, F., et al. (2013). Limits of normality of quantitative thoracic CT analysis. *Crit. Care* 17:R93. doi: 10.1186/cc12738

Currie, G., Hawk, K. E., Rohren, E., Vial, A., and Klein, R. (2019). Machine Learning and Deep Learning in Medical Imaging: intelligent Imaging. *J. Med. Imaging Radiat. Sci.* 50, 477–487. doi: 10.1016/j.jmir.2019.09.005

Dong, X., Lei, Y., Wang, T., Thomas, M., Tang, L., Curran, W. J., et al. (2019). Automatic multiorgan segmentation in thorax ct images using u-Net-gan. *Med. Phys.* 46, 2157–2168. doi: 10.1002/mp.13458

Gattinoni, L., Caironi, P., Cressoni, M., Chiumello, D., Ranieri, V. M., Quintel, M., et al. (2006). Lung recruitment in patients with the acute respiratory distress syndrome. *N. Engl. J. Med.* 354, 1775–1786.

Gattinoni, L., Pelosi, P., Vitale, G., Pesenti, A., D'Andrea, L., and Mascheroni, D. (1991). Body position changes redistribute lung computed-tomographic density in patients with acute respiratory failure. *Anesthesiology* 74, 15–23. doi: 10.1097/00000542-199101000-00004

Gattinoni, L., and Pesenti, A. (2005). The concept of "baby lung". *Intensive Care Med.* 31, 776–784. doi: 10.1007/s00134-005-2627-z

Gattinoni, L., Pesenti, A., Avalli, L., Rossi, F., and Bombino, M. (1987). Pressure-volume curve of total respiratory system in acute respiratory failure. Computed tomographic scan study. *A. Rev. Respir. Dis.* 136, 730–736. doi: 10.1164/ajrccm/136.3.730

Gattinoni, L., Presenti, A., Torresin, A., Baglioni, S., Rivolta, M., Rossi, F., et al. (1986). Adult respiratory distress syndrome profiles by computed tomography. *J. Thorac. Imaging* 1, 25–30.

Gerard, S. E., Herrmann, J., Kaczka, D. W., Musch, G., Fernandez-Bustamante, A., and Reinhardt, J. M. (2020). Multi-Resolution convolutional neural Networks for fully automated segmentation of acutely injured lungs in multiple species,". *Med. Image Anal.* 60:101592. doi: 10.1016/j.media.2019.101592

Gerard, S. E., Herrmann, J., Xin, Y., Martin, K. T., Rezoagli, E., Ippolito, D., et al. (2021). CT image segmentation for inflamed and fibrotic lungs using a multi-resolution convolutional neural Network. *Sci. Rep.* 11:1455. doi: 10.1038/s41598-020-80936-4

Ghosh, S., Chaki, A., and Santosh, K. C. (2021). Improved U-Net architecture with VGG-16 for brain tumor segmentation. *Phys. Eng. Sci. Med.* doi: 10.1007/s13246-021-01019-w [Epub ahead of print].

Glorot, X., and Bengio, Y. (2010). Understanding the difficulty of training deep feedforward neural Networks. *Proc. Thirteenth Int. Conf. Artif. Intell. Stat.* 9, 249–256.

Goodfellow, I., Bengio, Y., and Courville, A. (2018). *Deep Learning*. Cambridge, Massachusetts: MIT Press.

Guimarães, P., Keller, A., Fehlmann, T., Lammert, F., and Casper, M. (2021). Deep-learning based detection of eosinophilic esophagitis. *Endoscopy* doi: 10.1055/a-1520-8116 [Epub ahead of print].

Hinton, G. E., Osindero, S., and Teh, Y.-W. (2006). A fast learning algorithm for deep belief Nets. *Neural Comp.* 18, 1527–1554. doi: 10.1162/neco.2006.18.7.1527

Hofmanninger, J., Prayer, F., Pan, J., Röhrich, S., Prosch, H., and Langs, G. (2020). Automatic lung segmentation in routine imaging is primarily a data diversity problem, not a methodology problem. *Eur. Radiol. Exp.* 4:50. doi: 10.1186/s41747-020-00173-2

Hojin, K., Jinhong, J., Jieun, K., Byungchul, C., Jungwon, K., Jeong, Y. J., et al. (2020). Abdominal multi-organ auto-segmentation using 3D-patch-based deep convolutional neural Network. *Sci. Rep.* 10:6204. doi: 10.1038/s41598-020-63285-0

Hu, X., Luo, W., Hu, J., Guo, S., Huang, W., Scott, M. R., et al. (2020). Brain SegNet: 3D local refinement Network for brain lesion segmentation. *BMC Med. Imaging* 20:17. doi: 10.1186/s12880-020-0409-2

Ioffe, S., and Szegedy, C. (2015). *Batch Normalization: Accelerating Deep Network Training by Reducing Internal Covariate Shift*. Available online at: https://arxiv.org/abs/1502.03167 (accessed on 17 Feb 2020).

Jalali, Y., Fateh, M., Rezvani, M., Abolghasemi, V., and Anisi, M. H. (2021). ResBCDU-Net: a Deep Learning Framework for Lung CT Image Segmentation. *Sensors* 21:268. doi: 10.3390/s21010268

Jeong, Y., Rachmadi, M. F., Valdés-Hernández, M. D. C., and Komura, T. (2019). Dilated Saliency U-Net for White Matter Hyperintensities Segmentation Using Irregularity Age Map. *Front. Aging Neurosci.* 11:150. doi: 10.3389/fnagi.2019.00150

Jünger, S. T., Hoyer, U. C. I., Schaufler, D., Laukamp, K. R., Goertz, L., Thiele, F., et al. (2021). Fully Automated MR Detection and Segmentation of Brain Metastases in Non-small Cell Lung Cancer Using Deep Learning. *J. Magn. Reson. Imaging* doi: 10.1002/jmri.27741 [Epub ahead of print].

Klapsing, P., Herrmann, P., Quintel, M., and Moerer, O. (2017). Automatic quantitative computed tomography segmentation and analysis of aerated lung volumes in acute respiratory distress syndrome-A comparative diagnostic study. *J. Crit. Care* 42, 184–191. doi: 10.1016/j.jcrc.2016.11.001

Kumar Singh, V., Abdel-Nasser, M., Pandey, N., and Puig, D. (2021). LungINFseg: segmenting COVID-19 Infected Regions in Lung CT Images Based on a Receptive-Field-Aware Deep Learning Framework. *Diagnostics* 11:158. doi: 10.3390/diagnostics11020158

LeCun, Y., Bengio, Y., and Hinton, G. (2015). Deep learning. *Nature* 521, 436–444.

Lei, Y., Fu, Y., Roper, J., Higgins, K., Bradley, J. D., Curran, W. J., et al. (2021). Echocardiographic image multi-structure segmentation using Cardiac-SegNet. *Med. Phys.* 48, 2426–2437. doi: 10.1002/mp.14818

Litjens, G., Kooi, T., Bejnordi, B. E., Setio, A. A. A., Ciompi, F., Ghafoorian, M., et al. (2017). A survey on deep learning in medical image analysis. *Med. Image Anal.* 42, 60–88.

Maas, A. L., Hannun, A. Y., and Ng, A. Y. (2013). Rectifier Nonlinearities Improve Neural Network Acoustic Models. *Proc. ICML* 30:3.

Ngene (2021). *DeepLTK Deep Learning Toolkit for LabView*. Available online at: https://www.ngene.co/deep-learning-toolkit-for-labview (accessed August 17, 2021).

Nowozin, S. (2014). "Optimal Decisions from Probabilistic Models: The Intersection-over-Union Case Published 2014 Mathematics, Computer Science," in *IEEE Conference on Computer Vision and Pattern Recognition* (Piscataway: IEEE), doi: 10.1109/CVPR.2014.77

Park, J., Yun, J., Kim, N., Park, B., Cho, Y., Park, H. J., et al. (2020). Fully Automated Lung Lobe Segmentation in Volumetric Chest CT with 3D U-Net: validation with Intra- and Extra-Datasets. *J. Digit. Imaging* 33, 221–230. doi: 10.1007/s10278-019-00223-1

Pelosi, P., D'Andrea, L., Vitale, G., Pesenti, A., and Gattinoni, L. (1994). Vertical gradient of regional lung inflation in adult respiratory distress syndrome. *Am. J. Respir. Crit. Care Med.* 149, 8–13. doi: 10.1164/ajrccm.149.1.8111603

Pelosi, P., Tubiolo, D., Mascheroni, D., Vicardi, P., Crotti, S., Valenza, F., et al. (1998). Effects of the prone position on respiratory mechanics and gas exchange during acute lung injury. *Am. J. Respir. Crit. Care Med.* 157, 387–393. doi: 10.1164/ajrccm.157.2.97-04023

Qiblawey, Y., Tahir, A., Chowdhury, M. E. H., Khandakar, A., Kiranyaz, S., Rahman, T., et al. (2021). Detection and Severity Classification of COVID-19 in CT Images Using Deep Learning. *Diagnostics* 11:893. doi: 10.3390/diagnostics11050893

Ronneberger, O., Fischer, P., and Brox, T. (2015). "U-Net: convolutional Networks for biomedical image segmentation," in *InMedical Image Computing and Computer-Assisted Intervention – MICCAI 2015. MICCAI 2015. Lecture Notes in Computer Science*, eds N. Navab, J. Hornegger, W. Wells, and A. Frangi (Cham: Springer), 234–241.

Saood, A., and Hatem, I. (2021). COVID-19 lung CT image segmentation using deep learning methods: U-Net versus SegNet. *BMC Med. Imaging* 21:19. doi: 10.1186/s12880-020-00529-5

Schwartz, J. T., Cho, B. H., Tang, P., Schefflein, J., Arvind, V., Kim, J. S., et al. (2021). Deep Learning Automates Measurement of Spinopelvic Parameters on Lateral Lumbar Radiographs. *Spine* 46, E671–E678. doi: 10.1097/BRS.0000000000003830

Seo, H., Badiei Khuzani, M., Vasudevan, V., Huang, C., Ren, H., Xiao, R., et al. (2020a). Machine learning techniques for biomedical image segmentation: an overview of technical aspects and introduction to state-of-art applications. *Med. Phys.* 47, e148–e167. doi: 10.1002/mp.13649

Seo, H., Huang, C., Bassenne, M., Xiao, R., and Xing, L. (2020b). Modified U-Net (mU-Net) With Incorporation of Object-Dependent High Level

Features for Improved Liver and Liver-Tumor Segmentation in CT Images. *IEEE Trans. Med. Imaging* 39, 1316–1325. doi: 10.1109/TMI.2019.2948320

Skourt, B. A., El Hassani, A., and Majda, A. (2018). Lung CT Image Segmentation Using Deep Neural Networks. *Procedia Comput. Sci.* 127, 109–113. doi: 10.1016/j.procs.2018.01.104

Sravani, K. (2019). Medical Image Segmentation Using Deep Learning Using SegNet. *IOSR J. Eng.* 09, 28–35.

Srivastava, N., Hinton, G., Krizhevsky, A., Sutskever, I., and Salakhutdinov, R. (2014). Dropout: a simple way to prevent neural Networks from overfitting. *J. Mach. Learn. Res.* 15, 1929–1958.

Sułot, D., Alonso-Caneiro, D., Ksieniewicz, P., Krzyzanowska-Berkowska, P., and Iskander, D. R. (2021). Glaucoma classification based on scanning laser ophthalmoscopic images using a deep learning ensemble method. *PLoS One* 16:e0252339. doi: 10.1371/journal.pone.0252339

Suzuki, K. (2017). Overview of deep learning in medical imaging. *Radiol. Phys. Technol.* 10, 257–273. doi: 10.1007/s12194-017-0406-5

Umapathy, L., Unger, W., Shareef, F., Arif, H., Martín, D., Altbach, M., et al. (2020). A Cascaded Residual UNET for Fully Automated Segmentation of Prostate and Peripheral Zone in T2-weighted 3D Fast Spin Echo Images. *ArXiv*. Available Online at: https://arxiv.org/ftp/arxiv/papers/2012/2012.13501.pdf (accessed August 17, 2021).

Wang, C., Shao, J., Lv, J., Cao, Y., Zhu, C., Li, J., et al. (2021). Deep learning for predicting subtype classification and survival of lung adenocarcinoma on computed tomography. *Transl. Oncol.* 14:101141. doi: 10.1016/j.tranon.2021.101141

Wang, Z., Zou, Y., and Liu, P. X. (2021). Hybrid dilation and attention residual U-Net for medical image segmentation. *Comput. Biol. Med.* 134:104449. doi: 10.1016/j.compbiomed.2021.104449

Yan, Y., and Zhang, D. (2021). . Multi-scale U-like Network with attention mechanism for automatic pancreas segmentation. *PLoS One* 16:e0252287. doi: 10.1371/journal.pone.0252287

Yasaka, K., Akai, H., Kunimatsu, A., Kiryu, S., and Abe, O. (2018). Deep learning with convolutional neural Network in radiology. *Jpn. J. Radiol.* 36, 257–272. doi: 10.1007/s11604-018-0726-3

Yi, P. H., Wei, J., Kim, T. K., Shin, J., Sair, H. I., Hui, F. K., et al. (2021). Radiology "forensics": determination of age and sex from chest radiographs using deep learning. *Emerg. Radiol.* doi: 10.1007/s10140-021-01953-y [Epub ahead of print].

Zhou, T., Canu, S., and Ruan, S. (2020). Automatic COVID-19 CT segmentation using U-Net integrated spatial and channel attention mechanism. *Int. J. Imaging Syst. Technol.* doi: 10.1002/ima.22527 [Epub ahead of print].

Zhou, Z., Siddiquee, M. M. R., Tajbakhsh, N., and Liang, J. (2018). UNet++: a Nested U-Net Architecture for Medical Image Segmentation. *Deep Learn. Med. Image Anal. Multimodal Learn. Clin. Decis. Support* 2018, 3–11. doi: 10.1007/978-3-030-00889-5_1

Conflict of Interest: The authors declare that the research was conducted in the absence of any commercial or financial relationships that could be construed as a potential conflict of interest.

Publisher's Note: All claims expressed in this article are solely those of the authors and do not necessarily represent those of their affiliated organizations, or those of the publisher, the editors and the reviewers. Any product that may be evaluated in this article, or claim that may be made by its manufacturer, is not guaranteed or endorsed by the publisher.

frontiers in Physiology

ORIGINAL RESEARCH
published: 18 October 2021
doi: 10.3389/fphys.2021.711273

Effects of Positive End-Expiratory Pressure on Lung Recruitment, Respiratory Mechanics, and Intracranial Pressure in Mechanically Ventilated Brain-Injured Patients

Chiara Robba[1,2†], Lorenzo Ball[1,2†], Stefano Nogas[1], Denise Battaglini[1], Antonio Messina[3], Iole Brunetti[1], Giuseppe Minetti[4], Lucio Castellan[4], Patricia R. M. Rocco[5] and Paolo Pelosi[1,2]*

[1] Anesthesia and Intensive Care, San Martino Policlinico Hospital, Istituto di Ricovero e Cura a Carattere Scientifico (IRCCS) for Oncology and Neurosciences, Genoa, Italy, [2] Department of Surgical Sciences and Integrated Diagnostics (DISC), University of Genoa, Genoa, Italy, [3] Humanitas Clinical and Research Center—Istituto di Ricovero e Cura a Carattere Scientifico (IRCCS), Rozzano, Italy, [4] Radiology Department San Martino Policlinico Hospital, Istituto di Ricovero e Cura a Carattere Scientifico (IRCCS) for Oncology and Neurosciences, Genoa, Italy, [5] Laboratory of Pulmonary Investigation, Carlos Chagas Filho Institute of Biophysics, Federal University of Rio de Janeiro, Rio de Janeiro, Brazil

OPEN ACCESS

Edited by:
Christopher G. Wilson,
Loma Linda University, United States

Reviewed by:
Sophie Lalande,
University of Texas at Austin, United States
Gabriele Valli,
Azienda Ospedaliera San Giovanni Addolorata, Italy

***Correspondence:**
Chiara Robba
kiarobba@gmail.com

[†] These authors have contributed equally to this work

Specialty section:
This article was submitted to Respiratory Physiology, a section of the journal Frontiers in Physiology

Received: 18 May 2021
Accepted: 09 September 2021
Published: 18 October 2021

Citation:
Robba C, Ball L, Nogas S, Battaglini D, Messina A, Brunetti I, Minetti G, Castellan L, Rocco PRM and Pelosi P (2021) Effects of Positive End-Expiratory Pressure on Lung Recruitment, Respiratory Mechanics, and Intracranial Pressure in Mechanically Ventilated Brain-Injured Patients. Front. Physiol. 12:711273. doi: 10.3389/fphys.2021.711273

Background: The pathophysiological effects of positive end-expiratory pressure (PEEP) on respiratory mechanics, lung recruitment, and intracranial pressure (ICP) in acute brain-injured patients have not been completely elucidated. The primary aim of this study was to assess the effects of PEEP augmentation on respiratory mechanics, quantitative computed lung tomography (qCT) findings, and its relationship with ICP modifications. Secondary aims included the assessment of the correlations between different factors (respiratory mechanics and qCT features) with the changes of ICP and how these factors at baseline may predict ICP response after greater PEEP levels.

Methods: A prospective, observational study included mechanically ventilated patients with acute brain injury requiring invasive ICP and who underwent two-PEEP levels lung CT scan. Respiratory system compliance (Crs), arterial partial pressure of carbon dioxide ($PaCO_2$), mean arterial pressure (MAP), data from qCT and ICP were obtained at PEEP 5 and 15 cmH_2O.

Results: Sixteen examinations (double PEEP lung CT and neuromonitoring) in 15 patients were analyzed. The median age of the patients was 54 years (interquartile range, IQR = 39–65) and 53% were men. The median Glasgow Coma Scale (GCS) at intensive care unit (ICU) admission was 8 (IQR = 3–12). Median alveolar recruitment was 2.5% of total lung weight (−1.5 to 4.7). PEEP from 5 to 15 cmH_2O increased ICP [median values from 14.0 (11.2–17.5) to 23.5 (19.5–26.8) mmHg, $p < 0.001$, respectively]. The amount of recruited lung tissue on CT was inversely correlated with the change (Δ) in ICP (rho = −0.78; $p = 0.0006$). Additionally, ΔCrs (rho = −0.77, $p = 0.008$), $\Delta PaCO_2$ (rho = 0.81, $p = 0.0003$), and ΔMAP (rho = −0.64, $p = 0.009$) were correlated with ΔICP. Baseline Crs was not predictive of ICP response to PEEP.

Conclusions: The main factors associated with increased ICP after PEEP augmentation included reduced Crs, lower MAP and lung recruitment, and increased $PaCO_2$, but none of these factors was able to predict, at baseline, ICP response to PEEP. To assess the potential benefits of increased PEEP in patients with acute brain injury, hemodynamic status, respiratory mechanics, and lung morphology should be taken into account.

Keywords: positive end expiratory pressure, intracranial pressure, brain injured patients, quantitative computed tomography, mechanical ventilation

INTRODUCTION

A substantial number of patients with acute brain injury require mechanical ventilation (Borsellino et al., 2016) due to both neurological and respiratory causes (Della Torre et al., 2017). The aim of mechanical ventilation is to optimize oxygen delivery and minimize lung and brain injury (Frisvold et al., 2019). The use of lung-protective ventilation strategies has been shown to reduce morbidity and mortality in acute respiratory distress syndrome (ARDS) and non-ARDS critically ill patients (Sutherasan et al., 2014; Serpa Neto et al., 2015; Simonis et al., 2018). However, strategies comprising the use of high positive end-expiratory pressure (PEEP) have been challenged in brain-injured patients because of concerns regarding their effects on cerebral hemodynamics (Nemer et al., 2011; Borsellino et al., 2016; Robba et al., 2020), in particular intracranial pressure (ICP). Possible mechanisms responsible for ICP augmentation after PEEP application include alveolar overdistension with the increase of arterial partial pressure of carbon dioxide ($PaCO_2$) levels, and hemodynamic instability (Caricato et al., 2005; Mascia et al., 2005; Nemer et al., 2011). To date, the pathophysiological interplay between intracranial changes, respiratory system mechanics, and alveolar recruitment has not been completely elucidated, and no specific recommendations are available regarding the optimal levels of PEEP to be applied in acute brain-injured patients (Robba et al., 2020). We, therefore, conducted an observational study whose primary aim was to investigate the effects of two levels of PEEP (5 and 15 cmH_2O) on respiratory mechanics, quantitative lung computed tomography (qCT) findings, and its relationship with ICP changes in brain-injured patients. Secondary aims included the assessment of the correlation between different factors (respiratory mechanics and qCT features) with the changes of ICP, and how these factors at baseline may predict ICP response after greater PEEP levels. Finally, we explored whether non-invasive neuromonitoring tools are able to assess changes of ICP following augmented PEEP levels. We hypothesized that the effect of greater PEEP levels on ICP depends on the amount of alveolar recruitment and respiratory mechanics.

METHODS

We followed the "Strengthening the Reporting of Observational Studies in Epidemiology (STROBE)" statement guidelines for observational cohort studies (**Supplementary Table 1**) (von Elm et al., 2014). This study was performed at San Martino Policlinico Hospital, Genoa, Italy, a tertiary academic hospital with neurocritical care facilities, from August 1, 2020, to March 8, 2021. The study was approved by the ethics review board "Comitato Etico Regione Liguria" (protocol n. CER Liguria: 23/2020). According to the local regulations, written consent was obtained from next of kin of the patients, as all patients were unconscious at the time of inclusion.

Inclusion and Exclusion Criteria

Inclusion criteria were critically ill adult patients who required intubation and invasive mechanical ventilation following acute brain injury (traumatic brain injury, TBI; subarachnoid hemorrhage, SAH; intracranial hemorrhage, ICH) admitted to the intensive care unit (ICU), requiring invasive ICP and other neuromonitoring tools (Transcranial Doppler, TCD and optic nerve sheath diameter, ONSD) and who underwent two-PEEP CT scan based on clinical indication with PEEP 5 and 15 cmH_2O. Exclusion criteria were the absence of informed consent; the absence of indications for invasive ICP monitoring (i.e., coagulopathy); the absence of temporal window for TCD evaluation; basal skull fracture with the cerebrospinal fluid leak, or ocular trauma for ONSD measurement; patients requiring contrast medium during CT for clinical reasons or having contraindications to higher PEEP (e.g., emphysema and undrained pneumothorax), or judged too instable to be safely transported to the CT facility (e.g., hemodynamic instability, need for high doses vasopressors, or acute and refractory increased ICP).

Data Collection and Patients' Management

Demographic, epidemiologic, and clinical data were obtained from electronic medical records of patients and collected by physicians trained in critical care at admission to the ICU and on the day when a double PEEP CT scan was obtained. Recorded data included admission demographics [age, gender, and body mass index (BMI)], comorbidities (asthma, chronic respiratory disease, hypertension, chronic cardiac disease diabetes mellitus, chronic kidney injury, and previous neurological disease), type of brain injury, neurological status at ICU admission (Glasgow Coma Scale, GCS), type of ICP monitoring (intraparenchymal and external ventricular drain), ICU complications, ICU length of stay (LOS), and Glasgow Outcome Score (GOS) at ICU discharge. Patients were sedated with propofol and/or midazolam and fentanyl, targeting the tidal volume of 6–8 ml per kg of predicted body weight (PBW), but increases were tolerated based on the driving pressure. The respiratory rate was titrated

to maintain pH between 7.35 and 7.45. On the day of CT scan, ventilatory data, respiratory mechanics, and blood gases parameters (i.e., inspired fraction of oxygen (FiO_2), PEEP, plateau pressure (Pplat), respiratory system compliance (Crs), tidal volume (VT), respiratory rate (RR), arterial and venous saturation of oxygen (SaO_2 and SvO_2), arterial pH (pHa), partial pressure of oxygen (PaO_2 and $PaCO_2$) were obtained at PEEP = 5 cmH_2O (T0) and at PEEP = 15 cmH_2O (T1). Vital signs, such as mean arterial pressure (MAP) and neuromonitoring parameters [ICP, ONSD, systolic, mean, and diastolic flow velocities (FVs, FVd, and FVm)] were also collected at T0 and T1.

Clinical Rationale for PEEP Test

The decision to perform a PEEP test was based on the judgment of the treating physician, if optimization of mechanical ventilation was required. PEEP test was performed in Volume-Controlled Ventilation aiming to target the tidal volume of 6–8 ml per kg/PBW. To date, no universal recommendations are available concerning the optimal PEEP levels in the invasively ventilated brain-injured patients (Robba et al., 2020). Therefore, in our institution, a PEEP test is performed to increasing PEEP from 5 to 15 cmH_2O, assessing both respiratory mechanics and cerebral hemodynamics. These values have previously been demonstrated to be safe and can lead to increased brain oxygenation, without the increase in ICP (Nemer et al., 2011). However, as greater PEEP levels may result in worsening of the respiratory mechanics with eventually increased alveolar hyperdistention (Mascia et al., 2005), two-PEEP CT, when possible, has become part of our routine clinical evaluation and has been performed in our institution in other groups of patients (Ball et al., 2021). Evaluation and calculation of gas exchanges, respiratory mechanics, and details on the protocol for two-PEEP CT acquisition and analysis are described in the ESM.

CT Scan Acquisition and Analysis

Images were acquired during expiratory breath-hold at 5 and 15 cmH_2O. The two scans were acquired in sequence, interleaved by 1–2 min of uninterrupted ventilation at PEEP 15 cmH_2O (Ball et al., 2021). This time of ventilation at 15 cmH_2O of PEEP was applied before repeating the CT scan (T1). For safety reasons, no recruitment maneuver was performed.

Lung segmentation was performed excluding big airway, vessels, and pleural effusion. Segmentations were performed using ITKSnap (http://www.itksnap.org), image analysis was performed with Matlab scripts (Mathworks, MA, USA), based on widely adopted numerical methods (Malbouisson et al., 2001). Alveolar recruitment was defined as the difference in the non-aerated compartment from PEEP 5–15 cmH_2O, divided by total lung weight at PEEP of 5 cmH_2O (Gattinoni et al., 2006).

Neuromonitoring

The indications for invasive ICP placement followed the latest Brain Trauma Foundation Guidelines (Carney et al., 2016). Ultrasound measurement was performed by a selected group of experienced operators (CR, SN, and DB) using a standardized insonation technique to reduce inter-operator variability. Ultrasound measurements were performed after PEEP augmentation and after repeating the second CT.

Transcranial Doppler was performed bilaterally on the middle cerebral artery (MCA) through the temporal window using a traditional 2-MHz transducer (Philips SparQ®) as previously described (Robba et al., 2017b). Non-invasive ICP estimation using TCD (ICP_{TCD}) was obtained using a previously validated formula (Rasulo et al., 2017). Ultrasound examination of the ONSD was performed using a 7.5 MHz linear ultrasound probe (Philips SparQ®) using the lowest possible acoustic power that could measure the ONSD. The probe was oriented perpendicularly in the vertical plane and at around 30° in the horizontal plane on the closed eyelids of both eyes of subjects in the supine position. Ultrasound gel was applied on the surface of each eyelid, and the measurements were made in the axial and sagittal planes of the widest diameter visible 3 mm behind the retina in both eyes. The final ONSD value was calculated as previously described (Robba et al., 2016, 2017a).

Statistical Analysis

An *a priori* sample size calculation was not feasible due to the lack of data on quantitative CT analysis in brain-injured patients, but our sample size was similar to previous physiologic studies regarding PEEP augmentation in ARDS or brain-injured patients (Mascia et al., 2005; Nemer et al., 2011; Mauri et al., 2016, 2020). Data are reported as median (interquartile range, IQR), if not otherwise specified. We compared data between groups with the Mann–Whitney *U* or Fisher's exact test, as appropriate. Variables acquired at two-PEEP levels were compared with the Wilcoxon signed-rank test. Changes of variables from PEEP 5 to PEEP 15 were calculated as Δ (value at PEEP 15 cmH_2O–value at PEEP 5 cmH_2O). Correlations were sought using Spearman's rho. A linear regression analysis was performed using ΔICP (invasive ICP) as the dependent variable and alveolar recruitment, ΔMAP, Crs, and $PaCO_2$ as independent variables. As an exploratory analysis, we modeled ΔICP as a function of clinically sound covariates using linear regression, adopting a variance inflation factor threshold of 5 as an acceptable limit for multi-collinearity. All statistical analyses were performed in SPSS Statistics, Version 25.0 (IBM Corp., Armonk, NY, USA). Significance was assumed at two-tailed $p < 0.05$.

RESULTS

General Characteristics

A total of 16 examinations (double PEEP quantitative CT and neuromonitoring, including invasive ICP, ONSD, and TCD) from 15 patients were included in the analysis (in one patient, the measures were obtained twice). The median age of the patients was 54 years (IQR = 39–65); 53.3% were men. Six patients (40%) were admitted for SAH, six after TBI (40%), and three (20%) for ICH (**Table 1**). The median GCS was eight (IQR = 3–12); intraparenchymal and intraventricular monitoring were inserted in seven (46.6%) and eight (53.3%) cases, respectively. One patient died in ICU (6.6%) and the median ICU LOS was 16 (IQR = 13–21) days.

TABLE 1 | Characteristics of the patients at ICU admission.

Demographics	
Gender, male, *n* (%)	8 (53.3%)
Age [years], median [IQR]	54 [39–65]
BMI [kg/m^2], median [IQR]	26.3 [25.5–27.9]
PBW [kg], median [IQR]	68.7 [57–78]
Comorbidities	
Respiratory disease, *n* (%)	3 (20)
Cardiovascular disease, *n* (%)	1 (6.6)
Cancer, *n* (%)	0 (0)
Neurologic disorders, *n* (%)	1 (6.6)
Moderate/severe liver disease, *n* (%)	1 (6.6)
End-stage kidney injury, *n* (%)	0 (0)
Hypertension, *n* (%)	7 (46.6)
Diabetes mellitus, *n* (%)	3 (20)
ICU characteristics	
Reason for ICU admission, *n* (%)	
TBI	6 (40)
SAH	6 (40)
ICH	3 (20)
GCS score, median [IQR]	8 [3–12]
Type of ICP monitor, *n* (%)	
Bold	7 (46.6)
EVD	8 (53.3)
Need for vasopressors, *n* (%)	13 (86.7)
ICU complications	
Respiratory failure, *n* (%)	1 (6.6)
Ventilator- associated pneumonia, *n* (%)	4 (26.6)
Cardiovascular, *n* (%)	2 (13.3)
Acute kidney injury, *n* (%)	0 (0)
Sepsis, *n* (%)	1 (6.6)
Vasospasm, *n* (%)	2 (13.3)
ICU discharge characteristics	
Mortality, *n* (%)	1 (6.6)
GOS, median [IQR]	4 [3–4]
ICU length of stay, median [IQR]	16 [13–21]

IQR, Interquartile range; n, number; BMI, body mass index; PBW, predicted body weight; ICU, intensive care unit; TBI, traumatic brain injury; SAH, subarachnoid hemorrhage; ICH, intracranial hemorrhage; GCS, Glasgow Coma Scale; ICP, intracranial pressure; EVD, external ventricular drain; GOS, Glasgow outcome score.

Effect of PEEP Augmentation on Respiratory Mechanics, Quantitative CT Findings, and ICP

Figure 1 shows two representative examples of CT images at 5 and 15 cmH_2O of PEEP in two patients with low and high alveolar recruitment. After greater PEEP levels, systemic oxygenation [PaO_2, from 96.4 (81–108) to 98 (85.4–148) mmHg; $p = 0.039$], and $PaCO_2$ [from 40 (36.8–44.9) to 44 (41.4–48.6) mmHg; $p = 0.034$] increased, while median Crs did not change (**Table 2** and **Figure 2**). Total lung volume was augmented after greater PEEP levels, as also the gas volume, but not total lung weight (**Table 2**). Median alveolar recruitment was 2.5% (−1.5–4.7). **Figure 3** illustrates the frequency distribution of Hounsfield units at 5 and 15 cmH_2O of PEEP. The increase of PEEP from 5 to 15 cmH_2O resulted in higher median invasive ICP values [14 (11.2–17.5) vs. 23.5 (19.5–26.8) mmHg, $p < 0.001$; **Figure 2**] and non-invasive ICP measured through TCD and of ONSD values. Higher PEEP also resulted in a significant reduction of cerebral perfusion pressure (CPP) [78 (71–81.7) vs. 63 (57.8–74.8) mmHg, $p = 0.001$; **Table 2**].

Correlation Between the Changes of Quantitative CT Variables, Respiratory Mechanics, and ICP

The variations of lung volume and gas volume evaluated at qCT analysis were not correlated with the changes of ICP (rho = 0.05; $p = 0.86$ and rho = −0.07; $p = 0.80$, respectively). However, the amount of recruited tissue was inversely correlated with ΔICP (rho = −0.78; $p = 0.0006$). ΔCrs, ΔPlateau pressure, Δ$PaCO_2$, and ΔMAP were significantly correlated with ΔICP (rho = −0.77; $p = 0.008$; rho = 0.54; $p = 0.0002$; rho = 0.81; $p = 0.0003$; rho = −0.64; $p = 0.009$, respectively; **Figure 4**).

At linear regression analysis, Δ$PaCO_2$ (regression coefficient B = 0.96, 95% CI from 0.1 to 1.8, $p = 0.028$) and ΔCrs (B = −0.41, 95% CI from −0.647 to −0.183, $p = 0.02$) were the only independently variables associated with ΔICP. We did not observe correlations between the ICP increase and the following parameters assessed at PEEP 5 cmH_2O: Crs, CO_2, MAP, ONSD, ICP_{TCD}, and invasive ICP ($p > 0.40$ in all correlations with ΔICP).

Correlation analysis between qCT variables, respiratory mechanics, and non-invasive ICP estimated through TCD and ONSD are presented in **Supplementary Table 2**. A significant correlation was found between the changes of ONSD and ICP (rho = 0.8096; $p = 0.0003$), but not between ICP_{TCD} and ICP (**Supplementary Figure 1**).

DISCUSSION

In a population of mechanically ventilated patients with acute brain injury, we found that (1) PEEP augmentation from 5 to 15 cmH_2O may lead to higher oxygenation, $PaCO_2$, and ICP values, with alveolar recruitment of 2.5% of total lung weight; (2) ICP increase with PEEP was correlated to higher $PaCO_2$, poor alveolar recruitment, reduction of Crs, and decreased MAP; (3) baseline values of Crs, $PaCO_2$, MAP, and ICP are not predictive for ICP increase with PEEP; and (4) changes in ONSD, but not ICP_{TCD}, are correlated to changes in ICP.

To our knowledge, this is the first study quantitatively assessing alveolar recruitment and its distribution in the whole lung in mechanically ventilated patients with acute brain injury and its associations with changes in ICP and main physiological and clinical parameters.

Acute brain-injured patients with a clinical indication for chest CT, such as respiratory failure, and/or suspect of pneumonia were included in the study. This explains why the alveolar recruitment induced by PEEP was 2.5% of total lung weight, similar to a previous cohort of patients with COVID-19 (Ball et al., 2021). In fact, in the healthy population, the average

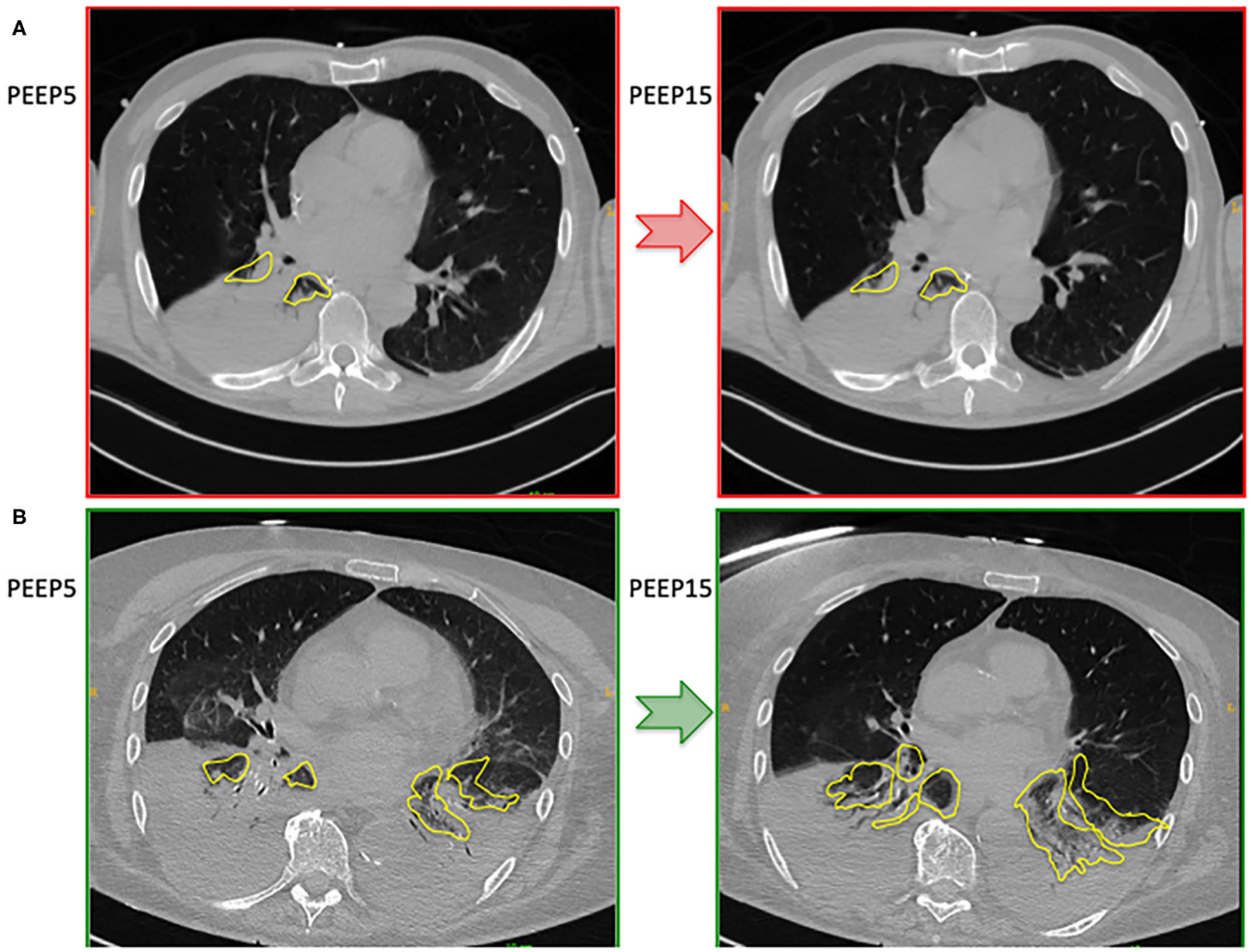

FIGURE 1 | Representative cases representing CT images at 5 and 15 cmH_2O of PEEP in a patient with poor alveolar recruitment **(A)** and good alveolar recruitment **(B)**.

lung weight is 930 g and gas volume 4,000 ml (Cressoni et al., 2013) in patients with ARDS-COVID-19, average lung weight is 1,500 g and gas volume 1,360 ml (Ball et al., 2021), whereas in our cohort of acute brain-injured patients average lung weight is 1,076 g and gas volume 1,693 ml.

Patients with acute brain injury admitted to ICU frequently require mechanical ventilation, and PEEP is often useful to support oxygenation, with the aim to ensure reliable oxygen delivery (Stevens et al., 2008; Borsellino et al., 2016; Del Sorbo et al., 2017) and minimize lung injury. However, mechanical ventilation and increased intrathoracic pressure can exert harmful effects on the brain due to complex physiological interactions between brain and lung compartments. The optimization of PEEP application in the general ICU population (Sutherasan et al., 2014; Algera et al., 2020) and in particular in patients with acute brain injury is still controversial. Recently, a systematic review of the literature revealed only marginal evidence for a specific ventilatory strategy in this group of patients (Robba et al., 2020), and only a few small physiologic studies have explored the effect of PEEP on intracranial dynamics (Caricato et al., 2005; Nemer et al., 2011). The use of higher PEEP may lead to possible negative hemodynamic effects, which could potentially lead to a reduction of MAP and therefore CPP. However, two small studies suggested that slow and progressive PEEP augmentation may be safe and can improve systemic and cerebral oxygenation without significant changes in ICP and CPP (Huynh et al., 2002; Nemer et al., 2011). Another important pathophysiological mechanism is the effect of respiratory mechanics on ICP. Caricato et al. (2005) demonstrated that in patients with low Crs (those with greater severity of lung injury and requiring higher PEEP), PEEP application had no important effects on cerebral and systemic hemodynamics. However, this finding was not confirmed in the present study. We observed a correlation between changes in ICP and worsening of Crs, but the absolute value of Crs at lower PEEP was not predictive for ICP increase with PEEP. We speculate that Crs measured at lower PEEP alone might not identify patients that will increase ICP at higher PEEP is not necessarily associated

TABLE 2 | Ventilator settings, respiratory mechanics, arterial blood gases, quantitative CT analysis, neuromonitoring data, and hemodynamics in our cohort at PEEP = 5 and 15 cmH_2O.

Parameter	PEEP = 5 (*N* = 16)	PEEP = 15 (*N* = 16)	*p*
Ventilator settings and arterial blood gases			
Tidal volume, median [IQR], ml/kg PBW	7.4 [6.9–7.9]	7.4 [6.9–7.9]	0.999
Respiratory rate, median [IQR], 1/min	21 [18–23]	21 [18–22]	0.257
Plateau pressure, median [IQR], cmH_20	21 [18–22]	30 [28–34]	<0.001
Respiratory system compliance, median [IQR], ml/cmH_20	30 [30–38]	34 [28–41]	0.759
Venous admixture, median [IQR], (%)	25.7 [15.1–32.3]	21.6 [15–31.2]	0.717
Ventilation ratio, median [IQR]	1.7 [1.5–2]	1.9 [1.7–2.2]	0.109
pH, median [IQR]	7.41 [7.36–7.45]	7.45 [7.39–7.48]	0.343
PaO_2, median [IQR], mmHg	96 [81–108]	98 [85–148]	0.039
SaO_2, median [IQR], mmHg	98 [97–100]	99 [97–99]	0.724
$PaCO_2$, median [IQR], mmHg	40 [37–45]	44 [41–49]	0.034
SvO_2, median [IQR], mmHg	72 [63–78]	75 [68–78]	0.453
PaO_2/FiO_2, median [IQR], mmHg	195 [163–216]	195 [171–296]	0.049
Quantitative computed tomography analysis			
Total lung volume (ml)	2,704 [2,360–3,574]	3,334 [2,883–4,228]	0.001
Total lung weight (g)	1,076 [915–1,368]	1,010 [884–1,365]	0.679
Gas volume (ml)	1,693 [1,204–2,292]	2,429 [1,862–2,864]	<0.001
Mean attenuation (HU)	−601 [-671 −−557]	−677 [-724 −−618]	0.001
Hyper-aerated tissue (g)	10 [3–17]	23 [14–32]	0.002
Hyper-aerated tissue (% of total lung weight)	0.8 [0.3–1.5]	2 [1.4–2.3]	0.001
Normally aerated tissue (g)	449 [382–592]	533 [402–655]	0.002
Normally aerated tissue (% of total lung weight)	45 [31.4–54.2]	48 [35–55]	0.008
Poorly aerated tissue (g)	250 [193–307]	199 [167–278]	0.023
Poorly aerated tissue (% of total lung weight)	22.4 [16.6–26.1]	19.7 [13.1–21.6]	0.017
Non-aerated tissue (g)	434 [213–563]	344 [189–567]	0.121
Non-aerated tissue (% of total lung weight)	30.1 [25–44.6]	31.2 [21.2–39]	0.017
Neuromonitoring			
ICP, median [IQR], mmHg	14 [11–17]	23 [19–26]	<0.001
CPP, median [IQR], mmHg	78 [71–82]	63 [58–75]	0.001
FVs, median [IQR], cm/s	112 [106–121]	97 [55–116]	0.036
FVd, median [IQR], cm/s	43 [32–51]	19 [15–27]	0.001
FVm, median [IQR], cm/s	65 [59–74]	46 [31–56]	0.001
ONSD, median [IQR], mm	4.5 [4.1–5.1]	5.8 [5.4–6.4]	0.001
ICP_{TCD}, median [IQR], mmHg	21 [18–25]	33 [31–45]	0.001
Hemodynamics			
Mean arterial pressure, median [IQR], mmHg	91 [87–97]	90 [84–94]	0.086

Data are presented as median [IQR, interquartile range]. IQR, interquartile range; PaO_2, arterial partial pressure of oxygen, SaO_2, arterial oxygen saturation; $PaCO_2$, arterial partial pressure of carbon dioxide; SvO_2, venous saturation of oxygen; PaO_2/FiO_2 (inspired fraction of oxygen); HU: Hounsfield Units; ICP, intracranial pressure; FVs, FVd, FVm, systolic, diastolic, mean flow velocity; ONSD, optic nerve sheath diameter; ICP_{TCD}, intracranial pressure measured with transcranial Doppler (TCD); CPP, cerebral perfusion pressure.

with the potential for lung recruitment. Patients with greater lung recruitment will improve lung gas distribution not resulting in ICP increase, while non-recruiters will over-inflate already aerated areas with a negative impact on dead space and possibly on venous return. In a prospective study that has 12 brain-injured patients, where 5 and 10 cmH_2O of PEEP was randomly applied, patients defined as recruiters increased Crs and PaO_2, while in non-recruiters Crs decreased and $PaCO_2$ increased. Furthermore, ICP and jugular saturation remained constant in recruiters but significantly increased in non-recruiters, showing a significant correlation between changes in ICP, compliance, and $PaCO_2$.

This suggests that PEEP may have a detrimental effect on ICP only when it causes alveolar hyperinflation leading to a significant increase in $PaCO_2$, whereas when PEEP leads to good alveolar recruitment, ICP does not change.

Our results and previous evidence suggest that a precise evaluation of respiratory mechanics and gas exchange modifications may be of great importance in the assessment of recruitment. Comparative studies have shown that the only

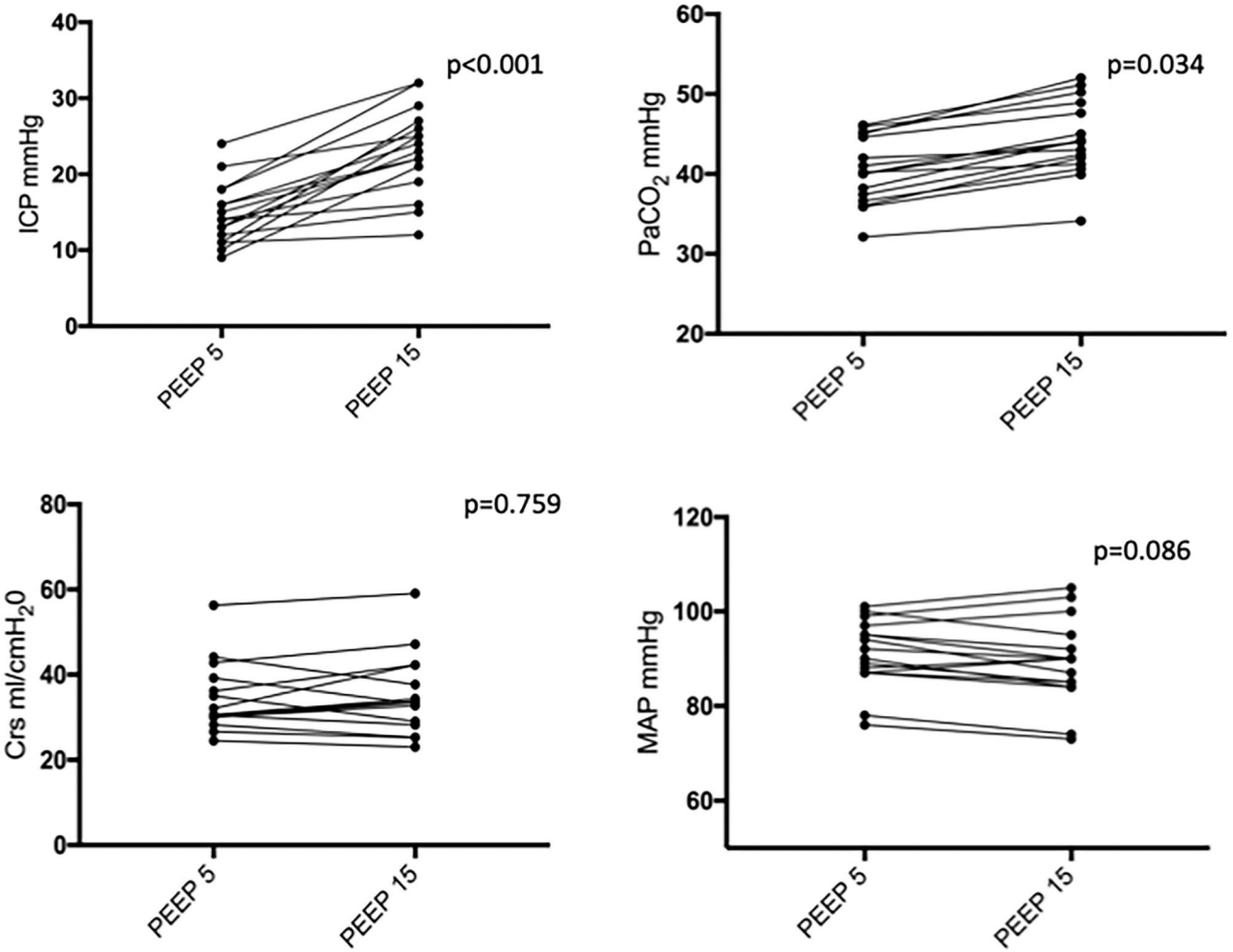

FIGURE 2 | Intracranial pressure (ICP), partial pressure of carbon dioxide ($PaCO_2$), respiratory system compliance (Crs), and mean arterial pressure (MAP) at PEEP of 5 and 15 cmH_2O. Black dots and lines represent individual patient data. PEEP, positive end-expiratory pressure.

possible method to evaluate the amount of collapsed lung tissue regaining inflation is the CT scan (Gattinoni et al., 2017), thus making our study unique in the description of the pathophysiological effects of PEEP on the intracranial compartment, based on the characteristics of lung morphology. Our results show that in patients with acute brain injury increased $PaCO_2$ and reduction of CPP and Crs with PEEP are the main factors associated with increased ICP. In fact, the potential mechanisms related to the overall ICP increase observed in our cohort might be related to the increase of $PaCO_2$ and reduction of CPP. However, as MAP did not change, this latter mechanism was probably related to a reduction of intracranial compliance consequent to the supine position, thus possibly reducing jugular venous outflow.

We also demonstrated that the amount of alveolar recruitment is an important determinant of changes in ICP, thus suggesting that in patients with good response to alveolar recruitment, which leads to the improvement of Crs without affecting hemodynamic status and without causing alveolar hyperdistension of patients and therefore increased $PaCO_2$, PEEP augmentation might be safe.

All in it, the principles for PEEP safety and titration in patients with acute brain injury seem not to be importantly different from those applied in the general ICU population and should take into account hemodynamic status, respiratory mechanics, and CT findings of patients (Ball et al., 2021). Indeed, a recent expert consensus (Robba et al., 2020) suggested that in brain-injured patients the levels of PEEP should be the same as for the general critically ill population. Similarly, a survey of the European Society of Intensive Care (Stocchetti et al., 2014) and a recent large multicenter study (Tejerina et al., 2021) suggest that moderate-high levels of PEEP are currently part of the clinical practice of neurocritical care physicians.

Finally, we explored the potential role of non-invasive ICP methods for the evaluation of changes of ICP after PEEP

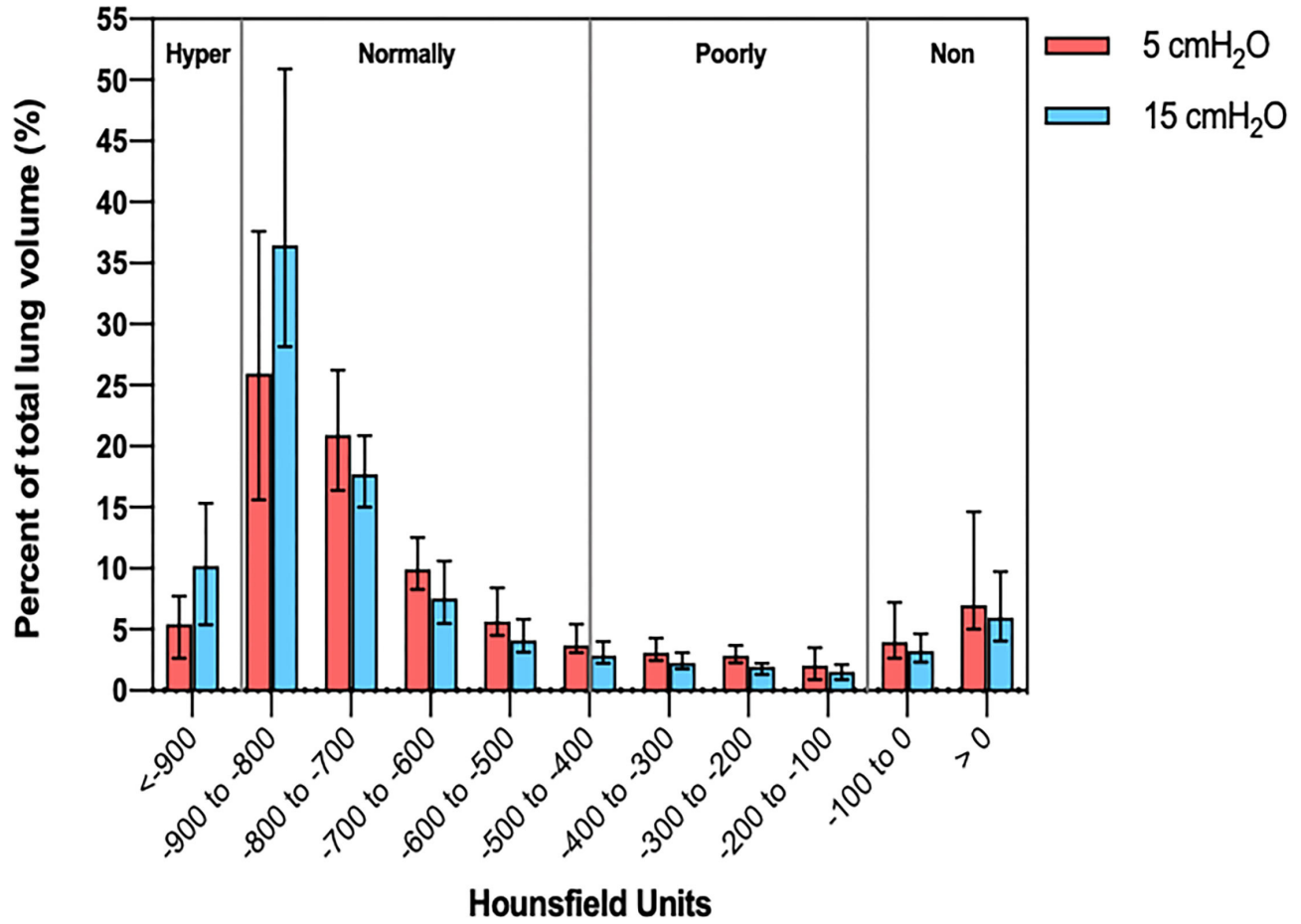

FIGURE 3 | Histogram distribution of lung volume aeration at 5 and 15 cmH_2O of PEEP. PEEP, positive end-expiratory pressure.

application. We found no significant correlation between non-invasive methods and qCT or respiratory mechanics data. This suggests that invasive ICP methods should be always considered as the gold standard for the evaluation of cerebral hemodynamics (Robba et al., 2015). However, changes in ONSD seem to be correlated with changes in ICP, thus making this tool a promising method for the bedside assessment of intracranial modifications when ICP is not available or contraindicated (Robba et al., 2018).

There are several limitations in our study that deserve to be mentioned. First, the sample size is small, despite similar to previous physiological studies exploring the effect of PEEP on lung recruitment (Mascia et al., 2005; Nemer et al., 2011; Mauri et al., 2016, 2020).

Second, in our center, a CT scan with double PEEP is routinely performed in selected patients with acute brain-injured patients, but only when CT is clinically indicated and in sufficiently stable patients. Therefore, patients were affected by brain damage of different nature and were heterogeneous as for comorbidities and lung damage.

Third, we cannot exclude that different ventilator setting may have led to different results (Gattinoni et al., 2006). However, we standardized mechanical ventilator settings, respiratory mechanics evaluation, and arterial blood gases measurement. In addition, we used a relatively short time for high PEEP exposure before repetition of CT. However, studies showed that most changes in volume and recruitment occur in this timeframe and that most respiratory units recruit below 30 cmH_2O (Katz et al., 1981; Crotti et al., 2001). In fact, we were able to detect a clear recruitment effect in some patients. In addition, more data and details regarding hemodynamics and cardiac performance would have added greater insights regarding the effect of PEEP on cardiac function; however, unfortunately, we do not routinely perform in our institution echocardiography or carotid flow assessment during PEEP challenge. Finally, patients were in a supine position during CT, and this might have led to an increase of ICP regardless of the implementation of PEEP.

CONCLUSIONS

Quantitative CT can help in the assessment of lung recruitability and the effect of different PEEP levels on ICP. The main factors associated with an increase of ICP after PEEP augmentation include worsening of Crs, reduction of MAP, low lung

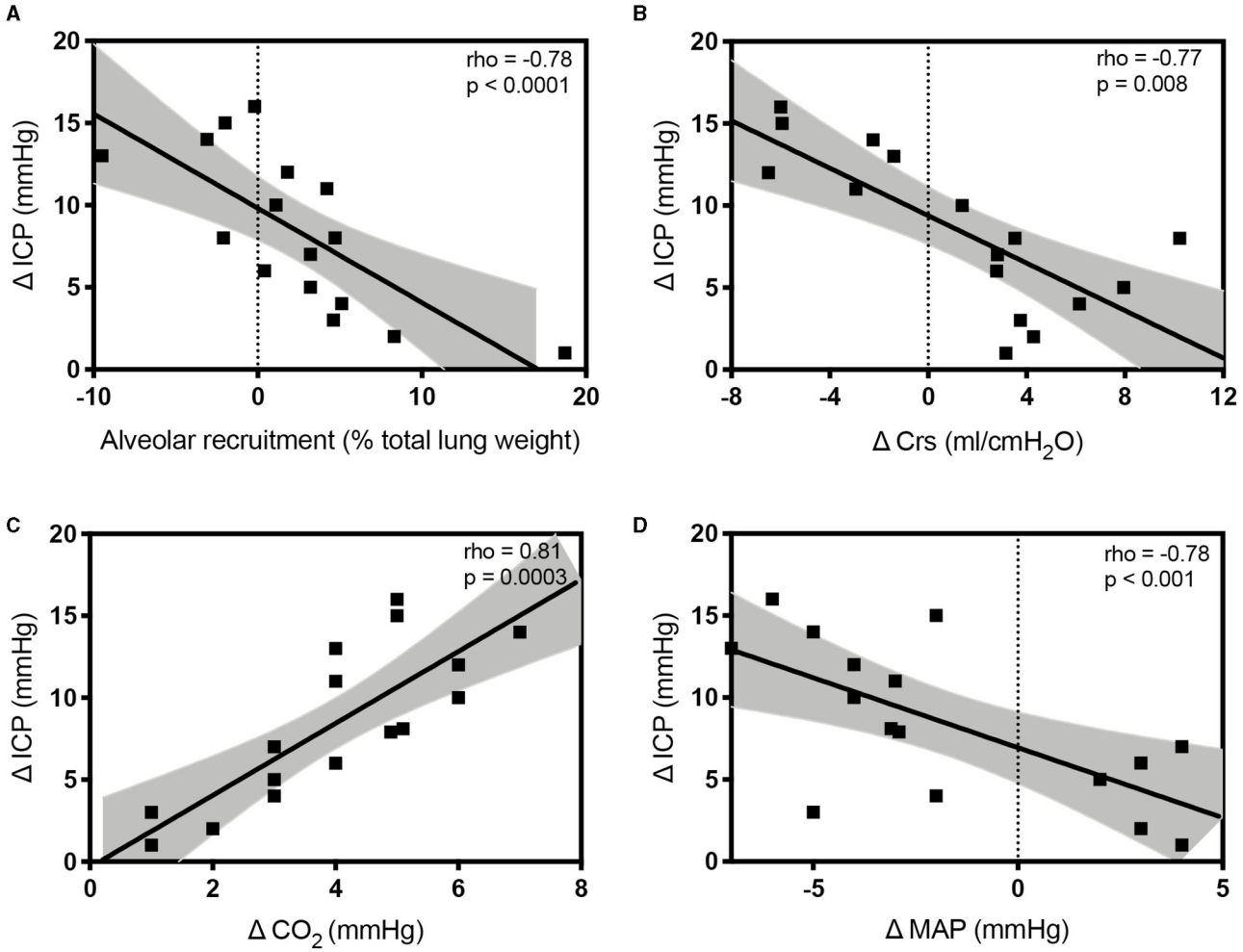

FIGURE 4 | Scatterplots showing the linear association and correlation between alveolar recruitment **(A)**, Δ respiratory system compliance (Crs; **B**), Δ carbon dioxide ($PaCO_2$; **C**), Δ mean arterial pressure (MAP; **D**) vs. Δ intracranial pressure (ICP) at different study time points. Dotted lines represent the 95% CIs for the linear regression.

recruitment, and increased $PaCO_2$. The potential benefits of PEEP augmentation in acute brain-injured patients should take into account hemodynamic status, respiratory mechanics, and lung morphology of patients. Further research is warranted to assess the effect of PEEP on ICP and the application of non-invasive ICP methods in this context.

DATA AVAILABILITY STATEMENT

The raw data supporting the conclusions of this article will be made available by the authors, without undue reservation.

ETHICS STATEMENT

The studies involving human participants were reviewed and approved by Comitato Etico Genova, Liguria. The patients/participants provided their written informed consent to participate in this study.

AUTHOR CONTRIBUTIONS

CR, LB, PR, and PP designed the study and the methods. CR, SN, and DB collected the data. LB and CR performed the statistical analysis. All the authors participated in data evaluation, analysis, manuscript revision, and final manuscript approval.

SUPPLEMENTARY MATERIAL

The Supplementary Material for this article can be found online at: https://www.frontiersin.org/articles/10.3389/fphys.2021.711273/full#supplementary-material

REFERENCES

Algera, A. G., Pisani, L., Serpa Neto, A., den Boer, S. S., Bosch, F. F. H., Bruin, K., et al. (2020). Effect of a lower vs. higher positive end-expiratory pressure strategy on ventilator-free days in ICU patients without ARDS: a randomized clinical trial. *J. Am. Med. Assoc.* 324, 2509–2520. doi: 10.1001/jama.2020.23517

Ball, L., Robba, C., Maiello, L., Herrmann, J., Gerard, S. E., Xin, Y., et al. (2021). Computed tomography assessment of PEEP-induced alveolar recruitment in patients with severe COVID-19 pneumonia. *Crit. Care*. 25:81. doi: 10.1186/s13054-021-03477-w

Borsellino, B., Schultz, M. J., Gama de Abreu, M., Robba, C., and Bilotta, F. (2016). Mechanical ventilation in neurocritical care patients: a systematic literature review. *Expert. Rev. Respir. Med.* 10, 1123–1132. doi: 10.1080/17476348.2017.1235976

Caricato, A., Conti, G., Corte, F., Della, M, A., Santilli, F., Sandroni, C., et al. (2005). Effects of PEEP on the intracranial system of patients with head injury and subarachnoid hemorrhage: the role of respiratory system compliance. *J. Trauma Inj. Infect. Crit. Care* 58, 571–576. doi: 10.1097/01.TA.0000152806.19198.DB

Carney, N., Totten, A. M., O'Reilly, C., Ullman, J. S., Hawryluk, G. W. J., Bell, M. J., et al. (2016). Guidelines for the management of severe traumatic brain injury, fourth edition. *Neurosurgery* 2016, 1–10. doi: 10.1227/NEU.0000000000001432

Cressoni, M., Gallazzi, E., Chiurazzi, C., Marino, A., Brioni, M., Menga, F., et al. (2013). Limits of normality of quantitative thoracic CT analysis. *Crit. Care*. 17:R93. doi: 10.1186/cc12738

Crotti, S., Mascheroni, D., Caironi, P., Pelosi, P., Ronzoni, G., Mondino, M., et al. (2001). Recruitment and derecruitment during acute respiratory failure. *Am. J. Respir. Crit. Care Med.* 164, 131–140. doi: 10.1164/ajrccm.164.1.2007011

Del Sorbo, L., Goligher, E. C., McAuley, D. F., Rubenfeld, G. D., Brochard, L. J., Gattinoni, L., et al. (2017). Mechanical ventilation in adults with acute respiratory distress syndrome: summary of the experimental evidence for the clinical practice guideline. *Ann. Am. Thorac Soc.* 14, S261–S270. doi: 10.1513/AnnalsATS.201704-345OT

Della Torre, V., Badenes, R., Corradi, F., Racca, F., Lavinio, A., Matta, B., et al. (2017). Acute respiratory distress syndrome in traumatic brain injury: how do we manage it? *J. Thorac Dis.* 9, 5369–5381. doi: 10.21037/jtd.2017.11.03

Frisvold, S. K., Robba, C., and Guérin, C. (2019). What respiratory targets should be recommended in patients with brain injury and respiratory failure? *Intens. Care Med.* 45, 683–686. doi: 10.1007/s00134-019-05556-7

Gattinoni, L., Caironi, P., Cressoni, M., Chiumello, D., Ranieri, V. M., Quintel, M., et al. (2006). Lung recruitment in patients with the acute respiratory distress syndrome. *N. Engl. J. Med.* 354, 1775–1786. doi: 10.1056/NEJMoa052052

Gattinoni, L., Collino, F., Maiolo, G., Rapetti, F., Romitti, F., Tonetti, T., et al. (2017). Positive end-expiratory pressure: how to set it at the individual level. *Ann. Transl. Med.* 5:288. doi: 10.21037/atm.2017.06.64

Huynh, T., Messer, M., Sing, R. F., Miles, W., Jacobs, D. G., Thomason, M. H., et al. (2002). Positive end-expiratory pressure alters intracranial and cerebral perfusion pressure in severe traumatic brain injury. *J. Trauma* 53, 488–492. doi: 10.1097/00005373-200209000-00016

Katz, J. A., Ozanne, G. M., Zinn, S. E., and Fairley, H. B. (1981). Time course and mechanisms of lung-volume increase with PEEP in acute pulmonary failure. *Anesthesiology* 54, 9–16. doi: 10.1097/00000542-198101000-00003

Malbouisson, L. M., Muller, J. C., Constantin, J. M., Lu, Q., Puybasset, L., Rouby, J. J., et al. (2001). Computed tomography assessment of positive end-expiratory pressure-induced alveolar recruitment in patients with acute respiratory distress syndrome. *Am. J. Respir. Crit. Care Med.* 163, 1444–1450. doi: 10.1164/ajrccm.163.6.2005001

Mascia, L., Grasso, S., Fiore, T., Bruno, F., Berardino, M., and Ducati, A. (2005). Cerebro-pulmonary interactions during the application of low levels of positive end-expiratory pressure. *Intens. Care Med.* 31, 373–379. doi: 10.1007/s00134-004-2491-2

Mauri, T., Eronia, N., Turrini, C., Battistini, M., Grasselli, G., Rona, R., et al. (2016). Bedside assessment of the effects of positive end-expiratory pressure on lung inflation and recruitment by the helium dilution technique and electrical impedance tomography. *Intens. Care Med.* 42, 1576–1587. doi: 10.1007/s00134-016-4467-4

Mauri, T., Spinelli, E., Scotti, E., Colussi, G., Basile, M. C., Crotti, S., et al. (2020). Potential for lung recruitment and ventilation-perfusion mismatch in patients with the acute respiratory distress syndrome from coronavirus disease 2019. *Crit. Care Med.* 48, 1129–1134. doi: 10.1097/CCM.0000000000004386

Nemer, S., Santos, R., Caldeira, J., Reis, P., Guimarães, B., Loureiro, T., et al. (2011). Positive end-expiratory pressure can increase brain tissue oxygen pressure in hypoxemic severe traumatic brain injury patients. *Crit. Care*. 15:P41. doi: 10.1186/cc10189

Rasulo, F. A., Bertuetti, R., Robba, C., Lusenti, F., Cantoni, A., Bernini, M., et al. (2017). The accuracy of transcranial Doppler in excluding intracranial hypertension following acute brain injury: a multicenter prospective pilot study. *Crit. Care*. 21:44. doi: 10.1186/s13054-017-1632-2

Robba, C., Bragazzi, N. L., Bertuccio, A., Cardim, D., Donnelly, J., Sekhon, M., et al. (2017a). Effects of prone position and positive end-expiratory pressure on noninvasive estimators of ICP: a pilot study. *J. Neurosurg. Anesthesiol.* 29, 243–250. doi: 10.1097/ANA.0000000000000295

Robba, C., Cardim, D., Donnelly, J., Bertuccio, A., Bacigaluppi, S., Bragazzi, N., et al. (2016). Effects of pneumoperitoneum and Trendelenburg position on intracranial pressure assessed using different non-invasive methods. *Br. J. Anaesth.* 117, 783–791. doi: 10.1093/bja/aew356

Robba, C., Cardim, D., Tajsic, T., Pietersen, J., Bulman, M., Donnelly, J., et al. (2017b). Ultrasound non-invasive measurement of intracranial pressure in neurointensive care: a prospective observational study. *PLoS Med.* 14:1002356. doi: 10.1371/journal.pmed.1002356

Robba, C., Donnelly, J., Bertuetti, R., Cardim, D., Sekhon, M. S., Aries, M., et al. (2015). Doppler non-invasive monitoring of ICP in an animal model of acute intracranial hypertension. *Neurocrit. Care* 23, 419–426. doi: 10.1007/s12028-015-0163-4

Robba, C., Poole, D., McNett, M., Asehnoune, K., Bösel, J., Bruder, N., et al. (2020). Mechanical ventilation in patients with acute brain injury: recommendations of the European Society of Intensive Care Medicine consensus. *Intens. Care Med.* 46, 2397–2410. doi: 10.1007/s00134-020-06283-0

Robba, C., Santori, G., Czosnyka, M., Corradi, F., Bragazzi, N., Padayachy, L., et al. (2018). Optic nerve sheath diameter measured sonographically as non-invasive estimator of intracranial pressure: a systematic review and meta-analysis. *Intens. Care Med.* 44, 1284–1294. doi: 10.1007/s00134-018-5305-7

Serpa Neto, A., Hemmes, S. N. T., Barbas, C. S. V., Beiderlinden, M., Biehl, M., Binnekade, J. M., et al. (2015). Protective versus conventional ventilation for surgery: a systematic review and individual patient data meta-analysis. *Anesthesiology* 123, 66–78. doi: 10.1097/ALN.0000000000000706

Simonis, F. D., Serpa Neto, A., Binnekade, J. M., Braber, A., Bruin, K. C. M., Determann, R. M., et al. (2018). Effect of a low vs intermediate tidal volume strategy on ventilator-free days in intensive care unit patients without ARDS. *J. Am. Med. Assoc.* 320, 1872–1880. doi: 10.1001/jama.2018.14280

Stevens, R. D., Lazaridis, C., and Chalela, J. A. (2008). The role of mechanical ventilation in acute brain injury. *Neurol. Clin.* 26, 543–563. doi: 10.1016/j.ncl.2008.03.014

Stocchetti, N., Picetti, E., Berardino, M., Buki, A., Chesnut, R. M., Fountas, K. N., et al. (2014). Clinical applications of intracranial pressure monitoring in traumatic brain injury : report of the Milan consensus conference. *Acta Neurochir.* 156, 1615–1622. doi: 10.1007/s00701-014-2127-4

Sutherasan, Y., Vargas, M., and Pelosi, P. (2014). Protective mechanical ventilation in the non-injured lung: review and meta-analysis. *Crit. Care.* 18:211. doi: 10.1186/cc13778

Tejerina, E. E., Pelosi, P., Robba, C., Peñuelas, O., Muriel, A., Barrios, D., et al. (2021). Evolution over time of ventilatory management and outcome of patients with neurologic disease. *Crit. Care Med.* 49, 1095–1106. doi: 10.1097/CCM.0000000000004921

von Elm, E., Altman, D. G., Egger, M., Pocock, S. J., Gøtzsche, P. C., and Vandenbroucke, J. P. (2014). The strengthening the reporting of observational

studies in epidemiology (STROBE) statement: guidelines for reporting observational studies. *Int. J. Surg.* 12, 1495–1499. doi: 10.1016/j.ijsu.2014.07.013

Conflict of Interest: The authors declare that the research was conducted in the absence of any commercial or financial relationships that could be construed as a potential conflict of interest.

Publisher's Note: All claims expressed in this article are solely those of the authors and do not necessarily represent those of their affiliated organizations, or those of the publisher, the editors and the reviewers. Any product that may be evaluated in this article, or claim that may be made by its manufacturer, is not guaranteed or endorsed by the publisher.

frontiers in Physiology

ORIGINAL RESEARCH
published: 22 November 2021
doi: 10.3389/fphys.2021.717266

Mechanical Power Correlates With Lung Inflammation Assessed by Positron-Emission Tomography in Experimental Acute Lung Injury in Pigs

Martin Scharffenberg[1], Jakob Wittenstein[1], Xi Ran[1,2], Yingying Zhang[1,3], Anja Braune[4], Raphael Theilen[1], Lorenzo Maiello[1,5], Giulia Benzi[1,6], Thomas Bluth[1], Thomas Kiss[1,7], Paolo Pelosi[5,8], Patricia R. M. Rocco[9], Marcus J. Schultz[10], Jörg Kotzerke[4], Marcelo Gama de Abreu[1,11,12] and Robert Huhle[1]*

[1] Department of Anesthesiology and Intensive Care Medicine, Pulmonary Engineering Group, University Hospital Carl Gustav Carus, Technische Universität Dresden, Dresden, Germany, [2] Department of Intensive Care, Chongqing General Hospital, University of Chinese Academy of Sciences, Chongqing, China, [3] Department of Anesthesiology, Affiliated Hospital of Southwest Medical University, Luzhou, China, [4] Department of Nuclear Medicine, University Hospital Carl Gustav Carus, Technische Universität Dresden, Dresden, Germany, [5] Anesthesia and Critical Care, San Martino Policlinico Hospital, IRCCS for Oncology and Neurosciences, Genoa, Italy, [6] Department of Clinical and Biological Sciences, Service of Anesthesia and Intensive Care, Ospedale di Circolo e Fondazione Macchi, University of Insubria, Varese, Italy, [7] Department of Anaesthesiology, Intensive-, Pain- and Palliative Care Medicine, Radebeul Hospital, Academic Hospital of the Technische Universität Dresden, Radebeul, Germany, [8] Department of Surgical Sciences and Integrated Diagnostics, University of Genoa, Genoa, Italy, [9] Laboratory of Pulmonary Investigation, Carlos Chagas Filho Institute of Biophysics, Federal University of Rio de Janeiro, Rio de Janeiro, Brazil, [10] Department of Intensive Care and Laboratory of Experimental Intensive Care and Anaesthesiology, Academic Medical Center, University of Amsterdam, Amsterdam, Netherlands, [11] Department of Intensive Care and Resuscitation, Anesthesiology Institute, Cleveland Clinic, Cleveland, OH, United States, [12] Department of Outcomes Research, Anesthesiology Institute, Cleveland Clinic, Cleveland, OH, United States

OPEN ACCESS

Edited by:
Christopher G. Wilson,
Loma Linda University, United States

Reviewed by:
Sam Bayat,
Université Grenoble Alpes, France
Gaetano Perchiazzi,
Uppsala University, Sweden

***Correspondence:**
Marcelo Gama de Abreu
gamadem@ccf.org

Specialty section:
This article was submitted to Respiratory Physiology, a section of the journal Frontiers in Physiology

Received: 30 May 2021
Accepted: 20 October 2021
Published: 22 November 2021

Citation:
Scharffenberg M, Wittenstein J, Ran X, Zhang Y, Braune A, Theilen R, Maiello L, Benzi G, Bluth T, Kiss T, Pelosi P, Rocco PRM, Schultz MJ, Kotzerke J, Gama de Abreu M and Huhle R (2021) Mechanical Power Correlates With Lung Inflammation Assessed by Positron-Emission Tomography in Experimental Acute Lung Injury in Pigs. Front. Physiol. 12:717266. doi: 10.3389/fphys.2021.717266

Background: Mechanical ventilation (MV) may initiate or worsen lung injury, so-called ventilator-induced lung injury (VILI). Although different mechanisms of VILI have been identified, research mainly focused on single ventilator parameters. The mechanical power (MP) summarizes the potentially damaging effects of different parameters in one single variable and has been shown to be associated with lung damage. However, to date, the association of MP with pulmonary neutrophilic inflammation, as assessed by positron-emission tomography (PET), has not been prospectively investigated in a model of clinically relevant ventilation settings yet. We hypothesized that the degree of neutrophilic inflammation correlates with MP.

Methods: Eight female juvenile pigs were anesthetized and mechanically ventilated. Lung injury was induced by repetitive lung lavages followed by initial PET and computed tomography (CT) scans. Animals were then ventilated according to the acute respiratory distress syndrome (ARDS) network recommendations, using the lowest combinations of positive end-expiratory pressure and inspiratory oxygen fraction that allowed adequate oxygenation. Ventilator settings were checked and adjusted hourly. Physiological measurements were conducted every 6 h. Lung imaging was repeated 24 h after first PET/CT before animals were killed. Pulmonary neutrophilic inflammation was assessed by normalized uptake rate of 2-deoxy-2-[^{18}F]fluoro-D-glucose (K_{iS}), and its difference between the two PET/CT was calculated (ΔK_{iS}). Lung aeration was assessed by lung CT

scan. MP was calculated from the recorded pressure–volume curve. Statistics included the Wilcoxon tests and non-parametric Spearman correlation.

Results: Normalized ^{18}F-FDG uptake rate increased significantly from first to second PET/CT ($p = 0.012$). ΔK_{iS} significantly correlated with median MP ($\rho = 0.738$, $p = 0.037$) and its elastic and resistive components, but neither with median peak, plateau, end-expiratory, driving, and transpulmonary driving pressures, nor respiratory rate (RR), elastance, or resistance. Lung mass and volume significantly decreased, whereas relative mass of hyper-aerated lung compartment increased after 24 h ($p = 0.012$, $p = 0.036$, and $p = 0.025$, respectively). Resistance and $PaCO_2$ were significantly higher ($p = 0.012$ and $p = 0.017$, respectively), whereas RR, end-expiratory pressure, and MP were lower at 18 h compared to start of intervention.

Conclusions: In this model of experimental acute lung injury in pigs, pulmonary neutrophilic inflammation evaluated by PET/CT increased after 24 h of MV, and correlated with MP.

Keywords: mechanical ventilation, acute respiratory distress syndrome, ARDS, ventilator- induced lung injury, VILI, mechanical power, pulmonary neutrophilic inflammation, ^{18}F-FDG

INTRODUCTION

Mechanical ventilation (MV) is often life-saving in critically ill patients with acute respiratory failure and/or acute respiratory distress syndrome (ARDS) (Bellani et al., 2016). However, MV may lead to ventilator-induced lung injury (VILI) (Dreyfuss and Saumon, 1998). Different mechanisms of VILI have been identified so far. High distending pressures may promote baro- and volutrauma, whereas repetitive aeration and collapse of alveoli may induce atelectrauma (Güldner et al., 2016). Inhomogeneous lung aeration can further aggravate mechanical stress and lung injury (Mead et al., 1970). Although certain measures to prevent VILI have been established (Acute Respiratory Distress Syndrome Network Brower et al., 2000; Amato et al., 2015), e.g., limitation of tidal volume (V_T) or airway plateau and driving pressures, discussion about adequate levels of positive end-expiratory pressure (PEEP) is ongoing, and the interplay among parameters is complex (Battaglini et al., 2021). Irrespectively of specific parameters, mechanical energy is inevitably transferred to the respiratory system in every single MV cycle, resulting in transferred mechanical power (MP) when multiplied with respiratory rate (RR). Although it has been known that the transferred energy, or power, is partly restored and dissipated in the respiratory system (Sassoon and Mahutte, 1998; Guttmann, 2010), the concept gained new attention recently when MP was proposed as the main determinant of VILI (Cressoni et al., 2016; Gattinoni et al., 2016), which is still under development (Huhle et al., 2018). Although recent research mainly focused on single ventilator parameters as VILI determinants, MP may summarize the potentially damaging effects of different parameters in one single variable. Yet, MP was shown to be associated with different characteristics of experimental lung injury, i.e., radiological signs of lung edema, lung wet/dry ratio, and histological features (Cressoni et al., 2016; Collino et al., 2019; Vassalli et al., 2020). In retrospective clinical trials, MP was associated with mortality in critically ill patients (Serpa Neto et al., 2018; Costa et al., 2021). However, its effects on the pulmonary neutrophilic inflammation as assessed by positron-emission tomography (PET)/computed tomography (CT) have not been determined yet, though neutrophilic inflammation is a mainstay in ARDS pathogenesis (Grommes and Soehnlein, 2011). In this study, we aimed to investigate the applied resulting MP and the neutrophilic pulmonary inflammation in a clinically relevant model of acute lung injury in pigs ventilated with fixed combinations of PEEP and inspiratory oxygen fractions (F_IO_2), as recommended by the ARDS network's low PEEP table (Brower et al., 2004). We hypothesized that neutrophilic inflammation correlates with MP.

Abbreviations: $\%E_2$, volume-dependent elastance; ΔK_{iS}, difference in K_{iS} between first and second lung imaging; ΔP, driving pressure; ΔPtrans, transpulmonary driving pressure; ^{18}F-FDG, 2-deoxy-2-[^{18}F]fluoro-D-glucose; $AaDO_2$, alveolo-arterial oxygen difference; ACCT, attenuation-correction computed tomography; ARDS, acute respiratory distress syndrome; CO, cardiac output; E, elastance; F_IO_2, inspiratory oxygen fraction; HU, hounsfield units; HR, heart rate; I:E, inspiratory to expiratory time ratio; IQR, interquartile range; K_{iS}, normalized ^{18}F-FDG uptake rate; ME, mechanical energy; MP, mechanical power; MV, mechanical ventilation; $PaCO_2$, arterial partial pressure of carbon dioxide; PaO_2, arterial partial pressure of oxygen; PaO_2/F_IO_2, horovitz index; P_{aw}, airway pressure; P_{peak}, peak airway pressure; PEEP, positive end-expiratory pressure; P_{eso}, esophageal pressure; P_{mean}, mean airway pressure; P_{plat}, mean plateau pressure; R, resistance; RR, respiratory rate; SV, stroke volume; VILI, ventilator-induced lung injury; V_T, tidal volume.

MATERIALS AND METHODS

The Institutional Animal Care and Welfare Committee and the Government of the State of Saxony, Germany, approved the study protocol (file 25-5131/474/31; 27.09.2019; Dr. B. Langen, Landesdirektion Sachsen). Animals received humane care according to German law and the Principles of Laboratory Animal Care formulated by the National Society for Medical

Research and the United States National Academy of Sciences Guide for the Care and Use of Laboratory Animals, and the Animal Research: Reporting of *in vivo* Experiments guidelines were followed.

Animal Preparation and Mechanical Ventilation

Eight female landrace pigs (35–51 kg) were intravenously anesthetized (ketamine, 15 mg/kg/h; midazolam, 1 mg/kg/h), orotracheally intubated, and mechanically ventilated. The following initial settings were used: Volume-controlled ventilation, tidal volume (V_T) 6 ml/kg, PEEP 5 cmH_2O, inspiratory to expiratory ratio (I:E) 1:1, inspired fraction of oxygen (F_IO_2) 1.0, RR adjusted to normocapnia, and inspiratory flow 35 L/min (Evita XL, Dräger, Lübeck, Germany). V_T was reduced if airway plateau pressure (Pplat) was $\geq$30 cmH_2O. The right carotid artery, jugular vein, and urinary bladder were catheterized under sterile conditions. A pulmonary artery thermodilution catheter and an esophageal balloon catheter (Cooper Surgical, Trumbull, CT, United States; filling volume 0.5 ml) were introduced. The correct position of the balloon catheter was confirmed as described elsewhere (Lanteri et al., 1994). Animals were paralyzed (atracurium, 3 mg/kg/h) throughout the whole experiment and received a balanced electrolyte infusion of 10 ml/kg/h during preparations and 4 ml/kg/h during intervention time, respectively. The mean arterial pressure (MAP) was kept >60 mmHg by means of norepinephrine and colloid infusion, as appropriate.

Lung Injury

Following instrumentation, lung injury was induced by repetitive lung lavage with warmed 0.9 % saline in a prone and supine position (37°C; 35 ml/kg; lavage pressure approximately 30 cmH_2O), until PaO_2/F_IO_2 was <200 mmHg for at least 30 min.

Experimental Protocol and Intervention Time

The sequence of events is depicted in **Figure 1**, which represents a subprotocol of a larger study on the effects of different MV on lung inflammation and function. After instrumentation and induction of lung injury, PET and CT scans were obtained under baseline MV settings, but PEEP of 10 cmH_2O. Later, MV was adjusted according to the ARDS network recommendations (Brower et al., 2004), as follows: volume-controlled ventilation, V_T 6 ml/kg, I:E 1:1, RR adjusted to normocapnia, and flow 35 L/min. The lowest possible fixed PEEP and F_IO_2 combination were applied according to the low PEEP table (Brower et al., 2004) to keep PaO_2 between 55 and 80 mmHg. Lung recruitment maneuvers were not applied. Ventilator settings were titrated within 30 min, and interventional time was started afterwards. Settings were checked hourly and adjusted if necessary. PET/CT lung imaging was repeated 24 h after first PET/CT, and animals were killed by intravenous bolus injection of 2 g thiopental and 50 ml 1 M potassium chloride.

Measurements

We recorded physiological variables and respiratory signals before (Baseline) and after inducing lung injury (Injury), at the start of intervention time (0 h) and every 6 h thereafter (6, 12, and 18 h), respectively. Blood gasses were analyzed using a commercially available device (ABL80, Radiometer, Brønshøj, Denmark) and cardiac output (CO) was determined by thermodilution method (MP70, Philips Healthcare, Eindhoven, the Netherlands). Stroke volume (SV) was calculated by dividing CO by heart rate (HR).

Respiratory Signals and Calculations

Respiratory signals were recorded using a LabVIEW-based software (National Instruments, Austin, TX, United States) and analyzed semi-automatically (MATLAB, R2019a, The MathWorks Inc., Natick, MA, United States). Airway (P_{aw})

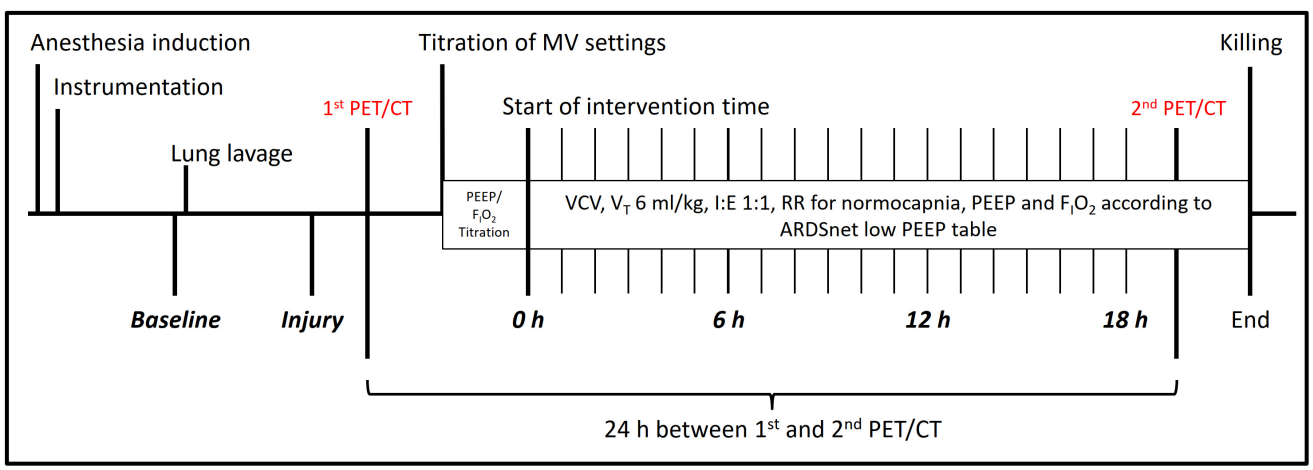

FIGURE 1 | Experimental time course. Experimental time course. PEEP, positive end-expiratory pressure; F_IO_2, inspiratory fraction of oxygen; VCV, volume-controlled ventilation; I:E, inspiratory to expiratory time ratio; RR, respiratory rate; ARDSnet, acute respiratory distress syndrome network.

and esophageal pressure (P_{eso}) were measured using differential pressure transducers (Sensortechnics GmbH, Puchheim, Germany) at the endotracheal tube and the balloon catheter, respectively. Furthermore, air flow and airway pressure signals were recorded from the ventilator using a serial interface. The ventilator's airway pressure signal was used for the offline synchronization of all recorded signals. Peak (P_{peak}) and mean (P_{mean}) airway pressure were determined as Paw maximum and average during one respiratory cycle from the respiratory tracings, respectively. Driving pressure (ΔP) and transpulmonary pressure (P_{trans}) were calculated as $P_{plat} - PEEP$ and $P_{aw} - Peso$, respectively. Transpulmonary driving pressure (ΔP_{trans}) was calculated as plateau − minimal P_{trans}. Elastance (E) and resistance (R) were derived by fitting the equation of motion to the acquired respiratory signals (multiple linear regression). The percentage of volume-dependent elastance ($\%E_2$) was determined as described elsewhere (Kano et al., 1994; Carvalho et al., 2013). MP was calculated using the recorded respiratory signals, which included continuous recordings of airway pressure and flow. V_T was calculated from the latter. First, mechanical energy by breath (ME) is defined as the numerical integral of the airway pressure and volume changes (Huhle et al., 2018), constituting the tidal pressure–volume curve (PV curve), see **Figure 2**. Second, ME was multiplied by RR to achieve MP. During each breath, energy is spend to overcome resistance and elastic forces; thus, the corresponding components, i.e., resistive and elastic power, can be calculated. Alveolo-arterial oxygen difference ($AaDO_2$) and venous admixture were calculated using standard formulas.

PET and CT

The PET-based assessment of tissue uptake rate of the radiotracer 2-deoxy-2-[^{18}F]fluoro-D-glucose (^{18}F-FDG) served as surrogate for neutrophilic pulmonary inflammation (Musch et al., 2007; Wadsak and Mitterhauser, 2010) and was measured by dynamic ^{18}F-FDG PET scans (Biograph Vision 600 PET/CT, Siemens Healthineers, Knoxville, TN, United States), as described elsewhere (Braune et al., 2019; Kiss et al., 2019; Wittenstein et al., 2020). In brief, a static low-dose CT scan (attenuation-correction computed tomography, ACCT, approximately 5 s) for attenuation correction of the following PET scan was performed at mean airway pressure hold and followed by injection of ^{18}F-FDG (∼200 MBq) and dynamic PET scan (26 cm craniocaudal field of view, 75 min) before the start of the intervention time. Blood samples were collected throughout the dynamic PET scan to assess the tracer's plasma activity (cross-calibrated gamma counter). These lung imaging procedures were repeated 24 h after first PET/CT. The dynamic PET scans were reconstructed using an OSEM 3D iterative reconstruction, applying point spread function (PSF) and time of flight and correcting for attenuation and scatter, into an image matrix size of 440 × 440, resulting in a voxel size of 1.65 mm × 1.65 mm × 2.0 mm. ACCTs co-registered to PET scans were used to semi-automatically create lung masks and calculate gas fractions by F_{Gas} = CT number [Hounsfield unit HU]/−1000 (Gattinoni et al., 2001). The ^{18}F-FDG uptake rate (K_i) was calculated using the Patlak model using the software Rover (ABX GmbH, Radeberg, Germany) (Schroeder et al., 2011; Torigian et al., 2009). K_i was then normalized to the tissue fraction (K_{iS}) (Wittenstein et al., 2020) as follows:

$$K_{iS} = \frac{Ki}{F_{Tissue}} = \frac{Ki}{(1 - F_{Gas} - F_{Blood})}, \quad (1)$$

where, K_{iS} stands for tissue-normalized ^{18}F-FDG uptake rate, F_{Gas} for gas fraction, and F_{Blood} for blood fraction derived using the Sokoloff model (Schroeder et al., 2011). Differences between lung imaging data before and after intervention time (second

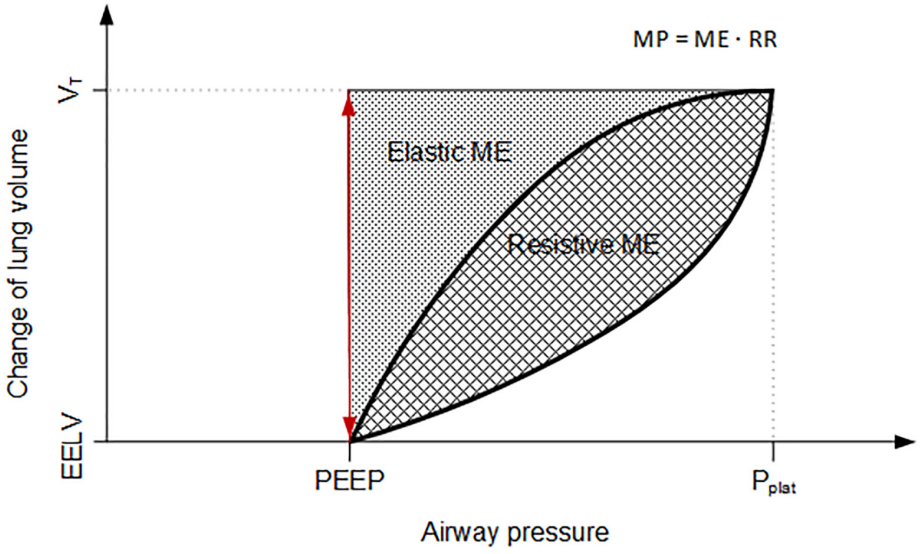

FIGURE 2 | Schematic pressure–volume curve for calculation of mechanical energy. Schematic visualization of changing lung volume and pressure per respiratory cycle, constituting the pressure–volume curve. MP, mechanical power; ME, mechanical energy; RR, respiratory rate; PEEP, positive end-expiratory pressure; P_{plat}, plateau airway pressure; V_T, tidal volume; EELV, end-expiratory lung volume.

PET/CT – first PET/CT) were calculated using median over the respective semi-automatically segmented lung regions of interest (ROIs). ROIs were segmented using a semi-automatic approach consisting of automated segmentation using a deep convolutional neural network algorithm trained on static CT scans from previous animal studies, followed by manual correction by two independent, trained physicians. Hyper (<−900 HU), normal (−900 to −500 HU), poor (−500 to 100 HU), and non-aerated (>−100 HU) lung compartment were computed as described elsewhere based on ACCT data (Hedenstierna et al., 1989).

Statistical Analysis

This study was exploratory in nature, and thus, its sample size was based on the experience of our group with previous studies on MV and neutrophilic inflammation (Kiss et al., 2019; Wittenstein et al., 2020). However, we defined K_{iS} as the primary outcome. Data are presented as median and interquartile range (IQR), if not stated differently. Statistical differences of variables between baseline and injury and between 0 and 18 h were analyzed using a paired non-parametric test (Wilcoxon test, asymptotic significance, two-sided). Association between median variables and inflammation was assessed using non-parametric spearman correlation. Statistics were performed using SPSS (version 27, IBM Corp., Armonk, NY, United States). Significance was accepted at $p < 0.05$. Graphs were created using GraphPad Prism (version 6.0, GraphPad Software, San Diego, CA, United States).

RESULTS

General Results

All eight animals were included in the analysis. Median body weight was 47.7 (8.0) kg. Animals received median 8 (3) lavages to reach the lung injury criteria. The median intervention time, i.e., time from start of intervention time to completion of last lung imaging, was 22.75 h (27 min). In total, animals received median doses of 174 (4) ml/kg of crystalloids, and 0.144 (1.863) μg/kg of norepinephrine during the intervention time. Median cumulative urine output was 67 (12) ml/kg.

Respiratory Variables

Table 1 shows the respiratory variables and **Figure 3** depicts the individual time course of MP for each experiment. After induction of experimental lung injury, RR, P_{peak}, P_{plat}, ΔP, peak P_{trans}, ΔP_{trans}, resistance, elastance, $\%E_2$, MP, elastic MP, resistive MP, $AaDO_2$, and venous admixture were significantly higher as compared to baseline. PaO_2 and PaO_2/F_IO_2 were significantly lower after injury than at baseline, whereas other variables

TABLE 1 | Respiratory variables.

Variable	Baseline	Injury	0 h	6 h	12 h	18 h	BL vs. Injury *p*	0 h vs. 18 h *p*
Tidal volume (ml/kg)	6.5 (0.2)	6.6 (0.2)	6.5 (0.2)	6.5 (0.2)	6.5 (0.2)	6.5 (0.3)	0.327	0.484
Respiratory rate (1/min)	25 (7)	31 (9)	31 (5)	22 (6)	19 (5)	17 (3)	**0.018**	**0.012**
F_IO_2 (0.0–1.0)	1.00 (0.03)	1.00 (0.00)	0.32 (0.09)	0.32 (0.01)	0.32 (0.01)	0.32 (0.02)	0.109	0.438
P_{peak} (cmH_2O)	19.2 (2.8)	36.9 (6.6)	28.9 (3.8)	29.3 (2.7)	30.6 (2.9)	30.1 (4.5)	**0.012**	0.889
P_{plat} (cmH_2O)	13.8 (1.1)	30.2 (4.9)	24.5 (2.3)	23.1 (3.9)	23.1 (3.5)	22.9 (3.1)	**0.012**	0.093
ΔP (cmH_2O)	8.8 (0.9)	25.3 (5.2)	19.1 (3.4)	18.1 (3.9)	18.3 (3.6)	18.2 (3.0)	**0.012**	0.779
$PEEP_{set}$ (cmH_2O)	5.0 (0)	5.0 (0)	5.0 (0)	5.0 (0)	5.0 (0)	5.0 (0)	–	–
$PEEP_{measured}$ (cmH_2O)	5.1 (0.3)	5.0 (0.2)	5.1 (0.1)	4.9 (0.2)	4.8 (0.2)	4.9 (0.1)	0.352	**0.011**
Resistance (cmH_2O s/l)	10.5 (4.0)	14.9 (1.8)	12.4 (2.0)	15.4 (2.3)	16.6 (3.4)	16.6 (5.6)	**0.012**	**0.012**
Elastance (cmH_2O/l)	26.2 (4.9)	83.0 (20.6)	57.3 (15.0)	56.3 (12.0)	56.3 (10.7)	54.7 (9.3)	**0.012**	0.484
$\%E_2$ (%)	−37.8 (0.4)	−12.6 (9.4)	−24.6 (3.5)	−28.3 (4.1)	−v28.6 (3.1)	−29.5 (4.0)	**0.012**	0.069
MP (J/min)	6.6 (2.9)	17.3 (10.4)	13.5 (4.9)	9.8 (3.5)	9.9 (2.6)	8.5 (2.2)	**0.012**	**0.012**
MP elastic (J/min)	4.5 (1.9)	11.8 (7.1)	9.1 (3.3)	6.7 (2.5)	6.7 (1.8)	5.7 (1.5)	**0.012**	**0.012**
MP resistive (J/min)	2.2 (1.0)	5.5 (3.3)	4.4 (1.6)	3.1 (1.0)	3.2 (0.8)	2.7 (0.7)	**0.012**	**0.017**
P_{trans} peak (cmH_2O)	8.8 (4.2)	25.1 (4.8)	18.4 (3.2)	17.9 (3.4)	18.6 (4.0)	18.7 (2.4)	**0.012**	0.889
P_{trans} endex (cmH_2O)	−3.5 (2.7)	−4.4 (2.0)	−3.9 (2.9)	−4.8 (2.8)	−4.3 (2.6)	−4.4 (0.8)	0.123	0.123
ΔP_{trans} (cmH_2O)	12.0 (4.0)	29.3 (4.5)	21.6 (4.5)	22.3 (3.3)	23.4 (2.3)	23.2 (3.7)	**0.012**	0.327
PaO_2 (mmHg)	530.3 (277.3)	100.5 (73.1)	106.0 (50.8)	109.5 (17.3)	110.5 (23.5)	105.5 (19.1)	**0.012**	0.327
$PaCO_2$ (mmHg)	55.7 (5.6)	50.2 (10.4)	46.4 (16.9)	54.0 (9.3)	51.3 (5.1)	60.2 (4.4)	0.161	**0.017**
pHa	7.37 (0.08)	7.37 (0.07)	7.42 (0.11)	7.40 (0.04)	7.42 (0.03)	7.40 (0.05)	0.528	0.236
PaO_2/F_IO_2 (mmHg)	528 (265)	101 (73)	301 (125)	352 (44)	349 (74)	320 (91)	**0.012**	0.208
$AaDO_2$ (mmHg)	115.1 (241.4)	549.8 (93.6)	79.4 (40.4)	45.0 (32.7)	49.0 (37.2)	50.8 (38.1)	**0.012**	0.036
Venous admixture (%)	8.8 (37.1)	47.6 (16.9)	21.1 (14.0)	14.7 (3.2)	10.9 (7.9)	14.6 (13.2)	**0.012**	0.327

Median (IQR); BL: baseline; V_T, tidal volume; F_IO_2, inspiratory oxygen fraction; P_{peak}, peak airway pressure; P_{plat}, plateau airway pressure; ΔP, driving pressure; PEEP, positive end-expiratory pressure; $\%E_2$, volume-dependent elastance; MP, mechanical power calculated from pressure–volume curve; P_{trans} peak, peak transpulmonary pressure; P_{trans} endex, end-expiratory transpulmonary pressure; ΔP_{trans}, transpulmonary driving pressure; PaO_2, arterial partial pressure of oxygen; $PaCO_2$, arterial partial pressure of carbon dioxide; pHa, arterial pH value; PaO_2/F_IO_2, Horovitz index; $AaDO_2$, alveolo-arterial oxygen difference. Comparisons baseline vs. injury and 0 h vs. 18 h: Wilcoxon test, asymptotic significance, two-sided, significance accepted at $p < 0.05$. Bold p-values show significant differences (all p-values below 0.05).

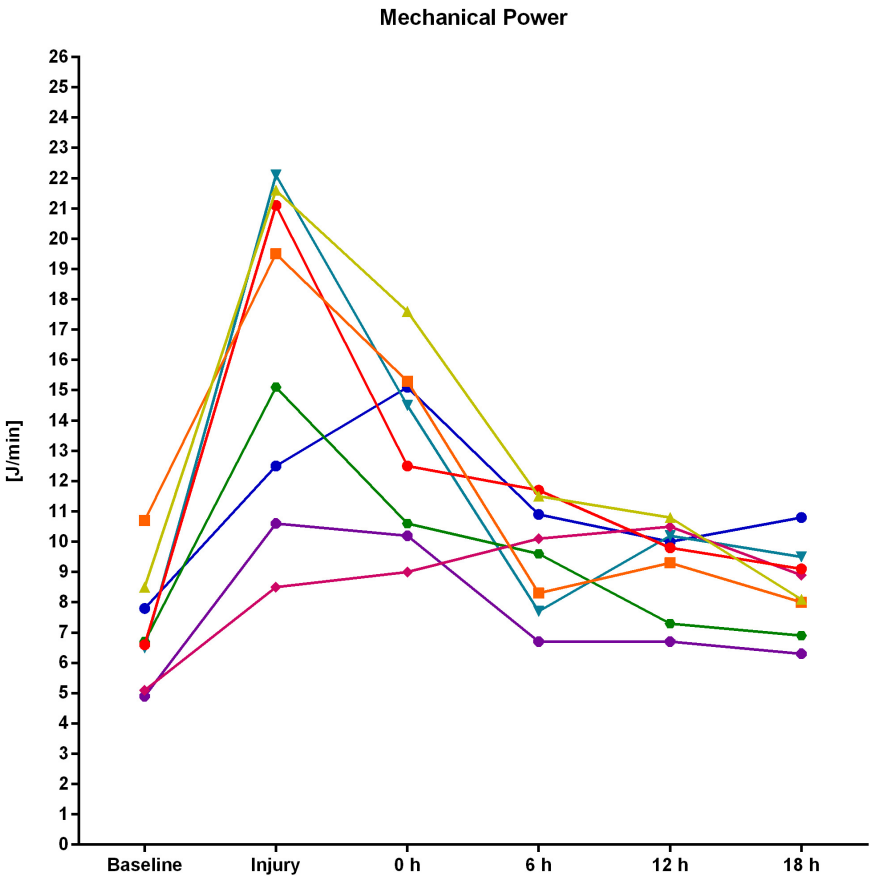

FIGURE 3 | Individual time course of mechanical power derived from the pressure–volume curve for each of the eight experiments.

did not differ significantly between these two pre-intervention time points. After 18 h of intervention, resistance and $PaCO_2$ were significantly increased, whereas RR, PEEP, MP, and elastic and resistive MP were significantly lower as compared to the start of the intervention. The remaining variables did not differ significantly between begin and end of the intervention time.

Neutrophilic Inflammation

Representative PET/CT scans are presented in **Figure 4**. As compared to the first PET/CT, K_{iS} was significantly higher after 24 h (second PET/CT 0.0320 (0.0203) min^{-1} vs. first PET/CT 0.0136 (0.0041) min^{-1}; $p = 0.012$; **Figure 5**). ΔK_{iS} significantly correlated with median MP derived from the PV curve (**Figure 6**) and with the median elastic and resistive MP components (**Table 2**). In contrast, the other respiratory variables did not correlate with ΔK_{iS} (**Table 2**).

Lung Aeration

Both median total lung mass and total pulmonary gas volume significantly decreased from first to second lung imaging [854.1 (177.2) vs. 635.6 (121.9) g, $p = 0.012$; and 850.7 (143.2) vs. 780.2 (185.9) ml, $p = 0.036$, respectively]. In relation to total lung mass in the corresponding PET/CT, the relative mass of hyper-aerated compartment of the lung increased significantly from the first to the second PET/CT scan [0.48 (0.45)% vs. 0.75 (0.64)%, $p = 0.025$]. The relative mass of normally, poorly, and non-aerated lung mass did not differ significantly between the scan before and after the intervention time (**Figure 7**). The net relative lung aeration, defined as sum of poorly, normally, and hyper-aerated lung compartments, did not differ between first and second PET/CT [69.4 (11.1)% vs. 67.1 (15.8)%, $p = 0.889$].

Hemodynamic Variables

Table 3 depicts the hemodynamic variables. As compared with baseline, MAP, mean pulmonary arterial pressure (MPAP), pulmonary capillary wedge pressure, and central venous pressure were significantly higher after induction of lung injury, whereas HR, SV, and CO did not differ significantly. The majority of hemodynamic variables did not differ significantly between start and end of intervention time, despite cardiac SV, which was significantly higher after 18 h of intervention time.

DISCUSSION

The main findings of the present study are in pigs ventilated mechanically according to the low PEEP table of the ARDS network: (1) pulmonary neutrophilic inflammation, as assessed

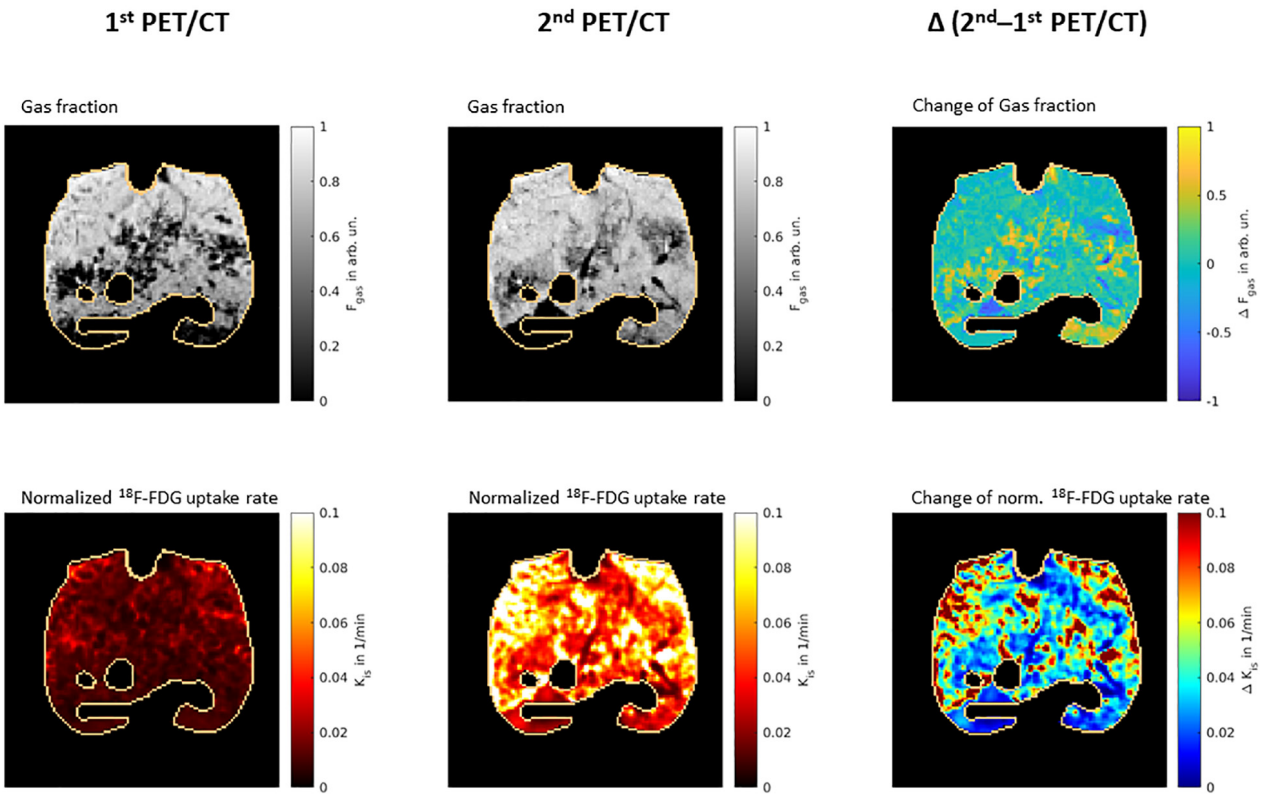

FIGURE 4 | Representative PET/CT scans. Representative PET/CT scans from one representative animal, showing gas fraction **(upper row)** and normalized ^{18}F-FDG uptake rate **(lower row)** from first **(left column)** and second lung scans **(middle column)**. The right column shows the difference between second and first scan after co-registration of ACCTs using Elastix Library. The lung masks are outlined in copper color. F_{gas}, gas fraction; arb. un., arbitrary units; ^{18}F-FDG, 2-deoxy-2-[^{18}F]fluoro-D-glucose; K_{is}, normalized uptake rate of 2-deoxy-2-[^{18}F]fluoro-D-glucose.

by PET/CT, increased significantly over time; (2) among all ventilatory variables investigated, only MP and its elastic and resistive components showed a positive correlation with neutrophilic inflammation; and (3) global pulmonary gas volume decreased whereas hyper-aerated relative lung mass increased over time.

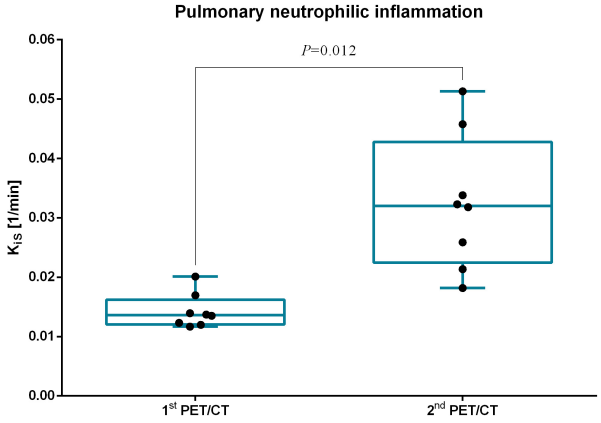

FIGURE 5 | Normalized ^{18}F-FDG uptake rate (K_{iS}) before and after intervention time. Normalized ^{18}F-FDG uptake rate (K_{iS}) before and after intervention time. PET/CT, positron-emission tomography; CT, computed tomography.

To the best of our knowledge, this is the first experimental study that prospectively investigated the relationship between MP and pulmonary neutrophilic inflammation as assessed with PET/CT. Previous studies were limited to a less sensitive assessment of VILI, including radiographic evidence of pulmonary edema, cumulative histological scores, and lung wet/dry ratio (Cressoni et al., 2016; Collino et al., 2019; Vassalli et al., 2020). Neutrophilic infiltration and inflammation is deemed to be a main pathological mechanism in the development and course of ARDS (Zemans et al., 2009; Grommes and Soehnlein, 2011; Matthay and Zemans, 2011).

A particular strength of our study is that we used MV settings of a clinically common MV concept in a model of moderate acute lung injury, rather than intentionally provoking lung injury by unusual or artificial settings or investigating the roles of certain ventilator parameters. Instead, we applied fixed PEEP/F_IO_2 combinations according to the ARDS network recommendations (low PEEP table) (Brower et al., 2004). Although large clinical trials did not reveal an outcome advantage of high over low PEEP in patients with ARDS (Brower et al., 2004; Meade et al., 2008; Mercat et al., 2008), MV concepts tolerating formation

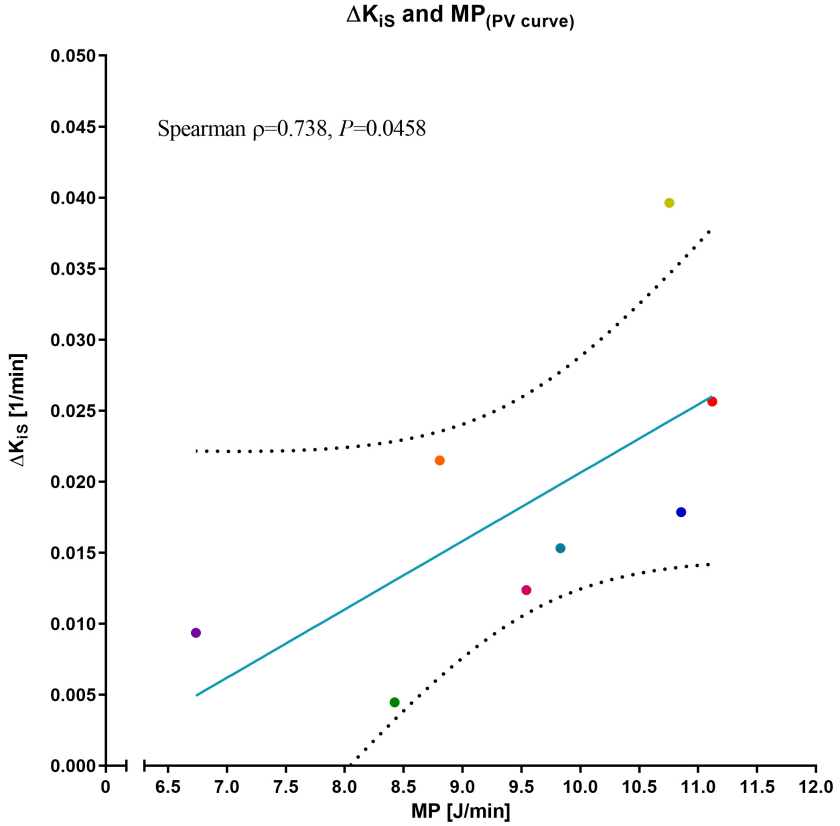

FIGURE 6 | Correlation of ΔK_{iS} and mechanical power. Normalized ^{18}F-FDG uptake rate, expressed as difference between the two PET/CT scans (ΔK_{iS}), and mechanical power (MP) as assessed from the pressure–volume curve; dotted lines: 95 % confidence band of the best-fit line. Correlation was assessed as non-parametric bivariate correlation (Spearman). Colors represent corresponding animals from **Figure 3**.

of atelectasis and moderate hypercapnia in order to avoid aggressive ventilation in terms of high distending pressures are under debate (Pelosi et al., 2018) and clinically favored. Use of the low PEEP table was recently shown to increase survival in patients with ARDS as compared with individualized but higher PEEP (Cavalcanti et al., 2017). In addition, titrating PEEP according to lung morphology did not improve outcome and even increased mortality if morphology was misclassified, respectively. Thus, as proposed earlier (Brower et al., 2004), fixed $PEEP/F_IO_2$ combinations should still be used for patients with ARDS (Chiumello et al., 2014; Battaglini et al., 2021), which justified our selected experimental setting.

The finding that MV at relatively low PEEP increased neutrophilic inflammation is in line with a previous experimental study by our group (Kiss et al., 2019). Therein, PEEP was titrated according to end-expiratory transpulmonary pressure allowing end-expiratory alveolar collapse. This approach was shown to increase neutrophilic inflammation as compared with higher PEEP under controlled MV (Kiss et al., 2019). In the present study, PEEP was titrated according to clinically common oxygenation thresholds, and according to the low $PEEP/F_IO_2$ table from the ARDS Net, yielding PEEP levels even lower than the titrated PEEP in the mentioned previous trial. Thus, it is not surprising that pulmonary neutrophilic inflammation was detected and even increased over time herein. Furthermore, median ΔP was higher than 15 cmH_2O throughout the intervention time, which was postulated as a threshold for

TABLE 2 | Correlation between respiratory variables and ΔK_{iS}.

Variable	Spearman ρ	*P*
MP (J/min)	0.738	**0.037**
MP elastic (J/min)	0.738	**0.037**
MP resistive (J/min)	0.738	**0.037**
P_{peak} (cmH_2O)	0.405	0.320
P_{plat} (cmH_2O)	0.310	0.456
ΔP (cmH_2O)	0.310	0.456
ΔP_{trans} (cmH_2O)	0.095	0.823
RR (1/min)	−0.108	0.798
Elastance (cmH_2O/l)	−0.357	0.385
Resistance (cmH_2O s/l)	0.452	0.260
$\%E_2$ (%)	0.262	0.531

Spearman coefficient ρ for correlation of displayed respiratory variables with ΔK_{iS}. MP, mechanical power obtained from pressure–volume curves; P_{peak}, peak airway pressure; P_{plat}, plateau airway pressure; ΔP, driving pressure; ΔP_{trans}, transpulmonary driving pressure; RR, respiratory rate; $\%E_2$, percentage of volume-dependent elastance. Statistical test two-sided, significance accepted at $p < 0.05$. Bold p-values show significant differences (all p-values below 0.05).

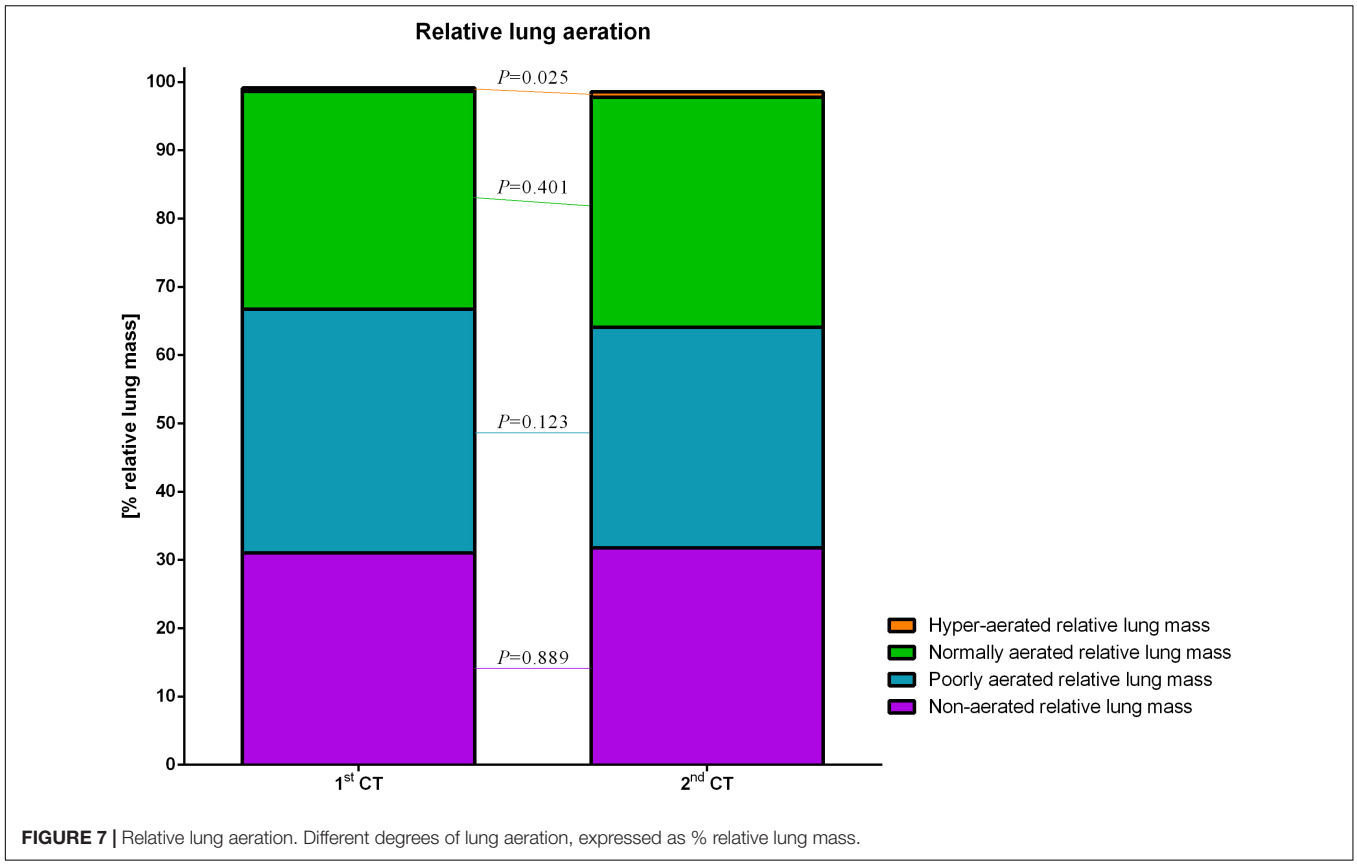

FIGURE 7 | Relative lung aeration. Different degrees of lung aeration, expressed as % relative lung mass.

TABLE 3 | Hemodynamic variables.

Variable	Baseline	Injury	0 h	6 h	12 h	18 h	BL vs. Injury *p*	0 h vs. 18 h *p*
MAP (mmHg)	72 (11)	85 (15)	81 (16)	75 (13)	74 (7)	76 (13)	**0.011**	0.127
MPAP (mmHg)	17 (4)	33 (4)	25 (5)	24 (5)	23 (6)	24 (10)	**0.012**	0.526
PCWP (mmHg)	9 (4)	11 (5)	7 (2)	8 (3)	8 (3)	8 (3)	**0.017**	0.053
CVP (mmHg)	6 (4)	9 (4)	5 (4)	5 (2)	6 (4)	6 (2)	**0.011**	0.139
HR (1/min)	96 (17)	94 (22)	120 (28)	98 (20)	94 (9)	104 (30)	0.092	0.058
SV (ml)	54 (10)	59 (12.0)	50 (15)	63 (19)	63 (9)	68 (13)	0.036	**0.012**
CO (l/min)	5.3 (1.0)	5.8 (1.8)	6.2 (2.4)	6.1 (2.6)	5.9 (1.9)	7.1 (2.1)	0.612	0.093

Median (IQR); BL, baseline; MAP, mean arterial pressure; MPAP, mean pulmonary arterial pressure; PCWP, pulmonary capillary wedge pressure; CVP, central venous pressure; HR, heart rate; SV, stroke volume; CO, cardiac output; comparisons baseline vs. injury and 0 h vs. 18 h, Wilcoxon test, asymptotic significance, two-sided, significance accepted at $p < 0.05$. Bold p-values show significant differences (all p-values below 0.05).

increased risk of mortality in a retrospective clinical analysis of patients with ARDS (Amato et al., 2015). Although existing meta-analyses are ambiguous, our finding of increased pulmonary neutrophilic inflammation might be recognized as contradictory to the observation that survival in ARDS may be higher with lower PEEP (Cavalcanti et al., 2017). However, in general, clinical outcomes are influenced by many effects, e.g., disease severity, comorbidities, ventilation settings potentially inducing VILI, and hemodynamics. One could hypothesize that there is a similar inflammatory response in patients with ARDS undergoing similar ventilator settings, but that other effects in the recent clinical trials, e.g., impaired hemodynamics, affect outcomes majorly as well. Our study cannot assess how clinically relevant our observed pulmonary inflammation is and direct comparison with the recent large clinical trials must be done cautiously. However, we focused on an established mechanism in ARDS pathophysiology, the neutrophilic inflammation, which served as VILI surrogate in many high-quality experimental studies.

Despite the time point directly after starting the intervention time (0 h), median MP was always lower than the initially postulated VILI threshold of 12 J/min (Cressoni et al., 2016). However, it was high at Injury and the start of intervention time (0 h). Thus, it is not surprising that there is neutrophilic inflammation, though MP was relatively low during intervention time. This is also in line with the findings from another experimental study, where the lowest power was also associated

with histological evidence of VILI (Collino et al., 2019). In a third experimental investigation, cumulative histological lung injury did not differ between MP around 14 and 29 J/min (Vassalli et al., 2020). In this regard, two major considerations have to be made. First, absolute MP values depend on the way of calculation. We used the respiratory tracings to assess MP, whereas different MP formulas have been postulated since the seminal publication in 2016 (Giosa et al., 2019). The major criticism regarding the initial formula was that there is incorrect mathematical modeling of the role of PEEP (Huhle et al., 2018), whereas others tried to reduce the formula's complexity (Marini and Jaber, 2016; Giosa et al., 2019). This issue needs further investigation. Second, different experimental models and settings preclude from direct comparison of certain MP values and their respective associated results.

Although ΔP, E, and V_T did not change and R increased during the intervention time, both RR and MP decreased, i.e., changed in the same direction. Of course, RR contributes linearly to MP; thus, RR and MP are closely linked mathematically. Still, one could hypothesize that it could be mainly RR contributing to VILI in our study. In fact, RR was associated with lung injury under certain circumstances (Rich et al., 2003). However, only MP correlated significantly with ΔK_{iS} in our study, whereas RR did not. The finding that MP but not is determinants, i.e., ΔP and RR, were associated with pulmonary neutrophilic inflammation may strengthen the potential role of MP regarding VILI as a unifying variable, summarizing the burden resulting from the clinically selected ventilator settings. For the first time, our study combined concepts of pulmonary neutrophilic inflammation and MP. Although the first is generally considered a cellular quantity indicative of VILI, the latter is discussed as a VILI determinant. MP depends on a number of factors including ventilator settings (ΔP, V_T, RR, etc.) and respiratory mechanics (R and E). Although driving pressure may reflect the mechanical burden, i.e., stress per breath alone, it does not reflect how often this mechanical stress is applied per unit of time. RR quantifies mechanical stress applied per unit of time. In a gross approximation, MP is the product of both RR and driving pressure. Consequently, although neither driving pressure nor RR are associated with neutrophilic inflammation, MP may still do because both do not necessarily covariate. In this investigation, we found an association of MP with neutrophilic inflammation supporting the notion that MP may be a determinant of VILI superior to the single respiratory components. Of note, this statistical association does not prove causality. During our intervention time, PEEP decreased significantly. However, its median difference between 0 and 18 h was only 0.2 cmH_2O, which we would not consider as clinically relevant. Thus, its contribution to the shown decrease of MP may have been negligible.

The CT scans revealed that both the total pulmonary gas volume decreased during the intervention time, whereas the relative mass of lung aeration compartments did not change substantially, despite the significantly increased hyper-aerated compartment. The decreased lung mass may be explained by a decrease of intrapulmonary fluid content, because lung lavage fluid partly remained in the airways and alveoli after induction of lung injury, but was removed by positive pressure ventilation and capillary/lymphatic resorption within the intervention time and before second CT. This is in line with our experiences with the lavage model. The total gas volume decreased most likely because first CT scan was performed at PEEP of 10 cmH_2O, whereas median PEEP was substantially lower at the moment of second CT ($\sim$5 cmH_2O). Interestingly, net relative lung aeration (defined as aerated relative lung mass in relation to total lung mass at respective CT scans) did not differ; thus, the atelectatic compartment remained stable. Accordingly, median end-expiratory transpulmonary pressure was negative throughout the intervention time, which promotes end-expiratory lung collapse and atelectasis formation. Furthermore, elastance, ΔP, and transpulmonary driving pressure did not differ significantly between start and end of the intervention time. The significant increase of $PaCO_2$ over time could suggest decreasing lung aeration, but venous admixture did not differ between 0 and 18 h. More likely, $PaCO_2$ increased because RR was decreased to keep arterial pH in a desired range. Within the aerated lung compartments, only relative hyper-aeration increased significantly. Although this was not accompanied by significant changes of $\%E_2$, it fits to the finding of increased K_{iS} in the second PET/CT.

As the only hemodynamic variable, SV significantly differed between 0 and 18 h. Most likely, hemodynamics were still impaired at 0 h related to the recent induction of lung injury. Already 6 h later, SV increased and remained stable or even increased until 12 and 18 h, respectively. The latter may reflect further hemodynamic stabilization or recovery, and may be related to the increasing cumulative intravenous fluid administration. In contrast, increased SV could be interpreted as a reaction to the increasing inflammatory status. However, HR, CO, MAP, and the need for norepinephrine did not change significantly, rendering this explanation less likely.

Possible Clinical Implications of the Findings

Because MP was associated with a major pathological mechanism of lung injury in ARDS, namely neutrophilic infiltration and inflammation, clinicians may consider adjusting MV to reduce MP, whereas providing minimally acceptable gas exchange.

Limitations

The present study knows limitations. First, this was a relatively small, explorative experimental trial in pigs to investigate prospectively the association of MP with pulmonary neutrophilic inflammation, which limits direct extrapolation to humans. Second, we used an injury model based on lung lavages only, precluding direct translation to different models. Third, we did not provoke different magnitudes of MP, which may limit the extrapolation to other MV settings or concepts, e.g., higher PEEP or open lung approach. However, we aimed to investigate the effects in an experimental model reflecting common clinical settings. Fourth, PEEP differed between the first and the second PET/CT. However, PEEP was adjusted according to defined criteria, did not differ between animals, and may reflect clinically relevant time course. Fifth, we assessed VILI in terms of

the metabolic activity as indicated by normalized ^{18}F-FDG uptake rate. Although other metabolically active cells may also accumulate this tracer, previous studies identified K_{iS} as a reliable VILI surrogate (Jones et al., 1997; Musch et al., 2007; Costa et al., 2010; Saha et al., 2013). We addressed only the short- to mid-term effects, resembling the very early phase of ARDS. Sixth, we did not evaluate histological VILI features, because other investigators have successfully completed histological analyses previously (Collino et al., 2019; Vassalli et al., 2020). In this regard, our study expands previous trials. Seventh, results are only valid for controlled ventilation, which we used herein. Results may differ in a clinical setting where spontaneous breathing is increasingly accepted nowadays, also within the first 24 h.

CONCLUSION

In experimental acute lung injury in pigs, MV according to the recommendations of the ARDS network and using the low PEEP/F_IO_2 table resulted in increased PET/CT-derived pulmonary neutrophilic inflammation, which correlated with MP.

DATA AVAILABILITY STATEMENT

The raw data supporting the conclusions of this article will be made available by the authors, without undue reservation.

ETHICS STATEMENT

The animal study was reviewed and approved by Landesdirektion Sachsen, Referat 25, Chemnitz.

AUTHOR CONTRIBUTIONS

MS, JW, RH, JK, PP, MJS, PR, and MG planned and designed the study. MS, JW, RH, XR, YZ, AB, RT, LM, and GB performed the experiments. MS, JW, MG, AB, RH, and JK planned, performed and analyzed the PET/CT image acquisition. MS, JW, RH, XR, YZ, RT, LM, GB, TB, TK, and MG were involved in the data analyses. YZ, RT, LM, and RH performed the lung segmentations (semi-automatic followed by manual correction), image data preprocessing, and co-registration. MS, JW, RH, and MG wrote the manuscript draft. All authors read and approved the submitted manuscript, and agreed to be accountable for the content of the work and its publication.

FUNDING

This study was funded by the European Society of Anaesthesiology and Intensive Care (ESAIC, former ESA) Grant Programme 2020 (ESAIC Research Support Grant 2020), a grant by the local Faculty of Medicine Carl Gustav Carus, Dresden (MeDDrive #60439), and a national grant of the German Research Council (Deutsche Forschungsgemeinschaft, DFG; Grant number GA 1256/8-1).

ACKNOWLEDGMENTS

We thank Sabine Müller and the research fellows of the Pulmonary Engineering Group, University Hospital Carl Gustav Carus, Technische Universität Dresden, Germany, for their assistance in conducting the experiments.

REFERENCES

Acute Respiratory Distress Syndrome Network, Brower, R. G., Matthay, M. A., Morris, A., Schoenfeld, D., Thompson, B. T., et al. (2000). Ventilation with lower tidal volumes as compared with traditional tidal volumes for acute lung injury and the acute respiratory distress syndrome. *N. Engl. J. Med.* 342, 1301–1308. doi: 10.1056/NEJM200005043421801

Amato, M. B. P., Meade, M. O., Slutsky, A. S., Brochard, L., Costa, E. L. V., Schoenfeld, D. A., et al. (2015). Driving pressure and survival in the acute respiratory distress syndrome. *N. Engl. J. Med.* 372, 747–755. doi: 10.1056/NEJMsa1410639

Battaglini, D., Sottano, M., Ball, L., Robba, C., Rocco, P. R. M., and Pelosi, P. (2021). Ten golden rules for individualized mechanical ventilation in acute respiratory distress syndrome. *J. Intens. Med.* Available online at: https://www.sciencedirect.com/science/article/pii/S2667100X21000049 (accessed March 19, 2021).

Bellani, G., Laffey, J. G., Pham, T., Fan, E., Brochard, L., Esteban, A., et al. (2016). Epidemiology, patterns of care, and mortality for patients with acute respiratory distress syndrome in intensive care Units in 50 Countries. *JAMA* 315, 788–800. doi: 10.1001/jama.2016.0291

Braune, A., Hofheinz, F., Bluth, T., Kiss, T., Wittenstein, J., Scharffenberg, M., et al. (2019). Comparison of static 18F-FDG-PET/CT (SUV, SUR) and dynamic 18F-FDG-PET/CT (Ki) for quantification of pulmonary inflammation in acute lung injury. *J. Nucl. Med.* 60, 1629–1634. doi: 10.2967/jnumed.119.226597

Brower, R., Lanken, P., MacIntyre, N., Matthay, M., Morris, A., Ancukiewicz, M., et al. (2004). Higher versus lower positive end-expiratory pressures in patients with the acute respiratory distress syndrome. *New Engl. J. Med.* 351, 327–336. doi: 10.1056/NEJMoa032193

Carvalho, A. R., Pacheco, S. A., de Souza Rocha, P. V., Bergamini, B. C., Paula, L. F., Jandre, F. C., et al. (2013). Detection of tidal recruitment/overdistension in lung-healthy mechanically ventilated patients under general anesthesia. *Anesth Analg.* 116, 677–684. doi: 10.1213/ANE.0b013e318254230b

Cavalcanti, A. B., Suzumura, ÉA., Laranjeira, L. N., Paisani, D., de, M., Damiani, L. P., et al. (2017). Effect of lung recruitment and titrated positive end-expiratory pressure (PEEP) vs low PEEP on mortality in patients with acute respiratory distress syndrome: a randomized clinical trial. *JAMA* 318, 1335–1345. doi: 10.1001/jama.2017.14171

Chiumello, D., Cressoni, M., Carlesso, E., Caspani, M. L., Marino, A., Gallazzi, E., et al. (2014). Bedside selection of positive end-expiratory pressure in mild, moderate, and severe acute respiratory distress syndrome. *Crit. Care Med.* 42, 252–264. doi: 10.1097/CCM.0b013e3182a6384f

Collino, F., Rapetti, F., Vasques, F., Maiolo, G., Tonetti, T., Romitti, F., et al. (2019). Positive end-expiratory pressure and mechanical power. *Anesthesiology* 130, 119–130. doi: 10.1097/ALN.0000000000002458

Costa, E. L. V., Musch, G., Winkler, T., Schroeder, T., Harris, R. S., Jones, H. A., et al. (2010). Mild endotoxemia during mechanical ventilation produces spatially heterogeneous pulmonary neutrophilic inflammation in sheep. *Anesthesiology* 112, 658–669. doi: 10.1097/ALN.0b013e3181cbd1d4

Costa, E. L. V., Slutsky, A., Brochard, L. J., Brower, R., Serpa-Neto, A., Cavalcanti, A. B., et al. (2021). Ventilatory variables and mechanical power in patients with acute respiratory distress syndrome. *Am. J. Respir. Crit. Care Med.* Available

online at: https://www.atsjournals.org/doi/abs/10.1164/rccm.202009-3467OC (accessed April 6, 2021).

Cressoni, M., Gotti, M., Chiurazzi, C., Massari, D., Algieri, I., Amini, M., et al. (2016). Mechanical Power and development of ventilator-induced lung injury. *Anesthesiology* 124, 1100–1108.

Dreyfuss, D., and Saumon, G. (1998). Ventilator-induced lung injury: lessons from experimental studies. *Am. J. Respir. Crit. Care Med.* 157, 294–323.

Gattinoni, L., Caironi, P., Pelosi, P., and Goodman, L. R. (2001). What has computed tomography taught us about the acute respiratory distress syndrome? *Am. J. Respir. Crit. Care Med.* 164, 1701–1711. doi: 10.1164/ajrccm.164.9.2103121

Gattinoni, L., Tonetti, T., Cressoni, M., Cadringher, P., Herrmann, P., Moerer, O., et al. (2016). Ventilator-related causes of lung injury: the mechanical power. *Intens. Care Med.* 42, 1567–1575. doi: 10.1007/s00134-016-4505-2

Giosa, L., Busana, M., Pasticci, I., Bonifazi, M., Macrì, M. M., Romitti, F., et al. (2019). Mechanical power at a glance: a simple surrogate for volume-controlled ventilation. *Intens. Care Med. Exp.* 7:61. doi: 10.1186/s40635-019-0276-8

Grommes, J., and Soehnlein, O. (2011). Contribution of neutrophils to acute lung injury. *Mol. Med.* 17, 293–307.

Güldner, A., Braune, A., Ball, L., Silva, P. L., Samary, C., Insorsi, A., et al. (2016). Comparative effects of volutrauma and atelectrauma on lung inflammation in experimental acute respiratory distress syndrome. *Crit. Care Med.* 44, e854–e865. doi: 10.1097/CCM.0000000000001721

Guttmann, J. (2010). HS-404.2 Energietransfer Beatmungsgerät-Patient – Kann man das weiter minimieren? *Anästh Int.* 51:527.

Hedenstierna, G., Lundquist, H., Lundh, B., Tokics, L., Strandberg, A., Brismar, B., et al. (1989). Pulmonary densities during anaesthesia. An experimental study on lung morphology and gas exchange. *Eur. Respir. J.* 2, 528–535.

Huhle, R., Serpa Neto, A., Schultz, M. J., and Gama de Abreu, M. (2018). Is mechanical power the final word on ventilator-induced lung injury?-no. *Ann. Transl. Med.* 6, 394.

Jones, H. A., Sriskandan, S., Peters, A. M., Pride, N. B., Krausz, T., Boobis, A. R., et al. (1997). Dissociation of neutrophil emigration and metabolic activity in lobar pneumonia and bronchiectasis. *Eur. Respir. J.* 10, 795–803.

Kano, S., Lanteri, C. J., Duncan, A. W., and Sly, P. D. (1994). Influence of nonlinearities on estimates of respiratory mechanics using multilinear regression analysis. *J. Appl. Physiol.* 77, 1185–1197. doi: 10.1152/jappl.1994.77.3.1185

Kiss, T., Bluth, T., Braune, A., Huhle, R., Denz, A., Herzog, M., et al. (2019). Effects of positive end-expiratory pressure and spontaneous breathing activity on regional lung inflammation in experimental acute respiratory distress syndrome. *Crit. Care Med.* 47, e358–e365.

Lanteri, C. J., Kano, S., and Sly, P. D. (1994). Validation of esophageal pressure occlusion test after paralysis. *Pediatr. Pulmonol.* 17, 56–62. doi: 10.1002/ppul.1950170110

Marini, J. J., and Jaber, S. (2016). Dynamic predictors of VILI risk: beyond the driving pressure. *Intens. Care Med.* 42, 1597–1600. doi: 10.1007/s00134-016-4534-x

Matthay, M. A., and Zemans, R. L. (2011). The acute respiratory distress syndrome: pathogenesis and treatment. *Annu. Rev. Pathol.* 6, 147–163.

Mead, J., Takishima, T., and Leith, D. (1970). Stress distribution in lungs: a model of pulmonary elasticity. *J. Appl. Physiol.* 28, 596–608. doi: 10.1152/jappl.1970.28.5.596

Meade, M. O., Cook, D. J., Guyatt, G. H., Slutsky, A. S., Arabi, Y. M., Cooper, D. J., et al. (2008). Ventilation strategy using low tidal volumes, recruitment maneuvers, and high positive end-expiratory pressure for acute lung injury and acute respiratory distress syndrome: a randomized controlled trial. *JAMA* 299, 637–645.

Mercat, A., Richard, J.-C. M., Vielle, B., Jaber, S., Osman, D., Diehl, J.-L., et al. (2008). Positive end-expiratory pressure setting in adults with acute lung injury and acute respiratory distress syndrome: a randomized controlled trial. *JAMA* 299, 646–655.

Musch, G., Venegas, J. G., Bellani, G., Winkler, T., Schroeder, T., Petersen, B., et al. (2007). Regional gas exchange and cellular metabolic activity in ventilator-induced lung injury. *Anesthesiology* 106, 723–735. doi: 10.1097/01.anes.0000264748.86145.ac

Pelosi, P., Rocco, P. R. M., and Gama de Abreu, M. (2018). Close down the lungs and keep them resting to minimize ventilator-induced lung injury. *Crit. Care* 22:72. doi: 10.1186/s13054-018-1991-3

Rich, P. B., Douillet, C. D., Hurd, H., and Boucher, R. C. (2003). Effect of ventilatory rate on airway cytokine levels and lung injury. *J. Surg. Res.* 113, 139–145. doi: 10.1016/S0022-4804(03)00195-1

Saha, D., Takahashi, K., de Prost, N., Winkler, T., Pinilla-Vera, M., Baron, R. M., et al. (2013). Micro-autoradiographic assessment of cell types contributing to 2-deoxy-2-[(18)F]fluoro-D-glucose uptake during ventilator-induced and endotoxemic lung injury. *Mol. Imag. Biol.* 15, 19–27. doi: 10.1007/s11307-012-0575-x

Sassoon, C. S. H., and Mahutte, C. K. (1998). *Work of Breathing During Mechanical Ventilation: Physiological Basis of Ventilatory Support*. New York, NY: Marcel Dekker Inc., 261–310.

Schroeder, T., Melo, M. F. V., and Venegas, J. G. (2011). Analysis of 2-[Fluorine-18]-Fluoro-2-deoxy-D-glucose uptake kinetics in PET studies of pulmonary inflammation. *Acad. Radiol.* 18, 418–423. doi: 10.1016/j.acra.2010.11.019

Serpa Neto, A., Deliberato, R. O., Johnson, A. E. W., Bos, L. D., Amorim, P., Pereira, S. M., et al. (2018). Mechanical power of ventilation is associated with mortality in critically ill patients: an analysis of patients in two observational cohorts. *Intens. Care Med.* 44, 1914–1922. doi: 10.1007/s00134-018-5375-6

Torigian, D., Chong, E., Schuster, S., Hofheinz, F., Rosenbaum, J., and Alavi, A. (2009). Feasibility and utility of ROVER software for 3D quantitative image analysis of FDG-PET in patients with diffuse large B-cell lymphoma (DLBCL). *J. Nuc. Med.* 50(Suppl. 2), 135–135.

Vassalli, F., Pasticci, I., Romitti, F., Duscio, E., Aßmann, D. J., Grünhagen, H., et al. (2020). Does Iso-mechanical Power lead to iso-lung damage?: an experimental study in a porcine model. *Anesthesiology* 132, 1126–1137. doi: 10.1097/ALN.0000000000003189

Wadsak, W., and Mitterhauser, M. (2010). Basics and principles of radiopharmaceuticals for PET/CT. *Eur. J. Radiol.* 73, 461–469. doi: 10.1016/j.ejrad.2009.12.022

Wittenstein, J., Scharffenberg, M., Braune, A., Huhle, R., Bluth, T., Herzog, M., et al. (2020). Effects of variable versus nonvariable controlled mechanical ventilation on pulmonary inflammation in experimental acute respiratory distress syndrome in pigs. *Br. J. Anaesth* 124, 430–439. doi: 10.1016/j.bja.2019.12.040

Zemans, R. L., Colgan, S. P., and Downey, G. P. (2009). Transepithelial migration of neutrophils: mechanisms and implications for acute lung injury. *Am. J. Respir. Cell Mol. Biol.* 40, 519–535. doi: 10.1165/rcmb.2008-0348TR

Conflict of Interest: MG received consultation fees from Dräger, Ambu, GE Healthcare, and ZOLL.

The remaining authors declare that the research was conducted in the absence of any commercial or financial relationships that could be construed as a potential conflict of interest.

Publisher's Note: All claims expressed in this article are solely those of the authors and do not necessarily represent those of their affiliated organizations, or those of the publisher, the editors and the reviewers. Any product that may be evaluated in this article, or claim that may be made by its manufacturer, is not guaranteed or endorsed by the publisher.

frontiers in Physiology

MINI REVIEW
published: 09 December 2021
doi: 10.3389/fphys.2021.762688

New Frontiers in Functional and Molecular Imaging of the Acutely Injured Lung: Pathophysiological Insights and Research Applications

*Guido Musch**

Department of Anesthesiology and Perioperative Medicine, University of Massachusetts Medical School, Worcester, MA, United States

This review focuses on the advances in the understanding of the pathophysiology of ventilator-induced and acute lung injury that have been afforded by technological development of imaging methods over the last decades. Examples of such advances include the establishment of regional lung mechanical strain as a determinant of ventilator-induced lung injury, the relationship between alveolar recruitment and overdistension, the regional vs. diffuse nature of pulmonary involvement in acute respiratory distress syndrome (ARDS), the identification of the physiological determinants of the response to recruitment interventions, and the pathophysiological significance of metabolic alterations in the acutely injured lung. Taken together, these advances portray multimodality imaging as the next frontier to both advance knowledge of the pathophysiology of these conditions and to tailor treatment to the individual patient's condition.

Keywords: positron-emission tomography, tomography X-ray computed, magnetic resoance imaging, ventilator-induced lung injury, acute lung injury, respiratory distress syndrome, respiratory physiological phenomena, isotopes

OPEN ACCESS

Edited by:
Patricia R. M. Rocco, Federal University of Rio de Janeiro, Brazil

Reviewed by:
Carmen Silvia Valente Barbas, University of São Paulo, Brazil
Gabriele Valli, Azienda Ospedaliera San Giovanni Addolorata, Italy

***Correspondence:**
Guido Musch
guido.musch@umassmed.edu
orcid.org/0000-0003-1170-8699

Specialty section:
This article was submitted to Respiratory Physiology, a section of the journal Frontiers in Physiology

Received: *22 August 2021*
Accepted: *17 November 2021*
Published: *09 December 2021*

Citation:
Musch G (2021) New Frontiers in Functional and Molecular Imaging of the Acutely Injured Lung: Pathophysiological Insights and Research Applications. Front. Physiol. 12:762688. doi: 10.3389/fphys.2021.762688

INTRODUCTION

Most reviews of imaging for acute lung injury start from the specific method and then derive, based on its technical and physical properties, the corresponding application. The approach of this review will be different. It will start from fundamental pathophysiologic and metabolic hallmarks of ventilator-induced and acute lung injury to derive the corresponding phenotypic trait that can be leveraged as an imaging target. Not aiming to be an exhaustive review of this topic, for which there are recent comprehensive papers (Cereda et al., 2019), the emphasis herein will be on phenotype-based imaging approaches that hold promise of significant new developments and applications as well as on the insights that such approaches have already yielded.

HETEROGENEOUS LOSS OF AERATION AND CONCENTRATED LUNG STRAIN

Since the late 1980s, it became clear that what had been previously considered a homogeneous loss of aeration throughout the lung of patients with acute respiratory distress syndrome

(ARDS) was instead heterogeneously distributed. Such loss involved only certain portions of the lung, most frequently the dependent, dorsal, and caudal regions, while often sparing the more anterior nondependent ones (Puybasset et al., 1998). A functional consequence of this heterogeneous loss of aeration is that the amount of lung available to accommodate tidal volume is reduced and hence potentially exposed to greater mechanical strain during ventilation (Gattinoni and Pesenti, 2005). Because the lung, in contrast to solid organs like the liver or the brain, contains gas, mechanical strain is accompanied by a change in gas volume and thus lung density and electrical impedance. This property has been leveraged by, respectively, computed and electrical impedance tomography to measure the regional distribution of tidal volumetric strain in mechanically ventilated patients with, and animal models of, ARDS. Computed tomography (CT) measures the *x*-ray absorbance of each "piece" (voxel) of lung, which is inversely proportional to its gas content. Multi-detector CT scanners allow coverage of the entire lung fields at very high spatial resolutions of 1–2 mm. This enables reconstruction of a detailed three-dimensional map of the distribution of lung gas volume vs. tissue volume. By taking CT scans at different phases of the respiratory cycle, such as end expiration and end inspiration, or at different end-expiratory pressures, one can derive information on the distribution of both static and dynamic lung strain. While CT has the definite advantage of a very high spatial resolution, its main limitations are: cost, radiation exposure, and extreme difficulty, if not inability, to use it as a bedside tool to guide ventilator strategy. Electrical Impedance Tomography (EIT) partially obviates these limitations, albeit at the expense of a much lower spatial resolution. In EIT, an electrode belt is placed around the chest and used to record cross-sectional voltages after stimulation with low-amperage alternating current. Changes in thoracic electrical impedance are related to changes in the amount of gas relative to lung tissue, edema, or blood volume, and hence have been used mainly to assess the regional distribution of ventilation and end-expiratory lung gas volume. A distillate of the findings of literally hundreds of studies performed with CT and EIT is:

a. Loss of aeration is predominant in dependent dorsal and caudal regions (Puybasset et al., 1998).
b. As a result, tidal volume distributes preferentially to the non-dependent ventral regions (Gattinoni et al., 1995; Spinelli et al., 2021), exposing them to increased and potentially injurious strain, which compounds the inflammatory process of ARDS and leads to ventilator-induced lung injury (VILI).
c. The increased vertical pleural pressure gradient of the edematous lung defines a transition zone of poorly aerated lung tissue that undergoes the greatest cyclical changes in lung density during the respiratory cycle. This zone is thought to act as a focus of propagation of subsequent injury (Cereda et al., 2017; Xin et al., 2018)
d. Recent evidence indeed suggests that lung regions that exhibit the greatest cyclical change in density with tidal volume at the start of a period of mechanical ventilation eventually become "injured" as defined by a stable increase of their density above −300 Hounsfield Units (Cereda et al., 2017);
e. All of the above phenomena can be partially reversed with positive end-expiratory pressure (PEEP) or prone positioning (Gattinoni et al., 1995; Cornejo et al., 2013; Xin et al., 2018).

TOMOGRAPHIC IMAGING OF INHALED GASES TO DERIVE MEASURES OF REGIONAL VENTILATION AND ALVEOLAR GEOMETRY

The above measurements of lung gas content with an external source be it of radiation or electricity, cannot directly trace the transport and distribution of inhaled gases to the alveolar airspace where gas exchange occurs. Several techniques were developed to overcome this limitation by administering inhaled gases that would yield a signal to be imaged. Herein, we will review three such techniques that hinge on three different imaging modalities, and the insights they provided.

Xenon is a radiodense gas and can thus be used as an inhaled contrast agent to study regional gas transport, ventilation, and lung strain with CT. Using this technique, Herrmann et al. (2021) recently demonstrated that multifrequency oscillatory ventilation, a new approach to oscillatory ventilation that uses more than one frequency in the ventilatory waveform, achieved fast gas transport rates, similar to conventional mechanical ventilation, but with much lower delivered volumes, comparable to high frequency oscillatory ventilation. This mode should thus afford the lower lung stretch of high frequency oscillation, while compensating the drawback of less efficient gas transport than conventional mechanical ventilation.

Another approach is to administer an inhaled radioactive gas, either a single photon, like krypton-81, or positron, like nitrogen-13 ($^{13}N_2$), emitter. The washin, equilibration, and washout kinetics can then be imaged by single photon emission computed tomography (SPECT) or positron emission tomography (PET), respectively. Using inhaled $^{13}N_2$, Wellman et al. (2014) showed that high PEEP decreases tidal strain in middle and dependent lung regions of mechanically ventilated sheep exposed to intravenous lipopolysaccharide, an experimental model for sepsis. Inhaled gas methods have also allowed validation of strain measurements derived from lung density changes against other measurements of regional mechanics such as specific ventilation (Wellman et al., 2010) and parenchymal marker displacement (Fuld et al., 2008).

A third approach is based on inhalation of hyperpolarized gases, in particular helium-3 (^{3}He) and xenon-129 (^{129}Xe), the distribution of which can be imaged with magnetic resoance imaging (MRI). ^{3}He has been used to measure the apparent diffusion coefficient (ADC) in models of ARDS and atelectasis during mechanical ventilation (Cereda et al., 2011, 2013a,b, 2016). Helium's small nucleus enables rapid diffusivity, which is limited only by the restriction imposed by the alveolar wall. The ADC is a measure of how freely and far a nucleus can diffuse within a specific medium. This diffusivity is decreased

by barriers that do not allow free passage of the nucleus, as are the alveolar walls in the lung. Consequently, the smaller is the size of the acinar space, the more restricted is the movement of ^{3}He and the lower is the ADC. This technique has thus been particularly valuable to yield insights on airspace size changes with atelectasis and PEEP. In particular, this technique has led to an appreciation of the importance of alveolar interdependence when considering the effects of alveolar overdistension and derecruitment (Cereda et al., 2011). Whereas classical thinking had these two phenomena occurring at high and low extremes of airway pressure, respectively, and in topographically distinct parts of the lung (non-dependent vs. dependent), ^{3}He MRI studies revealed that ADC of ventilated airspaces increases during ventilation at low airway pressure that promotes atelectasis, that this increase is reversed by alveolar recruitment maneuvers (Cereda et al., 2011), and that the highest ADC increase tends to colocalize with the loss of aeration in dependent dorsal regions (Cereda et al., 2016). In a saline-lavage model of ARDS (Cereda et al., 2013a), surfactant depletion resulted in a wider distribution of ADC, shifted toward higher ADC values. Combined application of PEEP and exogenous surfactant restored ADC values and distribution similar to those before lavage (**Figure 1**). In another study, application of PEEP to initially healthy but derecruited lungs resulted in reversal of ADC-hysteresis, with smaller ADC values on the descending than on the ascending limb of the pressure-ADC curve as opposed to the whole lung pressure-volume curve (Cereda et al., 2013b). Taken together, these results have been interpreted to indicate that alveolar derecruitment leads to overstretching of airspaces that remain open, due to alveolar interdependence. Interalveolar traction forces between open and atelectatic airspaces in the same or contiguous regions are relieved by alveolar recruitment, which results in a greater number of open airspaces, with consequent reduction of the forces and smaller and more homogenous distribution of alveolar size.

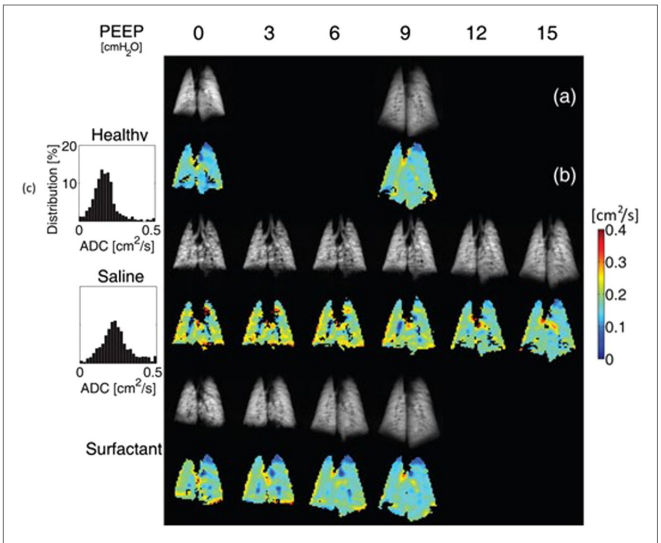

FIGURE 1 | Effect of positive end-expiratory pressure (PEEP), surfactant depletion by saline lavage, and exogenous surfactant administration on helium-3 (^{3}He) spin density **(A)** and alveolar size as inferred by apparent diffusion coefficient (ADC) for ^{3}He **(B)** in a coronal slice of rat lung. At PEEP = 0 cmH_2O, saline lavage shifted the ADC distribution toward higher values and increased its variance **(C)**, consistent with greater heterogeneity of aerated acini's size and alveolar overdistension, as it can be appreciated by yellow and red speckling on the lung ADC map. PEEP and surfactant reduced this speckling, both individually and through a combined effect that resulted in restoration of an ADC map similar to the healthy state (Modified from Cereda et al., 2013a).

TOMOGRAPHIC IMAGING OF SHUNT, EDEMA, AND VASCULAR PERMEABILITY

A pathophysiological hallmark of ARDS is increased pulmonary vascular permeability, which leads to interstitial and intraalveolar edema. The functional consequence of edema is shunt, whereby gas exchange with pulmonary capillary blood is impeded. These physiological alterations, and their topographical distribution, can be measured with PET of several isotopes. The key concept here is that the delivery of the tracer by inhalation is not useful because, by definition, inhaled tracer cannot reach regions of shunt, which are not ventilated. Therefore, even techniques like ^{129}Xe MRI, which can measure gas transport efficiency in healthy lungs from the loss of ^{129}Xe signal to the blood phase as Xe is absorbed into the pulmonary circulation (Ruppert et al., 2019), do not yield a measurable signal in shunting regions.

One approach to circumvent this roadblock is to administer a gaseous tracer in saline solution intravenously, so that it can reach shunting regions, which are perfused. Historically, the first gas used for this purpose was sulfur hexafluoride, as part of the multiple inert gas elimination technique. A necessary prerequisite for measuring "true" shunt is that such gas must have very low solubility in blood so that it entirely diffuses into the gas phase of non-shunting units at first pass, and is retained only in shunting units. A gas that has similarly low solubility and also the advantage of a positron emitting isotope is nitrogen. The corresponding PET technique to measure regional pulmonary perfusion and shunt is based on the intravenous administration of [^{13}N]nitrogen ($^{13}N_2$) in saline solution (Galletti and Venegas, 2002; Vidal Melo et al., 2003). A bolus of $^{13}N_2$ gas dissolved in 20–30 ml of saline is infused intravenously at the beginning of a 30- to 60-s apnea while the pulmonary kinetics of $^{13}N_2$ is measured with sequential PET frames. Because of the low solubility of nitrogen in blood and tissues (partition coefficient between water and air is 0.015 at 37°C); virtually all infused $^{13}N_2$ diffuses into the airspace of aerated alveoli at first pass, where it accumulates in proportion to regional perfusion (Musch et al., 2002). However, if alveoli are perfused but not aerated, for example because they are atelectatic or flooded with edema, $^{13}N_2$ kinetics shows an early peak of tracer activity, reflecting perfusion to that region, followed by an exponential decrease for the remainder of apnea, as $^{13}N_2$ to shunting units is carried away by ongoing blood flow. The magnitude of this decrease is proportional to regional shunt, and robust estimates of regional perfusion and shunt

fraction can be derived by applying a mathematical model to the pulmonary kinetics of a $^{13}N_2$–saline bolus, measured by PET during apnea (Galletti and Venegas, 2002; O'Neill et al., 2003).

A distillate of the main findings obtained with this technique is:

a. Surfactant depletion is accompanied by alveolar derecruitment in dependent regions without major perfusion redistribution toward non-dependent regions. As a result, substantial shunt develops in dependent lung regions in the supine position (de Prost et al., 2011);
b. Interventions aimed at recruiting alveoli with increased airway pressure, such as recruitment maneuvers and PEEP, exert two competing effects on the determinants of oxygenation: on one hand they promote re-aeration of derecruited airspaces, thus favoring an improvement of oxygenation, on the other they divert blood flow toward regions that remain derecruited, thus favoring an increase of shunted perfusion and a worsening of oxygenation. The net result of these two effects determines whether oxygenation improves or worsens, and the change in oxygenation can be precisely predicted based on the effect of these interventions on regional shunted blood flow (Musch et al., 2004, 2008);
c. Prone positioning restores gas exchange to the dorsal lung in a model of surfactant depletion while only minimally increasing shunted perfusion to the ventral, dependent lung, with consequent dramatic improvement in blood gases (Richter et al., 2005).

Shunt is a functional consequence of edema. Using intravascular tracers that freely diffuse across the endothelium into edematous regions, it is possible to quantify the regional distribution of pulmonary perfusion and extravascular extracellular lung water, i.e., edema fluid. One such technique is based on PET imaging of the pulmonary kinetics of ^{15}O-water ($H_2{}^{15}O$) to measure regional perfusion and lung water, coupled with PET blood volume scans after inhalation of ^{11}C- or ^{15}O-carbon monoxide to subtract pulmonary blood volume from regional water (Mintun et al., 1986). Extravascular lung water can then be obtained by subtracting intravascular water from regional water. This technique thus allows determination of regional pulmonary blood flow and extravascular lung water (i.e., edema). Main findings obtained with this technique and other PET techniques that measure regional blood flow are:

Perfusion redistributes away from dependent edematous lung regions in oleic acid-induced lung injury (Gust et al., 1998), to a much greater extent than observed in the lung lavage model (Musch et al., 2004, 2008; de Prost et al., 2011). This redistribution, which acts to preserve arterial oxygenation, is impaired by intravenous endotoxin, thus worsening oxygenation. Because endotoxin blunts hypoxic pulmonary vasoconstriction (Brimioulle et al., 2002; Easley et al., 2009; Fernandez-Bustamante et al., 2009), this observation implies that vascular smooth muscle contraction is responsible for at least part of the observed perfusion redistribution in this model;

Studies in patients with ARDS using the $H_2{}^{15}O$ technique have also revealed lack of substantive perfusion redistribution away from edematous regions (Schuster et al., 2002), suggesting that hypoxic pulmonary vasoconstriction is, at least to some extent, impaired, similarly to the experimental endotoxin studies (Gust et al., 1998);

Redistribution of perfusion away from injured regions, similar to the oleic acid model, was instead demonstrated after unilateral endobronchial instillation of hydrochloric acid, a model for gastric aspiration, using PET of ^{68}Ga labeled microspheres to measure perfusion in rats (Richter et al., 2015).

Edema in ARDS is a consequence of increased pulmonary vascular permeability. This pathophysiological abnormality can be leveraged with PET by imaging the regional distribution of the pulmonary transcapillary escape rate of a radiolabeled protein, such as ^{68}Ga-transferrin or ^{11}C-methylalbumin, between the intravascular and extravascular space (Schuster et al., 1998). The most consequential insight into ARDS provided by this technique was a dissociation between the topographical distribution of pulmonary vascular permeability increase and that of the resultant edema (Sandiford et al., 1995). Whereas permeability was similarly increased in ventral and dorsal lung regions, extravascular lung density was significantly higher in dorsal, dependent regions, than in ventral, nondependent ones. This finding suggests that even when the inflammatory process involves the entire lung parenchyma, the resultant edema is heterogeneously distributed and tends to concentrate in dependent regions, most likely as a consequence of the effect of gravity.

In addition to PET, a technique that has recently emerged as a potentially useful clinical tool to image the mismatch between pulmonary gas and blood volume distribution is contrast-enhanced dual energy CT. Two CT scans with different radiation energy are simultaneously acquired and then processed to reconstruct the spatial distribution of pulmonary blood volume, a surrogate for pulmonary perfusion (Fuld et al., 2013). Using this technique, Ball et al. (2021) showed that patients with ARDS due to SARS-CoV-2 requiring invasive mechanical ventilation showed both a ventro-dorsal and cranio-caudal gradient in blood volume opposite to that in gas volume, with the result that regions with low gas-to-blood content (i.e., mismatch) increased from ventral to dorsal and from cranial to caudal. Interestingly, however, there were also areas of nonaerated lung that did not appear to contain blood, especially in dependent regions, consistent with pulmonary vascular thrombosis in opacities due to SARS-CoV-2 ARDS.

LEVERAGING ANAEROBIC METABOLISM AS AN IMAGING BIOMARKER FOR NEUTROPHILIC INFLAMMATION

Acute respiratory distress syndrome and VILI are characterized by a neutrophilic inflammatory response. Neutrophils have very few mitochondria and hence rely primarily on glycolysis for their energy needs. A corollary of this phenotypic trait is that, because glycolysis has low energy yield, activated neutrophils increase their glucose consumption and lactate production

disproportionately to other cell types to satisfy their increased energy requirement. This trait can be leveraged by two different metabolic imaging modalities: PET of 2-[^{18}F]fluoro-2-deoxy-D-glucose ([^{18}F]FDG) and MRI of hyperpolarized [1-^{13}C]pyruvate. In the former modality, the positron emitting glucose analog [^{18}F]FDG is taken up by cells through facilitative glucose transporters and phosphorylated by hexokinase to [^{18}F]FDG-6-phosphate, which cannot proceed further along the glycolytic pathway and thus accumulates in proportion to cellular metabolic rate. Substantive experimental and clinical evidence has established PET measurement of [^{18}F]FDG uptake as a tool to noninvasively assess the activation of inflammatory cells in the noncancerous lung (Jones et al., 1994; Chen and Schuster, 2004). In particular, the increase in [^{18}F]FDG uptake during VILI was shown to be largely attributable to neutrophils (Musch et al., 2007) and, to a lesser extent, other cell populations such as macrophages and type 2 epithelial cells (Saha et al., 2013). The main insights into the pathophysiology of acute and ventilator-induced lung injury afforded by PET of [^{18}F]FDG are:

a. Inflammatory cell metabolic activation is an early event in the pathogenesis of lung injury, as increased [^{18}F]FDG uptake precedes impairment of pulmonary gas exchange in an acute smoke inhalation model of lung injury (Musch et al., 2014) and development of lung densities in an endotoxemia model with superimposed mechanical ventilation (Wellman et al., 2016);
b. The topographical distribution of [^{18}F]FDG uptake reflects, at least in part, that of mechanical lung strain. Regions of lung that are most exposed to the biophysical determinants of VILI also show increased [^{18}F]FDG uptake (Wellman et al., 2014; Motta-Ribeiro et al., 2018; Retamal et al., 2018). This topographical heterogeneity of [^{18}F]FDG uptake is enhanced by the infusion of low-dose endotoxin concomitantly with mechanical ventilation (Costa et al., 2010), a model for clinical sepsis, and reduced by protective ventilation with high PEEP and low tidal volume (de Prost et al., 2013);
c. Importantly, regions of lung that present increased [^{18}F]FDG uptake on PET also reveal gene expression patterns indicative of activation of specific inflammatory pathways, adhesion molecules, and epithelial and endothelial stretch markers (Wellman et al., 2016; Motta-Ribeiro et al., 2018). In addition, parameters derived from [^{18}F]FDG kinetic modeling correlate with specific aspects of the inflammatory response, such as neutrophil infiltration and cytokine expression (de Prost et al., 2014);

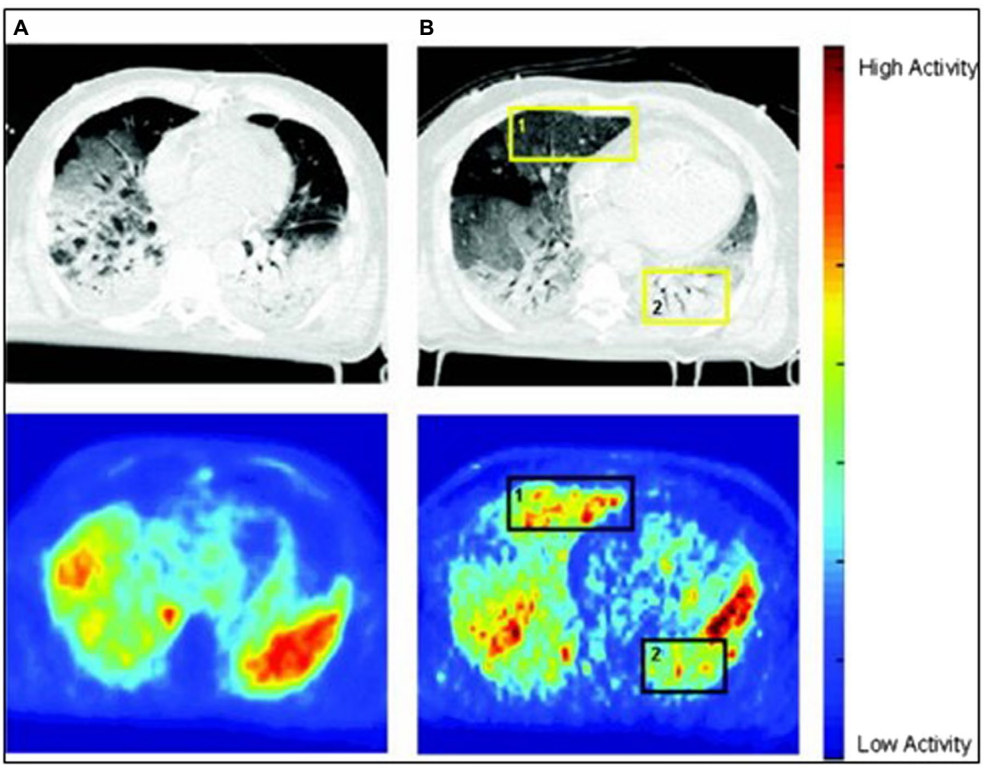

FIGURE 2 | Computed tomography (CT) scans (upper row) and positron emission tomography (PET) scans of [^{18}F]FDG uptake (bottom row) in two patients with acute respiratory distress syndrome (ARDS). In patient **A**, [^{18}F]FDG uptake is highest in regions of increased lung density on CT, suggesting that these opacities are inflamed and possibly responsible for ARDS. In contrast, in patient **B**, there is a dissociation between [^{18}F]FDG signal and density, with increased [^{18}F]FDG uptake in nondependent normally aerated regions of both lungs. A hypothesis is that, in this case, the [^{18}F]FDG signal mainly reflects ventilator-induced lung injury (VILI), as these are the regions exposed to mechanical ventilation (Reproduced from Bellani et al., 2009).

TABLE 1 | Main advantages and limitations of lung imaging modalities.

	Advantages	Limitations
EIT	Bedside availability	Poor spatial resolution
	Easy implementation	Limited lung volume sampled
CT	High spatial resolution	Radiation exposure
	Speed of acquisition (can image the entire lung volume)	Limited ability to image biologic processes
	Gated acquisition possible	
PET	Image biologic processes	Radiation exposure
	Tracer kinetic modeling	Lower spatial resolution
	Gated acquisition possible	Longer acquisition times
MR	High spatial resolution	Requires hyperpolarized gases to image ventilation
	Radiation free	
		Limited ability to image biologic processes

d. Whereas there is consistent evidence that volutrauma leads to increased pulmonary [^{18}F]FDG uptake (Musch et al., 2007; Güldner et al., 2016), results have been conflicting on the role of so called "atelectrauma." Studies in both animal models (Güldner et al., 2016) and patients (Bellani et al., 2011) have not been able to conclusively demonstrate increased [^{18}F]FDG uptake in regions of cyclical tidal recruitment-derecruitment, which are the expected origin of atelectrauma;
e. In patients with ARDS, the distribution of lung opacities on CT does not necessarily overlap with that of [^{18}F]FDG uptake measured by PET (Bellani et al., 2009; Cressoni et al., 2016). In some patients, the highest [^{18}F]FDG uptake occurs in areas that appear consolidated on CT, suggesting that the primary inflammatory process responsible for ARDS is also responsible for the increased PET signal. In other patients, instead, the PET signal is higher in regions with normal aeration. The increased signal in these aerated and ventilated regions could reflect the iatrogenic injury from mechanical ventilation (**Figure 2**).

Some of the above findings were recently corroborated by metabolic imaging of hyperpolarized [1-^{13}C]pyruvate in a hydrochloric acid instillation model of ARDS with superimposed VILI. This MRI method showed increased lactate production, consistent with neutrophilic inflammation, when acid instillation was followed by ventilation with no PEEP. The increased lactate localized predominantly to the dependent dorsal lung in this model, together with increased proton signal intensity consistent with the development of increased lung density from exudate, consolidation, or atelectasis. Protective ventilation with PEEP prevented the increase in lactate signal after acid instillation (Pourfathi et al., 2018).

Main advantages and limitations of the pulmonary imaging modalities presented in this review are summarized in **Table 1**.

CONCLUSION

Over the past 4 decades, substantive evolution in image technology and processing has enabled application of an array of imaging methods to study the acutely injured lung. These methods have yielded fundamental insights into the pathophysiology of VILI and of the gas exchange impairment and inflammatory response of ARDS.

AUTHOR CONTRIBUTIONS

The author confirms being the sole contributor of this work and has approved it for publication.

FUNDING

Funding for this article was provided by the Department of Anesthesiology and Perioperative Medicine and University of Massachusetts Medical School.

REFERENCES

Ball, L., Robba, C., Herrmann, J., Gerard, S. E., Xin, Y., Mandelli, M., et al. (2021). Collaborators of the GECOVID group. Lung distribution of gas and blood volume in critically ill COVID-19 patients: a quantitative dual-energy computed tomography study. *Crit. Care* 25:214. doi: 10.1186/s13054-021-03610-9

Bellani, G., Guerra, L., Musch, G., Zanella, A., Patroniti, N., Mauri, T., et al. (2011). Lung regional metabolic activity and gas volume changes induced by tidal ventilation in patients with acute lung injury. *Am. J. Respir. Crit. Care Med.* 183, 1193–1199. doi: 10.1164/rccm.201008-1318OC

Bellani, G., Messa, C., Guerra, L., Spagnolli, E., Foti, G., Patroniti, N., et al. (2009). Lungs of patients with acute respiratory distress syndrome show diffuse inflammation in normally aerated regions: a [^{18}F]-fluoro-2-deoxy-D-glucose PET/CT study. *Crit. Care Med.* 37, 2216–2222. doi: 10.1097/CCM.0b013e3181aab31f

Brimioulle, S., Julien, V., Gust, R., Kozlowski, J. K., Naeije, R., and Schuster, D. P. (2002). Importance of hypoxic vasoconstriction in maintaining oxygenation during acute lung injury. *Crit. Care Med.* 30, 874–880. doi: 10.1097/00003246-200204000-00027

Cereda, M., Emami, K., Kadlecek, S., Xin, Y., Mongkolwisetwara, P., Profka, H., et al. (2011). Quantitative imaging of alveolar recruitment with hyperpolarized gas MRI during mechanical ventilation. *J. Appl. Physiol.* 110, 499–511. doi: 10.1152/japplphysiol.00841.2010

Cereda, M., Emami, K., Xin, Y., Kadlecek, S., Kuzma, N. N., Mongkolwisetwara, P., et al. (2013a). Imaging the interaction of atelectasis and overdistension in surfactant-depleted lungs. *Crit. Care Med.* 41, 527–535. doi: 10.1097/CCM.0b013e31826ab1f2

Cereda, M., Xin, Y., Emami, K., Huang, J., Rajaei, J., Profka, H., et al. (2013b). Positive end-expiratory pressure increments during anesthesia in normal lung result in hysteresis and greater numbers of smaller aerated airspaces. *Anesthesiology* 119, 1402–1409. doi: 10.1097/ALN.0b013e3182a9b0c1

Cereda, M., Xin, Y., Goffi, A., Herrmann, J., Kaczka, D. W., Kavanagh, B. P., et al. (2019). Imaging the injured lung: mechanisms of action and clinical use. *Anesthesiology* 131, 716–749. doi: 10.1097/ALN.0000000000002583

Cereda, M., Xin, Y., Hamedani, H., Bellani, G., Kadlecek, S., Clapp, J., et al. (2017). Tidal changes on CT and progression of ARDS. *Thorax* 72, 981–989. doi: 10.1136/thoraxjnl-2016-209833

Cereda, M., Xin, Y., Hamedani, H., Clapp, J., Kadlecek, S., Meeder, N., et al. (2016). Mild loss of lung aeration augments stretch in healthy lung regions. *J. Appl. Physiol.* 120, 444–454. doi: 10.1152/japplphysiol.00734.2015

Chen, D. L., and Schuster, D. P. (2004). Positron emission tomography with [18F] fluorodeoxyglucose to evaluate neutrophil kinetics during acute lung injury. *Am. J. Phys. Lung Cell. Mol. Phys.* 286, L834–L840. doi: 10.1152/ajplung.00339.2003

Cornejo, R. A., Díaz, J. C., Tobar, E. A., Bruhn, A. R., Ramos, C. A., González, R. A., et al. (2013). Effects of prone positioning on lung protection in patients with acute respiratory distress syndrome. *Am. J. Respir. Crit. Care Med.* 188, 440–448. doi: 10.1164/rccm.201207-1279OC

Costa, E. L., Musch, G., Winkler, T., Schroeder, T., Harris, R. S., Jones, H. A., et al. (2010). Mild endotoxemia during mechanical ventilation produces spatially heterogeneous pulmonary neutrophilic inflammation in sheep. *Anesthesiology* 112, 658–669. doi: 10.1097/ALN.0b013e3181cbd1d4

Cressoni, M., Chiumello, D., Chiurazzi, C., Brioni, M., Algieri, I., Gotti, M., et al. (2016). Lung inhomogeneities, inflation and [^{18}F]2-fluoro-2-deoxy-D-glucose uptake rate in acute respiratory distress syndrome. *Eur. Respir. J.* 47, 233–242. doi: 10.1183/13993003.00885-2015

de Prost, N., Costa, E. L., Wellman, T., Musch, G., Tucci, M. R., Winkler, T., et al. (2013). Effects of ventilation strategy on distribution of lung inflammatory cell activity. *Crit. Care* 17:R175. doi: 10.1186/cc12854

de Prost, N., Costa, E. L., Wellman, T., Musch, G., Winkler, T., Tucci, M. R., et al. (2011). Effects of surfactant depletion on regional pulmonary metabolic activity during mechanical ventilation. *J. Appl. Physiol.* 111, 1249–1258. doi: 10.1152/japplphysiol.00311.2011

de Prost, N., Feng, Y., Wellman, T., Tucci, M. R., Costa, E. L., Musch, G., et al. (2014). 18F-FDG kinetics parameters depend on the mechanism of injury in early experimental acute respiratory distress syndrome. *J. Nucl. Med.* 55, 1871–1877. doi: 10.2967/jnumed.114.140962

Easley, R. B., Mulreany, D. G., Lancaster, C. T., Custer, J. W., Fernandez-Bustamante, A., Colantuoni, E., et al. (2009). Redistribution of pulmonary blood flow impacts thermodilution-based extravascular lung water measurements in a model of acute lung injury. *Anesthesiology* 111, 1065–1074. doi: 10.1097/ALN.0b013e3181bc99cf

Fernandez-Bustamante, A., Easley, R. B., Fuld, M., Mulreany, D., Hoffman, E. A., and Simon, B. A. (2009). Regional aeration and perfusion distribution in a sheep model of endotoxemic acute lung injury characterized by functional computed tomography imaging. *Crit. Care Med.* 37, 2402–2411. doi: 10.1097/CCM.0b013e3181a02354

Fuld, M. K., Easley, R. B., Saba, O. I., Chon, D., Reinhardt, J. M., Hoffman, E. A., et al. (2008). CT-measured regional specific volume change reflects regional ventilation in supine sheep. *J. Appl. Physiol.* 104, 1177–1184. doi: 10.1152/japplphysiol.00212.2007

Fuld, M. K., Halaweish, A. F., Haynes, S. E., Divekar, A. A., Guo, J., and Hoffman, E. A. (2013). Pulmonary perfused blood volume with dual-energy CT as surrogate for pulmonary perfusion assessed with dynamic multidetector CT. *Radiology* 267, 747–756. doi: 10.1148/radiol.12112789

Galletti, G. G., and Venegas, J. G. (2002). Tracer kinetic model of regional pulmonary function using positron emission tomography. *J. Appl. Physiol.* 93, 1104–1114. doi: 10.1152/japplphysiol.00910.2001

Gattinoni, L., Pelosi, P., Crotti, S., and Valenza, F. (1995). Effects of positive end-expiratory pressure on regional distribution of tidal volume and recruitment in adult respiratory distress syndrome. *Am. J. Respir. Crit. Care Med.* 151, 1807–1814. doi: 10.1164/ajrccm.151.6.7767524

Gattinoni, L., and Pesenti, A. (2005). The concept of "baby lung". *Intensive Care Med.* 31, 776–784. doi: 10.1007/s00134-005-2627-z

Güldner, A., Braune, A., Ball, L., Silva, P. L., Samary, C., Insorsi, A., et al. (2016). Comparative effects of volutrauma and atelectrauma on lung inflammation in experimental acute respiratory distress syndrome. *Crit. Care Med.* 44, e854–e865. doi: 10.1097/CCM.0000000000001721

Gust, R., Kozlowski, J., Stephenson, A. H., and Schuster, D. P. (1998). Synergistic hemodynamic effects of low-dose endotoxin and acute lung injury. *Am. J. Respir. Crit. Care Med.* 157, 1919–1926. doi: 10.1164/ajrccm.157.6.9704110

Herrmann, J., Gerard, S. E., Reinhardt, J. M., Hoffman, E. A., and Kaczka, D. W. (2021). Regional gas transport During conventional and oscillatory ventilation assessed by xenon-enhanced computed tomography. *Ann. Biomed. Eng.* 49, 2377–2388. doi: 10.1007/s10439-021-02767-2

Jones, H. A., Clark, R. J., Rhodes, C. G., Schofield, J. B., Krausz, T., and Haslett, C. (1994). In vivo measurement of neutrophil activity in experimental lung inflammation. *Am. J. Respir. Crit. Care Med.* 149, 1635–1639. doi: 10.1164/ajrccm.149.6.7516252

Mintun, M. A., Ter-Pogossian, M. M., Green, M. A., Lich, L. L., and Schuster, D. P. (1986). Quantitative measurement of regional pulmonary blood flow with positron emission tomography. *J. Appl. Physiol.* 60, 317–326. doi: 10.1152/jappl.1986.60.1.317

Motta-Ribeiro, G. C., Hashimoto, S., Winkler, T., Baron, R. M., Grogg, K., Paula, L. F. S. C., et al. (2018). Deterioration of regional lung strain and inflammation during early lung injury. *Am. J. Respir. Crit. Care Med.* 198, 891–902. doi: 10.1164/rccm.201710-2038OC

Musch, G., Bellani, G., Vidal Melo, M. F., Harris, R. S., Winkler, T., Schroeder, T., et al. (2008). Relation between shunt, aeration, and perfusion in experimental acute lung injury. *Am. J. Respir. Crit. Care Med.* 177, 292–300. doi: 10.1164/rccm.200703-484OC

Musch, G., Harris, R. S., Vidal Melo, M. F., O'Neill, K. R., Layfield, J. D. H., Winkler, T., et al. (2004). Mechanism by which a sustained inflation can worsen oxygenation in acute lung injury. *Anesthesiology* 100, 323–330. doi: 10.1097/00000542-200402000-00022

Musch, G., Layfield, J. D. H., Harris, R. S., Vidal Melo, M. F., Winkler, T., Callahan, R. J., et al. (2002). Topographical distribution of pulmonary perfusion and ventilation, assessed by PET in supine and prone humans. *J. Appl. Physiol.* 93, 1841–1851. doi: 10.1152/japplphysiol.00223.2002

Musch, G., Venegas, J. G., Bellani, G., Winkler, T., Schroeder, T., Petersen, B., et al. (2007). Regional gas exchange and cellular metabolic activity in ventilator-induced lung injury. *Anesthesiology* 106, 723–735. doi: 10.1097/01.anes.0000264748.86145.ac

Musch, G., Winkler, T., Harris, R. S., Vidal Melo, M. F., Wellman, T. J., de Prost, N., et al. (2014). Lung [^{18}F]fluorodeoxyglucose uptake and ventilation-perfusion mismatch in the early stage of experimental acute smoke inhalation. *Anesthesiology* 120, 683–693. doi: 10.1097/01.anes.0000435742.04859.e8

O'Neill, K., Venegas, J. G., Richter, T., Harris, R. S., Layfield, J. D. H., Musch, G., et al. (2003). Modeling kinetics of infused 13NN-saline in acute lung injury. *J. Appl. Physiol.* 95, 2471–2484. doi: 10.1152/japplphysiol.00401.2003

Pourfathi, M., Cereda, M., Chatterjee, S., Xin, Y., Kadlecek, S., Duncan, I., et al. (2018). Lung metabolism and inflammation during mechanical ventilation; an imaging approach. *Sci. Rep.* 8:3525. doi: 10.1038/s41598-018-21901-0

Puybasset, L., Cluzel, P., Chao, N., Slutsky, A. S., Coriat, P., and Rouby, J. J. (1998). A computed tomography scan assessment of regional lung volume in acute lung injury. *Am. J. Respir. Crit. Care Med.* 158, 1644–1655. doi: 10.1164/ajrccm.158.5.9802003

Retamal, J., Hurtado, D., Villarroel, N., Bruhn, A., Bugedo, G., Amato, M. B. P., et al. (2018). Does regional lung strain correlate With regional inflammation in acute respiratory distress syndrome During nonprotective ventilation? An experimental porcine study. *Crit. Care Med.* 46, e591–e599. doi: 10.1097/CCM.0000000000003072

Richter, T., Bellani, G., Harris, R. S., Vidal Melo, M. F., Winkler, T., Venegas, J. G., et al. (2005). Effect of prone position on regional shunt, aeration, and perfusion in experimental acute lung injury. *Am. J. Respir. Crit. Care Med.* 172, 480–487. doi: 10.1164/rccm.200501-004OC

Richter, T., Bergmann, R., Musch, G., Pietzsch, J., and Koch, T. (2015). Reduced pulmonary blood flow in regions of injury 2 hours after acid aspiration in rats. *BMC Anesthesiol.* 15:36. doi: 10.1186/s12871-015-0013-0

Ruppert, K., Xin, Y., Hamedani, H., Amzajerdian, F., Loza, L., Achekzai, T., et al. (2019). Measurement of regional 2D gas transport efficiency in rabbit lung using hyperpolarized ^{129}Xe MRI. *Sci. Rep.* 9:2413. doi: 10.1038/s41598-019-38942-8

Saha, D., Takahashi, K., de Prost, N., Winkler, T., Pinilla-Vera, M., Baron, R. M., et al. (2013). Micro-autoradiographic assessment of cell types contributing to 2-deoxy-2-[18F]fluoro-D-glucose uptake during ventilator-induced and endotoxemic lung injury. *Mol. Imaging Biol.* 15, 19–27. doi: 10.1007/s11307-012-0575-x

Sandiford, P., Province, M. A., and Schuster, D. P. (1995). Distribution of regional density and vascular permeability in the adult respiratory distress syndrome. *Am. J. Respir. Crit. Care Med.* 151, 737–742. doi: 10.1164/ajrccm/151.3_Pt_1.737

Schuster, D. P., Anderson, C., Kozlowski, J., and Lange, N. (2002). Regional pulmonary perfusion in patients with acute pulmonary edema. *J. Nucl. Med.* 43, 862–870.

Schuster, D. P., Markham, J., and Welch, M. J. (1998). Positron emission tomography measurements of pulmonary vascular permeability with 68Ga-

transferrin or 11C-methylalbumin. *Crit. Care Med.* 26, 518–525. doi: 10.1097/00003246-199803000-00026

Spinelli, E., Kircher, M., Stender, B., Ottaviani, I., Basile, M. C., Marongiu, I., et al. (2021). Unmatched ventilation and perfusion measured by electrical impedance tomography predicts the outcome of ARDS. *Crit. Care* 25:192. doi: 10.1186/s13054-021-03615-4

Vidal Melo, M. F., Layfield, D., Harris, R. S., O'Neill, K., Musch, G., Richter, T., et al. (2003). Quantification of regional ventilation-perfusion ratios with PET. *J. Nucl. Med.* 44, 1982–1991.

Wellman, T. J., de Prost, N., Tucci, M., Winkler, T., Baron, R. M., Filipczak, P., et al. (2016). Lung metabolic activation as an early biomarker of acute respiratory distress syndrome and local gene expression heterogeneity. *Anesthesiology* 125, 992–1004. doi: 10.1097/ALN.0000000000001334

Wellman, T. J., Winkler, T., Costa, E. L., Musch, G., Harris, R. S., Venegas, J. G., et al. (2010). Measurement of regional specific lung volume change using respiratory-gated PET of inhaled ^{13}N-nitrogen. *J. Nucl. Med.* 51, 646–653. doi: 10.2967/jnumed.109.067926

Wellman, T. J., Winkler, T., Costa, E. L., Musch, G., Harris, R. S., Zheng, H., et al. (2014). Effect of local tidal lung strain on inflammation in normal and lipopolysaccharide-exposed sheep. *Crit. Care Med.* 42, e491–e500. doi: 10.1097/CCM.0000000000000346

Xin, Y., Cereda, M., Hamedani, H., Pourfathi, M., Siddiqui, S., Meeder, N., et al. (2018). Unstable inflation causing injury. Insight from prone position and paired computed tomography scans. *Am. J. Respir. Crit. Care Med.* 198, 197–207. doi: 10.1164/rccm.201708-1728OC

Conflict of Interest: The author declares that the research was conducted in the absence of any commercial or financial relationships that could be construed as a potential conflict of interest.

frontiers in Physiology

REVIEW
published: 06 January 2022
doi: 10.3389/fphys.2021.721951

Ten Years of Pediatric Lung Ultrasound: A Narrative Review

Anna Maria Musolino[1], Paolo Tomà[2], Cristina De Rose[3], Eugenio Pitaro[1], Elena Boccuzzi[1], Rita De Santis[3], Rosa Morello[3], Maria Chiara Supino[1], Alberto Villani[4], Piero Valentini[3] and Danilo Buonsenso[3,5,6]*

[1] Pediatric Emergency Unit, Department of Emergency and General Pediatrics, Bambino Gesù Children's Hospital, IRCCS, Rome, Italy, [2] Department of Imaging, Bambino Gesù Children's Hospital, IRCCS, Rome, Italy, [3] Department of Woman and Child Health and Public Health, Fondazione Policlinico Universitario A. Gemelli IRCCS, Rome, Italy, [4] General Pediatric and Infectious Disease Unit, Internal Care Department, Bambino Gesù Children's Hospital, Rome, Italy, [5] Dipartimento di Scienze Biotecnologiche di Base, Cliniche Intensivologiche e Perioperatorie, Università Cattolica del Sacro Cuore, Rome, Italy, [6] Global Health Research Institute, Istituto di Igiene, Università Cattolica del Sacro Cuore, Rome, Italy

Lung diseases are the most common conditions in newborns, infants, and children and are also the primary cause of death in children younger than 5 years old. Traditionally, the lung was not thought to be a target for an ultrasound due to its inability to penetrate the gas-filled anatomical structures. With the deepening of knowledge on ultrasound in recent years, it is now known that the affected lung produces ultrasound artifacts resulting from the abnormal tissue/gas/tissue interface when ultrasound sound waves penetrate lung tissue. Over the years, the application of lung ultrasound (LUS) has changed and its main indications in the pediatric population have expanded. This review analyzed the studies on lung ultrasound in pediatrics, published from 2010 to 2020, with the aim of highlighting the usefulness of LUS in pediatrics. It also described the normal and abnormal appearances of the pediatric lung on ultrasound as well as the benefits, limitations, and possible future challenges of this modality.

Keywords: lung ultrasound, LUS, children, pediatrics, imaging, lung disease

OPEN ACCESS

Edited by:
Patricia R. M. Rocco, Federal University of Rio de Janeiro, Brazil

Reviewed by:
Steven Mink, University of Manitoba, Canada
Luigi Vetrugno, University of Udine, Italy

***Correspondence:**
Piero Valentini
piero.valentini@policlinicogemelli.it

Specialty section:
This article was submitted to Respiratory Physiology, a section of the journal Frontiers in Physiology

Received: *07 June 2021*
Accepted: *17 November 2021*
Published: *06 January 2022*

Citation:
Musolino AM, Tomà P, De Rose C, Pitaro E, Boccuzzi E, De Santis R, Morello R, Supino MC, Villani A, Valentini P and Buonsenso D (2022) Ten Years of Pediatric Lung Ultrasound: A Narrative Review. Front. Physiol. 12:721951. doi: 10.3389/fphys.2021.721951

INTRODUCTION

Lung diseases are the most common conditions in newborns, infants, and children and are also the primary causes of death in children younger than 5 years old (Liu et al., 2015b). Therefore, accurate and timely diagnosis is extremely important in order to enable efficient treatment and to improve the prognosis of patients with lung diseases.

In the past, the diagnosis of lung disease in the pediatric population mainly depended on chest X-ray (CXR) and/or computed tomography (CT). However, CXR may not be efficient bedside, requires transfer to specific radiological settings with all the infectious risks for patients and operators, and exposes the patient to ionizing radiation. Ultrasound imaging is based on the reflection and scattering of ultrasound (US) beam occurring at the interfaces between different media.

Traditionally, the lung was not thought to be a target for ultrasound waves due to their inability to penetrate the gas-filled anatomical structures. With the deepening of knowledge on ultrasound in recent years, it is now known that the affected lung produces ultrasound artifacts resulting from the abnormal tissue/gas/tissue interface when US waves penetrate lung tissue. Such artifacts are the basis of lung ultrasound (LUS) application in the clinic (Coley, 2011; Joshi et al., 2019).

Until recently, LUS has been underutilized for evaluation of the lung in pediatrics. Over the years, its applications have changed and its main indications in the pediatric population have expanded. Hence, ultrasound, which was previously used mainly to confirm the presence and nature of pleural effusion as well as to differentiate solid from cystic masses, was later used to evaluate the lung as well. To date, LUS is a frequently used diagnostic tool in daily pediatric clinical practice among clinicians and radiologists, but its application is not yet widely accepted, despite the numerous literature data.

This review analyzed the studies on LUS in pediatrics, published from 2010 to 2020, with the aim of highlighting the usefulness of pediatric LUS. It also described the normal and abnormal appearances of the pediatric lung on ultrasound as well as the benefits, limitations, and possible future challenges of this modality.

METHODS

Our work is a narrative review that included articles from October 2010 to February 2020.

To be included in the review, papers needed to focus on pediatric experience with lung ultrasound to diagnose different pathological conditions.

The bibliographic database named PubMed was chosen to identify potentially relevant documents using keywords "lung children ultrasound" and "lung children echography." The articles published between October 2010 and February 2020, written in French or English, and concerning the pediatric age including the neonatal age, were taken into consideration.

Papers that did not fit into the conceptual framework of this review or that dealt with the ultrasound experience of adult patients were excluded.

We grouped the studies according to the topic: ultrasound techniques and images; pneumonia; bronchiolitis; pneumothorax; neonatal ultrasound; wheezing.

Furthermore, each section has been divided by year (**Supplementary Materials**).

INDICATIONS, LIMITATIONS, AND USE OF LUNG ULTRASOUND IN THE PEDIATRIC POPULATION OVER THE LAST 10 YEARS

Until recently, LUS has been underutilized for evaluation of the lung in pediatrics. The bony chest and the presence of air within the lungs were thought to interfere with the transmission of US. Currently, it is known that ultrasonography is suitable for the pediatric chest due to the lack of significant subcutaneous fat. Additionally, the pediatric chest wall is only partially ossified, providing additional acoustic windows that are not available in older children or adults. The thymus also allows for adequate acoustic windows for the evaluation of the anterior chest and mediastinum. Non-ossified sternal and costal cartilage which appears relatively hypoechoic in US gradually ossifies with aging thus decreasing acoustic access (Coley, 2011; Joshi et al., 2019).

Over the years, the applications of LUS have changed and its main indications in children have expanded.

From 2010 to 2015: Lung Ultrasound as a Support Diagnostic Tool

In the first years during which lung ultrasound was used in pediatric clinical practice, the authors were rather skeptical of its use for which they emphasized its limits rather than advantages and limited its use to a few conditions, in clinical practice, mainly in support of other radiological investigations.

The most common indication for LUS was *to evaluate the opacities detected by CXR and the pleural abnormalities* (Coley, 2011; Joshi et al., 2019). For example, it allowed differentiating whether the cause of a completely opaque hemithorax was parenchymal or pleural disease (or both) guiding the appropriate direction of therapy and the eventual thoracic surgery.

Other classic applications of LUS in children – in support of classical radiology – were the *evaluation of mediastinal widening and the study of chest wall lesions*. Specifically, focal masses were studied by LUS to determine their location and whether they were solid or cystic (Coley, 2011; Joshi et al., 2019).

Reviewing the studies performed up to that moment in the pediatric field, several authors (Supakul and Karmazyn, 2013; Tomà and Owens, 2013; Trinavarat and Riccabona, 2014) concluded that the exclusive approach with LUS instead of CXR could only be applicable in case of assessment of large areas of consolidation in contact with the pleural surface or a suitable acoustic window and for the presence of pleural effusions. They (Supakul and Karmazyn, 2013; Tomà and Owens, 2013; Trinavarat and Riccabona, 2014) stated that CXR was the primary imaging modality for evaluating respiratory disease and that chest CT should typically be performed when better pathology characterization or surgical planning was needed.

However, according to other authors (Coley, 2005; Riccabona, 2008; Chira et al., 2011; Mong et al., 2012), LUS could be used in the evaluation of lesions/diseases that appeared to be occult on chest radiography.

From 2010 to 2015: Lung Ultrasound, More Limits Than Advantages?

Most of the authors (Supakul and Karmazyn, 2013; Tomà and Owens, 2013; Trinavarat and Riccabona, 2014) – reviewing the papers carried out up to 2013–2014 – underlined the limits of the use of LUS in children and the weaknesses of the idea of regularly replacing CXR with LUS.

These limitations included the following: (1) the lack of studies in the pediatric population aimed at evaluating the pathology of the broncho-tracheal airways; (2) the need for contact between the diseased lung portion and the pleural surface and the need to find an adequate acoustic window; (3) the fact that acoustic phenomena are not always directly convertible into images of the human body as direct biomarkers; (4) the difficult sonographic differentiation between consolidation and atelectasis due to the conflicting opinions of the different

authors up to that moment (2014). In this regard, Lichtenstein et al. (2009), hypothesized that in infectious lung disease LUS shows an alveolar consolidation with air bronchograms with a specificity of 94% and a sensitivity of 61% for the diagnosis of pneumonia (Lichtenstein et al., 2009; Tomà and Owens, 2013). On the other hand, Riccabona (2008), stated that ultrasound cannot reliably differentiate between atelectasis caused by pneumonia and other causes and that caution is needed about the significance of small areas of subpleural lung consolidation and pleural line abnormalities (Kim et al., 2000; Riccabona, 2008; Caiulo et al., 2013). (5) The comparison of LUS was with CXR in the studies performed. Instead, the gold standard for the respiratory disease should be lung CT, which cannot be used habitually for ethical reasons of radiation exposure (Supakul and Karmazyn, 2013; Tomà and Owens, 2013; Trinavarat and Riccabona, 2014); (6) the fundamental dependence on the patient's clinical information before performing LUS and the usefulness of having the most recent CXR because, according to the authors (Supakul and Karmazyn, 2013; Tomà and Owens, 2013; Trinavarat and Riccabona, 2014), it would allow to guide the study in the area of interest. In addition, other studies (Tomà, 2013a,b; Tomà and Owens, 2013; Trovato et al., 2013a,b; Trovato and Sperandeo, 2013) on a larger population did not confirm the usefulness of using B-lines/vertical artifacts in the differential diagnosis of dyspnea due to poor specificity. These studies did not also find sufficient evidence for the use of LUS as a substitute for CXR in diagnosing pneumonia.

Nevertheless, the same authors of these reviews conducted up to 2014 (Supakul and Karmazyn, 2013; Tomà and Owens, 2013; Trinavarat and Riccabona, 2014), following the ALARA principle, also stated that LUS should be promoted in pediatric respiratory disease as a valuable imaging tool while respecting of its restrictions and limitations that could be overcome by adding diagnostic tool. The author's further state that it is not important to stick to the old concept of technique choice substitution. Surely the best results are obtained by choosing case by case and by integrating the different tools.

All things considered, such reviews (Supakul and Karmazyn, 2013; Tomà and Owens, 2013; Trinavarat and Riccabona, 2014) have limitations: few articles have been analyzed on pediatric lung disease (Caiulo et al., 2013) and some of them also have a low number of cases. Most of the reported studies were performed on adults in an emergency setting. The objective evaluation of experimental data of studies on the pediatric population and those increasingly produced worldwide has been neglected (Shah et al., 2013).

Since 2015: Lung Ultrasound and the Reassessment of Its Use

For many years the new LUS applications remained strictly within the confines of adult critical care units. Over the years, several authors (Kim et al., 2000; Copetti et al., 2008; Mong et al., 2012; Reissig et al., 2012; Caiulo et al., 2013) proposed translating this acquired experience in adults for LUS application in children. This trend has prompted a re-evaluation of the classic ultrasound patterns, contemporarily introducing a new sonographic semiotic.

In this regard, over the years, evolving technology and greater understanding of the artifacts of LUS allowed for its greater applicability of the pediatric chest (Kim et al., 2000; Copetti et al., 2008; Mong et al., 2012; Reissig et al., 2012; Caiulo et al., 2013).

The new clinical and preclinical phase studies (Volpicelli et al., 2012; Soldati et al., 2015; Martelius et al., 2016; Sferrazza Papa et al., 2017; Buonsenso et al., 2020) describe the B-lines as vertical hyperechoic reverberations that move in synchrony with the lung and then as key artifacts in the interpretation of the lung ultrasound findings. According to this new point of view, the physiological basis of B lines is represented by a decreased lung aeration and they generally indicate an ultrasound non-specific finding (Volpicelli et al., 2012; Soldati et al., 2015; Sferrazza Papa et al., 2017). However, its quantitative characterization and according to the most recent studies also qualitative can be indicative of an ultrasound pattern more specific.

Multiple B-lines are seen in congestive heart disease, interstitial lung disease, respiratory infections, and neonates. B-lines could also be observed in a limited number of healthy individuals (Volpicelli et al., 2012; Soldati et al., 2015; Sferrazza Papa et al., 2017; Buonsenso et al., 2020).

In this field, Martelius et al. (2016) performed the first study on the pediatric population. They prospectively evaluated 60 patients (0 to 18 years) who underwent chest CT for different clinical reasons and compared the extent of parenchymal changes observed with the number of B-lines on sonography. No pathological findings were detected on CT in 30 cases; in the others, parenchymal changes were seen in the anterolateral regions. The number of B-lines on LUS was found to consistently increase with the growing extent of parenchymal changes on CT. Parenchymal changes on CT associated with a significantly increased B- line count often included ground-glass opacities, interlobular septal thickening, parenchymal bands, and atelectasis. The results of this study suggested that B-lines were considered to be highly non-specific in children and not useful to differentiate pathologic processes of the lung parenchyma. However, the authors proposed LUS as a screening and follow-up tool for estimating the extent of parenchymal changes in children with respiratory symptoms, taking into account that few published data were available on LUS findings in healthy individuals.

Moreover, in a large population with multiple respiratory conditions, one could expect one-third of the lung ultrasound studies to show a B-line pattern in at least one thoracic area, with etiology varying between different age groups. Since this pattern could be attributed to a wide range of conditions, its interpretation cannot withstand analysis of the distribution, extension, and severity of the B-line pattern along with accurate clinical correlation (Sferrazza Papa et al., 2017).

In 2017, Yousef (2017) published a study in which the population was represented by pediatric patients of the cardiac intensive unit undergoing congenital heart surgery. Patients underwent both CXR and LUS in the post-operative time. On LUS, the number of B-lines increased proportionally with the increase in extravascular lung water (EVLW) and progressed

to white lungs which are the equivalent of the ground glass appearance on chest X-rays and CT. The results of this study are highly interesting. The authors reported a significant positive correlation between early B-line scores, obtained during the first hours after surgery, and short-term clinical outcomes. The author concluded that in consideration of the inability to see non-superficial lesions, LUS can be used as a complement to the CXR in order to improve patient care (who is at risk to develop or who has already developed cardiogenic pulmonary edema) and reduce accumulated radiation doses.

In the following years, Soldati and other authors (Soldati et al., 2016, 2019; Soldati and Demi, 2017) through studies on physical models clarified the concept of the sonographic interstitial syndrome (SIS). It is a characteristic ultrasound picture of the hyperdense and unconsolidated superficial lung characterized by the presence of multiple vertical, patched, or diffuse artifacts (B lines) that fan out from the lung wall interface (see dedicated paragraph "Imagine Findings").

In the presence of edema, ARDS, interstitial lung disease, non-consolidating pneumonia, and contusions, part of the lung volume originally occupied by air can be replaced with water, connective tissue, cells, hyaline membrane, or edematous tissue, eventually creating acoustic traps for the US beam containing a medium that is physically (in terms of acoustic impedance) very different from the surrounding environment (air). Vertical artifacts or B-lines are artifactual and not real images and in their variable aspect, indicate a loss of peripheral lung aeration (without tissue consolidation) due to interstitial disease or simply to lung deflation without histological alterations.

The transition from vertical artifacts to consolidation is a continuum with something similar to the transition between the ground glass and consolidation in chest CT, where ground glass is due to thickening of the interstitium and/or the presence of fluid and/or the presence of collapsed areas and/or increased circulation. In a sense, the vertical artifacts have some correspondence with ground glass, even if they are already present in sufficient conditions to create acoustic channels that anatomically do not reach the entity of the ground glass.

Soldati et al. (2016, 2019); Soldati and Demi (2017) through studies on physical models explain how B-lines or vertical artifacts cannot easily differentiate the causes in the absence of an analysis of their appearance. The same authors demonstrated on physical models that the B lines are heterogeneous entities in terms of aggregation and visual structure, the nature of which is linked to the superficial histological characteristics of their wavelength.

Vertical artifacts generated by a fibrotic or inflammatory lung have a different appearance from those generated by cardiogenic edema (see dedicated paragraph "Imagine Findings").

In the context of the re-evaluation of LUS applications in pediatric clinical practice, different studies, that compared the use of LUS vs. CXR and vs. pulmonary auscultation in the evaluation of pulmonary consolidations and other injuries, had new goals which were as follows: (1) to understand if LUS could be a diagnostic tool not only supporting diagnostic chest X-ray; (2) to reassess the implementation of the LUS as point-of-care ultrasound (PoCUS).

Some authors (Berant et al., 2015; Chen et al., 2015; Zhang, 2015; Coca Pérez et al., 2016; Cox et al., 2017) have re-evaluated the implementation of the LUS as PoCUS intended as bedside ultrasound examination of the patient by the physician in charge mainly in the Pediatric Intensive Units (PIU) and in the Pediatric Emergency Departments (PED).

In this study, LUS was compared to CXR in the diagnosis of pulmonary diseases. The authors evaluated the following: (1) the characterization of non-specific areas of the white lung on chest x-ray; (2) the detection of small subpleural consolidations not detected on chest x-ray; (3) the diagnosis and monitoring of acute pulmonary edema in patients with acute heart disease; (4) the early diagnosis and post-treatment follow-up of respiratory complications in children with acute respiratory disease such as atelectasis and secondary pneumothorax; (5) the guiding to the complex alveolar recruitment maneuver in small patients with acute respiratory distress and areas of atelectasis; (6) the diagnosis and characterization of the pleural effusion when less than 10 ml. Several authors (Berant et al., 2015; Chen et al., 2015; Zhang, 2015; Coca Pérez et al., 2016; Cox et al., 2017) stated that there are limitations to CXR such as poor image quality, presence of artifacts, the time required to obtain the image and exposure to ionizing radiation. It was also shown (Berant et al., 2015; Chen et al., 2015; Zhang, 2015; Coca Pérez et al., 2016; Cox et al., 2017) that CXR is insensitive for detecting small volumes of pleural fluid less than 200 ml and is not able to define the nature of the pleural fluid. Some studies (Chen et al., 2015; Cox et al., 2017) confirmed a sensitivity and a specificity of POCUS for the diagnosis and follow-up of the most common pediatric and neonatal lung diseases higher than that of CXR.

There are also limitations to CT, the gold standard for the diagnosis of respiratory pathology, including its high cost, reduced availability, high radiation exposure, and difficulty in transporting the patient out of the hospitalization unit (Chen et al., 2015; Cox et al., 2017). So, the authors (Chen et al., 2015; Cox et al., 2017) proposed LUS as a convenient, non-invasive, safe, and radiation-free tool that can be quickly performed at the patient's bed without the need to move, to help in the differentiation of lung diseases and to become a reference instrument for the monitoring of respiratory dynamics and the follow-up of respiratory diseases (Chen et al., 2015; Cox et al., 2017). According to them (Chen et al., 2015; Cox et al., 2017), the clinical information collected at the bedside is essential to guide care quickly and correctly and decrease uncertainty so giving the LUS a fundamental role in the diagnostic and therapeutic process of respiratory diseases.

In a prospective study, Lovrenski et al. (2016) compared LUS with auscultation findings. In children with clinical suspicion of pneumonia, LUS showed positive findings of lung consolidations to a greater extent than auscultation which, on the contrary, was to a greater extent associated with negative findings. According to the authors, moreover, a craniocaudal size of subpleural consolidation of less than 30 mm significantly reduced the possibility of auscultator detection (in approximately 95% of auscultator examinations). In addition, the use of an additional trans-abdominal US approach, along with the standard trans-thoracic approach, could be expected to result in a further

increase in US sensitivity for the diagnosis of pneumonia, which was already high (the sign referred to as "dynamic air bronchogram" had a reported positive predictive value of 97% for the diagnosis of pneumonia) (Lovrenski et al., 2016).

Some authors (Copetti, 2016; Lovrenski et al., 2016; Cox et al., 2017; Lovrenski, 2020) based on their review studies, stated that whenever lung US is consistent with clinical and laboratory findings and auscultation, chest radiographs might be avoided. Furthermore, when clinical findings are uncertain, but a classic LUS pneumonic pattern is evident (for example, lung parenchyma consolidation with branched air bronchogram), we should consider avoiding chest radiography, using lung US to monitor the effects of therapy.

In conclusion, studies performed over the last few years report that one of the most valuable aspects of LUS application is its utility in the follow-up of pneumonia helping clinicians to make proper therapeutic adjustments if needed without exposure to radiation. It enables detection of early stages of necrotizing pneumonia by revealing minor areas of necrosis, which often cannot be seen on CXR.

Moreover, it allows a significant reduction in the number of chest CT and CXR in children with necrotizing pneumonia, both early and extensive ones, and sometimes allows even avoidance of chest CT, especially when the clinical course of the disease shows a regression of symptoms and improvement of laboratory findings. Of course, CT should be employed in complicated cases and when the clinical course of the disease is not improving.

Although most studies report that trans-thoracic examination is sufficient, the trans-abdominal (trans-hepatic and trans-splenic) approach can increase the sensitivity of lung US in detecting pneumonia by recognizing patterns other than normal mirror-image phenomenon, which represent a supradiaphragmatic projection of the liver and spleen. (Copetti, 2016; Lovrenski et al., 2016; Cox et al., 2017; Joshi et al., 2019; Lovrenski, 2020).

Since 2018, several authors have begun to conduct studies in specific settings - not only in pediatric and neonatal ICUs - with the aim of defining specific ultrasound patterns for each disease with the possibility of creating ultrasound scores for the various pediatric lung diseases. In this way, LUS could be used as a non-invasive clinical marker to evaluate the evolution of a particular acute or chronic lung disease and the response to therapy (see the section "The main fields of application of LUS in pediatrics").

TECHNIQUE AND METHOD OF SCANNING

As for the scanning technique and method, there was substantial homogeneity among the different studies that were included in this review.

Lung Ultrasound Scanning Mode

The ribs in neonates and small infants have low mineral content, thus allowing trans osseous scanning, especially in the parasternal region where the ribs are cartilaginous (Shah and Greenberg, 2017; Joshi et al., 2019). This can be done through the trans-sternal and trans-costal approaches.

Although most studies report trans-thoracic examination as sufficient, trans-abdominal (trans-hepatic and trans-splenic) approach can increase the sensitivity of LUS in detecting pneumonia or SIS areas (Copetti, 2016; Lovrenski et al., 2016; Cox et al., 2017; Joshi et al., 2019; Lovrenski, 2020). According to some authors (Joshi et al., 2019), evaluation of the diaphragm, the subdiaphragmatic space as well as the liver and spleen should form part of the protocol as lung consolidation and empyema may be secondary to a liver abscess.

Probes and Transducers

The type and frequency of transducer used would vary with the age of the patient and the location of the lesion.

Linear transducers with high frequency with a small footprint are preferred to perform sagittal and intercostal scans in neonates and infants. In addition, the linear probe is the best choice for studying the dynamics of breath-dependent motion as well as pleural line abnormalities.

Lower-frequency transducers are used for older children and overweight or obese adolescents (Lovrenski et al., 2016). Curved array transducers are used to insonate between ribs, below the diaphragm, or from the suprasternal notch (Joshi et al., 2019; Strzelczuk-Judka et al., 2019).

In particular, all the studies used a high-resolution linear probe 10 MHz or more. However, the use of both high-frequency linear probes and lower or intermediate frequency linear probes (Zhang, 2015; Lovrenski et al., 2016; Martelius et al., 2016; Song et al., 2017; Strzelczuk-Judka et al., 2019; Tripathi et al., 2019) and low-frequency convex probes have been used in the same studies (Lovrenski et al., 2016; Strzelczuk-Judka et al., 2019; Tripathi et al., 2019).

Two studies (Ho et al., 2015; Yadav et al., 2017) only used the convex probe which, however, did not bring about changes in the execution of the ultrasound investigation and the evaluation of the images.

Scanning Protocol and Examination Position

Most of the LUS studies in the pediatric population have been performed in critically ill patients with or without respiratory distress in the pediatric emergency departments or pediatric/neonatal intensive care units (Cattarossi, 2014; Zhang, 2015; Song et al., 2017, 2018; Yousef, 2017; Tripathi et al., 2019). Therefore, patients were scanned in the supine position. Only if conditions allowed, they were scanned in sitting or reclining position.

In the case of stable patients, each hemithorax is divided into six regions using two longitudinal lines (anterior and posterior axillary line) and two axial lines (one above the diaphragm and the other 1 cm above the nipples). The lung areas are the anterior (between the sternum and the anterior axillary line), the lateral (between the anterior and posterior axillary lines), and the posterior (between the posterior axillary line and

the spine) (Lovrenski et al., 2016; Martelius et al., 2016; Weerdenburg et al., 2016; Yousef, 2017; Strzelczuk-Judka et al., 2019; Lovrenski, 2020).

For a comprehensive examination, the 12 lung areas are sequentially scanned from right to left, cranial to caudal until the diaphragm is revealed, and anterior to posterior.

IMAGING FINDINGS

There has been a complete consensus among all the studies with respect to the imaging criteria required for diagnosing the various respiratory conditions. Most of the studies clarify that US findings are considered physiological and pathological and describe the LUS pathological findings mainly translating the experience gained from the adult population into pediatric clinical practice.

Normal Pattern of the Lung (Figure 1 and Electronic Supplementary Video 1)

The LUS findings of a normal lung (Copetti et al., 2008; Lichtenstein and Mauriat, 2012; Volpicelli et al., 2012; Lichtenstein, 2014; Chen et al., 2015; Saraogi, 2015; Shah and Greenberg, 2017; Joshi et al., 2019) are represented by:

- **The pleural line** represents the normal lung surface (an intense interface due to high variation of impedance from the chest wall to lung parenchyma) and results in a single smooth regular hyperechogenic line with a thickness of lesser than.5 mm below the rib line, formed by sound waves reflected from the parietal and visceral pleura. A normal pleural line is characterized by the presence of sliding: a "to and fro" movement of lung surface synchronized with respiration (Copetti et al., 2008; Volpicelli et al., 2012; Chen et al., 2015; Shah and Greenberg, 2017; Joshi et al., 2019).

In pathological conditions, the pleural line can be absent or present with a thickness more than.5 mm or with a coarse and irregular appearance with or without evidence of small subpleural consolidation; just as pleural sliding can be absent or poorly represented (Copetti et al., 2008; Volpicelli et al., 2012; Chen et al., 2015; Shah and Greenberg, 2017; Joshi et al., 2019).

- **A-lines,** echogenic horizontal lines parallel and equidistant from each other, which indicate the presence of normally aerated lung. The lung and the soft tissues differ in their acoustic characteristics causing reflection of the ultrasound waves from the lung surface creating reverberation artifacts that are configured in these lines (Copetti et al., 2008; Lichtenstein and Mauriat, 2012; Lichtenstein, 2014; Chen et al., 2015; Joshi et al., 2019).

The search, identification, and evaluation of these US findings of normality are performed in B-mode (Copetti et al., 2008; Lichtenstein and Mauriat, 2012; Volpicelli et al., 2012; Lichtenstein, 2014; Chen et al., 2015; Saraogi, 2015; Shah and Greenberg, 2017; Joshi et al., 2019).

Pneumothorax (Figure 2 and Electronic Supplementary Video 2)

The accuracy of US as a first-line investigation for detection of pneumothorax (PTX) is almost comparable to the accuracy of CT and far exceeds the accuracy of plain radiographs (Coley, 2011; Volpicelli, 2011; Chen et al., 2015; Chen and Zhang, 2015; Zhang, 2015; Coca Pérez et al., 2016; Raimondi et al., 2016; Cox et al., 2017; Joshi et al., 2019).

According to the US signs of PTX, there is an agreement between the various studies taken into consideration. In particular, it is identified by:

- **Absence of lung sliding** (specificity and sensitivity of 91.1 and 95.3%, respectively**) and absence B-lines**, both identified in B-mode, originating from the visceral pleura (negative predictive value of 99.2–100%).
- **Lung point**, (specificity and sensitivity of 100 and 79%, respectively), identified in B-mode, the point at which normal sliding disappears because of the presence of air in the pleural cavity (**Electronic Supplementary Video 2**).
- **Double lung point**, (Zhang, 2015), identified in B-mode, whose presence indicates limited pneumothorax so indicating conservative management. Between two lung points, there is no lung sliding or B-line, suggesting separation of visceral and parietal pleura. Laterally to the points, the pleural sliding and B-line signs are evident. Both lung points move simultaneously with respiration.
- **The barcode sign**, identified and studied in M-mode, occurs as there is no motion of the chest wall and no motion of the lung due to the presence of air in the pleural cavity. This is seen as multiple parallel horizontal lines resembling a bar code. It is represented by the transition from the normal lung (linear granular pattern) to the pneumothorax (linear pattern) (**Figure 2**).

Pleural Effusion (Figures 3, 4A)

The role of LUS in confirming the presence of pleural effusion is well established (Coley, 2011; Prithviraj and Suresh, 2014; Berant et al., 2015; Cox et al., 2017; Joshi et al., 2019; Toma et al., 2019).

Lung ultrasound (LUS) is a useful and safe tool for evaluating pleural effusion because it allows the distinction between effusion and lung consolidations and has greater accuracy in detecting pleural effusion than bedside CXR. CXR can detect the presence of pleural effusion in patients in an orthostatic position only if the volume of the effusion is at least 200 mL and the sensitivity of this method decreases in the supine position, while LUS can detect effusions as small as 10-20 mL (Coley, 2011; Prithviraj and Suresh, 2014; Berant et al., 2015; Cox et al., 2017; Joshi et al., 2019; Toma et al., 2019).

Lung ultrasound (LUS) evaluation of a patient in a sitting or standing position is better because it allows for more precise quantification of pleural effusion and the visualization of small amounts of fluid in the pleural cavity. In this position, the free fluid will collect in decline space while it will be found in a posterior location with the patient supine.

In addition, ultrasound allows the identification of adjacent structures: chest wall, hemidiaphragm (over the liver or spleen),

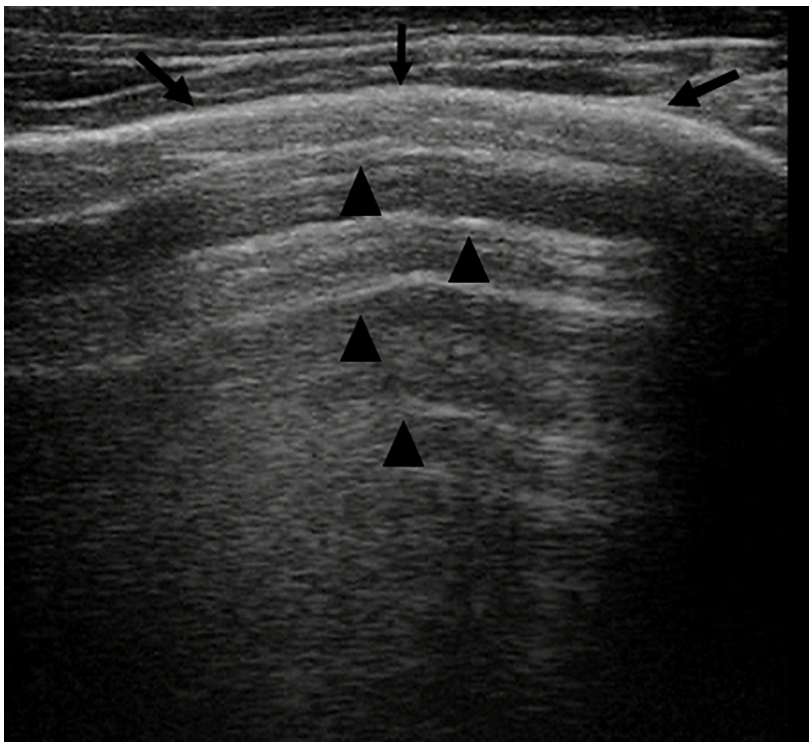

FIGURE 1 | Grayscale lung ultrasound examination (transverse scan between intercostal fields; linear probe with 12 MHz frequency) shows a normal lung ultrasound pattern: hyperechoic, regular, and smooth pleural line with a thickness of less than 0.5 mm (*arrows*), pleural sliding present, and normally represented characterized by "to and fro" movement of lung surface synchronized with respiration (**Electronic Supplementary Video 1**). Below the pleural line, lung ultrasound imagines show A-lines (*arrowheads*): echogenic horizontal lines parallel and equidistant from each other which indicate the presence of normally aerated lung.

and visceral pleural surface. This is important, especially in the case of an invasive procedure, in order to avoid organ injury (Coley, 2011; Prithviraj and Suresh, 2014; Berant et al., 2015; Cox et al., 2017; Joshi et al., 2019; Toma et al., 2019).

Unlike CXR, US can provide information on the nature of the pleural fluid. It is superior to CT in characterizing the nature of pleural fluid collections and can help guide percutaneous drainage. However, in complicated and refractory cases CT may be a better option, especially if surgery is planned (Coley, 2011; Prithviraj and Suresh, 2014; Berant et al., 2015; Cox et al., 2017; Joshi et al., 2019; Toma et al., 2019).

Pleural effusions have a different echogenicity on US depending on the underlying causes (Coley, 2011; Prithviraj and Suresh, 2014; Berant et al., 2015; Cox et al., 2017; Joshi et al., 2019; Toma et al., 2019).

- **Transudative effusions** (**Figure 4A**) appear as a space (usually anechoic) between the parietal and visceral pleura that changes depending on the patient's position. The lung appears with varying degrees of compression and, depending on the amount of fluid, also moves with breathing ("sinusoid sign") or heartbeat ("pulse sign").
- **Exudative effusions** (**Figure 3**) show echoes that suggest the presence of debris (cell, blood fibrin). Fibrin can be observed in exudative effusions but the amount, distribution, and organization in septa or loculi differ from patient to patient, depending on the cause of the effusion and the time from the onset.

The additional presence of a thickened pleura or pulmonary consolidation with dynamic air bronchogram may suggest **the infectious nature of the pleural effusion** (Coley, 2011; Prithviraj and Suresh, 2014; Berant et al., 2015; Cox et al., 2017; Joshi et al., 2019; Toma et al., 2019).

The presence of a diffuse sign of lung congestion (B-lines or vertical artifacts) suggests **transudative effusion during heart failure** (Yousef, 2017) (**Figure 4**).

Although various US methods for quantifying the volume of pleural effusions have been described, all require several measurements. Many authors believe that knowing the exact amount of fluid is of limited usefulness in clinical practice.

A qualitative approach may be useful, summarized in the **Table 1** below (Prina et al., 2014). Additionally, LUS can help estimate the effect of pleural effusion on lung parenchyma by allowing visualization of different degrees of collapse (Prina et al., 2014).

Lung Consolidations (Figures 5–8)

When a lung area loses its normal aeration due to an inflammatory event or collapse of the airways, a consolidation is created in the lung parenchyma, and the displayed image is a real image and not an artifact (Coley, 2011; Chen et al., 2015;

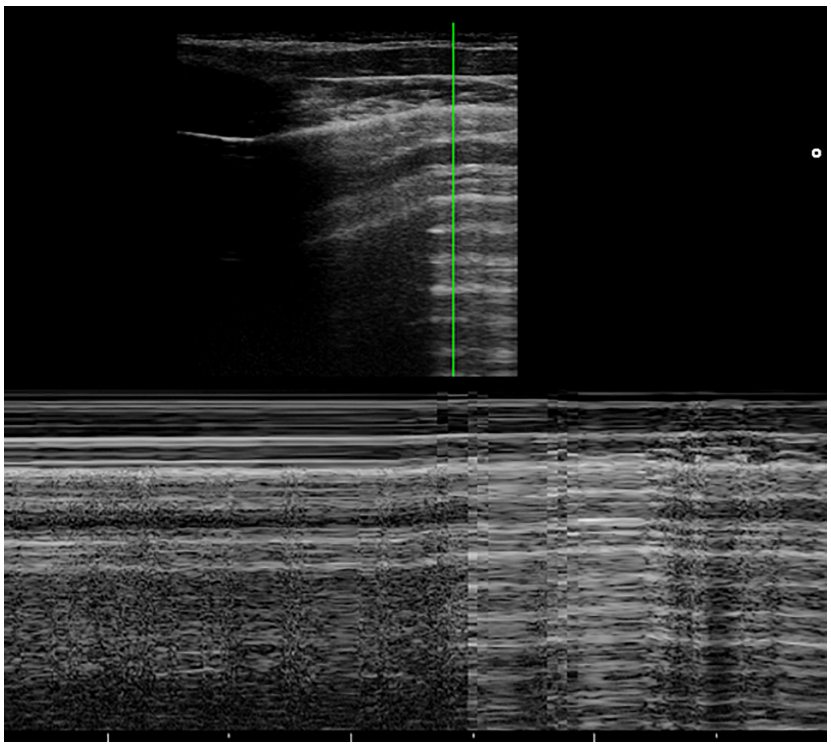

FIGURE 2 | The grayscale lung ultrasound examination (transverse scan between the intercostal fields; linear probe with a frequency of 12 MHz) of a 15-year-old boy with left apical pneumothorax shows the *Barcode sign* identified in M-mode as a transition from the normal lung (*linear granular pattern on the right of the figure*) to the pneumothorax (*linear pattern on the left of the figure*). The grayscale lung ultrasound examination (transverse scan between the intercostal fields; linear probe with a frequency of 12 MHz) of a 16-year-old boy with right apical pneumothorax, shows the *Lung Point sign* identified in B-mode as the point where normal sliding disappears due to the presence of air in the pleural cavity.

Coca Pérez et al., 2016; Lovrenski et al., 2016; Claes et al., 2017; Cox et al., 2017; Joshi et al., 2019; Lovrenski, 2020). In fact, within the consolidated area we can recognize:

- **Hepatization** (**Figure 5**), which is defined as that area of the lung without air that mimics the appearance of the liver. In consolidations, alveoli are replaced with fluid and inflammatory debris resulting in hepatization of the lung that is characterized in the US by a hypoechoic aspect and Doppler vessels (Chen et al., 2015; Cox et al., 2017; Joshi et al., 2019).
- **Dynamic air bronchograms** (**Figure 6**; **Electronic Supplementary Video 3**), the branching echogenic foci within a consolidation, represent the residual air within the bronchi and some of the alveoli. They are represented by hyperechoic images of air bubbles moving within the airways with a centrifugal respiratory progression in inspiration. The presence of dynamic air bronchogram is associated with pneumonia identification in approximately 70–97% of cases and with the exclusion of an atelectasic area and/or bronchial obstruction (Lichtenstein et al., 2009; Chen et al., 2015; Cox et al., 2017; Joshi et al., 2019; Lovrenski, 2020).
- **Fluid or mucus bronchograms** (**Figure 5**), identified by ultrasound in B-Mode and by Color-Doppler, are represented by echo-free tubular structures without any perfusion signal. The air in the bronchi is replaced by fluid. Their presence is associated with the identification of pneumonia (Chen et al., 2015; Joshi et al., 2019; Lovrenski, 2020).
- **Normal branching pattern of vessels within the consolidated lung**, identified by ultrasound in B-Mode and by Color-Doppler, is useful for differentiating a lung consolidation air from a mass (Chen et al., 2015; Joshi et al., 2019).
- **Linear, parallel, and static bronchograms** (**Figure 7**) are hyperechoic images of air bubbles that do not move inward during breathing and are parallel to each other. Their presence is usually associated with the identification of atelectasis. In fact, in atelectasis, the lung appears hypoechoic, triangular in shape with crowding of the bronchi due to loss of lung volume. Only a few of these can have air within them (Chen et al., 2015; Coca Pérez et al., 2016; Joshi et al., 2019; Lovrenski, 2020).
- **Extremely small subpleural consolidations** (**Figure 8**) with sizes of less than 5–0.1 mm with or without adjacent single or confluent B-lines, whose presence is associated with abnormal ventilated areas or Viral pneumonia or Bronchiolitis (Lovrenski et al., 2016; Lovrenski, 2020).

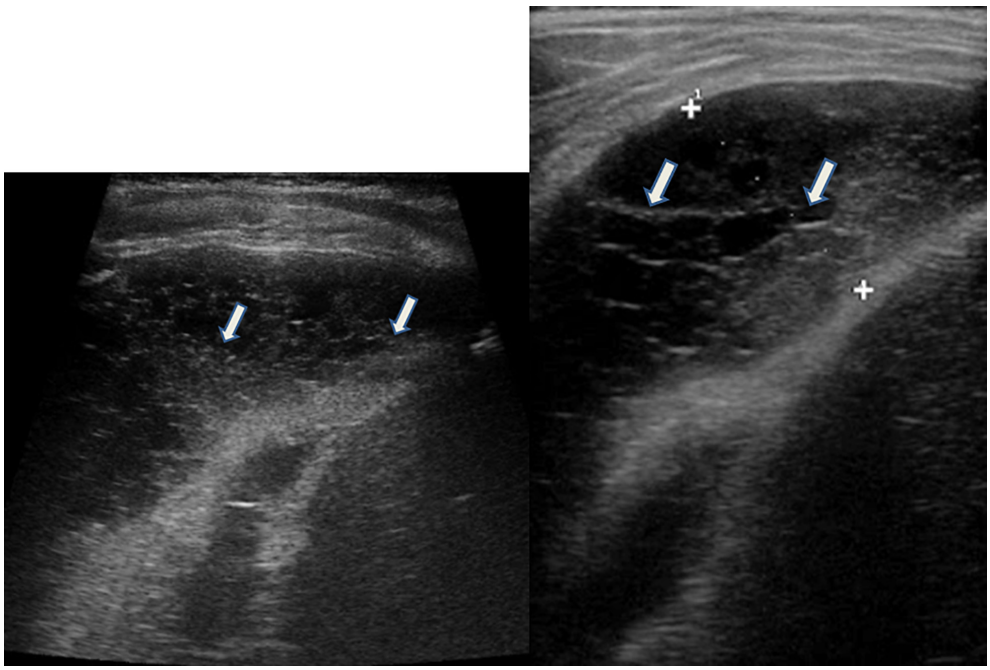

FIGURE 3 | Grayscale lung ultrasound examination (transverse scan between intercostal fields; linear probe with 12 MHz frequency) of a 5-year-old child with pneumococcal pleuropneumonia (complicated by pleural empyema), shows exudative pleural effusion, with internal echoes non-homogeneously distributed: it is fibrinous, plural-septate, and concamerated and with thickened septa (*arrows*).

- **Areas of breakdown/small areas of lung necrosis and lung abscess.** The small areas of lung necrosis appear as areas of decreased echogenicity with no color Doppler flow within a region of pulmonary consolidation. Larger abscesses can develop a thick wall and air-fluid levels may be seen if there is cavitation or if the abscess communicates with the bronchial tree. They are commonly seen in staphylococcal cases of pneumonia, where pneumatoceles can also occur, as well as in acute necrotizing cases of pneumonia (Coley, 2011; Claes et al., 2017; Joshi et al., 2019).

Sonographic Intesitial Syndrome (Figures 4, 9)

Coley, 2011; Cattarossi, 2014; Chen et al., 2015; Coca Pérez et al., 2016; Martelius et al., 2016; Sferrazza Papa et al., 2017; Yousef, 2017; Joshi et al., 2019; Soldati et al., 2019; Buonsenso et al., 2020.

Vertical artifacts of B-lines are seen as vertically oriented artifacts and indicate an abnormality in the interstitial or alveolar compartment. They extend from the pleural line to the edge of the screen.

B-lines or vertical artifacts, in their variable appearances, indicate a loss of peripheral lung aeration (without tissue consolidation, therefore indicating an artifactual image) due to interstitial disease or simply to lung deflation without histologic changes. However, B-lines could not be sufficient to differentiate the causes without an analysis of their appearance.

The fetal lung has a high fluid content hence B-lines can be seen even on the first day of life in neonates without respiratory distress and they usually disappear by the third day. Furthermore, B-lines can also be seen in healthy individuals especially in newborns and/or infants (Buonsenso et al., 2020). B lines are also seen to a greater extent in pulmonary edema, interstitial lung disease, infections, lung contusion, and atelectasis.

Recent studies (Soldati et al., 2019; Buonsenso et al., 2020) have shown that the vertical artifacts have a different appearance depending on the underlying cause: for example, those generated from a fibrotic lung have a different appearance from those generated by cardiogenic edema. Several authors (Soldati et al., 2019) are currently trying to understand and interpret the causes of these differences by performing preclinical studies (e.g., vertical artifacts can be thicker, brighter, and longer than others, each bearing different acoustic information).

In recent years, Soldati et al. (2019) generated a different point of view, demonstrating on physical models that B-lines are heterogeneous entities in terms of aggregation and visual structure, the nature of which is linked to the superficial histologic characteristics of the lung.

Therefore, rather than simply developing algorithms to count artifacts, it could be much more useful to develop new software that, with the help of artificial intelligence, is able to extract quantitative and qualitative information from the vertical artifacts.

- **Cardiogenic origin** (**Figure 4**) can be characterized by: typical B-lines or vertical artifacts (laser-like, bright) with the septal disposition (early stage); modulated B-lines (early stage); regular pleural line; the presence of pleural

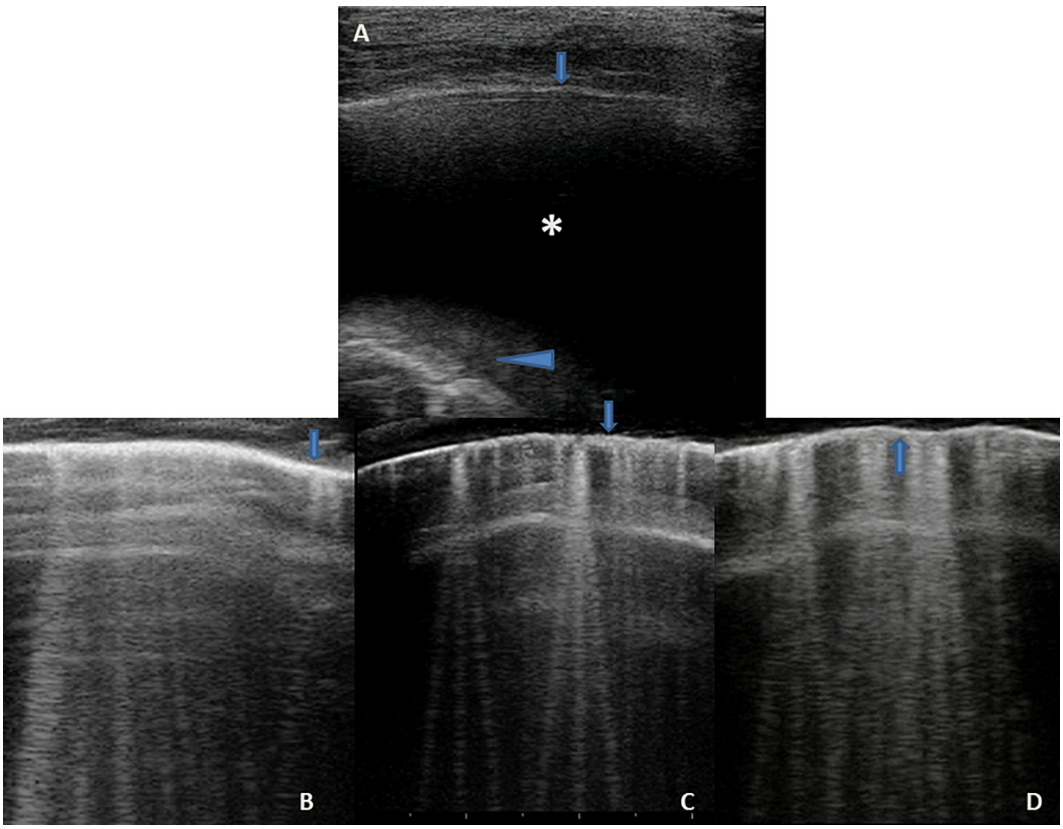

FIGURE 4 | Grayscale lung ultrasound examination (transverse scan between intercostal fields; linear probe with 12 MHz frequency) of a 10-year-old child with congestive heart disease resulting from untreated rheumatic carditis, shows in Panel **(A)**, on the basal posterior-lateral fields on the right, an anechoic pleural effusion (*asterisk*) that appears like an anechoic space between the parietal (*arrow*) and visceral pleura (*arrowhead*) below which lung appears atelectasis. Panels **(B,C)** show the SIS pattern of the upper right and left fields, respectively; Panel **(D)** shows that of the right lower/basal fields: the pleural line is regular (*arrows*); vertical artifacts or B-lines are separated, laser-like artifacts, with gravitational course spreading from the pleural line to the bottom of the screen and they show an internal sequence of alternating horizontal bands and homogeneous distribution in the affected spaces. Ultrasound picture compatible with the septal pattern of early CPE (Soldati and Demi, 2017; Soldati et al., 2019). CPE, cardiogenic pulmonary edema; SIS, sonographic interstitial syndrome.

sliding; diffuse pulmonary involvement without spared areas (bilaterally); absence of consolidations, pleural nodules or pleural irregularities. Furthermore, they are all characteristics that can take on a dynamic aspect depending on the patient's position, the effects of the exercise and therapy (Coca Pérez et al., 2016; Martelius et al., 2016; Sferrazza Papa et al., 2017; Yousef, 2017; Joshi et al., 2019; Soldati et al., 2019; Buonsenso et al., 2020).

- **Pneumogenic origin** (**Figure 9**) can be characterized by: unusual septal disposition of B-lines; blurred, uneven, coalescent B-lines and white lung; non-modulated B-lines or pseudo-B-lines; irregular pleural line; reduced pleural sliding; monofocal or multifocal, patchy or inhomogeneous involvement; consolidations, subpleural nodules or micronodules (generating pseudo-B-lines). Furthermore, the US features do not have dynamic aspects and do not change with the patient's position, therapy, or movements (Soldati et al., 2019; Buonsenso et al., 2020).

In the context of neonatal pathology, however, the differential diagnosis of the interstitial syndrome commonly falls between the respiratory distress syndrome (RDS) and Transient Tachypnea of Newborn (Joshi et al., 2019) (see specific section on the neonatal disease).

THE MAIN FIELDS OF APPLICATION OF LUNG ULTRASOUND IN PEDIATRICS

Pneumothorax

The detection of PTX is a growing interest section within pediatric PoCUS even if most of what is reported is based

TABLE 1 | Lung ultrasound assessment of pleural fluid and its estimate of volume.

Quantification	Ultrasound visualization	Volume estimation mL
Minimal	Costophrenic angle	≤ 100
Small	Range, one probe	100–500
Moderate	Range, two probes	500–1.500
Large or Massime	Range, three or more probes	> 1500

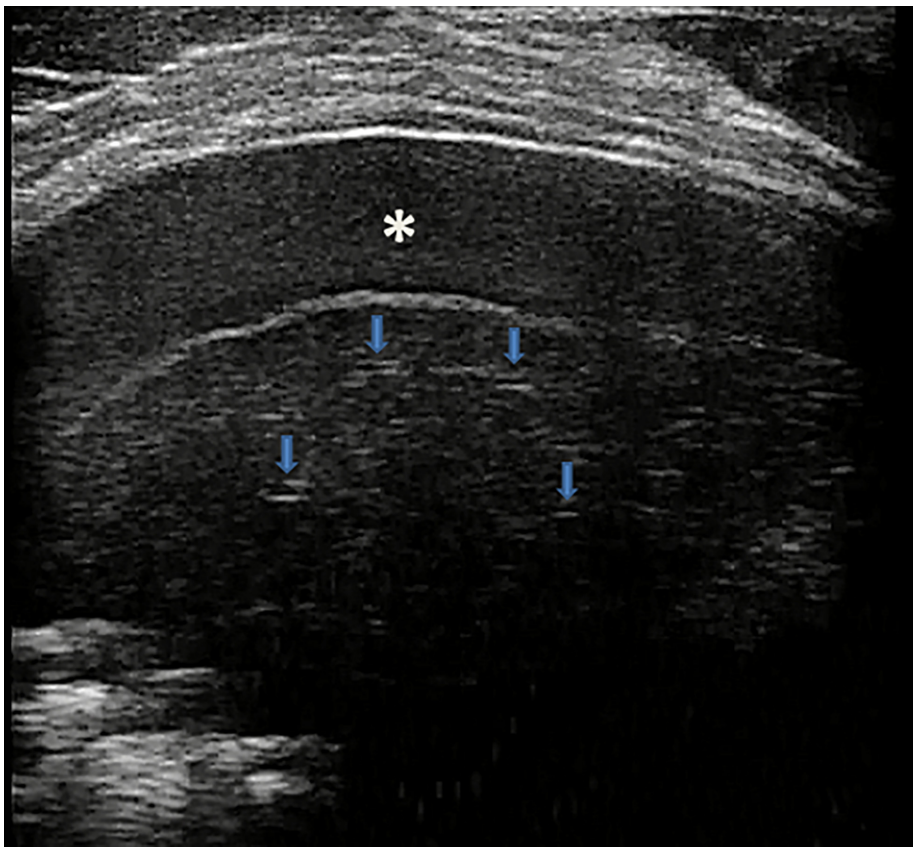

FIGURE 5 | Grayscale lung ultrasound examination (transverse scan between intercostal fields; linear probe with 12 MHz frequency) of a 7-year-old boy with bacterial lobar pneumonia, shows hepatized subpleural consolidation with fluid bronchograms (*arrows*) and fibrinous inflammatory reactive pleural effusion (*asterisk*).

on descriptive cases of retrospective works. Pneumothorax is defined as the pathological presence of air between the parietal and visceral pleura resulting in collapsing of the lung. In its extreme degree, tension PTX is a life-threatening event leading to increased intrathoracic pressure, elevated central venous pressure, and decreased venous return with consequent reduced cardiac output, bradycardia, and ultimately cardiac arrest. Symptoms of PTX may be extremely variable including chest pain, shortness of breath, cough, and increases in heart rate or breathing until respiratory failure. PTX is traditionally classified as spontaneous, traumatic, or iatrogenic and its diagnosis is based on a combination of clinical suspicion along with supporting imaging studies. Computed tomography remains the gold-standard imaging test in the evaluation of PTX, but it is limited by its high radiation exposure, especially in pediatric age, and the need of transporting critically ill patients. So, the most widely used method for bedside evaluation is CXR even if its diagnostic sensitivity is well known to be limited in the supine position with a small pneumothorax (Volpicelli, 2011). These are the reasons why POCUS is getting an ongoing interest in the diagnosis of PTX, although its application in pediatric age is once again deriving mainly from observations conducted on the adult population (Volpicelli, 2011; Volpicelli et al., 2012; Chen and Zhang, 2015; Liu et al., 2017).

Lung ultrasound (LUS) diagnostic accuracy for PTX has been confirmed and can even reach 100% in sensitivity, specificity, positive and negative predictive value (Volpicelli et al., 2012; Raimondi et al., 2016). The diagnosis of PTX by LUS is as reliable as conventional CXR in neonatal age and even more sensitive especially for small PTXs (Deng et al., 2020). Lung ultrasound can help with rapid and timely diagnosis and thus in bedside treatment (Deng et al., 2020) and PTX can even be earlier detected by applying LUS rather than by using only X-ray (Szymońska et al., 2019); furthermore, LUS application in the follow-up of diagnosed PTXs significantly reduces the CTXs performed (Szymońska et al., 2019) and limits the exposure to ionizing radiation (Szymońska et al., 2019; Deng et al., 2020).

There may be some limitation in the ability of LUS to assess the volume of PTX that would be required for choosing surgical vs. conservative treatment. Although there is not a close correlation between the extension on the chest wall and the volume of the intrapleural air, the localization of the lung point in the supine patient allows predicting the extension of PTX through a semi quantification of the volume: large and small PTX (Volpicelli, 2011).

Lung ultrasound (LUS) can therefore be definitely considered the novel approach for PTX evaluation, due to the advantages of timeliness and its high accuracy and reliability.

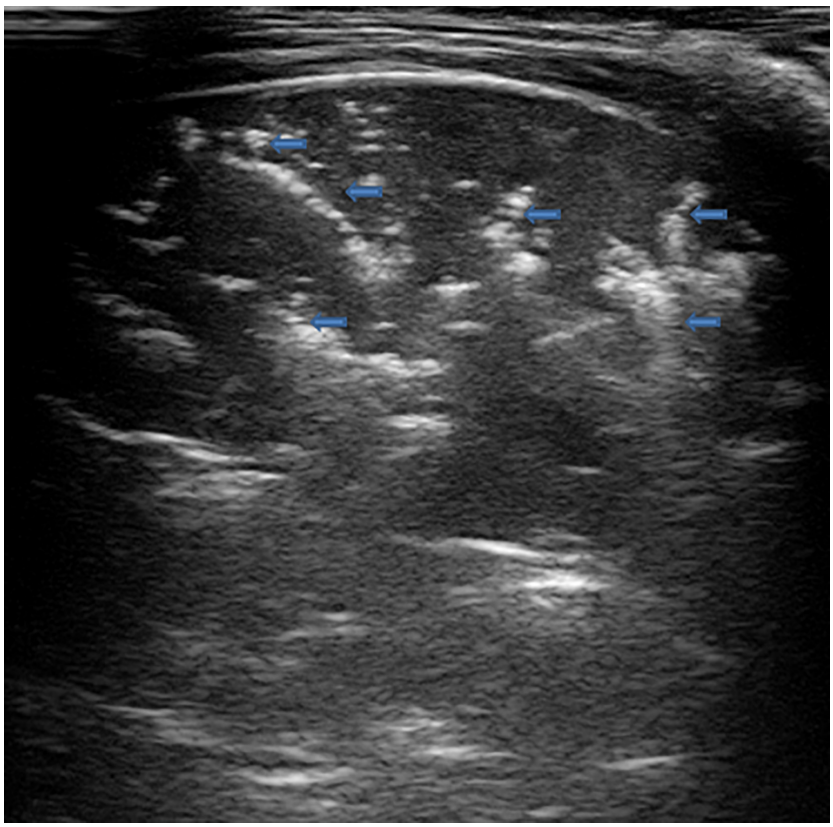

FIGURE 6 | Grayscale lung ultrasound examination (transverse scan between intercostal fields; linear probe with 12 MHz frequency) of a 5-year-old boy with bacterial pneumonia lobar, shows subpleural consolidation of an inflammatory/infectious nature with numerous elements of surface dynamic arborized bronchograms (*arrows*) – (**Electronic Supplementary Video 3**) and deep fluid bronchogram.

For the ultrasound diagnostic criteria of pneumothorax (Volpicelli, 2011; Volpicelli et al., 2012; Chen and Zhang, 2015; Liu et al., 2017) see the specific section in "Imaging findings."

Neonatal Respiratory Diseases

In the past years, neonatal respiratory diseases have been a diagnostic dilemma for the clinician due to the low sensitivity and specificity of their signs and symptoms and the CXR has not always been able to solve the diagnostic challenge since inter- and intra-observer variability has always been wide.

Lung ultrasound (LUS) may be useful in detecting congenital lung diseases such as pulmonary sequestration, congenital pulmonary airway malformation, and congenital diaphragmatic hernia. Although most of these congenital conditions are detected *in utero* and CT is needed for surgical road-mapping, it is not uncommon to find them accidentally during an abdominal US exam or when referral diagnosis points to another pulmonary condition, such as pneumonia (Lovrenski, 2018; Yousef et al., 2018).

In recent years, LUS is becoming a useful tool in neonatal intensive care units (Avery et al., 1966; Persson and Hanson, 1998; Lichtenstein et al., 2004; Bober and Swietliński, 2006; Copetti and Cattarossi, 2007; Copetti et al., 2008; El-Malah et al., 2015; Liu et al., 2015a; Kurepa et al., 2018; Raimondi et al., 2018; Corsini et al., 2019; Deng et al., 2020) with a variety of differential diagnoses including RDS, transient tachypnea of the newborn, meconium aspiration syndrome, neonatal pneumonia, pulmonary hemorrhage, pneumothorax and bronchopulmonary dysplasia (Lovrenski, 2020).

Some authors (Cattarossi et al., 2010; Cattarossi, 2014; Lovrenski, 2020) have supported the validity of LUS to follow the dynamics of interstitial lung fluid clearance in the postnatal hours, to accurately detect the presence of interstitial and/or alveolar fluid in RDS with ultrasound images that are in full concordance with the clinical course of RDS, but not with x-ray. Lung US showed a sensitivity of 95.6% and a specificity of 94.4%, with a positive predictive value of 91.6% and a negative predictive value of 97.1% for RDS, and a sensitivity of 93.3% and a specificity of 96.5% with a positive predictive value of 96.5% and a negative predictive value of 93.4% for transient tachypnea of the newborn in a more recent article (Liang et al., 2018).

Some authors (Cattarossi et al., 2010; Cattarossi, 2014; Liang et al., 2018) strongly suggest the use of LUS in neonatal age as a first-line imaging technique. The main potential of LUS in the neonatal intensive care unit lies in a dynamic follow-up of changes in the pulmonary condition of neonates; in these cases, LUS can help neonatologists in decision-making in this more vulnerable group of children. Nevertheless, the

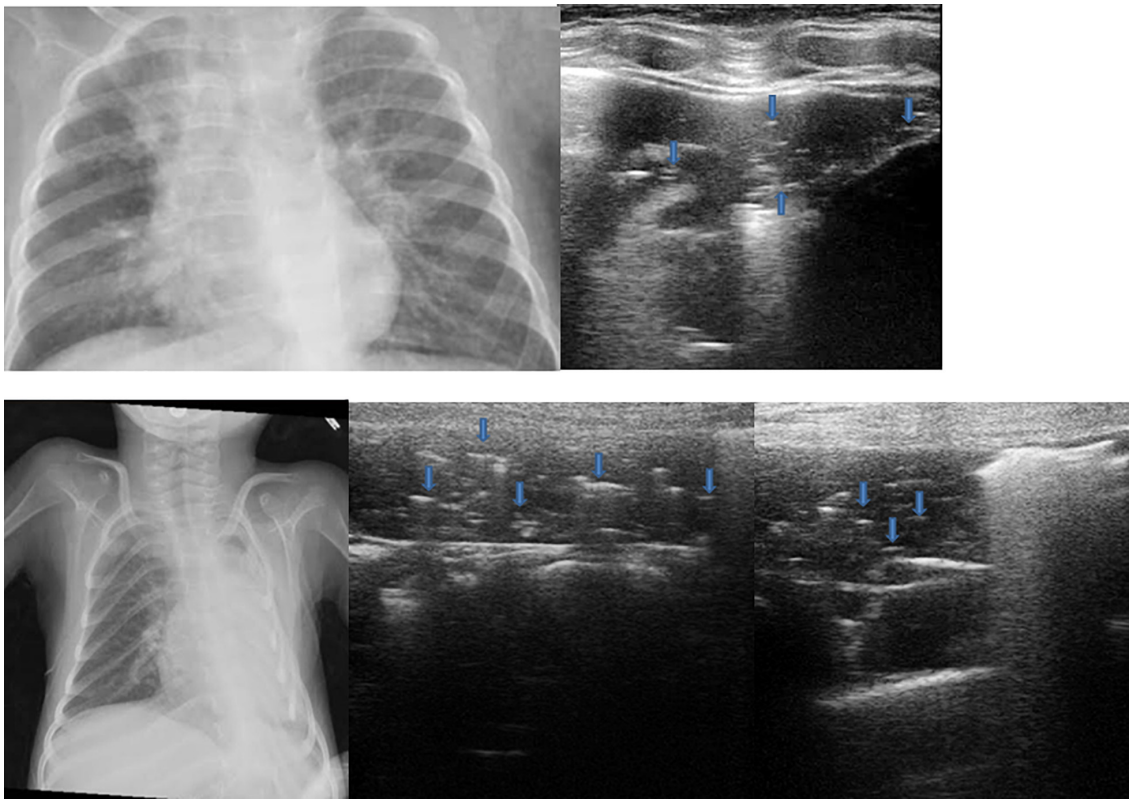

FIGURE 7 | The upper part of the figure shows chest X-ray and lung ultrasound images of a 7-year-old girl with uncontrolled asthma and an ongoing severe asthma attack, with no clinical or laboratory signs of infections. The chest X-ray shows non-specific areas of reduced transparency in the right apical and right basal sites. Grayscale lung ultrasound examination (transverse scan between intercostal fields; linear probe with 12 MHz frequency) shows – on the right paracardiac area – subpleural consolidation with hyperechoic images of air bubbles (static aerial bronchograms, *arrows*) that do not move inward during breathing and are parallel to each other. Their presence is associated with the identification of atelectasis, supported by the clinical and laboratory context of the patient being examined. The lower part of the figure shows chest X-ray and lung ultrasound images of a 4-year-old girl with neuromuscular pathology in nocturnal non-invasive ventilation with ongoing respiratory exacerbation without laboratory and clinical signs of infections. The chest X-ray shows a completely white left lung not well definable. Grayscale lung ultrasound examination (transverse scan between intercostal fields; linear probe with 12 MHz frequency) shows the entire left lung's subpleural consolidations with hyperechoic images of air bubbles (static aerial bronchograms, *arrows*) static and parallel to each other. Their presence is associated with the identification of left pulmonary atelectasis. The ultrasound suspicion is supported by the clinical and laboratory context of the patient being examined.

combination of diagnostic modalities in neonatal intensive care units is essential (Lovrenski, 2020). Chest X-rays are still needed to detect the exact position of lines and tubes, as well as air-leak syndromes (especially pneumomediastinum, pneumopericardium, and interstitial emphysema).

The most encountered applications of LUS in the context of neonatal pathology are RDS and transient tachypnea of the newborn (TTN):

Respiratory distress syndrome (RDS) is one of the most frequent pathological conditions of a newborn. It can occur at birth or in the first hours of life with tachypnea (respiratory rate over 70), dyspnea, gasping, hypotension, pallor, and tachycardia and it moves toward a usual resolution between the second and the fourth day of life. Its principal risk factors are prematurity, because of the lack of surfactant (which begins to be produced from the 24th gestational week), and gestational diabetes, because of fetus hyperinsulinism that interferes with glucocorticoids axes and with surfactant production. The condition is traditionally diagnosed by CXR that shows typical ground glass images.

By LUS, B lines associated with irregularity of the pleural line and subpleural consolidations can lead to the "white lung" condition frequently observed in neonates affected with RDS. A debate about the real concordance between CXR and LUS is ongoing in the literature (Bober and Swietliński, 2006; Copetti et al., 2008; El-Malah et al., 2015; Liu et al., 2015b; Blank et al., 2018; Corsini et al., 2019), although Corsini et al. (2019) described a concordance between LUS and X-Ray of 91%. They also made a comparison in terms of diagnosis time: almost 9 min for LUS vs. 50 min for CXR. Moreover, they proposed a theoretical training of 2 h for novice sonographers and a 30 min hands-on training. The sonographers performed LUS with a successive blinded evaluation by an expert sonographer and a perfect concordance between CXR and LUS was described after 25 performed exams.

Transient tachypnea of newborns (TTN) is a postnatal condition due to a delay in fetal fluid clearance. Principal risk factors are gestational diabetes and cesarean section, considering that in vaginal delivery there is lung compression which would remove excess fluid (Avery et al., 1966;

Persson and Hanson, 1998). Kurepa et al. (2018) described the presence of B-lines (not white lung), thickened pleural line, and presence of a typical sign: the double lung points which consists of a straight difference in upper (no B lines) and lower (presence of B lines), in neonates with TTN (Kurepa et al., 2018).

Differential diagnosis between RDS and TTN is not always easy on CXR, but it can allow physicians to differ clinical strategies: the administration of surfactant is performed in RDS while in TTN only ventilation is sufficient. Double lung point has a high sensitivity (although it is reported to vary from 76.6 to 100%) and specificity (100%) in TTN (Lichtenstein et al., 2004; Copetti and Cattarossi, 2007).

Differentiating RDS from TTN

	RDS	TTN
B Lines	Bilateral confluent B-lines No double lung point	Very compact B lines in the inferior pulmonary fields, not so compact in superior lung field - "Double Lung point"
Pleural Line	Thickened and irregular	Normal regular echogenic
Evolution of B Line	Persists, no change even after surfactant	Disappears by day two coinciding with clinical improvement
Lung Consolidation	Associated lung consolidation may be seen	No lung consolidation

RDS: Respiratory Distress Syndrome; TTN: Transient Tachypnea of Newborn (Joshi et al., 2019).

- *Pneumothorax (PTX)* can also be detected in newborns. Deng et al. (2020) described a cohort of 86 newborns diagnosed PTX by LUS and CXR. In neonates, LUS was more sensitive and more specific for early detection of PTX. Indeed, the absence of B lines, absence of sliding sign, and presence of lung point reached a sensitivity of 100, 100, and 94%, respectively (Deng et al., 2020).
- *Atelectasis* can also be studied by LUS; it is usually described in newborns under mechanical ventilation with no sufficient pressure (Kurepa et al., 2018).
- *Meconium aspiration syndrome* usually shows an LUS finding characterized by one or more consolidations with associated thickened pleura and air bronchograms non-uniformly distributed (Kurepa et al., 2018).

Pneumonia

Pneumonia remains the leading cause of death globally in children under the age of five.

The first study about the role of LUS in the diagnosis and management of pneumonia was conducted by Caiulo et al. (2013). It's a single-blind observational study performed on 102 children evaluated in a PED, with the aim of evaluating LUS findings both in the diagnosis and in the follow-up of pneumonia and comparing the sensitivity and specificity of LUS vs. CXR. The authors proved that LUS is a simple and reliable imaging tool, not inferior to CXR in identifying pleuropulmonary lesions in children with suspected pneumonia.

However, according to Tomà (2013a), the use of LUS as a diagnostic tool for infectious respiratory diseases in children would not have been safe if based on the criteria used in studies that involved adult patients. Don et al. (2013) also suggested that to understand the role of LUS in the diagnosis of pediatric pneumonia, further studies with larger, multicenter test samples would be needed, since, until 2014, only a few studies with small sample sizes have been published (Gargani et al., 2012; Shah et al., 2013).

The study of Reissig and Copetti (2014) reviewed the various studies performed up to then on the pediatric population and defined the US characteristics of pneumonia as a hypoechogenic area with: poorly defined borders, presence of B-lines at the far-field margin, less echogenic pleural line in the area affected by the lung consolidation and reduced or absent lung sliding. Furthermore, branching echogenic structures representing air bronchograms were described in the area of the infected zone in the context of consolidations.

Subsequently, several studies that focused on the pediatric population were published in the literature (Copetti and Cattarossi, 2008; Reissig et al., 2012; Chiappini et al., 2013; Audette and Parent, 2016; Milliner and Tsung, 2017; Pervaiz et al., 2018; Xin et al., 2018). The most used study model was the prospective one, but we also took into consideration the other studies whose scientific validity is lower (case report, letter to editor, commentary, meta-analysis, and reviews). In the present review, 27 studies (Gereige and Laufer, 2013; Shah et al., 2013; Esposito et al., 2014; Liu et al., 2014; Reali et al., 2014; Chavez et al., 2015; Iorio et al., 2015; Pereda et al., 2015; Urbankowska et al., 2015; Ambroggio et al., 2016; Claes et al., 2017; Guerra et al., 2016; Hajalioghli et al., 2016; Ianniello et al., 2016; Jones et al., 2016; Ključevšek, 2016; Boursiani et al., 2017; Ellington et al., 2017; Man et al., 2017; Milliner and Tsung, 2017; Yadav et al., 2017; Yilmaz et al., 2017; Biagi et al., 2018; Liang et al., 2018; Pervaiz et al., 2018; Xiao et al., 2018; Zhan et al., 2018; Lissaman et al., 2019; Najgrodzka et al., 2019; Tsou et al., 2019; Yan et al., 2020) evaluated LUS in terms of sensitivity and specificity regarding the diagnosis of pneumonia. The individual studies' sensitivity ranged from 87 to 100 (94%; IQR: 89–97%) and specificity ranged from 85 to 100% (with an average of 94%; IQR: 86–98%).

Among the 27 studies, 8 of these (Shah et al., 2013; Liu et al., 2014; Reali et al., 2014; Boursiani et al., 2017; Balk et al., 2018; Biagi et al., 2018; de Souza et al., 2019; Lissaman et al., 2019) compared sensitivity and specificity of LUS vs. CRX. CXR sensitivity ranged from 82 to 95, while CXR specificity ranged from 90 to 100. These studies suggest that LUS examination can detect lung consolidation and the other ultrasound features of pneumonia in children with the similar accuracy and reliability

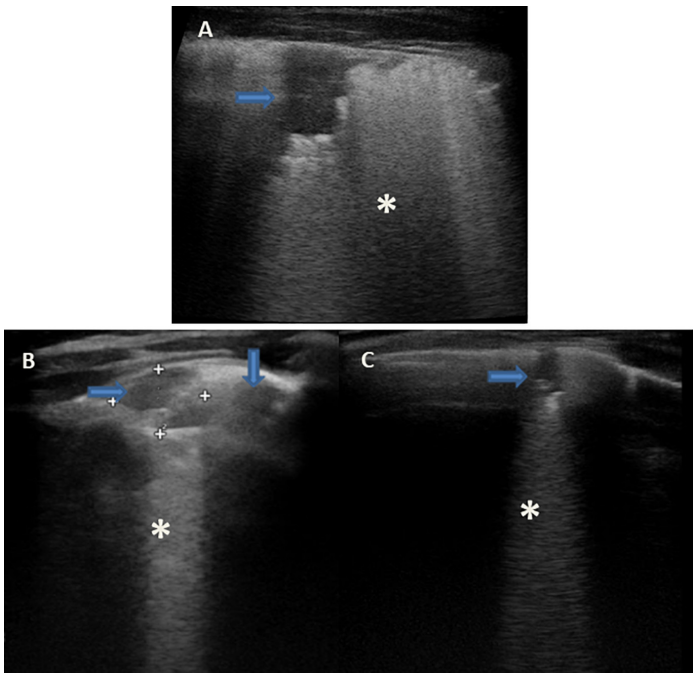

FIGURE 8 | Grayscale lung ultrasound examination (transverse scan between intercostal fields; linear probe with 12 MHz frequency) of children with viral lower respiratory tract infection [**(A)**: 2-year-old boy with H1N1 Influenza pneumonia; **(B,C)**: 8-month-old infant with Respiratory Syncytial Virus bronchiolitis]. Lung ultrasound findings show sonographic interstitial syndrome (SIS) with areas of the white lung with multiple, coalescent vertical artifacts (B-lines, asterisks) and small subpleural consolidations (hypoechoic areas, *arrows*) less than 1 centimeter in size associated with areas of "white lung" or confluent B-lines (*asterisks*).

as chest radiographs with the benefits of no exposure to ionizing radiation and savings in cost and time, both in diagnosis and in follow-up.

Furthermore, several studies have demonstrated the superiority of LUS in identifying even minimal pleural effusion that occurs with pneumonia (Shah et al., 2013; Reali et al., 2014; Balk et al., 2018; de Souza et al., 2019) with a sensitivity of LUS that is higher compared to CXR.

One variable that influenced the specificity is the size of the lesion. In fact, in the work of Shah et al. (2013) the specificity rises from 89 to 97% in children with consolidation greater than 1 cm. According to Biagi et al. (2018), the specificity reaches 98.4% when there are >1 cm consolidations. Another variable regarding sensitivity and specificity seems to be age. According to Liu et al. (2014), a large area of lung consolidation with irregular margins had 100% sensitivity and 100% specificity for the diagnosis of neonatal pneumonia.

Two studies deviate from the results of the previous ones. In one study, Lissaman et al. (2019) reported that LUS sensitivity was 91% (95% CI: 78 to 98%) and specificity was 68% (95% CI: 54 to 80%). However, in this regard, the sonographers were a first-year pediatric emergency medicine fellow and a final-year medical student, both without prior US experience but trained specifically for this study by an emergency physician with 5 years of POCUS experience and a Diploma in Diagnostic Ultrasound. In the other study (Biagi et al., 2018) the diagnosis of consolidations by LUS showed a high sensitivity of 93% but low specificity (14% for expert operators and 25% for novice operators). However, in this study, although CXR was used as the gold standard, LUS and CXR were not always performed consecutively and changes in the lung disease process may have occurred due to the time elapsed between the two imaging studies. Also, the sample size is very small, in which only 23 patients were recruited.

Although lung CT is considered the gold standard for the diagnosis of pneumonia, for reasonable ethical reasons no studies have subjected patients to lung CT except in case of clinical need. In most studies, LUS was therefore compared with CXR, the widely used diagnostic tool to diagnose pediatric Community-Acquired Pneumonia (pCAP).

On the other hand, the other authors, evaluated the diagnostic accuracy of *LUS in the diagnosis of pneumonia by comparing it with clinical diagnosis defined by WHO guidelines* (Chavez et al., 2015). They showed that the WHO algorithm did not agree with the results of POCUS in over a third of children and had an overall low performance compared to point-of-care ultrasound to identify lung consolidation. One of the future challenges of LUS may be precisely that of being able to improve cases of pneumonia management in limited-resource settings. To test this possibility, Lenahan et al. (2018), with their multicenter pilot study, proposed to pilot LUS in Mozambique and Pakistan and to generate evidence regarding the use of LUS as a diagnostic tool for childhood pneumonia.

In conclusion, the main purpose of all the studies was to evaluate whether LUS can be used as an alternative method to X-ray in the diagnosis of pneumonia. The consensus opinion

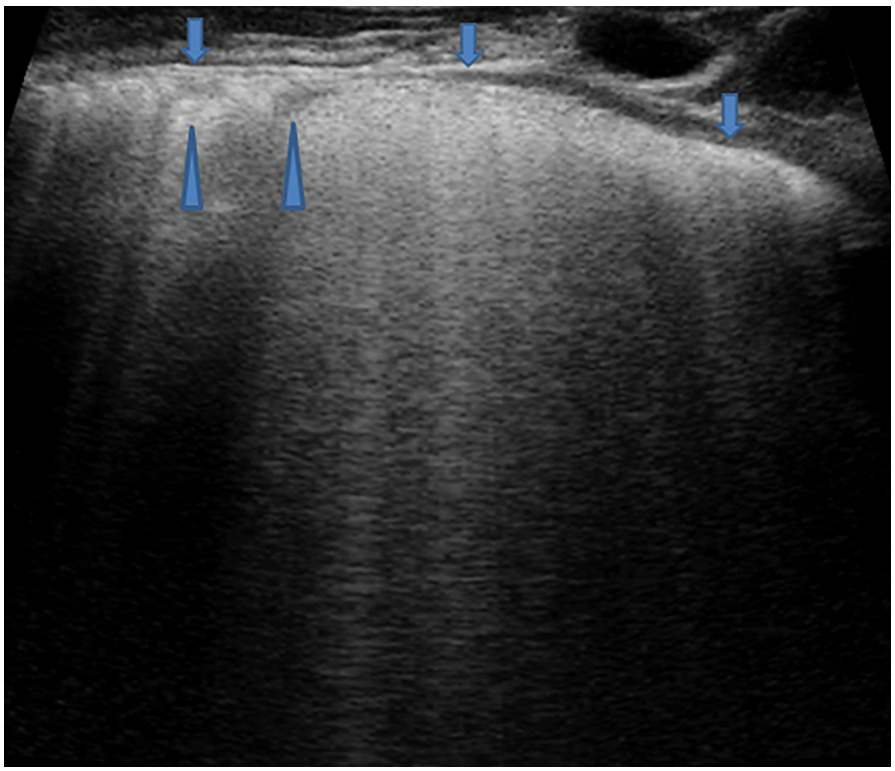

FIGURE 9 | Grayscale lung ultrasound examination (transverse scan between intercostal fields; linear probe with 12 MHz frequency) of a 4-year-old boy with viral pneumonia – due to Coronavirus (non-COVID-19), Bocavirus, and Metapneumovirus coinfection- requiring respiratory assistance with High- flow nasal oxygen at the pediatric department. It shows sonographic interstitial syndrome (SIS) which is characterized by blurred, uneven, coalescent B-lines and white lung; irregular pleural line *(arrows);* reduced pleural sliding; multifocal inhomogeneous involvement; subpleural microconsolidations (generating pseudo-B-lines) *(arrowheads).*

of the aforementioned studies is that LUS has been proposed as a method with better sensitivity and specificity than CXR. The advantage of LUS is not only relative to the diagnosis of pneumonia, but also the lack of exposure to X-rays and the possibility of performing the examination at the patient's bed as well as performing a follow-up.

However, some open questions did emerge. In particular, the question regarding how to determine when a negative LUS requires further evaluation with CXRs or whether it is safe not to prescribe antibiotics in cases of suspected pneumonia when LUS is normal or only shows interstitial syndrome or very small sonographic consolidations. Moreover, there is the need to standardize the appropriate protocol to interpret the LUS findings in childhood pneumonia and the need for international guidelines about the LUS use for pneumonia diagnosis. Future studies should focus on these aspects.

Future studies should also focus on ultrasound-based etiological diagnosis. Not only the presence or absence of the inflammatory event but the etiological hypothesis by which LUS could lead to a change in the current antibiotic therapy thereby encouraging personalized antibiotic treatment.

Bronchiolitis

Bronchiolitis is a typical lower respiratory tract infection that usually affects children in the first two years of life. Its etiology is viral and more frequently it's caused by Respiratory Syncytial Virus (RSV) (Meissner, 2016).

Bronchiolitis physiopathology is characterized by edema, increased production of mucus, and necrosis of cells of the small airway causing obstruction of distal bronchioles (Meissner, 2016).

In recent years, the clinical evaluation of children affected by bronchiolitis has been completed with LUS (Miller, 1995; Jaszczołt et al., 2018), exploiting the advantages of ultrasound especially in young children (non-invasive, non-ionizing radiation tool characterized by a rapid, affordable, point-of-care imaging modality that allows both real-time diagnosis and follow-up of respiratory diseases).

According to LUS findings (Caiulo et al., 2011; Basile et al., 2015; Cohen et al., 2017; Di Mauro et al., 2019; Supino et al., 2019), the ultrasound pattern of bronchiolitis is not specified in an absolute sense. We can find it for example in the case of pneumonia of viral origin. It is characterized by the presence of a thickened pleura that reflects ultrasound waves from the sliding sign and by the presence of long vertical artifacts/B-lines and small subpleural consolidations. B-line/vertical artifacts derive from interstitial inflammation and/or disventilation. Inflammation in particular can be such as to also affect the alveolar component and therefore such as to cause the formation of a consolidation which can then become macroscopic and

also characterized by elements of dynamic air bronchogram (Basile et al., 2015; Supino et al., 2019). Basile et al. (2015) proposed a US pattern classification that can be associated with the clinical classification. It has been described as having a good concordance between clinical condition and US pattern, highlighting a worse clinical course for those patients who have a subpleural consolidation with a diameter greater than 10 mm (Basile et al., 2015; Jaszczołt et al., 2018; Supino et al., 2019).

Lung ultrasound (LUS) shows better sensitivity than CXR in the detection of subpleural parenchymal consolidations of small dimensions (1–2 cm) (Jaszczołt et al., 2018) and it is also able to detect bacterial superinfection by detecting large consolidations and aerial bronchograms (Biagi et al., 2018).

In conclusion, considering the advantages of LUS over chest radiography in detecting and characterizing bronchiolitis findings and considering that there is a good concordance between clinical condition and ultrasonographic pattern (Caiulo et al., 2011), LUS is especially important in the follow-up to avoid repeated chest radiographs. However, considering that the LUS findings of bronchiolitis are not specific, integration with clinical and laboratory data remains important in the diagnostic approach to the child with suspected bronchiolitis.

Wheezing and Asthma

A field in which the use of LUS is not still well defined or is in development is that of asthmatic pathology. The studies available in the last ten years (from 2010 to 2020) in the literature are very few.

In the PED, children frequently present with respiratory distress and concomitant wheeze. Clinicians need to determine whether the pathophysiological process is one such as bronchiolitis, asthma, or pneumonia. The management of the aforementioned common conditions of childhood is dramatically different (Varshney et al., 2016; Dankoff et al., 2017).

A point-of-care tool that could differentiate between etiologies and/or guide the management of children with respiratory tract infections and wheeze would prove useful to the emergency care of these patients.

Varshney et al. (2016), performed the first study, a prospective study, featuring LUS findings in 94 children $\leq$2 years of age presenting to the PED with signs of a respiratory tract infection and wheeze. Among this category of children, a positive LUS seems to distinguish between clinical syndromes by ruling in pneumonia and ruling out asthma.

In 2017 same authors (Dankoff et al., 2017) performed the first study, a prospective study, characterizing lung ultrasound findings in children (aged between 2 and 17 years) with a moderate to severe acute asthma exacerbation. This study demonstrated that 45% of pediatric patients had a positive lung ultrasound during their acute respiratory presentation, of which 90% had a final physician diagnosis of asthma and 10% had asthma/pneumonia. Positive lung ultrasound was defined as the presence of $\geq$ 1 of the following findings: $\geq$ 3 B-lines per intercostal space, consolidation, and/or pleural abnormalities. Although the authors (Dankoff et al., 2017) have shown that pulmonary ultrasound is positive even in the course of asthma, they have not been able to define whether asthma, both in the acute phase and in the stability phase, is characterized by a specific LUS pattern.

Future prospective studies, better on larger pediatric populations, are needed to determine the usefulness and reliability of this tool in the clinical practice of asthma disease taking into account of (1) other diagnostic tests - and not just clinical evaluation associated with LUS evaluation - such as microbiological tests from the airways, chest X-ray, lung function assessment; (2) the treatment of acute asthma attack and any background therapy performed; (3) changes in the LUS findings and other clinical and instrumental assessments before and after the administration of therapy for acute attack; (4) characterization of the ultrasound lung pattern in patients with stable asthma and its comparison with other instrumental and functional evaluations.

Lung Ultrasound in Other Specific Settings

Lung Ultrasound After Cardiac Surgery

The performance of LUS approaches that of chest CT and surpasses that of CXR for diagnosing lung diseases that occur frequently after cardiac surgery, including consolidation, pleural effusion, pulmonary edema, and pneumothorax (Ashton-Cleary, 2013). Song et al. (2018) published a randomized controlled trial with the aim of assessing the utility of perioperative LUS and the effect of US-guided recruitment maneuver in pediatric cardiac surgery taking into account that the optimization of perioperative respiratory care is crucial for improving outcomes after pediatric cardiac surgery. Lung ultrasound findings (degree of consolidations, B-lines, and pleural effusion) were characterized and evaluated following the evaluation method described by Song et al. (2017). According to the authors, perioperative LUS examination followed by ultrasound-guided recruitment maneuver helped decrease postoperative desaturation events and shortened the duration of mechanical ventilation in pediatric cardiac patients.

In particular, among 120 children included in the analysis (aged 5 years or less and divided into 60 in the control group and 60 in the intervention group), the postoperative desaturation occurred more in the control group. LUS scores were better in the intervention group than in the control one. Duration of mechanical ventilation was longer in the control group than in the intervention group. In this way, the authors encouraged more active LUS application in pediatric cardiac surgery (Song et al., 2018).

Also, according to Tripathi et al. (2019), who performed a prospective observational study at PICU using the ultrasound image acquisition protocol in the critically ill (Lichtenstein, 2014), LUS provides actionable quantitative data and it's useful to monitor lung recruitment and other dynamic changes.

Lung Ultrasound in Cystic Fibrosis

The aim of the pilot study of Strzelczuk-Judka et al. (2019) was to evaluate the diagnostic value of LUS in children with *Cystic Fibrosis (CF)* compared to a CXR scoring system and to assess the diagnostic value of the recently developed LUS score CF-USS (Cystic Fibrosis Ultrasound Score), devised based

on the modified Chrispin Norman score and the bronchiolitis score reported by Caiulo and colleagues who applied LUS in patients with bronchiolitis, which is also present in CF patients (Brasfield et al., 1980; Helbich et al., 1999; Caiulo et al., 2011, 2013; Strzelczuk-Judka et al., 2019). In each patient, the authors evaluated: – the quality and quantity of any fluid in the pleural space; - the shape and thickness of the pleural line, the lung sliding sign; – A-lines and B-lines artifacts (number, localization, and morphology, including single ones, "lung rockets" complexes and "white lung" images) and – the alveolar consolidations (number, dimensions, localization, morphology, presence of bronchogram and its air or fluid characteristic and vascularization). Lung ultrasound findings were also classified according to CF-USS. According to the authors, LUS should be a supplementary examination in scheduled follow-up visits in pediatric patients with CF, and the CF-USS scoring system could provide clinicians with valuable information on disease progression. The CF-USS results correlated with the conventional x-ray modified Chrispin–Norman score. Moreover, the authors emphasize that LUS could constitute an invaluable tool for the diagnosis of subpleural consolidations (Strzelczuk-Judka et al., 2019).

However, according to the authors of the studies described above (Song et al., 2018; Strzelczuk-Judka et al., 2019; Tripathi et al., 2019), LUS has low negative predictive values and negative examinations and cannot rule out lung pathology. Limitations of LUS would include the inability to visualize consolidations separated from the pleura and larger airways. The numerous clinical conditions in which B-line artifacts could be present also make it difficult to recommend LUS as the only diagnostic modality in some categories of patients such as those with underlying lung diseases (e.g., CF) (Song et al., 2018; Strzelczuk-Judka et al., 2019; Tripathi et al., 2019).

DISADVANTAGES OF LUNG ULTRASOUND

Many studies have commented on the disadvantages of LUS. These disadvantages included the following (Copetti, 2016; Lovrenski et al., 2016; Cox et al., 2017; Lovrenski, 2020): (1) the inability to visualize the paravertebral regions (beneath the scapulae); (2) the difficulty in examining some patients who are characterized as hypoechogenic (e.g., patients with obesity, subcutaneous emphysema, dressings/wounds); (3) the non-optimal position in which patients with acute respiratory distress and dyspnea are often found, which limits the examination of some lung areas; (4) the air leak syndromes (pneumomediastinum, pneumopericardium, and interstitial emphysema) which couldn't be easily identified by LUS; (5) the areas of air trapping and hypoalveolarization that characterize much of the child's chronic pathology; (6) the errors that may occur if the operator is not properly trained and experienced.

Furthermore, in the context of infectious pulmonary disease, specifically pneumonia, LUS findings are considered non-specific from an etiological point of view and need to be compared and associated with clinical and laboratory findings in order to determine the true etiology of pulmonary changes. No studies have yet investigated the role of LUS in the etiological diagnosis of pediatric pneumonia.

WHAT ARE THE FUTURE DIAGNOSTIC CHALLENGES OF LUNG ULTRASOUND?

Lung ultrasound (LUS) in pediatrics could be used to expand and improve its diagnostic capabilities in several ways. These would include the better capability in the following aspects. First, in the differential diagnosis between viral and bacterial lower respiratory infections and diagnosis of interstitial pneumonia in which the application of LUS could determine the etiological diagnosis of pneumonia in children which could improve antibiotic stewardship (Berant et al., 2015; Han et al., 2018). Second, in the qualitative, quantitative, and objective characterization of vertical artifacts in each of the childhood respiratory diseases, which include chronic disabling ones, through the development of artificial intelligence to identify more specific ultrasound patterns and to create ultrasound scores as is going on for lung infection by COVID-19 (Soldati et al., 2020; Vetrugno et al., 2020). Third, in the use of contrast-enhanced lung ultrasound in complicated pneumonia, both intravenous and intracavitary: intravenous contrast-enhanced US can accurately diagnose "necrotizing" pneumonia and delineate pleural effusion, while intracavitary contrast-enhanced US can identify the location and patency of the thoracic catheter and show the presence of loculations (Lovrenski, 2020). Fourth, in the correlation of LUS with clinical parameters, mechanical ventilation parameters in the context of neonatal and pediatric intensive care; LUS also has the potential for enabling a more focused pulmonary rehabilitation of these children after extubating, targeting precisely to the poorly ventilated areas that need treatment. Finally, in the correlation between LUS and CT findings by performing LUS after each chest CT, which is the gold standard of lung diseases, which could be indicated for other reasons.

CONCLUSION

The greatest potential of LUS belongs to the dynamic follow-up of pulmonary conditions, making many everyday decisions easier for clinicians and enabling a higher quality of treatment and faster recovery of children. For some conditions, such as lung consolidations of both infectious and non-infectious nature, LUS can be considered the first-choice tool for the diagnosis and follow-up of pediatric lung diseases.

Conversely, whenever there is a discrepancy between LUS and other findings (clinical and laboratory), CXR or CT (in more complicated cases) should be performed. This kind of approach would probably reduce the number of CXRs significantly.

Importantly, one of the biggest advantages of LUS is its availability, especially in developing countries (Buonsenso and De Rose, 2021), because it is often easier to bring the ultrasound device to children than to conduct the children to ultrasound rooms of distant hospitals. Unlike most US techniques, LUS

does not require a high-tech ultrasound device: old ultrasound devices and two US probes (convex and linear) are sufficient to provide the necessary information. Fortunately, LUS techniques are easy to perform and master so they are very convenient both outside and inside hospitals; however, as in any other aspect of life, experience is important for lung US, as well (Lovrenski, 2020). The best results are obtained by choosing case by case by integrating the different diagnostic tools.

In conclusion, over the past 10 years, LUS has enhanced our ability to diagnose many pediatric respiratory conditions. Further studies are ongoing that will help us to integrate LUS with the other more commonly used diagnostic modalities to an even greater extent.

AUTHOR CONTRIBUTIONS

All authors have read and approved the manuscript for submission, and have made a substantial contribution to the conception, design, gathering of data, and contribution to the writing and intellectual content of the article.

SUPPLEMENTARY MATERIAL

The Supplementary Material for this article can be found online at: https://www.frontiersin.org/articles/10.3389/fphys.2021.721951/full#supplementary-material

REFERENCES

Ambroggio, L., Sucharew, H., Rattan, M. S., O'Hara, S. M., Babcock, D. S., Clohessy, C., et al. (2016). Lung Ultrasonography: A Viable Alternative to Chest Radiography in Children with Suspected Pneumonia? *J. Pediatr.* 176, 93.e–98.e. doi: 10.1016/j.jpeds.2016.05.033

Ashton-Cleary, D. T. (2013). Is thoracic ultrasound a viable alternative to conventional imaging in the critical care setting? *Br. J. Anaesth.* 111, 152–160. doi: 10.1093/bja/aet076

Audette, L. D., and Parent, M. C. (2016). BET 3: Bedside lung ultrasound for the diagnosis of pneumonia in children. *Emerg. Med. J. EMJ* 33, 589–592. doi: 10.1136/emermed-2016-206047.3

Avery, M. E., Gatewood, O. B., and Brumley, G. (1966). Transient tachypnea of newborn. Possible delayed resorption of fluid at birth. *Am. J. Dis. Children* 111, 380–385. doi: 10.1001/archpedi.1966.02090070078010

Balk, D. S., Lee, C., Schafer, J., Welwarth, J., Hardin, J., Novack, V., et al. (2018). Lung ultrasound compared to chest X-ray for diagnosis of pediatric pneumonia: A meta-analysis. *Pediatr. Pulmonol.* 53, 1130–1139. doi: 10.1002/ppul.24020

Basile, V., Di Mauro, A., Scalini, E., Comes, P., Lofù, I., Mostert, M., et al. (2015). Lung ultrasound: a useful tool in diagnosis and management of bronchiolitis. *BMC Pediatr.* 15:63. doi: 10.1186/s12887-015-0380-1

Berant, R., Kwan, C., and Fischer, J. (2015). Emergency Point-of-Care Ultrasound Assessment of Whiteout Lung in the Pediatric Emergency Department. *Pediatr. Emerg. Care* 31, 872–875. doi: 10.1097/PEC.0000000000000635

Biagi, C., Pierantoni, L., Baldazzi, M., Greco, L., Dormi, A., Dondi, A., et al. (2018). Lung ultrasound for the diagnosis of pneumonia in children with acute bronchiolitis. *BMC Pulmonary Med.* 18:191. doi: 10.1186/s12890-018-0750-1

Blank, D. A., Kamlin, C., Rogerson, S. R., Fox, L. M., Lorenz, L., Kane, S. C., et al. (2018). Lung ultrasound immediately after birth to describe normal neonatal transition: an observational study. Archives of disease in childhood. *Fetal Neonatal Edition* 103, F157–F162. doi: 10.1136/archdischild-2017-312818

Bober, K., and Swietliński, J. (2006). Diagnostic utility of ultrasonography for respiratory distress syndrome in neonates. *Med. Sci. Monit.* 12, CR440–CR446.

Boursiani, C., Tsolia, M., Koumanidou, C., Malagari, A., Vakaki, M., Karapostolakis, G., et al. (2017). Lung Ultrasound as First-Line Examination for the Diagnosis of Community-Acquired Pneumonia in Children. *Pediatr. Emerg. Care* 33, 62–66. doi: 10.1097/PEC.0000000000000969

Brasfield, D., Hicks, G., Soong, S., Peters, J., and Tiller, R. (1980). Evaluation of scoring system of the chest radiograph in cystic fibrosis: a collaborative study. *AJR* 134, 1195–1198. doi: 10.2214/ajr.134.6.1195

Buonsenso, D., and De Rose, C. (2021). Implementation of lung ultrasound in low- to middle-income countries: a new challenge global health? *Eur. J. Pediatr.* 2021, 1–8. doi: 10.1007/s00431-021-04179-9

Buonsenso, D., Soldati, G., Curatola, A., Morello, R., De Rose, C., Vacca, M. E., et al. (2020). Lung Ultrasound Pattern in Healthy Infants During the First 6 Months of Life. *J. Ultrasound Med.* 39, 2379–2388. doi: 10.1002/jum.15347

Caiulo, V. A., Gargani, L., Caiulo, S., et al. (2013). Lung ultrasound characteristics of community-acquired pneumonia in hospitalized children. *Pediatr. Pulmonol.* 48, 280–287. doi: 10.1002/ppul.22585

Caiulo, V. A., Gargani, L., Caiulo, S., Fisicaro, A., Moramarco, F., Latini, G., et al. (2011). Lung ultrasound in bronchiolitis: comparison with chest X-ray. *Eur. J. Pediatr.* 170, 1427–1433. doi: 10.1007/s00431-011-1461-2

Cattarossi, L. (2014). Lung ultrasound: diagnostic and therapeutic issues. *Acta Bio Med. Atenei Parmensis* 85, 25–29.

Cattarossi, L., Copetti, R., Poskurica, B., and Miserocchi, G. (2010). Surfactant administration for neonatal respiratory distress does not improve lung interstitial fluid clearance: echographic and experimental evidence. *J. Perinatal Med.* 38, 557–563. doi: 10.1515/jpm.2010.096

Chavez, M. A., Naithani, N., Gilman, R. H., Tielsch, J. M., Khatry, S., Ellington, L. E., et al. (2015). Agreement Between the World Health Organization Algorithm and Lung Consolidation Identified Using Point-of-Care Ultrasound for the Diagnosis of Childhood Pneumonia by General Practitioners. *Lung* 193, 531–538. doi: 10.1007/s00408-015-9730-x

Chen, L., and Zhang, Z. (2015). Bedside ultrasonography for diagnosis of pneumothorax. *Quantitat. Imaging Med. Surg.* 5, 618–623. doi: 10.3978/j.issn.2223-4292.2015.05.04

Chen, S. W., Zhang, M. Y., and Liu, J. (2015). Application of lung ultrasonography in the diagnosis of childhood lung diseases. *Chin. Med. J.* 128, 2672–2678. doi: 10.4103/0366-6999.166035

Chiappini, E., Venturini, E., Galli, L., Novelli, V., and de Martino, M. (2013). Diagnostic features of community-acquired pneumonia in children: what's new? *Acta Paediatr.* 102, 17–24. doi: 10.1111/apa.12502

Chira, R., Chira, A., and Mircea, P. A. (2011). Thoracic wall ultrasonography - normal and pathological findings. Pictorial essay. *Med. Ultrasonogr.* 13, 228–233.

Claes, A. S., Clapuyt, P., Menten, R., Michoux, N., and Dumitriu, D. (2017). Performance of chest ultrasound in pediatric pneumonia. *Eur. J. Radiol.* 88, 82–87. doi: 10.1016/j.ejrad.2016.12.032

Coca Pérez, A., Vázquez Martínez, J. L., Pérez Caballero, Macarrón, C., Tapia Moreno, R., and Stanescu, S. (2016). Utilidad de la ecografía pulmonar a pie de cama en cuidados intensivos pediátricos [Bedside lung ultrasound in paediatric intensive care]. *Anales Pediatr.* 84, 57–59. doi: 10.1016/j.anpedi.2015.05.006

Cohen, J. S., Hughes, N., Tat, S., Chamberlain, J. M., Teach, S. J., and Boniface, K. (2017). The Utility of Bedside Lung Ultrasound Findings in Bronchiolitis. *Pediatr. Emerg. Care* 33, 97–100. doi: 10.1097/PEC.0000000000000820

Coley, B. D. (2005). Pediatric chest ultrasound. *Radiol. Clin. North Am.* 43, 405–418.

Coley, B. D. (2011). Chest sonography in children: current indications, techniques, and imaging findings. *Radiol. Clin. North Am.* 49, 825–846. doi: 10.1016/j.rcl.2011.06.008

Copetti, R. (2016). Is lung ultrasound the stethoscope of the new millennium? Definitely yes! *Acta Med. Acad.* 45, 80–81. doi: 10.5644/ama2006-124.162

Copetti, R., and Cattarossi, L. (2007). The 'double lung point': an ultrasound sign diagnostic of transient tachypnea of the newborn. *Neonatology* 91, 203–209. doi: 10.1159/000097454

Copetti, R., and Cattarossi, L. (2008). Ultrasound diagnosis of pneumonia in children. *Radiol. Med.* 113, 190–198. doi: 10.1007/s11547-008-0247-8

Copetti, R., Cattarossi, L., Macagno, F., Violino, M., and Furlan, R. (2008). Lung ultrasound in respiratory distress syndrome: a useful tool for early diagnosis. *Neonatology* 94, 52–59. doi: 10.1159/000113059

Corsini, I., Parri, N., Gozzini, E., Coviello, C., Leonardi, V., Poggi, C., et al. (2019). Lung Ultrasound for the Differential Diagnosis of Respiratory Distress in Neonates. *Neonatology* 115, 77–84. doi: 10.1159/000493001

Cox, M., Soudack, M., Podberesky, D. J., and Epelman, M. (2017). Pediatric chest ultrasound: a practical approach. *Pediatr. Radiol.* 47, 1058–1068. doi: 10.1007/s00247-017-3896-8

Dankoff, S., Li, P., Shapiro, A. J., Varshney, T., and Dubrovsky, A. S. (2017). Point of care lung ultrasound of children with acute asthma exacerbations in the pediatric ED. *Am. J. Emerg. Med.* 35, 615–622. doi: 10.1016/j.ajem.2016.12.057

de Souza, T. H., Nadal, J., Peixoto, A. O., Pereira, R. M., Giatti, M. P., Soub, A., et al. (2019). Lung ultrasound in children with pneumonia: interoperator agreement on specific thoracic regions. *Eur. J. Pediatr.* 178, 1369–1377. doi: 10.1007/s00431-019-03428-2

Deng, B. Y., Li, N., Wu, W. S., He, X. G., Li, J. F., Huang, T. L., et al. (2020). Use of Neonatal Lung Ultrasound for the Early Detection of Pneumothorax. *Am. J. Perinatol.* 37, 907–913. doi: 10.1055/s-0039-1688999

Di Mauro, A., Ammirabile, A., Quercia, M., Panza, R., Capozza, M., Manzionna, M. M., et al. (2019). Acute Bronchiolitis: Is There a Role for Lung Ultrasound? *Diagnostics* 9:172. doi: 10.3390/diagnostics9040172

Don, M., Barillari, A., Cattarossi, L., Copetti, R., and Italian-Slovenian Group on Lung Ultrasound for Pediatric Pneumonia. (2013). Lung ultrasound for paediatric pneumonia diagnosis: internationally officialized in a near future? *Acta Paediatr.* 102, 6–7. doi: 10.1111/apa.12002

Ellington, L. E., Gilman, R. H., Chavez, M. A., Pervaiz, F., Marin-Concha, J., Compen-Chang, P., et al. (2017). Lung ultrasound as a diagnostic tool for radiographically-confirmed pneumonia in low resource settings. *Respirat. Med.* 128, 57–64. doi: 10.1016/j.rmed.2017.05.007

El-Malah, H. E.-D. G. M., Hany, S., Mahmoud, M. K., and Ali, A. M. (2015). Lung ultrasonography in evaluation of neonatal respiratory distress syndrome. *Egypt J. Radiol. Nucl. Med.* 46, 469–474.

Esposito, S., Papa, S. S., Borzani, I., Pinzani, R., Giannitto, C., Consonni, D., et al. (2014). Performance of lung ultrasonography in children with community-acquired pneumonia. *Ital. J. Pediatr.* 40:37. doi: 10.1186/1824-7288-40-37

Gargani, L., Forfori, F., Giunta, F., and Picano, E. (2012). Imaging polmonare dell'influenza H1N1 [Lung ultrasound imaging of H1N1 influenza]. *Recent Prog. Med.* 103, 23–25. doi: 10.1701/1022.11154

Gereige, R. S., and Laufer, P. M. (2013). Pneumonia. *Pediatr. Rev.* 34, 438–456. doi: 10.1542/pir.34-10-438

Guerra, M., Crichiutti, G., Pecile, P., Romanello, C., Busolini, E., Valent, F., et al. (2016). Ultrasound detection of pneumonia in febrile children with respiratory distress: a prospective study. *Eur. J. Pediatr.* 175, 163–170. doi: 10.1007/s00431-015-2611-8

Hajalioghli, P., Nemati, M., Dinparast Saleh, L., and Fouladi, D. F. (2016). Can Chest Computed Tomography Be Replaced by Lung Ultrasonography With or Without Plain Chest Radiography in Pediatric Pneumonia? *J. Thoracic Imaging* 31, 247–252. doi: 10.1097/RTI.0000000000000209

Han, J., Xiang, H., Ridley, W. E., and Ridley, L. J. (2018). Jellyfish sign: Pleural effusion. *J. Med. Imaging Radiat. Oncol.* 62(Suppl. 1):33. doi: 10.1111/1754-9485.20_12785

Helbich, T. H., Heinz-Peer, G., Eichler, I., Wunderbaldinger, P., Götz, M., Wojnarowski, C., et al. (1999). Cystic fibrosis: CT assessment of lung involvement in children and adults. *Radiology* 213, 537–544. doi: 10.1148/radiology.213.2.r99nv04537

Ho, M. C., Ker, C. R., Hsu, J. H., Wu, J. R., Dai, Z. K., and Chen, I. C. (2015). Usefulness of lung ultrasound in the diagnosis of community-acquired pneumonia in children. *Pediatr. Neonatol.* 56, 40–45. doi: 10.1016/j.pedneo.2014.03.007

Ianniello, S., Piccolo, C. L., Buquicchio, G. L., Trinci, M., and Miele, V. (2016). First-line diagnosis of paediatric pneumonia in emergency: lung ultrasound (LUS) in addition to chest-X-ray (CXR) and its role in follow-up. *Br. J. Radiol.* 89:20150998. doi: 10.1259/bjr.20150998

Iorio, G., Capasso, M., De Luca, G., Prisco, S., Mancusi, C., Laganà, B., et al. (2015). Lung ultrasound in the diagnosis of pneumonia in children: proposal for a new diagnostic algorithm. *PeerJ* 3:e1374. doi: 10.7717/peerj.1374

Jaszczołt, S., Polewczyk, T., Dołęga-Kozierowska, M., Woźniak, M., and Doniec, Z. (2018). Comparison of lung ultrasound and chest X-ray findings in children with bronchiolitis. *J. Ultrasonogr.* 18, 193–197. doi: 10.15557/JoU.2018.0029

Jones, B. P., Tay, E. T., Elikashvili, I., Sanders, J. E., Paul, A. Z., Nelson, B. P., et al. (2016). Feasibility and Safety of Substituting Lung Ultrasonography for Chest Radiography When Diagnosing Pneumonia in Children: A Randomized Controlled Trial. *Chest* 150, 131–138. doi: 10.1016/j.chest.2016.02.643

Joshi, P., Vasishta, A., and Gupta, M. (2019). Ultrasound of the pediatric chest. *Br. J. Radiol.* 92, 20190058. doi: 10.1259/bjr.20190058

Kim, O. H., Kim, W. S., Kim, M. J., et al. (2000). US in the diagnosis of pediatric chest diseases. *Radiographics* 20, 653–671. doi: 10.1148/radiographics.20.3.g00ma05653

Ključevšek, D. (2016). Lung ultrasonography: A new imaging approach in diagnosis of pneumonia in children. *Acta Med. Acad.* 45, 76–77. doi: 10.5644/ama2006-124.160

Kurepa, D., Zaghloul, N., Watkins, L., and Liu, J. (2018). Neonatal lung ultrasound exam guidelines. *J. Perinatol.* 38, 11–22. doi: 10.1038/jp.2017.140

Lenahan, J. L., Volpicelli, G., Lamorte, A., Jehan, F., Bassat, Q., and Ginsburg, A. S. (2018). Multicentre pilot study evaluation of lung ultrasound for the management of paediatric pneumonia in low-resource settings: a study protocol. *BMJ Open Respirat. Res.* 5:e000340. doi: 10.1136/bmjresp-2018-000340

Liang, H. Y., Liang, X. W., Chen, Z. Y., Tan, X. H., Yang, H. H., Liao, J. Y., et al. (2018). Ultrasound in neonatal lung disease. *Quant. Imaging Med. Surg.* 8, 535–546.

Lichtenstein, D. A. (2014). Lung ultrasound in the critically ill. *Ann. Intens. Care* 4:1. doi: 10.1186/2110-5820-4-1

Lichtenstein, D. A., and Mauriat, P. (2012). Lung Ultrasound in the Critically Ill Neonate. *Curr. Pediatr. Rev.* 8, 217–223. doi: 10.2174/157339612802139389

Lichtenstein, D. A., Lascols, N., Mezière, G., and Gepner, A. (2004). Ultrasound diagnosis of alveolar consolidation in the critically ill. *Intens. Care Med.* 30, 276–281. doi: 10.1007/s00134-003-2075-6

Lichtenstein, D., Mezière, G., and Seitz, J. (2009). The dynamic air bronchogram. A lung ultrasound sign of alveolar consolidation ruling out atelectasis. *Chest* 135, 1421–1425. doi: 10.1378/chest.08-2281

Lissaman, C., Kanjanauptom, P., Ong, C., Tessaro, M., Long, E., and O'Brien, A. (2019). Prospective observational study of point-of-care ultrasound for diagnosing pneumonia. *Arch. Dis. Childhood* 104, 12–18. doi: 10.1136/archdischild-2017-314496

Liu, J., Cao, H. Y., Wang, H. W., and Kong, X. Y. (2015a). The Role of Lung Ultrasound in Diagnosis of Respiratory Distress Syndrome in Newborn Infants. *Iran. J. Pediatr.* 25:e323. doi: 10.5812/ijp.323

Liu, J., Chi, J. H., Ren, et al. (2017). Lung ultrasonography to diagnose pneumothorax of the newborn. *Am. J. Emerg. Med.* 35, 1298–1302. doi: 10.1016/j.ajem.2017.04.001

Liu, J., Liu, F., Liu, Y., Wang, H. W., and Feng, Z. C. (2014). Lung ultrasonography for the diagnosis of severe neonatal pneumonia. *Chest* 146, 383–388. doi: 10.1378/chest.13-2852

Liu, L., Oza, S., Hogan, D., et al. (2015b). Global, regional, and national causes of child mortality in 2000-13, with projections to inform post-2015 priorities: an updated systematic analysis. *Lancet* 385, 430–440. doi: 10.1016/S0140-6736(14)61698-6

Lovrenski, J. (2018). Pulmonary sequestration as an incidental finding of pediatric abdominal ultrasound. *J. Health Sci. Med. Res.* 37, 61–66. doi: 10.1007/s00383-014-3572-0

Lovrenski, J. (2020). Pediatric lung ultrasound - pros and potentials. *Pediatr. Radiol.* 50, 306–313. doi: 10.1007/s00247-019-04525-y

Lovrenski, J., Petrović, S., Balj-Barbir, S., Jokić, R., and Vilotijević-Dautović, G. (2016). Stethoscope vs. ultrasound probe - which is more reliable in children with suspected pneumonia? *Acta Medica Acad.* 45, 39–50. doi: 10.5644/ama2006-124.155

Man, S. C., Fufezan, O., Sas, V., and Schnell, C. (2017). Performance of lung ultrasonography for the diagnosis of communityacquired pneumonia in hospitalized children. *Med. Ultrasonogr.* 19, 276–281. doi: 10.11152/mu-1027

Martelius, L., Heldt, H., and Lauerma, K. (2016). B-lines on pediatric lung sonography: comparison with computed tomography. *J. Ultrasound Med.* 35, 153–157. doi: 10.7863/ultra.15.01092

Meissner, H. C. (2016). Viral Bronchiolitis in Children. *New Engl. J. Med.* 374, 62–72. doi: 10.1056/NEJMra1413456

Miller, R. W. (1995). Special susceptibility of the child to certain radiation-induced cancers. *Environ. Health Perspect.* 103(Suppl. 6), 41–44. doi: 10.1289/ehp.95103s641

Milliner, B., and Tsung, J. W. (2017). Lung consolidation locations for optimal lung ultrasound scanning in diagnosing pediatric pneumonia. *J. Ultrasound Med.* 36, 2325–2328. doi: 10.1002/jum.14272

Mong, A., Epelman, M., and Darge, K. (2012). Ultrasound of the pediatric chest. *Pediatr. Radiol.* 42, 1287–1297.

Najgrodzka, P., Buda, N., Zamojska, A., Marciniewicz, E., and Lewandowicz-Uszyńska, A. (2019). Lung Ultrasonography in the Diagnosis of Pneumonia in Children-A Metaanalysis and a Review of Pediatric Lung Imaging. *Ultrasound Quart.* 35, 157–163. doi: 10.1097/RUQ.0000000000000411

Pereda, M. A., Chavez, M. A., Hooper-Miele, C. C., Gilman, R. H., Steinhoff, M. C., Ellington, L. E., et al. (2015). Lung ultrasound for the diagnosis of pneumonia in children: a meta-analysis. *Pediatrics* 135, 714–722. doi: 10.1542/peds.2014-2833

Persson, B., and Hanson, U. (1998). Neonatal morbidities in gestational diabetes mellitus. *Diabet. Care* 21(Suppl. 2), B79–B84.

Pervaiz, F., Chavez, M. A., Ellington, L. E., Grigsby, M., Gilman, R. H., Miele, C. H., et al. (2018). Building a prediction model for radiographically confirmed pneumonia in peruvian children: from symptoms to imaging. *Chest* 154, 1385–1394. doi: 10.1016/j.chest.2018.09.006

Prina, E., Torres, A., and Carvalho, C. R. (2014). Lung ultrasound in the evaluation of pleural effusion. *J. Brasil. Pneumol.* 40, 1–5. doi: 10.1590/S1806-37132014000100001

Prithviraj, D., and Suresh, A. (2014). Chest Ultrasonography-A quick and accurate diagnostic tool in pediatric emergency department and intensive care unit. *Int. J. Sci. Stud.* 2, 59–56.

Raimondi, F., Rodriguez Fanjul, J., Aversa, S., Chirico, G., Yousef, N., De Luca, D., et al. (2016). Lung Ultrasound for Diagnosing Pneumothorax in the Critically Ill Neonate. *J. Pediatr.* 175, 74.e–78.e. doi: 10.1016/j.jpeds.2016.04.018

Raimondi, F., Yousef, N., Migliaro, F., Capasso, L., and De Luca, D. (2018). Point-of-care lung ultrasound in neonatology: classification into descriptive and functional applications. *Pediatr. Res.* 2018, 1–8. doi: 10.1038/s41390-018-0114-9

Reali, F., Sferrazza Papa, G. F., Carlucci, P., Fracasso, P., Di Marco, F., Mandelli, M., et al. (2014). Can lung ultrasound replace chest radiography for the diagnosis of pneumonia in hospitalized children? *Respirat. Int. Rev. Thorac. Dis.* 88, 112–115. doi: 10.1159/000362692

Reissig, A., and Copetti, R. (2014). Lung ultrasound in community-acquired pneumonia and in interstitial lung diseases. *Respirat. Int. Rev. Thoracic Dis.* 87, 179–189. doi: 10.1159/000357449

Reissig, A., Copetti, R., and Kroegel, C. (2012). Current role of emergency ultrasound of the chest. *Crit. Care Med.* 39, 839–845. doi: 10.1097/CCM.0b013e318206d6b8

Riccabona, M. (2008). Ultrasound of the chest in children (mediastinum excluded). *Eur. Radiol.* 18, 390–399. doi: 10.1007/s00330-007-0754-3

Saraogi, A. (2015). Lung ultrasound: Present and future. *Lung Ind.* 32, 250–257. doi: 10.4103/0970-2113.156245

Sferrazza Papa, G. F., Pellegrino, G. M., Volpicelli, G., Sferrazza Papa, S., Di Marco, F., Mondoni, M., et al. (2017). Lung Ultrasound B Lines: Etiologies and Evolution with Age. *Respirat. Int. Rev. Thorac. Dis.* 94, 313–314. doi: 10.1159/000479034

Shah, C., and Greenberg, S. B. (2017). "The Pediatric Chest," in *Diagnostic Ultrasound*, 5th Edn, Chap. 50, eds C. Rumack and D. Levine (Amsterdam: Elsevier), 1701–1729.

Shah, V. P., Tunik, M. G., and Tsung, J. W. (2013). Prospective evaluation of point-of-care ultrasonography for the diagnosis of pneumonia in children and young adults. *JAMA Pediatr.* 167, 119–125. doi: 10.1001/2013.jamapediatrics.107

Soldati, G., and Demi, M. (2017). The use of lung ultrasound images for the differential diagnosis of pulmonary and cardiac interstitial pathology. *J. Ultrasound* 20, 91–96. doi: 10.1007/s40477-017-0244-7

Soldati, G., Demi, M., Inchingolo, R., Smargiassi, A., and Demi, L. (2016). On the Physical Basis of Pulmonary Sonographic Interstitial Syndrome. *J. Ultrasound Med.* 35, 2075–2086. doi: 10.7863/ultra.15.08023

Soldati, G., Demi, M., Smargiassi, A., Inchingolo, R., and Demi, L. (2019). The role of ultrasound lung artifacts in the diagnosis of respiratory diseases. *Expert Rev. Respirat. Med.* 13, 163–172. doi: 10.1080/17476348.2019.156599760

Soldati, G., Smargiassi, A., Inchingolo, R., Buonsenso, D., Perrone, T., Briganti, D. F., et al. (2020). Proposal for International Standardization of the Use of Lung Ultrasound for Patients With COVID-19: A Simple, Quantitative, Reproducible Method. *J. Ultrasound Med.* 39, 1413–1419. doi: 10.1002/jum.15285

Soldati, G., Smargiassi, A., Inchingolo, R., Sher, S., Nenna, R., Valente, S., et al. (2015). Lung Ultrasonography and Vertical Artifacts: The Shape of Air. *Respirat. Int. Rev. Thorac. Dis.* 90:86. doi: 10.1159/000430483

Song, I. K., Kim, E. H., Lee, J. H., Kang, P., Kim, H. S., and Kim, J. T. (2018). Utility of Perioperative Lung Ultrasound in Pediatric Cardiac Surgery: A Randomized Controlled Trial. *Anesthesiology* 128, 718–727. doi: 10.1097/ALN.0000000000002069

Song, I. K., Kim, E. H., Lee, J. H., Ro, S., Kim, H. S., and Kim, J. T. (2017). Effects of an alveolar recruitment manoeuvre guided by lung ultrasound on anaesthesia-induced atelectasis in infants: a randomised, controlled trial. *Anaesthesia* 72, 214–222. doi: 10.1111/anae.13713

Strzelczuk-Judka, L., Wojsyk-Banaszak, I., Zakrzewska, A., and Jończyk-Potoczna, K. (2019). Diagnostic value of chest ultrasound in children with cystic fibrosis - Pilot study. *PLoS One* 14:e0215786. doi: 10.1371/journal.pone.0215786

Supakul, N., and Karmazyn, B. (2013). Ultrasound of the pediatric chest–the ins and outs. *Semin. Ultrasound CT MR* 34, 274–285. doi: 10.1053/j.sult.2012.12.001

Supino, M. C., Buonsenso, D., Scateni, S., Scialanga, B., Mesturino, M. A., Bock, C., et al. (2019). Point-of-care lung ultrasound in infants with bronchiolitis in the pediatric emergency department: a prospective study. *Eur. J. Pediatr.* 178, 623–632. doi: 10.1007/s00431-019-03335-6

Szymońska, I., Wentrys, Ł, Jagła, M., Olszewska, M., Wasilewska, W., Smykla, B., et al. (2019). Lung ultrasound reduces the number of chest X-rays in newborns with pneumothorax. *Dev. Period Med.* 23, 172–177. doi: 10.34763/devperiodmed.20192303.172177

Tomà, P. (2013a). Lung ultrasound characteristics of community acquired pneumonia. *Pediatr. Pulmonol.* 48, 1041–1042.

Tomà, P. (2013b). Lung ultrasound in bronchiolitis. *Eur. J. Pediatr.* 172:713. doi: 10.1007/s00431-013-1941-7

Tomà, P., and Owens, C. M. (2013). Chest ultrasound in children: critical appraisal. *Pediatr. Radiol.* 43, 1427–1426. doi: 10.1007/s00247-013-2756-4

Toma, T. P., Trigiani, M., Zanforlin, et al. (2019). Competence in thoracic ultrasound. *Panminerva Med.* 61, 344–366. doi: 10.23736/S0031-0808.18.03577-2

Trinavarat, P., and Riccabona, M. (2014). Potential of ultrasound in the pediatric chest. *Eur. J. Radiol.* 83, 1507–1518. doi: 10.1016/j.ejrad.2014.04.011

Tripathi, S., Ganatra, H., Martinez, E., Mannaa, M., and Peters, J. (2019). Accuracy and reliability of bedside thoracic ultrasound in detecting pulmonary pathology in a heterogeneous pediatric intensive care unit population. *J. Clin. Ultrasound JCU* 47, 63–70. doi: 10.1002/jcu.22657

Trovato, G. M., and Sperandeo, M. (2013). Sounds, ultrasounds, and artifacts: which clinical role for lung imaging? *Am. J. Respir. Crit. Care Med.* 187, 780–781. doi: 10.1164/ajrccm.187.7.780

Trovato, G. M., Rollo, V. C., Martines, G. F., et al. (2013a). Thoracic ultrasound in the differential diagnosis of severe dyspnea: a reappraisal. *Int. J. Cardiol.* 167, 1081–1083. doi: 10.1016/j.ijcard.2012.10.057

Trovato, G. M., Sperandeo, M., and Catalano, D. (2013b). Thoracic ultrasound guidance for access to pleural, peritoneal, and pericardial space. *Chest* 144, 1735–1173. doi: 10.1378/chest.13-1475

Tsou, P. Y., Chen, K. P., Wang, Y. H., Fishe, J., Gillon, J., Lee, C. C., et al. (2019). Diagnostic Accuracy of Lung Ultrasound Performed by Novice Versus Advanced Sonographers for Pneumonia in Children: A Systematic Review and Meta-analysis. *Acad. Emerg. Med.* 26, 1074–1088. doi: 10.1111/acem.13818

Urbankowska, E., Krenke, K., Drobczyński, Ł, Korczyński, P., Urbankowski, T., Krawiec, M., et al. (2015). Lung ultrasound in the diagnosis and monitoring of community acquired pneumonia in children. *Respirat. Med.* 109, 1207–1212. doi: 10.1016/j.rmed.2015.06.011

Varshney, T., Mok, E., Shapiro, A. J., Li, P., and Dubrovsky, A. S. (2016). Point-of-care lung ultrasound in young children with respiratory tract infections and wheeze. *Emerg. Med. J.* 33, 603–610. doi: 10.1136/emermed-2015-205302

Vetrugno, L., Bove, T., Orso, D., Bassi, F., Boero, E., and Ferrari, G. (2020). Lung Ultrasound and the COVID-19 "Pattern": Not All That Glitters Today Is Gold Tomorrow. *J. Ultrasound Med.* 39, 2281–2282. doi: 10.1002/jum.15327

Volpicelli, G. (2011). Sonographic diagnosis of pneumothorax. *Intens. Care Med.* 37, 224–232. doi: 10.1007/s00134-010-2079-y

Volpicelli, G., Elbarbary, M., Blaivas, M., et al. (2012). International Liaison Committee on Lung Ultrasound (ILC-LUS) for International Consensus Conference on Lung Ultrasound (ICC-LUS) (2012). International evidence-based recommendations for point-of-care lung ultrasound. *Intens. Care Med.* 38, 577–591. doi: 10.1007/s00134-012-2513-4

Weerdenburg, K. D., Kwan, C. W., and Fischer, J. W. (2016). Point-Of-Care Ultrasound Findings Associated With Foreign Body Aspiration in the Pediatric Emergency Department. *Pediatr. Emerg. Care* 32, 486–488. doi: 10.1097/PEC.0000000000000842

Xiao, T. T., Jin, M., Ju, R., Yang, S., Gao, S. Q., Jiang, Y., et al. (2018). Zhongguo dang dai er ke za zhi. *Chin. J. Contemp. Pediatr.* 20, 444–448. doi: 10.7499/j.issn.1008-8830.2018.06.003

Xin, H., Li, J., and Hu, H. Y. (2018). Is Lung Ultrasound Useful for Diagnosing Pneumonia in Children?: A Meta-Analysis and Systematic Review. *Ultrasound Quart.* 34, 3–10. doi: 10.1097/RUQ.0000000000000330

Yadav, K. K., Awasthi, S., and Parihar, A. (2017). Lung Ultrasound is Comparable with Chest Roentgenogram for Diagnosis of Community-Acquired Pneumonia in Hospitalised Children. *Ind. J. Pediatr.* 84, 499–504. doi: 10.1007/s12098-017-2333-1

Yan, C., Hui, R., Lijuan, Z., and Zhou, Y. (2020). Lung ultrasound vs. chest X-ray in children with suspected pneumonia confirmed by chest computed tomography: A retrospective cohort study. *Exp. Therapeut. Med.* 19, 1363–1369. doi: 10.3892/etm.2019.8333

Yilmaz, H. L., Özkaya, A. K., Sarı Gökay, S., Tolu Kendir, Ö, and Şenol, H. (2017). Point-of-care lung ultrasound in children with community acquired pneumonia. *Am. J. Emerg. Med.* 35, 964–969. doi: 10.1016/j.ajem.2017.01.065

Yousef, N. (2017). To B or not to B; that might just be the question. The use of lung ultrasound in pediatric cardiac intensive care. *Pediatr. Pulmonol.* 52, 421–422. doi: 10.1002/ppul.23558

Yousef, N., Mokhtari, M., Durand, P., et al. (2018). Lung ultrasound findings in congenital pulmonary airway malformation. *Am. J. Perinatol.* 35, 1222–1227. doi: 10.1055/s-0038-1645861

Zhan, C., Grundtvig, N., and Klug, B. H. (2018). Performance of Bedside Lung Ultrasound by a Pediatric Resident: A Useful Diagnostic Tool in Children With Suspected Pneumonia. *Pediatr. Emerg. Care* 34, 618–622. doi: 10.1097/PEC.0000000000000888

Zhang, Z. (2015). Double lung point in an 18-month-old child: a case report and literature review. *J. Thorac. Dis.* 7, E50–E53. doi: 10.3978/j.issn.2072-1439.2015.01.14

Conflict of Interest: The authors declare that the research was conducted in the absence of any commercial or financial relationships that could be construed as a potential conflict of interest.

Publisher's Note: All claims expressed in this article are solely those of the authors and do not necessarily represent those of their affiliated organizations, or those of the publisher, the editors and the reviewers. Any product that may be evaluated in this article, or claim that may be made by its manufacturer, is not guaranteed or endorsed by the publisher.

frontiers in Physiology

ORIGINAL RESEARCH
published: 04 February 2022
doi: 10.3389/fphys.2021.725865

Automatic Lung Segmentation and Quantification of Aeration in Computed Tomography of the Chest Using 3D Transfer Learning

Lorenzo Maiello[1,2], Lorenzo Ball[2], Marco Micali[2], Francesca Iannuzzi[2], Nico Scherf[3], Ralf-Thorsten Hoffmann[4], Marcelo Gama de Abreu[1,5,6], Paolo Pelosi[2] and Robert Huhle[1]**

[1] Pulmonary Engineering Group, Department of Anaesthesiology and Intensive Care Therapy, University Hospital Carl Gustav Carus, Technische Universität Dresden, Dresden, Germany, [2] Department of Surgical Sciences and Integrated Diagnostics, IRCCS AOU San Martino IST, University of Genoa, Genoa, Italy, [3] Max Planck Institute for Human Cognitive and Brain Sciences, Leipzig, Germany, [4] Department of Diagnostic and Interventional Radiology, University Hospital Carl Gustav Dresden, Technische Universität Dresden, Dresden, Germany, [5] Department of Intensive Care and Resuscitation, Anesthesiology Institute, Cleveland Clinic, Cleveland, OH, United States, [6] Department of Outcomes Research, Anesthesiology Institute, Cleveland Clinic, Cleveland, OH, United States

OPEN ACCESS

Edited by:
Joseph M. Reinhardt, The University of Iowa, United States

Reviewed by:
Sam Bayat, Université Grenoble Alpes, France
Sandeep Bodduluri, University of Alabama at Birmingham, United States

***Correspondence:**
Lorenzo Maiello
lore.maiello@gmail.com
Robert Huhle
robert.huhle@tu-dresden.de

Specialty section:
This article was submitted to Respiratory Physiology, a section of the journal Frontiers in Physiology

Received: *15 June 2021*
Accepted: *21 December 2021*
Published: *04 February 2022*

Citation:
Maiello L, Ball L, Micali M, Iannuzzi F, Scherf N, Hoffmann R-T, Gama de Abreu M, Pelosi P and Huhle R (2022) Automatic Lung Segmentation and Quantification of Aeration in Computed Tomography of the Chest Using 3D Transfer Learning. Front. Physiol. 12:725865. doi: 10.3389/fphys.2021.725865

Background: Identification of lung parenchyma on computer tomographic (CT) scans in the research setting is done semi-automatically and requires cumbersome manual correction. This is especially true in pathological conditions, hindering the clinical application of aeration compartment (AC) analysis. Deep learning based algorithms have lately been shown to be reliable and time-efficient in segmenting pathologic lungs. In this contribution, we thus propose a novel 3D transfer learning based approach to quantify lung volumes, aeration compartments and lung recruitability.

Methods: Two convolutional neural networks developed for biomedical image segmentation (uNet), with different resolutions and fields of view, were implemented using Matlab. Training and evaluation was done on 180 scans of 18 pigs in experimental ARDS ($u2Net_{Pig}$) and on a clinical data set of 150 scans from 58 ICU patients with lung conditions varying from healthy, to COPD, to ARDS and COVID-19 ($u2Net_{Human}$). One manual segmentations (MS) was available for each scan, being a consensus by two experts. Transfer learning was then applied to train $u2Net_{Pig}$ on the clinical data set generating $u2Net_{Transfer}$. General segmentation quality was quantified using the Jaccard index (*JI*) and the Boundary Function score (*BF*). The slope between *JI* or *BF* and relative volume of non-aerated compartment (S_{JI} and S_{BF}, respectively) was calculated over data sets to assess robustness toward non-aerated lung regions. Additionally, the relative volume of ACs and lung volumes (LV) were compared between automatic and MS.

Results: On the experimental data set, $u2Net_{Pig}$ resulted in $JI = 0.892$ [0.88 : 091] (median [inter-quartile range]), $BF = 0.995$ [0.98 : 1.0] and slopes $S_{JI} = -0.2$ {95% conf. int. $-0.23 : -0.16$} and $S_{BF} = -0.1$ $\{-0.5 : -0.06\}$. $u2Net_{Human}$ showed similar performance compared to $u2Net_{Pig}$ in *JI*, *BF* but with reduced robustness $S_{JI} = -0.29$ $\{-0.36 : -0.22\}$ and $S_{BF} = -0.43$ $\{-0.54 : -0.31\}$. Transfer learning improved overall $JI = 0.92$ [0.88 : 0.94], $P < 0.001$, but reduced robustness $S_{JI} = -0.46$ $\{-0.52 : -0.40\}$,

and affected neither $BF = 0.96$ [0.91 : 0.98] nor $S_{BF} = -0.48$ {−0.59 : −0.36}. $u2Net_{Transfer}$ improved *JI* compared to $u2Net_{Human}$ in segmenting healthy ($P = 0.008$), ARDS ($P < 0.001$) and COPD ($P = 0.004$) patients but not in COVID-19 patients ($P = 0.298$). ACs and LV determined using $u2Net_{Transfer}$ segmentations exhibited $< 5\%$ volume difference compared to MS.

Conclusion: Compared to manual segmentations, automatic uNet based 3D lung segmentation provides acceptable quality for both clinical and scientific purposes in the quantification of lung volumes, aeration compartments, and recruitability.

Keywords: uNet, COVID-19, lung segmentation, ARDS, Jaccard index, deep learning, transfer learning, lung recruitment

1. INTRODUCTION

The ongoing COVID-19 pandemic has focused attention on Acute Lung Injury and the Acute Respiratory Distress Syndrome (ARDS), a disease mainly characterized by impaired gas exchange driven by an inflammatory state of the lung (Ferguson et al., 2012; The ARDS Definition Task Force*, 2012). Optimal treatment of this pathology is currently being debated and different approaches have been proposed (Amato et al., 2009; Calfee et al., 2014; Coppola et al., 2018; Pelosi et al., 2018; Hodgson et al., 2019; Robba et al., 2020). One of the main clinical questions remaining is how to choose the best ventilator strategy.

The primary objectives of mechanical ventilation (MV) are maintaining physiological blood oxygen and carbon dioxide concentrations. However, MV itself may induce further damage to the lung parenchyma. This process is known as Ventilator Induced Lung Injury (VILI) (Slutsky, 1999; Slutsky and Ranieri, 2013). The concept of protective ventilation has thus been introduced (Network, 2009) to minimize VILI. While pathophysiological pathways leading to biotrauma (Curley et al., 2016), volutrauma (Güldner et al., 2016), barotrauma (Anzueto et al., 2004), and atelectrauma (Tsuchida et al., 2012; Güldner et al., 2016) have been identified, the clinical challenge of individual patient ventilator settings to minimize VILI still remains. The titration of ventilatory parameters is often approached by integrating functional assessments of gas exchange, mechanical properties of the lung and radiological findings. Both gas exchange parameters and lung mechanics can be reliably measured bedside, leading to useful assessments of ventilation to perfusion matching, dead space estimation, and mechanical stress on the lung. Conversely, important radiological findings such as aeration compartments and recruitability are often only assessed qualitatively. Clinicians often rely on all of these sources of information in deciding to perform interventions such as positive end-expiratory pressure (PEEP) setting, recruitment maneuvers, prone positioning, pharmacologic interventions, or extra-corporeal circulation (Battaglini et al., 2021).

The classification and quantification of lung regions on computer tomographic (CT) data may also be used to guide ventilatory strategies (Pelosi et al., 2011; Cereda et al., 2019; Robba et al., 2020). While often used in research settings (Ball et al., 2017), this is, however, not routinely performed in clinical settings since it requires costly manual lung segmentation by trained physicians. The challenge of segmenting pathologic lung parenchyma originates from the fact that non-aerated lung tissue is not distinguishable from nearby structures by either its Hounsfield unit nor by its pattern. Segmenting lung parenchyma thus requires knowledge regarding the anatomical boundary and shape of the lung. For this reason the several deterministic algorithms previously proposed (Hu et al., 2001; Karmrodt et al., 2006; Cuevas et al., 2009; Mansoor et al., 2014; Noshadi et al., 2017) either lack in accuracy or are prone to fail if any one of their numerous constituting assumptions is not met, which typically occurs in ARDS.

The segmentation challenge posed by pathologic lung parenchyma has been recently successfully tackled using artificial intelligence (AI) based algorithms such as convolutional neural networks (CNN) (Shelhamer et al., 2017). The SegNet (Badrinarayanan et al., 2017) architecture was used successfully for the automatic segmentation of healthy and injured lung scans from experimental and clinical data alike (Gerard et al., 2020). More recently polymorphism was added, further increasing the robustness of the algorithm in segmenting poorly or non-aerated lung regions on CT scans with up to 25% volume of the non-aerated lung compartment (Gerard et al., 2021). Such U-net like architectures constitute an improvement compared to previous CNNs, mainly in context feedback. These architectures are thus particularly well suited to scarce segmentation problems with only limited available data (Ronneberger et al., 2015). For example, U-nets have been applied to medical image recognition and tasks such as brain tumor segmentation (Çiçek et al., 2016). When applied to the task of lung parenchyma segmentation, U-nets have shown promising results on healthy chest CTs by Ait Skourt et al. (2018) and on 2D slices (Zhou et al., 2021) and 3D volumes (Müller et al., 2020) of COVID-19 CT scans.

Given these promising results, in this contribution we propose a three-dimensional U-net based algorithm for segmenting lungs across different pathological states. We develop our system using experimental CT data. The resulting algorithm can be run on personal computers. We further train and evaluate this algorithm on data from a cohort of ICU patients with both non-respiratory diseases and respiratory disease, including COVID-19. We

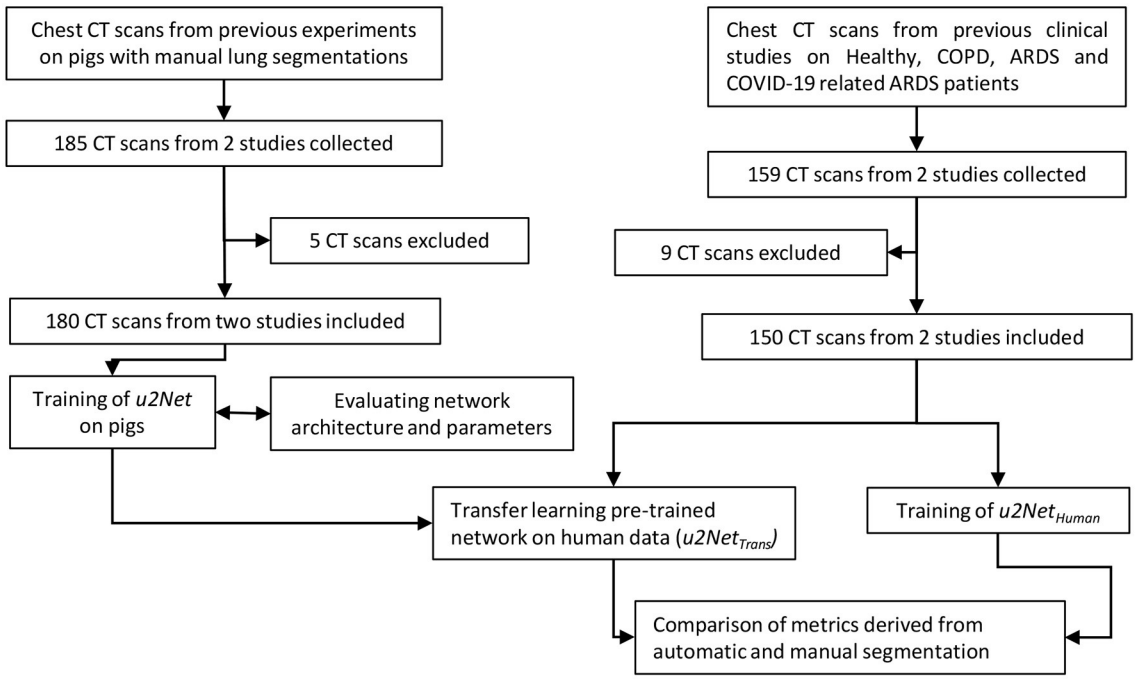

FIGURE 1 | Flow chart of the design process applied (CT scans were excluded if manual segmentations were of poor quality).

perform the evaluation of the system in terms of the correct determination of aeration compartments and lung volumes.

2. MATERIALS AND METHODS

2.1. Study Design

The present study is aimed at developing a reliable and time-efficient method for lung segmentation in pathological conditions using available data sets for future application. To this end, we employed only previously gathered research data sets with granted appropriate ethics committee approvals. Data had already been annonymized within the original study.

The study was conducted in three phases. First, we compiled the animal data set and used it to select the better of two possible network architectures. We then used the clinical data set to test *ex-novo* training vs. transfer learning from the animal data set. Finally, we evaluated if our approach was acceptable for research and clinical applications. To do so we compared measures derived from lung CT segmentations, such as aeration compartments, effective lung volume and recruitability, as calculated from CNN-segmentations against the same measures calculated from manual CT segmentations. An outline of the process is shown in **Figure 1**.

2.2. Convolutional Neural Network

The architecture implemented here stems from U-net structures, that apply convolutions to different image resolutions. Our architecture expands the same concept to 3D volumes. U-nets use down-sampling on the encoding path of the image processing, before applying convolutions, to modify the resolution of the image itself and then implement a symmetric up-sampling and concatenation of the results before the final convolution layer (Sudre et al., 2017) (**Figure 2**).

This algorithm of U-nets is composed of two networks that operate in series, as suggested by Gerard et al. (2020). For the first network CT data was down-sampled to $64 \times 64 \times 64$ voxel. This network has the task of determining general shape and size of the lung. A second network fine tunes the segmentation using as input both the output from the first network and the full-scale CT, re-sampled at one millimeter isotropic voxel for standardization across data sets. The second network operates by dividing the data into tiles that can be managed by a current desktop computer, but has only a partial view of the CT and relies on the output of the first network for information about size and shape.

Hyper parameters chosen for all networks based on previous literature were: three encoding steps, 32 first encoder filters, and $3 \times 3 \times 3$ convolutional filters. At every encoder level convolution (Stride $1 \times 1 \times 1$ voxel, same padding), batch normalization, and linear rectification was performed twice followed by max pooling. CT data were not augmented. However, both clinical data sets included implicit data augmentation, since scans at different resolution and different CT reconstruction kernels were used. Training was performed using an Adam solver and an initial learning rate of 10^{-4} with the DICE loss function. Weights were initialized according to He et al. (2015).

Architectures and network training were implemented in Matlab using the Deep Learning Toolbox (Mathworks Inc.,

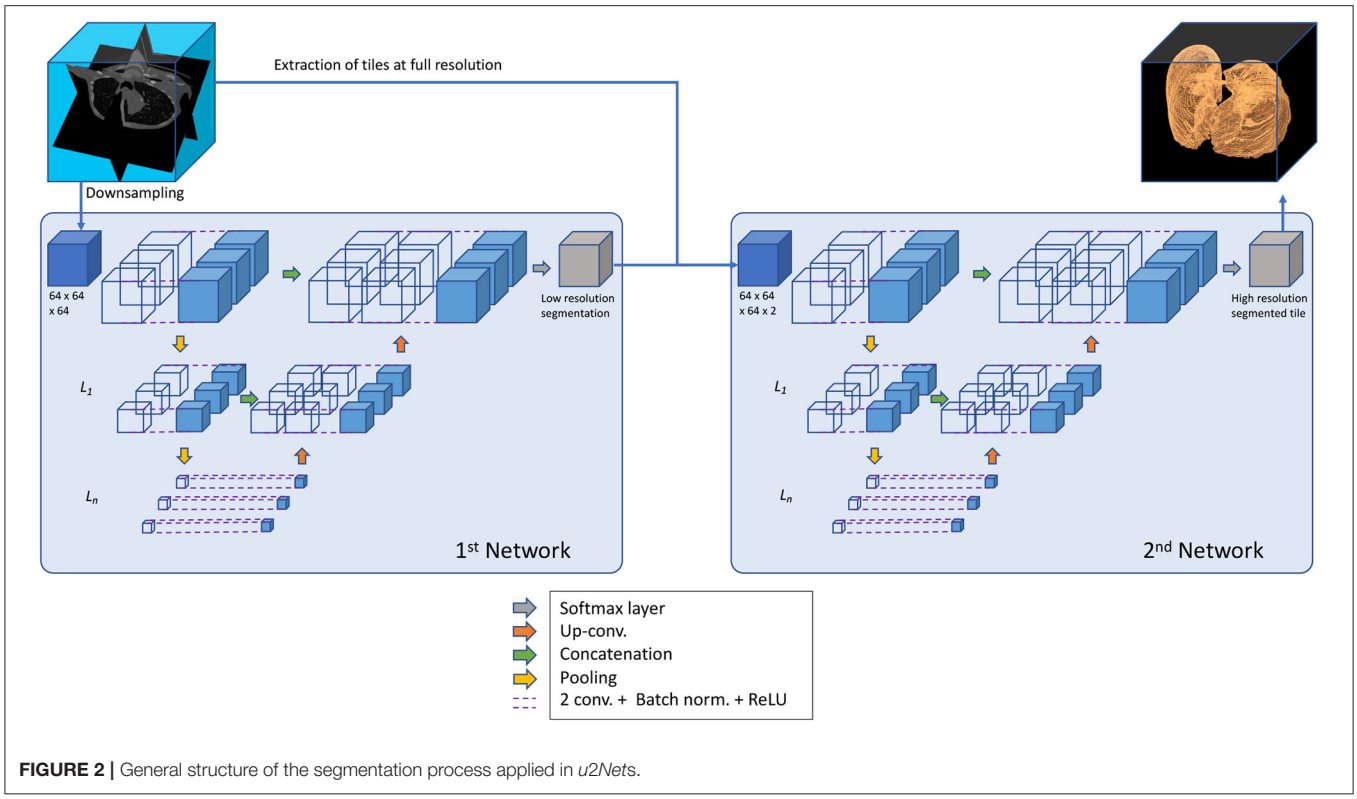

FIGURE 2 | General structure of the segmentation process applied in *u2Net*s.

Natwick, MA, USA). Training and validation were run in parallel on multiple GPUs on the High Performance Cluster (HPC) at the centre of information services and high performance computing (ZIH) at the TU-Dresden, Germany.

Two connected neuronal networks $u2Net_{64}$ were implemented in series and the role of the second networks field of view on the transversal plane ($64 \times 64 \times 64$ voxel - $u2Net_{64}$) or ($128 \times 128 \times 32$ voxel - $u2Net_{128}$) was investigated on experimental data. The algorithm yielding highest performance on the experimental data was then used to perform training and evaluation on clinical data only ($u2Net_{Human}$).

Finally, we tested the usefulness of transfer learning. Specifically, a u2Net with the same architecture as $u2Net_{Human}$ was initially trained on the pig data set. The resulting network weights and biases were then kept constant on all layers except the final convolution and classification layers. These weights were re-trained on the human data set, with increased weight and bias learning rate factors to optimize the computational costs of training. The resulting network ($u2Net_{Trans}$) was then compared to $u2Net_{Human}$.

2.3. Data Sets

CT scans from two completed animal experimental studies and two clinical studies were used (**Supplementary Table 1**). One manual segmentation was available for each scan. Each manual segmentation had been performed and corrected by two experienced experts. These data were employed for the training and parametrization of the described neural network algorithms.

2.3.1. Experimental Data

68 scans from 11 animals were taken from previously completed experimental study (Güldner et al., 2014). This study investigated the effects of different degrees of spontaneous breathing during biphasic positive airway pressure (BIPAP) ventilation on neutrophilic inflammation in a double-hit ARDS model composed of repeated lung lavage with Horowitz ratio below 200 *mmHg* for 30 min. CT scans were acquired using Siemens Biograph 16 Hirez PET/CT (Siemens Knoxville, TN, USA) at a resolution of $0.4x0.4x1\ mm$. Scans were taken during end-expiratory occlusion at an airway pressure of 10 cmH_2O of 10*s*. The study protocol was approved by local animal care committee (Landesdirektion Dresden, Dresden, Germany). Further protocol details are described elsewhere (Güldner et al., 2014).

A further 112 scans from 7 animals were taken from an unpublished experimental study performed at the University Hospital Carl Gustav Carus, TU Dresden, Germany. The study was performed on non-injured pig lungs with negative end-expiratory airway pressure of as low as $-12\ cmH_2O$. The CT scans (Kernel: BF30f, Resolution: $0.59x0.59x3\ mm$) were acquired using SOMATOM Definition Edge (Siemens Healthineers, Erlangen, Germany) in supine position during end-expiratory and end-inspiratory hold of 10 s with a PEEP of 5 cmH_2O as well as negative externally applied abdominal pressure (NEAP) at the airway of 0, −5, −8, and $-12\ cmH_2O$. The Institutional Animal Care and Welfare Committee of the State of Saxony, Germany approved all animal procedures (DD24.1-5131/474/422).

A total of 180 static CT scans from pigs were thus used for training and 5-fold cross validation as described below.

2.3.2. Clinical Data

Patient CT scans were collected from previously published studies with available manual segmentations performed by expert radiologists. A total of 159 scans from healthy, COPD and ARDS patients from the University Hospital San Martino in Genoa, Italy, were included in the current study. One set of 112 scans were taken from a previous study assessing the influence of reconstruction kernels and slice thickness on the estimation of aeration compartments across pathological conditions (Ball et al., 2016) (KERNEL). A further set of 44 scans from 18 patients were taken from another previous study investigating the effects of PEEP levels (8 and 16 cmH_2O) on alveolar recruitment in mechanically ventilated COVID-19 patients (Ball et al., 2021) (PEEP). Change of relative mass of non- and poorly aerated compartments from $PEEP = 16\,cmH_2O$ to $PEEP = 8\,cmH_2O$ was used to quantify recruitable lung tissue in a sub-set of 12 COVID-19 patients.

Data acquisition protocols, patient demographic data, ethics committee approval and further details can be found online in the original publications (Ball et al., 2016, 2021).

2.4. Five-Fold Cross Validation

Due to the relative scarcity of segmented CT scans,rather than splitting our experimental data in fixed training and validation sets, we instead employed a 5-fold cross validation procedure. This means that each network was trained five times and for each iteration 80% of available scans were randomly selected for training and the respective remaining 20% were used for validation.

2.5. Evaluation of Segmentation Quality

Performance of the automatic segmentation was assessed in two categories:

1. Similarity was assessed by:
   - Jaccard Index (*JI*), the ratio of number of elements of the intersection and the number of elements of the union of two sets - thus quantifying similarity - defined by

$$JI = Jaccard(GT, PR) = \frac{|GT \cap PR|}{|GT \cup PR|} \tag{1}$$

     where ground truth (*GT*) and the prediction (*PR*) correspond to logical masks (true or false) specifying whether a voxel belongs to the lung ROI or not. In our case GT corresponds to the manual segmentation. Perfect overlap between GR and PR results in a Jaccard Index of 1, whereas no intersection would result in a Jaccard Index of 0.
   - The Jaccard index is related to the popular Sørensen–Dice coefficient according to

$$DICE = \frac{2 \cdot JI}{1 + JI}. \tag{2}$$

     In the current study we decided to use *JI* instead of *DICE* since the former allows for a more granular analysis, especially for values close to $JI = 1$ (**Supplementary Figure 1**).

2. Contour agreement was assessed by:
   - Boundary Function score (BF-score) was calculated as proposed by Csurka et al. (2013). Briefly, precision and recall per class *c* are defined as:

$$P^c = \frac{1}{|B_{PR}|} \sum_{z \in B^c_{PR}} \left[d(z, B^c_{GT}) < \theta \right] \tag{3}$$

     and

$$R^c = \frac{1}{|B_{GT}|} \sum_{z \in B^c_{GT}} \left[d(z, B^c_{PR}) < \theta \right] \tag{4}$$

     with boundary map of the ground truth B^c_{GT}, boundary map of the predicted segmentation B^c_{PR}, Euclidean distance *d*, and distance error tolerance θ (chosen to be 0.75% of the image diagonal). The BF-score for class *c* is then derived by

$$BF^c = \frac{2 \cdot P^c \cdot R^c}{R^c + P^c} \tag{5}$$

     where a perfect BF-score of 1 indicates that both segmentation boundaries are within the distance error tolerance θ of each other.
   - Average symmetric surface distance (*ASSD*) was calculated (Yeghiazaryan and Voiculescu, 2018) as:

$$ASSD(B_{PR}, B_{GT}) = \frac{1}{|B_{PR}| + |B_{GT}|} \times \left(\sum_{x \in B_{PR}} d_{min}(x, B_{GT}) + \sum_{y \in B_{GT}} d_{min}(y, B_{PR}) \right). \tag{6}$$

     A comparison of both measures *BF* and *ASSD* in an *in-silico* example may be found in the **Supplementary Figure 2**.

We anticipated that the segmentation quality of the proposed algorithm would depend on the degree of lung injury and, more specifically, on the size of non-aerated lung regions of the

TABLE 1 | Segmentation quality metrics for the networks $u2Net_{64}$ and $u2Net_{128}$ on the experimental data set.

	$u2Net_{64}$	$u2Net_{128}$	Sign.
DICE (arb. un.)	0.942 [0.93..0.95]	0.955 [0.95..0.96]	$P < 0.001$
JI (arb. un.)	0.891 [0.88..0.9]	0.913 [0.9..0.93]	$P < 0.001$
BF (arb. un.)	0.993 [0.97..1]	0.997 [0.98..1]	$P = 0.009$
ASSD (mm)	1.149 [1.01..1.78]	0.899 [0.79..1.25]	$P < 0.001$
S_{JI} (arb. un.)	−0.15 {−0.19.. − 0.12}	−0.2 {−0.23.. − 0.17}	
S_{BF} (arb. un.)	−0.049 {−0.09..0}	−0.082 {−0.13.. − 0.04}	

values as median [iqr] and slope {95% conf. int.} respectively; with Sørensen–Dice coefficient (DICE), Jaccard index (JI), BF-score (BF), and average symmetric surface distance (ASSD) and their respective slopes S_{JI} and S_{BF}; statistics according to Wilcoxon test.

respective scan. To quantify the robustness of the segmentation method, we took the slope S_{JI} between JI and the relative volume of non-aerated compartments, defined by voxel value $< -100\,HU$ (V_{nA} in *arb.un.*) of the respective manually segmented region of interest (ROI) of the lung. This slope was determined by fitting the following linear equation over all scans in the respective data set:

$$JI = S_{JI} \cdot V_{nA} + C \tag{7}$$

TABLE 2 | Relative volume of aeartion compartments and effective lung volume (*ELV*) as determined using the networks lung ROI predictions $u2Net_{64}$ and $u2Net_{128}$ on the experimental data set.

	Ref. mask	$u2Net_{64}$	***P* =**	$u2Net_{128}$	***P* =**
V_{nA} (%)	12.3 ± 8.5	15.9 ± 8.0	< 0.001	15.8 ± 8.0	< 0.001
V_{poor} (%)	25.6 ± 8.1	25.6 ± 7.2	0.971	25.7 ± 7.2	0.952
V_{norm} (%)	56.0 ± 16.6	51.5 ± 14.5	0.007	51.7 ± 14.5	0.009
V_{hype} (%)	3.5 ± 3.6	3.4 ± 3.5	0.879	3.4 ± 3.5	0.876
ELV (*ml*)	757 ± 259	768 ± 262	0.879	768 ± 262	0.876

values as mean ± sd; P-values indicate difference compared to reference mask from two sample T-test; with rel. volume of non-aerated (V_{nA}), poorly-aerated (V_{poor}), normally aerated (V_{norm}) and hyper-aerated (V_{hype}).

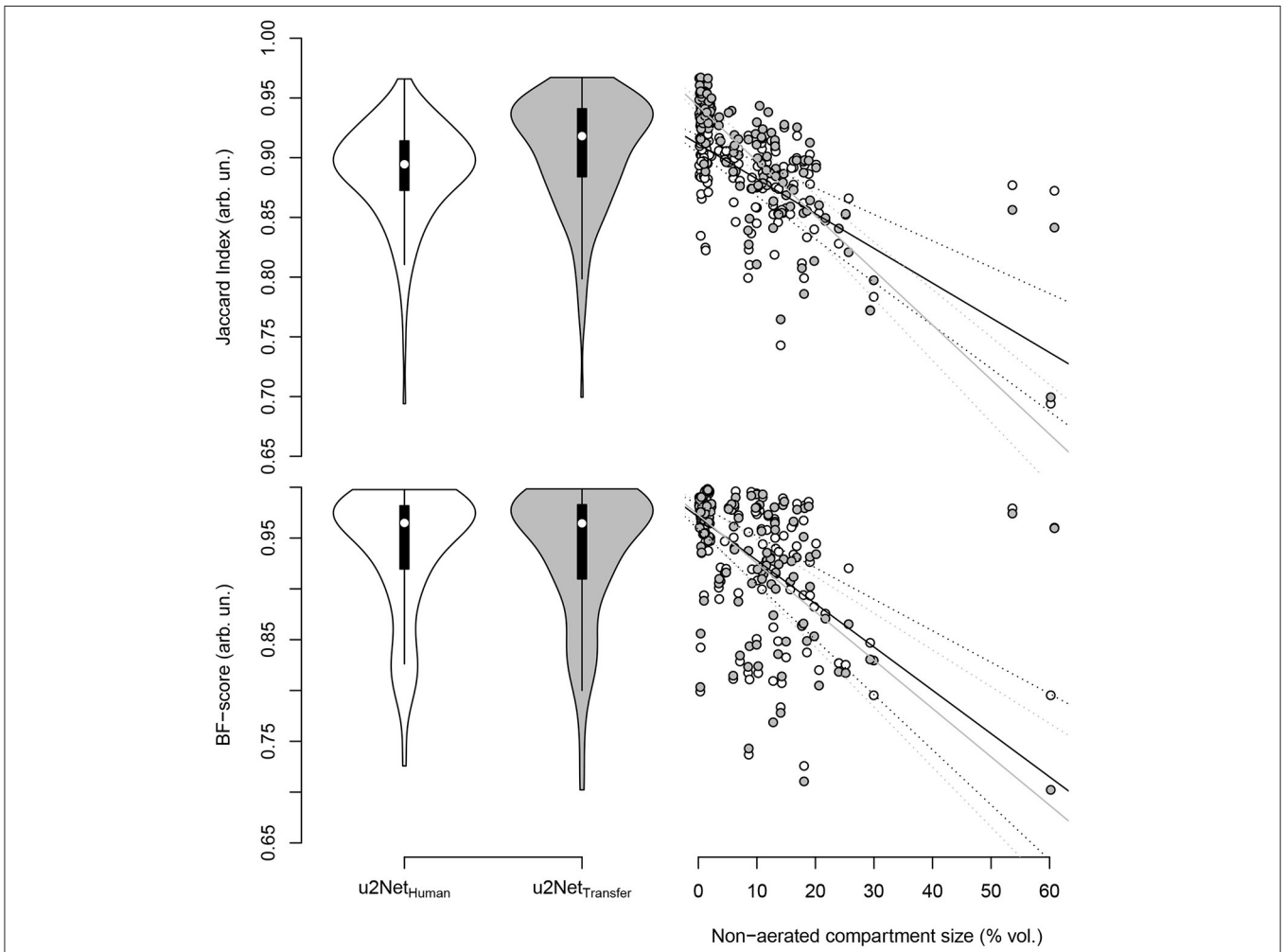

FIGURE 3 | Jaccard index **(top)** and BF-score **(bottom)** for networks trained from human data only ($u2Net_{Human}$, "white") and through transfer learning of networks trained on animal CT data ($u2Net_{Transfer}$, "grey.") In the right column the respective measure over relative size of the non-aerated compartment in % volume and its linear regressions with slopes S_{JI} and S_{BF}, as well as their respective confidence intervals.

TABLE 3 | Segmentation quality metrics for the two networks trained on human data only $u2Net_{Human}$ and on both experimental and clinical data sequentially $u2Net_{Transfer}$.

	$u2Net_{Human}$	$u2Net_{Transfer}$	Sign.
DICE (arb. un.)	0.937 [0.93..0.95]	0.957 [0.94..0.97]	$P < 0.001$
JI (arb. un.)	0.882 [0.86..0.91]	0.918 [0.88..0.94]	$P < 0.001$
BF (arb. un.)	0.965 [0.92..0.98]	0.964 [0.91..0.98]	$P = 0.917$
ASSD (mm)	1.678 [1.2..2.51]	1.493 [0.7..2.45]	$P = 0.003$
S_{DICE} (arb. un.)	−0.12 {−0.15.. − 0.08}	−0.19 {−0.22.. − 0.17}	
S_{JI} (arb. un.)	−0.2 {−0.26.. − 0.14}	−0.34 {−0.39.. − 0.29}	
S_{BF} (arb. un.)	−0.246 {−0.34.. − 0.16}	−0.303 {−0.39.. − 0.21}	
S_{ASSD} (mm)	4.011 {2.2..5.82}	6.257 {4.34..8.17}	

Values as median [iqr] and slope {95% conf. int.} respectively; Sørensen–Dice coefficient (DICE), with Jaccard index (JI), BF-score (BF) and F-score (BF), and average symmetric surface distance (ASSD) as well as their respective slopes S_{DICE}, S_{JI}, S_{BF}, and S_{ASSD}; statistics according to Wilcoxon test.

A robust segmentation algorithm should be independent of the degree of the non-aerated compartment size, thus resulting in a $S_{JI} = 0\,(arb.un.)$. Any negative/positive slope would instead indicate worse/better segmentation quality for non-aerated lung regions. The slopes S_{DICE}, S_{BF}, and S_{ASSD} were calculated the same way and have similar interpretation.

2.6. Aeration Compartment Size and Effective Lung Volume

The analysis of lung aeration compartments based on CT data is performed in Matlab (Mathworks Inc., Natwick, MA, USA). We employed commonly accepted thresholds dividing segmented lungs into four compartments using Hounsfield Unit (HU) value: Hyper-aerated $< -900, -900 <$ normally aerated < -500, $-500 <$ poorly aerated < -100, and non-aerated > -100. The relative size *%volume* of each compartment within the automatically segmented lung ROI was compared to the one determined by manual segmentation. The effective lung volume (ELV) was determined as the gas volume within the automatically segmented lung ROI and compared to ELV as determined using the manual segmentation.

2.7. Statistical Analysis

Statistical analyses were performed using non-parametric Wilcoxon test and slope differences assessed by confidence intervals. Agreement between relative aeration compartment sizes computed using automatic and manual segmentations was evaluated as proposed by Bland and Altman (1986). Statistical analyses were performed using the R statistical programming language (R Core Team, 2021). Statistical significance was accepted for $P < 0.05$.

3. RESULTS

3.1. Performance on Experimental Data Sets

The network designed with a wider transversal input $u2Net_{128}$ outperformed the network designed with a wider longitudinal view across all quality features (**Table 1**). Additionally, the two network architectures did not differ in terms of robustness relative to non-aerated lung volume: slopes S_{JI} and S_{BF} did not differ between $u2Net_{64}$ and $u2Net_{128}$.

Both *u2Net*s slightly over-estimated relative volume of non-aerated and under-estimated relative volume of normally aerated lung regions, while relative volumes of poorly and hyper-aerated as well as *ELV* did not differ significantly (**Table 2**).

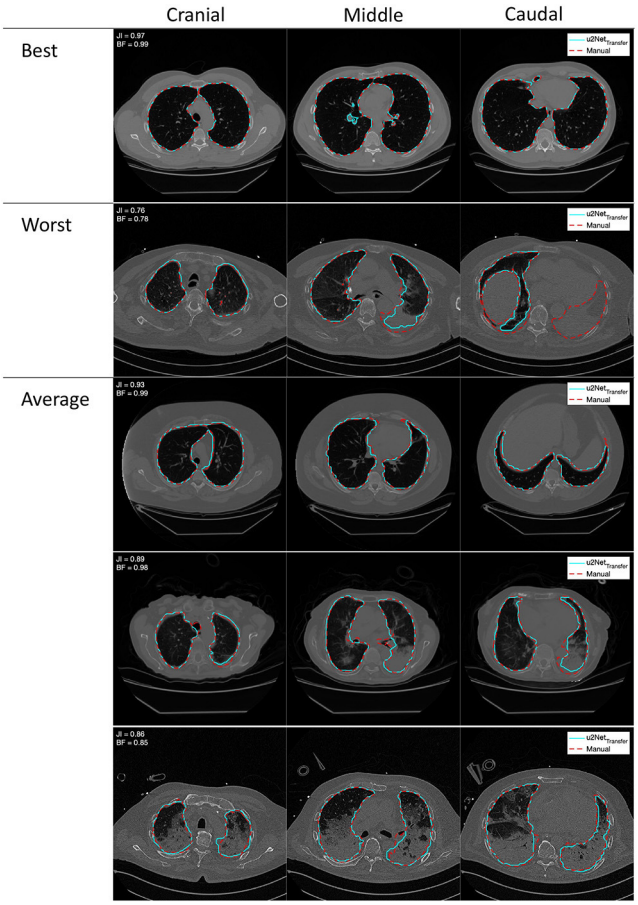

FIGURE 4 | Outlines of best, worst, and average segmentations generated from the double resolution architecture $u2Net_{Transfer}$ (cyan) compared to the manual segmentation (red), overlayed on the relative coronal CT slice. Images in each row come from a single scan progressing cranio-caudally from left to right.

3.2. Performance on Clinical Data

DICE and Jaccard index increased ($P < 0.001$, both), while *ASSD* decreased ($P = 0.003$) and BF-score did not differ ($P = 0.917$) for $u2Net_{Transfer}$ compared to $u2Net_{Human}$. Absolute slopes on similarity S_{DICE} and S_{JI} increased while slopes on contour agreement measures did not differ S_{BF} and S_{ASSD} (**Figure 3** and **Table 3**). Three slices in caudal to cranial sequence for representative scans of the $u2Net_{Transfer}$ segmentations are shown in **Figure 4**.

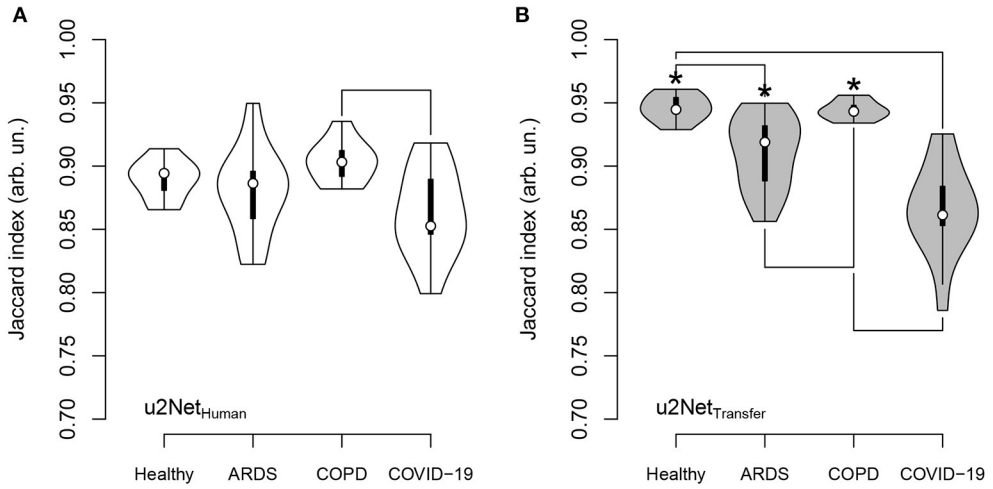

FIGURE 5 | Jaccard index for $u2Net_{Human}$ **(A)** and $u2Net_{Transfer}$ **(B)** and its dependence on clinical diagnosis; significance was tested using Kruskal-Wallis test followed by Nemenyi test; asterisk (*) indicates difference between networks; lines between diagnosis indicate difference between diagnosis; significance accepted at $P < 0.05$.

3.2.1. Dependence on Diagnosis

The Jaccard Index computed from the predictions of $u2Net_{Human}$ differed only between scans from COPD compared to COVID-19 patients ($P = 0.006$) in (**Figure 5**). Conversely the predictions of the network transfer learned $u2Net_{Transfer}$ showed a significantly higher JI for scans of healthy lungs and COPD patients compared to scans from ARDS ($P < 0.05$) and COVID-19 patients ($P < 0.05$). Additionally, Jaccard Index was higher for all diagnosis except COVID-19 in the $u2Net_{Transfer}$ vs. $u2Net_{Human}$ networks. The total volume of the lung ROI determined by $u2Net_{Transfer}$ differed from that determined through manual segmentation by $3.1 \pm 189.5\,ml$ (**Supplementary Figure 4**).

3.2.2. Aeration Compartments

The relative mass of hyper-aerated lung regions as determined by the $uNet2_{Transfer}$ segmentations had the smallest mean difference compared to that obtained through manual segmentation ($-0.09 \pm 0.66\,\%mass$, $LoA - 1.37 : 1.2$) followed by normally- ($-0.35 \pm 4.69\,\%mass$, $LoA - 9.55 : 8.84$), non- ($-0.77 \pm 3.98\,\%mass$, $LoA - 8.51 : 7.11$), and poorly-aerated compartments ($1.00 \pm 3.06\,\%mass$, $LoA - 4.99 : 6.99$), respectively (**Figure 6**). Independent of the compartment the Limits of agreement of the difference between both methods was well below 10%. For statistics on the relative volume of each aeration compartment refer to **Supplementary Figure 3**.

The relative mass of non- and poorly aerated compartments increased from $PEEP = 16\,cmH_2O$ to $PEEP = 8\,cmH_2O$. The value determined using the $u2Net_{Transfer}$ segmentation was highly correlated with the value obtained via manual segmentation (**Figure 7**) with limits of agreement below 2%.

3.2.3. Effective Lung Volume

The determination of effective lung volume using $u2Net_{Transfer}$ automated segmentation showed a difference with LV obtained through manual segmentations of $20.6 \pm 61.9\,ml$ (**Figure 8**). Additionally, total lung volume determination by automated and manual segmentations may be found in **Supplementary Figure 4**.

3.3. Computational Time

The proposed segmentation algorithm was tested on a commercially available personal computer equipped with an Intel i5 CPU and 8 *GB* of RAM. On this system, the algorithm could output low-resolution lung segmentation in under 20 s and a full resolution analysis in approximately 15 min.

4. DISCUSSION

The main findings of this investigation can be summarized as follows. We developed and evaluated a three-dimensional U-net based algorithm for time-efficient segmentation of the lung parenchyma. The algorithm, consisting of two deep networks concatenated in series, yielded satisfactory performance, sufficient for potential clinical applications using quantitative non-aerated compartment volumetry. Training the network using transfer learning across species improved the segmentation quality on the Human data sets in all patient groups except COVID-19. The sizes of the aeration compartments and the effective lung volume could be determined with limits of agreement of 5% with manual segmentation. The analyses assessing the dependence of the Jaccard index and the BF-score on the relative non-aerated lung volume (S_{JI} and S_{BF}, respectively) revealed that our proposed algorithm is able to perform robust segmentation of the diseased lungs.

The sub-analysis of lung recruitability shown in **Figure 7** from a subset of patients with available manual segmentations at $PEEP = 8\,cmH_2O$ and $PEEP = 16\,cmH_2O$ shows a strong correlation between the two methods ($R^2 = 0.975$). This, combined with the near-perfect correlation in determining ELV ($R^2 = 0.999$) shown in **Figure 8** and the Bland-Altman analysis

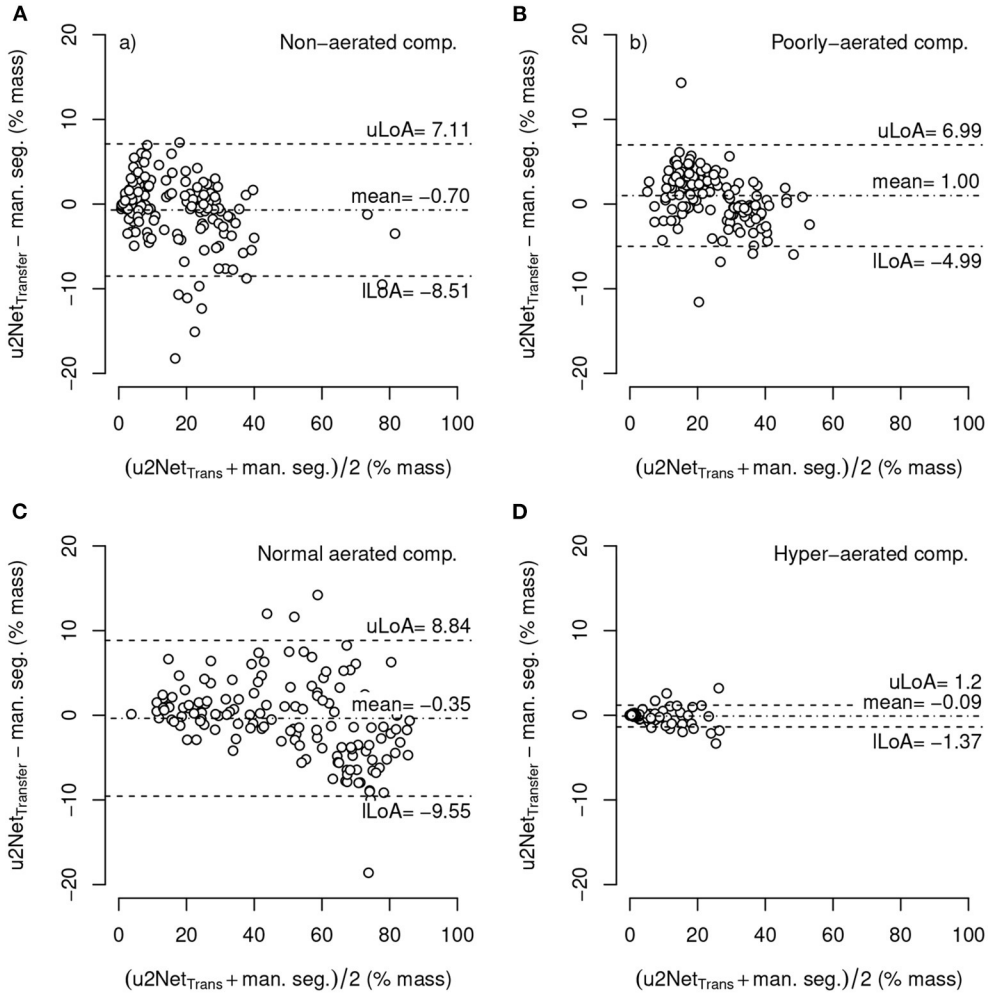

FIGURE 6 | Bland-Altman-plot of relative mass non-aerated **(A)**, poorly-aerated **(B)**, normally-aerated **(C)** and hyper-aerated **(D)** compartments using mask segmented by *u2Net*$_{Transfer}$ compared to manual segmentations; with upper and lower limits of agreement (mean ±1.96·standard deviation) *uLoA* and *lLoA*, respectively.

of aeration compartments shown in **Figure 6**, suggests that our proposed approach is sufficient for the task of monitoring modifications of poor and non-aerated lung tissue.

The results presented here demonstrate that AI-based analysis of CT scans yield fast and efficient evaluations of lung aeration compartments. Such algorithms should therefore be tested more widely, especially given the potential benefits of the derived parameters to the management of ventilatory strategies in ARDS. The varying performance of the algorithms in different pathological conditions reflects the anatomical alteration of the healthy lung, an intrinsic property of lung pathologies. In COPD, emphysema will enhance HU difference between parenchyma and surrounding structures, while in ARDS (and especially COVID-19) consolidated lung regions have intrinsically difficult boundaries to identify on CT scans, even for human experts. Upon visual examination of the worst scan as shown in **Figure 4** our algorithm is able to identify even the completely collapsed parenchyma, albeit with some uncertainty. This highlights the need, in developing data-driven approaches, for databases that span all required pathological conditions. The degree of detail that can be expected also suggests that this approach is suited for gross delineation of lung volumes and further research is needed to develop a system capable of finer distinction of blood vessels and airways.

One of the strengths of this technique is that it is operator-independent and highly reproducible. More importantly, if coupled with a simple threshold-based algorithm for identifying lung aeration compartments, this method can be used to quantify the degree of atelectasis or hyper-distension of lung parenchyma. The aforementioned qualities of AI-based analysis also reduce the cost of analyzing repeated CT scans, making it possible to follow the trend of pathological modifications over time and evaluate the effectiveness of interventions for both research and clinical purposes.

Quantitative analysis of aeration compartments could thus be implemented in decision making algorithms and contribute

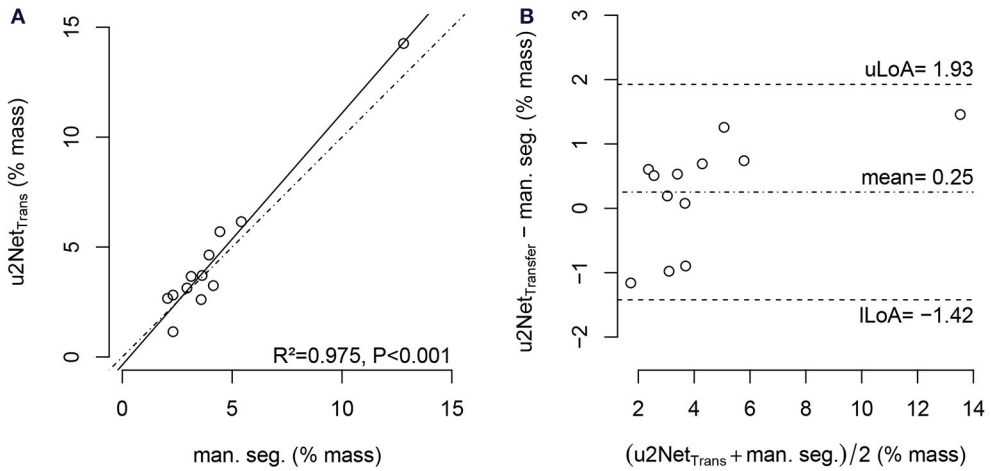

FIGURE 7 | Regression plot **(A)** and Bland-Altman-analysis **(B)** of relative non-aerated and poorly aerated lung mass from $PEEP = 16cmH_2O$ to $PEEP = 8cmH_2O$ in COVID-19 scans using manual segmentation and automatic segmentation from $u2Net_{Transfer}$; with upper and lower limit of agreement (mean ±1.96· standard deviation) *uLoA* and *lLoA*, respectively.

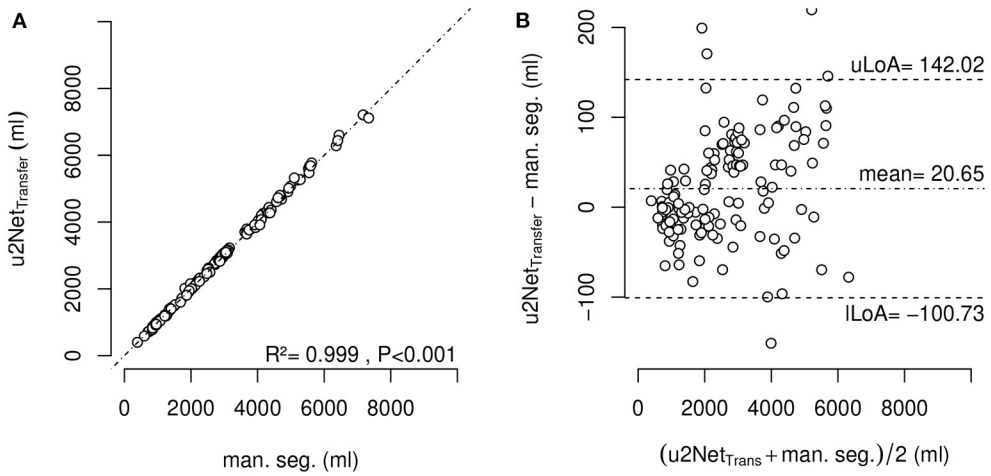

FIGURE 8 | Effective lung volume (ELV) measured using segmentation by $u2Net_{Transfer}$ over ELV measured using manual segmentation **(A)** and corresponding Bland-Altman-Analysis **(B)**; with upper and lower limit of agreement (mean ±1.96·standard deviation) *uLoA* and *lLoA*, respectively.

to the standardization of treatment across different settings and intensive-care units. The efficiency and accuracy of this method are appropriate for analysis of large data sets for research on lung disease that have until now been difficult to access.

This method may have potential clinical applications. While currently tidal volume is usually titrated to predicted body-weight, this method allows easy access to an estimation of lung tissue available for ventilation and can contribute to further development of lung protective strategies. Moreover, if coupled with dual-PEEP CT scans, it allows for an estimation of recruitability of the lung and can aid the clinician in the decision for recruitment maneuvers and PEEP setting. Finally, the quantification of non-aerated lung parenchyma could also be used to stratify severity and inform prognosis in ARDS.

The proposed transfer learned algorithm showed a lower performance compared to SegNet based LungSeg algorithm ($DICE = 0.96$ compared to $DICE = 0.98$) (Gerard et al., 2021) which may be explained by the lower number of available scans, the more heterogeneous diagnosis, and larger non-aerated relative lung regions in the data set.

Performance of the algorithm presented here was similar to the 3D uNet-based approaches trained on COVID-19 scans only with $DICE = 0.96$ (Müller et al., 2020). Although the latter had a better performance compared to the results on COVID-19 scans presented here ($DICE = 0.93$), it may be anticipated that the algorithm presented here may perform better on non-COVID ICU thorax CTs. Compared to 2D-uNet algorithms, our results indicate a slightly better performance on lung healthy patients ($DICE =$

0.95 vs. $DICE = 0.97$) (Ait Skourt et al., 2018) and outperformed results on COVID-19 patients (Zhou et al., 2021) ($DICE = 0.83$).

In evaluating the performance of lung segmentation algorithms in ARDS, we advocate for the use of a metric that takes into account the degree of non-aerated lung parenchyma present in the training and validation data sets. To this end, we propose a straight-forward slope index based on Jaccard and BF metrics. Low slopes in the experimental data set, compared to the human data set, suggest higher robustness toward non-aerated lung regions in the experimental data set, that might be explained by a more homogeneous nature of the surfactant depleted models. In the human data set both slope measures showed higher absolute value potentially due to the origin of non-aerated lung regions being more diverse and thus more heterogeneously distributed. This idea is supported by the fact that the transfer trained network indeed showed an increased Jaccard slope, compared to the network only trained on clinical data. A similar performance criterion had been implemented by Gerard et al. (2021) using the slope of DICE and ASSD with respect to relative volume of non-aerated lung compartments. Recalculation of the S_{DICE} in arb. un. to DICE slope in $\%^{-1}$ yielded a value of $-0.0012\,\%^{-1}$ for the human only trained algorithm and $-0.0019\,\%^{-1}$ for the transfer trained algorithm, both values being lower than the lowest value $0.003\,\%^{-1}$ reported by Gerard et al. (2021). Our algorithm trained on human data sets only showed lower ASSD slope with $0.04\,mm\%^{-1}$ compared to the one by Gerard et al. (2021) ($0.07\,mm\%^{-1}$), while the transfer learned algorithm showed similar values $0.06\,mm\%^{-1}$.

This study has several limitations. Firstly, the training and evaluation were performed on scans from a relatively low number of distinct animals/patients using five-fold cross validation. While our results are in keeping with others previously published, it is likely that training our proposed system on larger data sets would yield better results. Secondly, animal data were taken only from experimental models of reversible atelectasis, not resembling heterogeneity and underlying cause of clinical ARDS. Thirdly, scans from different computed tomographic scanners, with different resolutions and kernels, were used for the applied lung volumetry. While this implies reduced comparability between the respective scans (Mascalchi et al., 2017), it may also be regarded as an advantage since the networks experienced a higher diversity during training and may therefore show higher performance during clinically diverse CT scan modalities (Hofmanninger et al., 2020). Fourthly, the data used for this investigations did only contain one manual segmentation for each CT scan. A comparison of the algorithm to inter-human manual segmentations could therefor not be performed. Finally, the deep learning convolutional neural network based approach consisting of two sequential networks had been proposed before (Gerard et al., 2021). The present manuscript describes a re-implementation in Matlab Deep Learning Toolbox trained and bench-marked on a limited data set focused on pathological lung segmentation in moderate ARDS where transferability between species was accounted for.

5. CONCLUSION

Automatic uNet based 3*D* lung segmentation showed good quality and thereby allowed reliable estimation of lung volumes, aeration compartment sizes, and lung recruitability in both animals and patients with different lung conditions.

DATA AVAILABILITY STATEMENT

The original contributions presented in the study are included in the article/**Supplementary Material**, further inquiries can be directed to the corresponding author.

ETHICS STATEMENT

The studies involving human participants were reviewed and approved by Comitato Etico Regione Liguria, Italy. The need for written informed consent was waived for retrospectively collected data. According to local regulations, consent was delayed after discharge for prospectively collected data in unconscious patients. The animal study was reviewed and approved by Institutional Animal Care and Welfare Committee of the State of Saxony, Germany.

AUTHOR CONTRIBUTIONS

LM and RH designed and developed the algorithm and performed the training and evaluation of the algorithm. MM, FI, R-TH, and LB performed the manual segmentation of the clinical data set. LM, LB, NS, PP, MG, and RH designed the investigation and analysis protocol. All authors drafted, corrected, and revised the original manuscript.

FUNDING

This work was made possible by institutional funds and in part by German Research Foundation (grant no. GA 1256/8-1).

ACKNOWLEDGMENTS

The authors are grateful to the Centre for Information Services and High Performance Computing [Zentrum für Informationsdienste und Hochleistungsrechnen (ZIH)] TU Dresden for providing its facilities for high throughput calculations.

SUPPLEMENTARY MATERIAL

The Supplementary Material for this article can be found online at: https://www.frontiersin.org/articles/10.3389/fphys.2021.725865/full#supplementary-material

REFERENCES

Acute Respiratory Distress Syndrome Network; Brower, R.G., Matthay, M. A., Morris, A., Schoenfeld, D., Thompson, B T., and Wheeler, A. (2009). Ventilation with lower tidal volumes as compared with traditional tidal volumes for acute lung injury and the acute respiratory distress syndrome. *Nat. Engl. J. Med.* 342, 1301–1308. doi: 10.1056/NEJM200005043421801

Ait Skourt, B., El Hassani, A., and Majda, A. (2018). Lung CT image segmentation using deep neural networks. *Procedia Comput. Sci.* 127, 109–113. doi: 10.1016/j.procs.2018.01.104

Amato, M. B. P., Barbas, C. S. V., Medeiros, D. M., Magaldi, R. B., Schettino, G. P., Lorenzi-Filho, G., et al. (2009). Effect of a protective-ventilation strategy on mortality in the acute respiratory distress syndrome. *New England J. Med.* 338, 347–354. doi: 10.1056/NEJM199802053380602

Anzueto, A., Frutos–Vivar, F., Esteban, A., Alía, I., Brochard, L., Stewart, T., et al. (2004). Incidence, risk factors and outcome of barotrauma in mechanically ventilated patients. *Intensive Care Med.* 30, 612–619. doi: 10.1007/s00134-004-2187-7

Badrinarayanan, V., Kendall, A., and Cipolla, R. (2017). SegNet: a deep convolutional encoder-decoder architecture for image segmentation. *IEEE Trans. Pattern Anal. Mach. Intell.* 39, 2481–2495. doi: 10.1109/TPAMI.2016.2644615

Ball, L., Brusasco, C., Corradi, F., Paparo, F., Garlaschi, A., Herrmann, P., Quintel, M., and Pelosi, P. (2016). Lung hyperaeration assessment by computed tomography: correction of reconstruction-induced bias. *BMC Anesthesiol* 16, 67. doi: 10.1186/s12871-016-0232-z

Ball, L., Robba, C., Maiello, L., Herrmann, J., Gerard, S. E., Xin, Y., et al., (2021). Computed tomography assessment of PEEP-induced alveolar recruitment in patients with severe COVID-19 pneumonia. *Crit. Care* 25, 81. doi: 10.1186/s13054-021-03477-z

Ball, L., Vercesi, V., Costantino, F., Chandrapatham, K., and Pelosi, P. (2017). Lung imaging: how to get better look inside the lung. *Ann. Transl. Med.* 5, 294. doi: 10.21037/atm.2017.07.20

Battaglini, D., Sottano, M., Ball, L., Robba, C., Rocco, P. R., and Pelosi, P. (2021). Ten golden rules for individualized mechanical ventilation in acute respiratory distress syndrome. *J. Intensive Med.* 1, 42–51. doi: 10.1016/j.jointm.2021.01.003

Bland, J. M., and Altman, D. G. (1986). Statistical methods for assessing agreement between two methods of clinical measurement. *Lancet* 1, 307–310. doi: 10.1016/S0140-6736(86)90837-8

Calfee, C. S., Delucchi, K., Parsons, P. E., Thompson, B. T., Ware, L. B., and Matthay, M. A. (2014). Subphenotypes in acute respiratory distress syndrome: latent class analysis of data from two randomised controlled trials. *Lancet Respiratory Med.* 2, 611–620. doi: 10.1016/S2213-2600(14)70097-9

Cereda, M., Xin, Y., Goffi, A., Herrmann, J., Kaczka, D. W., Kavanagh, B. P., et al. (2019). Imaging the injured lung: mechanisms of action and clinical use. *Anesthesiology* 131, 716–749. doi: 10.1097/ALN.0000000000002583

Çiçek, Ö., Abdulkadir, A., Lienkamp, S. S., Brox, T., and Ronneberger, O. (2016). 3D U-net: learning dense volumetric segmentation from sparse annotation. *ArXiv160606650 Cs*.

Coppola, S., Froio, S., and Chiumello, D. (2018). Higher vs. lower PEEP in ARDS: just one part of the whole. *J. Thorac. Disc.* 10, 56–59. doi: 10.21037/jtd.2017.12.46

Csurka, G., Larlus, D., and Perronnin, F. (2013). "What is a good evaluation measure for semantic segmentation?," in *Proceedings of the British Machine Vision Conference* 32.1–32.11 (Bristol).

Cuevas, L. M., Spieth, P. M., Carvalho, A. R., Gama de Abreu, M., and Koch, E. (2009). "Automatic lung segmentation of helical-CT scans in experimental induced lung injury," in *4th European Conference of the International Federation for Medical and Biological Engineering, IFMBE Proceedings*, eds J. Vander Sloten, P. Verdonck, M. Nyssen, and J. Haueisen (Berlin: Springer), 764–767.

Curley, G. F., Laffey, J. G., Zhang, H., and Slutsky, A. S. (2016). Biotrauma and ventilator-induced lung injury: clinical implications. *Chest* 150, 1109–1117. doi: 10.1016/j.chest.2016.07.019

Ferguson, N. D., Fan, E., Camporota, L., Antonelli, M., Anzueto, A., Beale, R., et al. (2012). The Berlin definition of ARDS: an expanded rationale, justification, and supplementary material. *Intensive Care Med.* 38, 1573–1582. doi: 10.1007/s00134-012-2682-1

Gerard, S. E., Herrmann, J., Kaczka, D. W., Musch, G., Fernandez-Bustamante, A., and Reinhardt, J. M. (2020). Multi-resolution convolutional neural networks for fully automated segmentation of acutely injured lungs in multiple species. *Med. Image Anal.* 60, 101592. doi: 10.1016/j.media.2019.101592

Gerard, S. E., Herrmann, J., Xin, Y., Martin, K. T., Rezoagli, E., Ippolito, D., et al. (2021). CT image segmentation for inflamed and fibrotic lungs using a multi-resolution convolutional neural network. *Sci. Rep.* 11, 1455. doi: 10.1038/s41598-020-80936-4

Güldner, A., Braune, A., Ball, L., Silva, P. L., Samary, C., Insorsi, A., et al. (2016). Comparative effects of volutrauma and atelectrauma on lung inflammation in experimental acute respiratory distress syndrome. *Crit. Care Med.* 44, e854–e865. doi: 10.1097/CCM.0000000000001721

Güldner, A., Braune, A., Carvalho, N., Beda, A., Zeidler, S., Wiedemann, B., Wunderlich, G., Andreeff, M., Uhlig, C., Spieth, P. M., Koch, T., Pelosi, P., Kotzerke, J., and Gama de Abreu, M. (2014). Higher levels of spontaneous breathing induce lung recruitment and reduce global stress/strain in experimental lung injury. *Anesthesiology* 120, 673–682. doi: 10.1097/ALN.0000000000000124

He, K., Zhang, X., Ren, S., and Sun, J. (2015). "Delving deep into rectifiers: surpassing human-level performance on ImageNet classification," in *2015 IEEE International Conference on Computer Vision (ICCV)* (Santiago), 1026–1034.

Hodgson, C. L., Cooper, D. J., Arabi, Y., King, V., Bersten, A., Bihari, S., et al. (2019). Maximal recruitment open lung ventilation in acute respiratory distress syndrome (PHARLAP). a phase II, multicenter randomized controlled clinical trial. *Amer. J. Respir. Crit. Care Med.* 200, 1363–1372. doi: 10.1164/rccm.201901-0109OC

Hofmanninger, J., Prayer, F., Pan, J., Röhrich, S., Prosch, H., and Langs, G. (2020). Automatic lung segmentation in routine imaging is primarily a data diversity problem, not a methodology problem. *Eur. Radiol. Exp.* 4, 50. doi: 10.1186/s41747-020-00173-2

Hu, S., Hoffman, E., and Reinhardt, J. (2001). Automatic lung segmentation for accurate quantitation of volumetric X-ray CT images. *IEEE Trans. Med. Imag.* 20, 490–498. doi: 10.1109/42.929615

Karmrodt, J., Bletz, C., Yuan, S., David, M., Heussel, C. P., and Markstaller, K. (2006). Quantification of atelectatic lung volumes in two different porcine models of ARDS†. *Brit. J. Anaesthesia* 97, 883–895. doi: 10.1093/bja/ael275

Mansoor, A., Bagci, U., Xu, Z., Foster, B., Olivier, K. N., Elinoff, J. M., et al. (2014). A generic approach to pathological lung segmentation. *IEEE Trans. Med. Imag.* 33, 2293–2310. doi: 10.1109/TMI.2014.2337057

Mascalchi, M., Camiciottoli, G., and Diciotti, S. (2017). Lung densitometry: why, how and when. *J. Thorac. Dis.* 9, 3319–3345. doi: 10.21037/jtd.2017.08.17

Müller, D., Rey, I. S., and Kramer, F. (2020). Automated chest CT image segmentation of COVID-19 lung infection based on 3D U-Net. *ArXiv200704774 Cs Eess*.

Noshadi, A., Kircher, M., Pollnow, S., Elke, G., Frerichs, I., and Dössel, O. (2017). Automatic lung segmentation in the presence of alveolar collapse. *Curr. Direct. Biomed. Eng.* 3, 807–810. doi: 10.1515/cdbme-2017-0188

Pelosi, P., Rocco, P. R., and de Abreu, M. G. (2011). Use of computed tomography scanning to guide lung recruitment and adjust positive-end expiratory pressure. *Curr. Opin. Crit. Care* 17, 268–274. doi: 10.1097/MCC.0b013e32834 4ddbc

Pelosi, P., Rocco, P. R. M., and de Abreu, M. G. (2018). Close down the lungs and keep them resting to minimize ventilator-induced lung injury. *Crit Care* 22, 1–8. doi: 10.1186/s13054-018-1991-3

R Core Team, T. (2021). *R: A Language and Environment for Statistical Computing*. (Vienna: R Foundation for Statistical Computing).

Robba, C., Battaglini, D., Ball, L., Patroniti, N., Loconte, M., Brunetti, I., et al. (2020). Distinct phenotypes require distinct respiratory management strategies in severe COVID-19. *Respirat. Physiol. Neurobiol.* 279: 103455. doi: 10.1016/j.resp.2020.103455

Ronneberger, O., Fischer, P., and Brox, T. (2015). "U-Net: convolutional networks for biomedical image segmentation," in *Medical Image Computing and Computer-Assisted Intervention – MICCAI 2015, Lecture Notes in Computer Science*, eds N. Navab, J. Hornegger, W. M. Wells, and A. F. Frangi, (Cham: Springer International Publishing), 234–241.

Shelhamer, E., Long, J., and Darrell, T. (2017). Fully convolutional networks for semantic segmentation. *IEEE Trans. Pattern Anal. Mach. Intell.* 39, 640–651. doi: 10.1109/CVPR.2015.7298965

Slutsky, A. S. (1999). Lung injury caused by mechanical ventilation. *Chest* 116, 9S–15S. doi: 10.1378/chest.116.suppl_1.9s-a

Slutsky, A. S., and Ranieri, V. M. (2013). Ventilator-induced lung injury. *Nat. Engl. J. Med.* 369, 2126–2136. doi: 10.1056/NEJMra1208707

Sudre, C. H., Li, W., Vercauteren, T., Ourselin, S., and Cardoso, M. J. (2017). Generalised Dice overlap as a deep learning loss function for highly unbalanced segmentations. *ArXiv170703237 Cs*, 10553:240–248.

The ARDS Definition Task Force* (2012). Acute Respiratory Distress Syndrome: the Berlin Definition. *JAMA*. 307, 2526–2533. doi: 10.1001/jama.2012.5669

Tsuchida, S., Engelberts, D., Peltekova, V., Hopkins, N., Frndova, H., Babyn, P., et al. (2012). Atelectasis causes alveolar injury in nonatelectatic lung regions. *Amer. J. Respir. Crit. Care Med.* 174, 279–289. doi: 10.1164/rccm.200506-1006OC

Yeghiazaryan, V., and Voiculescu, I. (2018). Family of boundary overlap metrics for the evaluation of medical image segmentation. *J. Med. Imag. (Bellingham).* 5:015006. doi: 10.1117/1.JMI.5.1.015006

Zhou, T., Canu, S., and Ruan, S. (2021). Automatic COVID-19 CT segmentation using U-Net integrated spatial and channel attention mechanism. *Int. J. Imag. Syst. Technol.* 31, 16–27. doi: 10.1002/ima.22527

Conflict of Interest: The authors declare that the research was conducted in the absence of any commercial or financial relationships that could be construed as a potential conflict of interest.

Advantages of publishing in Frontiers

OPEN ACCESS
Articles are free to read for greatest visibility and readership

FAST PUBLICATION
Around 90 days from submission to decision

HIGH QUALITY PEER-REVIEW
Rigorous, collaborative, and constructive peer-review

TRANSPARENT PEER-REVIEW
Editors and reviewers acknowledged by name on published articles

Frontiers
Avenue du Tribunal-Fédéral 34
1005 Lausanne | Switzerland

Visit us: www.frontiersin.org
Contact us: frontiersin.org/about/contact

REPRODUCIBILITY OF RESEARCH
Support open data and methods to enhance research reproducibility

DIGITAL PUBLISHING
Articles designed for optimal readership across devices

FOLLOW US
@frontiersin

IMPACT METRICS
Advanced article metrics track visibility across digital media

EXTENSIVE PROMOTION
Marketing and promotion of impactful research

LOOP RESEARCH NETWORK
Our network increases your article's readership